Mathematics of Planet Earth 9

Henk Schuttelaars
Arnold Heemink
Eric Deleersnijder *Editors*

The Mathematics of Marine Modelling

Water, Solute and Particle Dynamics in Estuaries and Shallow Seas

MPE

Springer

Mathematics of Planet Earth

Volume 9

This series provides a variety of well-written books of a variety of levels and styles, highlighting the fundamental role played by mathematics in a huge range of planetary contexts on a global scale. Climate, ecology, sustainability, public health, diseases and epidemics, management of resources and risk analysis are important elements. The mathematical sciences play a key role in these and many other processes relevant to Planet Earth, both as a fundamental discipline and as a key component of cross-disciplinary research. This creates the need, both in education and research, for books that are introductory to and abreast of these developments.

Springer's MoPE series will provide a variety of such books, including monographs, textbooks, contributed volumes and briefs suitable for users of mathematics, mathematicians doing research in related applications, and students interested in how mathematics interacts with the world around us. The series welcomes submissions on any topic of current relevance to the international Mathematics of Planet Earth effort, and particularly encourages surveys, tutorials and shorter communications in a lively tutorial style, offering a clear exposition of broad appeal.

Henk Schuttelaars · Arnold Heemink ·
Eric Deleersnijder
Editors

The Mathematics of Marine Modelling

Water, Solute and Particle Dynamics in Estuaries and Shallow Seas

Springer

Editors
Henk Schuttelaars
Department of Applied Mathematics
Delft University of Technology
Delft, The Netherlands

Arnold Heemink
Department of Applied Mathematics
Delft University of Technology
Delft, The Netherlands

Eric Deleersnijder
Institute of Mechanics, Materials and Civil Engineering (IMMC) and Earth and Life Institute (ELI)
Université Catholique de Louvain
Louvain-la-Neuve, Belgium

ISSN 2524-4264 ISSN 2524-4272 (electronic)
Mathematics of Planet Earth
ISBN 978-3-031-09558-0 ISBN 978-3-031-09559-7 (eBook)
https://doi.org/10.1007/978-3-031-09559-7

This Springer imprint is published by the registered company Springer Nature Switzerland AG
The registered company address is: Gewerbestrasse 11, 6330 Cham, Switzerland

Preface

Coastal regions are strongly impacted by human interventions and climate change. Sea level rise and increased storminess threaten coastal safety; changes in intensity and duration of rainfall strongly impact intrusion of salt which may endanger the availability of fresh water. Examples of human interventions are the measures to mitigate these adverse climate effects, but also interventions are driven by, for example, economic (e.g., deepening of shipping channels, sand mining) and environmental (e.g., construction of large-scale wind parks) reasons. Unfortunately, such interventions may have unintended negative impacts due to the many conflicting interests in these regions: for example, channel deepening may be an excellent choice from an economic point of view, but it may result in a deterioration of the coastal safety and ecological values of the system under consideration. To oversee the multi-faceted impact of interventions and climate change, the dynamics of coastal seas, estuaries, and tidal inlets have to be well-understood. Only with such understanding, coastal managers can make well-balanced decisions that take all aspects into account. Mathematical modeling of marine systems becomes increasingly important to provide the insights necessary for decision making.

Over the past few decades, the mathematical modeling cycle has become instrumental in understanding the dynamics of coastal seas, estuaries, and tidal inlet systems. In this cycle, new mathematical models are developed or existing models are improved upon, advanced solution techniques are developed and employed to solve these highly complex nonlinear models, and the model outcomes are analyzed using state-of-the-art mathematical techniques and, if possible, compared to field and laboratory observations.

In this contribution, we focus on mathematical techniques available to study various topics from marine sciences in estuaries and coastal seas. Since only a limited number of topics can be treated, we restrict ourselves to the discussion of mathematical models on water motion and transport of pollutants and sediments by the water motion. In the first chapter, the basic mathematical concepts to obtain the governing equations are summarized and the final system of equations to model the water motion in coastal regions is given. In the next chapters, specific aspects of water motion are discussed: water waves in isotropic and anisotropic media, (near-shore)

waves, and barotropic tides. This is followed by a detailed review of 2D-turbulence modeling and parameterization of turbulent dispersion. In the final chapters, river plumes, mathematical techniques to model transport phenomena, morphodynamic modeling of the bathymetry and geometry, and accurately model drying and flooding are discussed.

The prerequisite mathematical knowledge varies, but most of the material should be accessible to advanced graduate students and early-stage researchers. In most chapters, there is a clear link with observations and practical challenges, allowing professionals outside academia and decision-makers to get a good insight into the various techniques underpinning the models often used and other methodologies that can be employed to tackle their real-world problems. In each chapter, there is an extensive list of references, ranging from general to highly specialized, allowing the interested reader to further explore these topics independently.

Delft, The Netherlands
February, 2022

Eric Deleersnijder
Arnold Heemink
Henk Schuttelaars

Contents

Contributors

Bokhove Onno School of Mathematics, University of Leeds, LS2 9JT, Leeds, UK

Clercx Herman J. H. Fluid Dynamics Laboratory, Department of Applied Physics, Eindhoven University of Technology, Eindhoven, MB, The Netherlands

Cushman-Roisin Benoit Thayer School of Engineering, Dartmouth College, Hanover, New Hampshire, USA

Dawson Clint Oden Institute for Computational Engineering and Sciences, The University of Texas at Austin, Austin, TX, USA

Deleersnijder Eric Université Catholique de Louvain, Ottignies-Louvain-la-Neuve, Belgium

de Swart Huib E. Institute for Marine and Atmospheric research, Department of Physics, Utrecht University, Utrecht, The Netherlands

Fringer Oliver Stanford University, Stanford, CA, USA

Gräwe Ulf Leibniz Institute for Baltic Sea Research Warnemünde (IOW), Rostock, Germany

Heemink Arnold Delft University of Technology, Delft, Netherlands

Hetland Robert D. Department of Oceanography, Texas A &M University, College Station, College Station, TX, USA

Kärnä Tuomas Finnish Meteorological Institute, Helsinki, Finland

Klingbeil Knut Leibniz Institute for Baltic Sea Research Warnemünde (IOW), Rostock, Germany

Lambrechts Jonathan Institute of Mechanics, Materials and Civil Engineering, Université catholique de Louvain, Louvain-la-Neuve, Belgium

Maas Leo R. M. Institute for Marine and Atmospheric Research (IMAU), Utrecht University, Utrecht, Netherlands

Ortleb Sigrun Department of Mathematics, University of Kassel, Kassel, Germany

Roos Pieter C. Water Engineering & Management, University of Twente, Enschede, The Netherlands

Samii Ali Department of Aerospace Engineering and Engineering Mechanics, The University of Texas at Austin, Austin, TX, USA

Schuttelaars H. M. Delft Institute of Applied Mathematics, Delft University of Technology, Delft, The Netherlands

Shah Syed Hyder Ali Muttaqi Sukkur Institute of Business Administration University, Sukkur, Pakistan

Umlauf Lars Leibniz Institute for Baltic Sea Research Warnemünde (IOW), Rostock, Germany

Zitman T. J. Department of Hydraulic Engineering, Delft University of Technology, Delft, The Netherlands

Chapter 1
Basic Equations of Marine Flows

Knut Klingbeil, Eric Deleersnijder, Oliver Fringer, and Lars Umlauf

Abstract The modeling of ocean basins, coastal seas, estuaries, and lagoons requires an adequate mathematical description of the state of the fluid in these systems. The state can be characterised by a set of macroscopic variables including density, velocity, temperature, concentrations of salt and other dissolved substances. The evolution of these state variables is governed by partial differential equations derived from physical laws. In this chapter the basic mathematical concepts for formulating the governing equations are summarized and the final set of governing equations is given.

1.1 Mathematical Description of Fluids

1.1.1 Fluids as Continuous Media

A fluid consists of an extremely large number of ions and molecules. However, it is usually not the microscopic information about all molecules (e.g. position, velocity, interaction), but a finite number of macroscopically averaged quantities that is of interest for the description of a fluid and its motion. Important macroscopic state variables are density ρ, velocity $\mathbf{v} = (u, v, w)$, temperature Θ, concentrations of salt S and suspended sediment c. As long as the mean free path of water molecules is smaller than the smallest scales over which gradients in the fluid occur, the fluid can be

K. Klingbeil (✉) · L. Umlauf
Leibniz Institute for Baltic Sea Research Warnemünde (IOW), Rostock, Germany
e-mail: knut.klingbeil@io-warnemuende.de

L. Umlauf
e-mail: lars.umlauf@io-warnemuende.de

E. Deleersnijder
Université Catholique de Louvain, Ottignies-Louvain-la-Neuve, Belgium
e-mail: eric.deleersnijder@uclouvain.be

O. Fringer
Stanford University, Stanford, CA, USA
e-mail: fringer@stanford.edu

H. Schuttelaars et al. (eds.), *The Mathematics of Marine Modelling*,
Mathematics of Planet Earth 9, https://doi.org/10.1007/978-3-031-09559-7_1

approximated as a continuous medium. Given that the mean free path of liquid water is $\mathcal{O}(10^{-10}\,\mathrm{m})$ and the smallest flow or density gradients in marine environments occur over scales of $\mathcal{O}(10^{-3}\,\mathrm{m})$, see e.g. Olbers et al. (2012), the continuum assumption is an extremely good approximation for all motions of interest. Therefore, the resulting state variables can be treated as continuous time-dependent field functions $\psi\,(\mathbf{x}, t)$, with the spatial coordinate $\mathbf{x} = (x, y, z)$ and time coordinate t.

1.1.2 Integral and Differential Formulations

Volume integration of continuous state variable functions introduced in Sect. 1.1.1 allows for the calculation of physical quantities like mass, momentum, angular momentum and energy. The first principles of classical mechanics and thermodynamics describe the evolution of mass, momentum and energy of a *material volume* of fluid. Material volumes consist of a fixed set of fluid elements bounded by material surfaces that follow the fluid and hence ensure that there is no flow into or out of the material volume. The temporal derivative with respect to the material volume is referred to as the *material derivative*, denoted by $\mathrm{D}/\mathrm{D}t$. The evolution of a state variable ψ is prescribed by a corresponding source term R, such that the prototype integral budget equation is given by $\frac{\mathrm{D}}{\mathrm{D}t}\int \psi \,\mathrm{d}V = \int R\,\mathrm{d}V$. Governing equations for integral flow quantities can be re-formulated in differential form with the help of the Leibniz integral rule. For an arbitrary continuous function ψ the resulting *Reynolds transport theorem* (Aris 1989) reads

$$\frac{\mathrm{D}}{\mathrm{D}t}\int \psi \,\mathrm{d}V = \int \partial_t \psi \,\mathrm{d}V + \oint \psi \underbrace{\frac{\mathrm{D}\mathbf{x}}{\mathrm{D}t}}_{=\mathbf{v}} \cdot \mathrm{d}\mathbf{A}, \tag{1.1a}$$

$$= \int \left[\partial_t \psi + \nabla \cdot (\mathbf{v}\psi)\right] \mathrm{d}V. \tag{1.1b}$$

In (1.1a), because the material surface moves with the fluid velocity, the material derivative of points on the material surface is equal to the fluid velocity $\mathbf{v} = \mathrm{D}\mathbf{x}/\mathrm{D}t$. Assuming (1.1b) is satisfied for any material volume, including one that is infinitesimally small, the prototype budget equation in differential form reads

$$\partial_t \psi + \nabla \cdot (\mathbf{v}\psi) = R. \tag{1.2}$$

Formulating the budget equations for mass, momentum and energy in differential form yields a set of coupled nonlinear partial differential equations for the state variables introduced in Sect. 1.1.1.

1.1.3 Averaging of Turbulent Flows

Coupled nonlinear differential equations can exhibit chaotic behaviour with solutions that are very sensitive to disturbances (Lorenz 1963). These solutions describe turbulent flows and exhibit strong fluctuations over a broad range of spatio-temporal scales (Foias et al. 2001). Solving the dynamics of the physical quantities on all scales, i.e. including the turbulent stirring down to the viscous scales, requires an impractical high spatio-temporal resolution. Furthermore, it is usually not one individual turbulent solution that is of interest, but properties of the mean flow. Mean flow quantities can be obtained by the application of a linear averaging operator $\langle\cdot\rangle$, commonly over space, time or ensemble realisations. If the operator commutes with the temporal and spatial derivatives, averaging of the prototype Eq. (1.2) yields an equation of identical form for the mean flow quantities, except for an additional turbulent flux $\boldsymbol{\tau}\,(\mathbf{v}, \psi)$ originating from the nonlinearity in the original equation:

$$\partial_t \langle\psi\rangle + \nabla \cdot (\langle\mathbf{v}\rangle \langle\psi\rangle) = \langle R\rangle - \nabla \cdot \underbrace{(\langle\mathbf{v}\psi\rangle - \langle\mathbf{v}\rangle \langle\psi\rangle)}_{=\boldsymbol{\tau}(\mathbf{v},\psi)}. \tag{1.3}$$

If the averaging operator is also idempotent, i.e. $\langle\langle\cdot\rangle\rangle = \langle\cdot\rangle$, it is called a *Reynolds average*. Only for a Reynolds average, e.g. the ensemble mean, the turbulent flux is represented by the correlation of fluctuations (second moments), i.e.

$$\boldsymbol{\tau}\,(\mathbf{v}, \psi) = \big\langle(\mathbf{v} - \langle\mathbf{v}\rangle)\,(\psi - \langle\psi\rangle)\big\rangle = \langle\mathbf{v}'\psi'\rangle \qquad \text{for Reynolds averages.} \tag{1.4}$$

Since turbulent stirring enlarges local gradients and the interfaces where molecular mixing can take place, the net effect of enhanced mixing in turbulent flows motivates to parameterise an unknown turbulent flux as a diffusive flux in terms of an eddy diffusivity and the known mean flow gradient (*eddy viscosity assumption* of Boussinesq).

1.2 Governing Equations

The governing equations are derived from the physical laws for mass conservation and the budget equations for linear and angular momentum, and energy. They are formulated following the prototype Eq. (1.2). A detailed derivation of each equation is beyond the scope of this book and the reader is referred to the excellent text books by Batchelor (1967), Griffies (2004) and Olbers et al. (2012). In marine modelling, several approximations are applied to simplify the set of equations. A very common approximation is the *Boussinesq approximation* (not to be mistaken for the eddy viscosity assumption of Boussinesq). As described by Young (2010), variations in density are only considered for buoyancy effects in the vertical momentum balance. In all other terms the density is replaced by a constant reference density ρ_0. The

buoyancy follows from a diagnostic *equation of state* which provides the density depending on salinity S, temperature Θ, and in case of Boussinesq fluids on depth instead of in-situ pressure (Roquet et al. 2015):

$$\rho = \rho(S, \Theta, z). \tag{1.5}$$

With the eddy viscosity assumption of Boussinesq, the set of governing equations for the mean-flow quantities (without brackets for brevity) is presented in the following. The emphasis of the vertical axis in geophysical applications motivates the assumption of *transverse isotropy* and the use of different eddy viscosities and diffusivities for vertical and horizontal turbulent fluxes.

1.2.1 Volume Conservation

Under the Boussinesq approximation it is not mass $\int \rho \, \mathrm{d}V$ anymore, but volume that is conserved. The original prognostic equation for density degenerates to the so-called *incompressibility constraint*,

$$\partial_x u + \partial_y v + \partial_z w = 0, \tag{1.6}$$

enforcing a divergence-free flow.

Kinematic boundary conditions further constrain the flow at bounding surfaces by prescribing the diasurface volume flux velocity (Griffies 2004). With the velocity of the bounding surface $\mathbf{v}_\mathrm{b}$ the conditions at a single-valued free surface $z = \eta(x, y, t)$ and impermeable bottom $z = -H(x, y, t)$ are given by

$$\nabla(z - \eta) \cdot (\mathbf{v} - \mathbf{v}_\mathrm{b}) = (E - P) \qquad \text{at } z = \eta, \tag{1.7a}$$

$$\nabla(z + H) \cdot (\mathbf{v} - \mathbf{v}_\mathrm{b}) = 0 \qquad \text{at } z = -H. \tag{1.7b}$$

In (1.7a) the volume flux velocity is prescribed in terms of evaporation E and precipitation P. Alternative formulations are

$$\partial_t \eta + u\partial_x \eta + v\partial_y \eta - w = -(E - P) \qquad \text{at } z = \eta, \tag{1.8a}$$

$$\partial_t H + u\partial_x H + v\partial_y H + w = 0 \qquad \text{at } z = -H. \tag{1.8b}$$

Boundary condition (1.8a) is used to determine the evolution of the free surface. In contrast, (1.8b) constrains the flow velocity at the bottom in terms of a prescribed bottom topography. The morphological evolution of the bottom $\partial_t H$ is either neglected or follows from a morphological model (see Chap. 10).

1.2.2 Salt Conservation

Seawater is a mixture of freshwater and salt. The fluid velocity $\mathbf{v}$ is defined as the center-of-mass (barycenter) velocity of the mixture. The mass fraction of salt in seawater defines the salinity S. The budget equation for salt in differential form reads

$$\partial_t S + \partial_x(uS) + \partial_y(vS) + \partial_z(wS) = \partial_x(K\partial_x S) + \partial_y(K\partial_y S) + \partial_z(\nu_t'\partial_z S). \quad (1.9)$$

The diffusive salt flux $\mathbf{j}_S = (-K\partial_x S, -K\partial_y S, -\nu_t'\partial_z S)$ on the right-hand side parameterizes the mean salt flux relative to the center-of-mass velocity (Beron-Vera et al. 1999; Nurser and Griffies 2019), with horizontal and vertical eddy diffusivities K and ν_t'. For salt there is a discontinuity at the surface and bottom boundaries, with no salt flux through them. Therefore, the analytical boundary condition requires the diffusive salt flux to compensate the advective one associated with (1.7a) and (1.7b):

$$\nabla(z-\eta)\cdot\mathbf{j}_S = -(E-P)S \qquad \text{at } z=\eta, \quad (1.10a)$$

$$\nabla(z+H)\cdot\mathbf{j}_S = 0 \qquad \text{at } z=-H. \quad (1.10b)$$

1.2.3 Heat Balance

An excellent representation of the heat of a seawater fluid element is the *Conservative Temperature* Θ (McDougall 2003). From the first law of thermodynamics the corresponding prognostic equation can be derived as

$$\partial_t\Theta + \partial_x(u\Theta) + \partial_y(v\Theta) + \partial_z(w\Theta) = \partial_x(K\partial_x\Theta) + \partial_y(K\partial_y\Theta) + \partial_z(\nu_t'\partial_z\Theta) + \frac{\partial_z I}{C_p\rho_0}, \quad (1.11)$$

with the specific heat capacity of water at constant pressure C_p and solar irradiance in I. The boundary condition for the diffusive temperature flux $\mathbf{j}_\Theta = (-K\partial_x\Theta, -K\partial_y\Theta, -\nu_t'\partial_z\Theta)$ with horizontal and vertical eddy diffusivities K and ν_t' reads as

$$\nabla(z-\eta)\cdot\mathbf{j}_\Theta = \frac{Q_s}{C_p\rho_0} \qquad \text{at } z=\eta, \quad (1.12a)$$

$$\nabla(z+H)\cdot\mathbf{j}_\Theta = 0 \qquad \text{at } z=-H. \quad (1.12b)$$

The surface heat flux Q_s consists of sensible, latent and long-wave radiation contributions.

1.2.4 Momentum Balance

The momentum balance provides prognostic equations for the velocity components. Considering Earth rotation and gravity these can be written as

$$\partial_t u + \partial_x(uu) + \partial_y(vu) + \partial_z(wu) - fv + f_c w = \partial_x T_{11} + \partial_y T_{21} + \partial_z T_{31} - \partial_x P_{nh} - \partial_x P_{hs}, \tag{1.13a}$$

$$\partial_t v + \partial_x(uv) + \partial_y(vv) + \partial_z(wv) + fu = \partial_x T_{12} + \partial_y T_{22} + \partial_z T_{32} - \partial_y P_{nh} - \partial_y P_{hs}, \tag{1.13b}$$

$$\partial_t w + \partial_x(uw) + \partial_y(vw) + \partial_z(ww) - f_c u = \partial_x T_{13} + \partial_y T_{23} + \partial_z T_{33} - \partial_z P_{nh}. \tag{1.13c}$$

In (1.13a)–(1.13c) $f = 2\Omega \sin\phi$ and $f_c = 2\Omega \cos\phi$ denote the Coriolis parameters with the spin rate of the Earth Ω and latitude ϕ, and T_{ij} the components of the turbulent stress tensor $\mathbf{T}$. Formulations for the stress tensor are given in Sect. 1.2.5. The dynamic pressure is already decomposed into hydrostatic and nonhydrostatic contributions. The hydrostatic pressure contribution is defined by the weight of the water column above,

$$\rho_0 P_{hs}(z) = p_a + \rho_0 g(\eta - z) + \int_z^\eta \big(\rho(z') - \rho_0\big)\, g \, \mathrm{d}z', \tag{1.14}$$

with p_a being atmospheric pressure at the surface and g the gravitational acceleration. Dynamic boundary conditions prescribe momentum fluxes through the surface and bottom,

$$\nabla(z - \eta) \cdot \mathbf{T} = \tau_s \qquad \text{at } z = \eta, \tag{1.15a}$$

$$\nabla(z + H) \cdot \mathbf{T} = \tau_b \qquad \text{at } z = -H, \tag{1.15b}$$

with τ_s and τ_b being surface and bottom stress vectors defined in opposite direction to the associated momentum fluxes. The bottom stress is usually reconstructed from a logarithmic velocity profile.

1.2.5 Common Formulations and Closures

Depending on the application and the scales of interest, different forms of the turbulent fluxes and different closures for the eddy viscosities and diffusivities have to be used.

Nonhydrostatic LES Equations

The governing equations for *Large eddy simulations (LES)* can be obtained when the averaging operator in (1.3) represents a sufficiently fine spatial filter such that the mean flow quantities still resolve the large energy-containing eddies down to the inertial subrange. Because the horizontal and vertical scales of motion are isotropic within the inertial subrange, the full momentum balance must be solved, which requires the solution of a three-dimensional elliptic Poisson equation for the nonhydrostatic pressure contribution.

In contrast to the large-scale eddies, which strongly depend on the geometry of the domain and thus obey no universal spectrum, the unresolved small-scale eddies are more likely to be homogeneous and isotropic and thus easier to model. The most common approach to modeling the turbulent stress in LES is to assume 3D isotropy for the eddy diffusivity A and its flow-dependent calculation following Smagorinsky (1963):

$$T_{ij} = A(\partial_i u_j + \partial_j u_i), \tag{1.16a}$$

$$A = (C_S \Delta)^2 \left(\frac{1}{2}(\partial_i u_j + \partial_j u_i) \frac{1}{2}(\partial_i u_j + \partial_j u_i) \right)^{1/2}. \tag{1.16b}$$

In (1.16b) summation is carried out over doubled indices, Δ is the filter width and $C_S = \mathcal{O}(0.1)$ is the Smagorinsky constant. Assuming 3D isotropy also implies equal horizontal and vertical eddy diffusivities for tracers, i.e. $K = \nu_t'$ in (1.9) and (1.11), which can be calculated in terms of a prescribed turbulent Prandtl number Pr_t:

$$K = A/Pr_t. \tag{1.17}$$

In LES the filter width Δ is a measure of the grid size, which must be of $\mathcal{O}(0.1\,\mathrm{m}) - \mathcal{O}(1\,\mathrm{m})$ to resolve the energy-containing eddies in typical marine applications. Therefore, LES is reserved for small-scale, idealized studies, although its application to real, field-scale problems continues to increase. For a more thorough overview of LES modeling, the reader is encouraged to refer to the texts by Pope (2000) and Rodi et al. (2013).

Hydrostatic Shallow Water Equations

In most geophysical applications the vertical scales of motion are much smaller than the horizontal ones. The flows usually take place in horizontal planes without significant vertical acceleration. These considerations motivate the *hydrostatic pressure assumption*, which degenerates the vertical momentum balance by neglecting (1.13c) so that the prognostic integration of w in (1.13c) is replaced by a diagnostic calculation from (1.6), see e.g. Klingbeil and Burchard (2013). Furthermore, the nonhydrostatic pressure contributions in (1.13a) and (1.13b) are neglected, i.e. $\partial_x P_{\mathrm{nh}} = \partial_y P_{\mathrm{nh}} = 0$. In addition, $f_c w$ is neglected in (1.13a) so that the Coriolis force stays orthogonal to the velocity and does not alter the kinetic energy of a fluid element.

The separation of horizontal and vertical scales also implies different viscosities in the horizontal and vertical direction (A and ν_t, respectively). Under this transverse isotropy two formulations of the stress tensor are common (Kamenkovich 1967; Smagorinsky 1993):

$$\begin{bmatrix} T_{11} & T_{21} & T_{31} \\ T_{12} & T_{22} & T_{32} \end{bmatrix} = \begin{bmatrix} 2A\partial_x u & A(\partial_x v + \partial_y u) & \nu_t \partial_z u \\ A(\partial_x v + \partial_y u) & 2A\partial_y v & \nu_t \partial_z v \end{bmatrix}, \tag{1.18a}$$

$$A = (C_S \Delta)^2 \left((\partial_x u)^2 + \frac{1}{2}(\partial_x v + \partial_y u)^2 + (\partial_y v)^2 \right)^{1/2}, \tag{1.18b}$$

or

$$\begin{bmatrix} T_{11} & T_{21} & T_{31} \\ T_{12} & T_{22} & T_{32} \end{bmatrix} = \begin{bmatrix} A(\partial_x u - \partial_y v) & A(\partial_x v + \partial_y u) & \nu_t \partial_z u \\ A(\partial_x v + \partial_y u) & -A(\partial_x u - \partial_y v) & \nu_t \partial_z v \end{bmatrix}, \tag{1.19a}$$

$$A = (C_S \Delta)^2 \left(\frac{1}{2}(\partial_x u - \partial_y v)^2 + \frac{1}{2}(\partial_x v + \partial_y u)^2 \right)^{1/2}. \tag{1.19b}$$

The horizontal eddy diffusivity of momentum A is either assumed to be constant, or calculated by the Smagorinsky closures given in (1.18b) and (1.19b), respectively. The horizontal eddy diffusivity for tracers K in (1.9) and (1.11) is usually derived in terms of a prescribed turbulent Prandtl number according to (1.17). Following Umlauf and Burchard (2005), the vertical turbulent diffusivities of momentum ν_t and tracers ν_t' can be obtained from a general algebraic second-moment closure in terms of the turbulent kinetic energy (TKE) k and its dissipation rate ε.

1.3 Summary

In this chapter the governing equations for marine flows were presented. For many applications the hydrostatic pressure assumption is valid. The resulting shallow water equations outlined in Sect. 1.2.5 form the basis for many studies and the remaining

chapters. Further details about the numerics of hydrostatic coastal ocean models can be found in Klingbeil et al. (2018).

References

Aris, R. 1989. Vectors. *Tensors and the basic equations of fluid mechanics*. Dover Publications. 978-0-486-66110-0.

Batchelor, G.K. 1967. *An introduction to fluid dynamics*. Cambridge University Press.

Beron-Vera, F.J., J. Ochoa, and P. Ripa. 1999. A note on boundary conditions for salt and freshwater balances. *Ocean Modelling* 1: 111–118.

Foias, C., O.P. Manley, R. Rosa, and R. Témam. 2001. Navier-Stokes equations and turbulence. In *Encyclopedia of mathematics and its applications*, vol. 83. Cambridge University Press. https://doi.org/10.1017/CBO9780511546754.

Griffies, S.M. 2004. *Fundamentals of ocean climate models*. Princeton University Press.

Kamenkovich, V.M. 1967. On the coefficients of eddy diffusion and viscosity in large-scale oceanic and atmospheric motions. *Izvestiya, Atmospheric and Oceanic Physics* 3: 1326–1333.

Klingbeil, K., and H. Burchard. 2013. Implementation of a direct nonhydrostatic pressure gradient discretisation into a layered ocean model. *Ocean Modelling* 65: 64–77.

Klingbeil, K., F. Lemarié, L. Debreu, and H. Burchard. 2018. The numerics of hydrostatic structured-grid coastal ocean models: state of the art and future perspectives. *Ocean Modelling* 125: 80–105.

Lorenz, E.N. 1963. Deterministic nonperiodic flow. *Journal of the Atmospheric Sciences* 20: 130–141.

McDougall, T.J. 2003. Potential enthalpy: A conservative oceanic variable for evaluating heat content and heat fluxes. *Journal of Physical Oceanography* 33: 945–963.

Nurser, A.J.G., and S.M. Griffies. 2019. Relating the diffusive salt flux just below the ocean surface to boundary freshwater and salt fluxes. *Journal of Physical Oceanography* 49: 2365–2376.

Olbers, D., J. Willebrand, and C. Eden. 2012. *Ocean dynamics*. Springer.

Pope, S.B. 2000. *Turbulent flows*. Cambridge University Press.

Rodi, W., G. Constantinescu, and T. Stoesser. 2013. *Large-Eddy simulation in hydraulics*. CRC Press.

Roquet, F., G. Madec, T.J. McDougall, and P.M. Barker. 2015. Accurate polynomial expressions for the density and specific volume of seawater using the TEOS-10 standard. *Ocean Modelling* 90: 29–43.

Smagorinsky, J. 1963. General circulation experiments with the primitive equations. *Monthly Weather Review* 91 (3): 99–164.

Smagorinsky, J. (1993). Some historical remarks on the use of nonlinear viscosities. In *Large eddy simulation of complex engineering and geophysical flows*, 3–36. Cambridge University Press. ISBN 9780521131339.

Umlauf, L., and H. Burchard. 2005. Second-order turbulence closure models for geophysical boundary layers. A review of recent work. *Continental Shelf Research* 25: 795–827.

Young, W.R. 2010. Dynamic enthalpy, conservative temperature, and the seawater Boussinesq approximation. *Journal of Physical Oceanography* 40: 394–400.

Chapter 2
Water Waves in Isotropic and Anisotropic Media: A comparison

Leo R. M. Maas

Abstract Restoring forces as gravity, Coriolis force or their combination, endow geo and astrophysical fluids with an anisotropy direction. Breaking the underlying hydrostatic or cyclostrophic force balances in fluids that are stratified in density or angular momentum results in obliquely-propagating internal waves. These waves differ in nearly every conceivable aspect from external, surface gravity and capillary waves. Differences between linear internal and external waves stem to a large part from the complementary way in which their frequency depends on the wave vector. While these differences may be hiding in symmetrically-shaped basins, these become fully apparent when the boundary shape breaks the symmetry imposed by the anisotropy. These underlying force balances also constrain any wave-driven mean flows. Interestingly, the lack of a clear force balance in a homogeneous, non-rotating fluid that is stratified in linear momentum, renders waves, perturbations on these shear flows, 'problematic'.

2.1 Introduction

Waves in isotropic media, like familiar sound and electromagnetic waves in three-dimensional space, or gravity waves in the two-dimensional plane of the water surface, behave quite differently from waves in anisotropic media. Inside fluids, the directions of gravity and/or background rotation provide the fluid with an anisotropy which strongly influences wave propagation inside stratified and/or rotating fluids. Gravity, rotation and a nontrivial shape of the fluid domain are important ingredients in the fields of geophysical and astrophysical fluid dynamics. This warrants consideration of the specific consequences of these properties, and a comparison between isotropic external and anisotropic internal waves. The aim of this paper is to juxtapose well-known properties of isotropic surface water waves with those exhibited by anisotropic waves in stratified/rotating fluids.

L. R. M. Maas (✉)
Institute for Marine and Atmospheric Research (IMAU), Utrecht University, Utrecht, Netherlands
e-mail: L.R.M.Maas@uu.nl

H. Schuttelaars et al. (eds.), *The Mathematics of Marine Modelling*,
Mathematics of Planet Earth 9, https://doi.org/10.1007/978-3-031-09559-7_2

In Sect. 2.2.1, we start by considering external waves: isotropic gravity waves propagating on the surface of homogeneous-density fluids. This deals with the specific nature of their dispersion relation, its implications for wave ray divergence and wave ray chaos, and the modifying influence of background rotation on long surface gravity waves. This leads to a brief discussion of Sverdrup, Poincaré and Kelvin waves (see also Chap. 4 of this book), as well as to amplitude and phase patterns displaying amphidromic points, phase-singularities where phase is multi-valued and vertical displacement vanishes.

Section 2.2.2 discusses two types of heterogeneous fluids that are density-stratified, supporting internal waves. The first type consists in layers of fluid that differ in density. Two-layer fluids allow for interfacial gravity waves that propagate horizontally along the average position of the interface, the pycnocline, which acts as a wave guide. These interfacial waves behave similar to surface waves because layers of uniform average depth inherit isotropy. The second type of internal gravity waves, found in continuously-stratified and particularly in uniformly-stratified fluids, obey another type of dispersion relation. Internal gravity waves propagate as beams, along paths that are inclined relative to the direction of gravity. A uniform water depth may again render the fluid superficially isotropic—up and downward propagating beams combine into vertically-standing, horizontally-propagating internal wave modes—but variations in water-depth reveal the true underlying anisotropic nature of stratified fluids. Upon reflection from sloping bottoms and side walls, internal wave beams lead to wave convergence and wave attractors.

Homogeneous-density fluids can still stratify, namely in linear momentum—known as shear flows—or in angular momentum, known as swirling flows. Both types of stratification support waves, although, as discussed in Sect. 2.3.1, those in the latter case are easier to observe. Solidly rotating fluids, for which the angular velocity is spatially uniform and constant, offer an important special case of swirling flows. When container motion produces this state the shear flow is deceptively simple. Upon passing through a viscous spin-up phase, observed from a co-rotating frame of reference, the flow recedes to a quiescent equilibrium state which obscures the underlying force balance. However, once this balance is perturbed it provides restoring Coriolis forces. Solid-body rotation invites a consideration of perturbations, called inertial waves, from within the co-rotating frame of reference, especially when the isotropy of the fluid domain is broken, discussed in Sect. 2.3.2.

The paper ends briefly discussing the effects of these waves on mean flows, Sect. 2.4, and gives some conclusions in the final Sect. 2.5.

2.2 Gravity Waves

Gravity waves arise both at free boundaries of fluid layers as external waves, as well as in their interiors as internal waves when the fluid is stratified in density. We discuss the far-reaching differences between these two types of waves, both with respect to their dispersion relations, reflection laws, as well as their regularity.

2.2.1 Surface Gravity Waves in Homogeneous Fluids

An inviscid, incompressible, non-rotating, quiescent uniform-density fluid does not support any hydrodynamic waves unless its surface is free and subject to gravity or capillary forces. These waves are external (boundary) waves as they propagate along the boundary of the fluid body. They are surface-trapped as wave-induced motions decay exponentially below the surface. These perturbations to the state of rest can be described by the linearised Euler equations. When vorticity is initially absent, the fluid will stay irrotational as vorticity is either created by friction at boundaries—a viscous process—or by baroclinic torques, due to misalignment of density and pressure gradients, excluded in a homogeneous-density fluid. Together with incompressibility this guarantees that the waves can be described by a scalar velocity potential, ϕ, that obeys a Laplace equation, $\nabla^2\phi = 0$, where $\nabla^2 = \partial_{xx} + \partial_{yy} + \partial_{zz}$ denotes the Laplacian operator. This elliptic equation, a sum of second-order spatial derivatives, determines the spatial structure of the waves in a Cartesian (x, y, z) frame of reference. Their temporal behaviour follows from boundary conditions describing continuity of pressure across the surface, and by requiring fluid parcels that sit at the surface to remain at the surface. Linear, constant-coefficient equations can be solved by complex space-time exponentials. The physical content of a particular wave is contained in its dispersion relation, $\omega(\mathbf{k})$, that describes how wave frequency, ω, depends on wavevector $\mathbf{k}$'s magnitude and direction.

Wave Dispersion in Isotropic Media

As for plane monochromatic acoustic and electromagnetic waves in isotropic three-dimensional space, gravity and capillary waves that propagate horizontally along the free surface have frequencies that depend only on wave vector magnitude $\kappa \equiv |\mathbf{k}|$ (or wavelength $\lambda = 2\pi/\kappa$), *not* on its direction. Restricting ourselves to gravity waves, the vertical structure of these external waves varies from exponentially-decaying, for short waves ($\kappa H \gg 1$), to vertically-uniform, for long waves ($\kappa H \ll 1$). Here H denotes uniform fluid depth. In these regimes, frequency ω varies from $\omega = \sqrt{g\kappa}$ to $\omega = \sqrt{gH}\kappa$, and the waves change from dispersive to dispersionless respectively. Here g denotes the acceleration of gravity. For any function, $\omega(\kappa)$, its restricted dependence on the wave vector immediately implies the familiar property that a wave group propagates its energy, related to that of its envelope, into the same direction as its individual crests and troughs. Energy is transported with the group velocity (the wave vector gradient of the wave frequency, $\mathbf{c}_g = \nabla_{\mathbf{k}}\omega = \mathbf{k}\,\kappa^{-1}\partial_\kappa\omega$), while crests and troughs—two particular phases of the wave—propagate at phase velocity, $\mathbf{c} = \omega\mathbf{k}/\kappa^2$, also pointing parallel to the wave vector $\mathbf{k}$. This alignment happens even when, due to a nonlinear dependence of wave frequency on wave vector magnitude, the waves constituting the group propagate at different speed, leading them to disperse and the wave group to spread. This type of dispersion relation obviously provides a constraint on the wavelength, which is fixed by the wave's frequency. Because of

this tight relationship between wave frequency and wavelength, in electromagnetism these are described by the single term 'color'.

Diverging External Waves and Wave Ray Chaos

Regardless of the horizontal shape of a container's vertical side-walls, a surface wave cannot change its frequency when it reflects. The amount of waves that will reflect off a wall is the same as the amount that are incident. The dependence of frequency on wave vector magnitude implies that the wavelength does not change either during reflection. Since the velocity vector produced by surface waves, $\mathbf{u} = \nabla\phi$, is given by the gradient of a velocity potential ϕ, it is parallel to the wave vector, $\mathbf{u} \parallel \mathbf{k}$. When waves are incident on a vertical wall, vanishing of the normal velocity component at the wall implies that normal wave vector components of incident and reflected waves have to match in magnitude while differing in sign. Together with the fact that wave vector magnitude cannot change during reflection this implies that the waves reflect specularly. This expresses the Snell-Descartes law, stating that a wave's angle of reflection relative to the wall's normal equals its angle of incidence.

While the presence of wave vector magnitude in the dispersion relation thus provides a constraint on the reflecting wave's length, the *absence* of the wave vector direction also has its significance: waves can adjust their propagation direction whenever there is reason to do so, for instance when they reflect from a curved vertical boundary. They will then scatter into multiple directions, at each point of the boundary reflecting specularly, see Fig. 2.1. This type of scattering reveals the natural tendency of surface gravity wave rays to diverge.

In an irregularly-shaped cavity, the unknown frequency of an arbitrarily located wave source can be extracted by measuring the wavelength (wave vector magnitude) over any part of the cavity. In an enclosed, but complex-shaped fluid basin, multiple reflections then give rise to 'wave ray chaos' (Berry 1981). Interestingly, surface waves still linger along a restricted set of periodic ray paths, where the rate of divergence is smallest. These paths stand out as 'scars': locations where those waves occur preferentially, see Fig. 2.2.

Rotational Modification of Long Surface Gravity Waves

When a homogeneous-density, free-surface fluid rotates, such as on Earth, the external waves—and especially the long, plane surface gravity waves—are modified. In a uniform-depth basin, rotating in an anticlockwise sense at rate Ω around an axis normal to the equilibrium surface, long waves are governed by the Rotating Shallow-Water Equations (RSWEs)

$$\begin{aligned} u_t - v &= -\zeta_x, \\ v_t + u &= -\zeta_y, \\ \zeta_t + u_x + v_y &= 0. \end{aligned} \tag{2.1}$$

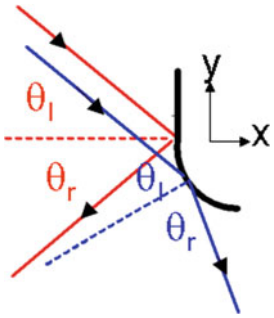

Fig. 2.1 Surface wave rays reflecting from curved vertical boundary

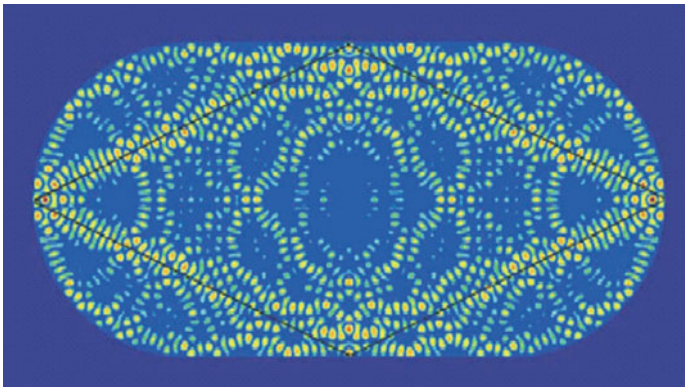

Fig. 2.2 Surface wave scars in a stadium showing large (yellow) and small (blue) amplitude disturbances. Solid lines show an unstable periodic orbit. Figure adapted from Heller (1984)

Here we use subscript-derivative notation and dimensionless variables. Time t is scaled with the Coriolis frequency $f = 2\Omega$. For convenience we take its expression as relevant in a laboratory model, instead of its geophysically-motivated expression $2\Omega \sin\varphi$ which in the traditional approximation would apply at latitude φ on a plane tangent to the Earth (Gerkema et al. 2008). The vertical, z, and surface elevation, ζ, are scaled with depth, H, horizontal (x, y)-coordinates with Rossby deformation radius, $R \equiv \sqrt{gH}/f$, and velocities, (u, v), with, $Rf = \sqrt{gH}$. As is well-known (see e.g. Gill (1982)), depending on geometric constraints, system rotation gives rise to Sverdrup, Poincaré and Kelvin waves (see Chap. 4 of this book). Over a uniform-depth sea, plane monochromatic Sverdrup waves $\propto e^{i(kx+ly-\omega t)}$ obey the dispersion relation

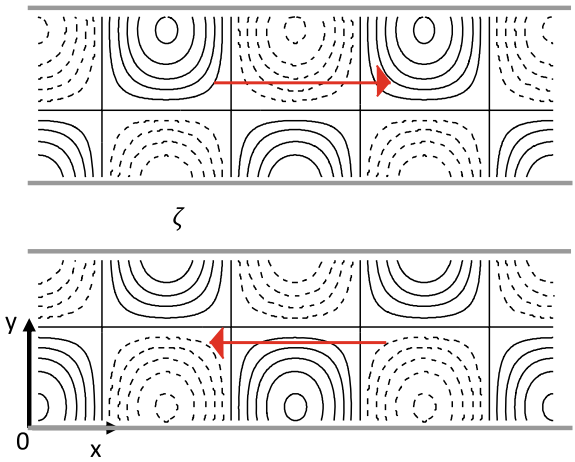

Fig. 2.3 Surface elevation ζ (solid and dashed for positive or negative displacements) for a Poincaré wave (sum of two Sverdrup waves) propagating in a channel into a direction indicated by the red arrow. Notice that nodal lines are displaced from the middle axis towards the coast that is on the right hand side, as seen from its propagation direction

$$\omega^2 = 1 + k^2 + l^2 = 1 + \kappa^2, \tag{2.2}$$

where $\mathbf{k} = (k, l) = \kappa(\cos\phi, \sin\phi)$, for waves propagating in direction ϕ relative to a pre-chosen orientation of the x-axis. The first term on the right-hand side represents the dimensionless Coriolis frequency, acting as low-frequency cut-off. Sverdrup waves occur on the infinite plane (Sverdrup 1926) and (2.1a,b) imply that system rotation induces elliptically-polarized currents. The presence of a vertical wall, at $y = 0$ say, requires a combination of incident and reflected Sverdrup waves—a Poincaré wave—to satisfy the impermeability condition, $\mathbf{u} \cdot \mathbf{n} = v = 0$, see Fig. 2.3 where $\mathbf{n}$ denotes a unit vector normal to the boundary directed outwards.

Kelvin waves, also propagating along one such a wall, simplify the dispersion relation to $\omega = k$, by having its transverse wavenumber $l = i$. In that case a low-frequency cut-off is absent. In order that the wave decays away from the wall as $y \to \infty$, only the positive sign of $\sqrt{k^2}$ is allowed. This implies propagation in positive x-direction. Regardless of wave frequency, this transverse decay occurs dimensionally always at the Rossby deformation scale, R.

External waves, such as short gravity waves, decaying exponentially below the surface, can be interpreted as a boundary wave whose dimension is reduced by one. Two-dimensionality of these waves is captured by integrating over the (vertical) decay direction. As horizontal currents associated with long waves are independent of the vertical coordinate, this decay is no longer visible. It occurs over a scale depth much larger than the fluid depth. Formally, these waves still present a dimensionally-reduced (surface trapped) wave feature. This can be treated as such by vertically integrating the equations. In the same vein, a Kelvin wave provides a further dimensional reduction, owing to its additional exponential decay, transverse to the coast. Integrating also over the direction perpendicular to the coast it can be described as a one-dimensional wave feature.

Amphidromic Wave Systems

In partially, or fully-enclosed rotating water bodies, such as inland seas and lakes, impermeability of its side walls requires a combination of Kelvin and Poincaré waves (see Chap. 4 of this book). This gives rise to intricate structures called *amphidromes*, see Fig. 2.4. Amphidromes are phase-singularities (points where phase is multi-valued) that coincide with nodal points: locations of zero elevation amplitude. Attempting to understand the spatial pattern of simultaneously observed tidal displacements along the North Sea's perimeter, Whewell (1833) inferred the presence of such points. He postulated their existence in an attempt to construct tidal co-phase lines—lines connecting points simultaneously reaching for instance high or low water. Solutions of the RSWEs also display 'spider-web like' structures, as found in (semi) rectangular and square basins of uniform depth (Proudman 1916; Taylor 1922; Rao 1966), and more recently in basins of variable bottom depth and boundary shape (Steinmoeller et al. 2019). These arise because rotationally-modified surface gravity waves need to satisfy an impermeability condition at boundaries. When cast in terms of the free surface elevation, ζ, this takes the form of an oblique-derivative (Robin) boundary condition, a weighted combination of Dirichlet and Neumann boundary conditions. Amphidromes already appear in straight, open channels, where they form due to two counter-propagating Kelvin waves, see Fig. 2.5 (Krauss 1973). Section 2.3.2 will discuss replicas of such structures in the interior inertial wave field, interestingly arising in fully confined (rigid-lid), homogeneous-density rotating fluids.

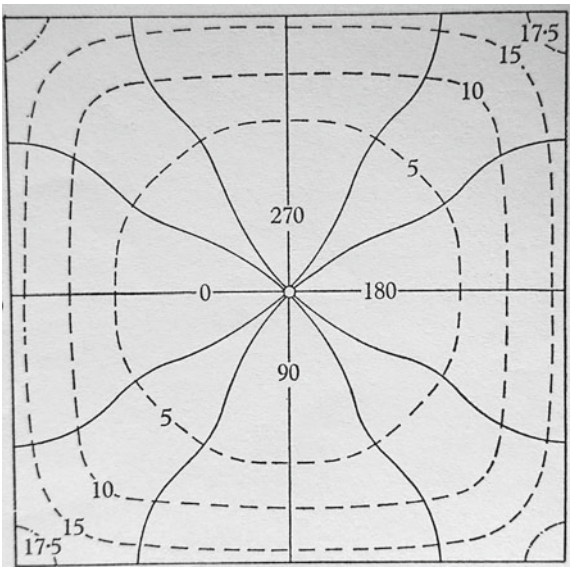

Fig. 2.4 Amplitude (dashed, arbitrary units) and phase lines (solid, each 30 °C) of the surface elevation for the computationally determined lowest frequency, rotationally-modified surface gravity wave in a rotating square basin. It displays a cyclonic amphidromic point in the centre where the amplitude vanishes and phase is multi-valued. Figure from Rao (1966)

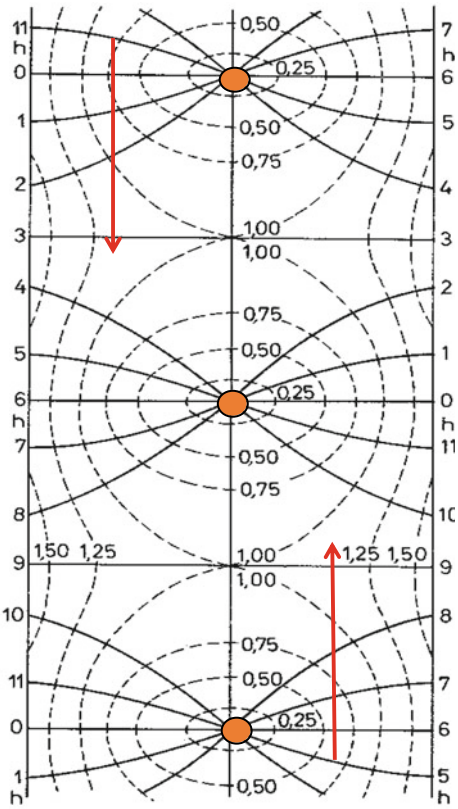

Fig. 2.5 Amplitude lines (dashed, arbitrary units) and phase lines (solid, each 30 °C) of the sea surface elevation produced by two counter-propagating Kelvin waves (propagation direction indicated by red arrows) of equal amplitude displaying amphidromic points (orange dots) where the amplitude vanishes and phase is multi-valued

2.2.2 Gravity Waves in Heterogeneous Media

Interfacial Waves

In the foregoing we interpreted surface waves in isotropic fluids as external or boundary waves. Alternatively, an external or boundary wave can be defined as a wave whose maximum displacement (in vertical or horizontal direction) occurs at the bounding surface. According to this definition, waves that have their maximum displacements below the free surface should be interpreted as internal waves. From that perspective, the waves that Franklin (1762) discovered at the interface between oil and water—two immiscible fluids of different density—might well be interpreted as internal waves, as their maximum displacements occur in the interior of the fluid. However, we refrain from this interpretation as waves still decay exponentially, below as well as above the interface. In that sense, these interfacial waves belong to the class of boundary waves, being external to the two fluid bodies of homogeneous-density that make up the two-layer fluid. Indeed, waves propagating at the interface between two fluid layers of different density but uniform depths are very akin to surface waves.

Apart from an additional, fluid-gas phase-transition, the free surface again separates two liquids differing in density (albeit by a factor thousand bigger than that between oil and water). Consequently, the dispersion relation satisfied by interfacial waves is very similar to that of surface waves. In particular, the frequency is again independent of wave vector direction, merely leading to a reduction of the acceleration of gravity by a factor equalling the ratio of the density difference between the two layers to their average density (Stokes 1847).

Two-layer stratification form one *end member* of the general class of density-stratified fluids. These are quite common in natural conditions, and occur for miscible fluids too. In shallow seas they form due to a combination of wind and tidal mixing that stir warm surface and cold bottom layers respectively, leaving a density jump at an interface in between. They also frequently occur near fjords, when fresh melt water spreads out over salty ocean water. It is in the latter situation that the existence and relevance of interfacial waves was first brought to light in an oceanographic context. These waves helped demystify the *dead-water* phenomenon encountered by Nansen at the end of the nineteenth century. Dead-water pertains to a sudden, sharp drop of a boat's speed when traversing a fjord (Nansen 1902). This loss of propulsion appears to occur when a boat's hull moves in the vicinity of an interface between low density fresh and high density salt fluid layers. When its velocity matches the interfacial wave speed it generates interfacial waves, leading the boat to suffer from excessive interfacial wave drag (Ekman 1904).

Wave Modes Versus Beams in Heterogeneous Fluids

Theoreticians also considered waves in three-layer, multi-layer, continuous and uniform stratifications (Rayleigh 1883; Burnside 1888; Love 1890). For internal gravity wave history, see the excellent review of Hinwood (1972). These waves are perturbations of a *hydrostatic equilibrium*,

$$(\rho_* + \rho(z))g = -\frac{dp}{dz}, \tag{2.3}$$

in which the downward-directed force of gravity, acting on fluid of local density consisting of a large constant ρ_* and a small depth-varying $\rho_0(z)$ part, balances the upward-directed pressure gradient force. This leads to a hybrid ensemble of boundary waves, propagating along interfaces, as well as, in the continuously-stratified fluid, to what could be called 'genuine internal waves'. The latter waves have their maximum displacements in the fluid interior and are not trapped to any particular interface. Initially, it was held expedient to assume the bottom to be parallel to the free surface, and consider a uniform-depth fluid. The benefit of this was that separation of variables was still possible, such that horizontally-propagating internal waves have a matching vertical structure. Approximating the surface as rigid, by requiring the vertical velocity to vanish at surface and bottom, the vertical modes are quantized by the finite depth. Indeed, this assumption on basin geometry and consequent

separability allowed for the computation of vertical modal solutions, even when the stratification was continuous yet non-uniform (Fjeldstad 1933; Groen 1948).

At the expense of a more fundamental, plane internal wave approach, that takes the form of an obliquely-propagating internal wave *beam*, this 'modal approach' subsequently dominated the interpretation and understanding of internal wave behaviour in the ocean. To be sure, the modal and beam approaches are reconcilable in uniform-depth, uniformly-stratified fluids, in which stability frequency $N(z)$ is assumed constant, a second *end-member* type of stratification. In Boussinesq approximation, the square of the stability frequency, $N^2 \equiv -g\rho_*^{-1} d\rho_0(z)/dz$, relates to the background density gradient. The beam's inclined orientation relative to gravity betrays that genuine internal waves propagate under a particular, fixed angle α, determined by the dispersion relation that perturbations satisfy:

$$\omega/N = \pm \cos\alpha. \tag{2.4}$$

In this case, angle α measures the direction of phase and group velocity vectors with respect to the horizontal and vertical, respectively. Assume the wave vector lies in the vertical (x,z)–plane in which the wave propagates, $\mathbf{k} = (k, 0, m) = \kappa(\cos\alpha, 0, \sin\alpha)$, then $\mathbf{c} = \omega\mathbf{k}/\kappa^2 = \omega\kappa^{-2}(k, 0, m) = \pm N \cos^2\alpha\kappa^{-1}(1, 0, \tan\alpha)$ (phase velocity) is perpendicular to group velocity vector $\mathbf{c_g} = \nabla_\mathbf{k}\omega = \partial_\alpha\omega\,\nabla_\mathbf{k}\alpha$, which evaluates to $\mathbf{c_g} = \pm N \sin\alpha\kappa^{-2}(m, 0, -k) = \pm N \sin^2\alpha\kappa^{-1}(1, 0, -\cot\alpha)$, although both share the same horizontal propagation direction.

The internal wave dispersion relation (2.4) betrays that a uniformly-stratified fluid is *transparent* to internal waves. 'Transparency' means that wave scattering occurs only at the boundary. Transparency can be maintained for some special non-uniform stratifications (Grimshaw et al. 2010). But to a good approximation it holds whenever the length scale over which the density gradient varies is large compared to the wavelength of the internal wave, so that $N = N(\varepsilon z)$, where ε denotes a small parameter and a WKB-approximation applies. For this situation, the inclination of a fixed-frequency ($\omega = constant$) wave can be obtained by a local application of the dispersion relation (2.4) and depth variations in amplitude and beam-inclination occur *adiabatically*, without any partial reflection or trapping inside the fluid (Hazewinkel et al. 2010b). This allows the vertical z-coordinate to be stretched, such that the equation describing the internal wave's spatial structure takes its canonical, hyperbolic form

$$\psi_{xx} - \psi_{zz} = 0. \tag{2.5}$$

Streamfunction $\psi(x, z)$ is introduced by virtue of two-dimensional incompressibility. Upon stretching the vertical, internal waves follow straight, inclined ray paths again. By contrast, when the density gradient varies rapidly, internal waves might also scatter inside the fluid on variations in the density gradient.

Internal Gravity Waves in Uniformly-Stratified Fluids

Adhering to the uniformly-stratified fluid in a basin of uniform depth, up and downward propagating beams of equal amplitude acquire a standing, sinusoidal vertical structure. Together with a complex exponential dependence on horizontal coordinate and time, these can obviously be interpreted as vertically-standing, horizontally-propagating modes. They present a seemingly straightforward extension of an interfacial wave. This interpretation however meets its limitations. It acquires horizontal, isotropic features due to depth-uniformity, which is lost in any real geophysical setting where depth variations scatter the incident beam.

Since an internal wave reflecting from a sloping bottom or side wall preserves its frequency, the dispersion relation implies that in this case the wave cannot change its wave vector inclination. This leads to anomalous, non-specular reflection. A single-frequency set of collinear waves differing in wave number magnitude and amplitude, defines an incident, compact wave beam of particular fixed inclination. This beam has a transverse width that will necessarily change when subject to *(de)focusing* reflections at an inclined boundary. Thus, depth-changes lead to a change of the wavelengths and amplitudes of the waves constituting the beam, see Fig. 2.6a. This precludes the persistence of a vertically-standing structure, built by beams of equal amplitude propagating in opposite vertical directions.

Converging Internal Waves and Wave Attractors

The ultimate fate of internal waves, generated by an oscillating cylinder, may not have been evident in the experiment shown in Fig. 2.6a. In confined basins, the focusing which internal wave beams experience upon bouncing at its boundaries, dominates

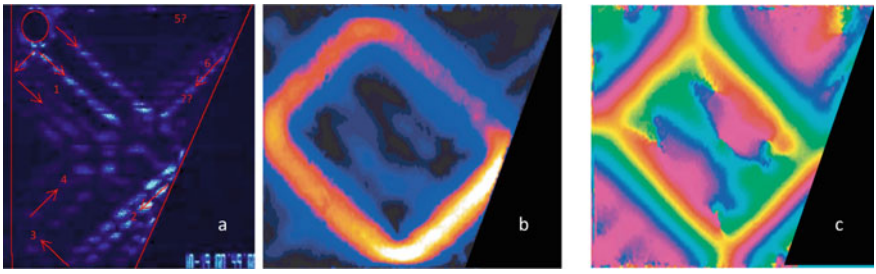

Fig. 2.6 Vertical transect of a uniformly-stratified fluid showing internal waves generated (**a**) by vertically-oscillating horizontal cylinder, located in the upper left (red circle) and **b**, **c** in a horizontally oscillating tank. The trapezoidal basin has rigid walls, both along the sloping and vertical side walls, as well as at top and bottom. (a) Arrows indicate the internal wave energy propagation direction. Successively reflected internal wave beams are numbered in sequential order. Courtesy of Frans-Peter Lam. **b** Amplitude (black: zero, white: most intense) and **c** phase (cyclic colors), adapted from Hazewinkel et al. (2010b)

over defocusing, leading to the formation of wave attractors, see Figs. 2.6b, c and 2.7a. Incident, focusing wave beams have larger scattering cross-sections than the reflected beams and *vice versa* for defocusing waves. Here the scattering cross-section refers to the width of the beam perpendicular to the energy propagation direction. The two are equal only for reflections from horizontal or vertical boundaries, which are parallel or perpendicular to the anisotropy direction. In that case the beam-width does not change upon reflection. Exceptionally, a net change of beam-width is also absent for special, nontrivially-shaped basins, when focusing of waves of particular frequencies (hence propagation angles) during some boundary reflections is exactly balanced by defocusing during other reflections. As a consequence, such basins possess a denumerable set of globally-resonant modes, see Fig. 2.7b. The latter property, exhibited for instance by trapezoidal domains, relies on the existence of residual symmetries (Maas and Lam 1995).

These situations can be interpreted geometrically by following individual characteristics (internal wave rays). Launching a ray from an arbitrarily located boundary point, upon reflection at any of the boundaries it will retain its inclination to the vertical. For these exceptional geometries and frequencies, after a number of reflections each ray path returns to its launching position and becomes part of a periodic orbit of finite length, forming a globally-resonant mode, see Fig. 2.7b. However, for all other frequencies in these basins—frequencies filling non-denumerable, continuous

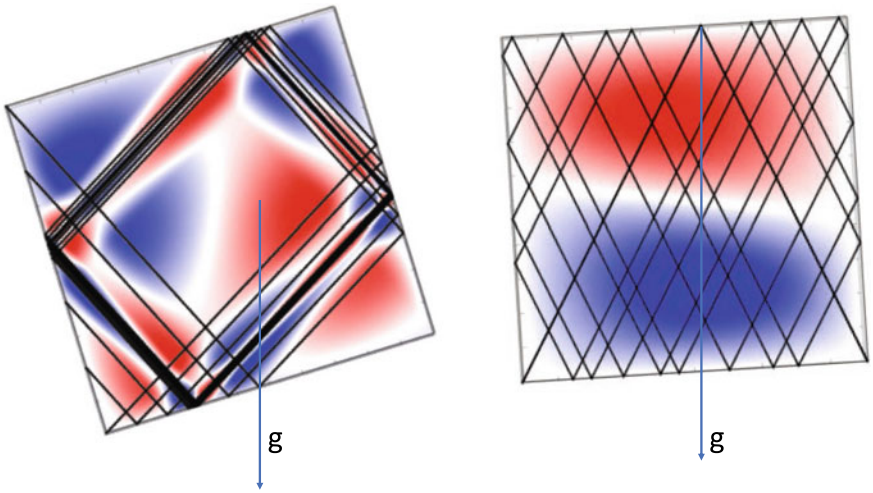

Fig. 2.7 Side view of internal gravity waves of two different frequencies in a uniformly-stratified fluid in a tilted square basin. Individual characteristics (lines) with which streamfunction field (color) is geometrically constructed (Maas and Lam 1995) retain their inclination relative to gravity, **g**, whose direction is indicated by an arrow. The generic response for arbitrary frequencies is given by wave attractors (left) and exhibits focusing of characteristics onto an attractor; the globally resonant modes (right) are exceptional, relying on periodicity of underlying individual characteristics. Courtesy of Stefan Kopecz

frequency bands—rays are non-periodic and infinitely long. Only a denumerable set of finite-length periodic orbits remains. These orbits attract all non-periodic orbits, see Fig. 2.7a where only one such attracting orbit exists.

For basins of generic shape that lack this residual symmetry, such as a parabolic basin, the basin shape breaks this residual symmetry too. There will be no exceptional frequencies, so no globally-resonant modes. Only a few periodic orbits remain, that attract all waves of a particular frequency. These limit cycles, *wave attractors*, are reached regardless of the wave's source location.

2.3 Inertial Waves

We will consider the implications of wave attractors later on, after taking a look at waves supported by shear flows, with, as important special case, the waves in swirling flows, and especially those in a solidly-rotating fluid. Owing to the anisotropy produced by rotation, combined with a symmetry-breaking basin shape, inertial waves supported by homogeneous-density, rotating fluids also show the presence of wave attractors.

2.3.1 Waves in Shear Flows

Homogeneous-density shear flows, $\mathbf{u} = (u, v, w) = (U(z), 0, 0)$, support waves which are stable manifestations of shear-flow perturbations. These form the complement of the much wider studied class of shear-flow instabilities (Drazin and Reid 1998; Carpenter et al. 2011). Since Squire's theorem asserts that two-dimensional perturbations turn unstable before three-dimensional disturbances do (Squire 1933) we consider two-dimensional, monochromatic plane wave perturbations $\propto e^{ik(x-ct)}$, governed by

$$\begin{aligned} ik(U-c)u + wU' + ikp &= 0, \\ ik(U-c)w + p' &= 0, \\ iku + w' &= 0, \end{aligned} \tag{2.6}$$

where a prime denotes a z-derivative. We describe these perturbations on a shear flow in terms of a streamfunction, $\psi = \Psi(z)e^{ik(x-ct)}$, that vanishes at the bottom and surface, $z = z_{1,2}$. Inserting perturbation velocities in these equations, $u = \partial\psi/\partial z$, $w = -\partial\psi/\partial x = -ik\psi$, yields Rayleigh's stability equation (Rayleigh 1879)

$$(U-c)\left(\frac{\partial^2\Psi}{\partial z^2} - k^2\Psi\right) - U''\Psi = 0. \tag{2.7}$$

Infer the stability of the shear flow by assuming that the frequency and thus phase speed is complex, $c = c_r + ic_i$. The presence of a non-zero imaginary part, c_i, signals

instability. Dividing (2.7) by $U - c$, multiplying by the complex-conjugate, Ψ^*, integrating between bottom and (rigid) surface (using integration by parts for the first term) and separating the real and imaginary parts, the latter is given by

$$c_i \int_{z_1}^{z_2} \frac{U''}{|U-c|^2} |\Psi|^2 \, dz = 0.$$

Parallel shear flows are stable ($c_i = 0$) when its background vorticity gradient U'' does not switch sign within the channel (Rayleigh's stability criterion). We will see an example shortly.

Waves in a Linear Shear Flow

A simple type of shear flow, a Couette flow, $U(z) = z$, lacking any curvature, $U'' = 0$, also supports waves propagating down a channel, $-1 \leq z \leq 1$, provided at some depth within the channel, z_c, the phase speed matches the background flow, $c = U(z_c)$: a critical layer. In this case, (2.7) is written (Drazin and Reid 1998)

$$\frac{\partial^2 \Psi}{\partial z^2} - k^2 \Psi = \delta(z - c), \tag{2.8}$$

allowing for exponentially-decaying waves on either side of the critical depth, $z_c = c$, and appropriately vanishing at the boundaries

$$\begin{aligned} \Psi(z) \propto \sinh k(c-1) \sinh k(z+1), \; -1 \leq z \leq c \\ \sinh k(c+1) \sinh k(z-1), \; c \leq z \leq 1. \end{aligned} \tag{2.9}$$

For any horizontal wave number, k, and any phase speed $|c| < 1$, this admits a continuous spectrum of waves, all trapped to their respective critical-depth. In a sense these all again belong to the class of isotropic boundary waves, as they decay exponentially away from the critical layer and do not propagate into the transverse z-direction.

For shear flows possessing curvature, a similar type of external wave exists at depth z_s where the shear flow has an inflection point, $U''(z_s) = 0$. Waves that propagate at a speed matching the local velocity at that depth, $U(z_s) = c$, can again be trapped at the critical layer $z = z_s$. But, in addition to waves belonging to the continuous spectrum, a discrete set of vertically-standing waves exists as we will see in the next subsection.

Waves in a Sinusoidal Shear Flow

Consider for example waves on a sinusoidal shear flow, $U = \sin z$, in a channel bounded by lines $z = z_{1,2}$, having, $z_1 \leq 0 \leq z_2$. This flow has an inflection point at $z = z_s = 0$. Then, for $c = 0$, its second derivative matches the prefactor of the first term in (2.7), and this equation factors into

$$\sin z \left(\frac{\partial^2 \Psi}{\partial z^2} + (1 - k^2)\Psi \right) = 0. \tag{2.10}$$

With the boundary conditions

$$\Psi = 0 \text{ at } z = z_1, z_2, \tag{2.11}$$

this equation has solutions

$$\Psi_s = \sin\left(n\pi \frac{z - z_1}{z_2 - z_1} \right), \quad k = \sqrt{1 - \frac{n^2\pi^2}{(z_2 - z_1)^2}}, \tag{2.12}$$

which are unstable, growing spatially (k imaginary) for integer $n > (z_2 - z_1)/\pi$. This shows that a finite number of neutral (wave) modes exist when $z_2 - z_1 > \pi$. This provides a counter-example to Rayleigh's criterion, showing that the presence of an inflection point is a necessary but not sufficient condition for all modes being unstable (Drazin and Howard 1962).

A channel lacking inflection points, $U''(z) \neq 0$, $z_1 \leq z \leq z_2$, is thus neutrally stable (i.e. c has zero imaginary part). It therefore still supports a discrete spectrum of neutral waves when $U(z)$ is concave and $U''/(U - c) < -k^2 < 0$. Concavity means that for any z in any part (z_-, z_+) of the fluid domain, where $z_1 \leq z_- \leq z \leq z_+ \leq z_2$, the average of the velocities at the end points of this interval is less than the velocity at any intermediate position, $|(U(z_+) + U(z_-))/2| < |U(z)|$. In a frame of reference moving with the waves, around the location where the phase speed matches the mean flow, the combined shear flow and waves manifest themselves in the form of Kelvin's 'cat-eye' flow pattern.

In these considerations, the effects of viscosity have sofar been left aside, the reason being that intuition would assign to viscosity an additional ability to stabilize wave motions. However, the contrary was proven to be true. As Darrigol (2005) recalls, Prandtl suspected that viscous stresses may induce a phase difference between wall-parallel and wall-transverse velocity components. In that case, energy, conveyed by the unperturbed mean flow U to the waves through Reynolds stress acting on mean-flow shear, might exceed viscous damping, leading to their instability and growth. This renders experimental study of stable waves on shear flows difficult if not impossible. Attention has thus shifted to the nonlinear regime, where large-amplitude waves may coexist with turbulence (Sun et al. 2015)), often in the form

of a self–sustained interaction of shear-flow perturbations with stream wise rolls (Waleffe 1997).

The geometry of the fluid basin receives little attention in these studies. In two-dimensional (x, z) settings, the shear flow $U(z)$ is compatible only with a uniform-depth channel having its boundaries at $z_{1,2} = constant$. But a consideration of geometry becomes pertinent when discussing waves on shear flows in three-dimensional domains, for which the *transverse* channel shape, $z = h(y)$, may become important. We will discuss the relevance of transverse topography in the context of axisymmetric shear flows in the next section.

Waves in Swirling Flows

In a *non-rotating*, cylindrical (r, θ, z) frame of reference, a special type of shear flow develops: a swirling flow. This is characterized by an axisymmetric, azimuthal flow of arbitrary radial dependence, $u_\theta = V(r)$, which is in *cyclostrophic balance*:

$$-\rho \frac{V^2}{r} = -\frac{dp}{dr}. \tag{2.13}$$

The outward directed centrifugal force is balanced by an inward directed pressure gradient force. Axisymmetric, monochromatic perturbations of this radially-dependent azimuthal flow allow for the introduction of a Stokes streamfunction, $\psi(r, z, t)$, as incompressibility implies that radial and vertical velocities can be obtained from $ru = \partial\psi/\partial z,\ rw = -\partial\psi/\partial r$. At this point the underlying cyclostrophic equilibrium state, (2.13), is lost out of sight, not only because the perturbation pressure is described by differences between the actual and the cyclostrophic pressure, but also because this perturbation pressure itself has been eliminated when deriving a vorticity equation by cross-differentiation and subtraction of the horizontal momentum equations. However, its importance will be stressed in Sect. 2.4.3, when discussing the implications that waves may have for mean flows.

The streamfunction's spatial part, $\psi = \Psi(r, z)e^{-i\omega t}$, is governed by

$$r\frac{\partial}{\partial r}\left(\frac{1}{r}\frac{\partial}{\partial r}\right)\Psi - \left(4\frac{\Omega_l^2}{\omega^2} - 1\right)\frac{\partial^2\Psi}{\partial z^2} = 0, \tag{2.14}$$

where Rayleigh's discriminant,

$$4\Omega_l^2(r) \equiv \frac{1}{r^3}\frac{dA^2}{dr} = 2\frac{V}{r}\left(\frac{V}{r} + \frac{dV}{dr}\right), \tag{2.15}$$

is, unconventionally, expressed as the square of the *local* Coriolis frequency, $2\Omega_l(r)$. This is twice the local rotation rate, Ω_l, that reduces to the constant rotation rate, Ω, in the case of solid-body rotation, $V = \Omega r$. Rayleigh's stability criterion, $\Omega_l^2(r) \geq 0$ for all r, implies that the square of the angular momentum, $A \equiv rV(r)$, must increase

monotonically with increasing radius (Rayleigh 1917). The square on A in (2.15) indicates that this criterion is insensitive to the direction of background rotation. For waves of frequency $|\omega| < 2|\Omega_l|$, the governing Eq. (2.14) has a negative sign in front of the last second-order derivative, which makes it a hyperbolic equation. This implies it supports a type of internal wave, called inertial or gyroscopic wave, discussed further in the next section. Inertial waves are, for example, observed in the swirling flow of liquid metal, when driven by a rotating and alternating electromagnetic field (Vogt et al. 2014).

In general, the r-dependence of the Rayleigh-discriminant implies these inertial waves are subject to scattering, trapping and tunnelling. The explicit, curvature-related radial dependence of the first term of (2.14) leads to additional amplitude variations. But an axisymmetric basin of maximum radius a and arbitrary axisymmetric depth profile $h(r)$ supports a cylindrically-rotating shear flow, described by

$$V = \sigma \frac{r^2}{a}. \tag{2.16}$$

This has local rotation rate

$$\Omega_l = \frac{\sqrt{6}\sigma}{2}\frac{r}{a} \tag{2.17}$$

and is transparent to low-frequency waves if $\omega \ll \sqrt{6}\sigma$. Transformed dimensionless radial, $s = r^2/2a^2$, and (stretched) vertical, $Z = z/H$, coordinates absorb the amplitude-decrease due to radial spreading. Here

$$H = \frac{a\sqrt{6}\sigma}{\omega}.$$

This transforms (2.14) into the canonical equation governing the spatial structure of monochromatic internal waves

$$\frac{\partial^2 \Psi}{\partial s^2} - \frac{\partial^2 \Psi}{\partial Z^2} = 0. \tag{2.18}$$

In basins of arbitrary radial shape, the method of characteristics can solve this equation (Maas and Lam 1995). It is prone to develop wave attractors for nearly all boundary shapes, $Z = h(s)/H$.

2.3.2 *Waves in Rotating Basins*

To describe perturbations, azimuthal flows $V(r)$ that possess arbitrary radial dependency do not favour any particular rotating coordinate frame over the inertial frame. However, when the flow is in solid-body rotation, $\Omega = constant$, and the azimuthal flow increases linearly with radius, $V = \Omega r$, it makes sense to use a frame of ref-

erence co-rotating with the flow. A transformed time-derivative then absorbs the advective terms and, as mentioned before, the Rayleigh discriminant becomes constant, $4\Omega_l^2 = 4\Omega^2$. In a cylindrical domain, this leads to separability of (2.14). A sinusoidal vertical dependency of Ψ splits-off from its radial, Bessel function dependence (Kelvin 1880). Requiring regularity at the origin, vanishing of Ψ at the cylinder boundaries, and periodicity in the azimuthal direction, together with impermeability constraints at top and bottom boundary, leads to a triple quantisation of these radial-azimuthal-vertical modes.

Intermezzo: Viscous Effects

When an axisymmetric, closed cylindrical domain is put into steady rotation, a solid-body rotating state is reached from the initial state of rest through a spin-up process. In axisymmetric basins this involves viscous Ekman boundary layers that transport momentum to the inviscid interior by means of a meridional circulation (Greenspan and Howard 1963; Weidman 1976). In non-axisymmetric basins, such as an *eccentrically*-positioned cylinder, or a basin of different shape, the fluid needs to respond 'instantaneously' when set into rotation. This is caused by a pressure torque which, in the incompressible description, transmits at once throughout the fluid domain. This is an approximation employed when pressure waves, propagating at the speed of sound, are much faster than any of the velocities involved. In this type of basin, the fluid's initial response is governed by vorticity conservation. The fluid aims to retain its initial state of zero absolute vorticity (Van Heijst 1989; Van Heijst et al. 1990)), so that, in the frame co-rotating with the container, it is initially described by a vortex having uniform anticyclonic vorticity. At later stages the flow is subject to viscous adjustment, due to friction at side-walls, bottom and top, occurring at the Ekman time scale, $E^{-1/2}\Omega^{-1}$, where Ekman number $E \equiv \nu/L^2\Omega \ll 1$ is defined in terms of kinematic molecular viscosity, ν, length scale, L, and time scale Ω^{-1}. During this phase, cyclonic vorticity develops. When the depth of the fluid is constant these processes lead to an arrangement of nearly circular cyclonic and anticyclonic cells that gradually decay on the still longer, diffusive timescale $E^{-1}\Omega^{-1} = L^2/\nu$. When the container depth varies, however, these cells keep on moving in an irregular fashion, and Ekman spin–up seems to be faster in the shallower parts of the fluid domain (Van Heijst et al. 1994; Li et al. 2012).

Linearized Rotating Euler Equations

For any boundary shape of a rotating container, $y = y_b(x)$, and for any location of the container relative to the rotation axis, solid-body rotation can be achieved (Van Heijst et al. 1994; Li et al. 2012). Viewed from the rotating, axial frame of reference, after spin-up, the fluid is in an apparent state of rest. In this steadily-rotating state, when fluid and bounding container move as a solid body, the effects of rotation and viscosity may no longer be visible. Yet, at any point within the fluid domain, the apparently

quiescent fluid retains a memory of the rotation. This is present in an exact balance of radially-outward centrifugal and radially-inward pressure gradient forces. Perturbing this quiescent state creates an imbalance which expresses itself in a combination of restoring Coriolis and pressure gradient forces that support *inertial waves*. These are the internal waves of a homogeneous-density, rotating fluid. They can be described in a uniformly-rotating Cartesian frame by the constant-coefficient, inviscid rotating linearized Euler equations

$$\begin{aligned} u_t - fv &= -p_x, \\ v_t + fu &= -p_y, \\ w_t &= -p_z, \\ \nabla \cdot \mathbf{u} &= 0. \end{aligned} \tag{2.19}$$

Here we use Cartesian velocity vector $\mathbf{u} = (u, v, w)$ and Coriolis parameter, $f = 2\Omega$, again assuming that the vertical z-direction aligns with the rotation axis. The *reduced* pressure p, contains deviations of the true pressure from the combined hydrostatic and cyclostrophic pressure, given by (2.3) and (2.13), respectively. Searching for monochromatic plane-wave solutions, $\propto e^{i(kx+ly+mz-\omega t)}$, with polar representation of wave vector $\mathbf{k} = (k, l, m) = \kappa(\cos\alpha\cos\phi, \cos\alpha\sin\phi, \sin\alpha)$, yields the inertial wave dispersion relation

$$\omega = \pm 2\Omega \sin\alpha, \tag{2.20}$$

which, as for internal gravity waves, is independent of wave vector magnitude κ. Indeed, this equation relates frequency to wave vector inclination relative to the horizontal plane, α, only. This is the hall-mark of internal waves. It complements the frequency—wave number, $\omega(\kappa)$, relationship typical for external waves.

The adjustment of fluids during spin-up or spin-down in basins of non-uniform depth, referred to above, is partly expressed by the inertial waves, described by (2.19). But, in fact, inertial waves arise under adjustment of the rotation rate in any container (Greenspan and Howard 1963; Cederlöf 1988; Oruba et al. 2017), whether forced by viscous or pressure forces. They especially occur when a container is deliberately forced at a frequency less than the Coriolis frequency, for instance by libration—a periodic modulation of the background rotation rate—or, as in nature, by tidal forces, when these waves are sustained (Maas 2001; Manders and Maas 2003, 2004; Bewley et al. 2007; Lamriben et al. 2011; Sibgatullin et al. 2017).

Inertial Waves in an Untilted Box

To solve (2.19) for free inertial waves in a rectangular box that has its sides either perpendicular or parallel to the rotation axis, we use depth H and Coriolis frequency $f = 2\Omega$ as length and inverse time scales (with velocity and reduced pressure scales equaling Hf and $(Hf)^2$, respectively). Note this implies that horizontal dimensions of the box are now measured in terms of H. This leads to the same set (2.19), except that now $f = 1$ and the bottom and surface of the rectangular box are at $z = 0, 1,$

respectively. As the normal velocities at these boundaries vanish, $w(0) = w(1) = 0$, the vertical velocity is expressed as a sum of vertically-standing modes, $w = \sum_{n=1}^{\infty} \partial\zeta_n/\partial t \sin n\pi z$, with ζ_n the vertical displacement field of the nth vertical mode. In turn, this implies $(u, v, p) = \sum_{n=1}^{\infty}(U_n, V_n, P_n)\cos n\pi z$. The vertical momentum equation then yields

$$P_n = \frac{1}{n\pi}\frac{\partial^2\zeta_n}{\partial t^2}. \tag{2.21}$$

Rescaling the horizontal coordinates $(X, Y) = n\pi(x, y)$, the *same* set of equations describes the horizontal structure of each of the modes, for which reason we suppress mode-index, n. In subscript-derivative notation these read (Maas 2003):

$$\begin{aligned} U_t - V &= -\zeta_{ttX}, \\ V_t + U &= -\zeta_{ttY}, \\ \zeta_t + U_X + V_Y &= 0. \end{aligned} \tag{2.22}$$

This set resembles the RSWEs (2.1), except that acceleration of the inertial wave vertical displacement field of mode n,

$$\frac{H}{n\pi}\frac{\partial^2\zeta_n}{\partial t^2}, \tag{2.23}$$

replaces gravitational acceleration multiplying the free surface displacement, $g\zeta$, which represents the reduced pressure of external, long surface gravity waves, giving due attention to the different meanings of ζ. Each mode obeys the same set of Eqs. (2.22), but finds the box's horizontal size to become larger as n increases. Clearly, as the nth mode scales with the decreasing depth scale, $1/n\pi$, the box's fixed horizontal size, L, increases for this mode to $L_n = n\pi L$.

Inserting plane-monochromatic waves $\propto e^{i(kX+lY-\omega t)}$ into (2.22) yields the dispersion relation

$$\omega^2 = \frac{1}{1+k^2+l^2} = \frac{1}{1+\kappa^2}. \tag{2.24}$$

Its right-hand side is the reciprocal of that for the RSWEs, (2.2). The Coriolis frequency now appears as *high-frequency* instead of low-frequency cut-off. Vertically-standing inertial modes, again behave as external waves, as their frequency now relates to wave vector magnitude of the horizontal wave vector, $\mathbf{k} = (k, l) = \kappa(\cos\phi, \sin\phi)$, like the vertically-standing internal gravity wave modes in a heterogeneous (especially, uniformly-stratified) fluid in a channel or box. As before, however, this apparent external nature of standing internal waves is superficial, owing to the particular orientation of the box, namely with its boundaries perpendicular or parallel to the rotation axis. Before investigating the true nature of inertial waves, which shows up when breaking this symmetry, we should mention how to determine the horizontal structure of inertial waves of this 'untilted' box.

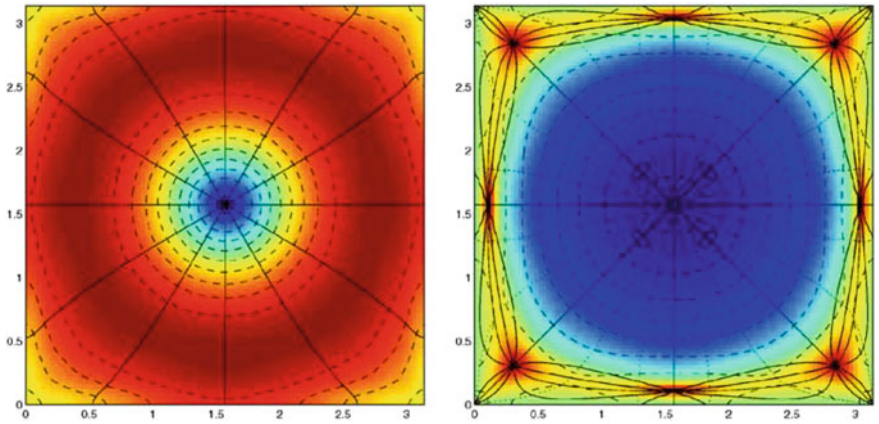

Fig. 2.8 Top view of inertial waves in a cube for the lowest-vertical, lowest-horizontal mode (highest subinertial frequency) of nominal dimensionless frequency $\omega \approx 2^{-1/2}$. Vertical displacement field amplitude (dashed) and phase (solid) (left) and velocity field (right, anticyclonically rotating current vector in blue; cyclonic in red; rectilinear, at walls, in green). For further explanation, see Maas (2003)

Proudman (1916) solved the RSWEs governing the rotationally-modified surface gravity waves in a box by using a Helmholtz decomposition of the horizontal velocity field,

$$\mathbf{u} = -\nabla\phi + \mathbf{e_z} \times \nabla\psi. \tag{2.25}$$

The velocity field is a sum of derivatives of a potential, ϕ, and streamfunction field, ψ. The challenge is to meet impermeability constraints at the box's vertical boundaries. Two-dimensional internal gravity waves need Dirichlet (zero streamfunction) conditions, and three-dimensional internal gravity waves Neumann (zero normal pressure derivative) conditions. Instead, rotationally-modified surface gravity waves require oblique-derivative boundary conditions. In this respect, inertial waves are more complicated than internal gravity waves. The latter execute rectilinear particle motions (within inclined beams), while, in linear approximation, the former follow inclined circular paths. Obviously, in an inviscid description, a side wall can be inserted when it is aligned with the internal gravity wave beam direction. But, circular particle paths, present in an inertial wave beam, are incompatible with any kind of side wall. Clearly, even in the inviscid approach, side walls must give rise to an adjustment of the inertial wave beam's velocity field, suggesting the presence of inviscid, 'wavy' boundary layers.

Proudman's method can also be used to determine the horizontal velocity, (U, V), and vertical displacement, ζ, of the vertically-standing inertial wave field. It leads to a generalized eigenvalue problem, which solves for eigenmodes of decreasing frequency and increasing spatial complexity, see Fig. 2.8. Indeed, as for the RSWEs, amphidromic systems are found (Maas 2003). This includes the fact that each phys-

ical mode (each eigenfrequency) contains an infinite series of Fourier modes, that is, an infinite set of scales, see in particular the corner regions in Fig. 2.8b. The fact that inertial waves are *scale-free* is exploited. The dispersion relation does not constrain the wave number. The interesting difference with rotationally-modified surface gravity waves is that, instead of just a single mode, inertial waves possess an infinite set of vertical modes. This means we might suspect eigenfrequency degeneracy: the eigenfrequency for mode n may be identical to that of another vertical mode m (which perceives the same horizontal domain as being m instead of n times its original horizontal size). The fundamental, beam-like nature of the inertial waves suggests degeneracy. The generalized eigenvalue problem has to be solved numerically. Therefore, a proof that the very same eigenfrequencies will show up for different vertical modes, true for two-dimensional anisotropic as well as for three-dimensional internal gravity waves (Maas 2003), stays a conjecture. In the case of a rotating cube, near-degeneracy is found for waves asymptoting at frequency $1/\sqrt{2}$, but this is no proof of finding the same eigenfrequencies (Wu et al. 2018) .

Inertial Waves in a Tilted Box

Adding an inclined sidewall (Maas 2001), tilting a rectangular box (Ogilvie 2005; Maas 2007), or changing the orientation of boundaries relative to the rotation axis' direction in other ways, implies that, as internal gravity waves, inertial waves will also be subject to focusing and defocusing reflections. In confined, two-dimensional fluid domains this leads to wave focusing dominance. Frequency-dependent orbits again appear to attract waves, regardless where they originate from. Bretherton (1964) inferred that inertial waves approach periodic orbits, giving a geometrical interpretation to prior analytical results by Stern (1963). Stern (1963) described waves in a homogeneous, rotating fluid confined to the equatorial region of a spherical shell, neglecting the vertical acceleration but retaining nontraditional (horizontal) Coriolis terms and noticing the presence of waves decaying polewards, see Maas (2001), Maas and Harlander (2007), Gerkema et al. (2008). Bretherton's (Bretherton 1964) periodic orbit is attracting (Stewartson 1971) and such wave attractors appear to form a broadband phenomenon (Israeli 1972): they exist in continuous frequency bands in which wave attractors have the same topology, experiencing the same amount of reflections at their boundaries. In such frequency windows, attractors have the same *winding number*, the same average angular progression during a single winding around the attractor (Manders et al. 2003). The winding number therefore acts as a topological invariant (Delplace et al. 2017). Instead of fixing the geometry and changing the frequency, this topological property can also be understood from a reverse perspective. Take for example the attractor in the left panel of Fig. 2.7 and keep the frequency, and therefore inclination fixed. Keeping also the attractor's four reflection points at the boundary fixed in space one can otherwise deform the remaining part of the boundary in whatever way one likes, and the attractor will persist as a limit cycle (John 1941). Different boundary deformations lead to differences in convergence rates (measured by the Lyapunov exponent), not in winding number. However, rectangles that are not

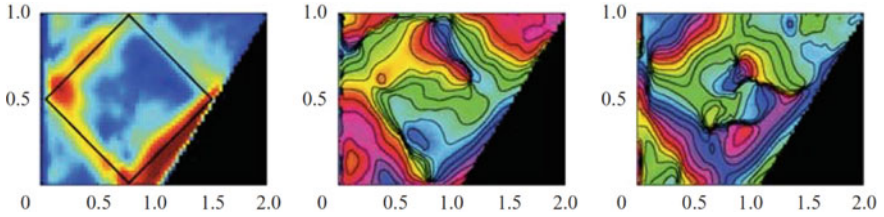

Fig. 2.9 Side view of inertial waves in a trapezoidal basin forced by the libration of a rotating tank. The modulation frequency aims at hitting a square-shaped attractor (solid lines). Visualisation of motions in a vertical sheet, a projection of the three-dimensional currents, is by means of Particle Image Velocimetry. Shown are current amplitude (left) and the phases of the two counter-rotating circular currents (middle and right) into which the current ellipses can be decomposed in the viewing plane. Notice phase lines parallel to attractor branches, indicating transverse phase propagation. For further explanation, see Manders and Maas (2003)

tilted remain exceptional. Ironically these are precisely the geometries favoured in textbooks for being solvable by the method of separation of variables. Lacking the generic appearance of wave attractors, these unfortunately give the completely false suggestion of overall regularity.

The interaction of inertial waves with sloping boundaries was studied experimentally in quasi two-dimensional, Cartesian settings, such as in trapezoidal rectangular basins (Maas 2001; Manders and Maas 2003, 2004; Brunet et al. 2019), see Fig. 2.9, in cylindrical settings such as a conical basin—a frustum—(Klein et al. 2014), and in spherical shells (Koch et al. 2013; Hoff et al. 2016a, b). In all cases, inertial waves, forced by libration of a tank, focus onto 'low-period wave attractors', attractors having the shortest length. Numerical studies, usually of a viscous nature, address the saturation of the amplitude-increase accompanying wave focusing. Saturation, both of focused internal gravity as well as inertial waves, is either due to the appearance of viscous, free boundary layers around the attractor (Rieutord and Valdettaro 1997; Dintrans et al. 1999; Rieutord 2001; Hazewinkel et al. 2008), or to the transfer of energy to other wave frequencies by nonlinear interactions when the fundamental wave experiences Triadic Resonant Instabilities (TRI) (Dauxois et al. 2018).

2.3.3 Three-dimensional Effects

While most studies have concentrated on quasi two-dimensional settings, whether in Cartesian, cylindrical or spherical geometries, inertial waves likely develop three-dimensional fine structure. This is already evident in the horizontal cross-sectional velocity field near the corners of the planar (untilted) box, see Fig. 2.8b. When basin shapes additionally break the reflectional symmetry of the obliquely propagating inertial waves, as in the tilted box or trapezoidal basin, it is a priori clear that wave attractors, located in planes perpendicular to the sloping sides, must adapt to the

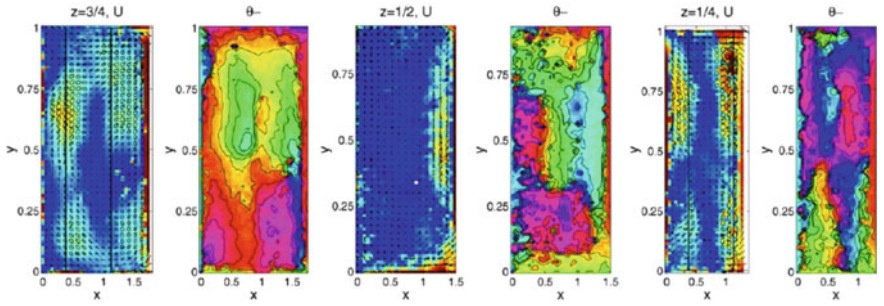

Fig. 2.10 Top view of observed velocity amplitude (U) and anticyclonic phase (θ_-) patterns of inertial waves in a homogeneous fluid contained in a trapezoidal basin. The tank has its sloping side, $z = x - 1$, at the right, for $1 \leq x \leq 2$. Shown are measurements at three heights: ($z = 3/4$, left two panels; $z = 1/2$, middle two panels; $z = 1/4$, right two panels). Inertial waves are forced by libration of the rotating tank. The libration frequency is such that in an infinitely-long trapezoidal basin the inertial wave would approach a rectangular-shaped attractor that intersects these levels at locations indicated by solid black lines. Velocities are dominated by anticyclonic motions. For further explanation, see Manders and Maas (2004)

presence of front and end side-walls. To phrase this differently, while inviscid internal gravity waves in a uniformly-stratified fluid are perfectly able to focus onto a set of wave attractors, all oriented perpendicular to the sloping boundary of a trapezoidal basin, so that their combined structure—the structure of a two-dimensional attracting manifold—is invariant in the along-slope horizontal direction, see Pillet et al. (2018), this is not possible for inertial waves in the same basin. The attracting manifold must change its form, or even its presence, when approaching the front and end walls. An experimental study, aimed at elucidating its structure, found the inertial wave attractor to become more intense but also squeezed on approaching the end walls, see Figs. 2.10 and 2.11. Moreover, wave energy slightly concentrated on the side of the trapezoidal basin that would, from a topographic Rossby wave perspective and given the presence of a sloping bottom, be associated with 'West'.

Other indications for nontrivial behaviour in three-dimensions comes from ray patterns. While rays and characteristics are often considered identical, correct in two-dimensional Cartesian settings, this is not true in three-dimensional or axisymmetric (quasi two-dimensional) domains. For this reason, in contrast to the two-dimensional case of a globally resonant mode, shown in Fig. 2.7b, in a spherical shell globally-resonant modes are not associated with periodicity of all characteristics (Rieutord et al. 2001). Curvature of the boundary implies that in the governing equation the leading second-order operator's characteristics are not identical to energy paths. Yet, this identification works well on small scales where curvature effects are negligible.

The dynamics of internal and inertial wave rays is interesting. The non-specular type of reflection experienced by rays propagating in a plane normal to a sloping bottom or side wall, leading to their focusing or defocusing, also affects the reflection of *obliquely* incident rays. By its elegance, Phillips' derivation of the reflection process of obliquely incident rays, formulated in an *inclined* plane defined by incident

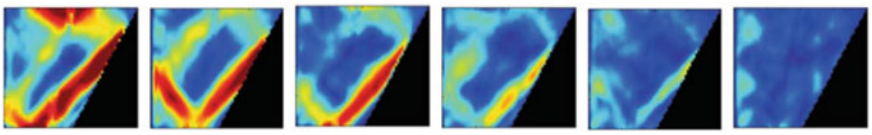

Fig. 2.11 Side views of velocity amplitude (U) measured at six different transects, from left to right at $y/L = 0.12, 0.18, 0.24, 0.30, 0.36, 0.42$ respectively. Notice the elongated character of the attractor close to the side wall at $y = 0$. Picture adapted from Manders and Maas (2003)

and reflected rays (Phillips 1963), obscures somewhat the *instantaneous refraction* accompanying focusing or defocusing reflections: a sudden change in horizontal propagation direction. Describing wave reflection instead in a frame-of-reference whose vertical axis is parallel to the anisotropy direction set by gravity or rotation axis, refraction is seen to occur simultaneously (Maas 2005). Interestingly, in three dimensions focusing of multiply-reflected wave rays onto a wave attractor in a vertical trapping plane is accompanied by another phenomenon that resembles ray behaviour in whispering galleries. Some rays avoid trapping onto a wave attractor by experiencing a sequence of focusing reflections that are exactly balanced by defocusing reflections. Reflection locations hug the line of critical depth, defined as the line connecting depth locations where ray slope equals bottom slope, see Fig. 2.12 (Maas 2005; Rabitti and Maas 2013; Pillet et al. 2019).

2.4 Discussion

The isotropy or anisotropy of a fluid depends on (i) the presence of an anisotropic restoring mechanism, such as gravity, system-rotation, or the presence of a magnetic field, so far undiscussed, (ii) a stratification of the fluid, such as in density or angular momentum, and (iii) the presence of inclined boundaries relative to the anisotropy direction.

The third aspect turns out to be vital. For even when a fluid's density is discretely-stratified in layers, and one might expect interfaces separating the layers to act as horizontal wave guides, see Sect. 2.2.2, or scatter obliquely incident waves into reflected and transmitted oblique waves, experiment shows otherwise (Hazewinkel et al. 2010a). In a fluid having twenty stratified layers of equal depth, differing incrementally in density and confined to a trapezoidal basin, a wave attractor of rectangular shape still forms, see Fig. 2.13. It is very similar in shape to the one found in the uniformly-stratified fluid, as visible in Fig. 2.6. The attractor shape becomes less visible when the number of layers is for instance halved (not shown).

The presence of restoring mechanisms allows us to define equilibrium states, in which a restoring force balances a pressure gradient force, such as the hydrostatic (2.3) and cyclostrophic (2.13) equilibria for density-stratified and rotating,

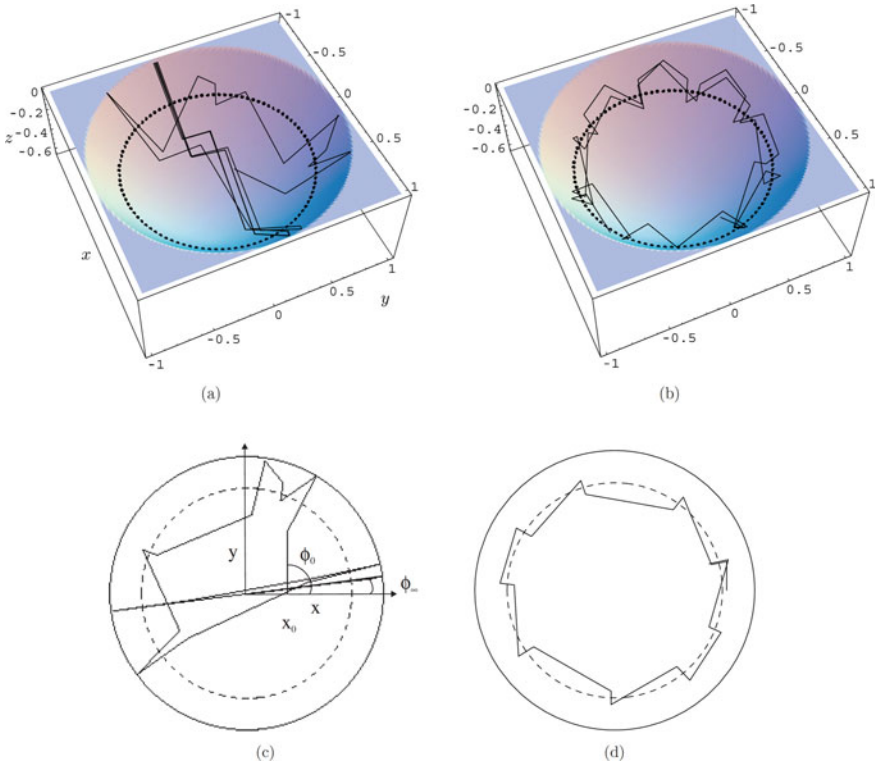

Fig. 2.12 Perspective (**a**, **b**) and top (**c**, **d**) views of rays launched in a uniformly-stratified fluid, confined to a paraboloidal container, either focusing onto a wave attractor (a,c) or propagating around in a whispering-gallery type of motion (b,d). The dashed circles shows critical depths, where bottom slope equals ray slope, determined by the ratio of wave and buoyancy (or Coriolis) frequencies. Picture adapted from Maas (2005)

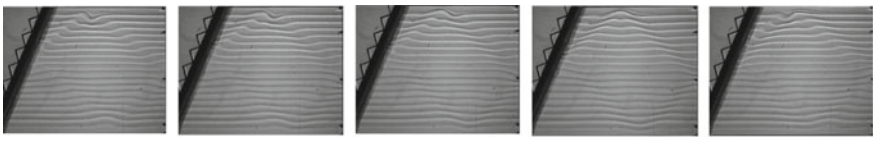

Fig. 2.13 Five subsequent snapshots of a video showing side views of a fluid that is discretely-stratified and that is being oscillated sideways periodically. The fluid contains twenty layers that are incrementally increasing in density downwards. Displacements of interfaces are visualized by shadowgraph. Picture adapted from Hazewinkel et al. (2010a)

homogeneous-density fluids, respectively. In plasmas, the presence of magnetic fields similarly invokes an equilibrium, described by the Grad-Shafranov equations (Goedbloed et al. 2019).

2.4.1 The Linear Shear Flow as 'Problematic' Equilibrium

Notice that waves in shear flows stratified in *linear* momentum, differ from those encountered in fluids stratified in density or angular momentum. Their existence is somewhat of a mystery (Hof et al. 2004). Despite the fact that rectilinear shear flows formally appear as stable solutions of the Euler equations, one cannot pinpoint an equilibrium state consisting in a similar balance of forces that, once disrupted, provides a restoring mechanism. Indeed, regarding the Euler equations as an asymptote of the Navier-Stokes equations in the limit that the Reynolds number $R = UL/\nu \to \infty$ approaches infinity (viscosity $\nu \to 0$), this limiting process, viewed as a state undergoing a large number of bifurcations while increasing the Reynolds number, generates more and more unstable solutions that should necessarily end in turbulence. This relates to the fact that particular classes of waves in shear flows are found in a very circumspect way. This is often done by viewing the rectilinear shear flow either as the limit of a swirling flow inside an annulus, whose cylinders, rotating at different speed, possess radii approaching infinity, or as the limit of a stably-stratified fluid, in which the stratification rate decreases to zero. Conspicuously these exactly correspond to the two previously mentioned cases for which force balances *can* easily be defined. In practice, real viscous pipe flows turn unstable and become turbulent at moderate speeds, generating longitudinal rolls, interacting with subsequently bifurcated transverse circulation cells (Hof et al. 2004). Moreover, because waves that are trapped to a critical layer in a shear flow have a wave frequency depending on wave vector magnitude, these best classify as isotropic again, as the isotropy concept is synonymous with an absence of any wave frequency dependence on wave vector direction.

2.4.2 Waves in Anisotropic Media

By contrast, in anisotropic media wave frequency depends on wave vector direction only, implying that perturbations of hydrostatic and cyclostrophic equilibria are unproblematic. The differences between waves in isotropic and anisotropic media have far-reaching implications. Isotropic water waves, such as surface gravity waves or internal waves in uniform-depth fluids, exhibit focal points when reflecting from convex vertical boundaries (such as a parabolic mirror). However, focusing occurs temporarily. Upon passing a focal point, waves diverge. In confined fluid domains, multiple side-wall reflections of such isotropic waves lead to wave ray chaos. It explains why one can illuminate a cave with a single candle, or why in a popular restaurant, conversations may be lost in a cacophony.

By contrast, anisotropic internal gravity and inertial waves almost always follow an *indefinite* geometric focusing principle. This occurs when they reflect from sloping boundaries that are neither parallel nor perpendicular to the anisotropy direction. As a consequence, despite the fact that linear equations govern these waves, the

geometrically (Maas and Lam 1995) or analytically (Maas 2009) constructed wave solutions exhibit self–similarity in real, Fourier and parameter spaces, features that are normally associated with nonlinear dynamical systems. Also, while isotropic waves in closed basins exhibit a discrete set of eigenfrequencies, the spectrum of anisotropic waves becomes continuous. These and other complementary properties of isotropic and anisotropic waves are discussed in Maas (2005), Brouzet et al. (2017), Sibgatullin and Ermanyuk (2019).

2.4.3 Mixing Due to Wave Focusing and Mean Flows

Let us look at one final aspect of these anisotropic media and their equilibria, namely the impact of waves on the mean state. Perturbations to a balanced hydrodynamic state—waves—may locally provoke mixing. Waves in anisotropic fluids focus onto wave attractors for nearly every shape of the fluid basin. While focusing, along-attractor velocity and shear amplify, and scales reduce. Attractors are therefore locations where mixing of anisotropic fluids can be expected to occur preferentially, either by immediately reaching down to the Kolmogorov scales, where viscous processes can mix, by means of wave breaking due to secondary shear-flow instabilities, or via triadic-wave interactions.

In this manner, local diapyncal (vertical) mixing of a density-stratified fluid leads to horizontal density and pressure gradients that force a horizontal mean flow, so that the mixed fluid will spread out along isopycnal surfaces. As rotating fluids contain a huge amount of energy, stored in rotational motion, weak mechanical forcing can similarly convey part of this large-scale intense flows (Le Bars et al. 2015). But mixing of a homogeneous-density, rotating fluid must pertain to mixing of the 'stuff' the fluid is stratified with: angular momentum. The underlying equilibrium state is thus relevant. The apparently quiescent initial state of a fluid that is in solid-body rotation, i.e. in a frame co-rotating with the container, is radially-stratified in angular momentum. Despite the fact that the (nonlinear) Euler equations are invariant with respect to coordinate translation, they do depend on the rotation axis' *location*. In case the fluid has a free surface this is easily visualised. After the spin-up process, the fluid is in solid-body rotation and the free surface shape will become paraboloidal; to be more precise, a *segment* of a paraboloidal surface. A segment that may or may not contain the paraboloid's minimum, depending on whether or not the rotation axis passes through the container. When that axis lies outside the container, the free surface will have its minimum at the point closest to the rotation axis.

The presence of this paraboloidal surface resolves the chicken-and-egg question whether, away from the rotation axis, the pressure is high because the free surface level is raised in favour of a reversed causality: the free surface is high because the pressure is high. To fully contain the fluid, imagine we use a rigid-lid instead of a free surface. The pressure in this solidly rotating fluid must still increase radially-outward, as fluid continues to be swept outwards by the centrifugal force, and the cyclostrophic balance will persist. While in a rotating, quiescent fluid we can perfectly

well describe perturbations as being governed by the linear, rotating Euler equations, it transpires that, in the same way as we neglect viscous effects after the spin-up phase in these equations, we must also have been neglecting compressibility. Despite liquids being nearly incompressible, during spin-up compressibility must have played a role in setting the higher pressure at larger radii, made visible by the free surface displacement when taking away the rigid lid.

This is relevant to what happens when mixing occurs in a rotating fluid, for instance due to wave focusing. In analogy to the isopycnal spreading of fluid following mixing of density-stratified fluids, mixing of fluids stratified in angular momentum will lead to a mixture spreading out along iso-angular momentum surfaces. But, its subsequent fate depends on the topology of these surfaces relative to the shape and size of the basin. Obviously, axial cylindrical fluid domains—cylinders whose axes coincide with the rotation axis—are special, as all iso-angular momentum surfaces fully lie within the fluid domain. In the presence of a sloping bottom, any mixing triggered by geometric focusing near a wave attractor can then drive a mean flow along a cylindrical iso-angular momentum surface that sits in the container above the attractor's focusing location at the bottom. It is uninhibited by obstructing side walls. Recent experiments on focusing inertial waves confirm the generation of such an axisymmetric mean flow, which however turns unstable and produces a sequence of barotropic cyclones (Boury et al. 2021). But non-axisymmetric boundaries are obviously more generic. When cylindrical iso-angular momentum surfaces are not or not completely contained within the cylinder these lead to regions where iso-angular momentum surfaces are obstructed. This occurs, for instance, in the corners outside the inscribed cylinder of rectangular axial containers. More pathologically this occurs for basins that lie completely outside the rotation axis, as for instance an eccentrically-positioned container on a large turn-table (Maas 2001). In that case, *all* angular momentum surfaces intersect the boundary and closed angular momentum surfaces are completely absent, see Fig. 2.14.

The notion of iso-angular momentum surfaces, and their potential blockage by boundaries, is reminiscent of that of geostrophic contours (Rhines and Young 1982). The latter are lines of equal potential vorticity, f/h, the ratio of planetary vorticity f and fluid depth, h. In geophysical context these lines are typically oriented in zonal direction because in the traditional approximation only the vertical component of planetary vorticity is taken into account. Variations in bottom topography, or, in a two-layer context, in equivalent depth, related to the interface depth, can force these lines to develop closed contours. Within these contours, circulation can strongly amplify and homogenise potential vorticity. We anticipate that the presence of closed iso-angular momentum surfaces may similarly homogenise angular momentum, even in uniform-depth, rigid-lid containers where potential vorticity is constant.

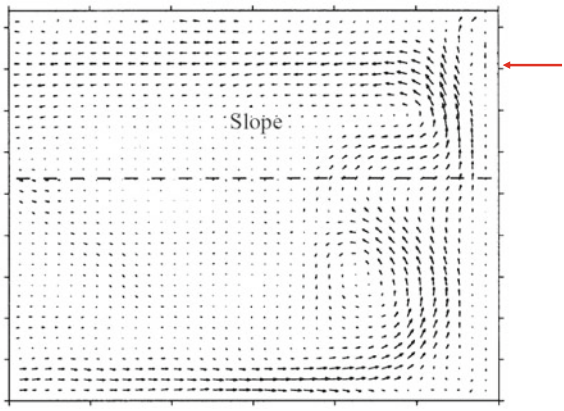

Fig. 2.14 Eulerian, vertically-uniform mean-flow observed by means of PIV in the top view of a homogeneous-density, rotating fluid situated in an eccentrically-located tank that is subject to libration. Observations extend over the right-half of the tank only. The angular momentum surfaces are roughly aligned with the figure's lower boundary. An attractor manifold develops (far from the vertical wall, at the right) over the location where it reflects from the slope, indicated by the red arrow. At the attractor, fluid differing in angular momentum is mixed, forcing this mean-flow. Picture adapted from Maas (2001)

2.5 Conclusion

A fluid layer supports waves that find their maxima and minima either at its boundaries or in its interior: external and internal waves, respectively. The former class encompasses capillary and surface and interfacial gravity waves, found in isotropic media. They obey a dispersion relation that relates frequency to wave vector magnitude. The latter class, encompassing internal gravity and inertial waves are found in anisotropic media. By contrast, their dispersion relations relate frequency to wave vector direction. The consequences of this difference in dispersion relation are multiple, best summarised by stating that the behaviour of internal waves is completely opposite and complementary to that of external waves.

In a field of gravity, anisotropy can be due to a stratification (non-uniformity) of the fluid's density. In a rotating fluid, anisotropy may be due to a radial stratification in angular momentum. These stratifications lend fluid parcels 'a memory', expressed in the material conservation of their density or angular momentum, respectively. Quiescent fluids that are stably stratified in density or angular momentum possess a balance between two opposing forces. Perturbing these states gives rise to a restoring mechanism, as one of the two forces will dominate.

Shear flows represent fluids that are stratified in linear momentum. With the exception of linear or parabolic shear flows, as present in Couette and Poiseuille flows, respectively, these flows do not themselves obey the Navier-Stokes equations. Under some stability conditions, these flows also support waves but lack an underlying balance of forces, making it harder to identify an internal restoring mechanism.

Acknowledgements Comments by Uwe Harlander and Evgeny Ermanyuk are gratefully acknowledged.

References

Berry, M.V. 1981. Regularity and chaos in classical mechanics, illustrated by three deformations of a circular 'billiard'. *European Journal of Physics* 2: 91.

Bewley, G.P., D.P. Lathrop, L.R.M. Maas, and K.R. Sreenivasan. 2007. Inertial waves in rotating grid turbulence. *Physics of Fluids* 19 (7): 071701.

Boury, S., I. Sibgatullin, E. Ermanyuk, N. Shmakova, P. Odier, S. Joubaud, L.R.M. Maas and T. Dauxois. 2021. Vortex cluster arising from an axisymmetric inertial wave attractor. *Journal of Fluid Mechanics*, 926 (A12).

Bretherton, F.P. 1964. Low frequency oscillations trapped near the equator. *Tellus* 16 (2): 181–185.

Brouzet, C., I.N. Sibgatullin, E.V. Ermanyuk, S. Joubaud, and T. Dauxois. 2007. Scale effects in internal wave attractors. *Physical Review Fluids* 2 (11): 114803.

Brunet, M., T. Dauxois, and P.-P. Cortet. 2019. Linear and nonlinear regimes of an inertial wave attractor. *Physical Review Fluids* 4 (3): 034801.

Burnside, W. 1888. On the small wave-motions of a heterogeneous fluid under gravity. *Proceedings of the London Mathematical Society* 1 (1): 392–397.

Carpenter, J.R., E.W. Tedford, E. Heifetz, and G.A. Lawrence. 2011. Instability in stratified shear flow: Review of a physical interpretation based on interacting waves. *Applied Mechanics Reviews* 64 (6): 060801.

Cederlöf, U. 1988. Free-surface effects on spin-up. *Journal of Fluid Mechanics* 187: 395–407.

Darrigol, O. 2005. *Worlds of flow: A history of hydrodynamics from the Bernoullis to Prandtl*. Oxford University Press.

Dauxois, T., S. Joubaud, P. Odier, and A. Venaille. 2018. Instabilities of internal gravity wave beams. *Annual Review of Fluid Mechanics* 50: 131–156.

Delplace, P., J.B. Marston, and A. Venaille. 2017. Topological origin of equatorial waves. *Science* 358 (6366): 1075–1077.

Dintrans, B., M. Rieutord, and L. Valdettaro. 1999. Gravito-inertial waves in a rotating stratified sphere or spherical shell. *Journal of Fluid Mechanics* 398: 271–297.

Drazin, P.G., and L.N. Howard. 1962. The instability to long waves of unbounded parallel inviscid flow. *Journal of Fluid Mechanics* 14 (2): 257–283.

Drazin, P.G., and W.H. Reid. 1998. *Hydrodynamic stability*. Cambridge University Press.

Ekman, V.W. 1904. On dead water. *Norwegian North Polar expedition 1893–1896, scientific results*, 5 (15): 1–152.

Fjeldstad, J.E. 1933. *Interne wellen. Geofysiske Publikasjoner* 10 (6): 1–35.

Franklin, B. 1762. Relating a curious instance of the effect of oil on water. *Complete Works, London* 2: 142, 1762.

Gerkema, T., J.T.F. Zimmerman, L.R.M. Maas, and H. Van Haren. 2008. Geophysical and astrophysical fluid dynamics beyond the traditional approximation. *Reviews of Geophysics* 46(2).

Gill, A.E. 1982. *Atmosphere-ocean dynamics*. Ac Press.

Goedbloed, H., R. Keppens, and S. Poedts. 2019. *Magnetohydrodynamics of laboratory and astrophysical plasmas*. Cambridge University press.

Greenspan, H.P., and L.N. Howard. 1963. On a time-dependent motion of a rotating fluid. *Journal of Fluid Mechanics* 17 (3): 385–404.

Grimshaw, R., E. Pelinovsky, and T. Talipova. 2010. Nonreflecting internal wave beam propagation in the deep ocean. *Journal of Physical Oceanography* 40 (4): 802–813.

Groen, P. 1948. *Contribution to the theory of internal waves*. KNMI, Mededelingen en verhandelingen; Serie B, Deel II, No. I.

Hazewinkel, J., P. van Breevoort, S.B. Dalziel, and L.R.M. Maas. 2008. Observations on the wavenumber spectrum and evolution of an internal wave attractor. *Journal of Fluid Mechanics* 598: 373–382.

Hazewinkel, J., L.R.M. Maas & S.B. Dalziel (2010a). Attractive internal wave patterns. arXiv:1010.1046 [physics.flu-dyn].

Hazewinkel, J., Chr. Tsimitri, L.R.M. Maas, and S.B. Dalziel. 2010. Observations on the robustness of internal wave attractors to perturbations. *Physics of Fluids* 22 (10): 107102.

Heller, E.J. 1984. Bound-state eigenfunctions of classically chaotic Hamiltonian systems: Scars of periodic orbits. *Physical Review Letters* 53 (16): 1515–1518.

Hinwood, J.B. 1972. The study of density-stratified flows up to 1945 part 2 internal waves and interfacial effects. *La Houille Blanche* 8 (709–722): 1972.

Hof, B., C.W.H. van Doorne, J. Westerweel, F.T.M. Nieuwstadt, H. Faisst, B. Eckhardt, H. Wedin, R.R. Kerswell, and F. Waleffe. 2004. Experimental observation of nonlinear traveling waves in turbulent pipe flow. *Science* 305 (5690): 1594–1598.

Hoff, M., U. Harlander, and C. Egbers. 2016. Experimental survey of linear and nonlinear inertial waves and wave instabilities in a spherical shell. *Journal of Fluid Mechanics* 789: 589–616.

Hoff, M., U. Harlander, and S.A. Triana. 2016. Study of turbulence and interacting inertial modes in a differentially rotating spherical shell experiment. *Physical Review Fluids* 1 (4): 043701.

Israeli, M. 1972. On trapped modes of rotating fluids in spherical shells. *Studies in Applied Mathematics* 51 (3): 219–237.

John, F. 1941. The dirichlet problem for a hyperbolic equation. *American Journal of Mathematics* 63 (1): 141–154.

Kelvin, Lord. 1880. On the oscillations of a columnar vortex. *Philosophical Magazine* 10: 155–168.

Klein, M., T. Seelig, M.V. Kurgansky, A. Ghasemi, I.D. Borcia, A. Will, E. Schaller, Chr. Egbers, and U. Harlander. 2014. Inertial wave excitation and focusing in a liquid bounded by a frustum and a cylinder. *Journal of Fluid Mechanics* 751: 255–297.

Koch, S., U. Harlander, Chr. Egbers, and R. Hollerbach. 2013. Inertial waves in a spherical shell induced by librations of the inner sphere: experimental and numerical results. *Fluid Dynamics Research* 45 (3): 035504.

Krauss, W. 1973. *Dynamics of the homogeneous and the quasihomogeneous ocean*, vol. 1. Borntraeger.

Lamriben, C., P.-P. Cortet, F. Moisy, and L.R.M. Maas. 2011. Excitation of inertial modes in a closed grid turbulence experiment under rotation. *Physics of Fluids* 23 (1): 015102.

Le Bars, M., D. Cébron, and P. Le Gal. 2015. Flows driven by libration, precession, and tides. *Annual Review of Fluid Mechanics* 47: 163–193.

Li, L., M.D. Patterson, K. Zhang, and R.R. Kerswell. 2012. Spin-up and spin-down in a half cone: A pathological situation or not? *Physics of Fluids* 24 (11): 116601.

Love, A.E.H. 1890. Wave-motion in a heterogeneous heavy fluid. *Proceedings of the London Mathematical Society* 1 (1): 307–316.

Maas, L.R.M. 2001. Wave focusing and ensuing mean flow due to symmetry breaking in rotating fluids. *Journal of Fluid Mechanics* 437: 13–28.

Maas, L.R.M. 2003. On the amphidromic structure of inertial waves in a rectangular parallelepiped. *Fluid Dynamics Research* 33 (4): 373–401.

Maas, L.M.R. 2005. Wave attractors: Linear yet nonlinear. *International Journal of Bifurcation and Chaos in Applied Sciences and Engineering* 15(9): 2757–2782.

Maas, L.R.M. 2007. Experiments on rotating flows: Impact of rotation on flow through tilted rectangular ducts. In *St. Petersburg Conference "Fluxes and Structures in Fluids"*, Ed. Yu. Chashechkin, 1–10.

Maas, L.R.M. 2009. Exact analytic self-similar solution of a wave attractor field. *Physica D* 238 (5): 502–505.

Maas, L.R.M., and U. Harlander. 2007. Equatorial wave attractors and inertial oscillations. *Journal of Fluid Mechanics* 570: 47–67.

Maas, L.R.M., and F.P.A. Lam. 1995. Geometric focusing of internal waves. *Journal of Fluid Mechanics* 300: 1–41.
Manders, A.M.M., and L.R.M. Maas. 2003. Observations of inertial waves in a rectangular basin with one sloping boundary. *Journal of Fluid Mechanics* 493: 59–88.
Manders, A.M.M., and L.R.M. Maas. 2004. On the three-dimensional structure of the inertial wave field in a rectangular basin with one sloping boundary. *Fluid Dynamics Research* 35 (1): 1–21.
Manders, A.M.M., J.J. Duistermaat, and L.R.M. Maas. 2003. Wave attractors in a smooth convex enclosed geometry. *Physica D* 186 (3–4): 109–132.
Nansen, F. 1902. The oceanography of the north polar basin. *The Norwegian North Polar Expedition 1893–1896. Scientific Results* 3(9).
Ogilvie, G.I. 2005. Wave attractors and the asymptotic dissipation rate of tidal disturbances. *Journal of Fluid Mechanics* 543: 19–44.
Oruba, L., A.M. Soward, and E. Dormy. 2017. Spin-down in a rapidly rotating cylinder container with mixed rigid and stress-free boundary conditions. *Journal of Fluid Mechanics* 818: 205–240.
Phillips, O.M. 1963. Energy transfer in rotating fluids by reflection of inertial waves. *Physics of Fluids* 6 (4): 513–520.
Pillet, G., E.V. Ermanyuk, L.R.M. Maas, I.N. Sibgatullin, and T. Dauxois. 2018. Internal wave attractors in three-dimensional geometries: Trapping by oblique reflection. *Journal of Fluid Mechanics* 845: 203–225.
Pillet, G., L.R.M. Maas, and T. Dauxois. 2019. Internal wave attractors in 3d geometries: A dynamical systems approach. *European Journal of Mechanics - B/Fluids* 77: 1–16.
Proudman, J. 1916. On the dynamical theory of tides. Part II. Flat seas. *Proceedings of the London Mathematical Society, 2nd Series* 18: 21–50.
Rabitti, A., and L.R.M. Maas. 2013. Meridional trapping and zonal propagation of inertial waves in a rotating fluid shell. *Journal of Fluid Mechanics* 729: 445–470.
Rao, D.B. 1966. Free gravitational oscillations in rotating rectangular basins. *Journal of Fluid Mechanics* 25 (03): 523–555.
Rayleigh, Lord. 1879. On the stability, or instability, of certain fluid motions. *Proceedings of the London Mathematical Society* 1 (1): 57–72.
Rayleigh, Lord. 1883. Investigation of the character of the equilibrium of an incompressible heavy fluid of variable density. *Proceedings of the London Mathematical Society* 14: 170–177.
Rayleigh, Lord. 1917. On the dynamics of revolving fluids. *Proceedings of the Royal Society A* 93 (648): 148–154.
Rhines, P.B., and W.R. Young. 1982. Homogenization of potential vorticity in planetary gyres. *Journal of Fluid Mechanics* 122: 347–367.
Rieutord, M. 2001. Ekman layers and the damping of inertial r -modes in a spherical shell: application to neutron stars. *Astrophysical Journal* 550 (1): 443–447.
Rieutord, M., and L. Valdettaro. 1997. Inertial waves in a rotating spherical shell. *Journal of Fluid Mechanics* 341: 77–99.
Rieutord, M., B. Georgeot, and L. Valdettaro. 2001. Inertial waves in a rotating spherical shell: Attractors and asymptotic spectrum. *Journal of Fluid Mechanics* 435: 103–144.
Sibgatullin, I.N., and E.V. Ermanyuk. 2019. Internal and inertial wave attractors: A review. *Journal of Applied Mechanics and Technical Physics* 60 (2): 284–302.
Sibgatullin, I.N., E. Ermanyuk, L.R.M. Maas, X. Xu, and T. Dauxois. 2017. Direct numerical simulation of three-dimensional inertial wave attractors. In *2017 Ivannikov ISPRAS Open Conference (ISPRAS)*, pp 137–143.
Squire, H.B. 1933. On the stability for three-dimensional disturbances of viscous fluid flow between parallel walls. *Proceedings of the Royal Society A* 142 (847): 621–628.
Steinmoeller, D.T., M. Stastna, and K.G. Lamb. 2019. Calculating basin-scale free oscillations in lakes on a rotating earth. *Ocean Modelling* 139: 101403.
Stern, M.E. 1963. Trapping of low frequency oscillations in an equatorial "boundary layer". *Tellus* 15 (3): 246–250.

Stewartson, K. 1971. On trapped oscillations of a rotating fluid in a thin spherical shell. *Tellus* 23 (6): 506–510.

Stokes, G.G. 1847. On the theory of oscillatory waves. *Transactions of the Cambridge Philosophical Society* 8: 441.

Sun, J., C.J. Nappo, L. Mahrt, D. Belušić, B. Grisogono, D.R. Stauffer, M. Pulido, C. Staquet, Q. Jiang, A. Pouquet, et al. 2015. Review of wave-turbulence interactions in the stable atmospheric boundary layer. *Reviews of Geophysics* 53 (3): 956–993.

Sverdrup, H.U. 1926. Dynamics of tides on the northern Siberian shelf. *Geophysics Publication* 4 (5): 76.

Taylor, G.I. 1922. Tidal oscillations in gulfs and rectangular basins. *Proceedings of the London Mathematical Society* 2 (1): 148.

Van Heijst, G.J.F. 1989. Spin-up phenomena in non-axisymmetric containers. *Journal of Fluid Mechanics* 206: 171–191.

Van Heijst, G.J.F., P.A. Davies, and R.G. Davis. 1990. Spin-up in a rectangular container. *Physics of Fluids* 2 (2): 150–159.

Van Heijst, G.J.F., L.R.M. Maas, and C.W.M. Williams. 1994. The spin-up of fluid in a rectangular container with sloping bottom. *Journal of Fluid Mechanics* 265: 125–159.

Vogt, T., D. Räbiger, and S. Eckert. 2014. Inertial wave dynamics in a rotating liquid metal. *Journal of Fluid Mechanics* 753: 472–498.

Waleffe, F. 1997. On a self-sustaining process in shear flows. *Physics of Fluids* 9 (4): 883–900.

Weidman, P.D. 1976. On the spin-up and spin-down of a rotating fluid. part 1. extending the Wedemeyer model. *Journal of Fluid Mechanics* 77(4): 685–708.

Whewell, W. 1833. Essay towards a first approximation to a map of cotidal lines. *Philosophical Transactions of the Royal Society of London* 147–236.

Wu, K., B.D. Welfert, and J.M. Lopez. 2018. Complex dynamics in a stratified lid-driven square cavity flow. *Journal of Fluid Mechanics* 855: 43–66.

Chapter 3
A Review of Nonlinear Boussinesq-Type Models for Coastal Ocean Modeling

Clint Dawson and Ali Samii

Abstract We review some of the key developments in wave models used in the coastal oceanography. To this end, we first recall the well-known shallowness, nonlinearity, and topography parameters, which are used to describe the dominant features in our problem. Next, we compare different wave models based on their assumptions on the magnitude of these parameters or based on the highest power of each parameter included in the model. We then choose a recent version of the Green–Naghdi equation and explain its derivation. Finally, we show some numerical results for this model, which were obtained using a hybridized discontinuous Galerkin solver.

3.1 Introduction

Coastal ocean models are used in a variety of applications; examples include predicting tidal cycles in coastal regions, operations of ports and military installations, modeling environmental conditions in bays and estuaries, and natural hazards such as hurricane storm surges and tsunamis. Flow in coastal regions, and even in deeper water, separates into long-wave and short-wave components (Holthuijsen 2007). Long-wave phenomena can be modeled using the standard shallow water equations. Short-waves require more complex mathematical treatment. Short-wave models are further categorized into phase-resolving and non-phase resolving models. Non-phase resolving models are typically used over large coastal and oceanic regions, since it is impossible to model each individual wave in the ocean. In the nearshore, where solitary waves are present, phase resolving models should be used. We focus on such models in this paper.

C. Dawson (✉)
Oden Institute for Computational Engineering and Sciences, The University of Texas at Austin, Austin, TX, USA
e-mail: clint@oden.utexas.edu

A. Samii
Department of Aerospace Engineering and Engineering Mechanics, The University of Texas at Austin, Austin, TX, USA
e-mail: a.samii@gmail.com

H. Schuttelaars et al. (eds.), *The Mathematics of Marine Modelling*,
Mathematics of Planet Earth 9, https://doi.org/10.1007/978-3-031-09559-7_3

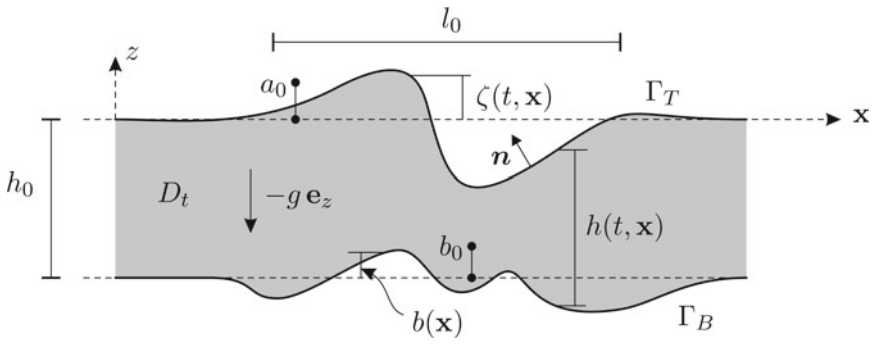

Fig. 3.1 Domain of the problem, employed notations, and the length scales

The numerical simulation of water waves near the coast requires a mathematical model which can include the highly nonlinear and dispersive properties of the wave regime in these areas. Although, the wave motion in such regions is a three dimensional process, the Boussinesq wave theory considers a polynomial distribution for the velocity field in the vertical direction and reduces the problem to a two dimensional description (Boussinesq 1872). In fact, Boussinesq's core assumption is the linear variation of the velocity field from zero at the bottom to a maximum value at the water surface. The conditions for validity of this assumption were not completely understood at the time, but it is now realized that if the fluid flow belongs to the shallow water regime, the polynomial variation of the velocity field can be well justified (Lannes 2013).

In order to identify the shallow water regime, we define three dimensionless parameters based on the typical length scales in our problem. As shown in Fig. 3.1, we consider a typical horizontal length scale (l_0), a typical water depth scale (h_0), a typical wave amplitude (a_0), and a typical topography scale (b_0). According to these scales, we define the *nonlinearity parameter* ($\varepsilon = a_0/h_0$), *topography parameter* ($\beta = b_0/h_0$), and the *shallowness parameter* ($\mu = h_0/l_0$). As can be inferred from its name, ε signifies the amount of nonlinear behavior in our problem. Meanwhile, the main assumption in the shallow water regime is $\mu \ll 1$, and if this assumption is in place, we can use the Boussinesq's technique to formulate a 2D problem from the original 3D setup. Hence, we do not need any special assumption on ε or β to develop the shallow water regime equations. However, in practice, in order to simplify the equations, one can assume that $\varepsilon = O(\mu^2)$ to get the weakly nonlinear equations. In this context, Peregrine (1967) was among the first ones to assume a quadratic variation for the vertical velocity and let $\varepsilon = O(\mu^2)$ to form what is now known as the *classical* Boussinesq equation. In this derivation, the terms of order μ^4 (such as $\varepsilon\mu^2$) were ignored to simplify the equations. In general, if we neglect the terms of order μ^N or higher in an approximate model, we call that model $O(\mu^N)$-*consistent* with the original water wave problem (or simply $O(\mu^N)$ model).

The $O(\mu^4)$ model of Peregrine has some limitations, the most important of which are its weak dispersive and nonlinear properties. In other words, it is not applicable to problems with relatively large μ's, and since its nonlinear properties are tuned to match its dispersion, it also does not perform well for moderately nonlinear waves. As a result, the phase velocities computed using this model are only valid for long waves with $kh_0 < 0.75$ (k being the wavenumber) (Madsen 2003). Among the studies which have tried to fix this issue (Nwogu 1993; Madsen et al. 2002; Barthélemy 2004), Witting pioneered the use of Padé approximation to obtain a good fit for the linear phase speed of the Stokes waves (Witting 1984). This approach was later pursued by Madsen et al. (1991), where they incorporated a spatial derivative of the water surface elevation to substitute a temporal derivative of the horizontal velocity. On a separate path, Nwogu (1993) proposed a new formulation based on the velocity at an arbitrary depth, instead of the velocity at the still water elevation, and obtained an improved matching for the linear celerity. The resulting dispersion relation was similar to the one obtained in Madsen et al. (1991). This techniques was later improved by others (Wei and Kirby 1995; Madsen and Sørensen 1992), and resulted in models with linear dispersion relations, which are valid up to $kh_0 = 6$. However, the issue of weak nonlinearity was still unresolved. An effort to relax the assumption on the nonlinearity parameter was to take $\varepsilon = O(\mu)$ and $\beta = O(\mu^2)$, and obtain $O(\mu^6)$-consistent equations, i.e. keeping terms such as $\varepsilon^2\mu^2$, $\varepsilon^3\mu^2$, and $\varepsilon\mu^4$ in the equations (Madsen and Schäffer 1998). In general, fixing both nonlinear and dispersive effects in the above coupled setting makes the equations very complicated, and designing numerical methods for them is not straightforward. One of the examples of such efforts was proposed in Gobbi et al. (2000), where the equation is $O(\mu^6)$-consistent with the original water wave problem, and contains up to fifth order derivatives. This results in a valid linear dispersion relation up to $kh_0 = 6$, and acceptable nonlinear properties up to $kh_0 = 3$.

In all of the above techniques, there is a coupling between the nonlinearity and shallowness assumption in the problem. As a result, they have inconsistent linear and nonlinear dispersion properties. However, if we can decouple these two features, we can inherit the nonlinear dispersive properties from the linear case. In one of the first efforts towards this goal (Agnon et al. 1999), the shoaling and dispersion are included in the model by solving the Laplace's equation with the kinematic boundary conditions, while the nonlinearity is treated using Euler's equation, based on Zakharov's methodology (Zakharov 1968). Based on this approach, other models were developed, which are shown to be valid for a wide range of wavenumbers up to $kh_0 = 25$ (Madsen et al. 2002; Madsen 2003). In order to enhance the dispersive behavior of these models for high bathymetry gradients, a new model was developed in Madsen et al. (2006).

Another group of methods for deriving the nonlinear dispersive wave equations, is based on using the so-called Dirichlet-Neumann (DN) operator. This operator was formulated by Craig et al. (1992), Craig and Sulem (1993), and its application to highly variable bathymetry was carried out in Artiles and Nachbin (2004a), Artiles and Nacbin (2004b). In the last decade, multiple works have been carried out to construct Serre-Green-Naghdi models (Serre 1953; Green and Naghdi 1976), which

Table 3.1 Orders of precision of different models and the corresponding nonlinearity (ε) and topography (β) parameters

Model	Precision	ε	β
(Saint-Venant) NSWE	$O(\mu^2)$	$O(1)$	$O(1)$
KdV (Korteweg and De Vries 1895)	$O(\mu^4)$	$O(\mu^2)$	0
Boussinesq-Peregrine (Peregrine 1967)	$O(\mu^4)$	$O(\mu^2)$	$O(\mu^2)$
Green–Naghdi (Serre 1953; Green and Naghdi 1976; Lannes and Bonneton 2009)	$O(\mu^4)$	O(1)	O(1)
Madsen and Schäffer (1998)	$O(\mu^6)$	$O(\mu)$	$O(\mu^2)$
Agnon et al. (1999)	$O(\mu^8)$	$O(\mu)$	$O(\mu^2)$

are $O(\mu^4)$-consistent, and are suitable for fully nonlinear ($\varepsilon = O(1)$) problems on arbitrary bathymetry ($\beta = O(1)$) (Lannes and Bonneton 2009; Bonneton et al. 2011; Lannes and Marche 2015). The main advantage in all of these works is their relatively straightforward computational implementation, due to their maximum order of spatial derivatives being three. It has been shown that by using different techniques such as introducing new tuning parameters, one can achieve a very good approximation to the dispersion relation using these $O(\mu^4)$ models (Chazel et al. 2009, 2011). Moreover, by dropping the assumption of water being irrotational, another group of models has been devised (Zhang et al. 2013, 2014; Castro and Lannes 2014). In Table 3.1 we have summarized the main features of a number of shallow water models based on the considered range of the dimensionless parameters.

In this article, we review the derivation of the irrotational $O(\mu^4)$-consistent equation for the fully nonlinear waves on an arbitrary bathymetry. We then show a set of numerical results based on a hybridized discontinuous Galerkin solver for this equation.

3.2 The Water Wave Problem

At a given time t, let D_t denote the subset of $\mathbb{R}^{d+1}$, which is filled with water (refer to Fig. 3.1). At a given point $(\boldsymbol{x}, z) \in D_t$, let $\mathbf{U}(t, \boldsymbol{x}, z) \in \mathbb{R}^{d+1}$ denote the velocity of a fluid particle. Meanwhile $\boldsymbol{u}(t, \boldsymbol{x}, z) \in \mathbb{R}^d$ and $w(t, X, z) \in \mathbb{R}$ are the horizontal and vertical components of the velocity. At this point, $p(t, \boldsymbol{x}, z)$ denotes the pressure. The acceleration of gravity, which acts in the vertical direction $(-g\mathbf{e}_z)$, is taken constant everywhere. Moreover, we use ∇ to denote the gradient in the horizontal direction and $\boldsymbol{\nabla}$ to denote $(\nabla, \partial_z)^T$. Similarly, we use Δ, and $\boldsymbol{\Delta}$ to denote ∇^2, and $\nabla^2 + \partial_z^2$,

respectively. Assuming the water to be inviscid, incompressible, and uniform, with irrotational motion, its flow is governed by the following equations:

$$\partial_t \mathbf{U} + (\mathbf{U}\cdot\boldsymbol{\nabla})\mathbf{U} = -\tfrac{1}{\rho}\boldsymbol{\nabla} p - g\mathbf{e}_z \qquad \text{in } D_t, \tag{3.1a}$$

$$\boldsymbol{\nabla}\cdot\mathbf{U} = 0 \qquad \text{in } D_t, \tag{3.1b}$$

$$\boldsymbol{\nabla}\times\mathbf{U} = 0 \qquad \text{in } D_t. \tag{3.1c}$$

Meanwhile, the particles on the top boundary ($z = \zeta(t,\mathbf{x})$) and the bottom boundary ($z = b(\mathbf{x})$) should not cross Γ_T and Γ_B:

$$\mathbf{U}\cdot\boldsymbol{n} = 0 \qquad \text{on } \Gamma_B, \tag{3.1d}$$

$$\partial_t\zeta + \nabla\zeta\cdot\boldsymbol{u} - w = 0 \qquad \text{on } \Gamma_T. \tag{3.1e}$$

Referring to Fig. 3.1, one can obtain the normal vector on Γ_T by taking the gradient of the equation: $z - \zeta(t,\boldsymbol{x}) = 0$ (which describes Γ_T) and get: $\boldsymbol{n}|_{\Gamma_T} = (-\nabla\zeta, 1)/\sqrt{1+|\nabla\zeta|^2}$. Hence, it is possible to write (3.1e) in the following form, as well:

$$\partial_t\zeta - \sqrt{1+|\nabla\zeta|^2}\,\mathbf{U}\cdot\boldsymbol{n} = 0, \quad \text{on } \Gamma_T. \tag{3.1e*}$$

Due to (3.1c), we can find a velocity potential function (Φ), such that $\boldsymbol{\nabla}\Phi = \mathbf{U}$. Substituting this into (3.1a), and assuming pressure at the water surface to be p_{atm}, (3.1a) becomes:

$$\partial_t\Phi + \tfrac{1}{2}|\boldsymbol{\nabla}\Phi|^2 + gz = -\tfrac{1}{\rho}(p - p_{\text{atm}}). \tag{3.2}$$

Next, we define ψ as the trace of Φ on the water surface, i.e. $\Phi|_{z=\zeta(\mathbf{x})} = \psi$. Accordingly, we can express (3.1b–d), in terms of the velocity potential, and get the following boundary value problem:

$$\boldsymbol{\Delta}\Phi = 0 \text{ in } D_t, \qquad \Phi = \psi \text{ on } \Gamma_T, \qquad \boldsymbol{\nabla}\Phi\cdot\boldsymbol{n} = 0 \text{ on } \Gamma_B. \tag{3.3}$$

Under proper regularity assumptions, the solution to the above system depends on ψ, and the parametrization of Γ_T, Γ_B using ζ, b. Hence, we identify the Dirichlet-Neumann operator ($\mathcal{G}[\zeta,b]$), which solves the above system for a given ψ and maps it as follows:

$$\mathcal{G}[\zeta,b] : \psi \mapsto \sqrt{1+|\nabla\zeta|^2}\,\partial_n\Phi|_{\Gamma_T} \tag{3.4}$$

or, equivalently (compare (3.1e) and (3.1e*)):

$$\mathcal{G}[\zeta,b] : \psi \mapsto -\nabla\zeta\cdot\nabla\Phi|_{\Gamma_T} + \partial_z\Phi|_{\Gamma_T} \tag{3.4*}$$

For a rigorous definition of this operator over its functional settings, we refer the interested reader to Lannes (2013). We use $\mathcal{G}$ to write (3.1e) in terms of the d-dimensional coordinates and unknowns, in the form:

$$\partial_t \zeta - \mathcal{G}[\zeta, b]\psi = 0. \tag{3.5}$$

Next, we want to express (3.3) independent of the vertical coordinate. Hence, we need to remove Φ, and its derivatives from this equation. Since, $\psi(t, \mathbf{x}) = \Phi(t, \mathbf{x}, \zeta(t, \mathbf{x}))$, we use the chain rule to get:

$$\partial_t \Phi = \partial_t \psi - \partial_z \Phi \, \partial_t \zeta \quad \text{on } \Gamma_T, \tag{3.6a}$$

$$\nabla \Phi = \nabla \psi - \partial_z \Phi \, \nabla \zeta \quad \text{on } \Gamma_T. \tag{3.6b}$$

For $\partial_z \Phi$, we start from (3.1e) and use (3.6) and the above relations to get:

$$\partial_z \Phi = \frac{\mathcal{G}[\zeta, b]\psi + \nabla \zeta \cdot \nabla \psi}{1 + |\nabla \zeta|^2} \quad \text{on } \Gamma_T. \tag{3.6c}$$

It will be fruitful if we can find a relationship between the DN operator and the depth averaged velocity. To this end, we can start from the definition of the average velocity, to get the following relation for the average momentum:

$$(h\bar{\mathbf{u}})(t, \mathbf{x}) = \int_{-h_0+b}^{\zeta} \nabla \Phi(t, \mathbf{x}, z) \, dz.$$

We then take the divergence of this formula in the horizontal direction, apply Leibnitz rule, employ $\boldsymbol{\Delta} \Phi = 0$, and use the boundary conditions (3.1d, e), to get:

$$\nabla \cdot (h\bar{\mathbf{u}}) = -\partial_z \Phi|_{\Gamma_T} + \nabla \zeta \cdot \nabla \Phi|_{\Gamma_T}$$

Comparing this with (3.1e), one has:

$$\mathcal{G}[\zeta, b]\psi = -\nabla \cdot (h\bar{\mathbf{u}}) \tag{3.7}$$

Consequently, we can substitute (3.6) into (3.2), and along with (3.5), we obtain the following system of equations:

$$\begin{cases} \partial_t \zeta + \nabla \cdot (h\bar{\mathbf{u}}) = 0, \\ \partial_t \psi + g\zeta + \dfrac{1}{2}|\nabla \psi|^2 - \dfrac{(\nabla \zeta \cdot \nabla \psi - \nabla \cdot (h\bar{\mathbf{u}}))^2}{2(1 + |\nabla \zeta|^2)} = 0. \end{cases} \tag{3.8}$$

3.2.1 *Dispersive Properties of the Linear Waves*

The dispersion relation corresponding to Eq. (3.8) can be obtained by writing this equation in terms of the perturbations of velocity potential and water surface about the rest state on a flat bathymetry, i.e. setting $\zeta = 0, b = 0$. This requires solving the

following BVP:

$$\boldsymbol{\Delta}\Phi = 0 \text{ in } D_t, \qquad \Phi = \psi \text{ on } \Gamma_T, \qquad \partial_z \Phi = 0 \text{ on } \Gamma_B, \tag{3.9}$$

along with the following linearized system of equations:

$$\begin{cases} \partial_t \zeta - \mathcal{G}[0,0]\psi = 0, \\ \partial_t \psi + g\zeta = 0. \end{cases} \tag{3.10}$$

Here, Γ_B is parametrized as $z = -h_0$. Now, we take the Fourier transform of (3.9) with respect to $\mathbf{x}$, to obtain the following problem in terms of the wave vector $\mathbf{k}$:

$$\partial_z^2 \hat{\Phi}(\mathbf{k}, z) = 0 \text{ in } D_t, \qquad \hat{\Phi} = \hat{\psi} \text{ on } \Gamma_T, \qquad \partial_z \hat{\Phi} = 0 \text{ on } \Gamma_B. \tag{3.11}$$

This results in the following solution:

$$\hat{\Phi}(\mathbf{k}, z) = \frac{\cosh[(z + h_0)|\mathbf{k}|]}{\cosh(h_0|\mathbf{k}|)} \hat{\psi}(\mathbf{k}). \tag{3.12}$$

Since, in the linearized case, $\boldsymbol{n}|_{\Gamma_T} = (\mathbf{0}, 1)$, we can simply write $\sqrt{1 + |\nabla\zeta|^2}\, \partial_n \Phi$ as $\partial_z \Phi$. Therefore, in the wavenumber domain we have the following:

$$\mathcal{G}[0,0]\hat{\psi} = \partial_z \hat{\Phi} = |\mathbf{k}| \tanh(|\mathbf{k}|h_0)\hat{\psi}(\mathbf{k}).$$

By substituting this into (3.10), we get the following equation for $\hat{\zeta}$:

$$\partial_t^2 \hat{\zeta}(\mathbf{k}) + g|\mathbf{k}| \tanh(h_0|\mathbf{k}|)\hat{\zeta}(\mathbf{k}) = 0.$$

By taking the Fourier transform of this equation with respect to t, we get the well-known dispersion relation of the linear water waves:

$$\omega(\mathbf{k}) = \sqrt{g|\mathbf{k}| \tanh(h_0|\mathbf{k}|)},$$

and the phase speed of linear waves at different wavenumbers ($k = |\mathbf{k}|$) can be computed using:

$$c(kh_0) = \sqrt{gh_0} \frac{\sqrt{\tanh(kh_0)}}{\sqrt{kh_0}} \tag{3.13}$$

If k in the above relation correspond to the length scale in our problem, i.e. $k = 2\pi/l_0$, then we obtain the typical celerity of gravity waves in our problem:

$$c_0 = \sqrt{gh_0 \nu}, \quad \text{with} \quad \nu = \frac{\tanh(2\pi\mu)}{2\pi\mu},$$

with μ being the shallowness parameter. One can clearly observe that μ characterizes the typical wavenumber in the problem. When we are dealing with very long waves ($\mu \ll 1$), we can assume that $\nu \simeq 1$. Thus the water waves are nondispersive in such cases, that is all of the wavelengths travel with the same speed. On the other hand, when we have intermediate values for μ, the longer waves travel faster than the shorter waves and the water waves show dispersive properties.

3.2.2 Scaling of Variables and Operators

In order to obtain the nondimensional equations, we should know the typical scales of coordinates, variable, and the corresponding operators. Here, we first introduce the time scale as the ratio of l_0 by c_0 (phase speed of linear waves): $t_0 = l_0/\sqrt{gh_0}$. Accordingly, we can define the nondimensional space and time coordinates (denoted with primes):

$$\mathbf{x}' = x/l_0, \quad z' = z/h_0, \quad t' = t/t_0, \tag{3.14}$$

and their corresponding differential operators:

$$\begin{gathered} \nabla' = l_0\nabla, \quad \boldsymbol{\nabla}' = l_0(\nabla, \mu\,\partial_z)^T, \quad \boldsymbol{\Delta}' = l_0^2(\nabla^2 + \mu^2\,\partial_z^2), \quad \partial_{t'} = t_0\partial_t, \\ \boldsymbol{\nabla} = \tfrac{1}{h_0}(\mu\,\nabla', \partial_{z'})^T, \quad \boldsymbol{\Delta} = \tfrac{1}{h_0^2}(\mu^2\,\nabla'^2 + \partial_{z'}^2). \end{gathered} \tag{3.15}$$

The scaling of ζ, b, and $h = \zeta + h_0 - b$ is straightforward:

$$\zeta' = \frac{\zeta}{a_0}, \quad b' = \frac{b}{b_0}, \quad h' = \frac{h}{h_0}. \tag{3.16}$$

We also want to find a typical scale for Φ. To this end, we first refer to (3.9), which states that Φ and ψ should have the same order of magnitude. Moreover, we look at the second equation of (3.10), which gives us a typical magnitude for ψ:

$$\begin{gathered} \frac{1}{t_0}\partial_{t'}\psi_0\psi' + ga_0\zeta' = 0 \Longrightarrow \psi_0 = \frac{a_0}{h_0}l_0\sqrt{gh_0}, \\ \Phi = \frac{\Phi}{\Phi_0}, \text{ with } \quad \Phi_0 = \psi_0. \end{gathered} \tag{3.17}$$

We also define a typical length scale for the horizontal velocity based on $\boldsymbol{u}_0 = \nabla\Phi_0$, or in terms of the nondimensional variables: $\boldsymbol{u}_0\boldsymbol{u}' = (\Phi_0/l_0)\nabla'\Phi'$. Thus, the dimensionless horizontal velocity can be defined as:

$$\boldsymbol{u}' = \frac{1}{\boldsymbol{u}_0}\boldsymbol{u}\,, \text{ with } \quad \boldsymbol{u}_0 = \frac{\Phi_0}{l_0} = \varepsilon\sqrt{gh_0}. \tag{3.18}$$

Before obtaining the nondimensionalized forms of the equations, we consider scaling the Dirichlet-Neumann operator. According to (3.4), we know that $\mathcal{G}[\zeta, b]\psi = \partial_z \Phi - \nabla\Phi \cdot \nabla\zeta$ on the water surface. By substituting the derivatives and variables from (3.14)–(3.18), we have:

$$\mathcal{G}[\zeta, b]\psi = \frac{\Phi_0}{h_0}(\partial_{z'}\Phi' - \mu^2\nabla'(\varepsilon\zeta') \cdot \nabla\Phi')|_{z'=\varepsilon\zeta'}.$$

Thus we define:

$$\mathcal{G}'[\varepsilon\zeta', \beta b']\psi' := (\partial_{z'}\Phi' - \mu^2\nabla'(\varepsilon\zeta') \cdot \nabla\Phi')|_{z'=\varepsilon\zeta'}, \tag{3.19}$$

to get:

$$\mathcal{G}[\zeta, b]\psi = \frac{\Phi_0}{h_0}\mathcal{G}'[\varepsilon\zeta', \beta b']\psi' \tag{3.20}$$

3.2.3 Nondimensionalization of Equations

Here, we first obtain the nondimensionalized version of the boundary value problem (3.3). Using the definitions in the previous section, this equation takes the form:

$$\mu^2\nabla'^2\Phi' + \partial_{z'}^2\Phi' = 0 \qquad \text{in } -1 + \beta b' \le z' \le \varepsilon\zeta', \tag{3.21a}$$

$$\Phi' = \psi' \qquad \text{on } z' = \varepsilon\zeta', \tag{3.21b}$$

$$\partial_{z'}\Phi' - \mu^2\nabla'(\beta b') \cdot \nabla'\Phi' = 0 \qquad \text{on } z = -1 + \beta b'. \tag{3.21c}$$

It will be useful to write (3.7) in the dimensionless form. This will be a straightforward application of definitions for ∇', Φ', h', and $\boldsymbol{u}'$:

$$\mathcal{G}'[\varepsilon\zeta', \beta b']\psi' = -\mu^2\,\nabla' \cdot (h'\bar{\boldsymbol{u}}')$$

Next, we substitute the above definitions of nondimensional variables and operators to write Eqs. (3.8) in the nondimensionalized form:

$$\begin{cases} \partial_{t'}\zeta' + \nabla' \cdot (h'\bar{\boldsymbol{u}}') = 0, \\ \partial_{t'}\psi' + \zeta' + \dfrac{\varepsilon}{2}|\nabla\psi'|^2 - \varepsilon\mu^2\,\dfrac{\left(\nabla'(\varepsilon\zeta') \cdot \nabla'\psi' - \nabla' \cdot (h'\bar{\boldsymbol{u}}')\right)^2}{2(1 + \varepsilon^2\mu^2|\nabla'\zeta'|^2)} = 0. \end{cases} \tag{3.22}$$

Now, we solve (3.21) exploiting the fact that $\mu \ll 1$. To this end, let us consider approximating the velocity potential based on the following asymptotic expansion:

$$\Phi'(t,\boldsymbol{x},z)=\sum_{n=0}^{N}\mu^{2n}\,\Phi'_n(t,\boldsymbol{x},z)+O(\mu^{2(N+1)}) \tag{3.23}$$

Hence, by including only the summation ($\sum_{n=0}^{N}\mu^{2n}\,\Phi'_n(t,\boldsymbol{x},z)$) in the right hand side, we approximate Φ up to $O(\mu^{2(N+1)})$, and the corresponding model would be $O(\mu^{2(N+1)})$–consistent with the original water wave problem. Although, the $O(\mu^4)$ model that we consider here will not have a very good precision for $kh_0>1.0$, there are techniques to improve its dispersive properties and increase its range of validity up to $kh_0=4$ (Chazel et al. 2009, 2011).

Now, if we substitute (3.23) to the boundary value problem (3.21), and arrange the terms with the same power of μ, we get:

$$\partial^2_{z'}\Phi'_n=\begin{cases}0, & \text{for } n=0,\\ -(\nabla')^2\Phi'_{n-1}, & \text{otherwise.}\end{cases} \tag{3.24}$$

Meanwhile, we let Φ'_0 satisfy the boundary condition on the top and set the homogeneous boundary condition for other Φ'_n's. Thus the boundary conditions find the form:

$$\Phi'_n=\begin{cases}\psi', & \text{for } n=0,\\ 0, & \text{otherwise,}\end{cases} \qquad \text{for} \quad z'=\varepsilon\zeta', \tag{3.25}$$

$$\partial_{z'}\Phi'_n=\begin{cases}0, & \text{for } n=0,\\ \beta\nabla' b'\cdot\nabla'\Phi'_{n-1} & \text{otherwise,}\end{cases} \qquad \text{for} \quad z'=-1+\beta b'. \tag{3.26}$$

We have to solve a simple ODE to obtain the solution to Φ'_0. Afterwards, the solution to Φ'_1 will be obtained by substituting Φ'_0 in the above equations and solving another ODE. The process is straightforward, and can be done using computer algebra software. Thus, we will have:

$$\Phi'_0=\psi' \tag{3.27a}$$

$$\Phi'_1=-\frac{\nabla'^2\psi'}{2}z'^2+\left[(-1+\beta b')\nabla'^2\psi'+\beta\nabla b'\cdot\nabla\psi\right]z + \frac{\nabla'^2\psi}{2}\left[h'^2-(1-\beta b')^2\right]-\beta(h'-1+\beta b')\nabla' b'\cdot\nabla'\psi' \tag{3.27b}$$

It is worthwhile noting that for an $O(\mu^2)$ model, i.e. $\Phi'=\Phi'_0$, the velocity potential is constant in depth. This means, the velocity field does not depend on the z-coordinate in the $O(\mu)$ models. An example of such models is the Saint-Venant equation, also known as the nonlinear shallow water equation (NSWE). Moreover, the vertical component of the velocity, i.e. $w'=\partial_{z'}\Phi'$ vanishes in these models. On the other hand, in $O(\mu^4)$ models, such as Green–Naghdi equation, the velocity varies quadratically in depth.

Next, let us obtain the velocity variation corresponding to Φ_0' and Φ_1'. In the nondimensionalized coordinates we have:

$$\bar{\boldsymbol{u}}_n' = \frac{1}{h'} \int_{-1+\beta b'}^{\zeta'} \nabla \Phi_n' \, dz'.$$

By substituting Φ_0' and Φ_1' from (3.27) into the above relation, and some algebraic manipulation, we can obtain $\bar{\boldsymbol{u}}_0'$ and $\bar{\boldsymbol{u}}_1'$:

$$\bar{\boldsymbol{u}}_0' = \nabla' \psi', \tag{3.28}$$

$$\bar{\boldsymbol{u}}_1' = -\mu^2 \mathcal{T}'[h', b'] \nabla' \psi', \tag{3.29}$$

where

$$\mathcal{T}'[h', b']\mathbf{w} = \mathcal{R}_1'[h', b'](\nabla' \cdot \mathbf{w}) + \beta \mathcal{R}_2'[h, b'](\nabla b' \cdot \mathbf{w}), \tag{3.30}$$

and,

$$\mathcal{R}_1'[h', b']w = -\frac{1}{3h'} \nabla'(h'^3 w) - \beta \frac{h'}{2} w \nabla' b', \tag{3.31a}$$

$$\mathcal{R}_2'[h', b']w = \frac{1}{2\,h'} \nabla'(h'^2 w) + \beta w \nabla' b'. \tag{3.31b}$$

Now, we can write the following relation for average velocity (dropping $[h', b']$ from $\mathcal{T}'$):

$$\bar{\boldsymbol{u}}' = \nabla' \psi' - \mu^2 \mathcal{T}' \nabla' \psi' + O(\mu^4) \tag{3.32}$$

Therefore, $\nabla' \psi' = \bar{\boldsymbol{u}}' + \mu^2 \mathcal{T}' \nabla \psi' + O(\mu^4)$. Substituting $\nabla' \psi'$ from this relation into itself will result in:

$$\begin{aligned} \nabla' \psi' =& \bar{\boldsymbol{u}}' + \mu^2 \mathcal{T}' \bar{\boldsymbol{u}}' + \mu^4 \mathcal{T}' \left(\mathcal{T}' \nabla' \psi' \right) + O(\mu^4) \\ \therefore \quad & \nabla' \psi' = \bar{\boldsymbol{u}}' + \mu^2 \mathcal{T}' \bar{\boldsymbol{u}}' + O(\mu^4). \end{aligned} \tag{3.33}$$

This relation is the last piece of machinery to derive the Green–Naghdi wave model. As an example of deriving an asymptotic wave model, we can start from (3.22), take the gradient of the second equation and drop all of the terms of order $O(\mu^2)$ to obtain the nonlinear shallow water equation (NSWE):

$$\begin{cases} \partial_{t'} \zeta' + \nabla' \cdot (h' \bar{\boldsymbol{u}}') = 0, \\ \partial_{t'} \bar{\boldsymbol{u}}' + \nabla' \zeta' + \varepsilon \bar{\boldsymbol{u}}' \cdot \nabla \bar{\boldsymbol{u}}' = 0. \end{cases}$$

We usually prefer the equations to be in terms of the conserved variables, i.e. h, $h\bar{\boldsymbol{u}}$. Hence, we use $\partial_{t'} h' = \varepsilon \partial_{t'} \zeta'$, and $\partial_{t'} \boldsymbol{u}' = [\partial_{t'}(h' \bar{\boldsymbol{u}}') + \varepsilon \bar{\boldsymbol{u}}' \nabla' \cdot (h' \bar{\boldsymbol{u}}')]/h$ in the second equation to obtain:

$$\begin{cases} \partial_{t'} h' + \varepsilon \nabla' \cdot (h' \bar{\boldsymbol{u}}') = 0, \\ \partial_{t'} (h' \bar{\boldsymbol{u}}') + \varepsilon \nabla' \cdot (h' \bar{\boldsymbol{u}}' \otimes \bar{\boldsymbol{u}}') + \dfrac{1}{\varepsilon} h' (\nabla' (h' + \beta b')) = 0. \end{cases}$$

Finally, we can write the equations with dimensions:

$$\begin{cases} \partial_t h + \nabla \cdot (h \bar{\boldsymbol{u}}) = 0, \\ \partial_t (h \bar{\boldsymbol{u}}) + \nabla \cdot (h \bar{\boldsymbol{u}} \otimes \bar{\boldsymbol{u}}) + g h \nabla h + g h \nabla b = 0. \end{cases}$$

3.2.4 Green–Naghdi Equation

The process for obtaining Green-Naghdi equation is similar to what we explained for NSWE; however, in the final step, instead of dropping all terms of order $O(\mu^{2N})$, with $N \geq 1$, we drop the terms of order $O(\mu^{2N})$, with $N \geq 2$. We encourage the interested readers to also consult the original materials, in which these equations were introduced (Lannes and Bonneton 2009; Lannes 2013). Now, let us write Green–Naghdi equation in terms of the dimensionless variables:

$$\begin{cases} \partial_{t'} \zeta' + \nabla' \cdot (h' \bar{\boldsymbol{u}}') = 0, \\ (I + \mu \mathcal{T}')(\partial_{t'} \bar{\boldsymbol{u}}') + \nabla' \zeta' + \varepsilon (\bar{\boldsymbol{u}}' \cdot \nabla') \bar{\boldsymbol{u}}' + \varepsilon \mu \mathcal{Q}' (\bar{\boldsymbol{u}}') = 0. \end{cases} \tag{3.34}$$

With, $\mathcal{T}'$ defined in (3.30), and $\mathcal{Q}'$ is defined in terms of $\mathcal{R}_1'$ and $\mathcal{R}_2'$, which were introduced in (3.31):

$$\mathcal{Q}'(\mathbf{w}) = \mathcal{R}_1' \left(\nabla' \cdot (\mathbf{w} \nabla' \cdot \mathbf{w}) - 2 (\nabla' \cdot \mathbf{w})^2 \right) + \beta \mathcal{R}_2' \left((\mathbf{w} \cdot \nabla')^2 b' \right) \tag{3.35}$$

It is observed that $\mathcal{Q}'$ contains up to third order derivatives of the velocity field, which we can avoid computing by introducing a new operator $\mathcal{Q}_1'$ as follows:

$$\mathcal{Q}_1'(\mathbf{w}) = \mathcal{T}' \left((\mathbf{w} \cdot \nabla) \mathbf{w} \right) - \mathcal{Q}'(\mathbf{w}). \tag{3.36}$$

Now, $\mathcal{Q}_1'$ contains up to second derivatives, and has the form:

$$\mathcal{Q}_1'(\mathbf{w}) = -2 \mathcal{R}_1' \left(\partial_{x'} \mathbf{w} \cdot \partial_{y'} \mathbf{w}^{\perp} + (\nabla' \cdot \mathbf{w})^2 \right) + \beta \mathcal{R}_2' \left(\mathbf{w} \cdot (\mathbf{w} \cdot \nabla') \nabla' b' \right) \tag{3.37}$$

Here, $\mathbf{w}^{\perp} = (-w_2, w_1)^T$; meanwhile, $\partial_{x'}$, and $\partial_{y'}$ are the partial derivatives with respect to x', and y' respectively. Using this definition, the equation (3.34) becomes:

$$\begin{cases} \partial_{t'} \zeta' + \nabla' \cdot (h' \bar{\boldsymbol{u}}') = 0, \\ (I + \mu \mathcal{T}') \left(\partial_{t'} \bar{\boldsymbol{u}}' + \varepsilon (\bar{\boldsymbol{u}}' \cdot \nabla') \bar{\boldsymbol{u}}' \right) + \nabla' \zeta' + \varepsilon \mu \mathcal{Q}_1' (\bar{\boldsymbol{u}}') = 0. \end{cases} \tag{3.38}$$

Similar to the previous section, we prefer the equations in terms of h', $h'\bar{\boldsymbol{u}}'$:

$$\begin{cases} \partial_{t'} h' + \varepsilon \nabla' \cdot (h' \bar{\boldsymbol{u}}') = 0, \\ \left(I + \mu h' \mathcal{T}' \frac{1}{h'}\right) \left(\partial_{t'} (h' \bar{\boldsymbol{u}}') + \varepsilon \nabla' \cdot (h' \bar{\boldsymbol{u}}' \otimes \bar{\boldsymbol{u}}')\right) + h' \nabla' \zeta' + \varepsilon \mu h' \mathcal{Q}_1'(\bar{\boldsymbol{u}}') = 0. \end{cases} \tag{3.39}$$

If we apply the inverse operator $\left(I + \mu h' \mathcal{T}' \frac{1}{h}\right)^{-1}$ on the second equation, we can simplify the numerical simulation of this equation. Afterwards, we go back to the unknowns with dimensions and the above system becomes:

$$\begin{cases} \partial_t h + \nabla \cdot (h \bar{\boldsymbol{u}}) = 0, \\ \partial_t (h \bar{\boldsymbol{u}}) + \nabla \cdot (h \bar{\boldsymbol{u}} \otimes \bar{\boldsymbol{u}}) + \left(I + \mu h \mathcal{T} \frac{1}{h}\right)^{-1} (g h \nabla \zeta + h \mathcal{Q}_1(\bar{\boldsymbol{u}})) = 0. \end{cases} \tag{3.40}$$

The operators $\mathcal{T}$ and $\mathcal{Q}_1$ with dimensions are according to (3.30) and (3.37) with $\beta = 1$, respectively. It is possible to modify this equation to get a set of equations with better dispersive properties (Chazel et al. 2011; Bonneton et al. 2011), or make it more suitable for large problems by avoiding the computation of the inverse operator $\left(I + \mu h' \mathcal{T}' \frac{1}{h}\right)^{-1}$ at each time step (Lannes and Marche 2015).

3.3 A Finite Element Discretization of the Green-Naghdi Equation

In this section, we give a very concise introduction to a hybridized discontinuous Galerkin (HDG) discretization of Eq. (3.40). The details of the proposed method will be reported in separate upcoming articles. In our numerical scheme, we use the well-known Strange splitting technique (Strang 1968) to decompose equation (3.40) to a hyperbolic (nonlinear shallow water equation) and a dispersive part. This splitting is known to be second order accurate if each of its components are at least second order accurate. Let us first consider $\mathcal{S}_1$ as the solution operator associated with the hyperbolic part of (3.40):

$$\begin{cases} \partial_t h + \nabla \cdot (h \boldsymbol{u}) = 0, \\ \partial_t (h \boldsymbol{u}) + \nabla (\frac{1}{2} g h^2) + \nabla \cdot (h \boldsymbol{u} \otimes \boldsymbol{u}) + g h \nabla b = 0. \end{cases} \tag{3.41}$$

Moreover, $\mathcal{S}_2$ is the solution operator for the dispersive part:

$$\begin{cases} \partial_t h = 0, \\ \partial_t (h \boldsymbol{u}) - g h \nabla \zeta + (1 + h \mathcal{T} \frac{1}{h} h)^{-1} \left[g h \nabla \zeta + h \mathcal{Q}_1(\boldsymbol{u}) \right] = 0. \end{cases} \tag{3.42}$$

The Strang splitting suggests that the solution operator corresponding to system (3.40) is: $\mathcal{S}(\Delta t) = \mathcal{S}_1(\Delta t/2) \mathcal{S}_2(\Delta t) \mathcal{S}_1(\Delta t/2)$. A graphical representation of the

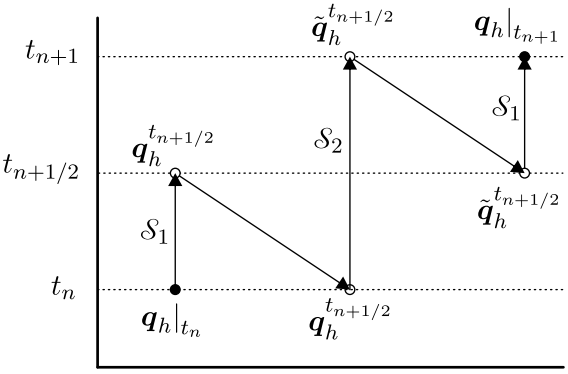

Fig. 3.2 The splitting technique used to solve the coupling between the hyperbolic and dispersive sub-problems. We start with $\boldsymbol{q}_h|_{t_n}$, and obtain $\boldsymbol{q}_h|_{t_{n+1}}$ at the end of the time step

employed technique is shown in Fig. 3.2. $\boldsymbol{q}_h$ in this figure stands for the unknown state, i.e. $\boldsymbol{q}_h = (h_h, h\mathbf{u}_h)$.

Although, Eq. (3.40) can be solved without the above splitting scheme, we prefer this approach, because we can apply different time discretization techniques to the hyperbolic and dispersive parts. For example, one can use an implicit time discretization for (3.41), and an explicit time integration for (3.42).

3.3.1 Notation

Let us consider the d-dimensional domain Ω and $\mathcal{T}_h = \{K\}$ as a finite collection of disjoint elements partitioning Ω (refer to Fig. 3.3). Let $\partial\mathcal{T}_h$ denote all of the faces of the elements in $\mathcal{T}_h$ (dashed lines in Fig. 3.3), and $\mathcal{E}_h$ be the set of faces in the mesh (continuous lines in Fig. 3.3). It is worthwhile mentioning that, while in $\mathcal{E}_h$, we count the common faces between two elements only once, the same common face is counted twice when we form $\partial\mathcal{T}_h$. Now, assume e is a common face between two elements K^+ and K^-, i.e. $e = \partial K^+ \cap \partial K^-$. We denote by $\mathbf{n}^\pm$ the unit normals of $K^\pm$ at e and use $[\![\cdot]\!]$ to show the jump of the information across e, e.g. $[\![\boldsymbol{F}\cdot\mathbf{n}]\!] = \boldsymbol{F}^+\cdot\mathbf{n}^+ + \boldsymbol{F}^-\cdot\mathbf{n}^-$,

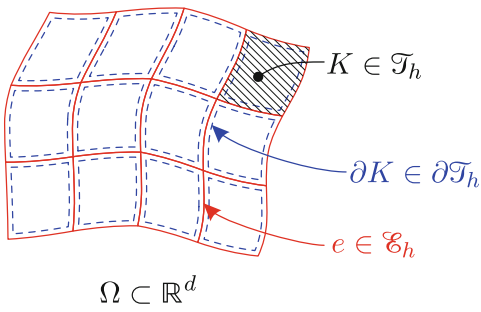

Fig. 3.3 Domain Ω with the discretization $\mathcal{T}_h$, the set of element faces ($\partial\mathcal{T}_h$), and the set of faces in the mesh ($\mathcal{E}_h$)

with $\boldsymbol{F}^{\pm}$ being the values of $\boldsymbol{F}$ corresponding to $K^{\pm}$. For the faces on the boundary of the domain, where $e \in \partial\mathscr{T}_h \cap \partial\Omega$, we define the jump based on the only contributing face, i.e. $[\![\boldsymbol{F}\cdot\mathbf{n}]\!] = \boldsymbol{F}\cdot\mathbf{n}$. Moreover, the average value of $\boldsymbol{F}$ at a common face is defined by $\{\{\boldsymbol{F}\}\} = (\boldsymbol{F}^{+} + \boldsymbol{F}^{-})/2$.

Throughout this section, we mainly use vector notation. However, for certain relations, the index notation can provide a more clear description. In those cases, we denote derivatives with respect to spatial coordinates with subscripts, i.e. $q_{i,j}$ denotes the derivative of the ith component of $\boldsymbol{q}$ with respect to the jth spatial coordinate. We also use $(v, w)_G$ to denote the inner product of functions v and w in $G \subset \mathbb{R}^d$, i.e. $(v, w)_G = \int_G vw\,\mathrm{d}G$. Furthermore, $\langle v, w\rangle_\Gamma$ denotes $\int_\Gamma vw\,\mathrm{d}\Gamma$, when $\Gamma \subset \mathbb{R}^{d-1}$.

3.3.2 Functional Setting

For each element $K \in \mathscr{T}_h$ and $p \geq 0$, let $\mathscr{Q}^p(K)$ denote the space of polynomials of degree at most p in each spatial direction. We choose our trial solution and test spaces as the set of square integrable functions over $\mathscr{T}_h$, such that their restriction to the domain of K belongs to $\mathscr{Q}^p(K)$; i.e.

$$\mathbf{V}_h^p := \{\boldsymbol{q} \in (L^2(\mathscr{T}_h))^{d+1} : \boldsymbol{q}|_K \in (\mathscr{Q}^p(K))^{d+1} \quad \forall K \in \mathscr{T}_h\}. \tag{3.43a}$$

The approximation spaces over the mesh skeleton ($\mathscr{E}_h$) are defined as:

$$\mathbf{M}_h^p := \{\boldsymbol{\mu} \in (L^2(\mathscr{E}_h))^{d+1} : \boldsymbol{\mu}|_e \in (\mathscr{Q}^p(e))^{d+1} \quad \forall e \in \mathscr{E}_h\}, \tag{3.43b}$$

$$\bar{\boldsymbol{M}}_h^p := \{\mu \in \left(L^2(\mathscr{E}_h)\right)^d : \mu|_e \in \left(\mathscr{Q}^p(e)\right)^d \quad \forall e \in \mathscr{E}_h\}. \tag{3.43c}$$

We also define the L^2-projection operator Π_∂, which maps a given $\boldsymbol{\xi} \in (L^2(\mathscr{E}_h))^{d+1}$ to the set of functions whose restriction to $e \in \mathscr{E}_h$ is in $(\mathscr{Q}^p(e))^{d+1}$, and Π_∂ satisfies:

$$\langle \Pi_\partial\boldsymbol{\xi} - \boldsymbol{\xi}, \boldsymbol{\mu}\rangle_e = 0, \quad \forall\boldsymbol{\mu} \in (\mathscr{Q}^p(e))^{d+1}.$$

3.3.3 Variational Formulation and Solution Procedure

Before we give the variational formulation for the hyperbolic and dispersive subproblems, we write (3.41) in the familiar conservation form:

$$\partial_t\boldsymbol{q} + \nabla\cdot\boldsymbol{F}(\boldsymbol{q}) = \boldsymbol{L} \quad \text{in } \Omega \subset \mathbb{R}^d, \tag{3.44}$$

with $\boldsymbol{L}$ being the source term, and

$$\boldsymbol{q} = \begin{Bmatrix} h \\ h\boldsymbol{u} \end{Bmatrix}, \quad \boldsymbol{F}(\boldsymbol{q}) = \begin{Bmatrix} h\boldsymbol{u} \\ h\boldsymbol{u} \otimes \boldsymbol{u} + \frac{1}{2} g h^2 \mathbf{I} \end{Bmatrix}. \tag{3.45}$$

Next, let us rewrite Eq. (3.42) as:

$$\begin{cases} \partial_t h = 0, \\ \partial_t (h\boldsymbol{u}) - gh\nabla\zeta + \boldsymbol{w}_1 = 0, \end{cases} \tag{3.46}$$

where $\boldsymbol{w}_1$ is obtained using:

$$(1 + h\mathcal{T}\frac{1}{h})\boldsymbol{w}_1 = gh\nabla\zeta + h\mathcal{Q}_1(\boldsymbol{u}). \tag{3.47}$$

Using definition (3.30) with $\beta = 1$, the above equation finds the following form:

$$\begin{aligned} \boldsymbol{w}_1 + h\mathcal{T}\left(\tfrac{1}{h}\boldsymbol{w}_1\right) = \boldsymbol{w}_1 &- \frac{1}{3}\nabla\left(h^3\nabla\cdot\left(\tfrac{1}{h}\boldsymbol{w}_1\right)\right) - \frac{h^2}{2}\nabla\cdot\left(\tfrac{1}{h}\boldsymbol{w}_1\right)\nabla b \\ &+ \frac{1}{2}\nabla\left(h\nabla b\cdot\boldsymbol{w}_1\right) + \nabla b\cdot\boldsymbol{w}_1\nabla b. \end{aligned} \tag{3.48}$$

We also expand the operator $\mathcal{Q}_1(\boldsymbol{u})$ in the right hand side of (3.47) as follows:

$$\begin{aligned} h\mathcal{Q}_1(\boldsymbol{u}) = &\frac{2}{3}\nabla\left(h^3\partial_x\boldsymbol{u}\cdot\partial_y\boldsymbol{u}^\perp + h^3(\nabla\cdot\boldsymbol{u})^2\right) + \frac{1}{2}\nabla\left(h^2\boldsymbol{u}\cdot(\boldsymbol{u}\cdot\nabla)\nabla b\right) \\ &+ h^2\left(\partial_x\boldsymbol{u}\cdot\partial_y\boldsymbol{u}^\perp + (\nabla\cdot\boldsymbol{u})^2\right)\nabla b + h\left(\boldsymbol{u}\cdot(\boldsymbol{u}\cdot\nabla)\nabla b\right)\nabla b. \end{aligned} \tag{3.49}$$

Based on above relations, (3.47) can be written as a system of first order equations:

$$\begin{cases} \nabla\cdot(\frac{1}{h}h\boldsymbol{w}_1) - h^{-3}w_2 = 0, \\ \boldsymbol{w}_1 - \frac{1}{3}\nabla(w_2) - \frac{1}{2h}w_2\nabla b + \frac{1}{2}\nabla(h\nabla b\cdot\boldsymbol{w}_1) \\ \qquad\qquad + \boldsymbol{w}_1\nabla b\otimes\nabla b = gh\nabla\zeta + h\mathcal{Q}_1(\boldsymbol{u}). \end{cases} \tag{3.50}$$

In the next two sections, we solve Eqs. (3.44) and (3.50).

Hyperbolic Part

We are looking for a piecewise polynomial solution $\boldsymbol{q}_h \in \mathbf{V}_h^p$ which satisfies Eq. (3.44) in the variational sense. Hence, for all $\boldsymbol{p} \in \mathbf{V}_h^p$ and every $K \in \mathcal{T}_h$, we want $\boldsymbol{q}_h$ to satisfy:

$$(\partial_t\boldsymbol{q}_h, \boldsymbol{p})_K + \langle \boldsymbol{F}_h^*, \boldsymbol{p}\rangle_{\partial K} - (\boldsymbol{F}(\boldsymbol{q}_h), \nabla\boldsymbol{p})_K - \boldsymbol{L}_h(\boldsymbol{p}) = 0. \tag{3.51}$$

Here, $\boldsymbol{F}_h^*$ is the *numerical flux*, an approximation to $\boldsymbol{F}(\boldsymbol{q})\cdot\mathbf{n}$ over the faces of the element K. Similar to the finite volume method, we can obtain a stable and convergent

solution by a proper choice of $\boldsymbol{F}_h^*$. In the hybridizable DG formulation, the numerical flux is defined through the numerical trace ($\widehat{\boldsymbol{q}}_h$), which is an approximation to $\boldsymbol{q}$ on the skeleton space ($\mathscr{E}_h$). Here, we consider the following form for $\boldsymbol{F}_h^*$:

$$\boldsymbol{F}_h^* = \boldsymbol{F}(\widehat{\boldsymbol{q}}_h) \cdot \mathbf{n} + \boldsymbol{\tau}(\boldsymbol{q}_h - \widehat{\boldsymbol{q}}_h), \tag{3.52}$$

where $\boldsymbol{\tau}$ is the stabilization parameter and its choice is important for obtaining a convergent and stable method. Here, we use the Lax-Friedrichs flux for this purpose (Samii et al. 2019). It is also worth mentioning that $\widehat{\boldsymbol{q}}_h$ is assumed to be single-valued on any given face in $\mathscr{E}_h$.

Next, we want to satisfy the flux conservation condition across the element faces. Since, the numerical flux is the only means of communication between elements, in all of the internal faces, we require that the projection of the jump of $\boldsymbol{F}_h^*$ onto $\mathbf{M}_h^p$ vanishes, i.e. $\Pi_\partial \left[\!\left[\boldsymbol{F}_h^*\right]\!\right] = 0$. On the other hand, over the domain boundary ($\partial\Omega$), we apply the boundary condition through the boundary operator $\boldsymbol{B}_h$. Hence, $\forall \boldsymbol{\mu} \in \mathbf{M}_h^p$, we want to have:

$$\langle \boldsymbol{F}_h^*, \boldsymbol{\mu} \rangle_{\partial\mathscr{T}_h \setminus \partial\Omega} + \langle \boldsymbol{B}_h, \boldsymbol{\mu} \rangle_{\partial\mathscr{T}_h \cap \partial\Omega} = 0 \tag{3.53}$$

Here, $\boldsymbol{B}_h$ is the boundary operator, and should be defined according to the applied conditions on $\partial\Omega$. The details of the employed boundary conditions can be found in other references (Samii et al. 2019).

We should solve Eqs. (3.51) and (3.53) to obtain the unknowns of the problem. We can substitute $\boldsymbol{F}_h^*$ from (3.52) into these two equations, and assemble (3.51) over all of the elements. Thus, the problem may be summarized as finding the approximate solution $(\boldsymbol{q}_h, \widehat{\boldsymbol{q}}_h) \in \mathbf{V}_h^p \times \mathbf{M}_h^p$, such that, for all $(\boldsymbol{p}, \boldsymbol{\mu}) \in \mathbf{V}_h^p \times \mathbf{M}_h^p$:

$$\begin{aligned}
&(\partial_t \boldsymbol{q}_h, \boldsymbol{p})_{\mathscr{T}_h} - (\boldsymbol{F}(\boldsymbol{q}_h), \nabla \boldsymbol{p})_{\mathscr{T}_h} + \langle \boldsymbol{\tau}\boldsymbol{q}_h, \boldsymbol{p} \rangle_{\partial\mathscr{T}_h} \\
&\qquad + \langle \boldsymbol{F}(\widehat{\boldsymbol{q}}_h) \cdot \mathbf{n}, \boldsymbol{p} \rangle_{\partial\mathscr{T}_h} - \langle \boldsymbol{\tau}\widehat{\boldsymbol{q}}_h, \boldsymbol{p} \rangle_{\partial\mathscr{T}_h} - \boldsymbol{L}_h(\boldsymbol{p}) = 0, \qquad (3.54a) \\
&\langle \boldsymbol{F}(\widehat{\boldsymbol{q}}_h) \cdot \mathbf{n}, \boldsymbol{\mu} \rangle_{\partial\mathscr{T}_h \setminus \partial\Omega} + \langle \boldsymbol{\tau}\boldsymbol{q}_h, \boldsymbol{\mu} \rangle_{\partial\mathscr{T}_h \setminus \partial\Omega} \\
&\qquad - \langle \boldsymbol{\tau}\widehat{\boldsymbol{q}}_h, \boldsymbol{\mu} \rangle_{\partial\mathscr{T}_h \setminus \partial\Omega} + \langle \boldsymbol{B}_h, \boldsymbol{\mu} \rangle_{\partial\mathscr{T}_h \cap \partial\Omega} = 0. \qquad (3.54b)
\end{aligned}$$

Considering Eq. (3.54), we use Newton-Raphson method to form a linearized equation in terms of the increments of $\boldsymbol{q}_h$ and $\widehat{\boldsymbol{q}}_h$. For the simplicity of the presentation, we consider backward Euler technique as the time integrator, with Δt being the current time step. Hence, denoting by $\boldsymbol{q}_h^{n-1}$ the values of $\boldsymbol{q}_h$ in the previous time level, and $(\bar{\boldsymbol{q}}_h, \bar{\widehat{\boldsymbol{q}}}_h) \in \mathbf{V}_h^p \times \mathbf{M}_h^p$ the corresponding values in the current iteration, we seek $(\delta\boldsymbol{q}_h, \delta\widehat{\boldsymbol{q}}_h) \in \mathbf{V}_h^p \times \mathbf{M}_h^p$ such that for all $(\boldsymbol{p}, \boldsymbol{\mu}) \in \mathbf{V}_h^p \times \mathbf{M}_h^p$, we have:

$$\begin{aligned}
&a_1(\delta\boldsymbol{q}_h, \boldsymbol{p}) + c_1(\delta\widehat{\boldsymbol{q}}_h, \boldsymbol{p}) + f_1(\boldsymbol{p}) = 0, \qquad (3.55a) \\
&c_2^T(\delta\boldsymbol{q}_h, \boldsymbol{\mu}) + c_3^T(\delta\boldsymbol{q}_h, \boldsymbol{\mu}) + e_1(\delta\widehat{\boldsymbol{q}}_h, \boldsymbol{\mu}) \\
&\qquad + e_2(\delta\widehat{\boldsymbol{q}}_h, \boldsymbol{\mu}) + f_2(\boldsymbol{\mu}) + f_3(\boldsymbol{\mu}) = 0. \qquad (3.55b)
\end{aligned}$$

with the bilinear forms and functionals defined as below:

$$
\begin{aligned}
a_1(\delta q_j,\, p_i) &= \frac{1}{\Delta t}(\delta q_j,\, \delta_{ij}\, p_i)_{\mathcal{T}_h} - \left(\frac{\partial F_{ik}}{\partial q_j}\delta q_j,\, p_{i,k}\right)_{\mathcal{T}_h} + \left\langle \tau_{ij}\delta q_j,\, p_i\right\rangle_{\partial\mathcal{T}_h},\\
c_1(\delta\hat{q}_j,\, p_i) &= \left\langle \left(\frac{\partial \hat{F}_{ik}}{\partial \hat{q}_j}n_k + \frac{\partial \tau_{ik}}{\partial \hat{q}_j}\bar{q}_k - \frac{\partial \tau_{ik}}{\partial \hat{q}_j}\bar{\hat{q}}_k - \tau_{ij}\right)\delta\hat{q}_j,\, p_i\right\rangle_{\partial\mathcal{T}_h},\\
f_1(p_i) &= \frac{1}{\Delta t}(\bar{q}_i - q_i^{n-1},\, p_i)_{\mathcal{T}_h} - \langle \hat{F}_{ij}n_j,\, p_i\rangle_{\partial\mathcal{T}_h} + \langle \tau_{ij}\bar{q}_j,\, p_i\rangle_{\partial\mathcal{T}_h}\\
&\quad - \langle \tau_{ij}\bar{\hat{q}}_j,\, p_i\rangle_{\partial\mathcal{T}_h} - (F_{ij},\, \partial_j p_i)_{\mathcal{T}_h} - L_i(p_i),\\
c_2^T(\delta q_j,\, \mu_i) &= \left\langle \tau_{ij}\delta q_j,\, \mu_i\right\rangle_{\partial\mathcal{T}\setminus\partial\Omega}, \quad c_3^T(\delta\boldsymbol{q}_h,\, \boldsymbol{\mu}) = \left\langle \frac{\partial \boldsymbol{B}_h}{\partial \boldsymbol{q}_h}\delta\boldsymbol{q}_h,\, \boldsymbol{\mu}\right\rangle_{\partial\Omega},\\
e_1(\delta\hat{q}_i,\, \mu_i) &= \left\langle \left(\frac{\partial \hat{F}_{ik}}{\partial \hat{q}_j}n_k + \frac{\partial \tau_{ik}}{\partial \hat{q}_j}\bar{q}_k - \frac{\partial \tau_{ik}}{\partial \hat{q}_j}\bar{\hat{q}}_k - \tau_{ij}\right)\delta\hat{q}_j,\, \mu_i\right\rangle_{\partial\mathcal{T}\setminus\partial\Omega},\\
e_2(\delta\widehat{\boldsymbol{q}}_h,\, \boldsymbol{\mu}) &= \left\langle \frac{\partial \boldsymbol{B}_h}{\partial \widehat{\boldsymbol{q}}_h}\delta\widehat{\boldsymbol{q}}_h,\, \boldsymbol{\mu}\right\rangle_{\partial\Omega},\\
f_2(\mu_i) &= \left\langle \hat{F}_{ij}n_j + \tau_{ij}\bar{q}_j - \tau_{ij}\bar{\hat{q}}_j,\, \mu_i\right\rangle_{\partial\mathcal{T}\setminus\partial\Omega}; \quad f_3(\boldsymbol{\mu}) = \langle \boldsymbol{B}_h,\, \boldsymbol{\mu}\rangle_{\partial\Omega}
\end{aligned}
\tag{3.56}
$$

In the above definitions, F_{ij}, $\hat{F}_{ij}$, and τ_{ij} denote the element at ith row and jth column of $\boldsymbol{F}(\bar{\boldsymbol{q}}_h)$, $\boldsymbol{F}(\bar{\widehat{\boldsymbol{q}}}_h)$, and $\boldsymbol{\tau}(\bar{\widehat{\boldsymbol{q}}}_h)$, respectively. Meanwhile, δ_{ij} denotes the Kronecker delta.

Dispersive Part

Now, we consider solving Eq. (3.50). To this end, we find $(\boldsymbol{w}_{1h},\, w_{2h}) \in \mathbf{V}_h^p$, and $\hat{\boldsymbol{w}}_{1h} \in \bar{\boldsymbol{M}}_h^p$ such that:

$$
\begin{cases}
(h^{-3}\, w_{2h},\, p_2) - \langle \hat{h}^{-1}\, \hat{\mathbf{w}}_{1h}\cdot\mathbf{n},\, p_2\rangle + \left(h^{-1}\, \boldsymbol{w}_{1h},\, \nabla p_2\right) = 0.\\
(\boldsymbol{w}_{1h},\, \mathbf{p}_1) - \frac{1}{3}\langle \mathbf{w}_{2h}^*\cdot\mathbf{n},\, \mathbf{p}_1\rangle + \frac{1}{3}\,(w_{2h},\, \nabla\cdot\mathbf{p}_1) - \frac{1}{2}\left(\frac{1}{h}\nabla b\, w_{2h},\, \mathbf{p}_1\right)\\
\qquad\qquad + \frac{1}{2}\langle \hat{h}\nabla b\cdot\hat{\boldsymbol{w}}_{1h},\, \mathbf{p}_1\cdot\mathbf{n}\rangle - \frac{1}{2}\,(h\nabla b\cdot\boldsymbol{w}_{1h},\, \nabla\cdot\mathbf{p}_1)\\
\qquad\qquad + (\nabla b\otimes\nabla b\, \boldsymbol{w}_{1h},\, \mathbf{p}_1) = l_{01}(\mathbf{p}_1),
\end{cases}
\tag{3.57}
$$

for all $(\mathbf{p}_1,\, p_2) \in \mathbf{V}_h^p$. Here, the definition of $l_{01}(\mathbf{p}_1)$ can be inferred by comparing the above system with (3.50); moreover, the numerical flux $\boldsymbol{w}_{2h}^*\cdot\mathbf{n}$ is defined as:

$$
\mathbf{w}_{2h}^*\cdot\mathbf{n} = w_{2h}\mathbf{I}\cdot\mathbf{n} + \boldsymbol{\tau}\left(\boldsymbol{w}_{1h} - \hat{\boldsymbol{w}}_{1h}\right),
\tag{3.58}
$$

where, $\mathbf{I}$ is the $d \times d$ identity matrix, and $\boldsymbol{\tau}$ is the stabilization parameter matrix. We will use a constant and uniform diagonal matrix for this purpose.

Next, we define the following bilinear forms and functionals:

$$
\begin{gathered}
a_{02}(w_{2h}, p_2) = (h^{-3} w_{2h}, p_2); \quad b_{01}^T(\boldsymbol{w}_{1h}, p_2) = (h^{-1}\boldsymbol{w}_{1h}, \nabla p_2); \\
c_{01}(\hat{\boldsymbol{w}}_1, p_2) = \langle \hat{h}^{-1}\hat{\boldsymbol{w}}_{1h} \cdot \mathbf{n}, p_2 \rangle; \quad b_{02}(w_{2h}, \mathbf{p}_1) = (\nabla w_{2h}, \mathbf{p}_1); \\
a_{01}(\boldsymbol{w}_{1h}, \mathbf{p}_1) = (\boldsymbol{w}_{1h}, \mathbf{p}_1) + (\nabla b \otimes \nabla b\, \boldsymbol{w}_{1h}, \mathbf{p}_1)\,; \\
d_{01}(\boldsymbol{w}_{1h}, \mathbf{p}_1) = \langle \tau \boldsymbol{w}_{1h}, \mathbf{p}_1 \rangle; \quad b_{03}^T(\boldsymbol{w}_{1h}, \mathbf{p}_1) = (h\nabla b \cdot \boldsymbol{w}_{1h}, \nabla \cdot \mathbf{p}_1) \\
a_{03}(w_{2h}, \mathbf{p}_1) = \left(\tfrac{1}{2} h \nabla b\, w_{2h}, \mathbf{p}_1\right); \\
c_{02}(\hat{\boldsymbol{w}}_{1h}, \mathbf{p}_1) = \langle \tau \hat{\boldsymbol{w}}_{1h}, \mathbf{p}_1 \rangle + \frac{3}{2} \langle \hat{h} \nabla b \cdot \hat{\boldsymbol{w}}_{1h}, \mathbf{p}_1 \cdot \mathbf{n} \rangle.
\end{gathered}
\tag{3.59}
$$

We are now able to write Eq. (3.57) as:

$$
\begin{cases}
A_{02} w_{2h} + B_{01}^T \boldsymbol{w}_{1h} - C_{01} \hat{\boldsymbol{w}}_{1h} = 0 \\
\left(A_{01} - \frac{1}{2} B_{03}^T - \frac{1}{3} D_{01}\right) \boldsymbol{w}_{1h} - \left(\frac{1}{2} A_{03} + \frac{1}{3} B_{02}\right) w_{2h} + \frac{1}{3} C_{02} \hat{\boldsymbol{w}}_{1h} = L_{01}
\end{cases}
\tag{3.60a}
$$

Finally, we also require that the numerical flux be conserved across element edges. In other words, we have:

$$
\langle \mathbf{w}_{2h}^* \cdot \mathbf{n}, \mu \rangle_{\partial \mathcal{T}_h \setminus \partial \Omega} + \langle \mathcal{B}_h, \mu \rangle_{\partial \mathcal{T}_h \cap \partial \Omega} = 0, \tag{3.60b}
$$

for all $\mu \in \bar{\boldsymbol{M}}_h^p$. Here $\mathcal{B}_h$ is the boundary operator, which can be defined based on the applied boundary conditions.

As a final remark, one should note that solving equation (3.47) involves computation of the 1st and 2nd order derivatives of the velocity vector. Among all other terms, we need to compute the term $\nabla\left(h^3 \partial_x \boldsymbol{u} \cdot \partial_y \boldsymbol{u}^\perp + h^3 (\nabla \cdot \boldsymbol{u})^2\right)$ in each element. If this computation is performed in a local manner in each element independent of the others, we lose a significant order of accuracy. It can be easily checked that by computing this term locally, our solution will not converge for elements with first order polynomial approximation. On the other hand, since we use this term in our weak formulation, one might consider using the integration by parts technique to transfer the gradient of the parentheses to the test function, and replace the flux of the terms in parentheses with a proper numerical flux. However, finding such a flux formulation for the extremely nonlinear terms like $(\nabla \cdot \boldsymbol{u})^2$ or $\partial_x \boldsymbol{u} \cdot \partial_y \boldsymbol{u}^\perp$ is not straightforward. Therefore, in this study we use a local discontinuous Galerkin technique to obtain approximations to $\nabla \mathbf{u}$ and $\nabla \nabla \mathbf{u}$. It is worthwhile to note that, $\nabla \mathbf{u}$ is a 2-tensor and $\nabla \nabla \mathbf{u}$ is a 3-tensor; As a result, we switch to index notation for clarity. We use u_i to denote the components of $\mathbf{u}$ and define the tensors r_{ij} (which contains the components of $\nabla \mathbf{u}$), and s_{ijk} (containing the components of $\nabla \nabla \mathbf{u}$) as follows:

$$
r_{ij} - \partial_j u_i = 0, \tag{3.61a}
$$

$$
s_{ijk} - \partial_k r_{ij} = 0. \tag{3.61b}
$$

Next, we write the variational formulations corresponding to these equations in an element ($K \in \mathcal{T}_h$):

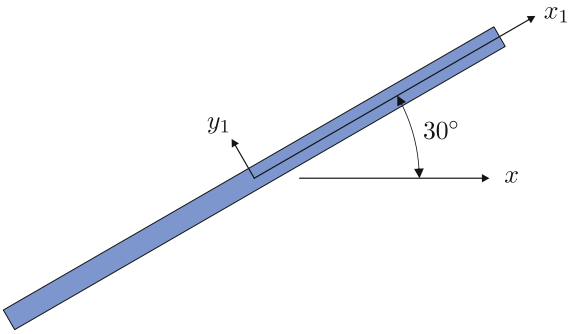

Fig. 3.4 Schematic plot of the domain of Example 1. The stripe is 20 m long and 0.2 m wide

$$\left(r_{ij}, \sigma_{ij}\right)_K = \langle \hat{u}_i, \sigma_{ij} n_j \rangle_{\partial K} - \left(u_i, \partial_j \sigma_{ij}\right)_K , \tag{3.62a}$$

$$\left(s_{ijk}, \eta_{ijk}\right)_K = \langle \hat{r}_{ij}, \eta_{ijk} n_k \rangle_{\partial K} - \left(r_{ij}, \partial_k \eta_{ijk}\right)_K . \tag{3.62b}$$

In these equations, $\hat{u}_i$ and $\hat{r}_{ij}$ are the numerical fluxes, which should be defined based on the values of u_i and r_{ij} in the two neighboring elements. In this study we use the centered fluxes (Bassi and Rebay 1997), i.e. $\hat{u}_i = \{\{u_i\}\}$, $\hat{r}_{ij} = \{\{r_{ij}\}\}$.

By using this technique, we can compute the derivatives of $\mathbf{u}$, and substitute them in (3.49) to compute $h\mathcal{Q}_1(\mathbf{u})$, and solve the system (3.60a) by an explicit time integration method.

3.4 Numerical Results

In this section, we present two numerical examples, for verification and validation of the presented technique. The purpose of the first example is to show the convergence properties of the numerical approximation with respect to the element size (Δx) and the polynomial order (p). In the second example we consider the amplifying effect of the reflection from a solid wall on the amplitude of a solitary wave. This kind of simulation is useful in the design of levees and dikes. We compare our numerical results with experimental data from the literature. In both of the numerical tests presented here, we use backward difference formula of second order for the hyperbolic part and the regular Runge-Kutta time integration technique for the dispersive part of the operator splitting. To solve the problem, we use our software which has been developed (Samii et al. 2016) using the libraries deal.II (Bangerth et al. 2016), PETSc (Balay et al. 2015), and MUMPS.

Example 1 In this example we consider the exact solution to the nonlinear Green-Naghdi equation on a flat bathymetry in one dimension. This solution, which is derived by Serre (1953), should match our numerical results with $b = -h_0$. This analytical solution is given by:

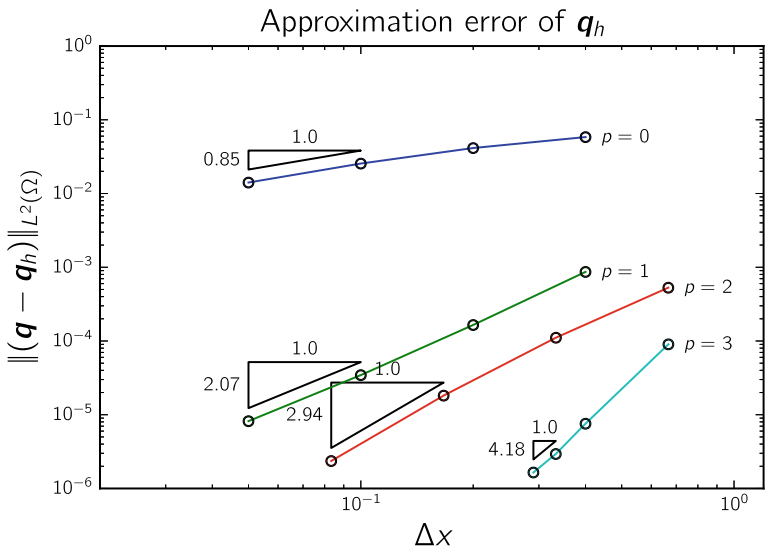

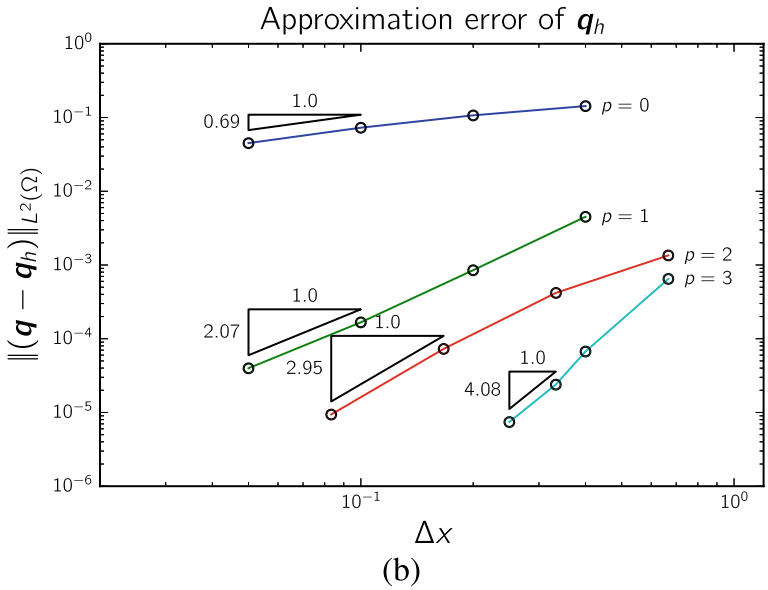

Fig. 3.5 The approximation errors and rates of convergence for different mesh sizes and polynomial orders **a**: $a_0/h_0 = 0.2$, **b**: $a_0/h_0 = 0.4$

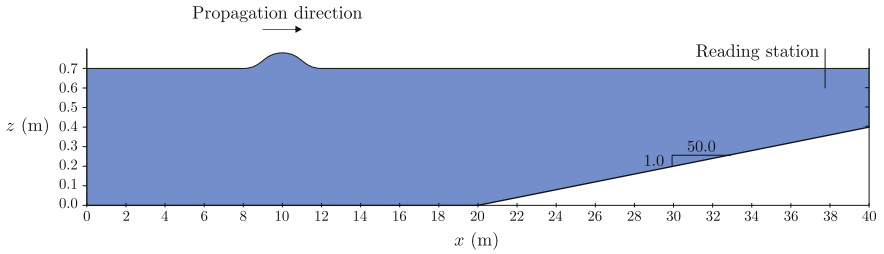

Fig. 3.6 The geometry of the numerical model of Example 2

$$h(t,x) = h_0 + a_0 \operatorname{sech}^2\left(\kappa(x - x_0 - c_0 t)\right), \tag{3.63a}$$

$$h\mathbf{u}(t,x) = c_0 h(t,x) - c_0 h_0, \tag{3.63b}$$

$$\kappa = \frac{\sqrt{3a_0}}{2h_0\sqrt{h_0 + a_0}}, \tag{3.63c}$$

$$c_0 = \sqrt{g(h_0 + a_0)} \tag{3.63d}$$

Here, we consider $h_0 = 0.5$, and two values for a_0/h_0, i.e. 0.05, 0.2. We solve the problem in the domain shown in Fig. 3.4. The domain is a stripe with 20 m length and 0.2 m width, and is oriented with an angle of 30° with respect to the x-axis. The reason for choosing a rotated domain is to include as many nonzero terms as possible in Eq. (3.47). Since we have rotated the domain, the x-coordinate in the analytical solution (3.63) should be replaced by x_1 (refer to Fig. 3.4). At all boundaries we consider solid wall conditions. In our numerical scheme, we assign the initial conditions according to the above $h, h\boldsymbol{u}$ at $t = 0$, $x_0 = -4$, and let the solitary wave propagate in the positive x_1-direction.

We compute the errors of the numerical results at time $t = 0.375$ s in the L^2-norm, i.e. $\|\boldsymbol{q} - \boldsymbol{q}_h\|_{L^2}$ with $\boldsymbol{q} = (h, h\boldsymbol{u})$. Next, we compute the corresponding rates of convergence on a set of successively refined meshes for polynomial orders $p = 0, 1, 2, 3$. The corresponding plots for $a_0/h_0 = 0.2, 0.4$ are shown in Fig. 3.5. We can observe that for $a_0/h_0 = 0.2$, the convergence rates are very close to the optimal rates, i.e. $p + 1$, for all orders of polynomial approximations. An important feature in these plots is the convergence of the results for $p = 0$ with the order 0.85. The same observation as above is also true for $a_0/h_0 = 0.4$, except the lower convergence rate for $p = 0$. As a final remark, it should be noted that in this example, the analytical solution of $\boldsymbol{u}$ is not exactly zero at the two ends of the domain i.e. $x_1 = \pm 10$ m. Hence, the error caused by applying the solid wall becomes the dominant error as we decrease the discretization errors. As a result we cannot achieve errors lower than 10^{-6} in this example.

Example 2 In this example we validate our numerical results against experimental data regarding the reflection of a solitary wave over a sloping beach (Dodd 1998; Walkley and Berzins 1999). The geometry of this problem is shown in Fig. 3.6. The

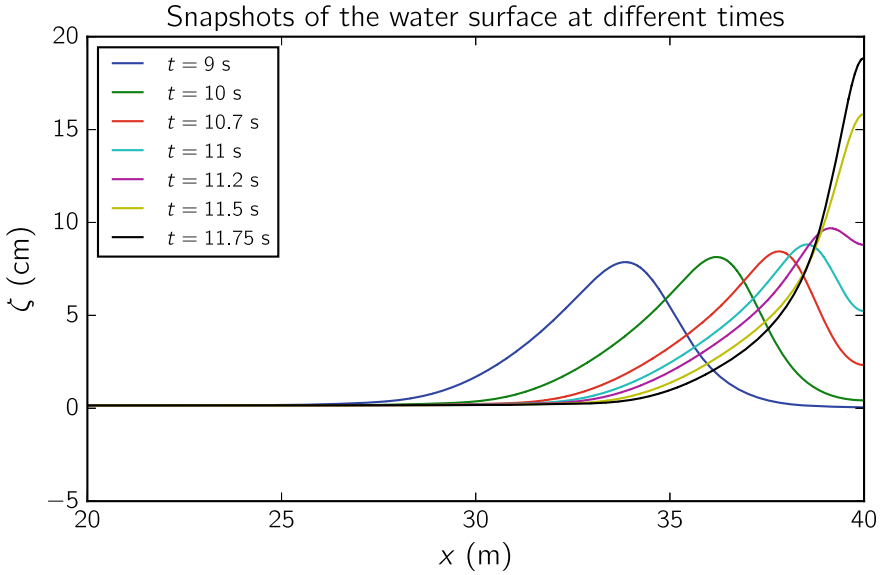

(a) For a_0 = 7 cm

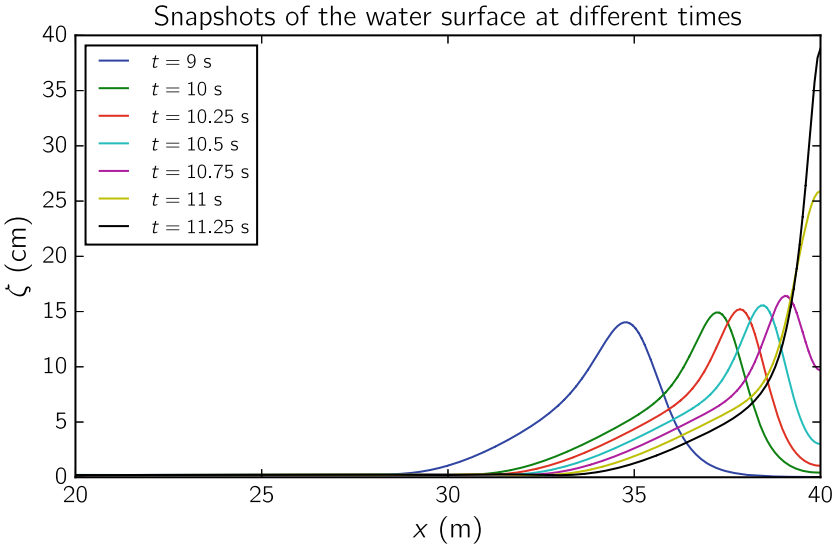

(b) For a_0 = 12 cm

Fig. 3.7 The snapshots of the water surface (ζ) in Example 2, at different times

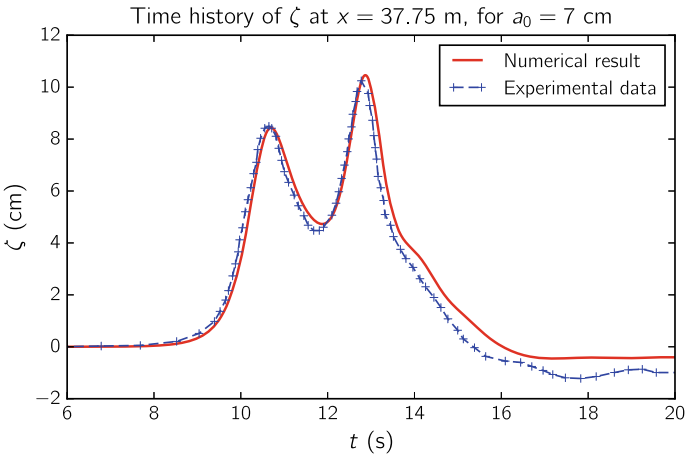

(a) For a_0 = 7 cm

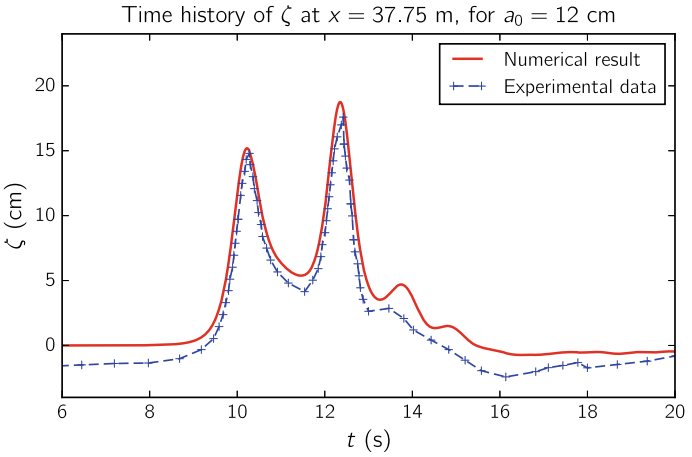

(b) For a_0 = 12 cm

Fig. 3.8 Time history of the water surface at reading station ($x = 37.75$ m) in Example 2

incident wave does not break prior to touching the wall; however, after the reflection its shape changes dramatically, which requires a fully nonlinear model to capture its behavior.

The numerical model is 40 m long, and the solid wall condition is applied at its both ends. The initial water depth is $h_0 = 0.7$ m, and two values are used for the initial wave amplitude, i.e. $a_0 = 7$ cm, and $a_0 = 12$ cm. The wave starts its propagation at $x = 10$ m (refer to Fig. 3.6), and the beach with the slope 1:50, starts at $x = 20$ m. The element size is 8 cm and we use first order elements to discretize the domain. The time history of water surface elevation at different locations in the domain is

available in the literature (Walkley and Berzins 1999). Here, we present our results for a reading station located at $x = 37.75$ m.

In Fig. 3.7, we show the snapshots of the water surface rise during the simulation for the initial amplitudes $a_0 = 7$ and 12 cm. In Fig. 3.8 we show the time history of the water surface elevation at the reading station with $x = 37.75$ m. The numerical technique have been able to capture the peaks in the experimental data quite well; however, as the reflected waves return from the wall, we can observe differences between numerical and experimental results.

3.5 Conclusions

In this paper, we have discussed various Boussinesq-Green-Naghdi models for approximating nearshore wave physics, and given some preliminary numerical results using the hybrid discontinuous Galerkin method. Future work will explore this methodology more fully for complex, two-dimensional domains, with adaptive mesh and time-step control.

Acknowledgements The authors wish to acknowledge the support of National Science Foundation grants ACI-1339801 and NSF-1854986.

References

Agnon, Y., P.A. Madsen, and H.A. Schäffer. 1999. A new approach to high-order Boussinesq models. *Journal of Fluid Mechanics* 399: 319–333.

Artiles, W., and A. Nachbin. 2004. Nonlinear evolution of surface gravity waves over highly variable depth. *Physical Review Letters* 93(23): 234501.

Artiles, W., and A. Nachbin. 2004. Asymptotic nonlinear wave modeling through the Dirichlet-to-Neumann operator. *Methods and Applications of Analysis* 11(4): 475–492.

Balay, S., S. Abhyankar, M.F. Adams, J. Brown, P. Brune, K. Buschelman, L. Dalcin, V. Eijkhout, W.D. Gropp, D. Kaushik, M.G. Knepley, L. Curfman McInnes, K. Rupp, B.F. Smith, S. Zampini and H. Zhang. 2015. PETSc users manual. Technical Report ANL-95/11 - Revision 3.6, Argonne National Laboratory.

Bangerth, W., D. Davydov, T. Heister, L. Heltai, G. Kanschat, M. Kronbichler, M. Maier, B. Turcksin and D. Wells. 2016. The deal.II library, version 8.4. *Journal of Numerical Mathematics* 24(3): 135–141.

Barthélemy, E. 2004. Nonlinear shallow water theories for coastal waves. *Surveys in Geophysics* 25 (3–4): 315–337.

Bassi, F., and S. Rebay. 1997. A high-order accurate discontinuous finite element method for the numerical solution of the compressible Navier-Stokes equations. *Journal of Computational Physics* 131(2): 267–279.

Bonneton, P., F. Chazel, D. Lannes, F. Marche, and M. Tissier. 2011. A splitting approach for the fully nonlinear and weakly dispersive Green-Naghdi model. *Journal of Computational Physics* 230: 1479–2498.

Boussinesq, J. 1872. Théorie des ondes et des remous qui se propagent le long d'un canal rectangulaire horizontal. en communiquant au liquide contenu dans ce canal des vitesses sensiblement pareilles de la surface au fond. *Journal de Mathematiques Pures et Appliquees* 55–108.

Castro, A., and D. Lannes. 2014. Fully nonlinear long-wave models in the presence of vorticity. *Journal of Fluid Mechanics* 759: 642–675.

Chazel, F., M. Benoit, A. Ern, and S. Piperno. 2009. A double-layer Boussinesq-type model for highly nonlinear and dispersive waves. *Proceedings of the Royal Society A* 465: 2319–2346.

Chazel, F., D. Lannes, and F. Marche. 2011. Numerical simulation of strongly nonlinear and dispersive waves using a Green-Naghdi model. *Journal of Scientific Computing* 48(1–3): 105–116.

Craig, W., C. Sulem, and P.-L. Sulem. 1992. Nonlinear modulation of gravity waves: a rigorous approach. *Nonlinearity* 5(2): 497–552.

Craig, W., and C. Sulem. 1993. Numerical simulation of gravity waves. *Journal of Computational Physics* 108(1): 73–83.

Dodd, N. 1998. Numerical model of wave run-up, overtopping, and regeneration. *Journal of Waterway, Port, Coastal, and Ocean Engineering* 124(2): 73–81.

Gobbi, M.F., J.T. Kirby, and G. Wei. 2000. A fully nonlinear Boussinesq model for surface waves. Part 2. Extension to *Journal of Fluid Mechanics* 405: 181–210.

Green, A.E. and P.M. Naghdi,. 1976. A derivation of equations for wave propagation in water of variable depth. *Journal of Fluid Mechanics* 78(2): 237–246.

Holthuijsen, L.H. 2007. *Waves in oceanic and coastal waters*. Cambridge Press.

Korteweg, D.J. and G. De Vries. 1895. XLI. On the change of form of long waves advancing in a rectangular canal, and on a new type of long stationary waves. *The London, Edinburgh, and Dublin Philosophical Magazine and Journal of Science* 39(240): 422–443.

Lannes, D., and P. Bonneton. 2009. Derivation of asymptotic two-dimensional time-dependent equations for surface water wave propagation. *Physics of Fluids* 21(1): 016601.

Lannes, D. 2013. *The water waves problem—mathematical analysis and asymptotics*. American Mathematical Society.

Lannes, D., and F. Marche. 2015. A new class of fully nonlinear and weakly dispersive Green-Naghdi models for efficient 2D simulations. *Journal of Computational Physics* 282: 238–268.

Madsen, P.A., R. Murray, and O.R. Sørensen. 1991. A new form of the Boussinesq equations with improved linear dispersion characteristics. *Coastal Engineering* 15(4): 371–388.

Madsen, P.A. and O.R. Sørensen. 1992. A new form of the boussinesq equations with improved linear dispersion characteristics. Part 2. A slowly–varying bathymetry. *Coastal Engineering* 18(3–4): 183–204.

Madsen, P.A., and H.A. Schäffer. 1998. Higher-order boussinesq-type equations for surface gravity waves: derivation and analysis. *Proceedings: Mathematical, Physical and Engineering Sciences* 356 (1749): 3123–3181.

Madsen, P.A., H.B. Bingham, and H. Liu. 2002. A new Boussinesq method for fully nonlinear waves from shallow to deep water. *Journal of Fluid Mechanics* 462: 1–30.

Madsen, P.A., H.B. Bingham, and H.A. Schäffer. 2003. Boussinesq-type formulations for fully nonlinear and extremely dispersive water waves: Derivation and analysis. *Proceedings: Mathematical, Physical and Engineering Sciences* 459(2033): 1075–1104.

Madsen, P.A., D.R. Fuhrman, and B. Wang. 2006. A Boussinesq-type method for fully nonlinear waves interacting with a rapidly varying bathymetry. *Coastal Engineering* 53 (5): 487–504.

Nwogu, O. 1993. Alternative form of Boussinesq equations for nearshore wave propagation. *Journal of Waterway, Port, Coastal, and Ocean Engineering* 119(6): 618–638.

Peregrine, D.H. 1967. Long waves on a beach. *Journal of Fluid Mechanics* 27(4): 815–827.

Samii, A., C. Michoski, and C. Dawson. 2016. A parallel and adaptive hybridized discontinuous Galerkin method for anisotropic nonhomogeneous diffusion. *Computer Methods in Applied Mechanics and Engineering* 304: 118–139.

Samii, A., K. Kazhyken, C. Michoski, and C. Dawson. 2019. A comparison of the explicit and implicit hybridizable discontinuous galerkin methods for nonlinear shallow water equations. *Journal of Scientific Computing* 80 (3): 1936–1956.

Serre, F. 1953. Contribution à l'étude des écoulements permanents et variables dans les canaux. *La Houille Blanche* 39(6): 830–872.

Strang, G. 1968. On the construction and comparison of difference schemes. *SIAM Journal on Numerical Analysis* 5 (3): 506–517.

Walkley, M., and M. Berzins. 1999. A finite element method for the one-dimensional extended Boussinesq equations. *International Journal for Numerical Methods in Fluids* 29(2): 143–157.

Wei, G., and J.T. Kirby. 1995. A fully nonlinear boussinesq model for surface waves. Part 1. Highly nonlinear unsteady waves. *Journal of Fluid Mechanics* 294: 71–92.

Witting, J.M. 1984. A unified model for the evolution nonlinear water waves. *Journal of Computational Physics* 56(2): 203–236.

Zakarhov, V.E. 1968. Stability of periodic waves of finite amplitude on the surface of a deep fluid. *Journal of Applied Mechanics and Technical Physics* 9(2): 190–194.

Zhang, Y., A.B. Kennedy, N. Panda, C. Dawson, and J.J. Westerink. 2013. Boussinesq-Green-Naghdi rotational water wave theory. *Coastal Engineering* 73: 13–27.

Zhang, Y., A.B. Kennedy, A.S. Donahue, J.J. Westerink, N. Panda, and C. Dawson. 2014. Rotational surf zone modeling for O(μ^4) Boussinesq-green-naghdi systems. *Ocean Modelling* 79: 43–53.

Chapter 4
Tides in Coastal Seas. Influence of Topography and Bottom Friction

Pieter C. Roos and Huib E. de Swart

Abstract Tides are important in various ways, e.g., by affecting navigation and coastal safety and by acting as a driver for sediment transport and seabed dynamics. To explain spatial patterns of tidal phase and range, observed in coastal seas around the world, we present an idealised process-based model. It solves the depth-averaged linearised shallow water equations, including the Coriolis effect and bottom friction, on schematised geometries with rectilinear coastlines and stepwise topographic variations. Based on an extended Klein-Gordon equation (accounting for bottom friction), Kelvin and Poincaré modes are identified as the fundamental wave solutions in a channel of uniform width and depth. We analyse their spatial structures and dynamic properties, addressing the roles of bottom friction and transverse topographic steps. The solution for a semi-enclosed basin, including topographic steps, is then obtained as a superposition of these wave modes, by applying a collocation technique. As an example, we present solutions that grossly explain the amphidromic system of the Gulf of California. Finally, we discuss the modelling approach and address the links with morphodynamics and climate change.

4.1 Introduction

Tides are the periodic water oscillations driven by the gravitational attraction of the moon and the sun. They constitute a fascinating phenomenon of both academic and practical interest.

To clarify this, it is useful to distinguish between 'vertical' and 'horizontal' tides. The *vertical tide* concerns the rise and fall of the free surface, with the difference between high and low water known as tidal range H. Figure 4.1 shows an example

P. C. Roos (✉)
Water Engineering & Management, University of Twente, Enschede, The Netherlands
e-mail: p.c.roos@utwente.nl

H. E. de Swart
Institute for Marine and Atmospheric research, Department of Physics, Utrecht University, Utrecht, The Netherlands
e-mail: h.e.deswart@uu.nl

H. Schuttelaars et al. (eds.), *The Mathematics of Marine Modelling*,
Mathematics of Planet Earth 9, https://doi.org/10.1007/978-3-031-09559-7_4

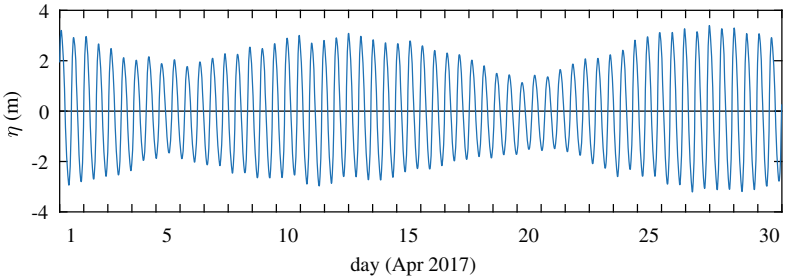

Fig. 4.1 Tidal record at Dover, UK, showing observed surface elevation versus time for April 2017. Mean elevation over this period used as vertical datum. Data from British Oceanographic Data Centre

of a tidal record at Dover, UK, with $H \sim 3 - 6$ m. It is dominated by a semi-diurnal cycle and further subject to other variations (spring-neap cycle, daily inequality) and weather effects. These water levels are important for coastal safety and for navigation, with so-called tidal windows allowing ship access to channels and harbours.

The *horizontal tide* refers to the oscillatory currents that are dynamically coupled to the vertical tide. In the North Sea, such currents are in the order of $0.1 - 1$ m s^{-1} (Davies and Kwong 2000). Apart from directly affecting navigation, tidal currents also have indirect implications. By eroding and transporting sand, they shape the seabed, thereby creating bed forms such as tidal sandbanks (De Swart and Yuan 2019) and sand waves (Besio et al. 2008). Also, by transporting other matter (mud, salt and nutrients), tidal currents affect turbidity, salt intrusion and the residence time of nutrients, which is important for water quality and ecology.

Let us now turn to tidal observations in more detail, particularly their temporal and spatial structure. Harmonic analysis enables decomposition of the tidal signal into different constituents. For the free surface elevation η as a function of time t, we may thus write

$$\eta = \sum_{n=1}^{N} \tfrac{1}{2} H_{c_n} \cos(\sigma_{c_n} t - \varphi_{c_n}), \tag{4.1}$$

thereby distinguishing N constituents c_n, each with an individual tidal range H_{c_n}, angular frequency σ_{c_n} and phase φ_{c_n}. Similar expressions hold for the components of the tidal current. The constituents include those directly following from celestial mechanics and those indirectly resulting from their nonlinear interaction (Parker 1993). Instead of a detailed derivation involving the tidal potential (Platzman 1982; Gerkema 2019), here we simply consider them as given (e.g., M2, S2, K1, O1; see Table 4.1) and mostly focus on the dominant one.

Observations from coastal seas around the world reveal intriguing spatial variations in tidal range and phase, so

$$H_{c_n} = H_{c_n}(x, y), \qquad \varphi_{c_n} = \varphi_{c_n}(x, y), \tag{4.2}$$

Table 4.1 Overview of the tidal constituents addressed in this chapter

Name c_n	Description	Period T (h)	Angular frequency σ (rad s^{-1})	σ/σ_{M2} (-)[a]
M2	Principal lunar semi-diurnal component	12.42	1.405×10^{-4}	1
S2	Principal solar semi-diurnal component	12.00	1.454×10^{-4}	1.035
K1	Luni-solar diurnal component	23.93	7.293×10^{-5}	0.519
O1	Principal lunar diurnal component	25.82	6.759×10^{-5}	0.481

[a]Relative to the angular frequency of the M2-tide

where we have introduced horizontal coordinates x and y. These patterns are visualised in so–called *amphidromic charts*, showing co-range and co-phase lines for a given constituent (Figs. 4.2 and 4.3). From the examples shown, we highlight the following features.

- Behaviour as a progressive wave along the coast, with a wavelength in the order of hundreds of kilometres. At the UK East Coast, for example, co-range lines are roughly parallel and co-phase lines perpendicular to the coastline.
- Cross-shore decay of tidal range with a typical length scale of about hundred kilometres in the North Sea.
- Cyclonic rotation[1] around locations with vanishing tidal range, known as (elevation) *amphidromic points*. These points can be real (inside basin) or virtual (outside basin, as in the Gulf of California).[2]
- In some cases, significant amplification of tidal range towards the shallow region at the head of the basin, such as in the Gulf of California.
- Local flow structure showing ellipses near closed end and bidirectional flow further away.

The goal of this chapter is to provide a generic process-based explanation of the amphidromic patterns observed in coastal seas as presented above. To position our work, we focus on barotropic tides[3] in basins that, from a dynamical point of view, can be termed both *shallow* and *wide*. These properties, to be quantified in the subsequent analysis, have implications for wave speed ('shallow') and emphasize

[1] Cyclonic means counterclockwise in the Northern Hemisphere and clockwise in the Southern Hemisphere.

[2] Next to these elevation amphidromic points, there are also *current amphidromic points*, i.e. locations where the tidal current ellipse reduces to a circle (Zongwan et al. 1995).

[3] Barotropic tides are associated with motion that is driven by gradients in sea level only; they are not affected by pressure gradient forces that result from density stratification. In the absence of friction, barotropic motion has no vertical structure.

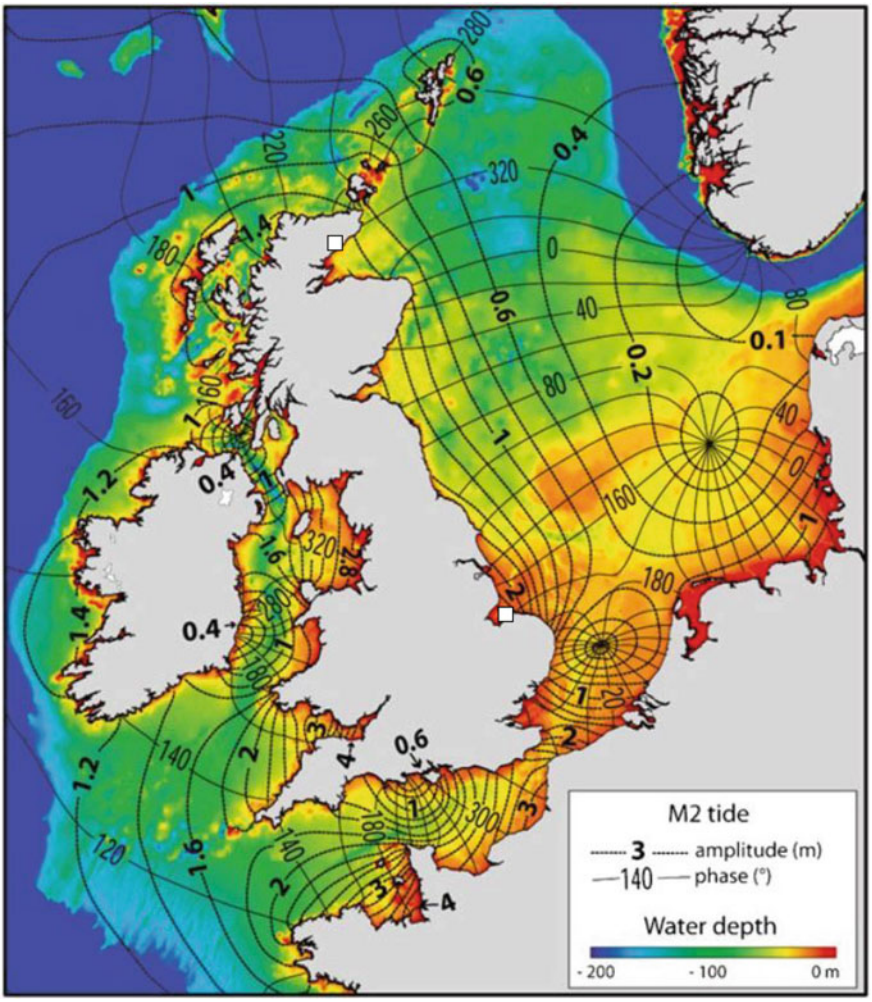

Fig. 4.2 Amphidromic chart of the semi-diurnal lunar tide (M2) in the North Sea, showing co-amplitude lines (half the tidal range) in m and co-phase lines in degrees. Colours in the background indicate water depth (Reynaud and Dalrymple 2012, after Sinha and Pingree 1997). Reprinted by permission from Springer: Springer, Principles of Tidal Sedimentology by R.A. Davis Jr. and R.W. Dalrymple, copyright (2012). The white squares along the UK East Coast denote the two tide stations Helmsdale (top) and Hunstanton (bottom) referred to in Sect. 4.3.2

the roles of bottom friction ('shallow') and the Coriolis effect ('wide'). As a result, we exclude narrow estuaries and tidal channels (or networks), for which lateral uniformity permits a cross-sectionally averaged approach (Friedrichs 2010; Talke and Jay 2020). Furthermore, as the basins are much smaller than the wavelength of

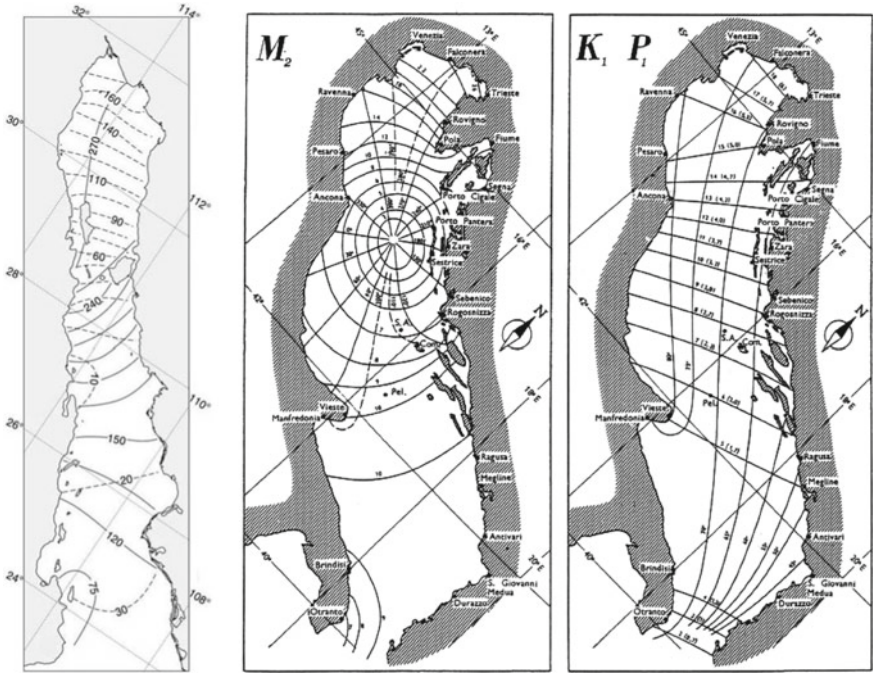

Fig. 4.3 Examples of amphidromic patterns from coastal seas around the world. Left: M2-tide in the Gulf of California, Mexico (Salas-de León et al. 2003), with co-phase in degrees (solid) and co-range in cm (dashed). Reprinted with permission from the American Geophysical Union. Middle and right: M2 and K1/P1 tides in the Adriatic Sea, with phase in degrees and range in cm, according to Polli (1960)

the directly forced tide (typically half the earth's circumference), they effectively *co-oscillate* with the tides in the adjacent larger oceans.

To achieve our goal, we adopt a so-called idealised process-based modelling approach, in which model geometry and the physical laws of water motion are both schematised, enabling analytical solutions that provide maximum insight. Specifically, we shall consider the linearised depth-averaged shallow water equations on the f plane, including bottom friction, in water bodies with rectilinear coastlines and step-wise topographic variations. Co-oscillation implies that the tidal potential can be neglected, so the system is forced only by elevations and/or currents at the open boundaries. Mathematically speaking, nonhomogeneities appear in the (open) boundary conditions rather than in the differential equations. In comparison to other texts on this topic (Pedlosky 1987; Gerkema 2019), the combined inclusion of bottom friction and topographic variations is the main innovation.

This chapter is organised as follows. Section 4.2 presents the model formulation, including the underlying assumptions and geometry. Then, in Sect. 4.3, we derive Kelvin and Poincaré modes as fundamental wave solutions in a channel section of uniform width and depth. Section 4.4 then demonstrates how superposition of these

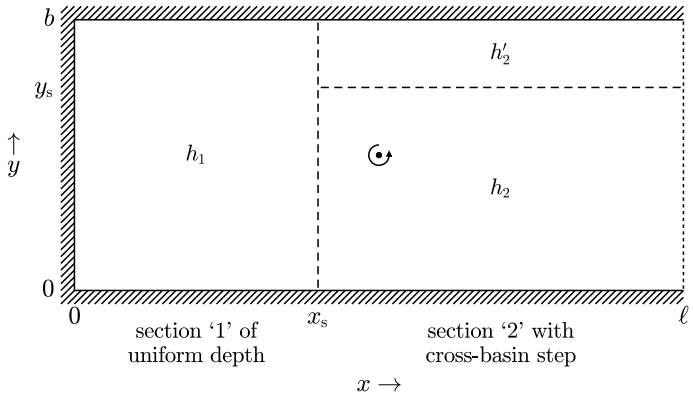

Fig. 4.4 Definition sketch of model geometry (top view), showing a semi-enclosed basin of length ℓ and width b. Along-basin and cross-basin topographic steps are denoted with dashed lines at $x = x_s$ and $y = y_s$, compartment depths with h_j and h'_j. In this example, we thus identify a section of uniform depth ($j = 1$) and a section with a single cross-basin step ($j = 2$). The open boundary at $x = \ell$ is represented by a dotted line

modes explains the amphidromic patterns occurring in large-scale basins with a specific topography. Section 4.5 contains a discussion of physical processes, implications (morphodynamics, climate change) and the model approach. Finally, we present our conclusions in Sect. 4.6.

4.2 Model Formulation

In our idealised process-based model, we consider a semi-enclosed rectangular basin of uniform width b and length ℓ (Fig. 4.4). Introducing along-basin and cross-basin coordinates x and y, the closed boundaries are located at $y = 0, b$ and $x = 0$. The depth h is spatially uniform, except across topographic steps, which are allowed parallel to either the x or y-direction.

Let us now turn to the description of the flow. We assume that the density ρ is constant, which makes the free surface elevation η, defined with zero spatial average, the primary variable of interest. As the horizontal scales of interest (tens to hundreds of km) are much larger than the vertical ones (tens to hundreds of m), we assume *shallow water flow* by which pressure gradients are proportional to gradients of the free surface elevation. Furthermore, we will not consider the vertical structure of the tide. We let u and v denote the *depth-averaged* velocity components in x and y-direction, respectively.

Next, we make the following assumptions about the relevant processes. First, to account for the *Coriolis effect*, the f plane approximation is adopted, with a Coriolis parameter that is set to a constant value

$$f = 2\Omega \sin\theta. \tag{4.3}$$

Here, $\Omega = 7.292 \times 10^{-5}$ rad s^{-1} is the angular frequency of the earth's rotation and θ is latitude. Second, we consider *linearised dynamics* because the Froude number $\mathrm{Fr} = U/(gh)^{1/2}$ is small (with velocity scale U and gravitational acceleration $g = 9.81$ m s^{-2}). This implies that the nonlinear advective terms can be neglected, as well as the contribution of the free surface displacement to the total water depth, i.e. $h + \eta \approx h$. Furthermore, we include *bottom friction* with the bed shear stress parameterised in a linear way (Prandle 1982). Finally, *co-oscillation* implies that the direct tidal forcing from the tidal potential is neglected.

With the above assumptions, the momentum and continuity equations are given by

$$\underbrace{\frac{\partial u}{\partial t} + \frac{ru}{h}}_{\mathcal{L}u} - fv = -g\frac{\partial \eta}{\partial x}, \tag{4.4a}$$

$$\underbrace{\frac{\partial v}{\partial t} + \frac{rv}{h}}_{\mathcal{L}v} + fu = -g\frac{\partial \eta}{\partial y}, \tag{4.4b}$$

$$\frac{\partial \eta}{\partial t} + h\left(\frac{\partial u}{\partial x} + \frac{\partial v}{\partial y}\right) = 0. \tag{4.4c}$$

Here, r is a linear friction coefficient (Prandle 1982), f the Coriolis parameter specified in Eq. (4.3) and g the gravitational acceleration. To facilitate the subsequent analysis, we have introduced the differential operator $\mathcal{L} = \frac{\partial}{\partial t} + \frac{r}{h}$, which combines inertial and frictional terms in the momentum equations.

At closed boundaries, the normal velocities must vanish. For the geometries under consideration, this boils down to

$$v = 0 \quad \text{at } y = 0, b, \tag{4.5a}$$

$$u = 0 \quad \text{at } x = 0. \tag{4.5b}$$

Our model is forced at its open boundary. For a given constituent with angular frequency σ, we prescribe the cross-basin profiles of tidal range H and phase φ:

$$\eta = \tfrac{1}{2}H(y)\cos\left(\sigma t - \varphi(y)\right) \quad \text{at } x = \ell. \tag{4.6}$$

Across topographic steps, we require continuity of elevation and normal transport. Depending on the type of step (longitudinal at $x = x_s$ or lateral at $y = y_s$), this is written as

$$\lim_{x\uparrow x_s}(\eta, hu) = \lim_{x\downarrow x_s}(\eta, hu), \tag{4.7a}$$

$$\lim_{y\uparrow y_s}(\eta, hv) = \lim_{y\downarrow y_s}(\eta, hv). \tag{4.7b}$$

Keeping the regular nature of tides in mind, we seek time-periodic solutions in dynamic equilibrium with the boundary forcing in Eq. (4.6). This means that the transient motion generated by starting from a certain initial condition has damped out due to bottom friction.

4.3 Fundamental Wave Solutions

In this section, we seek wave solutions in a channel section of uniform width. Our derivation, which involves the Klein-Gordon equation (Sect. 4.3.1), leads to the identification of the Kelvin wave (Sect. 4.3.2) and Poincaré waves (Sect. 4.3.3). The analysis is presented for a channel with uniform depth; the case with a single transverse step is treated separately in Sect. 4.3.4 (Roos and Schuttelaars 2009). We closely follow Pedlosky (1987), but extend it to account for bottom friction and a transverse topographic step.

4.3.1 Derivation with Klein-Gordon Equation

Let $\phi = (\eta, u, v)$ symbolically denote the state of the system. For a given frequency σ, we write

$$\phi = \mathrm{Re}\left\{\tilde{\phi}(y)\exp(\mathrm{i}[kx - \sigma t]\right\}, \tag{4.8}$$

with complex amplitudes $\tilde{\phi}(y) = (\tilde{\eta}(y), \tilde{u}(y), \tilde{v}(y))$ that are functions of the cross-channel coordinate y, and $\mathrm{Re}\{\cdot\}$ denoting the real part. The wave number $k = k_r + \mathrm{i}k_i$, also complex, is to be determined from the analysis below. The boundary conditions are as in Eq. (4.5a); they imply $\tilde{v}(0) = \tilde{v}(b) = 0$.

Before proceeding, we first derive an important general result.

We start by deriving the so-called *polarisation equations*, which relate the individual velocity components to the free surface elevation:

$$\left(\mathcal{L}^2 + f^2\right) u = -g\mathcal{L}\frac{\partial \eta}{\partial x} - fg\frac{\partial \eta}{\partial y}, \tag{4.9a}$$

$$\left(\mathcal{L}^2 + f^2\right) v = -g\mathcal{L}\frac{\partial \eta}{\partial y} + fg\frac{\partial \eta}{\partial x}. \tag{4.9b}$$

They follow from eliminating either v or u from the momentum equations (4.4a)–(4.4b).

Then, multiplying Eqs. (4.9) with h, taking their divergence and applying the continuity equation (4.4c) leads to a single equation for η only. This is the 'extended' *Klein-Gordon equation*:

$$\left(\mathcal{L}^2 + f^2\right)\frac{\partial \eta}{\partial t} - gh\mathcal{L}\left(\frac{\partial^2 \eta}{\partial x^2} + \frac{\partial^2 \eta}{\partial y^2}\right) = 0, \tag{4.10}$$

here, unlike its classical formulation, accounting for bottom friction. It serves as the governing equation for the wave solutions derived in this section. To arrive at Eq. (4.10), it is essential that h and r are spatially uniform. In the case without bottom friction ($r = 0$, so $\mathcal{L} = \frac{\partial}{\partial t}$), time integration of Eq. (4.10), while assuming wave-like solutions, recovers the regular Klein-Gordon equation (Pedlosky 1987). If also the Coriolis effect were neglected ($f = 0$), this would further reduce to the classical shallow-water wave equation $\frac{\partial^2 \eta}{\partial t^2} - gh\left(\frac{\partial^2 \eta}{\partial x^2} + \frac{\partial^2 \eta}{\partial y^2}\right) = 0$. As can be shown, also the flow velocity components must satisfy the extended Klein-Gordon equation, so in Eq. (4.10) one may freely replace η with either u or v.

The next step is to substitute our solution (4.8) into the extended Klein-Gordon equation (4.10). Upon defining the complex frictional correction factor

$$\gamma = \sqrt{1 + \mathrm{i}\mu}, \qquad \text{with } \mu = \frac{r}{\sigma h}, \tag{4.11}$$

implying $\gamma = 1$ in the absence of friction, it follows that $\mathcal{L} = -\mathrm{i}\gamma^2\sigma$ and we find

$$\frac{\partial^2 \tilde{\eta}}{\partial y^2} + \alpha^2 \tilde{\eta} = 0, \qquad \text{with } \alpha^2 = \frac{\gamma^2\sigma^2 - \gamma^{-2} f^2}{gh} - k^2. \tag{4.12}$$

The general solution to this differential equation reads

$$\tilde{\eta}(y) = A\cos\alpha y + B\sin\alpha y, \tag{4.13}$$

with constants A and B that follow from the boundary conditions in Eq. (4.5a). With the aid of the polarisation equation (4.9b), these are written in matrix form according to

$$\begin{bmatrix} fk & \alpha\gamma^2\sigma \\ fk\cos\alpha b - \alpha\gamma^2\sigma\sin\alpha b & \alpha\gamma^2\sigma\cos\alpha b + fk\sin\alpha b \end{bmatrix} \begin{bmatrix} A \\ B \end{bmatrix} = \begin{bmatrix} 0 \\ 0 \end{bmatrix}. \quad (4.14)$$

This system has non-trivial solutions only if the determinant of the coefficient matrix vanishes. With the definition of the parameter α in Eq. (4.12), we obtain the following condition:

$$\left([\gamma^2\sigma]^2 - f^2\right)\left(k^2 - \frac{\gamma^2\sigma^2}{gh}\right)\sin\alpha b = 0. \quad (4.15)$$

This equation contains three roots. The second and third are associated with Kelvin and Poincaré waves, to be analysed in the following subsections. In doing so we will adopt parameter values, inspired by the coastal seas of Sect. 4.1 and further aimed at exposing the key properties (Table 4.2). The first only exists without bottom friction; in that case it has been shown to add no information to the Kelvin wave (Pedlosky 1987).

4.3.2 Kelvin Wave

The second root in Eq. (4.15) corresponds to the so-called *Kelvin wave*. It permits two values of the wave number, i.e.

$$k = k_0^{\oplus} = +\gamma K, \qquad k = k_0^{\ominus} = -\gamma K, \qquad \text{with } K = \frac{\sigma}{\sqrt{gh}}, \quad (4.16)$$

corresponding to a progressive wave travelling in either the positive or negative x-direction. The wave number equals that of a shallow water wave ($\pm K$), modified by the frictional correction factor γ defined in Eq. (4.11). A subscript '0' has been added, because, as we shall see in Sect. 4.3.3, the Kelvin wave serves as the lowest mode in a family of wave solutions.

Using Eq. (4.16), the coefficient in Eq. (4.12) reduces to $\alpha = \pm \mathrm{i}\gamma^{-1} f(gh)^{-1/2}$. The elevation and velocity amplitudes, as defined in Eq. (4.8), are given by

$$\tilde{\phi}_0^{\oplus} = \left(\tilde{\eta}_0^{\oplus}, \tilde{u}_0^{\oplus}, \tilde{v}_0^{\oplus}\right) = (Z, U, 0)\exp\left(\frac{-fy}{\gamma\sqrt{gh}}\right), \quad \text{with } U = \frac{Z}{\gamma}\sqrt{\frac{g}{h}}, \quad (4.17a)$$

$$\tilde{\phi}_0^{\ominus} = \left(\tilde{\eta}_0^{\ominus}, \tilde{u}_0^{\ominus}, \tilde{v}_0^{\ominus}\right) = (Z, -U, 0)\exp\left(\frac{-f[b-y]}{\gamma\sqrt{gh}}\right). \quad (4.17b)$$

Table 4.2 Overview of model parameters and values (as used in Figs. 4.5, 4.7, 4.8, 4.9 and 4.10)

Symbol	Description	Value	Unit(s)
h	Water depth*	20	m
θ	Latitude	50	°N
σ	Angular frequency	1.405×10^{-4}	rad s^{-1}
r	Friction coefficient	5.0×10^{-4}	m s^{-1}
b	Channel/basin width	$300^{\text{Fig. 4.5}}$, $700^{\text{Figs. 4.7,4.8}}$, $200^{\text{Figs. 4.9,4.10}}$	km
ℓ	Basin length$^{\text{Fig. 4.10}}$	600	km
x_s	Position of along-basin step$^{\text{Fig. 4.10}}$	150	km
f	Coriolis parameter, Eq. (4.3)	1.12×10^{-4}	rad s^{-1}
μ	Dimensionless friction coefficient, Eq. (4.11)	0.18	–
K	Shallow water wave number, Eq. (4.16)	1.00×10^{-5}	rad m^{-1}
R	Rossby deformation radius, Eq. (4.18)	125	km
b_{crit}	Critical channel width, Eq. (4.23)	519	km
λ_0	Kelvin wavelength	$626^{\dagger\text{Figs. 4.5a,4.9a}}$, $624^{\text{Figs. 4.5b,4.9b}}$	km
λ_1	Wavelength of 1st Poincaré mode$^{\dagger\ddagger\text{Fig. 4.7a}}$	1584	km
L_2	Decay length of 2nd Poincaré mode$^{\dagger\ddagger\text{Fig. 4.7b}}$	149	km
L_3	Decay length of 3rd Poincaré mode†‡	83	km

*N.B.: in Fig. 4.10 we use a reference depth of $h = 40$ m and a shallow region of $h = 20$ m), †Without bottom friction, ‡For channel width $b = 700$ km.

In these expressions, Z represents the coastal elevation amplitude[4] at $(x, y) = (0, 0)$ and $(0, b)$, respectively, and U is the coastal velocity amplitude.

Let us now highlight the key properties of the Kelvin wave (Fig. 4.5, using parameter values from Table 4.2), first for the case without bottom friction ($r = 0$, so $\gamma = 1$, Fig. 4.5a):

- Nondispersive progressive shallow water wave with wave speed $(gh)^{1/2}$ and the along-channel velocity in phase with the free surface elevation.
- Exponential decay in the cross-channel direction with the so-called *Rossby deformation radius*

[4] For $f > 0$, Z is the *maximum* elevation amplitude of the Kelvin wave as it decreases when moving to the other coast. Conversely, for $f < 0$, Z is the *minimum* coastal amplitude.

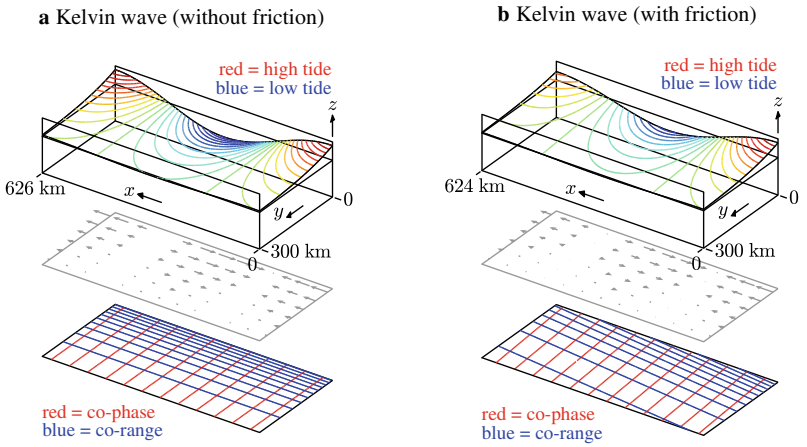

Fig. 4.5 Visualisation of Kelvin wave in a channel section of uniform width and depth in the Northern Hemisphere, propagating from right to left: **a** without friction, **b** with friction. The top panels show a three-dimensional snapshot of the surface elevation (coloured contours, high tide in red and low tide in blue). The middle panels show the corresponding instantaneous depth-averaged velocity (grey arrows). The bottom panels show the co-range lines (blue) and co-phase lines (red). Parameter values as in Table 4.2, with the frictional case chosen such that amplitude decay in the direction of propagation is already visible over one wavelength

$$R = \frac{\sqrt{gh}}{|f|} \tag{4.18}$$

as e-folding length scale. This enables us to quantify the 'wide' basins mentioned in the Introduction as basins with $b = \mathcal{O}(R)$ (or larger). For $b \ll R$, the cross-channel structures in Eq. (4.17) are nearly uniform, indicating that the Coriolis effect only marginally affects the solution.

- Facing the direction of propagation, the Kelvin wave 'hugs' the coast on its right (Northern Hemisphere, Fig. 4.5a) or on its left (Southern Hemisphere).
- Vanishing cross-channel velocity, i.e. $v = 0$, in the entire domain. This implies that the presence of the opposite coastline is not essential: the Kelvin wave in Eq. (4.17a) also exists as a wave solution in a semi-infinite water domain bounded by a single straight coastline at $y = 0$.
- Shore-parallel co-range lines, along which $\tilde{\eta}(y)$ is constant, and shore-normal co-phase lines, along which $\exp(\mathrm{i}kx)$ is constant (bottom panel of Fig. 4.5a).
- Dynamics of a progressive shallow water wave in the along-coast direction and *geostrophy* in the shore-normal direction. The latter implies a balance between the cross-shore pressure-gradient acceleration $-g\frac{\partial \eta}{\partial y}$ and the Coriolis acceleration fu of the alongshore flow (see Eq. (4.4b) and recall that $v = 0$).

Bottom friction ($r > 0$, so $\gamma \neq 1$) distorts the above picture (Fig. 4.5b). The along-channel velocity has a phase lead with respect to the surface elevation. The wave number $k = k_\mathrm{r} + \mathrm{i}k_\mathrm{i}$ is complex, implying exponential amplitude decay in the direc-

tion of propagation as well as a reduced wave speed

$$c = \frac{\sigma}{k_r} = \pm\sqrt{gh}\left[\frac{1}{2} + \frac{1}{2}\sqrt{1 + \left(\frac{r}{\sigma h}\right)^2}\right]^{-1/2}, \tag{4.19}$$

and, hence, a shorter wavelength $\lambda = 2\pi/k_r$. The dependency of wave speed on tidal frequency demonstrates that bottom friction makes the wave dispersive. Also cross-channel decay is affected, but the absence of cross-channel flow ($v = 0$) continues to hold in the entire domain. The above is reflected in the co-range and co-phase lines, which become skewed and no longer perpendicular (bottom panel of Fig. 4.5a).

To illustrate these Kelvin wave properties in a more quantitative sense, let us turn to the UK East Coast. The shore-parallel co-range lines and shore-normal co-phase lines in Fig. 4.2 suggest a near-perfect Kelvin wave propagating southward. Here we shall combine coastal data from the UK Admiralty Tide Tables (Admiralty 2009) with Kelvin wave theory to estimate tidal wavelength, water depth, Rossby deformation radius and coastal velocity amplitudes.

From the tidal phases as observed at coastal tide stations between Helmsdale and Hunstanton (Fig. 4.6) and using $k = \frac{\mathrm{d}\varphi}{\mathrm{d}x}$ with phase φ as introduced in Eq. (4.2), we thus find a wavelength estimate of $\lambda_{M2} = 1.05 \times 10^3$ km. Assuming a frictionless Kelvin wave speed of $c = \lambda/T = (gh)^{1/2}$, this corresponds to an 'effective' water depth of 57 m. In turn, with $\theta \sim 55°$N as typical latitude, we obtain a Rossby deformation radius of $R \sim 197$ km. This suggests that the tidal range is halved roughly at a distance of $R \ln 2 \approx 137$ km from the coast. As shown by Table 4.3, redoing this for the other constituents (S2, K1, O1) leads to roughly similar values of h and R.

As an alternative (not carried out here), one may also estimate the Rossby deformation radius directly from the co-range lines in Fig. 4.2 and use this to compute the 'effective' water depth. Finally, using $U = Z(g/h)^{1/2}$, the observed coastal tidal range of $H_{M2} \sim 1.66$ m corresponds to a coastal velocity amplitude of $U_{M2} \sim 0.35$ m s^{-1}. The results for the other constituents are shown in Table 4.3.

Table 4.3 Parameters used in Kelvin wave fit of UK East Coast (Fig. 4.6)

Symbol	Description	Value				Unit(s)
		M2	S2	K1	O1	
k	Wave number	0.60	0.63	0.35	0.30	$\times 10^{-5}$ rad m^{-1}
λ	Wavelength	1.05	1.00	1.80	2.12	$\times 10^{3}$ km
h	'Effective' water depth	57	54	44	53	m
R	Rossby deformation radius	197	193	175	191	km
H	Coastal tidal range	1.66	0.55	0.12	0.14	m
U	Coastal velocity amplitude	0.35	0.12	0.03	0.03	m s^{-1}

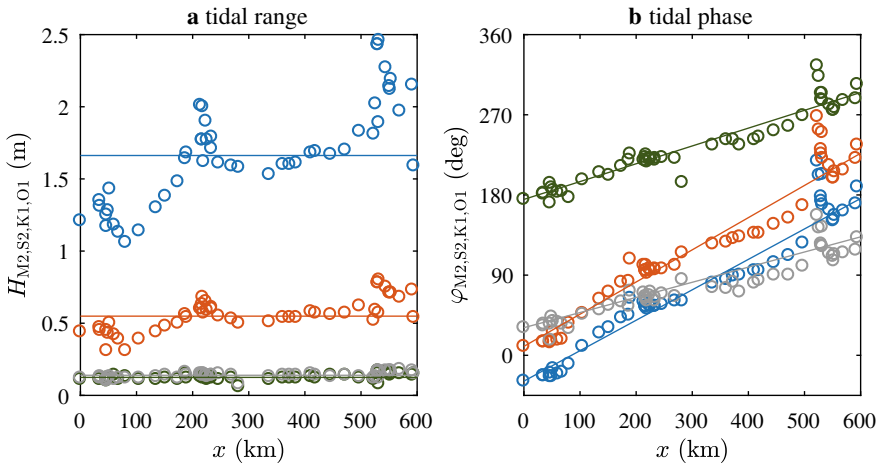

Fig. 4.6 Observations of M2 (blue circles), S2 (red), K1 (green) and O1 (grey) for coastal tide stations between Helmsdale and Hunstanton (UK, see Fig. 4.2): **a** tidal range H, **b** tidal phase φ. Data plotted as a function of the distance x on the straight line Helmsdale-Hunstanton, upon which each tide station's location has been projected ($x = 0$ corresponding to Helmsdale). The straight solid lines represent the fits of mean tidal range (left) and $\frac{d\varphi}{dx}$ (right). Data from UK Admiralty (Admiralty 2009)

4.3.3 Poincaré Waves

The third root of Eq. (4.15) corresponds to the set of infinitely many wave solutions known as *Poincaré waves*. As implied by the condition $\sin \alpha b = 0$, these modes are characterised by transverse wave numbers

$$\alpha_n = \frac{n\pi}{b}, \qquad \text{for } n = 1, 2, 3, \ldots . \tag{4.20}$$

Substitution of Eq. (4.20) into Eq. (4.12) leads to expressions for the wave number:

$$k_n^{\oplus} = \sqrt{\gamma^2 K^2 - \gamma^{-2} R^{-2} - \alpha_n^2}, \qquad k_n^{\ominus} = -k_n^{\oplus}, \tag{4.21}$$

which is the dispersion relationship for Poincaré waves. Here, γ, K and R are as defined in Eqs. (4.11), (4.16) and (4.18).

On the basis of Eq. (4.21), we thus identify two sets of countably infinite modes, labeled $n = 1, 2, 3, \ldots$ and characterised by wave numbers, the real and imaginary parts of which are either positive ($k_n^{\oplus}$) or negative ($k_n^{\ominus}$).

With the aid of the polarisation equations (4.9), the cross-channel structures of the surface elevation and flow field are found to be

$$\tilde{\phi}_n^{\oplus} = \begin{pmatrix} \tilde{\eta}_n^{\oplus} \\ \tilde{u}_n^{\oplus} \\ \tilde{v}_n^{\oplus} \end{pmatrix} = \begin{pmatrix} Z \\ \frac{k_n^{\oplus}}{\gamma K} U \\ 0 \end{pmatrix} \cos \alpha_n y + \begin{pmatrix} \frac{-f k_n^{\oplus}}{\alpha_n \gamma^2 \sigma} Z \\ \frac{-f K}{\alpha_n \gamma \sigma} U \\ \frac{\mathrm{i}\gamma K}{\alpha_n} \left[1 - \frac{k_n^{\oplus 2}}{\gamma^2 K^2} \right] U \end{pmatrix} \sin \alpha_n y. \tag{4.22}$$

For the other family, replace $^{\oplus}$ with $^{\ominus}$. As degree of freedom, we have chosen to specify the elevation amplitude Z at $(x, y) = (0, 0)$. The velocity scale U is as defined in Eq. (4.17a).

Let us now highlight the key properties of Poincaré waves, first for the case without bottom friction ($r = 0$, so $\gamma = 1$, Figs. 4.7 and 4.8).

- Unlike frictionless Kelvin waves, Poincaré waves are dispersive. This is reflected in the curved lines of σ versus k (Figs. 4.8a, c, d).
- Governed by the sinusoidal structure for the cross-channel flow velocity amplitude, the structures of elevation are also harmonic. The phase lag of 90° between u and v implies that the end point of the depth-averaged velocity vector describes an elliptical path during a tidal cycle.
- In the absence of bottom friction, Poincaré waves are either *free* (characterised by a real wave number $k_n = k_{n,\mathrm{r}}$) or *evanescent* (purely imaginary wave number $k_n = \mathrm{i}k_{n,\mathrm{i}}$). This is seen from the filled dots in Figs. 4.8a, b. For evanescent waves, the amplitude decays exponentially in the positive or negative x-direction with an e-folding decay length that is given by $L_n = |k_{n,\mathrm{i}}|^{-1}$.
- For any channel system, there is always a finite number $n_\star$ of free modes (possibly zero, $1 \le n \le n_\star$) and an infinite number of evanescent modes ($n > n_\star$). For the

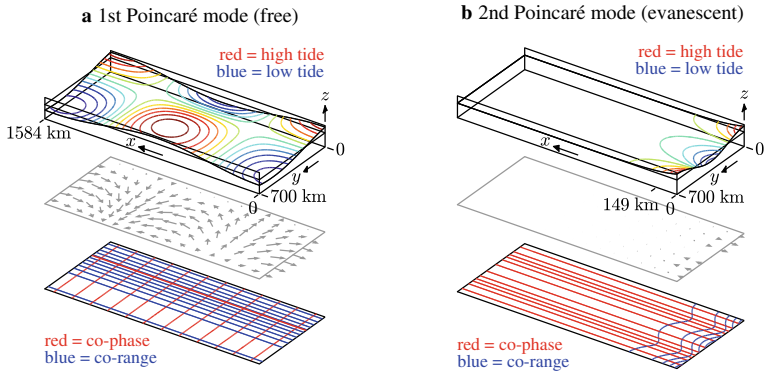

Fig. 4.7 Visualisation of Poincaré waves, in a channel section of uniform width and depth in the Northern Hemisphere (without bottom friction): **a** example of free mode propagating from right to left ($n = 1$), **b** example of evanescent mode exponentially decaying from right to left ($n = 2$). Analogous to Fig. 4.5, the sketch contains snapshots of surface elevation (top, with high tide in red and low tide in blue) and depth-averaged velocity (middle), as well as co-range and co-phase lines (blue and red in bottom panel, resp.). Parameter values as in Table 4.2, with channel width chosen such that the first mode is free and the second evanescent

example in Fig. 4.8, it follows that $n_\star = 1$. For these evanescent modes, the decay length L_n decreases with increasing n. In other words, the evanescent mode with the lowest index has the largest decay length, namely $L_{n_\star+1}$.

- In particular, provided that $\sigma > |f|$, there is a critical channel width b_{crit}, given by

$$b_{\text{crit}} = \pi \sqrt{\frac{gh}{\sigma^2 - f^2}}\,, \tag{4.23}$$

such that all Poincaré modes are evanescent if $b < b_{\text{crit}}$. Conversely, a finite number of free modes exist if $b > b_{\text{crit}}$. This follows from requiring the square root in Eq. (4.21) to have a vanishing argument for $n = 1$. Equivalently, one may derive a critical depth h_{crit} such that all Poincaré modes are evanescent if $h > h_{\text{crit}}$. Finally, for $\sigma \leq |f|$, all Poincaré modes are evanescent regardless width or depth.

Analogous to the Kelvin wave, the inclusion of bottom friction distorts the above picture. The wave numbers experience a shift in the complex plane: the free modes attain a nonzero imaginary part and the evanescent modes a nonzero real part (open dots in Figs. 4.8a, b). Also, changes in phase of velocity with respect to elevation take place.

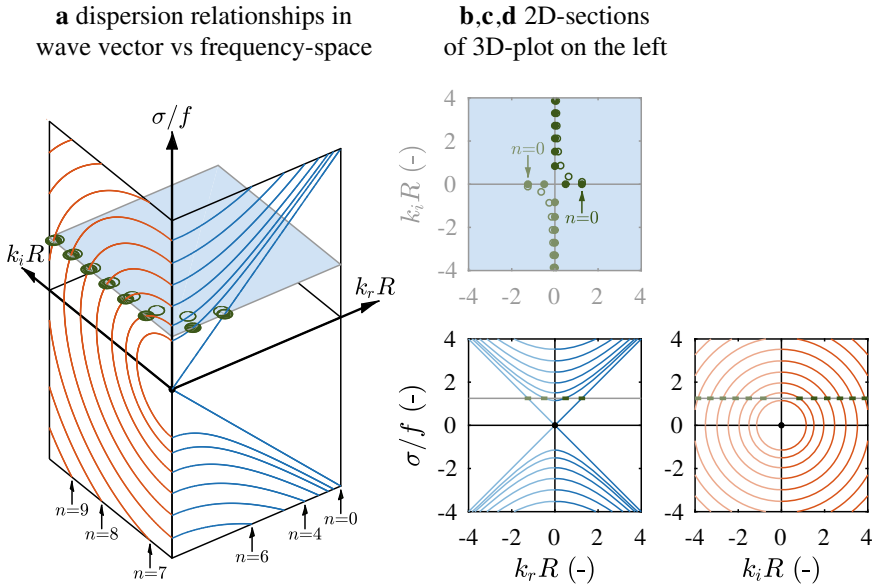

Fig. 4.8 Dispersion relationships (4.16) and (4.21) of Kelvin and Poincaré modes presented in dimensionless form. Plotted is the dimensionless frequency σ/f versus the real and imaginary parts $(k_\mathrm{r}R, k_\mathrm{i}R)$ of the dimensionless wave number (with Rossby deformation radius R): **a** Three-dimensional visualisation in $(k_\mathrm{r}R, k_\mathrm{i}R, \sigma/f)$-space (without bottom friction). The filled dots on the light-blue plane show the modes obtained for $\sigma/f = 1.25$, with free modes along the real axis and evanescent modes along the imaginary axis. The indices at the bottom show the Kelvin mode ($n = 0$) and Poincaré modes ($n = 1, 2, 3, \ldots$). **b** Two-dimensional plot of these modes ($\sigma/f = 1.25$) in the complex $(k_\mathrm{r}R, k_\mathrm{i}R)$-plane, with $n = 0$ denoting the Kelvin modes. The open dots in a,b show how the modes shift when bottom friction is included ($\mu = \frac{r}{\sigma h} = 0.18$). **c**,**d** 2D-sections showing σ/f versus *real* part $k_\mathrm{r}R$ (blue, whenever kR is real) and *imaginary* part $k_\mathrm{i}R$ (red, whenever kR is imaginary). Parameter values in Table 4.2, corresponding to a dimensionless channel width $b/R = 5.6$

4.3.4 *Wave Solutions with a Transverse Topographic Step*

Wave solutions in a channel section with a single cross-channel topographic step (at $y = y_\mathrm{s}$, see Sect. 4.2 in Fig. 4.4) consist of a solution in the lower compartment and one in the upper compartment (Roos and Schuttelaars 2009). We thus extend Eq. (4.8) to

$$\phi = \begin{cases} \mathrm{Re}\left\{\tilde{\phi}(y)\exp(\mathrm{i}[kx - \sigma t]\right\} & \text{for } 0 \le y \le y_\mathrm{s}\ (\text{'lower'}), \\ \mathrm{Re}\left\{\tilde{\phi}'(y)\exp(\mathrm{i}[kx - \sigma t]\right\} & \text{for } y_\mathrm{s} \le y \le b\ (\text{'upper'}), \end{cases} \tag{4.24}$$

with wave number k and cross-channel structures $\tilde{\phi}(y) = (\tilde{\eta}, \tilde{u}, \tilde{v})$ and $\tilde{\phi}'(y) = (\tilde{\eta}', \tilde{u}', \tilde{v}')$. Quantities in the upper compartment are denoted with a prime, those

in the lower compartment without a prime. Apart from different depths $h \neq h'$, we also allow different friction coefficients $r \neq r'$.

Since ϕ must be a solution to the model equations (4.4), each component must also satisfy the extended Klein-Gordon equation (4.10). Additionally, the solution must satisfy the closed boundary condition (4.5a) and the matching conditions across the topographic step in Eq. (4.7b). In fact, the latter force the wave number k in Eq. (4.24) to be identical in both compartments.

For a given wave number k (to be determined below), the cross-channel structure of the cross-channel velocity is written as

$$\tilde{v}(y) = \frac{C \sin \alpha y}{h \sin \alpha y_s}, \qquad \tilde{v}'(y) = \frac{C \sin \alpha' y'}{h' \sin \alpha' y'_s}, \qquad \text{with } y' = y - b, \tag{4.25}$$

in which we have introduced the coefficients

$$\alpha = \sqrt{\gamma^2 K^2 - \gamma^{-2} R^2 - k^2}, \qquad \alpha' = \sqrt{\gamma'^2 K'^2 - \gamma'^{-2} R'^2 - k^2}. \tag{4.26}$$

The solution in Eq. (4.25) has been constructed such that it automatically satisfies all of the above conditions, except continuity of elevation across the topographic step, i.e. except $\tilde{\eta}(y_s) = \tilde{\eta}'(y_s)$. This last requirement serves as solvability condition for the existence of non-trivial wave solutions. A numerical search routine, minimising $|\tilde{\zeta}(y_s) - \tilde{\zeta}'(y_s)|$, is then used to identify the wave numbers k, thus fixing the values of the coefficients α and α' according to Eq. (4.26). Expressions for the cross-channel structures of surface elevation $\tilde{\eta}$ and $\tilde{\eta}'$ as well as along-channel velocity $\tilde{u}$ and $\tilde{u}'$ are given in the Appendix.

The procedure outlined above identifies modified versions of each Kelvin and Poincaré mode in the two families, characterised by a shift in wave number and a deformed cross-channel structure. The presence of the two closed channel boundaries prevents new modes from arising here, e.g. the so-called double Kelvin wave that may propagate along a depth discontinuity in an infinite water domain (Longuet-Higgins 1968).

4.4 Amphidromic Patterns in Semi-enclosed Basins

In this section, we demonstrate how superpositions of the wave solutions derived in Sect. 4.3 explain amphidromic patterns in semi-enclosed basins. As an important first result, it is shown analytically that two Kelvin waves in a channel already produce an amphidromic system (Sect. 4.4.1). Then, Taylor's problem of Kelvin wave reflection in a semi-enclosed basin is addressed, presenting the solution method (Sect. 4.4.2) and properties of the solution (Sect. 4.4.3), the latter including application to the Gulf of California. In fact, an extended version of Taylor's problem is considered here, as we include bottom friction (Rienecker and Teubner 1980) and topographic steps (Roos and Schuttelaars 2009) (as well as a finite basin length). The Gulf of

California serves as a typical example with an important role for both bottom friction and topographic variations.

4.4.1 Superposition of Two Kelvin Waves

Consider the situation with two Kelvin waves, simultaneously travelling in opposite directions along opposite coastlines of a channel section of uniform width and depth. Following Eqs. (4.8) and (4.17), the surface elevation of this superposition is written as

$$\begin{aligned}\eta = \mathrm{Re}\big\{ & Z_0^{\oplus} \exp(-\delta y) \exp(\mathrm{i}[k_0^{\oplus} x - \sigma t]) \\ & + Z_0^{\ominus} \exp(-\delta[b-y]) \exp(\mathrm{i}[k_0^{\ominus} x - \sigma t])\big\},\end{aligned} \tag{4.27}$$

with coastal amplitudes $Z_0^{\oplus} = |Z_0^{\oplus}| \exp(\mathrm{i}\varphi_0^{\oplus})$ and $Z_0^{\ominus} = |Z_0^{\ominus}| \exp(\mathrm{i}\varphi_0^{\ominus})$, wave numbers $k_0^{\oplus} = -k_0^{\ominus} = k_\mathrm{r} + \mathrm{i}k_\mathrm{i}$ and complex coefficient $\delta = \delta_\mathrm{r} + \mathrm{i}\delta_\mathrm{i} = \gamma^{-1} f/(gh)^{-1/2}$. Equation (4.27) can be rewritten into real notation according to

$$\eta = Z\left[\exp(-\psi)\cos(\xi - \chi) + \exp(\psi)\cos(\xi + \chi)\right], \tag{4.28}$$

where we have introduced the short-hand notation

$$Z = |Z_0^{\oplus}| \exp(-\delta_\mathrm{r} y_\star), \qquad \text{with } y_\star = \frac{1}{2} b + \frac{1}{2}\delta_\mathrm{r}^{-1} \log(|Z_0^{\oplus}|/|Z_0^{\ominus}|), \tag{4.29a}$$

$$\psi = k_\mathrm{i} x + \delta_\mathrm{r}(y - y_\star), \tag{4.29b}$$

$$\xi = k_\mathrm{r} x - \delta_\mathrm{i}(y - \tfrac{1}{2} b) + \tfrac{1}{2}[\varphi_0^{\oplus} - \varphi_0^{\ominus}], \tag{4.29c}$$

$$\chi = \sigma t + \tfrac{1}{2}\delta_\mathrm{i} b - \tfrac{1}{2}[\varphi_0^{\oplus} + \varphi_0^{\ominus}]. \tag{4.29d}$$

Using trigonometric identities, we may now rewrite Eq. (4.28) into the form of Eqs. (4.1)–(4.2), i.e.

$$\eta(x, y, t) = H(x, y) \cos(\sigma t - \varphi(x, y)), \tag{4.30}$$

with analytical expressions for tidal range H and phase φ:

$$H(x, y) = 4Z\left(\cosh^2\psi \cos^2\xi + \sinh^2\psi \sin^2\xi\right), \tag{4.31a}$$

$$\tan\varphi(x, y) = \tanh\psi \tan\xi. \tag{4.31b}$$

This result reveals the existence of amphidromic points, characterised by zero tidal range (Fig. 4.9). The requirement $H = 0$ implies (i) $\psi = 0$ and (ii) $\xi = (p + \frac{1}{2})\pi$ with integer p. The former condition defines a line through $(x, y) = (0, y_\star)$ that is either coast-parallel (in the case without bottom friction; Fig. 4.9a) or tilted (with bottom friction; Fig. 4.9b). The latter condition locates the actual amphidromes on

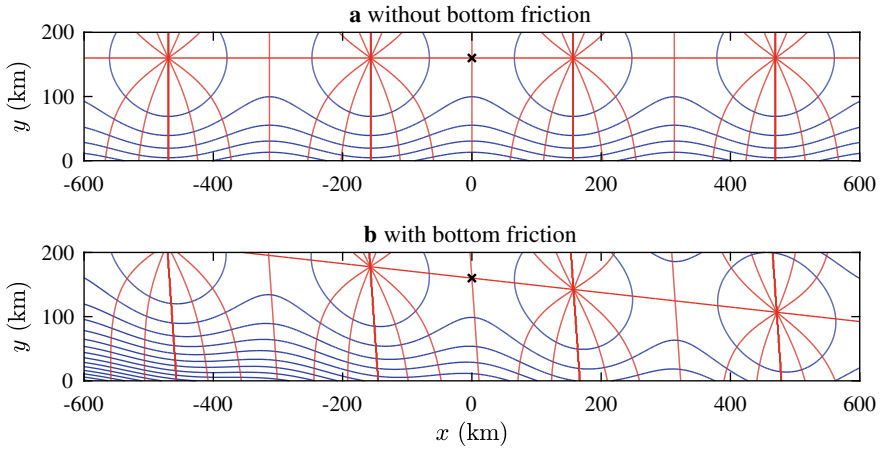

Fig. 4.9 Amphidromic chart (red=co-phase, blue=co-range) of the superposition of two Kelvin waves in a channel section of uniform width and depth according to the analytical solution in Eq. (4.31). **a** Without bottom friction, the amphidromic points are found on a coast-parallel line, here located slightly off the centerline (due to different coastal amplitudes). **b** With bottom friction, the amphidromes are located on a tilted line, leading to real and virtual amphidromes. In both examples, the point $(x, y) = (0, y_\star)$ in Eq. (4.29a), where both amplitudes are equal, is denoted with a black cross (here, $y_\star = 160$ km). Parameter values as in Table 4.2

this line, which may be inside or outside the channel (real or virtual). The presence of a transverse topographic step (as in Sect. 4.2 in Fig. 4.4) would distort the above amphidromic pattern, since the two Kelvin waves will then have slightly different wavelengths.

We conclude that the interference pattern of two Kelvin waves, propagating in opposite directions, produces an amphidromic system. The cross-channel positions of the amphidromic points depend on the relative amplitudes, which in turn is also affected by bottom friction. However, the case of a basin with a closed end (Fig. 4.4a, b) is not solved by any superposition of two Kelvin waves, as they cannot satisfy the closed boundary condition in Eq. (4.5b). How to overcome this difficulty, often referred to as *Taylor's problem*, is tackled in the next subsection.

4.4.2 Solution to Extended Taylor Problem

Let us now turn to the so-called *Taylor problem* (Taylor 1922) of tidal motion in a semi-enclosed basin of uniform width, with a closed boundary at $x = 0$. The classical version of this problem concerns an infinitely long basin of uniform depth, forced by an incoming Kelvin wave from $+\infty$, in the absence of bottom friction. Here we consider a different version of the problem: as before, we include bottom friction, allow for topographic steps, and further we consider a basin of finite length ℓ with

specified elevation amplitude and phase according to Eq. (4.2) as the open boundary condition at $x = \ell$ (Fig. 4.4). In our description below, we shall first ignore the topographic steps; how to include those is explained further below.

Different from the form of the individual wave solutions of Eq. (4.8) in Sect. 4.3, the solution $\phi = (\eta, u, v)$ is now more generally written as

$$\phi = \mathrm{Re}\left\{\hat{\phi}(x, y)\exp(-\mathrm{i}\sigma t)\right\}, \tag{4.32}$$

with complex amplitudes $\hat{\phi}(x, y) = (\hat{\eta}(x, y), \hat{u}(x, y), \hat{v}(x, y))$ that depend on both horizontal coordinates x and y.

The solution is then written as a (truncated) superposition of Kelvin and Poincaré modes according to

$$\hat{\phi}(x, y) = \sum_{n=0}^{N} a_n^{\oplus}\tilde{\phi}_n^{\oplus}(y)\exp(\mathrm{i}k_n^{\oplus}x) + \sum_{n=0}^{N} a_n^{\ominus}\tilde{\phi}_n^{\ominus}(y)\exp(\mathrm{i}k_n^{\ominus}[x-\ell]), \tag{4.33}$$

with nonzero[5] truncation number N and involving $2(N + 1)$ dimensionless complex coefficients $a_n^{\oplus}$ and $a_n^{\ominus}$. By construction, the solution presented here automatically satisfies the model equations (4.4) and the closed boundary conditions at $y = 0, b$ in Eq. (4.5a).

To satisfy also the two remaining conditions, i.e. the closed boundary condition at $x = 0$ in Eq. (4.5b) and the prescribed elevation amplitude and phase at $x = \ell$ in Eq. (4.6), we apply a so-called *collocation method* (Brown 1973). To this end, we define $N + 1$ lateral points $y_n = bn/N$ and we require that

$$\hat{u}(0, y_n) = 0, \qquad \hat{\zeta}(\ell, y_n) = \tfrac{1}{2}H(y_n)\mathrm{Re}\left\{\exp(\mathrm{i}\varphi(y_n))\right\} \quad \text{for } n = 0, 1, \ldots, N, \tag{4.34}$$

with tidal range H and phase φ taken from Eq. (4.6). This set of $2(N + 1)$ conditions leads to a linear system for the $2(N + 1)$ coefficients $a_n^{\oplus}$ and $a_n^{\ominus}$, which can be solved using standard techniques. It should be noted that the final solution in Eqs. (4.32) and (4.33) is independent of the value chosen for the elevation scale Z of the individual wave solutions in Eqs. (4.17) and (4.22).

Finally, some remarks on the solution method are in order.

- Generally, taking a truncation number of $N = \mathcal{O}(10)$ already produces a qualitatively correct picture of the solution (see Sect. 4.4.3). Further increasing N improves the accuracy of the solution mainly in the vicinity of the collocation points. While orthogonality conditions for Kelvin and Poincaré waves have been derived (Ripa and Zavala-Garay 1999), whether they actually form a complete set remains an open mathematical problem.

[5] Choosing $N = 0$ would effectively bring us back to the superposition of two Kelvin waves only, as already analysed in Sect. 4.4.1.

- The above procedure can be easily adjusted to cover the classical version of Taylor's problem. Instead of the second condition in Eq. (4.34), one should then choose a nonzero value of $a_0^{\ominus}$, force $a_n^{\ominus} = 0$ for all $n = 1, 2, \ldots, N$ and solve the set of $N + 1$ remaining equations resulting from the first condition in Eq. (4.34).
- Alternatively, the presence of an along-basin topographic step, at some $x = x_s$, is incorporated by defining separate expressions as in Eq. (4.33) for each compartment (Roos and Schuttelaars 2009). The increase in number of coefficients is then exactly balanced by the additional matching conditions across the step: one should require Eq. (4.7a) to be satisfied at all points (x_s, y_n) for $n = 0, 1, \ldots, N$.
- The presence of a cross-basin topographic step, at some $y = y_s$ poses no complications either. One can readily take the modified wave solutions as derived in Sect. 4.3.4. One should choose the truncation number N such that the transverse position y_s of the step does not coincide with any of the collocation points, since the longitudinal velocity is not uniquely defined there.

4.4.3 Application to Basins Around the World

A three-dimensional sketch of the solution to the Taylor problem is shown in Fig. 4.10. It shows a snapshot of the surface elevation (top) and the corresponding instantaneous flow field (bottom). For simplicity, this pertains to the classical Taylor problem, i.e. excluding bottom friction and imposing an incoming Kelvin wave rather than a prescribed elevation profile at the open boundary.

As it turns out, near the basin's closed end the depth-averaged flow velocity vector describes ellipses (also shown in the bottom panel of Fig. 4.10). Physically, this is due to the Coriolis effect: it effectively turns the reflection of the tidal wave at the basin's head into a cyclonic rotation of a Kelvin wave. Mathematically, this is seen in the Poincaré modes generated to satisfy the closed boundary condition at the basin's head ($x = 0$). In this subcritical case ($b < b_{\text{crit}}$) all Poincaré modes are evanescent, implying that further away the solution is effectively the superposition of the incoming and reflected Kelvin waves, for which the flow aligns with the along-basin direction. This alignment is actually visible because the decay length of the first Poincaré mode is smaller than the basin length.

Next, the four examples in Fig. 4.11 show the solution to the extended Taylor problem, restricting to the amphidromic charts. They particularly illustrate the (separate and combined) effects of including bottom friction and a shallow region near the basin's head. For this example with a subcritical basin width ($b < b_{\text{crit}}$, so all Poincaré modes are evanescent[6]), we highlight the following properties.

[6] As pointed in Sect. 4.3.3, this definition applies to the frictionless case.

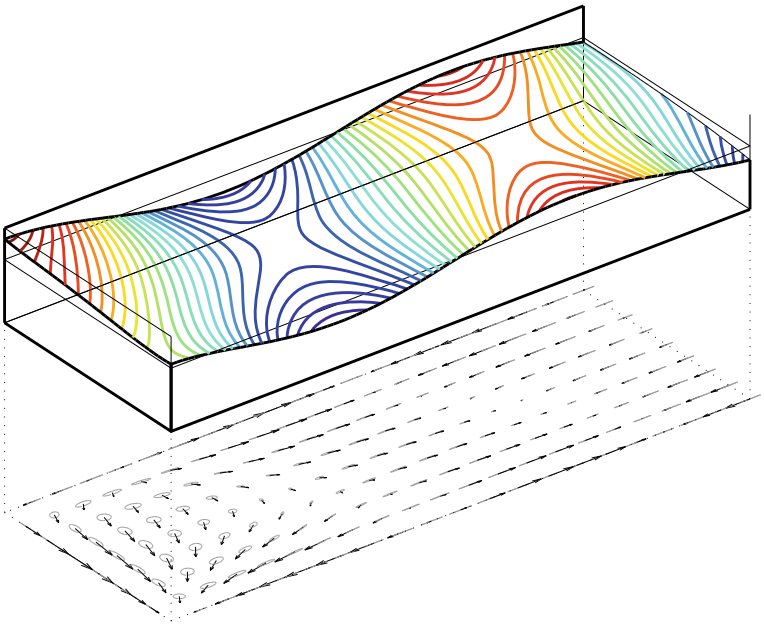

Fig. 4.10 Example of Taylor's solution, showing snapshot of the surface elevation (top, high tide in red, low tide in blue), as well as the corresponding depth-averaged flow vector (bottom), which describes ellipses during the tidal cycle. The basin's closed end is on the left-hand side, the open boundary on the right-hand side

- Without bottom friction, the reflected Kelvin wave has the same amplitude as the incoming Kelvin wave. As a result, amphidromic points are on the centerline of the basin.[7]
- Bottom friction distorts the picture in a similar fashion as in the plain superposition of two Kelvin waves (see Sect. 4.4.1 and Fig. 4.9). However, now the two Kelvin waves are connected by the reflection process at the closed end, which involves evanescent Poincaré modes bound to $x = 0$. As a result, amphidromic points shift toward the lower coastline ($y = 0$).
- Including a shallow region near the basin's head may lead to tidal amplification, and thus to higher values of the tidal range.
- The combined effect of bottom friction and the shallow part may enhance the shift of amphidromes away from the centerline (also see application to the Gulf of California below).

[7] For supercritical basins, i.e. basins with $b > b_{\text{crit}}$, this is not true since tidal wave energy is also reflected in a free Poincaré mode. This leads to a more complex amphidromic pattern resulting from the interference of these modes.

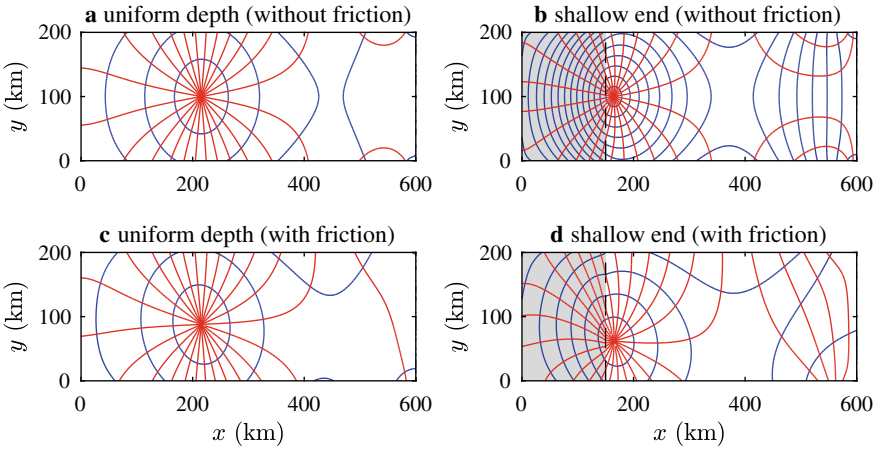

Fig. 4.11 Four examples of amphidromic charts (red=co-phase, blue=co-range) showing the solution to the extended Taylor problem. **a** Reference case with uniform depth of 40 m, no bottom friction. **b** Including a shallow zone near the basin's head (20 m deep, grey shade), no friction. **c** Uniform depth, now including friction. **d** Including both shallow zone and friction. Parameter values as in Table 4.2. All solutions are forced by an M2-tide with a uniform tidal range of $H = 1$ m at the open boundary (on the right). Contours are shown every 0.5 m

To apply and test our model, let us consider the Gulf of California (Hendershott and Speranza 1971; Carbajal and Backhaus 1998; Marinone 2000). This elongated basin is characterised by mixed semi-diurnal tides and a large tidal range in the northern part (spring tidal range close to 10 m). Typical is the virtual amphidromic point occurring for the semi-diurnal tides (Fig. 4.3).

Our procedure consists of the following four steps (Roos and Schuttelaars 2009).

1. We define a rectangular model geometry $PQRS$ that provides a good fit of the coastline. It has length $\ell = 1223$ km, width $b = 166$ km and an orientation/positioning as shown in Fig. 4.12a.
2. We perform orthogonal projections of the available tide stations on the model boundary (Fig. 4.12a). This enables us to plot observed ranges and phases (Carbajal and Backhaus 1998) as a function of a single coordinate: the distance along the perimeter $PQRS$.
3. Based on bathymetry (Fig. 4.12), we choose a division in two compartments, separated by a single longitudinal topographic step at $x_s = 350$ km: a shallow compartment with $h_1 = 100$ m near the basin's head and a deep compartment with $h_2 = 1200$ m.
4. Using a representative latitude $\theta = 27.5°$N, we perform model simulations varying both amplitude and phase of the incoming Kelvin wave. Note that this implies a different open boundary condition than in Eq. (4.2).

Results for the M2, S2, K1 and O1-tides are shown in Figs. 4.12c-f. In particular, the non-monotonous curve of the semi-diurnal phases φ_{M2} and φ_{S2} along the basin perimeter indicates the presence of a *virtual amphidromic point* (see Sect. 4.1 and Fig. 4.3). Such a pattern occurs when the amplitude of the reflected Kelvin wave is much weaker than that of the incoming Kelvin wave. Physically, this is caused by the enhanced dissipation due to bottom friction of the (locally amplified) tide in the shallow zone near the basin's head. This mechanism is also illustrated by the example in Fig. 4.10, although in that example the dissipation is too weak for the amphidrome to become virtual.

We conclude that our extended Taylor model, in spite of its strong schematisations, can adequately reproduce the patterns of tidal range and phase, as observed along the Gulf of California's coastline.

In other examples, the amphidromic patterns in basins with other length, widths, water depth and tidal ranges can be notably different. For example, the Adriatic Sea also has a shallow zone near the head, but tides and hence tidal dissipation are relatively weak, such that the amphidromes are still real and not virtual (Hendershott and Speranza 1971; Roos and Schuttelaars 2009). Alternatively, the asymmetric depth profile in the Persian Gulf leads to different Kelvin wavelengths on either side of the basin of the incoming and reflected Kelvin waves. Finally, basins characterised by (stepwise) variations in basin width are touched upon in Sect. 4.5.

4.5 Discussion

The model approach described in this chapter has been introduced as *idealised process-based* (Sect. 4.1), in other texts also referred to as exploratory (Murray 2003). This choice is motivated by our goal to provide a generic explanation of the amphidromic patterns starting from the physical processes. Here, the obtained insights immediately stem from the structure of the solution, i.e. a superposition of fundamental wave solutions. These wave solutions can be found analytically, which greatly facilitates interpretation and understanding of the tidal dynamics. As a specific example, we highlight the identification of the Rossby deformation radius $R = \sqrt{gh}/|f|$ as typical length scale for cross-shore decay of a Kelvin wave.

One of the challenges in idealised process-based modelling is thus to seek schematisations of model geometry and process formulations that allow for efficient and insightful solution techniques, while still realistic for the problem at hand. Examples in our extended Taylor model are the linearised bottom stress parameterisation, as well as the use of rectilinear coastlines and stepwise topographic changes. Clearly, too strong schematisation jeopardise model validity. For example, other studies allowed stepwise width variations have been adopted, e.g., to model the Labrador Sea/Davis Strait/Baffin Bay system (Godin 1965) and the North Sea (Roos et al. 2011).

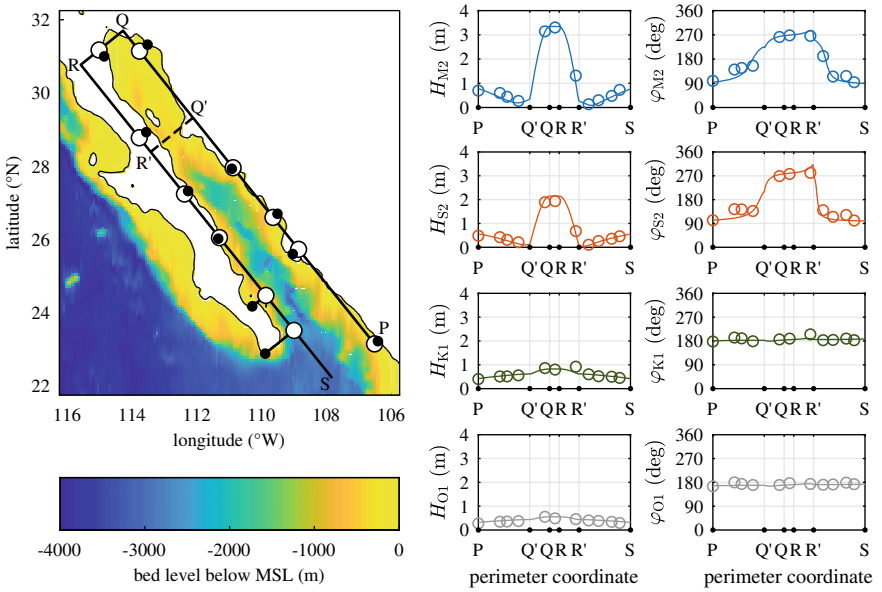

Fig. 4.12 Left: bathymetric chart of the Gulf of California with shallow region near closed end. Also shown is the rectangular model basin $PQRS$ with topographic step $Q'R'$ (dashed line) as well as tide stations (black dots) and their projections onto the model basin boundary (open circles). Right: comparison between model results (solid line) and observations (Carbajal and Backhaus 1998) (open circles). From top to bottom, this is done for the range and phase of M2, S2, K1 and O1, plotted as a function of the perimeter coordinate along $PQRS$

This idealised modelling approach contrasts with complex simulation models, which adopt state-of-the-art process formulation in numerical techniques aimed at accurate solutions with a high level of detail. We argue that, ideally, the two approaches are used in support of each other: complex models to reveal patterns, idealised models to unravel the underlying physics of the patterns found.

The knowledge and insights on barotropic tides as presented in this chapter constitute a basis for further studies that involve tides. For example, models have been developed to investigate the dynamics of secondary, nonlinear tides that are generated by nonlinear terms in the equations of motion (Iannello 1977; Parker 1993; Maas and Doelman 2002). Nonlinear tides include overtides, which are higher harmonics of a principal tidal constituent (e.g., M4, M6 are overtides of M2) and tidal residuals. Their manifestation implies that tidal records are asymmetrical, e.g. they show different durations of flood and ebb periods and/or different peak flood currents and ebb currents. Tides also nonlinearly interact with wind-driven flow (tide-surge interactions), wind waves and river flow (tide-fluvial interactions). These aspects are reviewed by Talke and Jay (2020).

Asymmetry of tidal currents is an important driver of net transport of matter, such as salt, nutrients and pollutants. An interesting application in this regard concerns the

demonstration of chaotic spreading of passive particles in a confined channel due to a simple current field that consists of a spatially uniform M2 tide and an alternating series of tidal residual eddies (Ridderinkhof and Zimmerman 1992). Furthermore, in shallow seas tidal currents are often sufficiently strong to erode sediment from the bottom and, when the currents are asymmetrical, they will also cause net transport of that sediment. These processes lead to the formation of turbidity maxima in estuaries (Burchard et al. 2018), and the emergence of bottom patterns: tidal sand ridges (De Swart and Yuan 2019), sand waves (Besio et al. 2008), tidal flats and bars (Seminara 2010), ebb-tidal deltas (De Swart and Zimmerman 2009), etcetera.

The theory of tides is further abundantly used to understand, reconstruct and predict alterations of tidal characteristics in seas and oceans. Nowadays, such alterations typically result from a mixture of naturally and anthropogenically induced changes in environmental conditions that occur on a wide spectrum of time scales. Examples are fluctuations in wind and river discharge, geometrical changes due to changes in mean sea level and shifts in positions of coastlines, as well as geometrical changes caused by construction of dams and dikes, deepening of fairways. Specific examples of studies that deal with changes in tides are given in the review by Talke and Jay (2020).

Tides are also an important source of turbulence, both directly and indirectly. The direct way is that turbulence is produced by the stress that tidal currents exert on a rough bottom. A more indirect way is through internal tides, which are generated by barotropic tides in stratified waters (density varies with depth) with an irregular bottom topography (Gerkema 2019). These internal waves break at steep slopes, such as those of underwater sea mountains and continental slopes, thereby creating turbulence. These turbulent motions are essential for the maintenance of the large-scale thermohaline circulation in the ocean and thus for the Earth's climate (Munk and Wunsch 1998).

4.6 Conclusions

Tides constitute a fascinating phenomenon of both theoretical and practical interest. Using idealised process-based models, solving only the essential physics on strongly schematised geometries, we have produced the gross features of tidal patterns in coastal basins around the world. The structure of the presented solutions, i.e. a superposition of fundamental wave solutions (Kelvin and Poincaré modes), leads to the following insights.

- The *Coriolis effect* is responsible for the typical cross-shore decay of tidal range away from the coast, a typical Kelvin wave property, and thus for the cyclonic wave propagation around amphidromic points in (sufficiently wide) semi-enclosed basins. Near the basin's closed end, tidal currents are elliptical, which is associated with the excitation of Poincaré waves.

- Dissipation due to *bottom friction* mainly causes a decay of tidal range in the direction of tidal wave propagation, implying a shift in the amphidromic points.
- *Topographic effects*, e.g. due to abrupt changes in depth, control tidal wave speed, which may lead to tidal amplification in shallow regions. In turn, this may enhance dissipation due to bottom friction, thus further affecting the amphidromic pattern.

Despite the strong schematisations, the idealised modelling approach is capable of grossly reproducing tidal patterns as observed in, e.g., the Gulf of California. Tidal patterns act as drivers in other studies of, e.g., morphodynamics, mixing and spreading of particles. Finally, the obtained insights and modelling techniques can be used to better understand the influence of large-scale changes due to climate change and large-scale human intervention.

Acknowledgements The tide gauge data used in Fig. 4.1 have been provided by the British Oceanographic Data Centre.

Appendix

Wave Solutions in Channel with Topographic Step

The cross-channel structures of elevation and along-channel velocity of the wave solutions in an infinite channel with a single transverse topographic step (Sect. 4.3.4) are given by

$$\tilde{\eta}(y) = \frac{\mathrm{i}C[f^2 - \gamma^4\sigma^2]\left[\alpha\gamma^2\sigma\cos\alpha y - fk\sin\alpha y\right]}{gh[\alpha^2\gamma^4\sigma^2 + f^2k^2]\sin\alpha y_\mathrm{s}}, \tag{4.35a}$$

$$\tilde{u}(y) = \frac{\mathrm{i}C[f^2 - \gamma^4\sigma^2]\left[\alpha k\cos\alpha y - \frac{f\sigma}{gh}\sin\alpha y\right]}{h[\alpha^2\gamma^4\sigma^2 + f^2k^2]\sin\alpha y_\mathrm{s}}. \tag{4.35b}$$

These expressions follow from subsequently combining the cross-channel velocity solution in Eq. (4.25) with the second polarisation equation (4.9b), and then substituting the result (4.35a) in the the first polarisation equation (4.9a). Expressions for $\tilde{\eta}'(y)$ and $\tilde{u}'(y)$ valid in the upper compartment are readily obtained by replacing the quantities $(\alpha, \gamma, h, y, y_\mathrm{s})$ in the above with $(\alpha', \gamma', h', y', y'_\mathrm{s})$.

References

Admiralty, British. 2009. *NP201-2010 Admiralty Tide Tables 2010, Volume 1*. United Kingdom Hydrographic Office.

Besio, G., P. Blondeaux, M. Brocchini, S.J.M.H. Hulscher, D. Idier, M.A.F. Knaapen, A.A. Németh, P.C. Roos, and G. Vittori. 2008. The morphodynamics of tidal sand waves: a model overview. *Coastal Engineering* 55 (7–8): 657–670.

Brown, P.J. 1973. Kelvin-wave reflection in a semi-infinite canal. *Journal of Marine Research* 31 (1): 1–10.

Burchard, H., H.M. Schuttelaars, and D. Ralston. 2018. Sediment trapping in estuaries. *Annual Review of Marine Science* 10: 371–395.

Carbajal, N., and J.O. Backhaus. 1998. Simulation of tides, residual flow and energy budget in the Gulf of California. *Oceanologica Acta* 21 (3): 429–446.

Davies, A.M. and S.C.M. Kwong. 2000. Tidal energy fluxes and dissipation on the European continental shelf. *Journal of Geophysical Research: Oceans* 105(C9): 21,969–21,989.

De Swart, H.E., and B. Yuan. 2019. Dynamics of offshore tidal sand ridges, a review. *Environmental Fluid Mechanics* 19 (5): 1047–1071.

De Swart, H.E., and J.T.F. Zimmerman. 2009. Morphodynamics of tidal inlet systems. *Annual Review of Fluid Mechanics* 41(7): 203–229.

Friedrichs, C.T. 2020. Barotropic tides in channelized estuaries. In *Contemporary issues in estuarine physics*, ed. A. Valle-Levinson, 27–61. Cambridge: Cambridge University Press.

Gerkema, T. 2019. *An introduction to tides*. Cambridge: Cambridge University Press.

Godin, G. 1965. The M2 tide in the Labrador Sea, Davis Strait and Baffin Bay. *Deep Sea Research* 12(4): 469–477.

Hendershott, M.C., and A. Speranza. 1971. Co-oscillating tides in long, narrow bays; the Taylor problem revisited. *Deep Sea Research* 18(10): 959–980.

Iannello, J.P. 1977. Tidally induced residual currents in estuaries of constant breadth and depth. *Journal of Marine Research* 35: 755–786.

Longuet-Higgins, M.S. 1968. On the trapping of waves along a discontinuity of depth in a rotating ocean. *Journal of Fluid Mechanics* 31(3): 417–434.

Maas, L.R.M., and A. Doelman. 2002. Chaotic tides. *Journal of Physical Oceanography* 32(3): 870–890.

Marinone, S.G. 2000. Tidal currents in the Gulf of California: intercomparisons among two- and three-dimensional models with observations. *Ciencas Marinas* 26(2): 275–301.

Munk, W., and C. Wunsch. 1998. Abyssal recipes II: energetics of tidal and wind mixing. *Deep Sea Research* 45(12): 1977–2010.

Murray, A.B. 2003. Contrasting the goals, strategies, and predictions associated with simplified numerical models and detailed simulations. In *Prediction in geomorphology*, vol. 135, ed. R.M. Iverson and P.R. Wilcock. Geophysical Monograph, 151–165. AGU: Washington, D.C.

Parker, B.B. 1993. *Tidal hydrodynamics*. New York: Wiley.

Pedlosky, J. 1987. *Geophysical fluid dynamics*. New York: Springer.

Platzman, G.W. 1982. Ocean tides and related waves. In: *Mathematical methods in the geophysical sciences, part 2: inverse problems, dynamo theory and tides*, ed. W.H. Reid, 239–292.

Polli, S. 1960. La propagazione delle maree nell' Adriatico. Technical Report **370**, Inst. Talassogr. Estratto da: Atti del 9. Convegno dell'Associazione geofisica italiana, Roma 20–21 novembre 1959.

Prandle, D. 1982. The vertical structure of tidal currents and other oscillatory flows. *Continental Shelf Research* 1(2): 191–207.

Reynaud, J.-Y. and R.W. Dalrymple. 2012. Shallow-marine tidal deposits. In *Principles of tidal sedimentology*, eds. R.A. Davis Jr. and R.W. Dalrymple, 335–369. Dordrecht: Springer.

Ridderinkhof, W., and J.T.F. Zimmerman. 1992. Chaotic stirring in a tidal system. *Science* 258(5085): 1107–1111.

Rienecker, M.M., and M.D. Teubner. 1980. A note on frictional effects in Taylor's problem. *Journal of Marine Research* 38(2): 183–191.

Ripa, P., and J. Zavala-Garay. 1999. Ocean channel modes. *Journal of Geophysical Research: Oceans* 104(C7): 15,479–15,494.

Roos, P.C., and H.M. Schuttelaars. 2009. Horizontally viscous effects in a tidal basin: extending Taylor's problem. *Journal of Fluid Mechanics* 640: 423–441.

Roos, P.C., J.J. Velema, S.J.M.H. Hulscher, and A. Stolk. 2011. An idealized model of tidal dynamics in the North Sea: resonance properties and response to large-scale changes. *Ocean Dynamics* 61 (12): 2019–2035.

Salas-de León, D.A., N. Carbajal-Pérez, M.A. Monreal-Gómez, and G. Barrientos-MacGregor. 2003. Residual circulation and tidal stress in the Gulf of California. *Journal of Geophysical Research: Oceans* 108 (C10): 3317.

Seminara, G. 2010. Fluvial sedimentary patterns. *Annual Review of Fluid Mechanics* 42: 43–66.

Sinha, B., and R.D. Pingree. 1997. The principal lunar semidiurnal tide and its harmonics: baseline solutions for M2 and M4 constituents in the North-West European continental shelf. *Continental Shelf Research* 17 (11): 1321–1365.

Talke, S.A., and D.A. Jay. 2020. Changing tides: the role of natural and anthropogenic factors. *Annual Review of Marine Science* 12: 121–151.

Taylor, G.I. 1922. Tidal oscillations in gulfs and rectangular basins. *Proceedings of the London Mathematical Society* 20(1): 148–181.

Zongwan, X., N., Carbajal and J. Südermann,. 1995. Tidal current amphidromic system in semi-enclosed basins. *Continental Shelf Research* 15(2–3): 219–240.

Chapter 5
Variational Water-Wave Modeling: From Deep Water to Beaches

Onno Bokhove

Abstract The mathematical and numerical modelling of free-surface water waves is considered from the viewpoint of variational principles combined with finite-element discretisations. Luke's classical variational principle (VP) is derived first, as opposed to Luke's (ingenious) positing of his VP, and forms the basis for three geometric or compatible finite-element water-wave models, two of which are validated against laboratory measurements and compared. Potential-flow wave dynamics in intermediate-depth water is coupled variationally to shallow-water beach dynamics, the latter modelling breaking waves, and illustrative numerics is shown to highlight the interactions between deeper water and shallow-water waves. Throughout, photographs of intricate wave interactions are used as illustrations.

5.1 Introduction

Water waves are ubiquitous on Earth, propagating on the free surface or interface between water and air, under the restoring influence of gravity. Water waves emerge when a (flat) water surface at rest is disturbed, e.g., when a stone is thrown in a quiescent pond, and the restoring force of gravity leads to wave propagation, the axisymmetric ripples with wave crests and troughs emanating after the stone has perturbed the water surface. When the acceleration vector due to gravity is locally (nearly) constant and unidirectional, the surface at rest will be (nearly) flat, while on larger planetary scales the free surface at rest will be curved, normal to the acceleration vector of gravity. We will consider water waves on smaller scales, on the order of centimetres to a few kilometres, thereby focussing on the scales of water-wave motion in laboratory channels, on ponds and lakes, near the shore and on fully-developed seas (cf. the photos in Figs. 5.1, 5.2, 5.3 and 5.4). The mathematical modelling of water waves, considered here, has a long history in fluid dynamics.

Predictive models for water-wave propagation started to emerge after the incompressible Euler or Navier-Stokes equations were formulated. Typically, for both linear

O. Bokhove (✉)
School of Mathematics, University of Leeds, LS2 9JT, Leeds, UK
e-mail: o.bokhove@leeds.ac.uk

H. Schuttelaars et al. (eds.), *The Mathematics of Marine Modelling*,
Mathematics of Planet Earth 9, https://doi.org/10.1007/978-3-031-09559-7_5

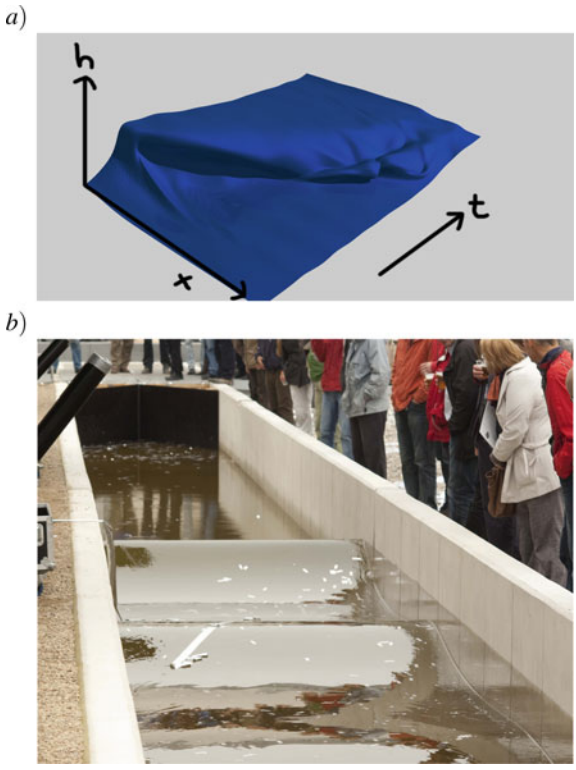

Fig. 5.1 **a** Rendering of a breaking wave in a vertical Hele-Shaw cell with water and air: it is a 2 mm–narrow cell with overall dimensions $0.7 \times 0.002 \times 0.24$ m^3 in which wave frequencies are used of circa 1 Hz (image courtesy: Wout Zweers, see also Bokhove et al. 2014; Thornton et al. 2014). Displayed is the time evolution of the overturning and splashing waterline as function of x and t. **b** A series of solitary water waves generated by lifting a sluice gate between different water levels is shown in a channel with approximate dimensions $45 \times 2 \times 1.2$ m^3, initially at rest, cf. Bokhove et al. (2011), Bokhove and Kalogirou (2016)

and nonlinear water-wave motion, the inviscid Navier-Stokes or Euler equations for an incompressible liquid (water) with a free surface and either an active or a passive gas (air) are considered to model water waves. Modelling of water waves focussed first mainly on linear wave propagation. We will, however, almost exclusively consider nonlinear water-wave dynamics even though we have used linear, exact solutions to verify our nonlinear numerical models in their small-amplitude limits. One of the first nonlinear models studied was the Korteweg-De-Vries (or KdV) equation (Drazin and Johnson 1989). It is an asymptotic subset of the three-dimensional potential-flow water-wave equations. These latter equations are, in turn, an exact subset of the incompressible Euler equations with a free surface, for the restricted case in which the three-dimensional velocity $\mathbf{u} = \nabla\phi$ is expressed in terms of a velocity potential ϕ. Here, both the velocity $\mathbf{u}$ and the velocity potential ϕ depend on the horizontal coordinates x and y, the vertical coordinate z, aligned in the opposite direction of the acceleration vector of gravity $\mathbf{g} = (0, 0, -g)^T$, and time t, with $g = 9.81$ m/s^2 the value near the Earth's surface. This nonlinear KdV–equation was derived in 1895 together with its famous solitary-wave or soliton solution, the famous sech–soliton by Korteweg and De Vries (Drazin and Johnson 1989). Both the KdV–equation and the potential-flow water-wave equations are inviscid and have a rich mathematical

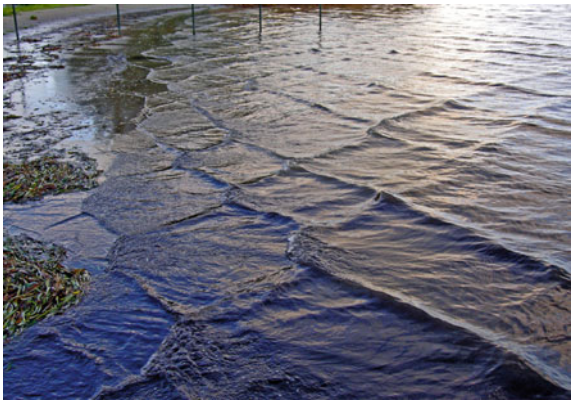

Fig. 5.2 Crossing waves near shorelines often show wave amplification with Mach stems, which may lead to localised wave breaking (as occurred for the cross-wave/Mach-stem in the foreground). Such shallow-water waves can be modelled approximately with the Kadomtsev-Petviashvili equation (Kadomtsev and Petviashvili 1970; Kodema 2010) or "two-dimensional KdV-equation", see also Ablowitz and Curtis (2013), Gidel et al. (2017). Photo courtesy V. Zwart

Fig. 5.3 Nonlinear unbroken waves start to shoal and break on the beach south of Newcastle. Photo O.B

and geometric structure intimately related to conservation laws and the phase-space dynamics of these systems (Drazin and Johnson 1989).

The geometric structure of such water-wave equations is the continuum or field extension of the geometric structure in classical mechanics; the latter mechanics was developed by Euler, Lagrange and Hamilton in the 17 and 18th centuries (Lanczos 1970; Marsden and Ratiu 1994). Classical mechanics concerns interacting mechanical or particle systems and results in a finite number of ordinary differential equations with functions of time. In contrast, the degrees-of-freedom (dofs) in space are infinite for fields, such as the velocity potential $\phi = \phi(x, y, z, t)$ and the water depth $h = h(x, y, t)$, and the dynamics are governed by partial differential equations. Here

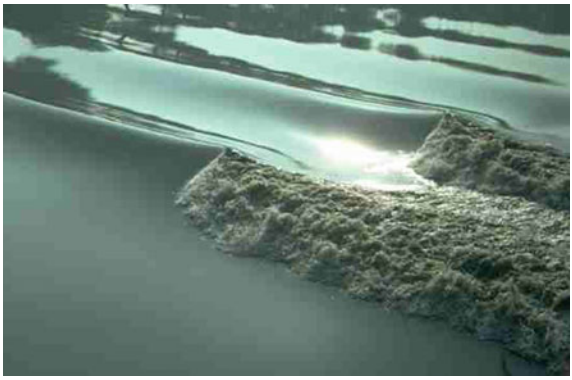

Fig. 5.4 Photograph of the Severn Bore, with a crest that is partially an unbroken solitary wave/undular bore in deep water and partially a spilling breaker along the shallow river bank, by the late D. Howell Peregrine, some of whose photographs and slides O.B. inherited. This photo was used as basis for one of the "Posters in the London Underground", i.e., for the "maths makes waves" poster

$z = h(x, y, t)$ is the nonoverturning free surface above the flat-bottom topography located at $z = 0$. We will use $h(x, y, t)$ later.

To introduce Hamilton's equations, consider the basic dynamics of a particle with mass m moving in one spatial dimension with position $q(t)$ and momentum $p(t)$ in an external potential $V(q)$. It is succinctly captured in the variational principle (VP)

$$0 = \lim_{\varepsilon\to 0}\int_0^T \frac{L(q+\varepsilon\delta q,\, p+\varepsilon\delta p) - L(q,p)}{\varepsilon}\,\mathrm{d}t = \delta\int_0^T L(q,p)\,\mathrm{d}t \quad (5.1a)$$

$$\equiv \delta\int_0^T p\dot{q} - H(p,q)\,\mathrm{d}t \equiv \delta\int_0^T p\dot{q} - \frac{1}{2}p^2/m - V(q)\,\mathrm{d}t \quad (5.1b)$$

$$= \int_0^T (\dot{q} - p/m)\delta p - (\dot{p} + \partial V(q)/\partial q)\,\delta q\,\mathrm{d}t + (p\delta q)|_{t=0}^{t=T} \quad (5.1c)$$

with Lagrangian $L(q, p)$, Hamiltonian $H(p, q)$ and final time T. Note that we also defined the functional derivative of the functional $\int_0^T L(q, p)\,\mathrm{d}t$ and used integration by parts in time. Given the arbitrariness of the variations δq and δp and by using end-point conditions $\delta q(0) = \delta q(T) = 0$, the two contributions in the integrand (5.1c) at $t = 0$ and $t = T$ are pointwise zero (in time). From (5.1c), we therefore obtain Hamilton's equations of motion (Lanczos 1970; Marsden and Ratiu 1994) as a first-order system in time:

$$\dot{q} = \frac{\partial H}{\partial p} = p/m \quad \text{and} \quad \dot{p} = F(q) \equiv -\frac{\partial H}{\partial q} = -\frac{\partial V}{\partial q} \quad (5.2)$$

with the central force $F(q)$ derived as the negative derivative of the potential $V(q)$. Combining (5.2) yields Newton's law of motion for a single particle in an external and central force, i.e.: $m\ddot{q} = F(q) = -V'(q)$. Hamilton's or Hamiltonian dynamics extends to more general mechanical and multi-particle systems in higher dimensions in which generalised coordinates $\mathbf{q}(t)$ and generalised momenta $\mathbf{p}(t)$ emerge for finite-dimensional systems, cf. Lanczos (1970), Marsden and Ratiu (1994). The reason to highlight such a straightforward example is that for infinite-dimensional systems such as water-wave hydrodynamics, these generalised coordinates and momenta will be replaced by fields. Despite this additional complexity, such an intrinsic structure of the variational principle (5.1) will be shown to be similar, and to remain recognisable, to that one for water-wave dynamics. For water-wave dynamics, the development of geometric and Hamiltonian dynamics took off with the works of Benney and Luke (1964), Luke (1967), Zakharov (1968) and Miles (1977) in the 1960 and 1970s. The work by Luke (1967) will be our starting point for describing water-wave dynamics.

A finite-dimensional example that is more closely related to the "pre-Luke" VP that we will present shortly in Sect. 5.2 is the following. Consider two nonlinear oscillators/springs moving in one dimension, denoted by $x = q_i$ (for $i = 1, 2$), with spatial coordinates $q_1 = q_1(t)$, $y_1 = 0$ and $q_2 = q_2(t)$, $y_2 = L$ or $\mathbf{q} = (q_1, q_2)^T$ with generalised momenta $\mathbf{p} = (p_1, p_2)^T$ and lateral y-direction, coupled together such that their separation is fixed by $\sqrt{(q_1 - q_2)^2 + L^2} = R$ with $R > L > 0$ constant. Based on specific initial conditions, we take $q_1 = q_2 + A$ with $A = \sqrt{R^2 - L^2}$. By again using suitable endpoint conditions, an example of a constrained VP and its variations is

$$
\begin{aligned}
0 =& \delta \int_0^T p_1\dot{q}_1 + p_2\dot{q}_2 - \frac{1}{2}p_1^2/m_1 - \frac{1}{2}p_2^2/m_2 - \frac{1}{3}k_1|q_1|^3 - \frac{1}{3}k_2|q_2|^3 \\
&\qquad + P(q_1 - q_2 - A)\,\mathrm{d}t \qquad (5.3a)\\
=& \int_0^T (\dot{q}_1 - p_1/m_1)\delta p_1 + (\dot{q}_2 - p_2/m_2)\delta p_2 - (\dot{p}_1 + k_1 q_1|q_1| - P)\delta q_1 \\
&\qquad - (\dot{p}_2 + k_2 q_2|q_2| + P)\delta q_2 + (q_1 - q_2 - A)\delta P\,\mathrm{d}t \qquad (5.3b)
\end{aligned}
$$

with a Lagrange multiplier or "pressure" $P = P(t)$ (Lanczos 1970; Marsden and Ratiu 1994) imposing the constraint $q_1 - q_2 - A = 0$, spring constants $k_{1,2} > 0$ and masses $m_{1,2}$. The resulting equations of motion follow directly from (5.3) using the arbitrariness of the variations $\delta\mathbf{q}$, $\delta\mathbf{p}$ as

$$
\begin{aligned}
&\delta q_1 :\ \dot{p}_1 + k_1 q_1|q_1| - P = 0, \quad \delta q_2 : \dot{p}_2 + k_2 q_2|q_2| + P = 0, && (5.4a)\\
&\delta p_1 :\ \dot{q}_1 = p_1/m_1, \quad \delta p_2 : \dot{q}_2 = p_2/m_2, \quad \delta P : q_1 - q_2 - A = 0. && (5.4b)
\end{aligned}
$$

The multiplier P is determined by taking twice the time derivative of the constraint yielding, first, that $p_1/m_1 - p_2/m_2 = 0$ and, second, that $P = (m_1 + m_2)(k_1 q_1|q_1|/m_1 - k_2 q_2|q_2|/m_2)/(m_1 m_2)$. This model is readily tested numerically

by using a sympletic integrator (Leimkühler and Reich 2009), with a forward timestep for $\mathbf{p}$ and a backward timestep for $\mathbf{q}$, that uses the update of $\mathbf{p}$ after first calculating the multiplier P. Initial conditions need to satisfy the constraint as well as $p_1/m_1 = p_2/m_2$. The timestepping described maintains these constraints exactly, which can be readily verified.

Taking Luke's variational principle as starting point may be a surprise since Luke states himself that "*No satisfactory solution seems known for the general problem of finding suitable Lagrangian functions. For the water wave problem, in particular, the pressure function used in (1) is more productive than the traditional form of the Lagrangian,* L^*, *equal to kinetic minus potential energy*" (Luke 1967). Luke found his variational principle presumably by insight. Cotter and Bokhove (2010) have, in contrast, shown that one can derive Luke's variational principle systematically from a Hamilton's action principle consisting of kinetic minus potential energy, with pairs of generalised field coordinates and conjugate momenta. There are several advantages for using such geometric formulations of hydrodynamics for water waves and, in particular, for coupling deep or intermediate water-wave dynamics to either moving structures such as elastic beams, buoys or ships or different, shallow-water hydrodynamic models. These advantages are based on the following "principles":

- The first principle is that, when damping and wave breaking are absent, the appropriate (coupled) models should contain a conservative limit.
- The second principle is that conservative, coupled wave-structure or coupled deep- and shallow-water systems should in a relatively straightforward manner consist of the sum of the variational principles of the separate systems. As a consequence the combined system remains consistent without spurious energy losses or gains.
- The third principle is that we directly discretise these (nonlinear and/or coupled) systems consistently in space and time, to obtain a space-time discrete algebraic variational (finite-element) system. Its variation then "semi-automatically" yields a stable and robust numerical scheme for advanced water-wave modelling.

We will employ finite-element methods (FEM) because the weak formulation inherent in FEM closely matches the weak formulation of variational principles. It is therefore a relatively small step—involving the finite-element expansion of the variables involved, their substitution and integration—to turn the relevant variational principle for continuum water-wave dynamics into a spatially discrete or space-time discrete variational principle. Variation of the latter algebraic principle then yields the final discretisation to be implemented. To facilitate the development of such variational discretisations, we have employed *Firedrake* "*…an automated system for the portable solution of partial differential equations using the finite element method*" to implement our numerical discretisations in an efficient manner (Rathgeber et al. 2016).

The beauty of water-wave dynamics lies in part in the abundance of water-wave phenomena surrounding us. We can, and most likely do, all observe water-wave motion on a daily basis. In what follows, we will both show photographs of water-wave phenomena (as in Figs. 5.1, 5.2, 5.3 and 5.4 using images from O.B.'s laboratory experiments and photographs from other people) as well as a range of numerical sim-

ulations from numerical models obtained following the above "principles", including simulation results from Bokhove and Kalogirou (2016) , Gagarina et al. (2014, 2016), Gidel et al. (2017), Gidel (2018).

This chapter has the following outline. Luke's VP is derived, as opposed to posited, in Sect. 5.2. In Sect. 5.3, Luke's VP is transformed from a time-dependent domain with a free surface and wavemaker to a fixed reference domain, resulting in Miles' VP in a transformed domain. Miles' VP then forms the basis to discuss three compatible numerical discretisations, directly based on the VP. Numerical results of two of the methods are compared and validated against wavetank experiments in Sect. 5.3.2, before we consider a novel discretisation of a third method in detail. A novel derivation of the variational coupling between a potential-flow water-wave model and a shallow-water model on the beach is investigated in Sect. 5.4, with illustrative numerical results. We conclude in Sect. 5.5 and finish with some future research directions.

5.2 Derivation of Luke's Variational Principle

In Cotter and Bokhove (2010), the starting point is a Lagrangian density L_{incr} consisting of the kinetic energy minus potential energy of a compressible fluid weakly constrained to be incompressible:

$$L_{incr} = \frac{1}{2} D|\mathbf{u}|^2 - gD(z - H_0) + P(1 - D) \tag{5.5}$$

with scaled density $D = D(x, y, z, t)$ such that density $\rho = \rho_0 D$ with constant water density ρ_0 and scaled pressure $P = p/\rho_0$ enforcing the constraint $1 - D = 0$. To instill dynamics, "Lin" constraints (named after C.C. Lin) were imposed on the space-time integral of L_{incr}, i.e., the continuity equation $\partial_t D + \nabla \cdot (D\mathbf{u}) = 0$ was enforced with a Lagrange multiplier ϕ and the kinematic condition for a single-valued free-surface was enforced by another Lagrange multiplier. By taking variations with respect to the velocity $\mathbf{u}$ it turns out that potential flow becomes a consequence, i.e. one derives that $\mathbf{u} = \nabla\phi$. After subsequent substitution of this relation $\mathbf{u} = \nabla\phi$ back into this Lin-constrained variational principle, the following "pre-Luke" variational principle (Cotter and Bokhove 2010) is shown to emerge:

$$0 = \delta \int_0^T \mathcal{L}_p[\phi, \tilde{\phi}, D, h]\, \mathrm{d}t \tag{5.6a}$$

$$= \delta \int_0^T \int_{\Omega_H} \int_0^h D\partial_t\phi + \frac{1}{2} D|\nabla\phi|^2 + gD(z - H_0) + P(D - 1)\, \mathrm{d}z\, \mathrm{d}x\, \mathrm{d}y\, \mathrm{d}t \tag{5.6b}$$

with $\tilde{\phi}(x,y,t) = \phi\,(x,y,h(x,y,t),t)$ in a domain with a flat bottom at $z=0$, vertical channel walls (for the moment), horizontal extent Ω_H and vertical extent $z \in [0,h]$, and a free surface at rest residing at $z = H_0$. Similar to the basic example with Hamilton's equations (5.2), variation of (5.6) yields Hamilton's equations,

$$\delta P: \quad D = 1 \tag{5.7a}$$

$$\delta D: \quad \partial_t \phi + \frac{1}{2}|\nabla\phi|^2 + g(z - H_0) = -P \tag{5.7b}$$

$$\delta\phi: \quad \partial_t D + \nabla\cdot(D\nabla\phi) = 0 \tag{5.7c}$$

$$\delta h: \quad \partial_t \phi + \frac{1}{2}|\nabla\phi|^2 + g(h - H_0) = 0 \quad \text{at} \quad z = h \tag{5.7d}$$

$$\delta\tilde{\phi}: \quad \partial_t h + \nabla\phi\cdot\nabla h = \partial_z\phi \quad \text{at} \quad z = h, \tag{5.7e}$$

in which we have used the constraint $D = 1$ at the free surface already, integration by parts in time with end-point conditions $\delta\phi(x,y,z,0) = \delta\phi(x,y,z,T) = 0$ (see Appendix 1), Gauss' law with $\hat{\mathbf{n}}\cdot\nabla\phi = 0$ at solid walls with the relevant outward normal $\hat{\mathbf{n}}$, and with outward normal $\hat{\mathbf{n}} = (-\nabla h, 1)^T/\sqrt{(1+|\nabla h|^2)}$ at the free surface located at $z = h(x,y,t)$.

The structure of (5.6) and (5.7) is the same as in (5.1) and (5.2), or as in (5.3) and (5.4), with the fields $\{\phi, \tilde{\phi}\}$ playing the role of generalised coordinates $\mathbf{q}$ and fields $\{D, h\}$ playing the role of generalised momenta $\mathbf{p}$. Pre-Luke's variational principle (5.6) does, however, have an additional constraint $D - 1 = 0$ relative to (5.1), but this is akin to the constraint $q_1 - q_2 - A = 0$ and Lagrange multiplier P in (5.3). After applying the constraint $D = 1$, Hamilton's equations (5.7) reduce to the well-known potential-flow water-wave equations with Laplacian $\nabla^2\phi = 0$ from (5.7c), dynamic boundary condition (5.7d) and kinematic boundary condition (5.7e), but we have an additional equation defining the fluid pressure P via (5.7b). By imposing constraint $D = 1$ directly onto pre-Luke's variational principle (5.6), we find Luke's variational principle

$$0 = \delta\int_0^T \mathcal{L}[\phi,\tilde{\phi},h]\,\mathrm{d}t = \delta\int_0^T\int_{\Omega_H}\int_0^h \partial_t\phi + \frac{1}{2}|\nabla\phi|^2 + g(z-H_0)\,\mathrm{d}z\,\mathrm{d}x\,\mathrm{d}y\,\mathrm{d}t \tag{5.8}$$

with, as Luke (1967) stressed in his remark quoted in the introduction, the (negative and scaled) pressure as integrand. The disadvantage of (5.8) in contrast to (5.6) is that it does not provide an explicit expression for the pressure P. For fluid-structure interactions involving water waves coupled to dynamic structures, this implies that there is no explicit mathematical expression for the value of the pressure on either the structure or at the waterline.

5.3 Transformed Luke's/Miles' Variational Principles with Wavemaker

In these more complex situations with fluids and structures as well as for numerical purposes, it is advantageous to transform the time-dependent domain to new coordinates in a fixed domain. Such a transformation is considered next and, to simplify the exposition, only within a *two-dimensional* domain $(x, z) \in \Omega$.

Consider water waves modelled as incompressible potential flow. The domain is bounded on the left side by a wavemaker at $x = W(z, t)$, from below by a flat bottom at $z = 0$, on the right side by a solid wall at $x = L_s$ and from above by a free surface parametrised as $\mathbf{X}_s = (X, Z)$. Here H_0 is the position of the free surface at rest for the case with the left boundary at $x = W(z, t) = 0$. The free surface is allowed to overturn as long as domain Ω stays singly-connected during the time interval $t \in [0, T]$ considered. The solenoidal velocity is now defined as $\mathbf{u} = (u, w) = \nabla\phi \equiv (\partial_x, \partial_z)\phi(x, z, t)$. Starting from Luke's variational principle (5.8) restriced to a vertical plane, the water-wave dynamics then arises from

$$0 = \delta \int_0^T \iint_\Omega \partial_t \phi + \frac{1}{2}|\nabla\phi|^2 + g(z - H_0)\,\mathrm{d}x\,\mathrm{d}z\,\mathrm{d}t. \tag{5.9}$$

As in Bridges and Donaldson (2011), we transform the space-time domain with $(x, z) \in \Omega$ and $t \in [0, T]$ to a cuboid $\xi \in [0, L_s]$, $\eta \in [0, H_0]$, $\tau \in [0, T]$ with $\tau = t$, while we have added a wavemaker. The required transformations are

$$\partial_t = \partial_\tau + \frac{J_1}{|J|}\partial_\xi + \frac{J_2}{|J|}\partial_\eta, \quad \partial_x = \frac{z_\eta}{|J|}\partial_\xi - \frac{z_\xi}{|J|}\partial_\eta, \quad \partial_z = -\frac{x_\eta}{|J|}\partial_\xi + \frac{x_\xi}{|J|}\partial_\eta, \tag{5.10a}$$

in which the determinantal minors

$$|J| = x_\xi z_\eta - x_\eta z_\xi, \quad J_1 = x_\eta z_\tau - x_\tau z_\eta, \quad J_2 = x_\tau z_\xi - x_\xi z_\tau \tag{5.10b}$$

arise from the three-dimensional space-time Jacobian

$$J = \begin{pmatrix} x_\xi & x_\eta & x_\tau \\ z_\xi & z_\eta & z_\tau \\ 0 & 0 & 1 \end{pmatrix}. \tag{5.10c}$$

Under transformations (5.10), Luke's variational principle (5.9) becomes

$$\begin{aligned} 0 = \delta \int_0^T \int_0^{L_s} \int_0^{H_0} & (x_\xi z_\eta - x_\eta z_\xi)\partial_\tau\phi + (x_\eta z_\tau - x_\tau z_\eta)\partial_\xi\phi + (x_\tau z_\xi - x_\xi z_\tau)\partial_\eta\phi \\ & + \frac{1}{2\,|J|}\left((x_\eta^2 + z_\eta^2)|\partial_\xi\phi|^2 - 2(x_\xi x_\eta + z_\xi z_\eta)\partial_\xi\phi\partial_\eta\phi + (x_\xi^2 + z_\xi^2)|\partial_\eta\phi|^2\right) \\ & + |J|g(z - H_0)\,\mathrm{d}\xi\,\mathrm{d}\eta\,\mathrm{d}\tau. \end{aligned} \tag{5.11}$$

Using (5.10b), it is straightforward to derive the geometric conservation law

$$\partial_\tau |J| + \partial_\xi J_1 + \partial_\eta J_2 = 0, \tag{5.12}$$

whence, by combining (5.11) and (5.12), we obtain

$$\begin{aligned} 0 = &\delta \int_0^T \int_0^{L_s} \int_0^{H_0} \partial_\tau (|J|\phi) + \partial_\xi (J_1 \phi) + \partial_\eta (J_2 \phi) + \\ &\frac{1}{2\,J|} \left((x_\eta^2 + z_\eta^2) |\partial_\xi \phi|^2 - 2(x_\xi x_\eta + z_\xi z_\eta) \partial_\xi \phi \partial_\eta \phi + (x_\xi^2 + z_\xi^2) |\partial_\eta \phi|^2 \right) \\ &+ |J| g (z - H_0) \, \mathrm{d}\xi \, \mathrm{d}\eta \, \mathrm{d}\tau. \end{aligned} \tag{5.13}$$

The above is the same as in Bridges and Donaldson (2011) but, due to the new wavemaker condition $x = W(z, \tau)$ at $\xi = 0$, new terms emerge when we integrate, term-by-term, $\partial_\tau (|J|\phi) + \partial_\xi (J_1 \phi) + \partial_\eta (J_2 \phi)$ in the variational principle (5.13). This demands that we adapt but also slightly extend the derivation given in Bridges and Donaldson (2011). The first integral term in (5.13) can be manipulated to yield

$$\begin{aligned} \delta \int_0^{H_0} \int_0^{L_s} \int_0^T \partial_\tau (|J|\phi) \, \mathrm{d}\tau \, \mathrm{d}\xi \, \mathrm{d}\eta &= \int_0^{H_0} \int_0^{L_s} \phi \left((\delta x)_\xi z_\eta + x_\xi (\delta z)_\eta \right. \\ &\left. - (\delta x)_\eta z_\xi - x_\eta (\delta z)_\xi \right) |_{\tau=0}^{\tau=T} + |J| \delta\phi |_{\tau=0}^{\tau=T} \, \mathrm{d}\xi \, \mathrm{d}\eta \\ &= \int_0^{H_0} \int_0^{L_s} \left(\phi \partial_\xi (z_\eta \delta x - x_\eta \delta z) + \phi \partial_\eta (x_\xi \delta z - z_\xi \delta x) \right) |_{\tau=0}^{\tau=T} \, \mathrm{d}\xi \, \mathrm{d}\eta = 0, \end{aligned} \tag{5.14}$$

where we have used end-point conditions $\delta\phi|_{\tau=0} = \delta\phi|_{\tau=T} = 0, \delta x|_{\tau=0} = \delta x|_{\tau=T} = 0$ and $\delta z|_{\tau=0} = \delta z|_{\tau=T} = 0$. The second integral term in (5.13) becomes

$$\begin{aligned} \int_0^{L_s} \int_0^{H_0} \partial_\xi \left((x_\eta z_\tau - x_\tau z_\eta) \phi \right) \, \mathrm{d}\xi \, \mathrm{d}\eta &= \int_0^{H_0} (x_\eta z_\tau - x_\tau z_\eta) \phi |_{\xi=0}^{\xi=L_s} \, \mathrm{d}\eta \\ &= \underline{\int_0^{H_0} z_\eta \partial_\tau W \phi |_{\xi=0} \, \mathrm{d}\eta}, \end{aligned} \tag{5.15}$$

since at $\xi = L_s$ also $x = L_s$, and therefore $x_\eta|_{\xi=L_s} = x_\tau|_{\xi=L_s} = 0$, while at $\xi = 0$ one has $x = W(z, \tau)$ such that $x_\eta = \partial_z W z_\eta, x_\tau = \partial_\tau W + \partial_z W z_\tau$ and $x_\eta z_\tau - x_\tau z_\eta = -z_\eta \partial_\tau W$. The third integral term in (5.13) becomes

$$\begin{aligned} \int_0^{L_s} \int_0^{H_0} \partial_\eta \left((x_\tau z_\xi - x_\xi z_\tau) \phi \right) \, \mathrm{d}\xi \, \mathrm{d}\eta &= \int_0^{L_s} (x_\tau z_\xi - x_\xi z_\tau) \phi |_{\eta=0}^{\eta=H_0} \, \mathrm{d}\xi \\ &= \underline{\int_0^{L_s} (x_\tau z_\xi - x_\xi z_\tau)|_{\eta=H_0} \tilde{\phi} \, \mathrm{d}\xi}, \end{aligned} \tag{5.16}$$

since $z = 0$ at $\eta = 0$ and thus $z_\xi|_{\eta=0} = z_\tau|_{\eta=0} = 0$. The outcome is therefore that there are two surface contributions, underlined in (5.15) and (5.16), one at the moving free surface $\eta = H_0$ and one at the moving wavemaker $\xi = 0$. The gravitational energy is also transformed as follows

$$\begin{aligned}
&\int_0^{L_s}\int_0^{H_0}(x_\xi z_\eta - x_\eta z_\xi)g(z-H_0)\,\mathrm{d}\xi\,\mathrm{d}\eta \\
&\quad=\int_0^{L_s}\int_0^{H_0}\partial_\eta\left(x_\xi(\frac{1}{2}gz^2-gH_0z)\right)-\partial_\xi\left(x_\eta(\frac{1}{2}gz^2-gH_0z)\right)\mathrm{d}\xi\,\mathrm{d}\eta \\
&\quad=\int_0^{L_s}x_\xi\frac{1}{2}gz^2-gH_0z|_{\eta=0}^{\eta=H_0}\,\mathrm{d}\xi-\int_0^{H_0}x_\eta\frac{1}{2}gz^2-gH_0z|_{\xi=0}^{\xi=L_s}\,\mathrm{d}\eta \\
&\quad=\int_0^{L_s}x_\xi g(\frac{1}{2}z^2-H_0z)|_{\eta=H_0}\,\mathrm{d}\xi+\int_0^{H_0}x_\eta g(\frac{1}{2}z^2-H_0z)|_{\xi=0}\,\mathrm{d}\eta,
\end{aligned}\tag{5.17}$$

again using the conditions at $\xi = L_s$ as well as $z = 0$ at $\eta = 0$.

Hence, for a domain with a flap-type wavemaker at ξ and a free surface at $\eta = H_0$, Luke's variational principle in transformed coordinates (5.13) becomes Miles' variational principle in transformed coordinates

$$\begin{aligned}
0=&\delta\int_0^T\int_0^{L_s}\Big(x_\tau z_\xi - x_\xi z_\tau)\tilde{\phi}+x_\xi g(\frac{1}{2}z^2-H_0z)\Big)|_{\eta=H_0}\,\mathrm{d}\xi \\
&+\int_0^{H_0}\Big(z_\eta\partial_\tau W\phi+x_\eta g(\frac{1}{2}z^2-H_0z)\Big)|_{\xi=0}\,\mathrm{d}\eta+\mathcal{K}\,\mathrm{d}\tau \\
\equiv&\delta\int_0^T\int_0^{L_s}\Big(x_\tau z_\xi - x_\xi z_\tau)\tilde{\phi}+x_\xi g(\frac{1}{2}z^2-H_0z)\Big)|_{\eta=H_0}\,\mathrm{d}\xi \\
&+\int_0^{H_0}\Big(z_\eta\partial_\tau W\phi+x_\eta g(\frac{1}{2}z^2-H_0z)\Big)|_{\xi=0}\,\mathrm{d}\eta \\
&+\int_0^{L_s}\int_0^{H_0}\frac{1}{2J}\Big((x_\eta^2+z_\eta^2)|\partial_\xi\phi|^2-2(x_\xi x_\eta+z_\xi z_\eta)\partial_\xi\phi\partial_\eta\phi \\
&\qquad+(x_\xi^2+z_\xi^2)|\partial_\eta\phi|^2\Big)\,\mathrm{d}\xi\,\mathrm{d}\eta\,\mathrm{d}\tau
\end{aligned}\tag{5.18}$$

with kinetic energy $\mathcal{K}$.

The challenge in the variation of Miles' variational principle (5.18) is that it results in variations of the variables $\{\phi, x, z\}$ whereas $\{x, z\}$ can only be independent at the free surface and partially independent at the moving wavemaker. Bridges and Donaldson (2011) provide an overview of models for the motion of $x(\xi, \eta, \tau)$ and $z(\xi, \eta, \tau)$, including (nonlinear) elliptical solvers for $\{x, z\}$ driven by the moving boundaries. Variation of the (nonlinear) elliptic solvers will lead to linear equations, for $\{\delta x, \delta z\}$, that relate the variations in the interior to the independent variations at the moving boundaries, denoted by $\{X, Z\}$. It is shown in Bridges and Donaldson (2011) that $\delta\mathcal{K}/\delta x = \delta\mathcal{K}/\delta z = 0$ in the interior, after one uses the transformed elliptic equation for ϕ in the interior. The motion of $\{x, z\}$ can in certain cases be specified and in other cases be imposed via Lagrange multipliers, the latter which has neither

been explored thoroughly in an analytical way nor in a numerical way. Consequently, the entire variation of (5.18) will lead to variations of only the variables $\{\phi, \tilde{\phi}, X, Z\}$. The numerical integration with finite-element methods (FEM) of (5.18) including (regular) mesh motion was explored for the first time in Gagarina et al. (2012, 2014) and Gidel (2018).

5.3.1 FEM and Mesh Motion

Hitherto, two numerical approaches have been developed and applied to evaluate and discretise (5.18) for domains with a piston wavemaker such that the boundary condition on the left-side of the channel becomes $x = W(z,t) = R(t)$. In the first approach, marked by I, two variations have been developed and employed. The difference is that in variation I.A, a continuous Galerkin FEM is used with, e.g., quadrilateral elements in the vertical $\{x,z\}$–plane, while in variation I.B a Galerkin FEM is used in the horizontal plane and higher-order Lagrange polynomials in one element in the vertical, in the transformed space and in three dimensions.

Variation I.A uses a space-time finite-element discretisation of Miles' variational principle in a two-dimensional $\{x,z\} \in [R, L_s] \times [0,h]$–plane, so without explicitly transforming it to the fixed reference domain in (5.18). The nodes of the (quadrilateral) mesh are moved in a regular fashion. In $\{x,z\} \in [R, L_w] \times [0,h]$, with $L_w < L_s$, the nodes are moved in the horizontal and vertical according to the method of lines, and in a linear fashion, such that the horizontal nodal movement at L_w is zero and is $R(t)$ on the piston wavemaker and, similarly, zero at the bottom at $z = 0$ and $h(x,t)$ at the non-overturning free surface. For $x > L_w$ nodes are only moving in the vertical. This prescription of the node movement implies that $\delta x = 0$ and that δz is uniquely and in a linear manner determined in terms of δh. The variation of the space-discrete variational principle then directly yields the discrete equations of motion. The detailed methodology is described in Gagarina et al. (2014, 2016).

Variation I.B in essence uses (5.18) with explicit expressions for the motion of x and z. We extend the description in Gidel (2018), where the wavemaker is a piston $W(z,t) = R(t)$, here to the general waveflap expression $x = W(z,t)$. The first transformation is from $\{x,z,t\}$ to $\{\chi, \tilde{z} = z, \tilde{t} = t\}$ with $\chi \in [0, L_w]$ and

$$x = \frac{W(\tilde{z},\tilde{t})L_w + \chi\left(L_w - W(\tilde{z},\tilde{t})\right)}{L_w}. \tag{5.19}$$

The second transformation is from $\{\chi = \xi, \tilde{z}, \tilde{t} = \tau\}$ to $\{\xi = \chi, \eta, \tau\}$ with

$$x(\xi,\eta,\tau) = \frac{\xi\left(L_w - W(\eta h/H_0,\tau)\right) + W(\eta h/H_0,\tau)L_w}{L_w} \text{ and } z(\xi,\eta,\tau) = \frac{\eta h}{H_0}, \tag{5.20}$$

where $h = h(\xi, \tau)$. Expressions (5.20) can be substituted into (5.18), with δx and δz uniquely and in a linear manner determined in terms of δh. The next step differs from variation I.A: first (Lagrange) polynomials are used in the variational principle to eliminate the vertical η–dependence by integration over these polynomials, leading to several predetermined matrices and vectors. It results in a reduced variational principle in terms of the horizontal spatial dimensions and time. Even though in the above we illustrated the approach in one horizontal dimension, Gidel (2018) extended the derivation to three dimensions and uses a priori an explicit coordinate transformation instead of the generic one developed to arrive at (5.18). The results are, by default, the same. Subsequently, this variational principle in the horizontal plane, based on polynomial expansions with one element in the vertical, is discretised using continuous Galerkin finite elements, on, e.g., quadrilateral elements in the horizontal. The variation of the now fully space-discrete variational principle then directly yields the space-discrete equations of motion. Both symplectic Euler and Störmer-Verlet time-stepping schemes, extended to include wave-forcing terms, have then been used to arrive at space-time discrete equations of motion. Alternatively, one can use (dis)continuous Galerkin finite-element methods in time (Bokhove and Kalogiro 2016; Gagarina et al. 2016) to first discretise the space-discrete variational principle in time as well, which variation subsequently leads to the same space-time discrete equations of motion. Approach I.B has been implemented in Firedrake (Rathgeber et al. 2016), such that the variations of the VP are essentially directly implemented in weak form, cf. the actual mathematical formulations. In Firedrake, details of the finite-element implementation are to a large extent hidden from the user, including matrix definitions, matrix assembly, nonlinear solvers, parallelisation (via MPI) and preconditioning.

In the second approach, marked by II, Miles' variational principle (5.18) is discretised in space using a continuous Galerkin FEM and two nonlinear elliptic solvers, one each for x and z, are used to determine $\{x(\xi, \eta, \tau), z(\xi, \eta, \tau)\}$. These nonlinear elliptic solvers and the gradients of x and z in (5.18) are discretised using finite-difference approximations and solved with an iterative successive overrelation method. Dirichlet boundary conditions for x and z are used at solid-wall boundaries and at the free surface one sets $x = X$ and $z = Z$. The variations of this finite-difference approximation of the nonlinear elliptic solvers for x and z are linear in δx and δz. This therefore again relates all interior domain variations of δx, δz, as in the previous approach I.A and I.B, in a linear fashion to the (free-)surface evariations δX, δZ. The equations for the variables $\{X, Z\}$ and $\phi(\xi, H_0, \tau)$ (at the free surface) are then stepped forward as conjugate variable pairs in time using a symplectic Störmer-Verlet time integrator, cf. Gagarina et al. (2012).

The results of these two approaches are geometric space-time discretisations of the potential-flow water-wave equations. We appear to be the first to have developed such an approach in a completely systematic and geometric manner. The advantage of such geometric space-time integrators above classical nongeometric ones is that there is no artifical numerical damping. For long-time simulations, wave-amplitudes are therefore preserved. A disadvantage may be that one has to use a partially implicit numerical discretisation, which is more costly to implement. Another disadvantage is that energy and motion cannot escape to smaller and smaller scales because there is no subgrid-scale

parameterization integrated in the discretisation. It depends on the numerical application at hand whether such a geometric approach is desirable or not.

Rogue waves are anomalously high waves, with at least twice the wave amplitude of the ambient sea (Dysthe et al. 2008). Their occurrance at sea is rare and difficult to predict, both statistically and deterministically. Understanding the occurrence of rogue waves is important because they have damaged or destroyed ships as well as maritime and coastal structures, see Nikolkina and Didenkulova (2011) for an overview of rogue-wave maritime disasters. Following our approach, we have successfully simulated these rogue-wave interactions in long-time simulations, also for a Benney-Luke approximation of the potential water-wave models, cf. Gagarina et al. (2014), Bokhove & Kalogirou (2016), Gidel et al. (2017), Gidel (2018). Some of these numerical results will be presented in Sect. 5.3.2.

5.3.2 Numerical Results: Comparison with Wave-Tank Experiments

The first two numerical approaches are compared with data from wave-tank experiments which have been collected at the Maritime Research Institute Netherlands (MARIN). MARINs Case 202002 is considered, which is one case in the suite of experimental test cases reported (Bunnik 2010). The wavetank at hand is 195.4 m long with a piston wavemaker at $x = R(t)$ and the water depth at rest is 1 m. The set-up is symmetric such that the experiments are effectively two dimensional in a vertical cross-section. Simulations are stopped before any wave reflections from the end of the tank are having an effect. The wavemaker signal is such that a rogue wave arises via wave focussing at circa $t = 109.5$ s and $x = 50$ m.

In approach I.A, using data from a probe around $x = 50$ m, the (finest) mesh size and timestep are determined based on linear wave-dispersion estimates, and are found to be $\Delta x = 0.00385$ m and $\Delta t = 0.001$ s. An exponential distribution of 20 mesh points is used in the vertical. In approach I.B, the numerical wave basin is 120 m long with a uniform mesh. The mesh size $\Delta x = 0.01$ m and timestep $\Delta t = 0.001$ s are again based on linear wave-dispersion estimates. Nine Lagrange degrees-of-freedom are taken into account in the vertical. The comparison between each simulation and the experimental data is shown as a time series in Figs. 5.5 and 5.6, while the corresponding Fourier spectra can be seen in Figs. 5.7 and 5.8, respectively. Both simulation approaches compare favourably with the experimental data and, hence, with another. The codes for Approach I.B have been parallised, a nearly automatic feature within the Firedrake FEM environment.

Third Approach

The third and novel geometrical approach to discretise (5.18) is developed next. It concerns the second principle stated in the introduction: that the variational principle

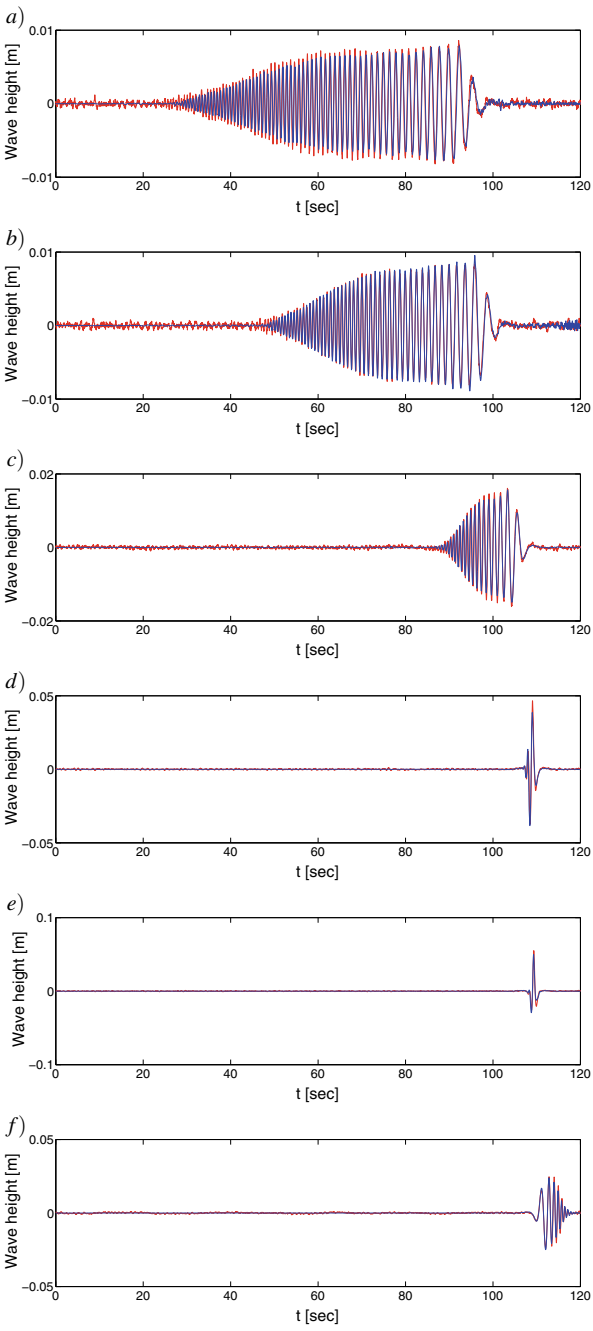

Fig. 5.5 Free surface $h(x, t)$ at various locations x as function of time t for numerical simulations using approach I.A (Störmer-Verlet scheme, denoted by SV: solid black lines) versus six experimental-probe measurements (red solid lines) in MARIN's wave tank a)-to-f) at $x = (10, 20, 40, 49.5, 50, 54)$ m. Figure 11, taken from Gagarina et al. (2014) taken with permission

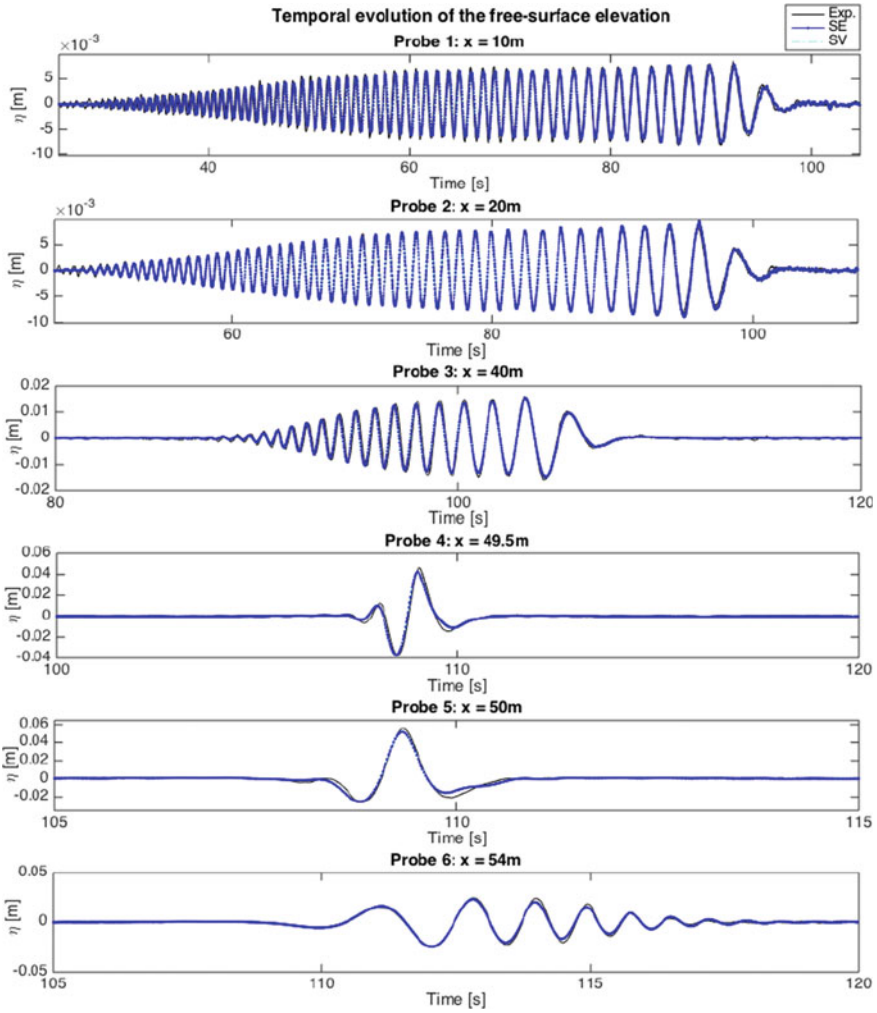

Fig. 5.6 Free surface $h(x,t)$ at various locations x as function of time t for numerical simulations using approach I.B (Symplectic Euler, denoted by SE: solid blue lines; SV: green dashed line) versus six experimental-probe measurements (black solid lines) in MARIN's wave tank at $x = (10, 20, 40, 49.5, 50, 54)$ m as indicated. Figure 3.20 from Gidel (2018) used with permission

of coupled models is the sum of the two variational principles. The first variational principle involved will be Miles' VP but, for simplicity, limited to the case with no variations in δx, and the second variational principle concerns the motion of z, renamed to $\bar{z}$, with the interior motion driven by the free-surface motion.

Rather than imposing the relation between $\{\delta x, \delta z\}$ and δh or $\{\delta X, \delta Z\}$ explicitly, as in the first two numerical approaches summarised above, additional equations for x and z will be imposed using Lagrange multipliers. We illustrate the

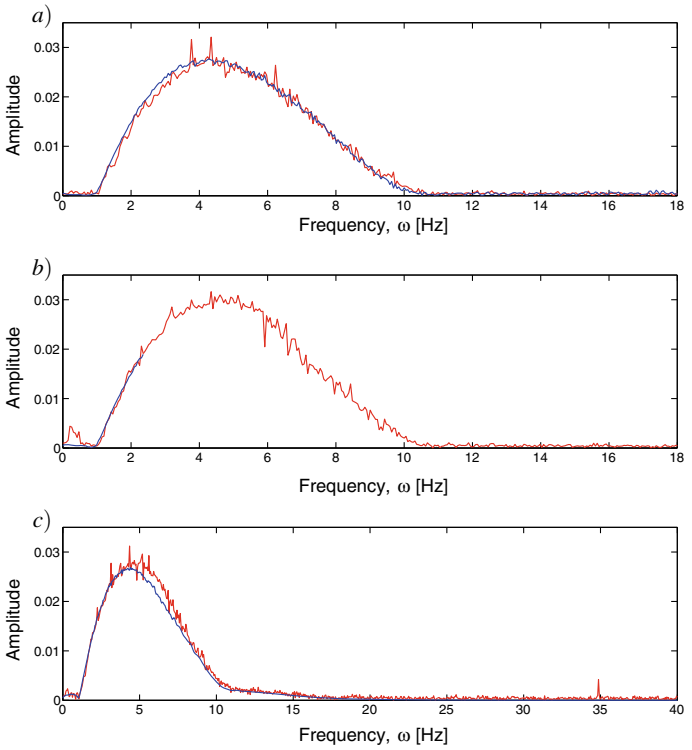

Fig. 5.7 Time spectra at probes 2, 3 and 5 at $x = (20, 40, 50)$ m for simulation approach I.A (blue lines) and the experiments (red lines) displayed as amplitude versus frequency (Fig. 13, from Gagarina et al. (2014), used with permission)

approach for a simplified version of (5.18), i.e., one without wavemaker such that $W(z, t) = 0$, and with $x = \xi$ such that $\delta x = 0$ and $\xi \in [0, L_s]$. One can either impose the constraint solution $z(\xi, \eta, \tau) - \eta Z(\xi, \tau)/H_0 = 0$, cf. (5.20), directly using a Lagrange multiplier $\lambda = \lambda(\xi, \eta, t)$, or one can impose the constraint differential equation $\bar{z}_{\eta\eta} = 0$ with boundary condition $\bar{z}(\xi, 0, \tau) = 0$ by adding additional interior integrals $\frac{1}{2}(\bar{z}_\eta)^2 + \lambda(z - \bar{z})$ and a boundary integral $\lambda_0(Z - z)$, thus indirectly imposing the "Dirichlet" boundary condition $\bar{z}|_{\eta=H_0} = Z$. Consequently, we take $\delta\bar{z}(\xi, 0, \tau) = \delta\bar{z}(\xi, H_0, \tau) = 0$. The latter second-order equation has, of course, the first constraint as solution: i.e., $\bar{z}(\xi, \eta, \tau) = \eta Z(\xi, \tau)/H_0$. In essence what we do, is glueing two different variational principles together, one for the dynamics given in (5.18) and one for the $\bar{z}$–movement i.e. $0 = \delta \int_0^{H_0} \frac{1}{2}(\bar{z}_\eta^2)\, \mathrm{d}\eta$. The approach in Bridges and Donaldson (2011) suggests to impose partial differential equations for z via a Lagrange multiplier λ, but the determination of the boundary conditions for λ has proven cumbersome and was left unresolved. Via the method outlined above, essentially renaming z into $\bar{z}$ before weakly equating them as shown in detail below, we avoid the issues surrounding the definition of boundary conditions for λ because we

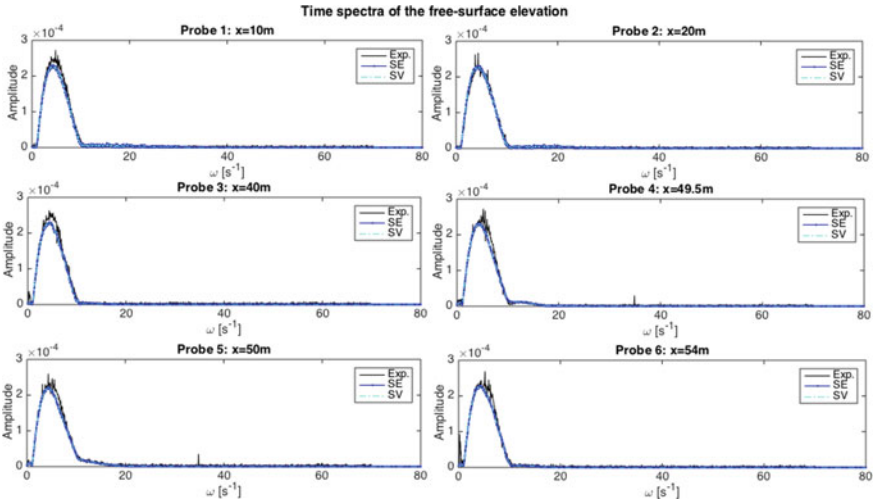

Fig. 5.8 Time spectra at probes 1-to-6 simulation for approach I.A. for the experiments, and simulations with SE and SV, as indicated. After Fig. 3.21 from Gidel (2018), used with permission

impose the (numerical) solution for $\bar{z}$. Before stating the augmented VP, we give a brief example of the idea and why it can work numerically.

Consider the second variational principle in isolation

$$0 = \delta\Big(\int_0^{H_0} \frac{1}{2}(\bar{z}_\eta)^2 + \lambda(z-\bar{z})\,\mathrm{d}\eta + \lambda_0(z-a)|_{\eta=H_0}\Big) \tag{5.21a}$$

$$= \int_0^{H_0} \bar{z}_\eta\delta\bar{z}_\eta - \lambda\delta\bar{z} + (z-\bar{z})\delta\lambda + \lambda\delta z\,\mathrm{d}\eta + \big(\lambda_0\delta z + (z-a)\delta\lambda_0\big)|_{\eta=H_0} \tag{5.21b}$$

$$= \int_0^{H_0} -(\bar{z}_{\eta\eta} + \lambda)\delta\bar{z} + (z-\bar{z})\delta\lambda + \lambda\delta z\,\mathrm{d}\eta + \big(\bar{z}_\eta\delta\bar{z} + \lambda_0\delta z + (z-a)\delta\lambda_0\big)|_{\eta=H_0} - (\bar{z}_\eta\delta\bar{z})|_{\eta=0}, \tag{5.21c}$$

with test function $\delta\bar{z}|_{\eta=0,H_0} = 0$, $\bar{z}(\eta=0) = 0$ and a a constant, yielding

$$\bar{z}_{\eta\eta} + \lambda = 0,\ \lambda = 0,\ z = \bar{z},\ \delta\lambda_0\colon z|_{\eta=H_0} = a,\ \delta z|_{\eta=H_0}\colon \lambda_0 = 0. \tag{5.21d}$$

For illustrative purposes, to discretise (5.21), we use continuous Galerkin finite-element expansions with piecewise linear basis functions $\boldsymbol{w}_i(\eta)$, e.g. $\bar{z} \approx \boldsymbol{w}_i\bar{z}_i$ and $z \approx \boldsymbol{w}_i z_i$ for indices $i,\ j = 1,\ldots,N$, with $i,\ j = 1$ at $\eta = 0$, $i,\ j = N$ at $\eta = H_0$ and $i',\ j' = 2,\ldots,N-1$, while using the Einstein summation convention for repeated indices. The variables and their variations belong to the following function spaces $\delta\bar{z} \in W^1_{0,H_0}$, $\{\bar{z},\delta z, z\} \in W^1_0$ and $\lambda \in W^1$ with W^1 the standard Sobolev space $H^1(\eta \in$

$[0, H_0]$) and with the subscripts on W^1 indicating where the variables belonging to that space are zero. The weak form (5.21b) yields that $\lambda = 0$ and $z = \bar{z}$ and thus is seen to be equivalent to the weak form $\int_0^{H_0} z_\eta \delta z_\eta \, \mathrm{d}\eta = 0$, and its boundary conditions, as intended by design. The finite-element spaces follow by restriction to the space of first-order polynomials on each element (here rods) with C^0–continuity. More explicitly, by direct substitution of the above expansions into the weak formulation (5.21b), and after defining mass and "Laplacian" matrices $M_{ij} = \int \boldsymbol{w}_i(\eta)\boldsymbol{w}_j(\eta)\,\mathrm{d}\eta$ and $A_{ij} = \int \boldsymbol{w}_i'(\eta)\boldsymbol{w}_j'(\eta)\,\mathrm{d}\eta$, we find that

$$\begin{aligned} &A_{i'j}\bar{z}_j - M_{i'j}\lambda_j = 0, \quad M_{ij}\lambda_j = 0 \Longrightarrow M_{i'j}\lambda_j = 0, \\ &M_{ij}(\bar{z}_j - z_j) = 0 \Longrightarrow z_j = \bar{z}_j, \quad \bar{z}_N = a, \end{aligned} \tag{5.22}$$

yielding that $\sum_{j'=2}^{N-1} A_{i'j'}\bar{z}_{j'} = -A_{i'N}a$, which is exactly what a direct continuous Galerkin finite-element discretisation with piecewise linear basis functions of $\bar{z}_{\eta\eta} = 0$ with Dirichlet conditions $\bar{z} = 0$ and $\bar{z} = a$ at $\eta = 0, H_0$ would yield. The example shows that it is required to introduce different variables $\bar{z}$ and z because variations $\delta\bar{z}$ and δz obey different conditions at $\eta = H_0$, but results are what one obtains in a classic FEM.

Similarly, we add the weak formulation of a differential equation for $\bar{z}$, the interior link $\lambda(z - \bar{z})$ and the free-boundary link $\lambda_0(Z - z)$ to the water-wave variational principle with Lagrange multipliers $\lambda(\xi, \eta, \tau)$ and $\lambda_0(\xi, \tau)$. At the free surface, define $\tilde{\phi} \equiv \phi(\xi, H_0, \tau)$. Variations of a simplified yet extended version of (5.18) become

$$\begin{aligned} 0 =& \delta \int_0^T \int_0^{L_s} \Big(-Z_\tau \tilde{\phi} + g(\frac{1}{2}Z^2 - H_0 Z) + \lambda_0(Z - z) \Big)\Big|_{\eta=H_0} \mathrm{d}\xi \\ &+ \int_0^{L_s} \int_0^{H_0} \frac{1}{2}\Big(z_\eta |\partial_\xi \phi|^2 - 2 z_\xi \partial_\xi \phi \partial_\eta \phi + \frac{(1 + z_\xi^2)}{z_\eta} |\partial_\eta \phi|^2 \Big) \\ &\quad + \frac{1}{2}(\bar{z}_\eta)^2 + \lambda(z - \bar{z}) \, \mathrm{d}\xi \, \mathrm{d}\eta \, \mathrm{d}\tau \end{aligned} \tag{5.23a}$$

$$\begin{aligned} =& \int_0^T \int_0^{L_s} \big((\partial_\tau \tilde{\phi} + g(Z - H_0) + \lambda_0)\delta Z - Z_\tau \delta\tilde{\phi} - \lambda_0 \delta z + (Z - z)\delta\lambda_0 \big)\big|_{\eta=H_0} \mathrm{d}\xi \\ &+ \int_0^{L_s} \int_0^{H_0} z_\eta \partial_\xi \phi \partial_\xi \delta\phi - z_\xi (\partial_\xi \phi \partial_\eta \delta\phi + \partial_\eta \phi \partial_\xi \delta\phi) + \frac{(1 + z_\xi^2)}{z_\eta} \partial_\eta \phi \partial_\eta \delta\phi \\ &+ \frac{1}{2}|\partial_\xi \phi|^2 \delta z_\eta - \partial_\xi \phi \partial_\eta \phi \delta z_\xi + \frac{z_\xi \delta z_\xi}{z_\eta} |\partial_\eta \phi|^2 - \frac{1}{2}\frac{(1 + z_\xi^2)\delta z_\eta}{z_\eta^2} |\partial_\eta \phi|^2 \\ &\quad + \bar{z}_\eta \delta\bar{z}_\eta + \lambda(\delta z - \delta\bar{z}) + (z - \bar{z})\delta\lambda \, \mathrm{d}\xi \, \mathrm{d}\eta \, \mathrm{d}\tau \end{aligned} \tag{5.23b}$$

$$
\begin{aligned}
&= \int_0^T \int_0^{L_s} \Big(\big(\partial_t \tilde{\phi} + g(Z - H_0) + \lambda_0\big)\delta Z + (Z - z)|_{\eta=H_0}\delta\lambda_0 \\
&\qquad + \big(\frac{1}{2}|\partial_\xi \phi|^2 - \frac{1}{2}\frac{(1+z_\xi^2)}{z_\eta^2}|\partial_\eta\phi|^2 - \lambda_0\big)|_{\eta=H_0}\delta z \\
&\qquad - \big(Z_\tau + \partial_\xi\phi z_\xi - \frac{(1+z_\xi^2)}{z_\eta}\partial_\eta\phi\big)\delta\phi\Big)\big|_{\eta=H_0}\,\mathrm{d}\xi \\
&+ \int_0^{L_s}\int_0^{H_0} \Big(-\partial_\xi(z_\eta\partial_\xi\phi) + \partial_\xi(z_\xi\partial_\eta\phi) + \partial_\eta(z_\xi\phi\partial_\xi\phi) - \partial_\eta\big(\frac{(1+z_\xi^2)}{z_\eta}\partial_\eta\phi\big)\Big)\delta\phi \\
&\quad + \Big(-\partial_\eta\big(\frac{1}{2}|\partial_\xi\phi|^2\big) + \partial_\xi(\partial_\xi\phi\partial_\eta\phi) - \partial_\xi\big(\frac{z_\xi}{z_\eta}|\partial_\eta\phi|^2\big) \\
&\quad + \partial_\eta\big(\frac{1}{2}\frac{(1+z_\xi^2)}{z_\eta^2}|\partial_\eta\phi|^2\big) + \lambda\Big)\delta z - (\bar{z}_{\eta\eta} + \lambda)\delta\bar{z} + (z - \bar{z})\delta\lambda\,\mathrm{d}\xi\,\mathrm{d}\eta\,\mathrm{d}\tau, \qquad (5.23c)
\end{aligned}
$$

in which we used the end-point conditions $\delta\bar{z}(\xi,\eta,0) = \delta\bar{z}(\xi,\eta,T) = 0$ and $\delta\bar{z}(\xi,0,t) = \delta\bar{z}(\xi,H_0,t) = 0$, and solid-wall boundary conditions at $\xi = 0, L_s$. The resulting equations of motion then follow via (5.23c) from the arbitrariness of the respective variations:

$$\delta Z : \partial_\tau\tilde{\phi} + g(Z - H_0) + \lambda_0 = 0 \quad \text{at} \quad \eta = H_0 \qquad (5.24a)$$

$$\delta z|_{\eta=H_0} : \lambda_0 = \frac{1}{2}|\partial_\xi\phi|^2 - \frac{1}{2}\frac{(1+z_\xi^2)}{z_\eta^2}|\partial_\eta\phi|^2 \quad \text{at} \quad \eta = H_0 \qquad (5.24b)$$

$$\delta\tilde{\phi} : Z_\tau + \partial_\xi\phi z_\xi = \frac{(1+z_\xi^2)}{z_\eta}\partial_\eta\phi \quad \text{at} \quad \eta = H_0 \qquad (5.24c)$$

$$\delta\phi : \partial_\xi(z_\eta\partial_\xi\phi) - \partial_\xi(z_\xi\partial_\eta\phi) - \partial_\eta(z_\xi\partial_\xi\phi) + \partial_\eta\big(\frac{(1+z_\xi^2)}{z_\eta}\partial_\eta\phi\big) = 0 \qquad (5.24d)$$

$$\delta z : \lambda = \partial_\eta\big(\frac{1}{2}|\partial_\xi\phi|^2\big) - \partial_\xi(\partial_\xi\phi\partial_\eta\phi) + \partial_\xi\big(\frac{z_\xi}{z_\eta}|\partial_\eta\phi|^2\big) - \partial_\eta\big(\frac{1}{2}\frac{(1+z_\xi^2)}{z_\eta^2}|\partial_\eta\phi|^2\big) = 0 \qquad (5.24e)$$

$$\delta\bar{z} : \bar{z}_{\eta\eta} + \lambda = 0 \qquad (5.24f)$$

$$\delta\lambda : \bar{z} = z \qquad (5.24g)$$

$$\delta\lambda_0 : z = Z \quad \text{at} \quad \eta = H_0. \qquad (5.24h)$$

Using the elliptic equation (5.24d) for ϕ into (5.24e) one derives, as noted, that $\lambda = 0$. The solution of $\bar{z}_{\eta\eta} = 0$ stated earlier is readily found using $\bar{z}_{\eta=H_0} = Z$ and $\bar{z}(\xi,0,t) = 0$. It is helpful to figure out a consistent time integration by first discretising time for (5.24). We leave that to the reader and instead directly give a complete space-time discretisation.

Time discretisation and weak formulation: To establish a time discretisation and in addition a suitable weak formulation, one starts from the second expression (5.23b), by discretising time using a first-order symplectic Euler scheme. The velocity potential is partitioned as follows: $\phi = \phi_1 + \varphi$ with $\phi_1(\xi, \eta, \tau) = \tilde{\phi}(\xi, \tau)\tilde{\varphi}(\eta)$ such that $\tilde{\varphi}_1(H_0) = 1$, $\tilde{\varphi}_1(0) = 0$ and $\varphi(\xi, H_0, t) = 0$ such that φ is clearly the interior contribution. This partitioning of the velocity potential is similar to the partitioning used in Kristina et al. (2014) for a different variational coupling problem. The function spaces of the variables are the following:

$$\begin{aligned}
&\{\tilde{\phi}(\xi, \tau), Z(\xi, \tau), \lambda_0(\xi, \tau)\} \in W^1(\eta = H_0) \cap X_h^k, \\
&\{\phi_1(\xi, \eta, \tau), \varphi(\xi, \eta, \tau), z(\xi, \eta, \tau), \bar{z}(\xi, \eta, \tau), \lambda(\xi, \eta, \tau)\} \in W^1(\Omega) \cap X_h^k \quad (5.25)
\end{aligned}$$

with $W^1(\Omega)$ the space of test functions and X_h^k the polynomials of order k on each element of a triangulation $\mathcal{T}_h = \{K\}$. This space $W^1(\Omega)$ is the standard Sobolev space H^1 with test function $\boldsymbol{w} \in H^1$, and in the two-dimensional case $||\boldsymbol{w}||_{\eta=c} = 0$ at the appropriate Dirichlet boundary with $c = 0$ or $c = H_0$ and $||\cdot||_{\eta=c}$ is the $L^2(\eta = c)$–norm at $\eta = c$. All functions are C^0–continuous, thus comprising a classical continuous Galerkin finite-element discretisation. *In the implicit, predictor step*, based on all arbitrary variations as test functions, except the one for δZ, the unknowns $Z^{n+1} = z^*|_{\eta=H_0}$, λ_0 and $\bar{z}^*$, z^*, φ^*, λ are jointly determined from

$$\begin{aligned}
0 = \int_0^T \int_0^{L_s} \Big(-\frac{(Z^{n+1} - Z^n)}{\Delta\tau}\delta\phi_1 - \lambda_0\delta z + (Z^{n+1} - z^*)\delta\lambda_0\Big)|_{\eta=H_0}\,\mathrm{d}\xi \\
+ \int_0^{L_s} \int_0^{H_0} z_\eta^*\partial_\xi\phi\partial_\xi\delta\varphi - z_\xi^*(\partial_\xi(\varphi^* + \phi_1^n)\partial_\eta\delta\varphi + \partial_\eta(\varphi^* + \phi_1^n)\partial_\xi\delta\varphi) \\
+ \frac{(1 + (z_\xi^*)^2)}{z_\eta^*}\partial_\eta(\varphi^* + \phi_1^n)\partial_\eta\delta\varphi\,\mathrm{d}\eta\,\mathrm{d}\xi \\
+ \int_0^{L_s} \int_0^{H_0} z_\eta^*\partial_\xi(\varphi^* + \phi_1^n)\partial_\xi\delta\phi_1 - z_\xi^*(\partial_\xi(\varphi^* + \phi_1^n)\partial_\eta\delta\phi + \partial_\eta(\varphi^* + \phi_1^n)\partial_\xi\delta\phi_1) \\
+ \frac{(1 + (z_\xi^*)^2)}{z_\eta^*}\partial_\eta(\varphi^* + \phi_1^n)\partial_\eta\delta\phi_1 \\
+ \frac{1}{2}|\partial_\xi(\varphi^* + \phi_1^n)|^2\delta z_\eta - \partial_\xi(\varphi^* + \phi_1^n)\partial_\eta(\varphi^* + \phi_1^n)\delta z_\xi \\
+ \frac{z_\xi^*\delta z_\xi}{z_\eta^*}|\partial_\eta(\varphi^* + \phi_1^n)|^2 - \frac{1}{2}\frac{(1 + (z_\xi^*)^2)\delta z_\eta}{(z_\eta^*)^2}|\partial_\eta(\varphi^* + \phi_1^n)|^2 \\
+ \bar{z}_\eta^*\delta\bar{z}_\eta + \lambda(\delta z - \delta\bar{z}) + (z^* - \bar{z}^*)\delta\lambda\,\mathrm{d}\xi\,\mathrm{d}\eta\,\mathrm{d}\tau. \quad (5.26a)
\end{aligned}$$

Note that ϕ_1^n is evaluated at the known, current time t^n and that z^*, $\bar{z}^*$, λ, λ_0 and φ^* are all aid variables. The latter highlights that the (discretised) elliptic equation for φ is rephrased as a Poisson problem with $\varphi = 0$ at the free surface rather than phrased as a (discretised) Laplace equation for ϕ. Similarly, $\bar{z}^*$ is solved weakly

via an elliptic equation, with Dirichlet boundary conditions, with the one at the free surface enforced via both Lagrange multipliers λ_0 and λ. *In the corrector step*, based on the arbitrary variations δZ as test functions, $\tilde{\phi}^{n+1}$ (underlined below) is solved using

$$0 = \int_0^T \int_0^{L_s} \left(\left(\frac{(\underline{\tilde{\phi}^{n+1}} - \tilde{\phi}^n)}{\Delta\tau} + g(Z^{n+1} - H_0) + \lambda_0 \right) \delta Z \right) \Big|_{\eta=H_0} \mathrm{d}\xi \, \mathrm{d}\tau, \quad (5.26b)$$

while again using the current value of the free-surface potential, i.e. $\tilde{\varphi}^n$, as well as the updates of variable Z^{N+1}, λ_0 and the aid variables φ^*, λ and z^*, which were all solved in the previous, implicit predictor step. It is clear that the predictor step contains the nonlinearities while the corrector step is linear in the unknowns. The above set-up for the time integration is in essence similar to the one in Gidel (2018) (cf. her expression (3.55)). The extension to mesh motion in two dimensions can proceed along similar lines of reasoning.

5.4 Coupling Water Waves to Shallow-Water Beach Hydraulics

In this section, the second principle stated in the introduction will be explored in a more physically motivated example for a model in which Miles' VP holds in a deep or intermediate water-depth region and a shallow-water model is used in a beach region (in which waves can break), cf. Figs. 5.3 and 5.4. It turns out that in Eulerian coordinates the only VP for shallow-water dynamics is one involving Clebsch variables. In one spatial dimension, shallow-water dynamics involves two fields: the water depth $h = h(x,t)$ and the horizontal velocity $u = u(x,t)$. In two dimensions, it involves three fields $h = h(x,y,t)$, $u = u(x,y,t)$ and an additional lateral velocity field $v = v(x,y,t)$. A description in terms of Clebsch variables involves four fields because the velocity is in that description rewritten as $u = \partial_x\tilde{\phi} + \pi\,\partial_x l$ with parcel label $l = l(x,t)$ and its conjugate $h\pi$ with $\pi = \pi(x,t)$, as well as h and its conjugate $\tilde{\phi}$. These take over the role of q and p in the examples in the introduction. In two spatial dimensions, the derivative $\partial_x(\cdot)$ is replaced by a two-dimensional gradient.

Rather than using Miles' VP, we use an extension of the potential-flow model in Cotter and Bokhove (2010), which contains both the three-dimensional potential-flow limit as well as the (horizontally) two-dimensional, depth-averaged shallow-water limit with surface velocities u and v. Hence, this new model contains the vertical component of the vorticity, $\partial_x v - \partial_y u$, while the other vortical components are, by construction, absent. We will consider a symmetric version of this model with no y–derivatives, except that the label reads $l(x,t) + y$, such that $v(x,t) = \partial_y\phi(x,z,t) + \pi(x,t)\partial_y\,(l(x,t) + y) = \pi(x,t)$. The vorticity then becomes $\partial_x v$.

The VP of the symmetric and coupled systems consists of the sum of the two VPs for the separate systems, with the extended potential-flow motion residing in

$x \in [0, L_c]$ with topography $z = b(x)$, and the shallow-water motion residing in $x \in [L_c, x_w(t)]$ with $x_w = x_w(t)$ the dynamic waterline point on the beach with fixed bottom topography $z = b(x)$. This "coupled VP" in Eulerian coordinates, with now $\phi(x, z, t) = \varphi(x, z, t) + \tilde{\phi}(x, t)$ and $\varphi(x, z = h(x, t), t) = 0$, thus reads

$$
\begin{aligned}
0 = \delta \int_0^T \mathcal{L}[\varphi, \tilde{\phi}, h, l, \pi]\,\mathrm{d}t \equiv \delta \int_0^T \int_0^{L_c} \tilde{\phi}\partial_t h + l\partial_t(h\pi) - \frac{1}{2}\,g(h+b)^2 + ghH_0\,\mathrm{d}x \\
- \int_{b(x)}^{b(x)+h(x,t)} \frac{1}{2}|\nabla\varphi + (u, v, 0)^T|^2\,\mathrm{d}z\,\mathrm{d}x \\
+ \int_{L_c}^{x_w(t)} \tilde{\phi}\partial_t h + l\partial_t(h\pi) - \frac{1}{2}\,h(u^2+v^2) - \frac{1}{2}\,g(h+b)^2 + ghH_0\,\mathrm{d}x\,\mathrm{d}t \qquad (5.27a) \\
= \int_0^T \int_0^{L_c} (\partial_t h + \partial_x(h\bar{u}))\,\delta\tilde{\phi} - (\partial_t\tilde{\phi} + \pi\partial_t l + \frac{1}{2}|\nabla\varphi + \mathbf{u}|^2 + g(h + b - H_0))|_{z=b+h}\delta h \\
- h(\partial_t l + \bar{u}\partial_x l + v)\delta\pi + (\partial_t(h\pi) + \partial_x(h\bar{u}\pi))\,\delta l \\
+ (\partial_x b(\partial_x\varphi + u) - \partial_z\varphi)|_{z=b}\delta\varphi|_{z=b} - \int_{b(x)}^{b(x)+h(x,t)} (\partial_{xx}\varphi + \partial_{zz}\varphi + \partial_x u)\delta\varphi\,\mathrm{d}z\,\mathrm{d}x \\
\underline{- \Big((h\bar{u})(\delta\tilde{\phi} + \pi\delta l)\Big)\,|_{x=L_c^-}} + \underline{\Big((hu)(\delta\tilde{\phi} + \pi\delta l)\Big)\,|_{x=L_c^+}}
\end{aligned}
$$

$$
\begin{aligned}
\underline{- \int_{b(x)}^{b(x)+h(x,t)} (\partial_x\varphi + u)\delta\varphi\,\mathrm{d}z\,|_{x\to L_c^-}} + \int_{L_c}^{x_w} (\partial_t h + \partial_x(hu))\,\delta\tilde{\phi} - (\partial_t\tilde{\phi} + \pi\partial_t l + B)\delta h \\
- h(\partial_t l + u\partial_x l + v)\delta\pi + (\partial_t(h\pi) + \partial_x(hu\pi))\,\delta l\,\mathrm{d}x\,\mathrm{d}t \qquad (5.27b)
\end{aligned}
$$

with $u = \partial_x\tilde{\phi} + \pi\partial_x l$ and $v = \pi$ for $x \in [0, x_w]$, Bernoulli function $B = (u^2 + v^2)/2 + g(h + b - H_0)$, (surface) velocity $\mathbf{u} = \mathbf{u}(x, t) = (u, v, 0)^T$ for $x \in [0, x_w]$, depth-averaged zonal flux $h\bar{u} = \int_{b(x)}^{b(x)+h(x,t)} \partial_x\varphi + u\,\mathrm{d}z$ for $x \in [0, L_c]$, and by using end-point conditions $\delta h(x, 0) = \delta h(x, T) = \delta(h\pi)(x, 0) = \delta(h\pi)(x, T) = 0$ and $h(x_w, t) = 0$ at the moving waterline $x_w(t)$. The resulting equations of motion in terms of the Clebsch variables, following directly from the arbitrariness of variations in (5.27b), are:

$$
\begin{aligned}
\delta\tilde{\phi}:&\ \partial_t h + \partial_x(h\bar{u}) = 0, \\
\delta h:&\ \partial_t\tilde{\phi} + \pi\partial_t l + \frac{1}{2}|\nabla\varphi + \mathbf{u}|^2 + g(h + b - H_0) = 0, \\
\delta\pi:&\ \partial_t l + \bar{u}\partial_x l + v = 0, \\
\delta l:&\ \partial_t(h\pi) + \partial_x(h\bar{u}\pi) = 0, \\
\delta\varphi:&\ \partial_{xx}\varphi + \partial_{zz}\varphi + \partial_x u = 0
\end{aligned} \qquad (5.28)
$$

in deep water for $x \in [0, L_c]$, with no normal flow $\partial_x b(\partial_x \varphi + u) - \partial_z \varphi = 0$ at the bottom $z = b$, and

$$\begin{aligned} \delta\tilde{\phi} : \partial_t h + \partial_x (hu) =& 0, \quad \delta h : \partial_t \tilde{\phi} + \pi \partial_t l + B = 0, \\ \delta\pi : \partial_t l + u\partial_x l + v =& 0, \quad \delta l : \partial_t (h\pi) + \partial_x (hu\pi) = 0 \end{aligned} \tag{5.29}$$

in shallow water for $x \in [L_c, x_w]$. Using the latter equation set and the definitions of u and $v = \pi$, and then by differentiating the Bernoulli equation with respect to x, it is straightforward to verify that the usual (symmetric) momentum equations emerge, i.e., $\partial_t u - v\partial_x v + \partial_x B = 0$ and $\partial_t v + u\partial_x v = 0$. Hence, this is a reduction from the four equations and variables in (5.29) to three equations for three variables. Likewise, the deep-water system (5.28) can be reduced to the variables $\{h, u, v, \varphi\}$, for details see Cotter and Bokhove (2010), Gagarina et al. (2013). The coupling between the two systems is contained in the underlined terms in (5.27), concerning fluxes at $x = L_c$ that need to balance:

$$\begin{aligned} \lim_{x \to L_c^+} (hu)\, \delta\tilde{\phi} &= \lim_{x \to L_c^-} \left(\int_{b(x)}^{b(x)+h(x,t)} (\partial_x \varphi + u) \delta\varphi \, \mathrm{d}z + h\bar{u}\, \delta\tilde{\phi} \right), \\ \lim_{x \to L_c^+} (hu)\pi\, \delta l &= \lim_{x \to L_c^-} h\bar{u}\pi\, \delta l. \end{aligned} \tag{5.30}$$

Coupling between a full, deep-to-intermediate-depth water-wave model to a shallow-water model is only meaningful when the depth-dependence of the full water-wave model has become sufficiently small or negligible. Hence, we assume that at $x = L_c$ the variations are asymptotically close such that

$$\delta l|_{x \to L_c^+} = \delta l|_{x \to L_c^+}, \quad \delta\tilde{\phi}|_{x \to L_c^+} = \frac{1}{h} \int_b^{b+h} \delta\varphi + \delta\tilde{\phi} \, \mathrm{d}z|_{x \to L_c^-}. \tag{5.31}$$

By using (5.31) in (5.30), we find that the deep-water flux is depth-independent

$$\lim_{x \to L_c^-} h(\partial_x \varphi + u) = \lim_{x \to L_c^+} (hu) \quad \text{as well as} \quad \lim_{x \to L_c^+} (hu\pi) = \lim_{x \to L_c^-} (h\bar{u}\pi) \tag{5.32}$$

Vice versa, $\delta\varphi|_{x=L_c^-} = 0$ in (5.30) leads to the shallow-water flux

$$hu|_{x=L_c^+} = h\bar{u}|_{x=L_c^-}. \tag{5.33}$$

These links between subsystems will be considered in the numerical coupling next.

Two different numerical techniques will be used for the two subsystems. The extended potential-flow water-wave model will be discretised using the spatially second-order variational technique established so far (Gidel 2018), while a classical first-order finite-volume method will be used in shallow water, cf. Audusse et al. (2004), Bokhove (2005). This finite-volume method can deal with breaking waves on the beach in the form of classic hydraulic bores (Whitham 1974). The finite-

volume method progresses the mean values of water depth and momentum forward in time on finite elements (or rods in one dimension). Communication between the elements is reached via a numerical flux vector $\mathbf{F}(\mathbf{U}_L, \mathbf{U}_R)$ with $\mathbf{U} \equiv (h, hu, hv)^T$ at each face (or node in one dimension), in which $\mathbf{U}_{L,R}$ are the limits of the mean values to the left and right of each face. At the coupling point $x = L_c$, this numerical flux needs to be determined by defining an appropriate $\mathbf{U}_L$ based on the values of variables in the potential-flow domain at $x = L_c^-$, while in the finite-element potential-flow domain, values from the shallow-water domain, i.e. $\mathbf{U}_R$ at $x = L_c^+$, will be used.

The finite-element weak formulation for the potential-flow is established, as in Sect. 5.3.1, by taking variations without integration by parts in space, while temporarily considering the shallow-water system to be continuous in space. For simplicity, we will set $l = \pi = v = 0$ in $x \in [0, L_c]$ and $\delta l = 0$ at $x = L_c^+$ in the shallow-water domain. The weak formulation we obtain is then as follows

$$
\begin{aligned}
0 = \int_0^T \int_0^{L_c} & \underline{\partial_t h\, \delta\tilde{\phi} + \int_{b(x)}^{b(x)+h(x,t)} (\nabla\varphi + \nabla\tilde{\phi})\, \mathrm{d}z \cdot \nabla\delta\tilde{\phi}} \\
& - \delta h\, \partial_t\tilde{\phi} + (\frac{1}{2}|\nabla\varphi + \tilde{\phi}|^2 + g(h + b - H_0))|_{z=b(x)+h(x,t)}\delta h\, \mathrm{d}x \\
& + \int_{b(x)}^{b(x)+h(x,t)} (\nabla\varphi + \nabla\tilde{\phi}) \cdot \nabla\delta\varphi\, \mathrm{d}z\, \mathrm{d}x + \underline{\left((hu)\delta\tilde{\phi}\right)|_{x=L_c^+}} \\
+ \int_{L_c}^{x_w} & (\partial_t h + \partial_x(hu))\, \delta\tilde{\phi} - (\partial_t\tilde{\phi} + \pi\partial_t l + B)\delta h \\
& - h(\partial_t l + u\partial_x l + v)\delta\pi + (\partial_t(h\pi) + \partial_x(hu\pi))\, \delta l\, \mathrm{d}x\, \mathrm{d}t. \qquad (5.34)
\end{aligned}
$$

Based on the arbitrariness of variations, we can take $\delta h = \delta\varphi = 0$ and $\delta\tilde{\phi} \neq 0$, such that only the underlined terms in (5.34) remain. Coupling to the shallow-water flux $(hu)_{x=L_c+}$ is then established in the continuity equation of the potential-flow model, cf. (5.32). Vice versa, we take $\mathbf{U}_L = \left(h, \int_b^{b+h} \partial_x(\varphi + \tilde{\phi})\, \mathrm{d}z\right)^T|_{x=L_c^-}$ in the numerical flux for the shallow-water model. The well-known HLL-approximation to the Godunov flux is used as the numerical flux $\mathbf{F}(\mathbf{U}_L, \mathbf{U}_R)$ (Bokhove 2005; LeVeque 1990). Briefly, the HLL-flux or Godunov flux uses (an approximation of) the shallow-water characteristics $u \pm \sqrt{gh}$ to establish whether information is (partially) entering or leaving the domain. Hence, providing the limiting values $\mathbf{U}_L|_{x=L_c^-}$ from the potential-flow model does not imply a priori that these values are used. That depends on whether the characteristic $u_L - \sqrt{gh_L} > 0$ is bigger than zero, such that information is estimated to enter the domain, or not, with $h_L u_L = \int_b^{b+h} \partial_x(\varphi + \tilde{\phi})_{x=L_c^-}\, \mathrm{d}z$ and $h_L = h|_{x=L_c^-}$, cf. (5.33). A consistent time discretisation is the partially implicit, first-order symplectic Euler time-stepping scheme, in which the continuity equation will be updated using a scheme implicit in the waterdepth, followed by an explicit step in $\tilde{\phi}$, in which the latter, explicit step the already updated value of h is used. For details, we refer to Gidel (2018) who simplified the timestepping in the shallow-water domain by only taking one explicit iterate of the symplectic Euler scheme into account and with good results. In addition, the dynamic waterline at $x = x_w(t)$ is

discretised using the technique of Audusse et al. (2004), in which the fixed numerical shallow-water domain $x \in [L_c, L]$ is extended to include an essentially dry part of the domain, i.e. for $x \in [x_w(t), L]$ as long as $x_w < L$. Only the potential-flow model is then partially solved in an implicit manner. Numerical results of waves generated by a wavemaker in the deep-water domain and dissipating by wave breaking on the beach will be presented in the next section. For further details on the implementation and numerical results presented next, we refer to Gidel (2018). The derivation of the variational coupling presented here is novel and an integrated version of the ones found in Klaver (2009), Kristina et al. (2014), Gidel (2018), for linear potential flow, a linear Boussinesq model and a nonlinear potential-flow model coupled to nonlinear shallow-water model, respectively. Note that Gidel (2018) contains an extra, stabilising, yet dissipative, coupling term.

5.4.1 Numerical Results: Damping of Waves on the Beach

Two simulations will be shown and interpreted in order to demonstrate the ability of the numerical coupling strategy derived earlier.

A first simulation is shown in Fig. 5.9 for a domain with potential flow in $x \in [0, L_c]$ and a shallow-water model on the beach beyond $x \in [L_c, L]$ with $L_c = 11$ m and $L = 12$ m. The beach starts at $x = 3$ m and a piston wavemaker, oscillating at $x = R(t)$ with a period of $T = 1.339$ s, generates the waves for a finite time. Based on linear dispersion of potential-flow water waves, the expected wave-length is $\lambda \approx 2$ m, as observed in Fig. 5.9. In that figure, a comparison is made between a simulation with a solid wall at $x = L_c$ and one with a transparant two-way boundary with a shallow-water model allowing for energy dissipation in hydraulic bores. In the simulation without wave breaking, standing waves occur due to the wave reflection, while in the simulation with the beach, wave reflection is minimal and nearly only unidirectional wave propagation occurs, towards the beach.

A long-time simulation is analysed next, involving three time intervals with wave generation, wave equilibration and wave damping respectively. The energy balance between the deep-water and shallow-water models as well as the total energy is displayed in Fig. 5.10. The wavemaker is switched on from $t \in [0, 68.03]$ s. The energy increases initially and starts to equilibrate, on average, after wave breaking commences on the beach around $t = 16$ s. Total energy dissipation for short-wave motion rapidly sets in after the wavemaker is switched off. Some long-wave motion remains, unaffacted by energy damping in the hydraulic bores, explaining why some of the energy remains. Due to the dissipative nature of the finite-volume shallow-water numerics, even in the absence of hydraulic bores, energy will eventually dissipate to zero, relative to the potential energy present in the system at rest.

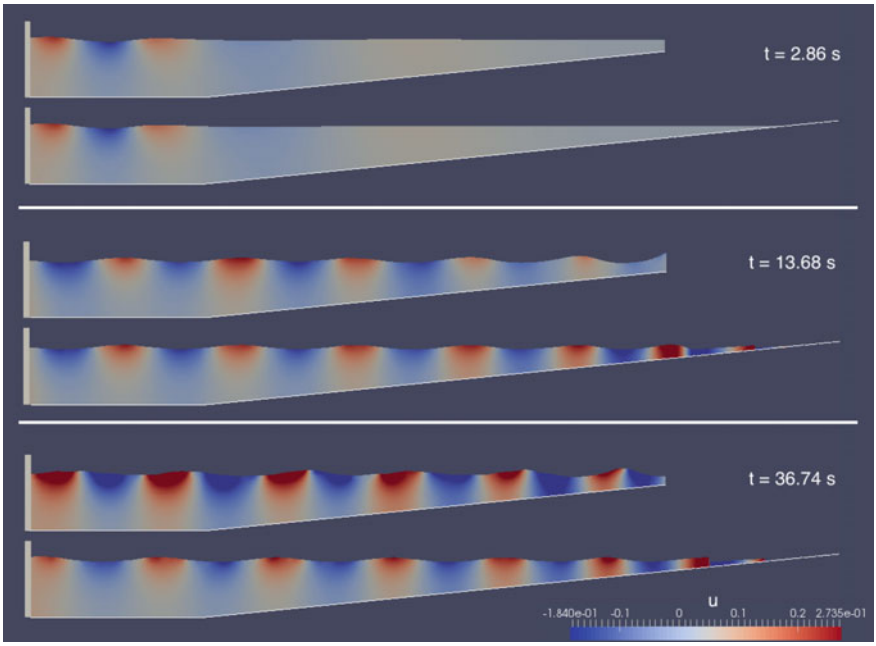

Fig. 5.9 The difference between simulations with a vertical wall at $x = L_c$ (top panel at a given time instance) and a shallow-water model over a beach (bottom panel) where wavebreaking will occur for $x \in [L_c, x_w(t)]$ is shown in three snapshots at $t = (2.86, 13.86, 36.74)$ s. The dynamic domain shape, topography and the free-surface are shown as well as the zonal velocity. At the coupling point, the potential-flow model is observed to be nearly depth-independent, a posteriori justifying the choice of the coupling at $x = L_c$. Figure 4.4 from Gidel (2018) used with permission

5.5 Summary and Conclusions

The central theme of this chapter has been the use of classical variational principles (VPs) for the modelling of water-waves in compatible and geometric numerical modelling of these free-surface waves. Both classical water-wave modelling in a two- or three-dimensional domain with fixed bottom and side walls as well as extensions to problems with wavemakers and coupling to shallow-water beaches with wave breaking have been considered. We started with a derivation of Luke's VP and linked the structure of a pre-Luke VP to the standard structure of a VP in classical mechanics. Subsequently, the domain with its moving free surface was transformed to a fixed reference domain in which the original coordinates become time-dependent variables, essentially describing the continuous form of the mesh motion required in the numerical modelling of water waves. We thus followed the first and third principles stated in the introduction: that the overal dynamics satisfies a VP in the conservative limit and that a space-time discretisation can follow "directly" from a discretisation of this VP for the continuum dynamics. Three types of mesh motion were considered,

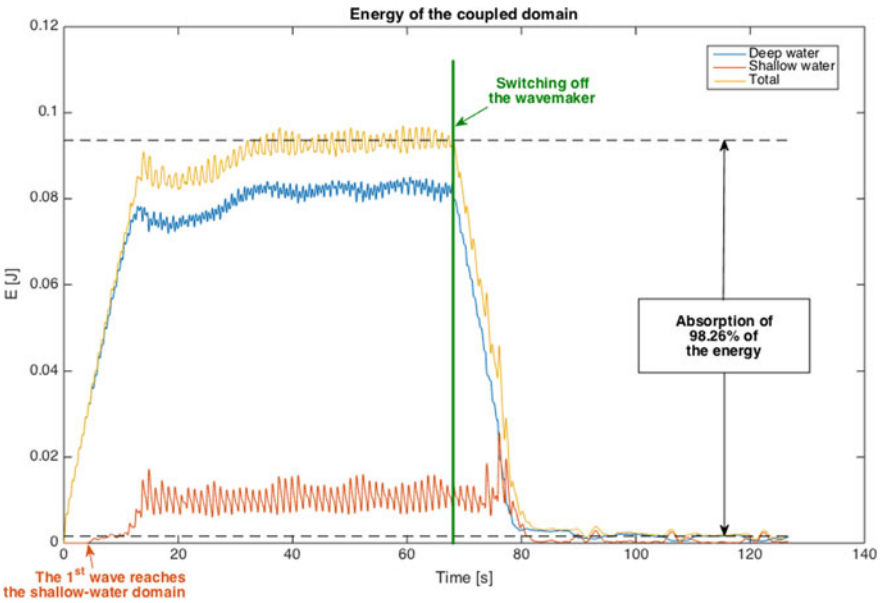

Fig. 5.10 The energy partitioning between the subsystems is considered: the wavemaker operates between $t \in [0, 68.03]$ s after which time it is switched off. The wavemaker initially leads to a (net) energy increase till wavebreaking at the beach starts to dissipate energy and the energy input and energy loss reach a (net) balance around $t = 35$ s. Figure 4.5 from Gidel (2018) used with permission

including a novel version for which we derived a VP coupling water-wave dynamics and mesh motion as the sum of the two separate VPs, cf. the second principle stated in our introduction, stating that coupled systems can be modelled by "straightforwardly" using the sum of the separate VPs. Another example of the second and third principles concerned the coupling and discretisation of VPs for potential-flow water waves in deep-to-intermediate-depth water coupled to breaking-wave dynamics on a shallow-water beach.

In summary, the key reasons to adopt a variational approach have been twofold: first, to ensure the stability, accuracy and speed of numerical discretisations by staying close to the variational structure of the original continuum dynamics and, second, to systematically formulate the dynamics of the coupled systems. We therefore finish by outlining a few future directions in the area of coupled variational fluid-structure systems, for which our variational approach has already shown to be fruitful:

- Variational and numerical coupling of water waves with wave-energy and ship dynamics is undertaken in Kalogirou et al. (2017), Bokhove et al. (2019). Rigid buoys and ships have been considered with translational and rotational degrees of freedom of the solid structures.

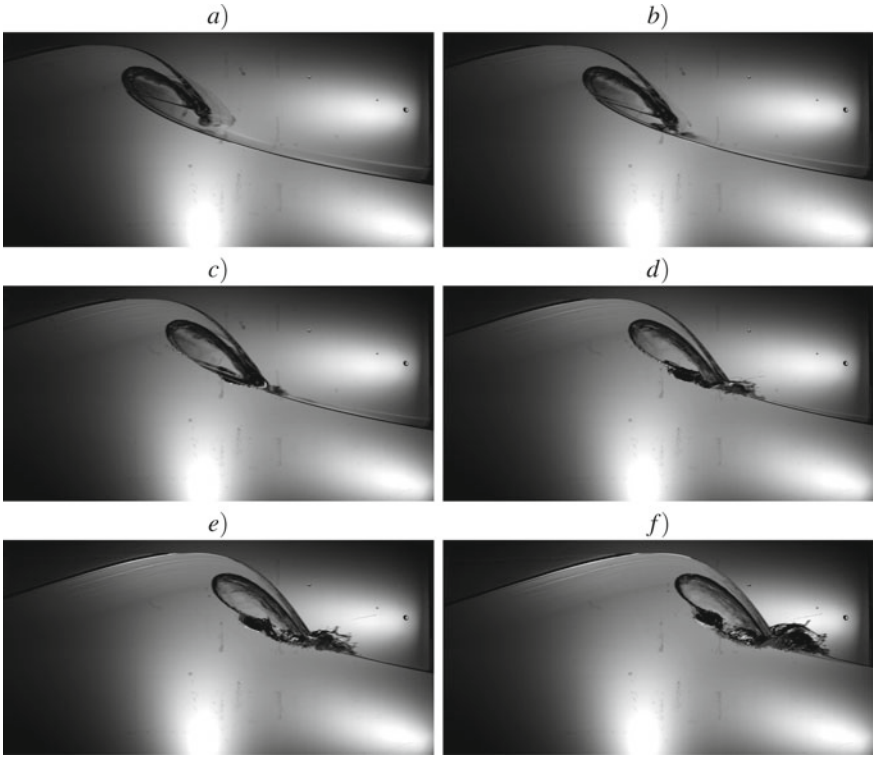

Fig. 5.11 Time sequence of a plunging breaker at (relative) times $t = (0.0, 0.011, 0.022, 0.033, 0.044, 0.055)$ s. Courtesy Olivier Kimmoun, Institut de Recherche sur les Phénomènes Hors Equilibre (IRPHE); images taken during the laboratory tour at IRPHE, at the workshop "Breaking Waves", on June 1st 2018 in Marseille, France

- Water waves have been coupled variationally to a nonlinear elastic beam representing a windturbine mast. Both this nonlinear formulation and stable variational numerics of the linearised problem have been established (Salwa et al. 2017).
- The variationally coupled wave-beach dynamics has been validated in Gidel (2018) and will be analysed further in Gidel et al. (2021). A further challenge is to find a suitable numerical discretisation of the unified potential-flow and shallow-water model derived in Cotter and Bokhove (2010), Gagarina et al. (2013), because the coupling point $x = L_c$ chosen a priori in Sect. 5.4, between breaking and nonbreaking waves, is intrinsically defined in this unified model.
- Wave slamming by breaking waves is an active topic of research but requires the introduction of dissipative effects in the wave breaking. Plunging breakers lead to changes in domain topology with droplets and bubbles, as seen in Fig. 5.11. Mixed variational and dissipative approaches have been explored, using models with (pseudo-)compressible effects, see, e.g. Salwa (2018).

Acknowledgements It is a pleasure to acknowledge Colin Cotter, Elena Gagarina and Anna Kalogirou for discussing and proofreading this chapter as well as the peacefulness of the ebbing and flooding tides at Hole's Hole in Devon. A special thank you goes to Floriane Gidel, Olivier Kimmoun and Wout Zweers for the use of their images. Funding by EU/EID project *Eagre: high-seas wave-impact modelling*, GA859983, is acknowledged.

Appendix 1: Variations in Pre-Luke's VP

While analysing the variations in (5.6), note furthermore that

$$\int_0^T \int_{\Omega_H} \int_0^h D\partial_t \delta\phi \,\mathrm{d}z\,\mathrm{d}x\,\mathrm{d}y\,\mathrm{d}t = \int_0^T \int_{\Omega_H} \int_0^h -\delta\phi\partial_t D + \partial_t(D\delta\phi)\,\mathrm{d}z\,\mathrm{d}x\,\mathrm{d}y\,\mathrm{d}t \tag{5.35a}$$

$$= -\int_0^T \int_{\Omega_H} \int_0^h \delta\phi\partial_t D\,\mathrm{d}z\,\mathrm{d}x\,\mathrm{d}y\,\mathrm{d}t + \int_0^T \frac{\mathrm{d}}{\mathrm{d}t} \int_{\Omega_h} \int_0^h D\delta\phi\,\mathrm{d}z\,\mathrm{d}x\,\mathrm{d}y\,\mathrm{d}t$$
$$- \int_0^T \int_{\Omega_H} D\partial_t h\delta\phi\,\mathrm{d}x\,\mathrm{d}y\,\mathrm{d}t \tag{5.35b}$$

$$= -\int_0^T \int_{\Omega_H} \int_0^h \delta\phi\partial_t D\,\mathrm{d}z\,\mathrm{d}x\,\mathrm{d}y\,\mathrm{d}t - \int_0^T \int_{\Omega_H} D\partial_t h\delta\phi\,\mathrm{d}x\,\mathrm{d}y\,\mathrm{d}t, \tag{5.35c}$$

in which the volumetric contribution at $t = 0$ and $t = T$ cancels, since $\delta\phi(x, y, z, 0) = \delta\phi(x, y, z, T) = 0$, and by assuming for the moment that Ω_h is time-independent. If Ω_h is time-dependent, for example in the presence of a wavemaker, then an extra term will emerge.

References

Ablowitz, M.J. and C.W. Curtis. 2013. Conservation laws and web–solutions for the Benney–Luke equation. *Proceedings of the Royal Society A: Mathematical, Physical and Engineering Sciences* 469(2152).

Audusse, E., F. Bouchut, M.O. Bristeau, R. Klein, and B. Perthame. 2004. A fast and stable well-balanced scheme with hydrostatic reconstruction for shallow water flows. *SIAM Journal on Scientific Computing* 25: 2050–2065.

Benney, D.J., and J.C. Luke. 1964. On the interactions of permanent waves of finite amplitude. *Journal of Mathematics and Physics* 43: 309–313.

Bokhove, O. 2005. Flooding and drying in discontinuous Galerkin finite-element discretizations of shallow-water equations. Part 1: one dimension. *Journal of Scientific Computing* 22: 47–82.

Bokhove, O., E. Gagarina, W. Zweers and A. Thornton. 2011. Bore Soliton Splash -van spektakel tot oceaangolf? *Nederlands Tijdschrift voor Natuurkunde* 77/12: 446–450 (In Dutch).

Bokhove, O., A.J. van der Horn, D. van der Meer, A.R. Thornton, and W. Zweers. 2014. On wave-driven "shingle" beach dynamics in a table-top Hele-Shaw cell. In *International conference coastal engineering proceedings*, vol. 15.

Bokhove, O and A. Kalogirou. 2016. Variational water wave modelling: from continuum to experiment. In *Lecture notes on the theory of water waves, London mathematical society lecture notes series*, vol. 426, eds. Bridges, Groves and Nicholls, 226–259.

Bokhove, O., A. Kalogirou, and W. Zweers. 2019. From bore-soliton-splash to a new wave-to-wire wave-energy model. *Water Waves* 1: 217–258.

Bridges, T.J., and N.M. Donaldson. 2011. Variational principles for water waves from the viewpoint of a time dependent moving mesh. *Mathematika* 57: 147–173.

Bunnik, T.H.J. 2010. Benchmark workshop on numerical wave modelling—description of test cases. Technical Report 70022-1-RD.

Cotter, C., and O. Bokhove. 2010. Water wave model with accurate dispersion and vertical vorticity. *Peregrine Commemorative Issue. Journal of Engineering Mathematics* 67: 33–54.

Drazin, P.G., and R.S. Johnson. 1989. *Solitons: An Introduction*. Cambridge: Cambridge University Press.

Dysthe, K., H.E. Krogstard, and P. Muller. 2008. Oceanic rogue waves. *Annual Review of Fluid Mechanics* 40: 287–310.

Gagarina, E., J.J.W. van der Vegt, V.R. Ambati and O. Bokhove. 2012. A Hamiltonian Boussinesq model with horizontally sheared currents. In *3rd international symposium on shallow flows*, 10. USA: Iowa City.

van der Gagarina, E.J.J.W., Vegt and O. Bokhove. 2013. Horizontal circulation and jumps in Hamiltonian water wave model. *Nonlinear processes in geophysics* 20: 483–500.

Gagarina, E., V.R. Ambati, J.J.W. van der Vegt, and O. Bokhove. 2014. Variational space-time DGFEM for nonlinear free surface waves. *Journal of Computational Physics* 275: 459–483.

Gagarina, E., V.R. Ambati, S. Nurijanyan, J.J.W. van der Vegt, and O. Bokhove. 2016. On variational and symplectic time integrators for Hamiltonian systems. *Journal of Computational Physics* 306: 370–389.

Gidel, F., O. Bokhove, and A. Kalogirou. 2017. Variational modelling of extreme waves through oblique interaction of solitary waves: application to Mach reflection. *Nonlinear Processes in Geophysics* 24: 43–60.

Gidel, F. 2018. *Variational water-wave models and pyramidal freak waves*. Ph.D. Thesis, University of Leeds.

Gidel, F., O. Bokhove T. Bunnik, G. Kapsenberg and M. Kelmanson. 2021. Experimental validation of variationally and numerically coupled wave-beach dynamics. In Preparation, based on Chapter 5 of Gidel [2018].

Kadomtsev, B.B., and V.I. Petviashvili. 1970. On the stability of solitary waves in weakly dispersive media. *Soviet Physics Doklad* 15: 539–541.

Kalogirou, A., O. Bokhove and D. Ham. 2017. Modelling of nonlinear wave-buoy dynamics using constrained variational methods. In *34th International Conference on Ocean, Offshore and Arctic Engineering–OMAE*.

Klaver, F. 2009. Coupling of numerical models for deep and shallow water. MSc Thesis. University of Twente, Netherlands. Supervisors: V.R. Ambati and O. Bokhove.

Kristina, W.O., Bokhove and E.W.C. van Groesen. 2014. Effective coastal boundary conditions for tsunami wave run-up over sloping bathymetry. *Nonlinear Processes in Geophysics* 21: 987–1005.

Kodama, Y. 2010. KP solitons in shallow water. *Journal of Physics A: Mathematical and Theoretical* 43: 434004.

Lanczos, C. 1970. *The variational principles of mechanics*. New York: Dover Publications.

Leimkühler, B., and S. Reich. 2009. *Simulating hamiltonian dynamics*. Cambridge: Cambridge University Press.

LeVeque, R.L. 1990. *Numerical methods for conservation laws*, Lectures in Mathematics. Birkhäuser.

Luke, J.C. 1967. A variational principle for a fluid with a free surface. *Journal of Fluid Mechanics* 27: 395–397.

Miles, J.W. 1977. On Hamilton's principle for surface waves. *Journal of Fluid Mechanics* 83: 153–158.

Rathgeber, F., D.A. Ham, L. Mitchell, M. Lange, F. Luporini, A.T.T. McRae, G. Bercea, G.R. Markall, and P.H.J. Kelly. 2016. Firedrake: automating the finite element method by composing abstractions. *ACM TOMS Transactions on Mathematical Software* 43: 1–27.

Marsden, J.E., and T.S. Ratiu. 1994. *Introduction to mechanics and symmetry*. Berlin: Springer.

Nikolkina, I., and I. Didenkulova. 2011. Rogue waves in 2006–2010. *Natural Hazards and Earth System Sciences* 11: 2913–2924.

Salwa, T.O., Bokhove and M. Kelmanson. 2017. Variational modelling of wave-structure interactions with an offshore wind-turbine mast. *Journal of Engineering Mathematics* 107: 61–85.

Salwa, T. 2018. *On variational modelling of wave slamming by water waves*. Ph.D. thesis. http://etheses.whiterose.ac.uk/23778/

Thornton, A.R., A.J. van der Horn, E. Gagarina, D. van der Meer, W. Zweers, and O. Bokhove. 2014. Hele-Shaw beach creation by breaking waves. *Environmental Fluid Dynamics* 14: 1123–1145.

Whitham, G.B. 1974. *Linear and nonlinear waves*. Wiley-Interscience.

Zakharov, V.E. 1968. Stability of periodic waves of finite amplitude on the surface of a deep fluid. *Journal of Applied Mechanics and Technical Physics* 9: 190–194.

Chapter 6
Quasi-2D Turbulence in Shallow Fluid Layers

Herman J. H. Clercx

Abstract Flows in thin fluid layers, like in the Earth's atmosphere or oceans, tend to behave as quasi-two-dimensional flows. Their dynamics is strikingly different from three-dimensional flows, and main features of the flow dynamics can be understood by considering two-dimensional (2D) fluid flows. Inviscid 2D flows are governed by conservation of vorticity due to absence of vortex stretching and tilting. Together with conservation of kinetic energy this results in the famous inverse energy cascade and the emergence and persistence of large-scale vortices. This also occurs in shallow fluid-layer flows even if they are neither purely inviscid nor perfectly two-dimensional. Basic phenomena for understanding the dynamics of 2D flows will be discussed and 2D flows on bounded domains, mainly dealing with the large-scale phenomenology of the flow, will be addressed: the self-organization of 2D turbulence in confined domains and the interaction of coherent structures with domain walls. This will be complemented with some observations from recent experiments on quasi-2D turbulence in shallow-fluid layers including the role and impact of bottom friction and out-of-plane motion on the flow evolution.

6.1 Introduction

Large-scale geophysical flows in the oceans and in the atmosphere basically consist of a relatively thin fluid layer (with typical thickness $\mathcal{H}$) with a large horizontal extent, where we denote the horizontal length scale with $\mathcal{L} \gg \mathcal{H}$. Flow phenomena on horizontal scales much larger than the thickness of the fluid layer (typically a few kilometers deep in the oceans or 10 km high in the atmosphere) behave predominantly as two-dimensional (2D) flows. The common justification is that a small vertical

H. J. H. Clercx (✉)
Fluid Dynamics Laboratory, Department of Applied Physics, Eindhoven University of Technology, P.O. Box 513, 5600 Eindhoven, MB, The Netherlands
e-mail: h.j.h.clercx@tue.nl

H. Schuttelaars et al. (eds.), *The Mathematics of Marine Modelling*,
Mathematics of Planet Earth 9, https://doi.org/10.1007/978-3-031-09559-7_6

length scale implies small characteristic vertical velocities due to mass conservation. In shallow coastal seas, estuaries or shallow lakes with depths in the range of 10–100 m and horizontal extents of tens or hundreds of kilometers one can assume, based on similar arguments as above, quasi-2D behaviour of large-scale flows. Even on the level of riverine flows, aspects of the dynamics of large-scale eddies can be analysed invoking two-dimensionality, see Uijttewaal (2014) for a recent overview. Besides the aspect ratio of vertical and horizontal length scales some other mechanisms may contribute to the process of two-dimensionalization of the flow. It is known that background rotation promotes two-dimensionality which is nicely illustrated by the Taylor-Proudman theorem (Proudman 1916; Taylor 1917). This theorem basically states that for steady inviscid rapidly rotating flows the fluid velocity will not change in the direction parallel to the background rotation. In the oceans the rotation of the Earth will contribute to two-dimensionalization of large-scale flows with characteristic horizontal length scales larger than about 100 km at low latitudes, gradually decreasing to about 20 km at high latitudes, and in the atmosphere for flow scales with a horizontal extent larger than typically 1000 km. In shallow coastal seas, estuarine flows or lakes a stable density stratification (by salinity or temperature effects or a combination of them) suppresses vertical motion as that would enhance potential energy content of the flow. Such flows have also a tendency to move predominantly in the horizontal plane, thus contributing to quasi-two-dimensionality of the flow. Note, however, that the type of two-dimensional flow is different depending on the mechanism enforcing it: shallow and stratified flows tend to be flat because of the constraints in the vertical while background rotation forms tall vertically-invariant columnar structures. This leads to competing effects when combining rotation with either shallowness or stratification; see, for example, Liechtenstein et al. (2005), Duran-Matute et al. (2012).

Also the presence of domain boundaries might be important. Consider, for example, closed or semi-closed basins such as the Gulf of California, the Gulf of Aden, or in the Mediterranean the Adriatic or Tyrrhenian Sea. They reveal the existence of arrays of vortical structures. A nice illustration of the flow in the Gulf of Aden, visualized by phytoplankton blooms, is shown in Fig. 6.1. We can indeed observe relatively large flow structures, including vortices with size almost the same as the width of the Gulf of Aden. Similar patterns have been observed for the Adriatic Sea, as reported by Falco et al. (2000), and for the Tyrrhenian Sea a few years earlier by Buffoni et al. (1997). The energy to drive such vortical flows is mostly supplied by the wind. Of course, one will never observe a perfect array of vortices as the wind varies, the coastal boundaries are irregular and the bottom topography affects the flow. Nevertheless, the basic flow phenomena, including the formation of arrays of domain-sized vortices is inherently related to the self-organization of 2D turbulent flows in confined (rectangular) geometries. Moreover, such arrays of vortices interact with domain boundaries, or are perturbed otherwise, inducing unsteady wiggling of these vortices. Such processes can lead to efficient transport and mixing of passive tracers (such as nutrients or salt) or inertial particles.

The quasi-two-dimensionality of many geophysical and environmental flows inspired research on the behaviour of 2D flows, including vortex dynamics and 2D

Fig. 6.1 A winter plankton bloom in the Gulf of Aden. In the image the swirling motion of the phytoplankton bloom in the basin-wide vortical structures is clearly visible. The image is composed of data acquired on February 12, 2018, by the MODIS on the Aqua Satellite of NASA. Credit NASA image by Norman Kuring, NASAś Ocean Biology Processing Group. Photograph courtesy of Joaquim Goes, Lamont Doherty Earth Observatory

turbulence. A few examples of studies motivated by environmental flows include turbulent wakes, large-scale flow structures and mixing processes in shallow flows (Chen and Jirka 1995; Uijttewaal and Booij 2000; Jirka 2001), grid-generated turbulence in a shallow fluid layer by Uijttewaal and Jirka (2003), and the dynamical behavior of monopolar and dipolar vortices in such shallow turbulent flows, see Lin et al. (2003), Sous et al. (2004), Sous et al. (2005). It has also motivated studies of the mechanisms promoting two-dimensionality by, for example, background rotation or density stratification. Regarding the fundamental aspects of (2D) turbulence, the reduction of dimensionality already attracted a lot of attention from a wide variety of scientists. These investigations have been of theoretical and numerical character, where two-dimensionality facilitates analysis and computations significantly by exploiting the reduction of dimensionality (2D instead of 3D computations, for some recent reviews with regard to numerical studies, see Clercx and Van Heijst (2009), Boffetta and Ecke (2012)), but also laboratory experiments turned out to be extremely worthwhile as such flows are easily accessible for flow diagnostics. The dynamics of vortices can be studied in rotating or density-stratified fluids, see the review by Van Heijst and Clercx (2009), and 2D turbulence can be studied experimentally in density stratified fluids, in shallow fluid layer experiments or in soap film experiments, see Danilov and Gurarie (2000), Tabeling (2002), Kellay and Goldburg (2002), Van Heijst et al. (2006), Van Heijst and Clercx (2009), Clercx and Van Heijst (2009).

In this chapter the focus will be on the large-scale flow phenomenology. It will start with a brief overview of the basic mechanisms in unbounded 2D turbulence in

Sect. 6.2 and the role of confinement on the dynamics of 2D turbulence in Sect. 6.3. In Sect. 6.4, the main features of the interaction of 2D vortex structures with (no-slip) walls will be discussed. In order to make a connection once again to shallow flows, 2D turbulence experiments in shallow fluids will briefly be reviewed in Sect. 6.5. We conclude with a brief summary of the most important observations in Sect. 6.6.

6.2 Two-Dimensional Turbulence

One of the most striking phenomena of 2D turbulence is the self-organization of the flow. This is clearly visualized in both laboratory experiments in rotating fluids, see Colin de Verdière (1980), Hopfinger et al. (1982), and in stratified fluids, see Boubnov et al. (1994), Yap and Van Atta (1993), Fincham et al. (1996), Maassen et al. (1999), Maassen et al. (2002). It has also been observed in shallow fluid layer and soap film experiments, see Couder (1984), Sommeria (1986), Tabeling et al. (1991), Kellay et al. (1995), Rutgers (1998), Rivera and Ecke (2005, 2016), and Akkermans et al. (2008a), and in many direct numerical simulations of either freely-evolving or forced 2D turbulence. Examples are the studies by McWilliams (1984), Legras et al. (1988), Santangelo et al. (1989), and Boffetta (2007). In the remaining part of this section some of the essential ingredients to understand the dynamics of 2D turbulence will be introduced.

6.2.1 Inertial Ranges in 2D Turbulence

One of the most striking differences between 2D and 3D turbulence concerns the weakly dissipative and self-organizing character of 2D turbulent flow compared to the highly dissipative character of 3D turbulence. Consider, for example, a simulation of freely-evolving 2D turbulence, where the flow field is initialized with a random vorticity field; see McWilliams (1984). This initial vorticity field does not contain any coherent vortex structures. During the evolution of the flow field from this initial vorticity distribution, large and approximately axisymmetric vorticity patches emerge as a result of subsequent vortex mergers. The typical lifetime of these vortices turns out to be long compared with the typical flow advection time scale. This self-organization process basically consists of transfer of kinetic energy from the smaller scales of the flow towards larger scales (merging of like-signed vortices) together with vorticity transport to the smaller scales. One can recognize the latter process as the elongation of vorticity filaments in between larger coherent structures. More recently, taking advantage of the increase in computing capabilities, (Boffetta 2007) illustrated this process with an extreme high-resolution simulation of forced 2D turbulence: the flow was forced at some intermediate length scale, and the kinetic energy supplied at the forcing length scale was transported almost completely to the larger and even domain-size scales (a process known as the inverse energy cascade).

Simultaneously, the enstrophy was transported downscale, in what we call the direct enstrophy cascade, to the viscous dissipation range. This is in agreement with the observation by McWilliams (1984) and both cascade ranges where already predicted by Kraichnan (1967, 1971).

From a phenomenological point of view the presence of an inverse energy cascade and a direct enstrophy cascade can be illustrated in the following way. The motion of an incompressible fluid with viscosity ν and density ρ in a plane is described by the 2D velocity field $\mathbf{v}(\mathbf{r}, t) = (u, v)$, with u and v its Cartesian components, and $\mathbf{r} = (x, y)$. The velocity field should satisfy conservation of mass,

$$\nabla \cdot \mathbf{v} = \frac{\partial u}{\partial x} + \frac{\partial v}{\partial y} = 0 \,. \tag{6.1}$$

Conservation of momentum is expressed by

$$\frac{\partial \mathbf{v}}{\partial t} + (\mathbf{v} \cdot \nabla)\mathbf{v} = -\frac{1}{\rho}\nabla p + \nu \nabla^2 \mathbf{v}, \tag{6.2}$$

where we assume that the flow is freely decaying (no injection of energy by external forcing). With the vorticity ω defined as $\omega = \frac{\partial v}{\partial x} - \frac{\partial u}{\partial y}$, we can reformulate Eq. (6.2) into the vorticity equation

$$\frac{\partial \omega}{\partial t} + (\mathbf{v} \cdot \nabla)\omega = \nu \nabla^2 \omega. \tag{6.3}$$

Define the kinetic energy E of the 2D flow as

$$E = \frac{1}{2}\int_{\mathcal{D}} |\mathbf{v}|^2 dA = \int E(k) dk, \tag{6.4}$$

with $\mathcal{D}$ the flow domain of interest, dA an infinitesimal area element of $\mathcal{D}$, $E(k)$ the energy spectrum and k the wave number. The enstrophy Ω is defined as

$$\Omega = \frac{1}{2}\int_{\mathcal{D}} \omega^2 dA = \int k^2 E(k) dk. \tag{6.5}$$

For the inviscid regime ($\nu = 0$), the kinetic energy is conserved (no dissipation), and the vorticity of a fluid element is also conserved as the vorticity Eq. (6.3) reduces to $\frac{D\omega}{Dt} = \frac{\partial \omega}{\partial t} + (\mathbf{v} \cdot \nabla)\omega = 0$. The latter conservation law also means that any function of the vorticity should be conserved too, thus also the enstrophy must be conserved for inviscid 2D flows. Suppose initially a Gaussian shape of the energy spectrum $E(k)$ which should broaden in time. However, broadening of the energy spectrum $E(k)$ with satisfying both conservation of energy and enstrophy (see Eqs. (6.4) and (6.5)), is only possible when the maximum of the spectrum shifts to lower wave numbers, and energy accumulates in larger-scale structures.

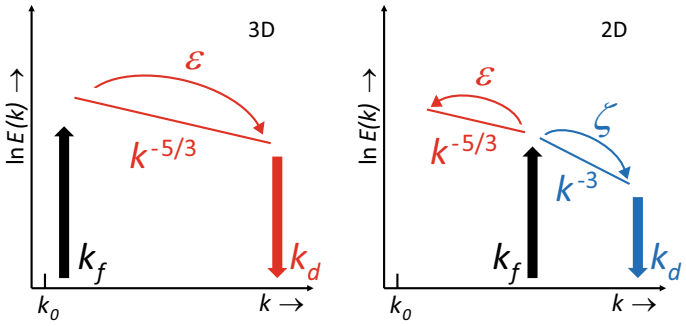

Fig. 6.2 Schematic representation of the inertial ranges in forced 3D turbulence with the direct energy cascade (left), and forced 2D turbulence with both the inverse energy cascade and the direct enstrophy cascade (right). The energy fluxes are denoted by ε (to large wave numbers in 3D and small wave numbers in 2D turbulence) and the enstrophy flux is denoted by ζ (to large wave numbers). The forcing wave number k_f is at the largest scales for the 3D case, but at intermediate scales for 2D turbulence; k_d denotes the dissipation wave number

The processes described above are in strong contrast with our experience with cascade processes in homogeneous and isotropic 3D turbulence. In 3D flows, processes like vortex stretching and tilting are present, playing a crucial role in the transfer of kinetic energy from large to small scales in the flow. In 2D flows, these two mechanisms are absent as the vorticity vector is always perpendicular to the plane of flow. In the 3D case, kinetic energy injected at a certain scale (mostly at large scales) is thus transported downscale via the inertial range to the smallest (Kolmogorov) scales where kinetic energy is dissipated.

Summarizing, in 2D turbulence kinetic energy is transported to and collected at the large scales of the flow, the coherent vortex structures. Onsager (1949), Fjørtoft (1953) already predicted on theoretical grounds the emergence of large-scale coherent vortices in 2D flows. In 3D turbulence kinetic energy is transported downscale and is being dissipated, see a schematic sketch of these processes in Fig. 6.2. This difference is responsible for many exciting, and at first sight, somewhat counter-intuitive phenomena that can be observed in large-scale quasi-2D flows.

6.2.2 2D Turbulence: The Early Years

Systematic investigations of homogeneous and isotropic 2D turbulence from a theoretical point of view, and also the first numerical attempts to simulate 2D turbulence, started some 50 years ago by Kraichnan (1967), Leith (1968), and Batchelor (1969). Kraichnan (1967) in his seminal contribution introduced a formal derivation of the scaling of the energy spectrum $E(k)$. He assumed conservation of energy and enstrophy only (in the inviscid limit), and based on that, he proposed for 2D forced turbulence the existence of a dual cascade which are known as the inverse

energy cascade and the direct enstrophy cascade. For the inverse energy cascade, assuming constant energy flux and no enstrophy flux, he found in the inertial range $E(k) \sim \varepsilon^{2/3} k^{-5/3}$. Here, ε is the constant rate of cascade of kinetic energy per unit mass and the expression is valid for $k_L \ll k \ll k_f$ with k_f the wave number at which forcing takes place (injection of energy) and k_L a representative wave number for the large-scale coherent structures. The proposed scaling looks very similar to the Kolmogorov scaling of the energy spectrum in the inertial range of 3D turbulence, but one should realize that the flux in the 3D case is in opposite direction, towards the small dissipative scales. For the inertial range of the direct enstrophy cascade, assuming a constant enstrophy flux and absence of an energy flux, he found a scaling of the spectrum according to $E(k) \sim \zeta^{2/3} k^{-3}$. In this case, ζ is the constant rate of cascade of mean-square vorticity, and the expression is valid for $k_f \ll k \ll k_\zeta$ with k_ζ the enstrophy dissipation scale. See Kraichnan (1971) for a discussion of a logarithmic correction to the energy spectrum in the direct enstrophy cascade range. Numerical simulations of forced 2D turbulence have been carried out since the prediction of the dual cascade, many providing supporting evidence for the dual cascade. As already mentioned before, the extreme high-resolution simulation by Boffetta (2007) has shown convincingly the existence of the dual cascade.

The analysis by Kraichnan (1967) concerned forced 2D turbulence. A few years after Kraichnan's contribution it was (Lilly 1971) who addressed 2D decaying (or freely-developing) turbulence with numerical simulations. One of his motivations was to confirm Kraichnan-Leith-Batchelor (KLB) theory, but also to test Batchelor's results on the time-dependent behavior of the kinetic energy $E(t)$, enstrophy $\Omega(t)$ and the palinstrophy $P(t) = \frac{1}{2} \int_{\mathcal{D}} |\nabla \omega|^2 dA \geq 0$ for decaying flows. From the Navier-Stokes equation for flows with finite viscosity ν one can rather straighforwardly derive the following relations, valid for freely-evolving flows on an unbounded or on a periodic domain:

$$\frac{dE(t)}{dt} = -2\nu\Omega(t) \quad \text{and} \quad \frac{d\Omega(t)}{dt} = -2\nu P(t). \tag{6.6}$$

Since the enstrophy and palinstrophy should always be positive (or zero), we can directly conclude that both the energy $E(t)$ and the enstrophy $\Omega(t)$ should decrease in course of time for decaying 2D turbulence. We can also conjecture that the enstrophy is always bounded by its initial value as $P(t) \geq 0$. In a natural way we then see that $\frac{dE(t)}{dt} \to 0$ for $\nu \to 0$. The study by Lilly (1971) indeed confirmed a few results from KLB theory, such as the k^{-3} scaling of the direct enstrophy cascade and the following asymptotic decay relations for $t \to \infty$ predicted by Batchelor (1969): $E(t) \propto t^{-1}$, $\Omega(t) \propto t^{-2}$, and $P(t) \propto t^{-3}$. However, many numerical studies employing higher resolutions gave deeper insights into both the scaling of the direct enstrophy cascade as the time behavior of energy, enstrophy, and palinstrophy. First of all, in the 1980s quite some evidence emerged about the presence of quite persistent weakly dissipative coherent vortices and the existence of a kind of quasi-steady equilibrium states, see, for example, Fornberg (1977), Matthaeus and Montgomery (1980) and Basdevant et al. (1981), and the already mentioned study

by McWilliams (1984). It was observed that the direct enstrophy cascade occurs as a transient state and often the spectrum steepened considerably, typically showing a k^{-5} scaling behavior (McWilliams 1984; Santangelo et al. 1989). Also a very-high resolution (4096^2 grid points) simulation of decaying 2D turbulence by Bracco et al. (2000) revealed a spectrum with a slope steeper than k^{-3}. Prime suspect of this behavior are the weakly dissipative coherent structures emerging during the decay process (destroying scale invariance); see Santangelo et al. (1989).

6.2.3 Coherent Structures and 2D Turbulence

Keeping the observations with regard to the scaling of the energy spectrum in the enstrophy cascade, and its possible cause, in mind several attempts have been undertaken to analyse theoretically and numerically the temporal evolution of the hierarchy of coherent vortices in such 2D decaying turbulent flows (Carnevale et al. 1991, 1992; Weiss and McWilliams 1993). In the scaling theory proposed by Carnevale et al. (1991), Carnevale et al. (1992) the time evolution of a few quantities have been derived. The vortex density $\rho(t) \propto t^{-\chi}$, the average vortex radius $r(t) \propto t^{-\chi/4}$, the average vortex separation $d(t) \propto t^{-\chi/2}$ and the average enstrophy $\Omega(t) \propto t^{-\chi/2}$, with χ undetermined. With numerical simulations the value $\chi \sim 0.72 - 0.75$ has been found, see Carnevale et al. (1992) and Weiss and McWilliams (1993). With this value it turns out that $\Omega(t) \propto t^{-0.36}$ and $\rho(t) \propto t^{-0.72}$. These scaling relations are remarkably different compared to the predictions by Batchelor (1969) who obtained: $\Omega(t) \propto t^{-2}$ and $\rho(t) \propto t^{-2}$. The high-resolution simulation by Bracco et al. (2000) confirmed the scaling relation for the enstrophy as predicted by the approach of Carnevale and coworkers. They actually found the same exponent for the long-time behavior of the enstropy: $\Omega(t) \propto t^{-0.36}$. In recent decades many more detailed studies have been reported, see Clercx and Van Heijst (2009) for an overview and references.

From this overview it seems quite evident that the presence of coherent structures in decaying 2D turbulence modifies the KLB-picture. In particular, scaling theories for the vortex population do not support the scaling theory put forward by Batchelor (1969) and the prediction of the scaling of the direct enstrophy cascade in decaying 2D turbulence (in contrast to forced 2D turbulence) is not always confirmed by numerical studies. A final issue concerns the so-called quasi-equilibrium final states. The sea of small-scale vortices will eventually evolve towards a final state by continuous merging processes, see Matthaeus and Montgomery (1980) and McWilliams (1984). Several studies with very-long time integrations have shown that eventually one large-scale dipolar quasi-equilibrium state will emerge (for decaying 2D Navier-Stokes turbulence on a square periodic domain), see Matthaeus et al. (1991).

6.3 2D Turbulence in Square, Rectangular and Circular Domains

Three-dimensional homogeneous and isotropic turbulence is an extremely valuable concept for studies of more general 3D turbulent flows. Although homogeneity and isotropy can be broken by the presence of the boundaries or by the forcing, they are quickly restored when going to smaller length scales. It is this assumption that underlies the Kolmogorov scaling of the energy spectrum in the inertial range. This means that for many fundamental studies, for example on turbulent mixing and inertial particle dispersion on length scales compatible with the inertial range, it may be sufficient to consider the relatively clean case of homogeneous and isotropic 3D turbulence. With the presence of an inverse energy cascade in 2D turbulence, without an energy sink at scales smaller than the domain size, energy is fed into the largest accessible scale. This implies direct interaction of energy-rich eddies with the domain walls, and in the case of no-slip boundary conditions these walls serve as a source of vorticity, even in the freely evolving case (without forcing). This is in strong contrast with 2D freely evolving unbounded (homogeneous and isotropic) turbulence. In that case the enstrophy is necessarily bounded by its initial value, see Batchelor (1969), and no vorticity sources are present.

One of the most striking differences between freely decaying 2D turbulence on a periodic domain and a similar decay process on a 2D confined domain is the shape of the quasi-steady final state. As already mentioned, this quasi-stationary final state on a periodic domain is basically a dipolar vortex, a structure with a patch of positive and a patch of negative vorticity (although under certain conditions exceptions may occur but are quite exceptional). For a square domain with walls, either free-slip (in case of inviscid flows), no-slip or stress-free (the latter two for flows with viscous effects included; the stress-free case will not be discussed here), the quasi-steady final state is different and are generally not a dipolar structure. A variety of statistical-mechanical approaches have been used for the analysis of final states of inviscid flows on confined domains; see Montgomery and Joyce (1974), Pointin and Lundgren (1976), and Chavanis and Sommeria (1996). Typical final states are a monopolar vortex on a square domain (Pointin and Lundgren 1976), a symmetric dipole, an asymmetric dipole or a monopole on a circular domain (depending on the control parameter $\Lambda = \Gamma/\sqrt{2E}$, with Γ the circulation and E the energy; see Chavanis and Sommeria (1996) for details), and a large ellipsoidal or two counter rotating vortices in a rectangular domain with length-to-width ratio of two (with a similar control parameter; see Chavanis and Sommeria (1996)).

6.3.1 Simulations of 2D Turbulence in Domains with No-Slip Walls

From now on, we will consider decaying 2D Navier-Stokes turbulence on confined domains with no-slip walls, which was the natural next step towards flows with realistic boundary conditions and, moreover, experimentally accessible flow configurations (Li and Montgomery 1996; Li et al. 1997; Maassen et al. 1999, 2002, 2003; Clercx et al. 1998, 1999, 2001; Schneider and Farge 2005, 2008; Keetels et al. 2010; Fang and Ouellette 2017).

We first focus on the quasi-steady final states. Here, some care is needed as the final state is always cessation of any flow. However, at an earlier stage during the decay process small-scale features are dissolved due to merging processes and sometimes disappear due to viscous dissipation. At a later stage, one final structure remains and is rather persistent for a very long time. This is what we call the quasi-steady final state. Some observations from both laboratory experiments of decaying quasi-2D turbulence in stratified fluids (Maassen et al. 1999, 2002, 2003) and direct numerical simulations (Clercx et al. 1998, 1999, 2001) with regard to the so-called quasi-steady final states are the following. In square containers, we found mostly a monopolar final state, and when the initial flow was more energetic, a tripolar state is found. The latter state is basically the result of the interaction of a rapidly rotating monopolar vortex that generates strong boundary layers at the no-slip wall. These boundary layers detach, roll up and form the satellite vortices. The minority of the end states in the numerical simulations had a dipolar-like character. Maybe the most remarkable result has been the phenomenon of spontaneous spin-up of the flow that initially had no angular momentum (Clercx et al. 1998). The higher the Reynolds number the more likely is spin-up to occur, with about 50% of the runs having a final state with clockwise rotation and the rest having counter-clockwise rotation (Keetels et al. 2010).

Spontaneous spin-up can be quantified by measuring the time evolution of the angular momentum $L(t)$ contained by the flow. The angular momentum is defined as

$$L(t) = \int_{\mathcal{D}} \hat{\mathbf{z}} \cdot (\mathbf{r} \times \mathbf{v}(\mathbf{r}, t)) dA, \tag{6.7}$$

with $\hat{\mathbf{z}}$ the unit vector normal to the plane of flow, the origin of the coordinate system (x, y) in the center of the container, and $\mathbf{r}$ the position vector. In the numerical experiments mentioned above, the angular momentum at $t = 0$ was negligible, $L(t = 0) = L_0 = 0$. The rate of change of angular momentum can straightforwardly be determined by taking the time derivative of Eq. (6.7) and substituting the Navier Stokes Eq. (6.2) into the resulting expression for $\frac{dL}{dt}$. It yields the following integral (in dimensionless form) over the boundary $\partial\mathcal{D}$ of the domain,

$$\frac{dL}{dt} = \int_{\partial\mathcal{D}} p(\mathbf{r}, t)\mathbf{r} \cdot d\mathbf{s} + \frac{1}{\mathrm{Re}} \int_{\partial\mathcal{D}} \boldsymbol{\omega}(\mathbf{r}, t)(\mathbf{r} \cdot \hat{\mathbf{n}}) ds. \tag{6.8}$$

Here, $\hat{\mathbf{n}}$ is a unit vector normal to the boundary, $d\mathbf{s}$ is an infinitesimal boundary element (tangential to the boundary) and ds its magnitude. This relation clearly shows that angular momentum production is due to a pressure contribution (inviscid) and a viscous contribution proportional to the vorticity generated at the boundary. The pressure contribution turns out to be the dominant term in the range of Reynolds numbers considered in the experiments and simulations. More extensive discussions on this phenomenon can be found in (Clercx et al. 1998; Clercx and Van Heijst 2009; Keetels et al. 2010).

In the experiments mentioned above and in most of the numerical studies, the integral scale Reynolds number $\mathrm{Re} = U_{rms}L/\nu$ (based on the initial root-mean-square velocity U_{rms}, the size of the container L, and the fluid kinematic viscosity ν) is relatively low. In the experiments, $1000 \lesssim \mathrm{Re} \lesssim 2000$, and in the numerical simulations, we typically have $1000 \lesssim \mathrm{Re} \lesssim 5000$, with a very few cases with $\mathrm{Re} = 10^4$ or 2×10^4. The more recent numerical simulations by Keetels et al. (2010) were carried out with significantly higher initial large-scale Reynolds number, up to $\mathrm{Re} = 10^5$. In Fig. 6.3, we show a typical evolution of decaying 2D turbulence on a square domain with no-slip rigid walls. The initial flow field consisted of an almost regular array of 10×10 Gaussian vortices. The positions of these vortices are all slightly disturbed to give the evolution a kick-start towards a fully turbulent flow. The quasi-steady final state that emerges after about 400 initial eddy turnover times is basically a relatively strong, but also relatively small monopolar vortex embedded in a large-scale swirling flow. Also several smaller vortices are embedded in this swirling background flow, and these vortices are mostly the result of detachment and roll up of boundary layers containing high-amplitude vorticity.

During the decay process the impact of the no-slip walls is large: many relatively small or even tiny vortices can be observed in each of the panels of Fig. 6.3. These small vortices are almost all generated at the no-slip walls, signifying a crucial difference between 2D decaying spatially unbounded turbulence and 2D decaying confined turbulence. It affects the vortex statistics, which is discussed in more detail in (Clercx and Van Heijst 2009), and also the enstrophy production and decay rate significantly. To illustrate the different decay scenarios, we show in Fig. 6.4 two snapshots from simulations starting with exactly the same initial conditions. The left panel shows the result with no-slip walls and the right panel those with periodic boundary conditions (Keetels et al. 2010).

6.3.2 *Quasi-Steady Final States: Laboratory Experiments*

Quasi-steady final states can also be explored in laboratory experiments. Here, and as a typical illustration, the decay scenarios of quasi-2D turbulence in laboratory experiments, carried out in a two-layer stratified fluid in circular containers (for experimental details, see Maassen et al. (1999)), are briefly discussed. See also Yap and Van Atta (1993) and Fincham et al. (1996) for similar experiments a few years earlier. Two sets of experiments in cylindrical containers have been carried out by

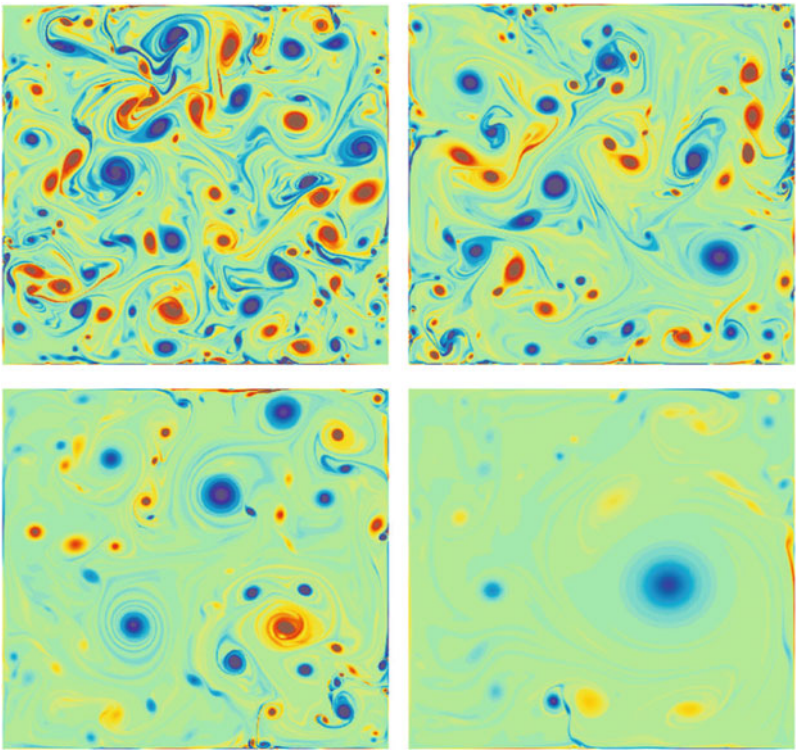

Fig. 6.3 A few vorticity snapshots showing the process of spontaneous spin-up. The Reynolds number of the simulation is $\mathrm{Re} = 5 \times 10^4$. The snapshots are taken at $\tau = 8, 24, 100$ and 400 eddy turnover times (with $\tau = 1$ corresponding to the initial eddy turnover of the initial vortices). The initial flow field consisted of an array of 10×10 vortices with positions slightly distorted to enhance the rapid evolution towards an irregular turbulent flow field. For computational details, see Keetels et al. (2010)

Maassen and collaborators, all in the spirit of (Li and Montgomery 1996; Chavanis and Sommeria 1996): a set with initially hardly any swirl ($L_0 \approx 0$) and a set with an initial condition with considerable swirl ($L_0 \neq 0$). The initial flow was generated by dragging a rake through the stratified fluid. At a large enough towing speed the wake behind each bar becomes turbulent, thus generating a turbulent initial flow field. Symmetric rakes result in $L_0 \approx 0$, and asymmetric rakes result in $L_0 \neq 0$, see Maassen et al. (1999) for details. The Reynolds number of the (initial) flow, now defined as $\mathrm{Re} = U_{rms} R/\nu$ with R the radius of the container, is $\mathrm{Re} \approx 4000$. The experiments with $L_0 \approx 0$ show the classical decay process. The small vortices, generated by initializing the flow, start the merge quickly with like-sign counterparts and the flow evolves towards a quadrupolar state. This evolution is due to a permanent interaction of the flow with the rigid circular no-slip walls. Finally, a more or less quasi-steady dipolar final state appears. The other set of experiments, with $L_0 \neq$

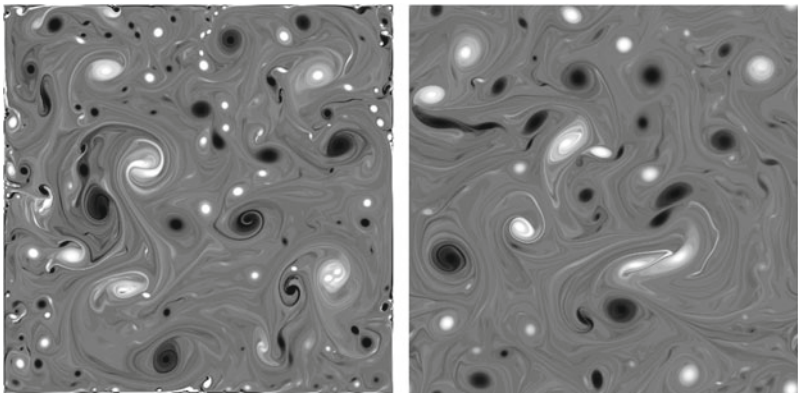

Fig. 6.4 Vorticity snapshots, taken at dimensionless time $\tau = 15$, from a simulation with no-slip rigid walls (left panel) and a simulation with periodic boundary conditions (right panel). The initial conditions were exactly the same for both numerical experiments and in both cases: $\mathrm{Re} = 10^5$. Dark and light grey represent positive and negative vorticity, respectively. Courtesy Keetels et al. (2010)

0, show basically a similar initial decay stage, but due to the swirl, a large-scale monopolar vortex forms instead of a quadrupolar or dipolar state. This monopolar vortex easily slides along the circular rigid walls, and less boundary-layer vorticity is produced in this case (compared to the square container). The experimental results are in very good agreement with the numerical simulations by Li et al. (1997). The experimentally observed quasi-steady states agree remarkably well with the predictions by Chavanis and Sommeria (1996) for inviscid flows in confined domains: a dipole when initially the circulation is zero, and a monopole when the initial condition contains circulation.

These experiments of decaying 2D turbulence in circular domains show that for $L_0 \approx 0$ the quasi-steady final state is a quadrupolar or dipolar structure, thus no spontaneous spin-up. Absence of spontaneous spin-up on circular domains was confirmed later on in numerical studies by Schneider and Farge (2005). This can be understood using Eq. (6.8). In circular domains, the pressure contribution to the production of angular momentum vanishes as $(\mathbf{r} \cdot \hat{\mathbf{n}}) = 0$, thus the dominant term vanishes for this particular geometry. The domain shape is thus relevant in determining the quasi-steady final state by flow-wall interaction.

In a similar spirit, laboratory experiments in two-layer density stratified fluids and numerical simulations have been carried out to explore the quasi-steady final states of 2D decaying turbulence in rectangular containers with aspect ratios $\delta = L/W$, with L the length and W the width of the container, varying from $\delta = 2$ to $\delta = 5$ (Maassen et al. 2003). The number of vortices N_f in the final quasi-steady cell pattern is in most experiments either $N_f = \delta$ or $N_f = \delta \pm 1$. This is not fully surprising, and is consistent with observations as shown in Fig. 6.1 for the gyres in the Gulf of Aden and the number of vortices observed in the Adriatic Sea. Another observation concerned the comparison of the present results, for the case $\delta = 2$, with results

of the quasi-steady final states in inviscid flows in domains with the same aspect ratio; see Pointin and Lundgren (1976) and Chavanis and Sommeria (1996). A clear discrepancy was reported which most likely is due to the role of the boundary layers present in the experiments but absent in the case of inviscid flows.

6.3.3 Forced 2D Turbulence on Confined Domains

The discussion above focuses solely on decaying 2D turbulence. However, the formation of domain-size monopolar vortices has also been observed in forced 2D turbulence in square domains. Both in experiments, see Sommeria (1986) and Paret and Tabeling (1998), and in numerical studies, see Molenaar et al. (2004) and Van Heijst et al. (2006). In particular the experimental study by Sommeria (1986) and numerical results reported by Van Heijst et al. (2006) revealed reversals of the swirl of the large-scale monopolar vortex. The time between reversals is orders of magnitude longer than the time scale needed for a reversal to occur, which is of the order of a few large-scale eddy turnover times. The initialization of these reversals was attributed to destabilizing disturbances such as small strong eddies (Sommeria 1986) but their origin was not entirely clear. In numerical studies of forced 2D turbulence in square domains with rigid no-slip sidewalls, with similar forcing length scale as the experiments by Sommeria, it became clear that the disturbances originate from formation and detachment of the boundary layers at the sidewall and subsequent roll up of the boundary-layer filaments into small strong vortices (Van Heijst et al. 2006). When strong enough, they may destabilize and potentially disintegrate the large-scale monopolar vortex. A new large-scale vortex will quickly build up after this event, with same or opposite rotation sense. As an illustration of this process three consecutive snapshots of the vorticity field from a forced 2D turbulence simulation in a square confined domain with no-slip sidewalls, provided by Molenaar et al. (2004), are shown in Fig. 6.5. The integral-scale Reynolds number of this simulation was approximately 3000. The snapshots are taken just before the collapse, during the collapse stage and just after it, when once again a domain-filling monopolar vortex has formed (with opposite sign vorticity in this case). The lower panel shows the normalized angular momentum computed according to Eq. (6.7) of the same run. It clearly shows the existence of domain-filling monopolar vortices over many turnover times and the collapse stages of relative short duration. Note that the vorticity snapshots in Fig. 6.5 are taken at $t = 800$, 900 and 1000, respectively. This kind of phenomena is a clear manifestation of the impact of rigid no-slip sidewalls on the dynamics of 2D turbulence.

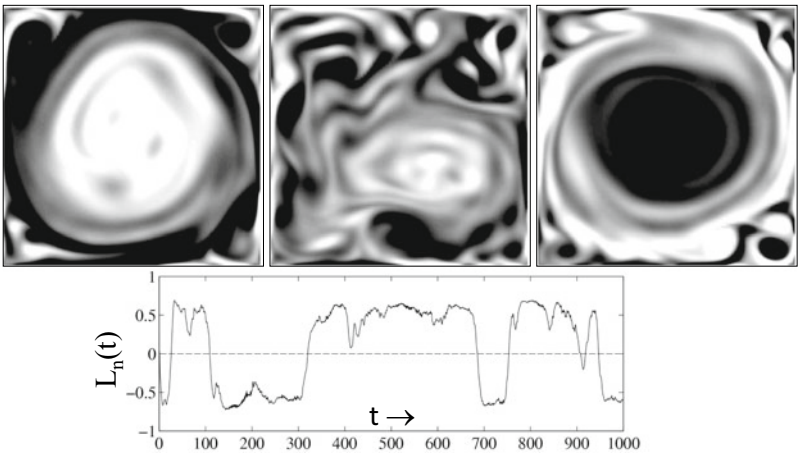

Fig. 6.5 Snapshots of the vorticity evolution from a forced 2D turbulence simulation in a square domain with no-slip walls. The snapshots are taken just before (left panel, $t = 800$) and just after (right panel, $t = 1000$) the sign reversal of a large monopolar vortex. The panel in the middle ($t = 900$) is taken during the collapse stage. Large negative values of vorticity are indicated with black, and white indicates large positive values of vorticity. The lower panel shows the normalized angular momentum of the flow in the square box, showing distinct phases of spin-up with collapse stages in between. Normalization is done with the angular momentum of uniform rotation with the same energy content $E(t)$ as the actual flow field. Courtesy Molenaar et al. (2004)

6.4 Interaction of Vortices with Walls

In the previous section, we have discussed the large-scale flow structures emerging during the decay of 2D turbulence in confined domains. There was a clear impact of the presence of rigid walls and the domain geometry on the quasi-stationary final states. However, we could also observe during the decay process the formation of many small-scale vortices containing high values of vorticity; see Figs. 6.3 and 6.4. The production of these small-scale vortices by detaching boundary layers also has a strong impact on the vortex statistics and the time evolution of the vortex density, vortex separation and the enstrophy is strongly affected when rigid no-slip walls are present. See for a further discussion of this particular aspect (Clercx and Van Heijst 2009). Such small-scale vortices might also be the cause of reversals of large-scale vortical structures in 2D forced turbulence in confined domains.

6.4.1 No-Slip Walls as Vorticity Sources

The formation of small-scale vortices near rigid no-slip walls indicate that flow-wall interactions are relevant for 2D turbulence in confined domains. It is expected that the larger and stronger the vortices, the larger their impact on the evolution of 2D

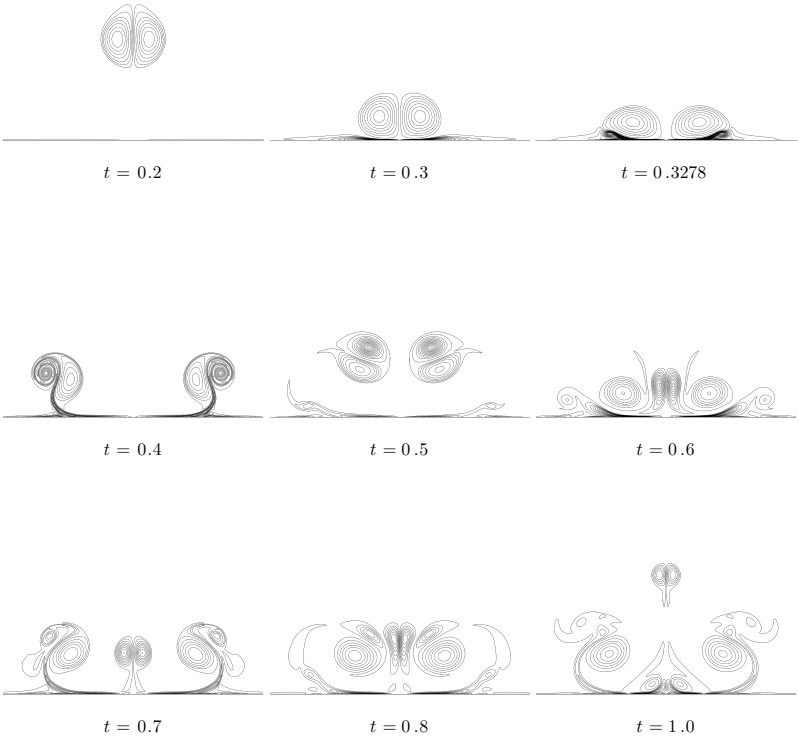

Fig. 6.6 Sequence of vorticity contour plots showing the flow evolution of a dipole-like vortex colliding with a rigid no-slip wall. The integral-scale Reynolds number, based on the initial speed and radius of the dipole, is Re = 2500. Courtesy Kramer et al. (2007)

turbulence. This is, in particular, due to the production of more intense boundary layers, that once again detach and create new strong vortices that travel to the interior. In other words, the rigid walls serve as a source of enstrophy, and this also implies enhanced dissipation of kinetic energy. One of the open questions here is what happens in the limit of vanishing viscosity, or in other words: what will happen when $\mathrm{Re} \to \infty$? Will there be a finite dissipation in the inviscid limit for 2D flows in confined geometries?

A variety of approaches can be used to tackle this problem. One of these is the dipole-wall collision experiment, see Fig. 6.6, which has recently been reviewed by Clercx and Van Heijst (2017). In particular, one can explore how vorticity production during a vortex-wall collision is enhanced and how this affects the dissipation of kinetic energy. For this purpose we need to introduce a slightly revised version of the evolution equation of the enstrophy, which was introduced in Sect. 6.2 for the unbounded or periodic domain. For domains bounded with no-slip walls we need to add an additional term, a boundary integral, yielding

$$\frac{d\Omega(t)}{dt} = -\frac{2}{\mathrm{Re}}P(t) + \frac{1}{\mathrm{Re}}\int_{\partial\mathcal{D}} \omega\frac{\partial\omega}{\partial n}ds, \tag{6.9}$$

with $\frac{\partial}{\partial n}$ the wall-normal derivative and ds an infinitesimal element of the boundary $\partial\mathcal{D}$. The time rate of change of the enstrophy is expressed in dimensionless form. The boundary integral may substantially increase the enstrophy at some instants of time, in such a way, that as a net effect, enstrophy is produced during vortex-wall collisions. Although the time rate of change of the kinetic energy will keep the same form, here in dimensionless quantities written as

$$\frac{dE(t)}{dt} = -\frac{2}{\mathrm{Re}}\Omega(t), \tag{6.10}$$

the persistence of enstrophy, or even the increase of enstrophy, will automatically imply stronger decay of the kinetic energy of the flow. Note that for 2D decaying flows on periodic domains the enstrophy is always bounded by its initial value (Batchelor 1969), thus the dissipation will reduce to zero in the inviscid limit, or: $\frac{dE(t)}{dt} \propto \mathrm{Re}^{-1} \to 0$ for $\mathrm{Re} \to \infty$. The question to be answered is whether the enstrophy production scales with the Reynolds number, which might be expected as the boundary layers generated during the vigorous vortex-wall collisions contains large amount of vorticity. Suppose that $\Omega \propto \mathrm{Re}^{\alpha}$ for $\mathrm{Re} \to \infty$. This would imply

$$\frac{dE}{dt} = -\frac{2}{\mathrm{Re}}\Omega \propto \mathrm{Re}^{\alpha-1}\,. \tag{6.11}$$

Obviously, when the enstrophy does not scale with the Reynolds number, or $\alpha = 0$, the original result is retrieved: $\frac{dE}{dt} \to 0$ when $\mathrm{Re} \to \infty$. In the case that $\alpha = 1$, or $\Omega \propto \mathrm{Re}$ for $\mathrm{Re} \to \infty$, we end up with constant energy dissipation in the inviscid limit, reminiscent to 3D turbulence. Some recent works have indeed indicated that $\alpha \neq 0$, but debate exists about its precise value and its potential implications; see Clercx and Van Heijst (2002, 2017), Sutherland et al. (2013), and Nguyen van yen et al. (2011, 2018), and values for α are found in the range 0.5–1.0.

6.4.2 *Vorticity Production by Dipole-Wall Collisions*

Exploration of vorticity production at walls is based on numerical experiments of dipole-wall collisions with a rigid flat wall (with no-slip boundary conditions), as for the first time investigated by Orlandi (1990). The original motivation of this kind of studies were related to the problem of trailing vortices from aircraft, which will interact with the ground during landing and take-off resulting in vortex rebounds. Later on, the mechanism for inviscid dipole-vortex rebounds became also a topic of interest in the geophysical flow community. There, vorticity production by stretching of vortex tubes in the presence of a sloping bottom in the coastal zone could be

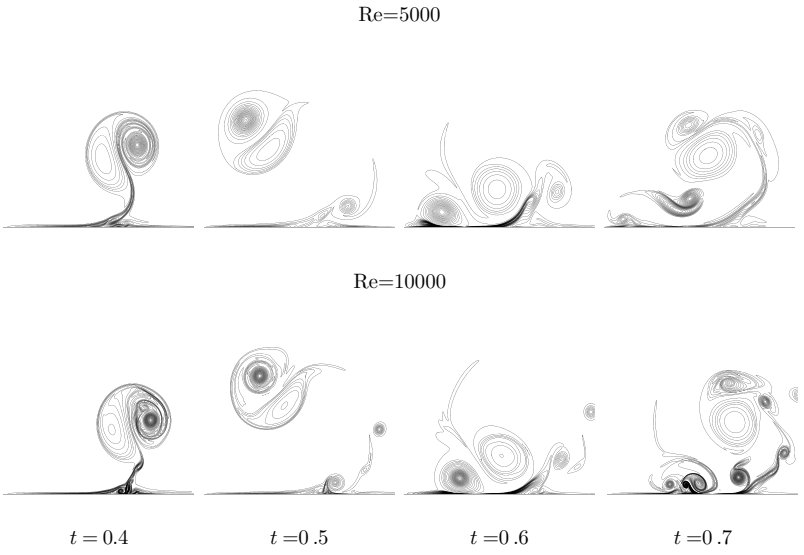

Fig. 6.7 Sequence of vorticity contour plots illustrating the flow evolution during a dipole-wall collision for $\mathrm{Re} = 5 \times 10^3$ (top panel) and $\mathrm{Re} = 10^4$ (bottom panel). The plots only show the right-hand side part of the domain as the dipole-wall collision is symmetric with regard to the dipole axis, see also Fig. 6.6. Courtesy Kramer et al. (2007)

used to parameterize aspects of 3D vortex dynamics for a 2D description of the inviscid rebound process (Carnevale et al. 1997). The complexity of dipole-wall collisions, with vortex rebounds already for relatively low Reynolds numbers, is nicely illustrated in Fig. 6.7. A brief review with regard to dipole-wall collisions is provided by Clercx and Van Heijst (2017).

First numerical observations of Reynolds-number dependency of enstrophy production during dipole-wall collisions were reported by Clercx and Van Heijst (2002). They revealed that $\Omega \propto \mathrm{Re}^{0.8}$ for $\mathrm{Re} \lesssim 2 \times 10^4$ and $\Omega \propto \mathrm{Re}^{0.5}$ for $\mathrm{Re} \gtrsim 2 \times 10^4$, with the Reynolds number based on the radius of the dipole R_d, and its self-induced traveling speed U_d. The scaling of the enstrophy implies $\frac{dE}{dt} \propto \mathrm{Re}^{-0.2}$ and $\frac{dE}{dt} \propto \mathrm{Re}^{-0.5}$ for the respective regimes. This scaling behavior turned out to be independent of the collision angle of the dipole with the rigid wall. A simple scaling analysis for the large-Reynolds number regime (where $\Omega \propto \mathrm{Re}^{0.5}$) is based on the following balance at the flat rigid wall (chosen parallel with the $x-$ axis of a reference frame),

$$-\nu \frac{\partial \omega}{\partial y}|_{\mathrm{wall}} = \frac{1}{\rho} \frac{\partial p}{\partial x}|_{\mathrm{wall}}, \tag{6.12}$$

which can directly be obtained from the Navier-Stokes equation. In the following, we assume that the boundary layer remains laminar (but unsteady), an assumption that eventually may break down at much higher Reynolds number values. When we

assume that the pressure distribution along the boundary is finite, we may immediately conclude from Eq. (6.12) that $\frac{\partial \omega}{\partial y}|_{\text{wall}} = \mathcal{O}(\text{Re})$ for large Reynolds number values. The boundary-layer thickness δ scales according to Prandtl's prediction: $\delta \propto \text{Re}^{-1/2}$. This immediately implies, using the predicted scaling of the vorticity gradient normal to the wall, that $\omega|_{\text{wall}} \propto \sqrt{\text{Re}}$. Provided that the Reynolds number is large enough (here $\text{Re} \geq 2 \times 10^4$), we can expect that the total enstrophy and palinstrophy in the flow will be dominated by the vorticity and vorticity gradient values in the boundary layer itself. We can then easily derive the following estimates: $\Omega \propto R_d \delta \omega^2|_{\text{wall}} \sim R_d \sqrt{\text{Re}}$. For the palinstrophy we can derive in a similar way: $P \propto R_d \delta (\frac{\partial \omega}{\partial y})^2|_{\text{wall}} \sim R_d \text{Re} \sqrt{\text{Re}}$. This is consistent with the scaling of the palinstrophy reported by Clercx and Van Heijst (2002): $P \propto \text{Re}^{1.5}$ for $\text{Re} \gtrsim 2 \times 10^4$ and $P \propto \text{Re}^{2.25}$ for $\text{Re} \lesssim 2 \times 10^4$. It is interesting to note that a scaling analysis for $\text{Re} \lesssim 10^4$ by Keetels et al. (2011) provided similar scaling exponents, $\Omega \propto \text{Re}^{3/4}$ and $P \propto \text{Re}^{9/4}$ (compared to $\text{Re}^{0.8}$ and $\text{Re}^{2.25}$, respectively, found by Clercx and Van Heijst (2002)).

In recent years, a few more studies emerged addressing the possible existence of extremely thin dissipation layers near the rigid wall, including the possible presence of a slip-velocity at the rigid wall (Nguyen van yen et al. 2011, 2018; Sutherland et al. 2013). Nguyen van yen et al. (2011) did a first attempt, based on a similar dipole-wall collision experiment as discussed above, to explore a possible Re-independent energy dissipation rate. In other words, they explored the possibility of the existence of $\frac{dE}{dt} \rightarrow \chi$ for $\text{Re} \rightarrow \infty$ with $\chi < 0$ and constant. Such behavior would be in sharp contrast with the standard result for 2D decaying turbulence in unbounded (or periodic) domains. In their analysis they complemented Prandtl's boundary layer argument with some theorems put forward by Kato (1984) on the dissipation rate in the vanishing viscosity limit and showed two scaling regimes for the enstrophy. For the early stage and initial collision stage they found $\Omega \propto \text{Re}^{0.5}$ and during the collision stage (and boundary-layer detachment) they found $\Omega \propto \text{Re}$. The latter regime implies indeed finite kinetic energy dissipation at ever larger Reynolds numbers. These results were subsequently critically examined by Sutherland et al. (2013) who provided supporting evidence of the earlier predicted scaling relation: $\frac{dE}{dt} \propto \text{Re}^{-0.5}$. We should however emphasize that the studies by Nguyen van yen et al. (2011) and Sutherland et al. (2013) do not actually extend the range of Reynolds numbers compared to (Clercx and Van Heijst 2002; Keetels et al. 2011). Therefore, we should still be careful to come to strong conclusions applicable for the vanishing viscosity limit.

The discussion on the dissipation rate in the vanishing viscosity limit is still ongoing; see Nguyen van yen et al. (2018). Moreover, the analysis presented so far are based on laminar Prandtl boundary layer theory and possible implications of boundary-layer detachment, but no deeper analysis is available for the case the boundary layers become fully turbulent, a scenario that is expected to become important when Re is further increased.

6.5 Review of 2D Turbulence Experiments in Shallow Fluids

In environmental flows, such as in estuaries and rivers (Uijttewaal 2014), suppression of vertical motion and subsequent quasi-two-dimensionalization occurs predominantly by the shallowness of the flow domain. Planetary rotation is almost irrelevant on these scales and density stratification is mostly not important (but not excluded in certain cases). For this reason shallow flow experiments have been used to study aspects of quasi-2D turbulence (Chen and Jirka 1995; Uijttewaal and Jirka 2003) and dynamics of coherent structures in shallow flows, including secondary out-of-plane motion (Jirka 2001; Lin et al. 2003; Sous et al. 2004, 2005; Akkermans et al. 2008a, 2010; Kelley and Ouellette 2011; Duran-Matute et al. 2010, 2011; Tithof et al. 2018).

This overview of shallow fluid layer experiments will focus on the larger scale flow phenomena such as the dynamics of vortices, the evolution of global integral quantities like energy and enstropy, and the eventual presence of 3D secondary flows. Quasi-steady final states belong to this class of phenomena but have already been discussed in Sect. 6.3. For an extensive discussion of the statistical properties of the velocity and vorticity field and the Lagrangian dispersion of tracers, also experimentally explored by means of shallow fluid layer and soap film experiments, the reviews by Tabeling (2002), Kellay and Goldburg (2002), Clercx and Van Heijst (2009), and Boffetta and Ecke (2012) can be consulted.

In the preceding section, we have discussed the implications of the lateral boundaries in 2D confined turbulence and their impact on a variety of physical processes, including coherent structure formation, vorticity production at rigid walls, and dissipation of kinetic energy. Shallow flows, both in geophysical systems and in laboratory experiments, need to be supported by a bottom, which implies an additional damping mechanism affecting the flow, thus an additional source of dissipation. Furthermore, the bottom will contribute to the emergence of 3D secondary flows. This damping mechanism and the weak 3D recirculation flows in these systems, are not represented in 2D (confined) turbulence. Their impact needs to be known for better understanding of the quasi-2D behavior of environmental and geophysical flows.

Since the mid-1980s the first experiments have been reported addressing a variety of aspects of 2D turbulence. In particular, several of the exciting theoretical and numerical findings based on KLB theory were put to a test, such as the inverse energy and direct enstrophy cascade, the associated energy and enstrophy fluxes, statistical quantities with regard to the fluctuating velocity and vorticity fields, vortex statistics of freely evolving 2D turbulence, Lagrangian dispersion properties of passive tracers (including pair dispersion), and last but not least, the emergence of so-called condensation phenomena (Smith and Yakhot 1993). The last phenomenon is a clear result of the inverse energy cascade as energy injected at some intermediate scale is transferred upwards to the largest scales, and eventually this inverse cascade is arrested by the finiteness of the container, a manifestation of confinement (see also the brief discussion in the last paragraph of Sect. 6.3).

Laboratory experiments can be carried out with a variety of generation mechanisms for quasi-2D flows. One could think of rapidly rotating homogeneous fluids, see, for example, the pioneering works by Colin de Verdière (1980) and Hopfinger et al. (1982), or in homogeneous density-stratified (or two-layer) fluids, see, for example, Yap and Van Atta (1993), Boubnov et al. (1994), Fincham et al. (1996), and Maassen et al. (1999). We will not further discuss this kind of experiments (but see Sect. 6.3 for some results on quasi-steady final states). We will focus on a discussion of experiments in shallow fluid layers where two-dimensionality is enforced by geometrical confinement only (and this will mostly exclude soap film experiments for which the interested reader is referred to Kellay and Goldburg (2002)).

6.5.1 Laboratory Experiments in Shallow Fluid Layers

The first shallow flow experiment aimed at verifying aspects of KLB-theory was reported by Sommeria (1986). His experiments were mostly focused on the measurement of the 2D inverse energy cascade which he was able to confirm. For this purpose he generated 2D turbulence in a shallow layer of mercury. By applying a uniform magnetic field (with the field lines perpendicular to the shallow mercury layer) 3D motions could be strongly suppressed. This approach resulted in a pretty horizontal velocity field in a substantial part of the mercury layer. Near the bottom plate a very thin viscous boundary layer is present which affects the flow in the core in the form of a linear damping, i.e. proportional to the local horizontal fluid velocity in the core. Larger coherent structures have larger velocities, and linear damping particularly affects these larger scales and potentially can serve as a sink of energy to arrest the inverse energy cascade at a certain scale.

As mercury has certain serious disadvantages, such as being inaccessible for optical diagnostics to measure the fluid velocity inside the fluid layer, but also its toxic properties (thus requiring quite some precautions to work safely) a different kind of experiment was necessary. A new setup was proposed not many years later by Tabeling et al. (1991) and Dolzhanskii et al. (1992), which initiated many laboratory investigations on 2D turbulence worldwide. These experiments have been carried out in a shallow layer of electrolyte and the forcing mechanism is based on the interaction of a current density with a magnetic field inducing the Lorentz force driving the fluid motion. For this purpose magnets are placed underneath the fluid layer and two electrodes are placed on opposite sides of the container providing a uniform electrical current that runs through the electrolyte to effectively force the fluid motion. To achieve quasi-2D flow the horizontal scale of motion L must be much larger than the fluid-layer thickness H. Under these conditions, it is usually assumed that due to mass conservation $w \approx (H/L)U$, with w and U the vertical and horizontal velocity scale, respectively. At first sight, the two-dimensionality of the flow can thus be tuned with the magnet size and fluid-layer thickness.

An important test for the shallow fluid layer setup was the comparison of experimentally obtained vortex statistics data with theoretical and numerical results

by Carnevale et al. (1991, 1992). Cardoso et al. (1994) found $\rho(t) \propto t^{\chi}$ with $\chi = 0.44 \pm 0.1$, quite different compared to the value reported by Carnevale and coworkers: $\chi \approx 0.72 - 0.75$. They also did not observe a rapid decrease of the area occupied by the vortices as expected from the approach by Carnevale and coworkers. Besides the fact that the integral-scale Reynolds number was of the order 1000–2000, so that the flow is affected by viscous dissipation, bottom friction could explain this deviation. Later, Akkermans et al. 2008b, a identified significant 3D recirculating flows in shallow fluid layers uncovered by stereo-PIV measurements (and confirmed in simulations) as another potential reason for deviations. Thus vertical confinement and bottom friction might complicate the picture considerably.

6.5.2 2D Turbulence with Rayleigh Friction

For the analysis of bottom friction it is often assumed that the vertical profile of the horizontal motion can be approximated by a Poiseuille profile (satisfying the boundary conditions at the no-slip bottom and stress-free surface). This allows us to reformulate the Navier Stokes Eq. (6.2) by replacing the viscous contribution $\nu(\partial^2\mathbf{v}/\partial z^2)$ by the term $-\lambda\mathbf{v}$. This linear damping term is known as Rayleigh friction and the bottom or Rayleigh friction coefficient takes the form $\lambda = \nu(\frac{\pi}{2H})^2$. We can now parameterize the quasi-2D flow in shallow fluid layers by the following dimensionless equation:

$$\frac{\partial \mathbf{v}}{\partial t} + (\mathbf{v}\cdot\nabla)\mathbf{v} = -\nabla p + \frac{1}{\mathrm{Re}}\nabla^2\mathbf{v} - \frac{1}{\mathrm{Re}_\lambda}\mathbf{v} + \mathbf{F}_L, \tag{6.13}$$

with $\mathbf{v}$ representing the horizontal flow field only, satisfying 2D mass conservation, Re_λ the ratio of the bottom-friction time scale and the large-scale eddy turnover time scale of the horizontal flow, and $\mathbf{F}_L$ the Lorentz force to drive the flow. In these shallow electrolyte solutions the typical integral scale Reynolds number is about 1000–2000.

Taking into account the presence of bottom friction an upgrade of this kind of experiments has been proposed few years later to suppress the effects of bottom friction (Marteau et al. 1995; Hansen et al. 1998). The new experiments consist of two thin layers of electrolyte on top of each other, the bottom layer heavier than the top layer, to reduce the impact of bottom friction (and to suppress vertical velocities). The flow is only effectively forced (in a similar way as described above) in the bottom layer. Coupling with the top layer occurs via the stress boundary condition at their interface. They repeated the experiments by Cardoso et al. (1994) and found the encouraging result $\chi \approx 0.70 \pm 0.1$. The observed decay scenario of the 2D turbulent flow was quite similar as in the 2D simulations (with similar integral-scale Reynolds number) reported by Clercx et al. (1999) and Wells and Afanasyev (2004). Moreover, their vortex statistics scenario turned out to be quite similar to those observed by Clercx and Nielsen (2000) and Clercx et al. (2003) for decaying

2D turbulence in confined domains. These shallow fluid experiments provide strong evidence that 2D turbulence decay scenarios follow those of 2D decaying and confined turbulence and not the vortex statistics scenario by Carnevale and coworkers. Quite remarkable, a similar stereo-PIV analysis by Akkermans et al. (2010) revealed that also in stratified two-layer shallow flows 3D recirculating flows of similar magnitude as in the single-layer experiments occur, implying that the two-layer solution is not extremely effective in suppressing vertical velocities. This puts into question the quasi-two-dimensionality of such flows. Although all these results are valuable for understanding quasi-2D turbulence, any interpretation of experimental data is still a delicate issue and should be done with care.

As laboratory experiments and confined 2D turbulence simulations appear to provide similar decay scenarios it might be helpful to have a closer look at decaying 2D flow with Rayleigh friction. The discussion below is based on Eq. (6.13) without forcing term. The dimensionless 2D vorticity equation is then

$$\frac{\partial \omega}{\partial t} + (\mathbf{v} \cdot \boldsymbol{\nabla})\omega = \frac{1}{\mathrm{Re}} \boldsymbol{\nabla}^2 \omega - \frac{1}{\mathrm{Re}_\lambda} \omega. \tag{6.14}$$

With the definitions of the kinetic energy and enstrophy of the flow, see Eqs. (6.4) and (6.5), we can derive the following expression for the time rate of change of the kinetic energy

$$\frac{dE(t)}{dt} = -\frac{2}{\mathrm{Re}} \Omega(t) - \frac{2}{\mathrm{Re}_\lambda} E(t). \tag{6.15}$$

By separating Rayleigh friction from ordinary 2D flow dynamics the energy is written as $E(t) = E_0(t)\mathrm{e}^{-2t/\mathrm{Re}_\lambda}$ and the enstrophy as $\Omega(t) = \Omega_0(t)\mathrm{e}^{-2t/\mathrm{Re}_\lambda}$, with $E_0(t)$ and $\Omega_0(t)$ the compensated energy and the enstrophy, respectively, we simplify Eq. (6.15) to

$$\frac{dE_0(t)}{dt} = -\frac{2}{\mathrm{Re}} \Omega_0(t). \tag{6.16}$$

This suggests that the 2D velocity field and the vorticity field can be written as $\mathbf{v}(\mathbf{r}, t) = \mathbf{v}_0(\mathbf{r}, t)\mathrm{e}^{-t/\mathrm{Re}_\lambda}$ and $\omega(\mathbf{r}, t) = \omega_0(\mathbf{r}, t)\mathrm{e}^{-t/\mathrm{Re}_\lambda}$, with $\mathbf{r} = (x, y)$ the dimensionless horizontal coordinates and t a dimensionless time. Substituting these expressions in Eq. (6.14), multiplying the full equation by $\mathrm{e}^{t/\mathrm{Re}_\lambda}$ and rescaling time to $t_* = \mathrm{Re}_\lambda(1 - \mathrm{e}^{-t/\mathrm{Re}_\lambda})$ the following equation is obtained:

$$\frac{\partial \omega_0}{\partial t_*} + (\mathbf{v}_0 \cdot \boldsymbol{\nabla})\omega_0 = \frac{1}{\mathrm{Re}_*} \boldsymbol{\nabla}^2 \omega_0, \tag{6.17}$$

with a renormalized Reynolds number, $\mathrm{Re}_* = \mathrm{e}^{-t/\mathrm{Re}_\lambda}\,\mathrm{Re}$. Note that this renormalized equation, first proposed by Hansen et al. (1998), is similar to the traditional 2D vorticity equation for $t \lesssim \mathrm{Re}_\lambda$ as then $t_* \approx t$. Moreover, $\lim_{\lambda \to 0}\ t_* = t$. With this renormalization 2D decaying flows with bottom friction behave as purely 2D decaying flows, but with a time-dependent Reynolds number, which can only evolve for a finite time (as $t_* \leq \mathrm{Re}_\lambda$).

Clercx et al. (2003) have tested the validity of the renormalized vorticity equation for a range of Re_λ in numerical simulations, and for a range of fluid-layer depths in laboratory experiments. Numerical simulations with initial integral-scale Reynolds numbers of 1000, 2000 and 5000 with $\mathrm{Re}_\lambda \in \{10, 20, 25, 33, 50, 100, \infty\}$ clearly show bottom-friction independent time evolution of the compensated energy $E_0(t)$ and for the compensated enstrophy $\Omega_0(t)$. For each Re the curves for different Re_λ collapse on each other, thus have the same scaling exponents independent of Re_λ. The scaling exponents of the average vortex radius, the mean vortex separation, the averaged normalized vorticity extremum, and the density of vortices, as obtained in our numerical simulations (all key quantities in the analysis by Carnevale et al. (1991), Carnevale et al. (1992)), turn out to be independent of bottom friction.

The analysis of data from laboratory experiments in shallow fluid layers (Clercx et al. 2003) reveals a more mixed picture. The experiments have been carried out in a container of horizontal dimensions of 52 × 52 cm, the diameter of the magnets is 25 mm and the magnets are positioned on a 10 × 10 chess-board-like pattern (minimum distance between the magnet centers is 50 mm). The fluid layer depth H is varied between 4 and 12 mm. The value of the Rayleigh friction λ can be estimated by the expression $\lambda = \frac{\pi^2 \nu}{4H^2}$. In these experiments, it is found that global quantities like $E_0(t)$, $\Omega_0(t)$, the average length scale l in the flow estimated by $l \approx \sqrt{E_0(t)/\Omega_0(t)}$ and the normalized vorticity extremum, $\omega_{ext}/\sqrt{E(t)}$ are virtually independent of the fluid layer depth (and in agreement with an earlier experiment by Danilov *et al.* (2002) which have been carried out with fluid layer depths of 2–6 mm). The experimental data for the average vortex density $\rho(t)$ and average vortex radius $r(t)$ are less conclusive. Power-law exponents are found for small fluid layer depths ($H \leq 8$ mm) that are in agreement with earlier reported results by Cardoso et al. (1994), but significantly larger power-law exponents are measured in the experiments with fluid layer depths between 8 and 12 mm. This would suggest that for integral quantities like the (compensated) energy and enstrophy the model of 2D turbulence with Rayleigh damping is a suitable model also implying that these integral quantities are not very sensitive to secondary 3D flow structures in shallow fluid layers. However, for the vortex statistics quantities like vortex density, vortex size and vortex separation the 2D flow model with Rayleigh damping does not provide a complete description.

6.5.3 *Secondary Flows in Quasi-2D Turbulence in Thin Fluid Layers*

During the last decade more attention has been paid to the influence of secondary 3D recirculations in shallow fluid layer experiments. The first detailed measurements were conducted by Akkermans et al. (2008a, b, 2010). Based on stereoscopic PIV and 3D numerical simulations, they analyzed the flow field within dipolar vortex structures in shallow fluid layers, with emphasis on the out-of-plane (vertical) velocity component. These stereoscopic PIV measurements have shown the presence of

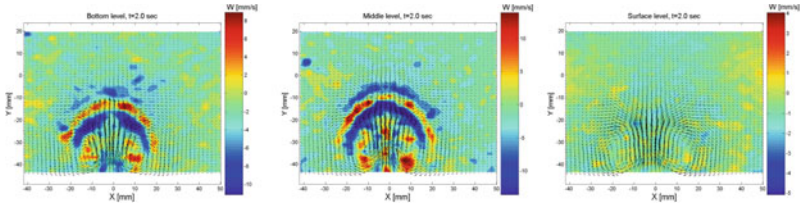

Fig. 6.8 Instantaneous velocity fields of a dipolar vortex in a horizontal plane by stereoscopic PIV measurements. The panels, from left to right, represent the flow near the bottom plate, at half height in the fluid layer and near the free surface, respectively. Vectors represent the horizontal velocity components (typically with a magnitude of a few cm/s in the vortex core) and the colors indicate the magnitude of the vertical velocity (5–10 mm/s). Courtesy Rinie Akkermans and Fluid Dynamics Laboratory, TU Eindhoven

significant, persistent (in time) and complex 3D flow structures, see the stereoscopic PIV data shown in Fig. 6.8. Full 3D numerical simulations revealed flow patterns with significant vertical motion largely consistent with the experimental data. Quite surprisingly, the flow patterns and out-of-plane motion appear independent of the applied boundary condition at the bottom, no-slip or stress-free. This might hint at the fact that bottom friction is not solely responsible for the 3D secondary flows, but it is basically vertical confinement and associated vertical gradients in the horizontal velocity field due to the boundary conditions; see Akkermans et al. (2008a) for an in-depth discussion. By measuring vertical slices of the horizontal motion in the fluid layer it became clear that a Poiseuille-like profile for the vertical variation of the horizontal velocity field is completely absent, both in experiments and in simulations. These conclusions are supported by the use of a global indicator of (lack of) two-dimensionality: the normalized horizontal divergence measured at several heights in the fluid layer,

$$\Lambda = \frac{H \int_{\mathcal{D}} |\nabla \cdot \mathbf{v}| dA}{L \int_{\mathcal{D}} |\omega_z| dA}. \tag{6.18}$$

Here, $\mathbf{v}$ is once again the horizontal velocity field (u, v), and ∇ represent the horizontal gradient operator. This measure clearly gives significant non-zero values (while for 2D flows it should be zero). For further discussions, see Albagnac et al. (2011), Duran-Matute et al. (2010, 2011, 2012).

The question is then if the degree of two-dimensionality can be improved through the use of a two-fluid-layer configuration. The finding that the 3D secondary flows in shallow fluid layers are due to vertical confinement and associated vertical gradients in the horizontal velocity field immediately implies that application of a stratified shallow two-layer system, aimed at reducing the effect of bottom friction, will not suppress out-of-plane motions significantly. A different set of experiments and simulations by Akkermans et al. (2010) has confirmed this conjecture. Two recent studies came with further supporting evidence, see Kelley and Ouellette (2011) for two-layer stratified shallow flows, and (Tithof et al. 2018). In this latter work the authors

compared three kinds of shallow flow experiments: a single fluid layer, a miscible two-layer system, and an immiscible two-layer system. They do not have access to all three components of the velocity field but used instantaneous 2D (horizontal) flow fields and quantified the out-of-plane motion using an approach from physical oceanography. The horizontal flow field is projected onto a stream function, boundary and potential modes, see for details (Kelley and Ouellette 2011), providing an alternative global indicator for two-dimensionality. This global indicator and the one in Eq. (6.18) resulted in similar conclusions with regard to how well two-dimensionality is or is not satisfied. Their conclusion, in agreement with those by Akkermans et al. (2008a, 2010), is basically that comparable levels of out-of-plane motion are measured for the single-layer case and the immiscible two-layer case, bringing strong doubt into the standard assumption since the 1990s that stratification enhances two-dimensionality.

6.5.4 Concluding Remarks

From this overview, it is important to realize that imposing a parameterization of bottom friction provides good results with regard to several global quantities, like the energy and enstrophy of the flow. However, they provide only a very qualitative description of the influence of 3D secondary flows (and do not cover the sources of it). Even a global measure as the averaged horizontal divergence is of limited value and deeper insight into the flow dynamics itself is required, for example, to understand what happens for flows in thin two-layer stratified fluids. This is still a matter of research. Several critical aspects with regard to quasi-2D flows in (stratified) shallow fluid layers need to be understood better. This kind of experiments nevertheless have provided useful insights with regard to the dynamics of 2D turbulence in the last few decades and we expect they continue to do so.

6.6 Summary

This chapter started with the observation that flows in thin fluid layers, like in the atmosphere of the Earth or in the oceans or coastal seas tend to behave quasi-two-dimensional under certain conditions. Several phenomena in such systems such as the formation and evolution of large-scale coherent structures, interaction of the flow with coastal boundaries, confinement effects, etc. can, at least partly, be comprehended with basic processes relevant in 2D fluid dynamics and, more specifically, 2D turbulence. In this chapter, the basic processes relevant for 2D turbulence have been reviewed with emphasis on a phenomenological description of these processes. With the applications in mind the role of horizontal confinement on flow organization is discussed and the role of lateral walls as vorticity source is highlighted. It describes processes that finds its counterparts in the oceans and coastal seas, see

Fig. 6.1 as one typical example. Finally, the use of laboratory set-ups to study such flows has been discussed in Sects. 6.3.2 and 6.5. I believe that the huge amount of knowledge collected in the last 50 years from fundamental 2D turbulence studies in general, but also the impact of lateral and bottom boundaries on their dynamics, and the quasi-2D behavior of such systems can contribute to our understanding of large-scale geophysical flows. This is a good example how numerical simulations and laboratory experiments of model systems can contribute to our understanding of geophysical systems.

Acknowledgements HJHC gratefully acknowledge financial support for the 2D Turbulence program from the Nederlandse Organisatie voor Wetenschappelijk Onderzoek I (NWO-I), the Netherlands (formerly known as Stichting voor Fundamenteel Onderzoek der Materie, FOM). The author would like to thank Dr. Matias Duran-Matute from Eindhoven University of Technology for carefully reading the manuscript and providing many suggestions for improvement.

References

Akkermans, R.A.D., A.R. Cieslik, L.P.J. Kamp, R.R. Trieling, H.J.H. Clercx, and G.J.F. Van Heijst. 2008. The three-dimensional structure of an electromagnetically generated dipolar vortex in a shallow fluid layer. *Physics Fluids* 20: 116601.

Akkermans, R.A.D., L.P.J. Kamp, H.J.H. Clercx, and G.J.F. Van Heijst. 2008. Intrinsic three-dimensionality in electromagnetically driven shallow flows. *Europhysics Letters* 83: 24001.

Akkermans, R.A.D., L.P.J. Kamp, H.J.H. Clercx, and G.J.F. Van Heijst. 2010. Three-dimensional flow in electromagnetically driven shallow two-layer fluids. *Physical Review E* 82: 026314.

Albagnac, J., L. Lacaze, P. Brancher, and O. Eiff. 2011. On the existence and evolution of a spanwise vortex in laminar shallow water dipoles. *Physics of Fluids* 23: 086601.

Basdevant, C., B. Legras, and R. Sadourny. 1981. A study of barotropic model flows: Intermittency, waves and predictability. *Journal of Atmospheric Sciences* 38: 2305–2326.

Batchelor, G.K. 1969. Computation of the energy spectrum in two-dimensional turbulence. *The Physics of Fluids Supply* 12: 233–239.

Boffetta, G. 2007. Energy and enstrophy fluxes in the double cascade of two-dimensional turbulence. *Journal of Fluid Mechanics* 589: 253–260.

Boffetta, G., and R.E. Ecke. 2012. Two-dimensional turbulence. *Annual Review of Fluid Mechanics* 44: 427–451.

Boubnov, B.M., S.B. Dalziel, and P.F. Linden. 1994. Source-sink turbulence in a stratified fluid. *Journal of Fluid Mechanics* 261: 273–303.

Bracco, A., J.C. McWilliams, G. Murante, A. Provenzale, and J.B. Weiss. 2000. Revisiting freely decaying two-dimensional turbulence at millennial resolution. *Physics Fluids* 12: 2931–2941.

Buffoni, G., P. Falco, A. Griffa, and E. Zambianchi. 1997. Dispersion processes and residence times in a semi-enclosed basin with recirculating gyres: An application to the Tyrrhenian Sea. *Journal of Geophysical Research* 102: 699–713.

Cardoso, O., D. Marteau, and P. Tabeling. 1994. Quantitative experimental study of the free decay of quasi-two-dimensional turbulence. *Physical Review E* 49: 454–461.

Carnevale, G.F., J.C. McWilliams, Y. Pomeau, J.B. Weiss, and W.R. Young. 1991. Evolution of vortex statistics in two-dimensional turbulence. *Physical Review Letters* 66: 2735–2737.

Carnevale, G.F., J.C. McWilliams, Y. Pomeau, J.B. Weiss, and W.R. Young. 1992. Rates, pathways, and end states of nonlinear evolution in decaying two-dimensional turbulence: Scaling theory versus selective decay. *Physics Fluids A* 4: 1314–1316.

Carnevale, G.F., O.U. Velasco Fuentes, and P. Orlandi. 1997. Inviscid dipole-vortex rebound from a wall or coast. *Journal of Fluid Mechanics* 351: 75–103.

Chavanis, P.H., and J. Sommeria. 1996. Classification of self-organized structures in two-dimensional turbulence: The case of a bounded domain. *Journal of Fluid Mechanics* 314: 267–297.

Chen, D., and G.H. Jirka. 1995. Experimental study of plane turbulent wakes in a shallow water layer. *Fluid Dynamics Research* 16: 11–41.

Clercx, H.J.H., and G.J.F. van Heijst. 2002. Dissipation of kinetic energy in two-dimensional bounded flows. *Physical Review E* 65: 066305.

Clercx, H.J.H., and G.J.F. van Heijst. 2009. Two-dimensional Navier-Stokes turbulence in bounded domains. *Applied Mechanics Reviews* 62: 020802.

Clercx, H.J.H., and G.J.F. van Heijst. 2017. Dissipation of coherent structures in confined two-dimensional turbulence. *Physics of Fluids* 29: 111103.

Clercx, H.J.H., and A.H. Nielsen. 2000. Vortex statistics for turbulence in a container with rigid boundaries. *Physical Review Letters* 85: 752–755.

Clercx, H.J.H., S.R. Maassen, and G.J.F. van Heijst. 1998. Spontaneous spin-up during the decay of 2D turbulence in a square container with rigid boundaries. *Physical Review Letters* 80: 5129–5132.

Clercx, H.J.H., S.R. Maassen, and G.J.F. van Heijst. 1999. Decaying two-dimensional turbulence in square containers with no-slip or stress-free boundaries. *Physics of Fluids* 11: 611–626.

Clercx, H.J.H., A.H. Nielsen, D.J. Torres, and E.A. Coutsias. 2001. Two-dimensional turbulence in square and circular domains with no-slip walls. *European Journal of Mechanics B Fluids* 20: 557–576.

Clercx, H.J.H., G.J.F. van Heijst, and M.L. Zoeteweij. 2003. Quasi-two-dimensional turbulence in shallow fluid layers: The role of bottom friction and fluid layer depth. *Physical Review E* 67: 066303.

Colin de Verdière, A. 1980. Quasi-geostrophic turbulence in a rotating homogeneous fluid. *Geophysical and Astrophysical Fluid Dynamics* 15: 213–251.

Couder, Y. 1984. Two-dimensional grid turbulence in a thin liquid film. *Journal der Physique Letters* 45: L353–L360.

Danilov, S.D., and D. Gurarie. 2000. Quasi-two-dimensional turbulence. *Physics Uspekhi* 43: 863–900.

Danilov, S., F.V. Dolzhanskii, V.A. Dovzhenko, and V.A. Krymov. 2002. Experiments on free decay of quasi-two-dimensional turbulent flows. *Physical Review E* 65: 036316.

Dolzhanskii, F.V., V.A. Krymov, and DYu. Manin. 1992. An advanced experimental investigation of quasi-two-dimensional shear flows. *Journal of Fluid Mechanics* 241: 705–722.

Duran-Matute, M., J. Albagnac, L.P.J. Kamp, and G.J.F. van Heijst. 2010. Dynamics and structure of decaying shallow dipolar vortices. *Physics of Fluids* 22: 116606.

Duran-Matute, M., R.R. Trieling, and G.J.F. van Heijst. 2011. Scaling and asymmetry in an electromagnetically forced dipolar flow structure. *Physical Review E* 83: 016306.

Duran-Matute, M., L.P.J. Kamp, R.R. Trieling, and G.J.F. van Heijst. 2012. Regimes of two-dimensionality of decaying shallow axisymmetric swirl flows with background rotation. *Journal of Fluid Mechanics* 691: 214–244.

Falco, P., A. Griffa, P.-M. Poulain, and E. Zambianchi. 2000. Transport properties in the Adriatic Sea as deducted from drifter data. *Journal of Physical Oceanography* 30: 2055–2071.

Fang, L., and N.T. Ouellette. 2017. Multiple stages of decay in two-dimensional turbulence. *Physics of Fluids* 29: 111105.

Fincham, A.M., T. Maxworthy, and G.R. Spedding. 1996. Energy dissipation and vortex structure in freely decaying, stratified grid turbulence. *Dynamics of Atmospheres and Oceans* 23: 155–169.

Fjørtoft, R. 1953. On the changes in the spectral distribution of kinetic energy for two-dimensional non-divergent flow. *Tellus* 5: 69–74.

Fornberg, B. 1977. Numerical study of 2-D turbulence. *Journal of Computational Physics* 25: 1–31.

Hansen, A.E., D. Marteau, and P. Tabeling. 1998. Two-dimensional turbulence and dispersion in a freely decaying system. *Physical Review E* 58: 7261–7271.

Hopfinger, E.J., F.K. Browand, and Y. Gagne. 1982. Turbulence and waves in a rotating tank. *Journal of Fluid Mechanics* 125: 505–534.

Jirka, G.H. 2001. Large scale flow structures and mixing processes in shallow flows. *Journal of Hydraulic Research* 39: 567–573.

Kato, T. 1984. Remarks on zero viscosity limit for nonstationary Navier-Stokes flows with boundary. In *Proceedings of the seminar on nonlinear partial differential equations*, pp. 85–98, MRSI, Berkely.

Keetels, G.H., H.J.H. Clercx, and G.J.F. van Heijst. 2010. On the origin of spin-up processes in decaying two-dimensional turbulence. *European Journal of Mechanics B Fluids* 29: 1–8.

Keetels, G.H., W. Kramer, H.J.H. Clercx, and G.J.F. van Heijst. 2011. On the Reynolds number scaling of vorticity production at no-slip walls during vortex-wall collisions. *Theoretical and Computational Fluid Dynamics* 25: 293–300.

Kellay, H., and W.I. Goldburg. 2002. Two-dimensional turbulence: A review of some recent experiments. *Reports on Progress in Physics* 65: 845–894.

Kellay, H., X.L. Wu, and W.I. Goldburg. 1995. Experiments with turbulent soap films. *Physical Review Letters* 74: 3975–3978.

Kelley, D.H., and N.T. Ouellette. 2011. Onset of three-dimensionality in electromagnetic thin-layer flows. *Physics of Fluids* 23: 045103.

Kraichnan, R.H. 1967. Inertial ranges in two-dimensional turbulence. *Physics of Fluids* 10: 1417–1423.

Kraichnan, R.H. 1971. Inertial-range transfer in two and three-dimensional turbulence. *Journal of Fluid Mechanics* 47: 525–535.

Kramer, W., H.J.H. Clercx, and G.J.F. van Heijst. 2007. Vorticity dynamics of a dipole colliding with a no-slip wall. *Physics of Fluids* 19: 126603.

Legras, B., P. Santangelo, and R. Benzi. 1988. High-resolution numerical experiments for forced two-dimensional turbulence. *Europhysics Letters* 5: 37–42.

Leith, C.E. 1968. Diffusion approximation for two-dimensional turbulence. *Physics of Fluids* 11: 671–673.

Li, S., and D. Montgomery. 1996. Decaying two-dimensional turbulence with rigid walls. *Physics Letters A* 218: 281–291.

Li, S., D. Montgomery, and W.B. Jones. 1997. Two-dimensional turbulence with rigid circular walls. *Theoretical and Computational Fluid Dynamics* 9: 167–181.

Liechtenstein, L., F.S. Godeferd, and C. Cambon. 2005. Nonlinear formation of structures in rotating stratified turbulence. *Journal of Turbulence* 6: N24.

Lilly, D.K. 1971. Numerical simulation of developing and decaying two-dimensional turbulence. *Journal of Fluid Mechanics* 45: 395–415.

Lin, J.C., M. Ozgoren, and D. Rockwell. 2003. Space-time development of the onset of a shallow-water vortex. *Journal of Fluid Mechanics* 485: 33–66.

Maassen, S.R., H.J.H. Clercx, and G.J.F. van Heijst. 1999. Decaying quasi-2D turbulence in a stratified fluid with circular boundaries. *Europhysics Letters* 46: 339–345.

Maassen, S.R., H.J.H. Clercx, and G.J.F. van Heijst. 2002. Self-organization of quasi-two-dimensional turbulence in stratified fluids in square and circular containers. *Physics of Fluids* 14: 2150–2169.

Maassen, S.R., H.J.H. Clercx, and G.J.F. van Heijst. 2003. Self-organization of decaying quasi-2D turbulence in stratified fluids in rectangular containers. *Journal of Fluid Mechanics* 495: 19–33.

Marteau, D., O. Cardoso, and P. Tabeling. 1995. Equilibrium states of two-dimensional turbulence: An experimental study. *Physical Review E* 51: 5124–5127.

Matthaeus, W.H., and D. Montgomery. 1980. Selective decay hypothesis at high mechanical and magnetic reynolds numbers. *Annals of the New York Academy of Sciences* 357: 203–222.

Matthaeus, W.H., W.T. Stribling, D. Martinez, S. Oughton, and D. Montgomery. 1991. Decaying, two-dimensional, Navier-Stokes turbulence at very long times. *Physics D* 51: 531–538.

McWilliams, J.C. 1984. The emergence of isolated coherent vortices in turbulent flow. *Journal of Fluid Mechanics* 146: 21–43.

Molenaar, D., H.J.H. Clercx, and G.J.F. van Heijst. 2004. Angular momentum of forced two-dimensional turbulence on a square no-slip domain. *Physics D* 196: 329–340.

Montgomery, D., and G.R. Joyce. 1974. Statistical mechanics of negative temperature states. *Physics of Fluids* 17: 1139–1145.

Nguyen van yen, R., M. Farge, and K. Schneider. 2011. Energy dissipating structures produced by walls in two-dimensional flows at vanishing viscosity. *Physical Review Letters* 106: 184502.

Nguyen van yen, N., M. Waidmann, R. Klein, M. Farge, and K. Schneider. 2018. Energy dissipation caused by boundary layer instability at vanishing viscosity. *Journal of Fluid Mechanics* 849: 676–717.

Onsager, L. 1949. Statistical hydrodynamics. *Nuovo Cimento* 6: 279–287.

Orlandi, P. 1990. Vortex dipole rebound from a wall. *Physics of Fluids A* 2: 1429–1436.

Paret, J., and P. Tabeling. 1998. Intermittency in the two-dimensional inverse cascade of energy: Experimental observations. *Physics of Fluids* 10: 3126–3136.

Pointin, Y.B., and T.S. Lundgren. 1976. Statistical mechanics of two-dimensional vortices in a bounded domain. *Physics of Fluids* 19: 1459–1470.

Proudman, J. 1916. On the motion of solids in a liquid possessing vorticity. *Proceedings of the Royal Society A* 92: 408–424.

Rivera, M.K., and R.E. Ecke. 2005. Pair dispersion and doubling time statistics in two-dimensional turbulence. *Physical Review Letters* 95: 194503.

Rivera, M.K., and R.E. Ecke. 2016. Lagrangian statistics in weakly forced two-dimensional turbulence. *Chaos* 26: 013103.

Rutgers, M.A. 1998. Forced 2D turbulence: Experimental evidence of simultaneous inverse energy and forward enstrophy cascades. *Physical Review Letters* 81: 2244–2247.

Santangelo, P., R. Benzi, and B. Legras. 1989. The generation of vortices in high-resolution, two-dimensional decaying turbulence and the influence of initial conditions on the breaking of self-similarity. *Physics of Fluids A* 1: 1027–1034.

Schneider, K., and M. Farge. 2005. Decaying two-dimensional turbulence in a circular container. *Physical Review Letters* 95: 244502.

Schneider, K., and M. Farge. 2008. Final states of decaying 2D turbulence in bounded domains: Influence of the geometry. *Physics D* 237: 2228–2233.

Smith, L.M., and V. Yakhot. 1993. Bose condensation and small-scale structure generation in a random force driven 2D turbulence. *Physical Review Letters* 71: 352–355.

Sommeria, J. 1986. Experimental study of the two-dimensional inverse energy cascade in a square box. *Journal of Fluid Mechanics* 170: 139–168.

Sous, D., N. Bonneton, and J. Sommeria. 2004. Turbulent vortex dipoles in a shallow water layer. *Physics of Fluids* 16: 2886–2898.

Sous, D., N. Bonneton, and J. Sommeria. 2005. Transition from deep to shallow water layer: formation of vortex dipoles. *European Journal of Mechanics-B/Fluids* 24: 19–32.

Sutherland, D., C. Macaskill, and D.G. Dritschel. 2013. The effect of slip length on vortex rebound from a rigid boundary. *Physics of Fluids* 25: 093104.

Tabeling, P. 2002. Two-dimensional turbulence: A physicist approach. *Physics Reports* 362: 1–62.

Tabeling, P., S. Burkhart, O. Cardoso, and H. Willaime. 1991. Experimental study of freely decaying two-dimensional turbulence. *Physical Review Letters* 67: 3772–3775.

Taylor, G.I. 1917. Motions of solids in fluids when the flow is not irrotational. *Proceedings of the Royal Society* 93: 99–113.

Tithof, J., B.C. Martell, and D.H. Kelley. 2018. Three-dimensionality of one- and two-layer electromagnetically driven thin-layer flows. *Physical Review Fluids* 3: 064602.

Uijttewaal, W.S.J. 2014. Hydrodynamics of shallow flows: Application to rivers. *Journal of Hydraulic Research* 52: 157–172.

Uijttewaal, W.S.J., and R. Booij. 2000. Effects of shallowness on the development of free-surface mixing layers. *Physics of Fluids* 12: 392–402.

Uijttewaal, W.S.J., and G.H. Jirka. 2003. Grid turbulence in shallow flows. *Journal of Fluid Mechanics* 489: 325–344.

Van Heijst, G.J.F., and H.J.H. Clercx. 2009. Laboratory modeling of geophysical vortices. *Annual Review of Fluid Mechanics* 41: 143–164.

Van Heijst, G.J.F., H.J.H. Clercx, and D. Molenaar. 2006. The effects of solid boundaries on confined two-dimensional turbulence. *Journal of Fluid Mechanics* 554: 411–431.

Weiss, J.B., and J.C. McWilliams. 1993. Temporal scaling behavior of decaying two-dimensional turbulence. *Physics of Fluids A* 5: 608–621.

Wells, J., and Ya..D.. Afanasyev. 2004. Decaying quasi-two-dimensional turbulence in a rectangular container: Laboratory experiments. *Geophysical and Astrophysical Fluid Dynamics* 98: 1–20.

Yap, C.T., and C.W. van Atta. 1993. Experimental studies of the development of quasi-two-dimensional turbulence in stably stratified fluid. *Dynamics of Atmospheres and Oceans* 19: 289–323.

Chapter 7
Turbulent Dispersion

Benoit Cushman-Roisin

Abstract This chapter proposes a novel method for the modeling of turbulent dispersion in the absence of buoyancy effects. Starting from a few salient observations, properties that an effective model should possess are identified, and a model is subsequently developed to incorporate these necessary properties. The model turns out to make use of fractional calculus and leads to a non-local operator, which is challenging from a computational perspective. Applications to dispersion by turbulent jets (round and planar) and the marine Ekman layer (surface and bottom) demonstrate the usefulness of the model.

7.1 Introduction

The purpose of this chapter is not to review the field observations, laboratory experiments, or turbulence-resolving numerical simulations that have contributed to our present knowledge of turbulent dispersion. Such reviews can be found in Csanady (1973), Fischer et al. (1979), Roberts and Webster (2002), Garrett (2006), and Cushman-Roisin (2013, and references therein). Rather, our purpose is to take the salient properties thus discovered and to formulate a modeling method that reproduces those properties without the need for resolution of turbulent fluctuations. Such non-eddy-resolving methods are necessary in the pursuit of large-scale ocean modeling, especially at the basin scale.

The vast majority of non-eddy-resolving models handle unresolved, sub-grid processes by means of an eddy diffusivity D_E (eddy viscosity ν_E for momentum), which is then made to vary heuristically with space and time according to the propensity of the broader flow to generate eddies via instabilities, such as shear instability. A prime example is the parameterization proposed by Joseph Smagorinsky (1963),

B. Cushman-Roisin (✉)
Thayer School of Engineering, Dartmouth College, Hanover, New Hampshire 03755, USA
e-mail: Benoit.Cushman-Roisin@dartmouth.edu

H. Schuttelaars et al. (eds.), *The Mathematics of Marine Modelling*,
Mathematics of Planet Earth 9, https://doi.org/10.1007/978-3-031-09559-7_7

$$D_E \sim \nu_E = \Delta x \Delta y \sqrt{\left(\frac{\partial u}{\partial x}\right)^2 + \left(\frac{\partial v}{\partial y}\right)^2 + \frac{1}{2}\left(\frac{\partial u}{\partial y} + \frac{\partial v}{\partial x}\right)^2}, \tag{7.1}$$

which increases with the divergence and shear of the local flow field under the reasoning that the greater the gradient of the velocity components, the greater the propensity of the flow to develop eddy-generating instabilities. Somewhat more sophisticated models, such as the family of $\mathtt{k}$ turbulence closure models ($\mathtt{k}$, $\mathtt{k}-\varepsilon$, $\mathtt{k}-\omega$; for a summary, see Cushman-Roisin and Beckers (2011), Sects. 14.3 and 14.4), solve an evolution equation for the turbulent kinetic energy $\mathtt{k}$ and make the eddy diffusivity (viscosity) dependent of the level of turbulent kinetic energy. For example (Umlauf and Burchard 2005), the eddy diffusivity may be expressed as:

$$D_E = C\,\frac{\mathtt{k}^2}{\varepsilon}, \tag{7.2}$$

in which the factor C depends on the velocity shear, and ε is the energy dissipation rate, which like $\mathtt{k}$ needs its own evolution equation. The function C and several terms in the evolution equations for $\mathtt{k}$ and ε are formulated based more on inferred phenomenology and empirical evidence than basic physics.

Likewise, in the presence of density stratification (Umlauf and Burchard 2005), the eddy diffusivity (viscosity) is made to depend on the local Richardson number in such a way that when buoyancy forces are stabilizing (destabilizing), the diffusivity is reduced (augmented). Again, the formulations are heuristic and accepted based more on post-model validation than pre-model physics. Some values have also been inferred from measurements of dispersion (e.g., Yanagi et al. 1982), by what might be called reverse engineering.

Aside from the fact that these parameterizations involve much heuristics and therefore stand on shaky grounds, the eddy diffusivity approach suffers from a major deficiency, namely that it predicts a growth proportional to the square root of time for the size of a tracer patch, with $L \simeq \sqrt{2D_E t}$ in which L is the size of the patch undergoing dispersion and t is time. A multiplicity of observations (Cushman-Roisin 2013) point out beyond a doubt that patch size in a turbulent flow environment grows rather like the first power of time or even faster (like $t^{\frac{3}{2}}$), and a better model ought to predict $L \simeq u_* t$ in which $u_* = \sqrt{2\mathtt{k}}$ is a turbulent velocity or $L \simeq \varepsilon^{\frac{1}{2}} t^{\frac{3}{2}}$ in which ε is the energy dissipation rate. A clear example (albeit from the atmosphere, not the ocean) is shown in Fig. 7.1. The unmistakable triangular shape of the plume indicates linear growth over distance, which in a larger-scale and therefore locally uniform wind corresponds to spreading proportional to the first power of time.[1] It should be noted that, for a case like this, spatially dependent eddy diffusivities as those proposed in (7.1) and (7.2) are of no use. The straight path of the plume indicates a uniform wind field from which we can presume homogeneous turbulence conditions

[1] Because buoyancy affects the vertical dispersion of hot plumes, it is more instructive when considering mechanical dispersion alone to use the horizontal view provided by aerial or satellite imagery than ground-level visualization that inevitably looks sideways.

Fig. 7.1 Aerial view of an ash and smoke plume emanating from the Mt. Etna volcano in Sicily, captured by the MODIS sensor onboard NASA's Terra satellite, on 27 October 2002. Note the unmistakable triangular shape of the plume, which indicates linear growth over time in the horizontal plane. *Photo credit* NASA

and thus a uniform eddy diffusivity. The fact that the plume does not widen like the square root of distance points to a fundamental flaw with the eddy diffusivity approach. Put another way, the mathematics of turbulent dispersion, at least in this case, should be governed by an operator other than a second derivative as in molecular diffusion. This argument was already voiced by Richardson and Stommel (1948) who remarked in the context of marine dispersion that "The variation of K depends on a geometrical quantity σ, and Fick's equation is also geometrical in so far as it contains $\partial^2/\partial x^2$. For this reason it is difficult to regard the variation of K as an outer circumstance detached from Fick's equation. There appears to be a fault in the equation itself." (Note: In this quote the quantities K and σ stand respectively for the diffusivity and patch size, noted D_E and L above.). Notwithstanding their own statement, Richardson and Stommel (1948) retained the eddy diffusivity concept and Fick's equation, preferring to rely on a diffusivity that grows as a power of patch size and proposing (in the present notation) $D_E \sim \sigma^\alpha$ with α varying from 1.0 to 1.4. In a follow-up study of turbulent dispersion in the sea, Stommel (1949) reiterated the conclusion that the Fickian model fails to describe horizontal diffusion in the sea.

Richardson and Stommel (1948) were not the only ones to suggest a patch-size-dependent diffusivity; others followed, including Okubo (1971) and Clark et al. (1996), among others. But this is wholly inadequate in modeling. Indeed, how could a model be so constructed when the system includes multiple overlapping patches at various stages of development? What should be the local value of D_E where an older, wider patch overtakes a more recent and smaller patch? To be effective, a model of turbulent dispersion ought to include a manner by which the vigor of dispersion automatically adapts to the spatial distribution of the tracer's concentration. The answer lies in the formulation of a different operator than the second derivative preceded by an eddy diffusivity. Put another way, turbulent dispersion in the environment proceeds in a qualitatively different manner than molecular diffusion with an enhanced and varying diffusivity, and one ought to pursue other mathematical formulations.

7.2 Model Requirements

Here, we are not interested in developing arguments about the statistics of dispersion such as considering the evolution of two-particle separation or moments of displacements (e.g., Taylor 1921; Richardson and Stommel 1948; Hunt 1985; Ferrari 2007). Instead, we are strongly directed toward the development of a mathematical tool that can readily be implemented in existing models, such as basin-wide oceanographic models, in which unresolved sub-grid scale processes can be represented on the resolving grid by means of calculations that provide the spatio-temporal evolution of concentration fields.

The considerations outlined in the preceding section lead us to formulate a model of turbulent dispersion that possesses the following three properties:

1. It must be based on physical principles rather than chiefly be validated after trials;
2. It should lead to patch growth proportional to the first or higher power of time; for example, in wall turbulence characterized by a eddy velocity $u_* = \sqrt{\tau_{wall}/\rho}$, it should lead to patch growth proportional to the first power of time ($L \sim u_* t$); and
3. It must be such that the vigor of dispersion automatically adapts to the spatial distribution of the tracer's concentration.

To establish a working model, it is helpful to recall the essence of turbulent dispersion. The cause of spreading is the eddy field inside which the tracer patch resides, with eddies moving, distorting and stirring the patch (Fig. 7.2). The eddies that are significantly larger than the patch sweep the latter around their orbits, merely changing its location without affecting its shape or size significantly. At the opposite end of the spectrum, the eddies much smaller than the patch size only stir the inside of the patch, while marginally increasing its extent along the edges. In contrast, the eddies of diameter comparable to the patch size greatly distort it, enlarge its overall extent by means of stretching, and cause the most dispersion. While the eddy population may remain statistically unchanged over time, the eddies take their turn in effecting dispersion, with the smaller eddies acting first when the patch is small and increasingly larger eddies acting sequentially as the patch widens. In terms of an eddy diffusivity, this means that the value of the diffusivity must somehow vary with the dominant scale of the patch. Thus, if the patch is characterized by a dominant wavenumber[2] $k \sim \frac{1}{L}$, the diffusivity must be a function of k, and as k evolves, so does the eddy diffusivity, locally and instantaneously without recording the time elapsed or distance covered since the start.

The rate of growth of the patch depends on how the orbital velocity changes with eddy size. Growth rate is constant in time when eddies all share the same orbital velocity scale regardless of diameter (as in wall turbulence characterized by a single orbital velocity u_*) or is increasing with time when larger eddies have larger orbital velocities (as in inertial turbulence cascade). Growth proportional to the square root of

[2] Note the subtlety in notation: straight $\mathtt{k}$ for the turbulent kinetic energy, now italic k for the wavenumber magnitude, and, a bit later, bold $\mathbf{k}$ for the wavenumber vector.

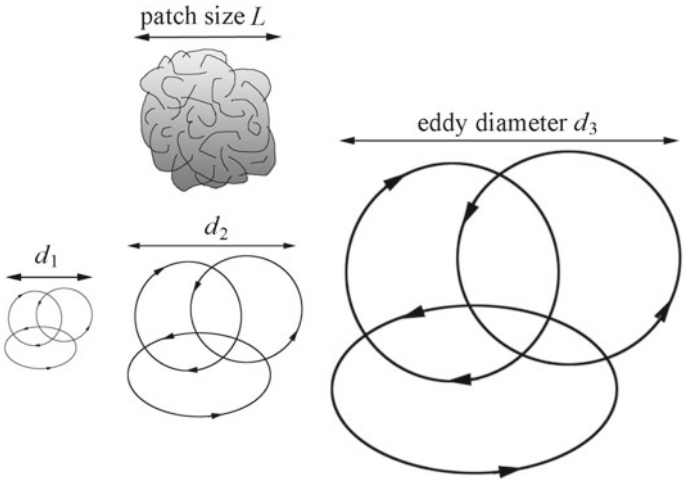

Fig. 7.2 Patch of a passive tracer of size L in a field of eddies of various scales. Eddies of diameter much shorter than the patch size ($d_1 << L$) stir the inside of the patch while marginally increasing its size along its edges. Eddies of size comparable to that of the patch ($d_2 \sim L$) greatly distort the patch and augment its size by means of stretching. Finally, eddies much larger than the patch ($d_3 >> L$) merely translate the patch around their orbits, causing large displacements but little dispersion. The conclusion is that the eddies that most effectively contribute to the enlargement of the patch are those of size comparable to the patch size. As the patch grows in time, eddies take their turn at being those of the most effective kind

time, as a constant diffusivity would have it, would imply growth that slows down in time (rate of growth proportional to $t^{-\frac{1}{2}}$) and would correspond to a situation where eddy orbital velocity decreases with increasing size, a situation never encountered in geophysical turbulence.

To put these elements in mathematical terms, let us assume that the eddy field is a collection of vortices of various sizes d with orbital velocity $u_*(d)$, i.e. with all eddies of comparable size having similar orbital velocities. The corresponding half-turnaround time is $\Delta t = \pi d/u_*(d)$, and over this time the displacement caused by the eddies of size d is one diameter. In terms of an eddy diffusivity, we would have

$$D_E = \frac{1}{2}\frac{dL^2}{dt} = L\frac{dL}{dt} = L\frac{d}{\Delta t} = \frac{1}{\pi}Lu_*(d). \tag{7.3}$$

As remarked earlier, the eddies contributing most to the dispersion are those with diameters comparable to the patch size. Thus, the dominant contribution to D_E is due to $d = \mathcal{O}(L)$ and

$$D_E = \mathcal{O}(Lu_*(L)), \tag{7.4}$$

or, in terms of the dominant wavenumber $k \sim L^{-1}$,

$$D_E = \mathcal{O}\left(\frac{u_*(k^{-1})}{k}\right). \tag{7.5}$$

In Fourier space, the diffusion term $D_E \nabla^2 c$ of a concentration field $c(\mathbf{x}, t)$ is $-k^2 D_E\ \hat{c}(\mathbf{k}, \mathbf{t})$, and the preceding considerations suggest that we replace this by

$$-\,k^2 D_E\ \hat{c} \quad \rightarrow \quad -C\ k u_*(k^{-1})\ \hat{c}, \tag{7.6}$$

with a constant dimensionless coefficient C in front and in which k stands for the magnitude of the three-dimensional wavenumber $\mathbf{k}$. The inverse Fourier transform provides the substitution expression in space:

$$D_E\ \nabla^2 c \quad \rightarrow \quad -C\ \frac{1}{(2\pi)^{\frac{3}{2}}} \iiint_{-\infty}^{\infty} k u_*(k^{-1})\ \hat{c}(\mathbf{k}, \mathbf{t})\ \mathbf{e}^{\mathbf{ik}\cdot\mathbf{x}}\ \mathbf{dk}. \tag{7.7}$$

For wall turbulence with uniform orbital velocity u_* across scales, the substituted dispersion operator ought to be

$$\frac{2Cu_*}{\pi^2} \iiint \frac{c(\mathbf{x}', t) - c(\mathbf{x}, t)}{|\mathbf{x}' - \mathbf{x}|^4}\, d\mathbf{x}\,, \tag{7.8}$$

while for the Kolmogorov inertial cascade with $u_*(k^{-1}) \simeq (\varepsilon/k)^{\frac{1}{3}}$, it is

$$(...)\ C\varepsilon^{\frac{1}{3}} \iiint \frac{c(\mathbf{x}', t) - c(\mathbf{x}, t)}{|\mathbf{x}' - \mathbf{x}|^{\frac{11}{3}}}\, d\mathbf{x}\,, \tag{7.9}$$

in which the triple integral covers the 3D infinite space.[3] We recognize here expressions of the fractional Laplacian (Kwaśnicki 2017).

7.3 Model Development

We now proceed to re-derive the preceding alternative expressions from basic physics. For this, we begin with the elementary advection equation for a passive tracer field $c(\mathbf{x}, t)$ in three dimensions:

$$\frac{\partial c}{\partial t} + \mathbf{u} \cdot \nabla c = 0, \tag{7.10}$$

in which the velocity field $\mathbf{u}$ is a three-dimensional random flow field with known probability density function (pdf) $f(\mathbf{u})$. Over a sufficiently short time interval Δt,

[3] The treatment of boundaries is delicate and will be addressed later in the context of one-dimensional modeling.

the patch is merely advected from $\mathbf{x} - \mathbf{u}\Delta t$ to $\mathbf{x}$, i.e., $c(\mathbf{x}, t + \Delta t) = c(\mathbf{x} - \mathbf{u}\Delta t, t)$, but since the value of $\mathbf{u}$ is one of many, the actual concentration will be the expected value over all possible values of $\mathbf{u}$:

$$c(\mathbf{x}, t + \Delta t) = \iiint c(\mathbf{x} - \mathbf{u}\Delta t, t)\ f(\mathbf{u})\ d\mathbf{u}. \tag{7.11}$$

Note in passing how we proceeded by solving the equation first and then averaging its solution, in complete reversal from Osborne Reynolds' original decomposition with an averaging of the equations first followed by (an attempt at) their solutions. Since the pdf of $\mathbf{u}$ must be normalized ($\iiint f(\mathbf{u})d\mathbf{u} = 1$), this can be rewritten as

$$\frac{c(\mathbf{x}, t + \Delta t) - c(\mathbf{x}, t)}{\Delta t} = \iiint \frac{c(\mathbf{x} - \mathbf{u}\Delta t, t) - c(\mathbf{x}, t)}{\Delta t}\ f(\mathbf{u})\ d\mathbf{u}. \tag{7.12}$$

Epps and Cushman-Roisin (2018) have shown that such an expression may be taken to the limit $\Delta t \to 0$ as long as the pdf $f(\mathbf{u})$ is a stable α-Lévy distribution (a family of pdf's with parameter $0 < \alpha \leq 2$), which we henceforth denote $f_\alpha(\mathbf{u})$. The general expression for this type of distribution is best given in terms of its inverse Fourier transform[4]:

$$f_\alpha(\mathbf{u}) = \frac{1}{(2\pi)^3} \iiint e^{-|\gamma \mathbf{k_u}|^\alpha}\ e^{i\mathbf{k_u}\cdot\mathbf{u}}\ d\mathbf{k_u} \tag{7.13}$$

in which the factor $\gamma > 0$ is a scaling factor (also called elasticity) with the same dimensions as $\mathbf{u}$, which is length per time here. For large argument $\mathbf{u}$ and for $\alpha < 2$, the tail of the distribution is given by Nolan (2006), Epps and Cushman-Roisin (2018):

$$f_\alpha(u) \simeq \frac{C_\alpha\ \gamma^\alpha}{|\mathbf{u}|^{\alpha+3}}\ , \tag{7.14}$$

in which the coefficient C_α is given by

$$C_\alpha = \frac{2^\alpha \Gamma\left(\frac{\alpha+3}{2}\right)}{\pi^{\frac{3}{2}} |\Gamma(-\frac{\alpha}{2})|}\ . \tag{7.15}$$

Particular values are $C_2 = 0$ (the pdf falls off exponentially rather than algebraically), $C_1 = \frac{1}{\pi^2}$ and $C_{2/3} = 0.066011$.

For $\alpha = 2$, the distribution is Gaussian (the only member of the family with non-algebraic tails):

$$f_2(\mathbf{u}) = \frac{1}{(4\pi)^{\frac{3}{2}}\gamma^3}\ e^{-\frac{|\mathbf{u}|^2}{4\gamma^2}}. \tag{7.16}$$

[4] We assume here velocity distributions with zero mean. Adding a mean component $\bar{\mathbf{u}}$ to $\mathbf{u}$ is relatively straightforward and yields the expected advection term $\bar{\mathbf{u}} \cdot \nabla c$ added to the time rate of change $\partial c/\partial t$.

The non-singular limit $\Delta t \to 0$ is obtained by taking $\gamma = \sqrt{D/\Delta t}$ so that Eq. (7.12) becomes

$$\frac{c(\mathbf{x}, t+\Delta t) - c(\mathbf{x}, t)}{\Delta t} = \left(\frac{1}{4\pi D}\right)^{\frac{3}{2}} \Delta t^{\frac{1}{2}} \iiint [c(\mathbf{x} - \mathbf{u}\Delta t, t) - c(\mathbf{x}, t)]\, e^{-\frac{|\mathbf{u}|^2 \Delta t}{4D}}\, d\mathbf{u}. \tag{7.17}$$

Defining the anterior position $\mathbf{x}' = \mathbf{x} - \mathbf{u}\Delta t$, switching from $\mathbf{u}$ to $\mathbf{x}'$ as the integration variable (with $d\mathbf{u} = -d\mathbf{x}/\Delta t^3$), and taking the limit of a vanishing time interval Δt, we obtain

$$\begin{aligned}
\frac{\partial c}{\partial t} &= \left(\frac{1}{4\pi D}\right)^{\frac{3}{2}} \lim_{\Delta t \to 0} \Delta t^{-\frac{5}{2}} \iiint [c(\mathbf{x}', t) - c(\mathbf{x}, t)]\, e^{-\frac{|\mathbf{x}' - \mathbf{x}|^2}{4D\Delta t}}\, d\mathbf{x}' \\
&= \left(\frac{1}{4\pi D}\right)^{\frac{3}{2}} \lim_{\Delta t \to 0} \Delta t^{-\frac{5}{2}} \iiint \left[\frac{1}{2}(x'-x)^2 \frac{\partial^2 c}{\partial x^2} + \frac{1}{2}(y'-y)^2 \frac{\partial^2 c}{\partial y^2} + \frac{1}{2}(z'-z)^2 \frac{\partial^2 c}{\partial z^2}\right] \\
&\qquad \times e^{-\frac{(x'-x)^2 + (y'-y)^2 + (z'-z)^2}{4D\Delta t}}\, d\mathbf{x}' \\
&= \frac{2D}{\pi^{\frac{3}{2}}} \iiint \left[\xi^2 \frac{\partial^2 c}{\partial x^2} + \eta^2 \frac{\partial^2 c}{\partial y^2} + \zeta^2 \frac{\partial^2 c}{\partial z^2}\right] e^{-\xi^2 - \eta^2 - \zeta^2}\, d\xi d\eta d\zeta = D\, \nabla^2 c.
\end{aligned} \tag{7.18}$$

Thus, we recover Fickian diffusion when taking $\alpha = 2$. Since this predicts patch growth proportional to the square root of time, it is deemed unsuitable to model turbulent dispersion, and we reject the possibility $\alpha = 2$.

Put another way, the probability density function of velocity fluctuations must have a so-called "fat tail" (that is, an algebraically decaying tail instead of an exponential tail) in order to be applicable to turbulence. This stands to reason since turbulence is characterized by a population of eddies, some of which may be as large as the entire domain, leading to the likelihood of displacements always as large as the patch size.

For $\alpha = 1$, the pdf is the Cauchy distribution,

$$f_1(\mathbf{u}) = \frac{1}{\pi^2} \frac{a u_*}{(|\mathbf{u}|^2 + a^2 u_*^2)^2}\,, \tag{7.19}$$

with $\gamma = a u_*$ (a being a free multiplicative constant), and Eq. (7.12) becomes

$$\begin{aligned}
\frac{\partial c}{\partial t} &= \frac{a u_*}{\pi^2} \lim_{\Delta t \to 0} \iiint \frac{c(\mathbf{x} - \mathbf{u}\Delta t, t) - c(\mathbf{x}, t)}{\Delta t} \frac{1}{(|\mathbf{u}|^2 + a^2 u_*^2)^2}\, d\mathbf{u}. \\
&= \frac{a u_*}{\pi^2} \lim_{\Delta t \to 0} \iiint \frac{c(\mathbf{x}', t) - c(\mathbf{x}, t)}{(|\mathbf{x}' - \mathbf{x}|^2 + a^2 u_*^2 \Delta t^2)^2}\, d\mathbf{x}' \\
&= C\, u_* \iiint \frac{c(\mathbf{x}', t) - c(\mathbf{x}, t)}{|\mathbf{x}' - \mathbf{x}|^4}\, d\mathbf{x}',
\end{aligned} \tag{7.20}$$

with $C = a/\pi^2$, in which we recognize the integral operator anticipated in (7.8). So, we are assured that this model will produce tracer patches that grow with the first power of time. In other words, the choice $\alpha = 1$ is suitable for the modeling of dispersion in shear turbulence characterized by a single turbulent velocity u_*. This is

the case, for example, near the surface of the ocean under the action of a wind stress $\tau_{wind} = \rho_{water} u_*^2$, in which the u_* value is unequivocally set by the surface stress.

The pdf for $\alpha = \frac{2}{3}$, which we anticipate to correspond to inertial turbulence (Kolmogorov cascade), cannot be expressed in simpler terms than expression (7.13), but its asymptotic behavior for large values of $\mathbf{u}$ is given in (7.14)–(7.15):

$$f_{2/3} \simeq \frac{C_{2/3}\, \gamma^{\frac{2}{3}}}{|\mathbf{u}|^{\frac{11}{3}}} \qquad \text{with} \qquad C_{2/3} = 0.066011. \tag{7.21}$$

Since inertial turbulence is governed by the energy dissipation rate ε of dimensions L^2/T^3, we now take $\gamma = a\sqrt{\varepsilon \Delta t}$, and Eq. (7.12) in the limit of $\Delta t \to 0$ becomes

$$\begin{aligned} \frac{\partial c}{\partial t} &= C_{2/3}\, a^{\frac{2}{3}} \lim_{\Delta t \to 0} (\varepsilon \Delta t)^{\frac{1}{3}} \iiint \frac{c(\mathbf{x} - \mathbf{u}\Delta t, t) - c(\mathbf{x}, t)}{\Delta t} |\mathbf{u}|^{-\frac{11}{3}}\, d\mathbf{u} \\ &= C\, \varepsilon^{\frac{1}{3}} \lim_{\Delta t \to 0} \frac{\Delta t^{\frac{1}{3}}}{\Delta t} \iiint [c(\mathbf{x}', t) - c(\mathbf{x}, t)] \left(\frac{|\mathbf{x}' - \mathbf{x}|}{\Delta t} \right)^{-\frac{11}{3}} \frac{d\mathbf{x}'}{\Delta t^3} \\ &= C\, \varepsilon^{\frac{1}{3}} \iiint \frac{c(\mathbf{x}', t) - c(\mathbf{x}, t)}{|x' - \mathbf{x}|^{\frac{11}{3}}}\, d\mathbf{x}', \end{aligned} \tag{7.22}$$

in which the two multiplicative constants were lumped into one, $C_{3/2}\, a^{\frac{2}{3}} = C$.

The general case $\alpha < 2$ is treated briefly as follows. The asymptotic expression of $f_\alpha(\mathbf{u})$ generates a factor $|\mathbf{u}|^{-\alpha-3}$, which after use of $\mathbf{u} = (\mathbf{x} - \mathbf{x}')/\Delta t$ provides a factor $\Delta t^{\alpha+3}$. This is in addition to the Δt^{-1} factor in $[c(\mathbf{x}', t) - c(\mathbf{x}, t)]/\Delta t$ and another factor Δt^{-3} arising from the change of variable $d\mathbf{u} = d\mathbf{x}/\Delta t^3$. The net is a factor $\Delta t^{\alpha-1}$. The limit $\Delta t \to 0$ will be meaningful only if this power of Δt is negated by a factor of opposing power in γ^α in the numerator of the asymptotic expression (7.14) of $f_\alpha(\mathbf{u})$. Thus, γ must be made proportional to $\Delta t^{\frac{1-\alpha}{\alpha}}$, and we write

$$\gamma = q^{\frac{1}{\alpha}}\, \Delta t^{\frac{1-\alpha}{\alpha}}, \tag{7.23}$$

with the quantity q having the dimensions L^α/T so that γ has the required dimensions of a velocity. This sets the rule to ascribe the value of α: Identify the physical quantity that governs the nature of the turbulent flow field, determine its dimensions, and then raise this quantity to the power that transforms its dimensions to the form L^α/T^1; the exponent of L then sets the value to be adopted for α. For example, in wall turbulence, the quantity governing the turbulent field is the friction velocity u_*, with dimensions L/T; thus, $\alpha = 1$ in this case. For inertial turbulence, the pertinent quantity is the energy dissipation rate ε with dimensions L^2/T^3, and the corresponding quantity is $q = \varepsilon^{\frac{1}{3}}$ of dimensions $L^{\frac{2}{3}}/T$, setting $\alpha = \frac{2}{3}$. This rule even applies to the non-turbulent regime of molecular diffusion, which is governed by a diffusivity D of dimensions L^2/T, thus requiring $\alpha = 2$.

In summary, we have developed an alternative to Fickian diffusion that should be preferable for modeling turbulent dispersion. It consists of a family of fractional

Laplacian operators with parameter $0 < \alpha < 2$. This is not entirely new, for fractional calculus has already been proposed for the modeling of dispersion in porous media (Schumer et al. 2001, 2009). The first case applies to the case of boundary turbulence (shear turbulence) where the turbulent velocity fluctuations are all, regardless of eddy size, on the order of the friction velocity imposed by the stress at the boundary, $u_* = \sqrt{\tau_{wall}/\rho}$, giving $\alpha = 1$. The equation governing the concentration $c(\mathbf{x}, t)$ of a passive tracer is (7.20), which with advection by the mean flow incorporated is:

$$\boxed{\frac{\partial c}{\partial t} + \bar{\mathbf{u}} \cdot \nabla c = C\, u_* \iiint \frac{c(\mathbf{x}', t) - c(\mathbf{x}, t)}{|\mathbf{x}' - \mathbf{x}|^4}\, d\mathbf{x}'.} \tag{7.24}$$

The second case applies in the case of inertial turbulence (Kolmogorov cascade) where the velocity fluctuations u_* vary with eddy size d according to $u_* = (\varepsilon d)^{\frac{1}{3}}$. The equation for concentration is (7.22), which with advection terms included is:

$$\boxed{\frac{\partial c}{\partial t} + \bar{\mathbf{u}} \cdot \nabla c = C\, \varepsilon^{\frac{1}{3}} \iiint \frac{c(\mathbf{x}', t) - c(\mathbf{x}, t)}{|\mathbf{x}' - \mathbf{x}|^{\frac{11}{3}}}\, d\mathbf{x}'.} \tag{7.25}$$

The general formulation for $0 < \alpha < 2$ is:

$$\boxed{\frac{\partial c}{\partial t} + \bar{\mathbf{u}} \cdot \nabla c = C\, q \iiint \frac{c(\mathbf{x}', t) - c(\mathbf{x}, t)}{|\mathbf{x}' - \mathbf{x}|^{\alpha+3}}\, d\mathbf{x}',} \tag{7.26}$$

in which the factor q with dimensions L^α/T is the physical quantity that governs the turbulent field.

The multiplicative constant C should depend on detailed statistics of the eddy field,[5] but practicality suggests to use them as tunable factors. Sources and sinks can be easily included as additional terms on the right-hand side. The triple integrals in (7.24) and (7.25) are two particular cases of the fractional Laplacian (Kwaśnicki 2017) as it can be shown that their Fourier transforms are $-k^\alpha \hat{c}$ (with $\alpha = 1, \frac{2}{3}$, respectively).

The preceding formulations were developed without specifying boundaries and thus apply strictly to an infinite domain in all three dimensions of space. The nature of boundary conditions accompanying the fractional Laplacian is a subject of current debate (Lischke et al. 2018). In practical situations, a first approximation is simply to restrict the triple integration to the finite physical domain. The weighing factor $\frac{1}{|\mathbf{x}'-\mathbf{x}|^{\alpha+3}}$ decays with distance, and the truncation to finite distances should not be a problem in the interior of the domain. Closer to the boundaries, a reflection term should preferentially be added, as discussed in the following section.

[5] For shear turbulence case, the value of C could perhaps be related to the ratio of the most probable velocity magnitude $|\mathbf{u}|$ to u_*.

7.4 Reduction to One Dimension with Boundaries

The preceding 3D formulations may be reduced to a single dimension in the case where the tracer concentration depends on a single spatial variable, say z in the vertical. In marine situations, this would be the case when vertical mixing occurs in the presence of much weaker gradients in the two horizontal dimensions. In such a case, the concentration spatial difference inside the integrals is $c(z', t) - c(z, t)$, and integration over x' and y' can be performed analytically prior to numerical implementation. The result is:

$$\frac{\partial c}{\partial t} + w\,\frac{\partial c}{\partial z} = C_1\,u_*\int \frac{c(z', t) - c(z, t)}{(z' - z)^2}\,dz' \tag{7.27a}$$

$$\frac{\partial c}{\partial t} + w\,\frac{\partial c}{\partial z} = C_1\,\varepsilon^{\frac{1}{3}}\int \frac{c(z', t) - c(z, t)}{|z' - z|^{\frac{5}{3}}}\,dz', \tag{7.27b}$$

for shear and inertial turbulence, respectively. The multiplicative constant C_1 in front of the dispersion operator is now designated with a subscript 1 to indicate that it corresponds to one dimension. The relation between the constants at 1 and 3 dimensions is:

$$C_1 = \pi\,\frac{\Gamma\left(\frac{\alpha+1}{2}\right)}{\Gamma\left(\frac{\alpha+3}{2}\right)}\,C, \tag{7.28}$$

yielding $C_1 = \pi C$ for $\alpha = 1$ (wall turbulence) and $C_1 = 0.248855\ C$ for $\alpha = \frac{2}{3}$ (inertial turbulence).

Strictly, these expressions apply for the infinite interval $-\infty < z < \infty$. When the domain is semi-infinite, say with a boundary at $z = 0$ so that $0 \le z < \infty$, the integral is restricted to this physical interval in return for one additional term that may be interpreted as a reflection term (Epps and Cushman-Roisin 2018)[6]. Since turbulence near a wall is most often of the shear turbulence type, only the u_* formulation needs to be considered:

$$\boxed{\frac{\partial c}{\partial t} + w\,\frac{\partial c}{\partial z} = C_1\,u_*\int_0^\infty [c(z', t) - c(z, t)]\left[\frac{1}{(z' - z)^2} + \frac{1}{(z' + z)^2}\right]\,dz'\,.} \tag{7.29}$$

The case of two boundaries (say $0 \le z \le H$) is more complicated and necessitates the addition of an infinite series of reflection terms (Epps and Cushman-Roisin 2018):

[6] The origin of these additional terms is found in the "bounce-back" condition of the probability density function in a Boltzmann kinetics framework.

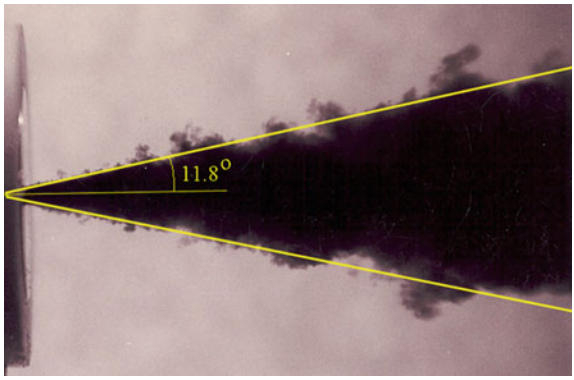

Fig. 7.3 A turbulent round jet of dyed water being discharged into clean water. The half-angle value of 11.8° tends to be universal at high Reynolds numbers. Photo taken in the Thayer School's Fluids Lab at Dartmouth College

$$\frac{\partial c}{\partial t} + w\,\frac{\partial c}{\partial z} = C_1\,u_* \int_0^H [c(z',t) - c(z,t)] \left\{ \frac{1}{(z'-z)^2} + \frac{1}{(z'+z)^2} \right.$$
$$\left. + \sum_{n=1}^{\infty} \left[\frac{1}{(2nH + z' + z)^2} + \frac{1}{(2nH + z' - z)^2} + \frac{1}{(2nH - z' + z)^2} + \frac{1}{(2nH - z' - z)^2} \right] \right\} dz' \,. \tag{7.30}$$

7.5 Application to Dispersion in Turbulent Jets

An interesting application is to dispersion caused by a turbulent jet because oftentimes contaminants are released by means of a smokestack or discharge pipe into the atmosphere or water body. We distinguish here the round jet from the planar jet.

7.5.1 Turbulent Round Jet

The turbulent round jet (Fig. 7.3) is created by a flow of velocity U and concentration c_0 exiting from a circular orifice of radius R and penetrating in an otherwise quiescent and pure fluid (no flow, no concentration). The quantity governing the "strength" of the jet is its momentum injection $\dot{m} = \rho(\pi R^2)U^2$, which is conserved all along the jet for lack of downstream pressure force.[7] Thus the quantity governing the

[7] It can be shown rather easily that there cannot be any pressure force across and down the jet as long as the pressure in the quiescent fluid away from the jet is uniform and radial acceleration is weak, thus ensuring conservation of momentum. Radial acceleration is weak because the jet is much longer than it is wide (so-called "thin jet approximation"). Note that in contrast mass is not conserved in the jet as it entrains fluid form the quiescent surroundings. The amount of tracer in the jet is conserved as long as the ambient fluid is tracer-free. The tracer concentration decreases by dilution with tracer-free fluid.

turbulence is $\dot{m}$, which leads us to adopting $q = RU$ with dimensions L^2/T, and we set $\alpha = 2$, which brings us exceptionally to using the classical diffusion model with D proportional to RU.

The governing equations in cylindrical coordinates with x directed along the centerline of the jet and r radially across it, and with the assumptions of axisymmetry, steady state and negligible radial momentum are:

$$\frac{\partial u}{\partial x} + \frac{1}{r}\frac{\partial}{\partial r}(rv) = 0 \tag{7.31a}$$

$$u\frac{\partial u}{\partial x} + v\frac{\partial u}{\partial r} = C\,RU\left(\frac{\partial^2 u}{\partial x^2} + \frac{\partial^2 u}{\partial r^2} + \frac{1}{r}\frac{\partial u}{\partial r}\right) \tag{7.31b}$$

$$u\frac{\partial c}{\partial x} + v\frac{\partial c}{\partial r} = C\,RU\left(\frac{\partial^2 c}{\partial x^2} + \frac{\partial^2 c}{\partial r^2} + \frac{1}{r}\frac{\partial c}{\partial r}\right), \tag{7.31c}$$

in which $u(x, r)$ is the downstream velocity, $v(x, r)$ is the radial velocity (positive outward and much weaker than u), and $c(x, r)$ is the tracer's concentration field. In both momentum and tracer equations, the diffusivity is taken as CRU, based on the assumption that in a turbulent environment all quantities can disperse at an equal rate because the stirring is caused by the shared turbulent velocity fluctuations.[8]

Because the jet is nearly unidirectional ($|v| \ll u$), mass conservation (7.31a) requires that the downstream variations be much weaker than the radial variations ($\frac{\partial}{\partial x} \ll \frac{\partial}{\partial r}$), and we may neglect downstream diffusion compared to cross-jet diffusion, reducing the momentum and concentration equations to

$$u\frac{\partial u}{\partial x} + v\frac{\partial u}{\partial r} = C\,RU\left(\frac{\partial^2 u}{\partial r^2} + \frac{1}{r}\frac{\partial u}{\partial r}\right) \tag{7.32a}$$

$$u\frac{\partial c}{\partial x} + v\frac{\partial c}{\partial r} = C\,RU\left(\frac{\partial^2 c}{\partial r^2} + \frac{1}{r}\frac{\partial c}{\partial r}\right), \tag{7.32b}$$

There are two upstream constraints that serve to set the velocity and concentration amplitudes, namely the influx of momentum and tracer at the jet's origin, which are both conserved along the jet:

$$\int_0^\infty u^2(r, x)\, 2\pi r\, dr = \pi R^2\, U^2 \tag{7.33a}$$

$$\int_0^\infty u(r, x)\, c(r, x)\, 2\pi r\, dr = \pi R^2\, U c_0. \tag{7.33b}$$

The above set of equations and constraints possesses a similarity solution of the form:

[8] There is evidence (Jischa and Rieke 1979) that the turbulent Prandtl (heat vs. momentum) and Schmidt (tracer vs. momentum) numbers depart from unity only when the molecular Prandtl and Schmidt numbers are much less than one, as in liquid metals, and the dependence of the departure depends on the Reynolds number of the flow, with smaller departures at high Reynolds numbers.

$$u(x,r) = \frac{RU}{x}\,\tilde{u}(\eta), \quad v(x,r) = \frac{RU}{x}\,\tilde{v}(\eta), \quad c(x,r) = \frac{Rc_0}{x}\,\tilde{c}(\eta) \tag{7.34}$$

with the similarity variable η defined as the ratio of spatial coordinates:

$$\eta = \frac{r}{x}. \tag{7.35}$$

We note that the equal powers of r and x in the numerator and denominator of η imply that the solution will represent a jet that widens linearly with distance, in agreement with observations (Pope 2000, page 100). The value $\eta = 0$ corresponds to the centerline.

The reduced equations governing the cross-jet profile functions $\tilde{u}(\eta)$, $\tilde{v}(\eta)$ and $\tilde{c}(\eta)$ are:

$$-\tilde{u} - \eta\,\frac{d\tilde{u}}{d\eta} + \frac{1}{\eta}\,\frac{d(\eta\tilde{v})}{d\eta} = 0 \tag{7.36a}$$

$$-\tilde{u}^2 - \eta\tilde{u}\,\frac{d\tilde{u}}{d\eta} + \tilde{v}\,\frac{d\tilde{u}}{d\eta} = C\left(\frac{d^2\tilde{u}}{d\eta^2} + \frac{1}{\eta}\,\frac{d\tilde{u}}{d\eta}\right) \tag{7.36b}$$

$$-\tilde{u}\tilde{c} - \eta\tilde{u}\,\frac{d\tilde{c}}{d\eta} + \tilde{v}\,\frac{d\tilde{c}}{d\eta} = C\left(\frac{d^2\tilde{c}}{d\eta^2} + \frac{1}{\eta}\,\frac{d\tilde{c}}{d\eta}\right). \tag{7.36c}$$

The accompanying constraints (7.33a)–(7.33b) become:

$$\int_0^\infty \tilde{u}^2(\eta)\;\eta\;d\eta = \frac{1}{2} \tag{7.37a}$$

$$\int_0^\infty \tilde{u}(\eta)\;\tilde{c}(\eta)\;\eta\;d\eta = \frac{1}{2}. \tag{7.37b}$$

Constraints (7.37a)–(7.37b) serve as substitutes for boundary conditions on $\tilde{u}(\eta)$ and $\tilde{c}(\eta)$, to which we add the obvious $\tilde{u} \to 0$ and $\tilde{c} \to 0$ for $\eta \to \infty$ because the jet is confined. Clearly, the solution for $\tilde{c}(\eta)$ will be the same as $\tilde{u}(\eta)$ because substitution of $\tilde{u}$ for $\tilde{c}$ in (7.36c) and (7.37b) reproduces (7.36b) and (7.37a), respectively.

Since these equations with a constant viscosity apply equally well to laminar flow, they are not new, and Schlichting (1933) has already found the solution, which can be expressed analytically:

$$\tilde{u}(\eta) = \tilde{c}(\eta) = \frac{3}{8C}\,\frac{1}{(1+a\eta^2)^2} \tag{7.38a}$$

$$\tilde{v}(\eta) = \frac{3}{16C}\,\frac{\eta\,(1-a\eta^2)}{(1+a\eta^2)^2}, \tag{7.38b}$$

in which the constant a is related to the dispersion coefficient by

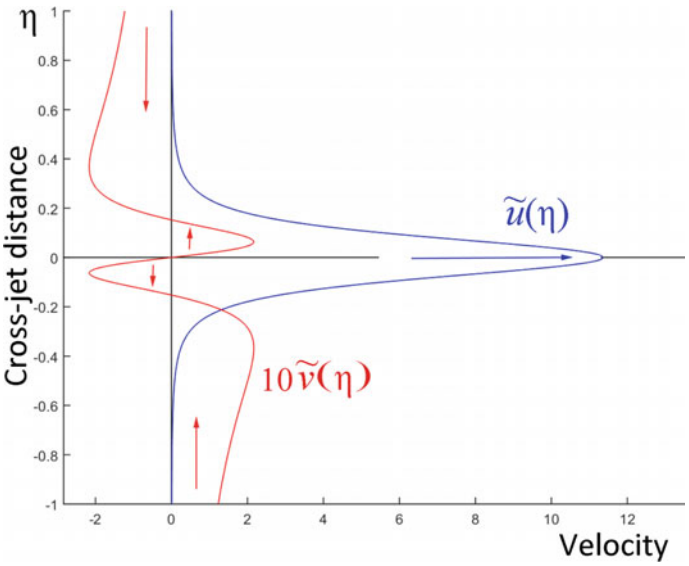

Fig. 7.4 Profiles of the downstream velocity $\tilde{u}(\eta)$ (in blue) and cross-jet radial velocity $\tilde{v}(\eta)$ (in red, multiplied by 10 to highlight its features) that are solutions to (7.36a)–(7.36b) and given by (7.38a)–(7.38b), for $C = 0.033$. While the jet velocity is fairly confined, the cross-jet velocity is not. Away from the jet, the latter contributes to flow toward the jet and, therefore, to entrainment into the jet. Around the center of the jet, the cross-flow reverses, contributing to jet divergence to compensate for the downstream convergence of the slowing jet velocity along the centerline

$$a = \frac{3}{64\,C^2}. \tag{7.39}$$

The jet velocity profile $\tilde{u}(\eta)$ is symmetric across the centerline, whereas the cross-jet velocity $\tilde{v}(\eta)$ is anti-symmetric across the centerline and reverses sign at $\eta = \pm 1/\sqrt{a}$. The lower the value of C, the faster the centerline velocity $(3/8C)$ and the narrower the jet ($\eta_{50\%} = 64(\sqrt{2}-1)C^2/3$). The profiles of $\tilde{u}(\eta)$ and $\tilde{v}(\eta)$ are plotted in Fig. 7.4 for $C = 0.033$. The jet velocity profile $\tilde{u}(\eta)$ (Fig. 7.5) is not Gaussian, with algebraic rather than exponential tails, but could be mistaken for Gaussian around the peak.

Back with dimensions in the (x,r) plane, the velocity and concentration fields are:

$$\begin{aligned} u(x,r) &= \frac{3RU}{8C\,x}\,\frac{1}{\left(1+a\frac{r^2}{x^2}\right)^2}, \quad v(x,r) = \frac{3RU\,r}{16C\,x^2}\,\frac{1-a\frac{r^2}{x^2}}{\left(1+a\frac{r^2}{x^2}\right)^2}, \\ c(x,r) &= \frac{3Rc_0}{8C\,x}\,\frac{1}{\left(1+a\frac{r^2}{x^2}\right)^2}. \end{aligned} \tag{7.40}$$

An important characteristic of the round jet is the rate at which it widens with downstream distance, called the spreading rate and defined from the distance $r_{50\%}$ at which the jet velocity drops to half of its centerline value:

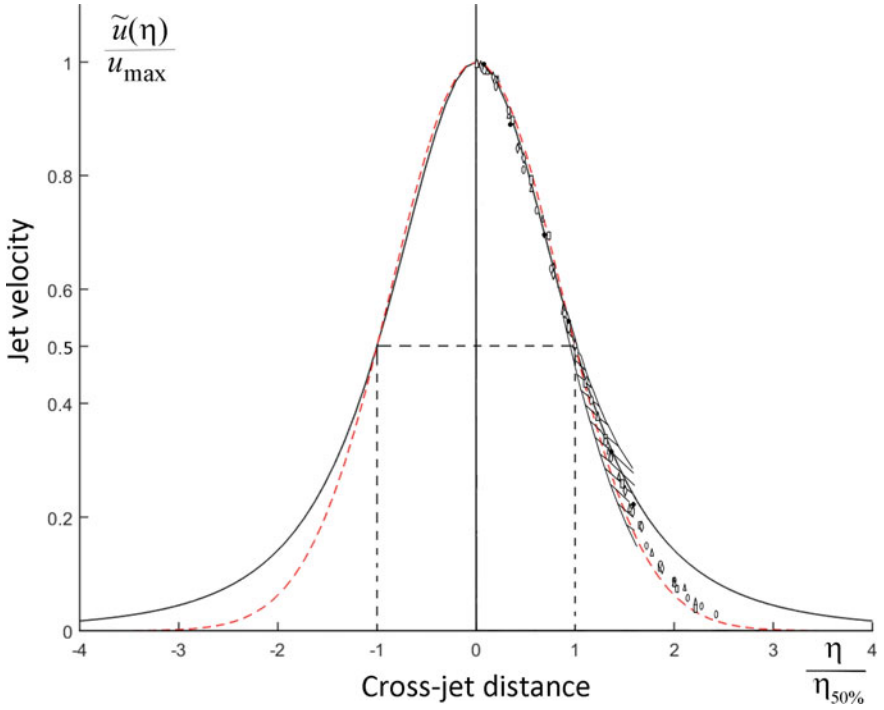

Fig. 7.5 Close-up on the downstream velocity profile (solid black line), re-scaled by centerline value versus $\eta/\eta_{50\%}$ in comparison with the best-fitting Gaussian distribution (red dashed line) and data from Wygnanski and Fiedler (1969) for $Re \approx 10^5$. The core of the jet has a very nearly Gaussian structure but has thicker tails. In the tail, the data seem to conform better with the Gaussian profile, but in this region at the edge of the jet, intermittency is very pronounced, and velocity values are highly variable, as sketched by Wygnanski and Fiedler (1969) by means of envelope lines and hatchings

$$S = \frac{r_{50\%}}{x} = \sqrt{\frac{\sqrt{2}-1}{a}} = 8C\sqrt{\frac{\sqrt{2}-1}{3}} = 2.973\ C. \tag{7.41}$$

Laboratory observations (Hussein et al. 1994) for $Re = 95,500$ give $S = 0.098 \pm 0.004$, yielding $C = 0.033 \pm 0.013$. This corresponds to a conical jet with half-angle of 11.8° when measured where velocity has dropped to 12% of its centerline value (Fig. 7.3).

While the concentration profile $\tilde{c}(\eta)$ is identical to the velocity profile $\tilde{u}(\eta)$ in the similarity solution, the measurement of concentration values in the laboratory is an independent endeavor. The experiments by Becker et al. (1967), who used oil smoke as a passive tracer in a turbulent air jet (with Schmidt number of about 38,000), confirm that the concentration profile, like the velocity profile, exhibits a similarity behavior, furthermore with a radius of half value increasing with downstream distance $0.106\ x$, which is nearly the same as that of velocity (Hussein et al. 1994). Figure

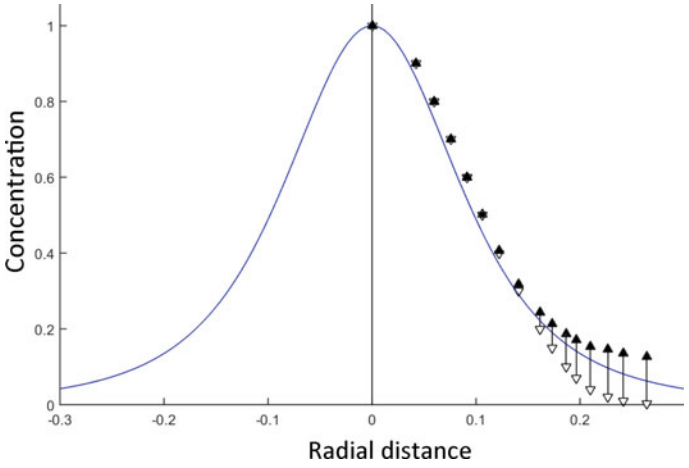

Fig. 7.6 Comparison of the concentration profile in a turbulent round jet as predicted by the similarity solution (7.38a) with $C = 0.033$ (normalized by centerline value) and laboratory data reported by Becker et al. (1967). The scatter in the data is primarily caused by turbulent fluctuations and turbulence intermittency at the edges, not experimental inaccuracies. The fit is excellent in both center of jet and at the edge

7.6 compares the similarity solution $\tilde{c}(\eta)$ given by (7.38a) to the laboratory data of Becker et al. (1967).

7.5.2 *Turbulent Planar Jet*

The turbulent planar jet is created by a flow of velocity U and concentration c_0 exiting from an elongated slit of width W and penetrating in an otherwise quiescent and pure fluid (no flow, no concentration). The quantity governing the "strength" of the jet is its momentum injection per unit length along the slit $\dot{m} = \rho W U^2$, which is conserved along the jet for lack of downstream pressure force (for the same reason as for the round jet). Thus the quantity governing the turbulence is $\dot{m}$, which leads us to adopting $q = \sqrt{WU^2}$ of dimensions $L^{\frac{3}{2}}/T$, with $\alpha = \frac{3}{2}$ in this case.

The governing equations in Cartesian coordinates with x directed downstream along the centerline of the jet, y transversely in the direction along the slit, and z across the jet, and with the assumptions of steady state, negligible cross-jet momentum, no variation in the $y-$direction are:

$$\frac{\partial u}{\partial x} + \frac{\partial w}{\partial z} = 0 \tag{7.42a}$$

$$u\,\frac{\partial u}{\partial x} + w\,\frac{\partial u}{\partial z} = C\,\sqrt{WU^2}\iiint \frac{u(\mathbf{x}') - u(\mathbf{x})}{|\mathbf{x}' - \mathbf{x}|^{\frac{9}{2}}}\,dx'dy'dz' \tag{7.42b}$$

$$u\,\frac{\partial c}{\partial x} + w\,\frac{\partial c}{\partial z} = C\,\sqrt{WU^2}\iiint \frac{c(\mathbf{x}') - c(\mathbf{x})}{|\mathbf{x}' - \mathbf{x}|^{\frac{9}{2}}}\,dx'dy'dz', \tag{7.42c}$$

in which $u(x, z)$ is the downstream velocity, $w(x, z)$ is the cross-jet velocity (much weaker than u), and $c(x, z)$ is the tracer's concentration field.

Applying now the assumption of much weaker dispersion in the downstream direction x than in the cross-jet direction z, as we did for the round jet, allows us to retain only the z variations in $[u(\mathbf{x}') - u(\mathbf{x})]$ and $[c(\mathbf{x}') - c(\mathbf{x})]$ inside the integrals and thus to integrate over x' and y' once and for all:

$$\iint_{-\infty}^{\infty} \frac{1}{[(x'-x)^2 + (y'-y)^2 + (z'-z)^2]^{\frac{9}{4}}}\,dx'dy' = \pi\,\frac{\Gamma\left(\frac{5}{4}\right)}{\Gamma\left(\frac{9}{4}\right)}\,\frac{1}{|z'-z|^{\frac{5}{2}}} = \frac{2.513274}{|z'-z|^{\frac{5}{2}}}. \tag{7.43}$$

The reduced equations are

$$u\,\frac{\partial u}{\partial x} + w\,\frac{\partial u}{\partial z} = C_1\sqrt{WU^2}\int_{-\infty}^{\infty} \frac{u(x, z') - u(x, z)}{|z'-z|^{\frac{5}{2}}}\,dz' \tag{7.44a}$$

$$u\,\frac{\partial c}{\partial x} + w\,\frac{\partial c}{\partial z} = C_1\sqrt{WU^2}\int_{-\infty}^{\infty} \frac{c(x, z') - c(x, z)}{|z'-z|^{\frac{5}{2}}}\,dz', \tag{7.44b}$$

with $C_1 = 2.513274\ C$. The injection of momentum and tracer, which are both conserved downstream, provide the following two conditions:

$$\int_{-\infty}^{\infty} u^2\,dz = WU^2 \tag{7.45a}$$

$$\int_{-\infty}^{\infty} uc\,dz = WUc_0. \tag{7.45b}$$

As for the round jet, a similarity solution exists, this time with

$$u(x, z) = U\sqrt{\frac{W}{x}}\,\tilde{u}(\eta), \quad w(x, z) = U\sqrt{\frac{W}{x}}\,\tilde{w}(\eta), \quad c(x, z) = c_0\sqrt{\frac{W}{x}}\,\tilde{c}(\eta) \tag{7.46}$$

with similarity variable

$$\eta = \frac{z}{x}, \tag{7.47}$$

which means that the jet widens linearly with downstream distance like the round jet, but the strength of the jet now decays with distance x like $1/\sqrt{x}$ instead of $1/x$. This is exactly what is observed (Pope 2000, page 135).

The equations governing the similarity profiles are:

$$-\frac{1}{2}\tilde{u} - \eta\,\frac{d\tilde{u}}{d\eta} + \frac{d\tilde{w}}{d\eta} = 0 \tag{7.48a}$$

$$-\frac{1}{2}\tilde{u}^2 - \eta\tilde{u}\,\frac{d\tilde{u}}{d\eta} + \tilde{w}\,\frac{d\tilde{u}}{d\eta} = C_1 \int_{-\infty}^{\infty} \frac{\tilde{u}(\eta') - \tilde{u}(\eta)}{|\eta' - \eta|^{\frac{5}{2}}}\, d\eta' \tag{7.48b}$$

$$-\frac{1}{2}\tilde{u}\tilde{c} - \eta\tilde{u}\,\frac{d\tilde{c}}{d\eta} + \tilde{w}\,\frac{d\tilde{c}}{d\eta} = C_1 \int_{-\infty}^{\infty} \frac{\tilde{c}(\eta') - \tilde{c}(\eta)}{|\eta' - \eta|^{\frac{5}{2}}}\, d\eta'. \tag{7.48c}$$

There is a single dimensionless parameter, C_1, which measures the strength of both momentum and tracer dispersion. Integration of (7.48a) from $w = 0$ along the centerline by symmetry yields:

$$\tilde{w} = \eta\tilde{u} - \frac{1}{2}\int_0^{\eta} \tilde{u}(\eta')\, d\eta'. \tag{7.49}$$

The injection conditions (7.45a)–(7.45b) that set the amplitudes of $\tilde{u}$ and $\tilde{c}$ reduce to:

$$\int_{-\infty}^{\infty} \tilde{u}^2(\eta)\, d\eta = 1 \tag{7.50a}$$

$$\int_{-\infty}^{\infty} \tilde{u}(\eta)\tilde{c}(\eta)\, d\eta = 1. \tag{7.50b}$$

As for the round jet, the solution for $\tilde{c}(\eta)$ will be the same as $\tilde{u}(\eta)$ because substitution of $\tilde{u}$ for $\tilde{c}$ in (7.48c) and (7.50b) reproduces (7.48b) and (7.50a), respectively.

In the absence of a known analytical solution, we proceed numerically as follows. An initial, bell-shape guess is made for the function $\tilde{u}(\eta)$ with amplitude set by (7.50a). From it, $\tilde{w}(\eta)$ is calculated using (7.49). The two functions are then inserted into the $x-$momentum Eq. (7.48b) in which a fake-time derivative $d\tilde{u}/dt$ is introduced on the left. This permits to update $\tilde{u}(\eta)$, on which condition (7.50a) is imposed again, and the steps are repeated until convergence. Figure 7.7 displays the two velocity profiles for $C_1 = 0.011$ ($C = 0.00438$), the value that yields a jet spreading rate $S = dz_{50\%}/dx = 0.1$ to match observations (Pope 2000, page 138). Figure 7.8 compares the half-jet profile obtained numerically with the solution obtained with constant eddy viscosity and laboratory data, both from Heskestad (1965).

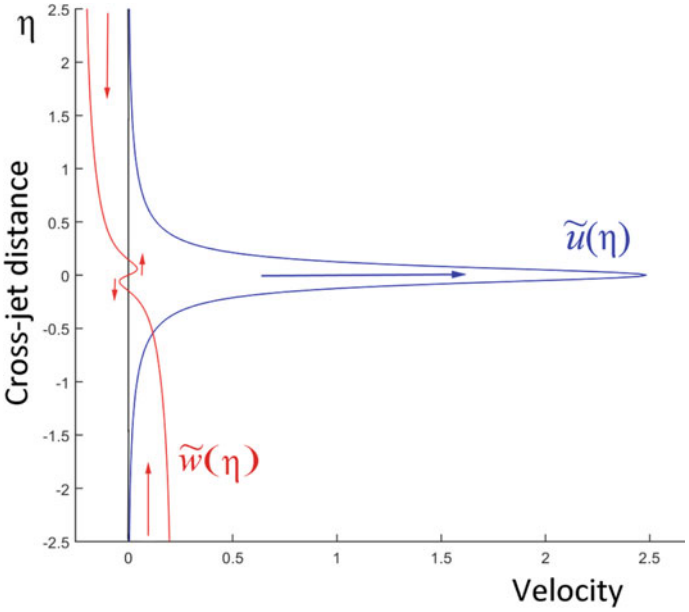

Fig. 7.7 Profiles of the downstream velocity $\tilde{u}(\eta)$ (in blue) and transverse velocity $\tilde{w}(\eta)$ (in red) that are solutions to (7.48a)–(7.48b), for $C_1 = 0.011$. While the jet velocity is fairly confined, the transverse velocity is not. Away from the jet, the latter contributes to flow toward the jet and, therefore, to entrainment into the jet. Around the center of the jet, the cross-flow reverses, contributing to jet divergence to compensate for the downstream convergence of the slowing jet velocity along the centerline

7.6 Turbulent Flow along a Wall—The Logarithmic Velocity Profile

It was shown in Sect. 7.4 that in the presence of a wall boundary at $z = 0$ and with $q = u_*$ as the governing quantity (case $\alpha = 1$), the dispersion operator is that given in (7.29):

$$\frac{\partial c}{\partial t} + w\,\frac{\partial c}{\partial z} = C_1\,u_* \int_0^\infty [c(z',t) - c(z,t)] \left[\frac{1}{(z'-z)^2} + \frac{1}{(z'+z)^2}\right] dz' \,. \quad (7.51)$$

We now apply this to unidirectional turbulent flow along a wall by replacing the concentration $c(z,t)$ by the velocity $u(z,t)$. In steady state and absence of a pressure gradient, the $x-$momentum equation reduces to a single term:

$$0 = C_1\,u_* \int_0^\infty [u(z') - u(z)] \left[\frac{1}{(z'-z)^2} + \frac{1}{(z'+z)^2}\right] dz'. \quad (7.52)$$

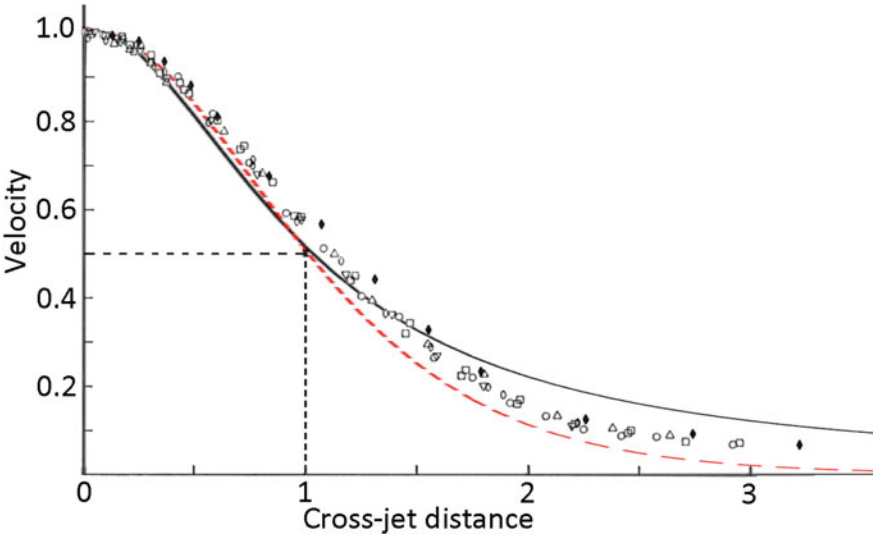

Fig. 7.8 Close-up on the downstream velocity profile (solid black line), re-scaled by centerline value versus $\eta/\eta_{50\%}$ in comparison with the analytical solution obtained for constant eddy viscosity (red dashed line) and data from Heskestad (1965) for $Re = 3.4 \times 10^4$. The data reveal a tail thicker than that predicted by the constant eddy diffusivity solution but thinner than that of the present solution. At the far end ($\eta/\eta_{50\%} \geq 3$), the laboratory data continue to show non-zero values in agreement with the heavy tail of the present solution and in contrast to the solution with constant eddy diffusivity

It can be shown (Cushman-Roisin and Jenkins 2006) that the exact solution to this integral equation with two degrees of freedom is:

$$u(z) = \frac{u_*}{\kappa} \ln \frac{z}{z_0}, \tag{7.53}$$

in which the factors κ and z_0 serve, respectively, has a multiplicative constant and an additive constant. We recognize here the well known logarithmic profile of velocity for turbulent flow along a wall with κ being the von Kármán constant and z_0 the roughness height.

Epps and Cushman-Roisin (2018) showed that the shear stress associated with the integral in (7.52) is:

$$\tau_{xz} = C_1 \rho u_* \int_0^\infty [u(z') - u(z)] \left[\frac{1}{z' - z} - \frac{1}{z' + z} \right] dz'. \tag{7.54}$$

The logarithmic velocity profile renders this stress constant, as it should be in a steady flow with no nonlinear advection and no pressure gradient. After substituting (7.53) in (7.54), we obtain:

$$\tau_{xz} = C_1 \rho u_* \int_0^\infty \frac{u_*}{\kappa} \ln\left(\frac{z'}{z}\right) \left[\frac{1}{z'-z} - \frac{1}{z'+z}\right] dz' = C_1 \rho \frac{u_*^2}{\kappa} \frac{\pi^2}{2} = \frac{\pi^2 C_1}{2\kappa} \rho u_*^2. \tag{7.55}$$

Since the turbulent velocity u_* is defined from the stress as $\tau_{xz} = \tau_{wall} = \rho u_*^2$, it follows that:

$$\frac{\pi^2 C_1}{2\kappa} = 1 \quad \rightarrow \quad C_1 = \frac{2\kappa}{\pi^2} = 0.0811. \tag{7.56}$$

for $\kappa = 0.40$. This suggests which value should be used for the constant C_1 when the quantity governing the turbulence is the turbulent velocity u_*. The corresponding constant in three dimensions is $C = C_1/\pi = 2\kappa/\pi^3 = 0.0258$. We note that this value is fairly close to the ones determined for turbulent jets from fit with observations, namely $C = 0.033$ for the round jet, $C_1 = 0.011$ for the planar jet.

7.7 Application to the Marine Ekman Layer

7.7.1 Surface Ekman Layer

The surface Ekman layer in the ocean is a manifestation of downward momentum dispersion from a wind stress at the surface.[9] The governing equations are those of Ekman dynamics (Cushman-Roisin and Beckers 2011, Chap. 8) except that we now substitute the preceding 1D turbulent dispersion operator to represent the frictional terms. In the absence of horizontal gradients (and thus of horizontal advection and a horizontal pressure force) and over an infinitely deep bottom, the equations to be solved are:

$$\frac{\partial u}{\partial t} - fv = C_1\, u_* \int_{-\infty}^0 [u(z',t) - u(z,t)] \left[\frac{1}{(z'-z)^2} + \frac{1}{(z'+z)^2}\right] dz' \tag{7.57a}$$

$$\frac{\partial v}{\partial t} + fu = C_1\, u_* \int_{-\infty}^0 [v(z',t) - v(z,t)] \left[\frac{1}{(z'-z)^2} + \frac{1}{(z'+z)^2}\right] dz', \tag{7.57b}$$

in which u_* is set by the stress exerted on the surface by the wind, $u_* = \sqrt{\tau_{wind}/\rho}$, which we take in the $x-$direction and constant over time suddenly started at $t = 0$ over an ocean initially at rest. The value of C_1 is given by (7.56) under the premise that the presence of rotation does not appreciably affect the nature of the shear turbulence near the surface. The second term inside the brackets in the integrand of (7.57a)–(7.57b) is included to take into account the presence of the surface boundary at $z = 0$. Boundary conditions are:

[9] Recall that a shear stress is a momentum flux.

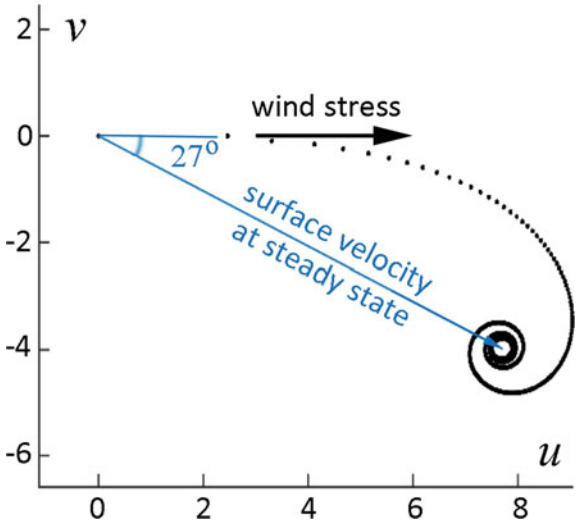

Fig. 7.9 Evolution of the surface velocity following the sudden imposition of a surface stress in the $x-$direction. Inertial oscillations are damped, and a steady flow is achieved. The surface velocity makes an angle of 27° to the right of the wind stress

$$\tau_x = \rho u_*^2, \quad \tau_y = 0 \qquad \text{at} \quad z = 0 \tag{7.58a}$$

$$u \to 0, \quad v \to 0 \qquad \text{as} \quad z \to -\infty. \tag{7.58b}$$

After scaling the velocity components by u_*, depth by u_*/f and time by $1/f$, we obtain the following dimensionless equations

$$\frac{\partial u}{\partial t} - v = C_1 \int_{-\infty}^{0} [u(z',t) - u(z,t)] \left[\frac{1}{(z'-z)^2} + \frac{1}{(z'+z)^2} \right] dz' \tag{7.59a}$$

$$\frac{\partial v}{\partial t} + u = C_1 \int_{-\infty}^{0} [v(z',t) - v(z,t)] \left[\frac{1}{(z'-z)^2} + \frac{1}{(z'+z)^2} \right] dz' \,. \tag{7.59b}$$

The solution proceeds numerically from rest after a suddenly imposed stress in the $x-$direction at $z = 0$ (enforced as a body force over the top grid cell) and until steady state is reached. Figure 7.9 shows that, after a several inertial oscillations, the flow settles into a steady state. Turbulent friction has a damping effect, as expected.

Steady-state velocity profiles (Fig. 7.10) show an interplay between the two velocity components hinting at veering with depth. If the depth of the Ekman layer is defined as the depth where the velocity magnitude has dropped to 5% of its surface value, the result is $0.63u_*/f$. This agrees with observations (Cushman-Roisin and Beckers 2011, page 255), both in its analytical expression as well as in its numerical value. The veering of the velocity with depth is prominently displayed in Fig. 7.11. The angle between surface stress and surface velocity is 27° (see also Fig. 7.9), noticeably lower than the 45° of the classical Ekman veering obtained with a constant eddy diffusivity. We also note from the time evolution shown in Fig. 7.9 that the angle between wind stress and surface velocity can be very much smaller

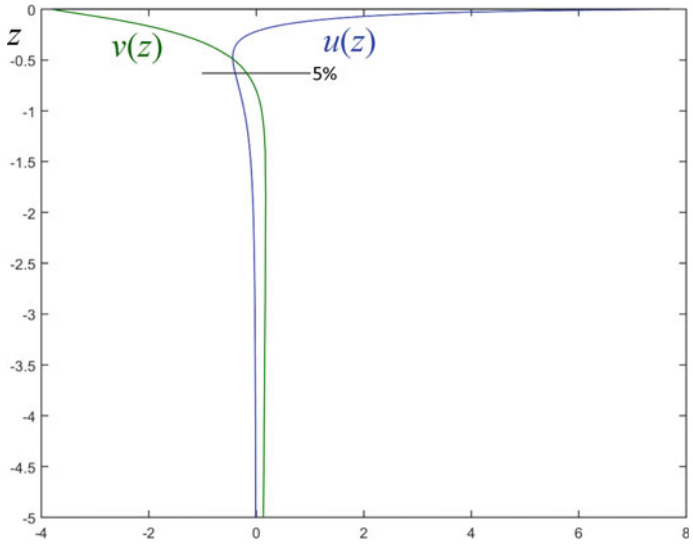

Fig. 7.10 Velocity profiles in the turbulent surface Ekman layer according to equations (7.59a)–(7.59b). The horizontal bar indicates the level at which the velocity magnitude has dropped to 5% of its surface value, serving as a measure of the Ekman layer depth

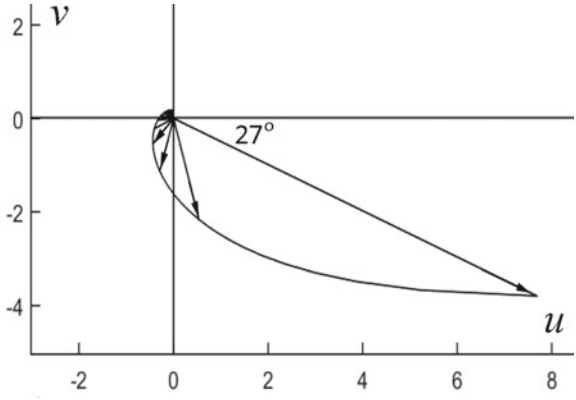

Fig. 7.11 Velocity hodograph for the surface Ekman layer. The angle between the surface velocity and the applied stress is 27°. A vector velocity is indicated every 0.15 dimensionless depth units (every 10 grid points with $\Delta z = 0.015$)

than the ultimate angle of 27° in the early part of the first inertial oscillation. Thus, in a situation with variable winds, the surface current can be expected to be more closely aligned with the wind than in steady state (Stacey et al. 1982).

7.7.2 Bottom Ekman Layer

The bottom Ekman layer differs from the surface Ekman layer by its forcing: Instead of being driven by an applied boundary stress and having a vanishing velocity at great distance, the bottom Ekman layer is driven by a non-zero geostrophic flow above and has a vanishing velocity at the boundary. The velocity equations are the same as (7.57a)–(7.57b) except for the bounds of integration now running upward from 0 to infinity. The boundary conditions are:

$$u = v = 0 \qquad \text{at} \quad z = 0 \tag{7.60a}$$

$$u \to u_g, \quad v \to v_g \qquad \text{as} \quad z \to \infty. \tag{7.60b}$$

By aligning the $x-$axis with the direction of the geostrophic flow, we take $v_g = 0$. After scaling the velocity components by u_g, height by u_g/f, and time by $1/f$, the equations reduce to

$$\frac{\partial u}{\partial t} - v = C_1 \, \lambda \int_0^\infty [u(z', t) - u(z, t)] \left[\frac{1}{(z' - z)^2} + \frac{1}{(z' + z)^2} \right] dz' \tag{7.61a}$$

$$\frac{\partial v}{\partial t} + u = C_1 \, \lambda \int_0^\infty [v(z', t) - v(z, t)] \left[\frac{1}{(z' - z)^2} + \frac{1}{(z' + z)^2} \right] dz' \,, \tag{7.61b}$$

in which $\lambda = u_*/u_g$. The value of C_1 remains that given in (7.56).

The numerical solution proceeds as follows: First, a guess value is made for the parameter λ since the bottom stress is not known *a priori*. The velocity field is initially set as the geostrophic flow throughout the water column ($u = 1, v = 0$), and the bottom value $u(z = 0)$ is suddenly set to zero to enforce no slip on the bottom boundary in accordance with (7.60a). The equations are then marched numerically in time until steady state is reached. Once the velocity profile is known, the two stress components are determined with use of (7.54), once with velocity $u(z)$ and once again with $v(z)$. The magnitude of the stress vector (nondimensionalized by ρu_g^2) yields a value for λ^2, and the resulting λ is compared to the initial guess. Iterations are performed until the starting and ending values of λ coincide. That value is found to be $\lambda = 0.0905$ for $C_1 = 0.0811$.

Figure 7.12 displays the velocity profiles. If the thickness of the bottom Ekman layer is defined as the height at which the magnitude of the velocity first reaches the magnitude of the geostrophic velocity aloft (Garratt 1992, page 287), as indicated by the horizontal bars across the velocity profiles in Fig. 7.12, the expression is

$$h = 0.34 \, \frac{u_*}{f}. \tag{7.62}$$

Not only is the expression proportional to the ratio u_*/f as observed, but the numerical coefficient is also within the range 0.2–0.4 derived from multiple observations of the neutral atmospheric boundary layer (Garratt 1992, page 288, and references

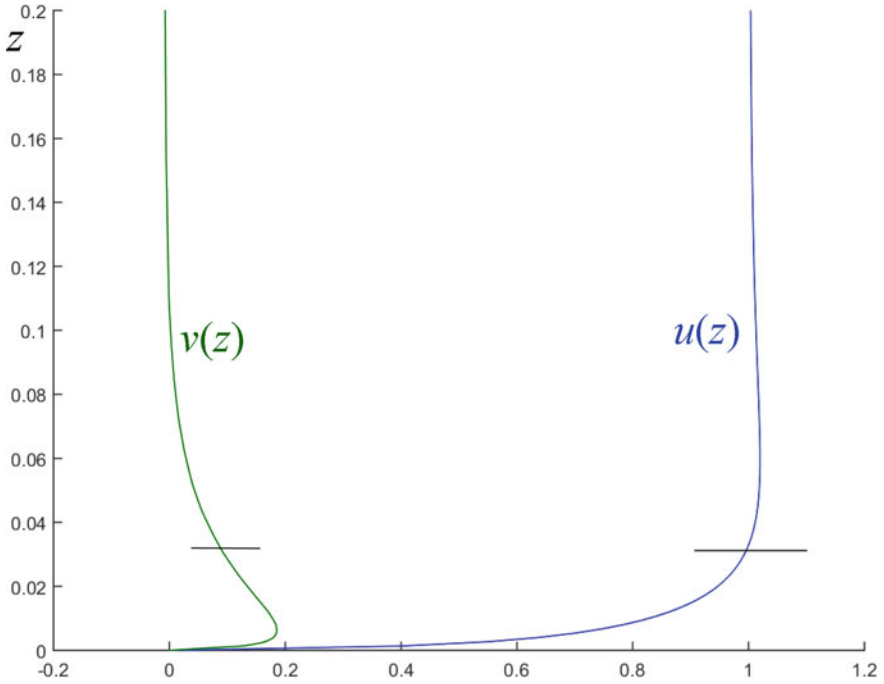

Fig. 7.12 Velocity profiles in the turbulent bottom Ekman layer according to equations (7.61a)–(7.61b) using 1501 grid points covering the finite domain $0 \leq z \leq 2$ (only the bottom 10% are shown here) and run until steady state is achieved. The horizontal bars across the velocity profiles indicate the level at which the velocity magnitude first equals the geostrophic value

therein) and 0.3–0.4 for bottom marine Ekman layers at various locations (Kundu 1976; Mercado and Van Leer 1976). Figure 7.13 displays the corresponding hodograph, revealing a small angle of 18° between near-bottom velocity and geostrophic flow aloft, confirming that in a turbulent situation the angle is much less than the 45° predicted by a theory with a constant diffusivity, as seen in observations. Perlin et al. (2007) quote a range of values between 10° and 23° for bottom Ekman layers in various coastal regions.

7.8 Conclusions

Notwithstanding the wide use of the eddy viscosity and diffusivity formulation in current marine models, it is argued that a fundamentally different approach is required for the proper modeling of turbulent dispersion in the ocean. The necessary ingredient is a mathematical operator that represents stirring by eddies of size comparable to the length scale of the instantaneous concentration field, and thus by eddies of

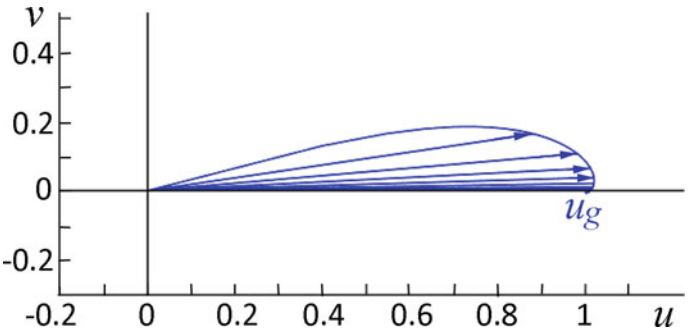

Fig. 7.13 Velocity hodograph for the bottom Ekman layer. The angle between the bottom velocity and the geostrophic flow aloft is 18°

increasingly longer scales as the concentration field widens over time. Put another way, the formulation needs to recognize in some automated way that, as a non-uniform distribution of a substance[10] evolves over time, the action of turbulence is to disperse this substance by the selective action of those eddies that occur on the same length scale as the distribution in that region and at that time. These arguments lead to an integral operator that replaces the classical diffusion operator:

$$D_E \nabla^2 c \quad \longrightarrow \quad C\, q \iiint \frac{c(\mathbf{x}', t) - c(\mathbf{x}, t)}{|\mathbf{x}' - \mathbf{x}|^{\alpha+3}}\, d\mathbf{x}', \tag{7.63}$$

in which C is a dimensionless constant, q is a dimensional variable characteristic of the local turbulent field, with dimensions L^α/T, and α is the power of L in the dimensions of q, which must lie between 0 and 2. Examples are $q = u_*$ with $\alpha = 1$ in wall turbulence and $q = \varepsilon^{\frac{1}{3}}$ with $\alpha = \frac{2}{3}$ for inertial turbulence. The possible case of multiple turbulent characterizations superimposed onto one another remains to be elucidated.

Formulation (7.63) was applied to cases of round and planar turbulent jets, showing the ability of the formulation to produce solutions in good agreement with laboratory data. Before a value was ascribed to the constant C, it was shown that the model possesses a similarity solution that matches the observed behavior, namely a centerline velocity decreasing with downstream distance at the correct power (1 for the round jet and $\frac{1}{2}$ for the planar jet) and a jet width increasing proportionally to downstream distance. After the value of the parameter C was adjusted to reproduce one feature of the solution, chosen here to be the angle at which the jet widens with downstream distance, the prediction of other information pertaining to the jet, such as its cross-stream velocity profile, followed without further tuning. What sets the value of C is not yet clear, but it appears that the various adjusted values are not too

[10] The word "substance" should be understood broadly here. It may be a passive scalar or an active scalar, such as temperature, or even momentum.

disparate ($0.0044 \leq C \leq 0.033$). Assignment of a value for C remains an area of inquiry.

The presence of a boundary causes the appearance a second, reflection-like term in the integrand of (7.63) (see (7.29) in the 1D case of wall turbulence). Application of this operator to the case of a turbulent flow along a wall reproduces the well known logarithmic profile. A connection is then possible between the von Kármán constant and the new constant C, which leads to $C = 0.0258$ ($C_1 = 0.0811$ in one dimension) for wall turbulence. There is then no parameter left to tune! Using this value, the formulation was applied to the surface and bottom Ekman layers, reproducing accurately the key aspects of observed turbulent Ekman layers in both atmosphere and ocean, namely angle of veering and Ekman layer thickness.

The integral operator in (7.63) demands that, at every grid point at every time step, differences be computed with values at all other grid points. This is computationally burdensome. The applications presented herein did not take any shortcut, but it is hoped that numerical modelers can find ways to reduce the number of calculations that are necessary to obtain approximate but accurate evaluations of the integrals. A point of departure is to recognize that differences become less important at larger distances by virtue of the increasing distance $|\mathbf{x}' - \mathbf{x}|$ raised to a power $\alpha + 3 > 3$ in the denominator. The questions are: How far or near can the integral be truncated to guarantee an acceptable approximation? Or, better, is there a way to approximate analytically the contributions of tails in order to avoid calculating differences across distant points at any time? Kämpf and Cox (2016) have begun this investigation.

Acknowledgements The author thanks Professor Brenden Epps of Dartmouth College for his assistance with the Lévy distributions and their asymptotic behavior, and the editors of this volume for their invitation, encouragements, and support.

References

Becker, H.A., H.C. Hottel, and G.C. Williams. 1967. The nozzle-fluid concentration field of the round, turbulent, free jet. *Journal of Fluid Mechanics* 30: 285–303.

Clark, J.F., P. Schlosser, M. Stute, and H.J. Simpson. 1996. $SF^6-{}^3He$ tracer release experiment: A new method of determining longitudinal dispersion coefficients in large rivers. *Environmental Science and Technology* 30: 1527–1532.

Csanady, G. T. 1973. *Turbulent Diffusion in the Environment*, 249 pp. Dordrecht: D. Reidel Publishing Co.

Cushman-Roisin, B., and A.D. Jenkins. 2006. On a non-local parameterisation for shear turbulence and the uniqueness of its solutions. *Boundary-Layer Meteorology* 118: 69–82.

Cushman-Roisin, B., and J.-M. Beckers. 2011. *Introduction to Geophysical Fluid Dynamics—Physical and Numerical Aspects*, 828 pp. Academic Press.

Cushman-Roisin, B. 2013. Turbulent dispersion. Chapter 21 in *Handbook of Environmental Fluid Dynamics—Volume 1: Overview and Fundamentals*, ed. H. J. S. Fernando, 263–271, CRC Press.

Epps, B. P., and B. Cushman-Roisin. 2018. Turbulence modeling via the fractional Laplacian. https://arxiv.org/pdf/1803.05286.pdf.

Ferrari, R. 2007. Statistics of dispersion in flows with coherent structures. In *Proceedings of the 15th 'Aha Huliko'a Hawaiian Winter Workshop on Extreme Events*, No. 23–26.

Fischer, H. B., E. J. List, R. C. Y. Koh, J. Imberger, and N. H. Brooks. 1979. *Mixing in Inland and Coastal Waters*, 483 pp. Academic Press.
Garratt, J. R. 1992. *The Atmospheric Boundary Layer*, 316 pp. Cambridge University Press.
Garrett, C. 2006. Turbulent dispersion in the ocean. *Progress in Oceanography* 70: 113–125.
Heskestad, G. 1965. Hot-wire measurements in a plane turbulent jet. *Journal of Applied Mechanics* 32 (4): 721–734.
Hunt, J.C.R. 1985. Turbulent diffusion from sources in complex flows. *Annual Review of Fluid Mechanics* 17: 447–485.
Hussein, H.J., S. Capp, and W.K. George. 1994. Velocity measurements in a high-Reynolds-number, momentum-conserving, axisymmetric, turbulent jet. *Journal of Fluid Mechanics* 258: 31–75.
Jischa, M., and H.B. Rieke. 1979. About the prediction of turbulent Prandtl and Schmidt numbers from modeled transport equations. *International Journal of Heat and Mass Transfer* 22: 1547–1555.
Kämpf, J., and D. Cox. 2016. Towards improved numerical schemes of turbulent lateral dispersion. *Ocean Modeling* 106: 1–11.
Kundu, P.K. 1976. Ekman veering observed near the ocean bottom. *Journal of Physical Oceanography* 6: 238–242.
Kwaśnicki, M. 2017. Ten equivalent definitions of the fractional Laplace operator. *Fractional Calculus and Applied Analysis* 20 (1): 7–51.
Lischke, A., G. Pang, M. Gulian, F. Song, C. Glusa, X. Zheng, Z. Mao, W. Cai, M. Meerschaert, M. Ainsworth, and G. E. Karniadakis. 2018. What is the fractional Laplacian? arXiv:1801.09767v1.
Mercado, A., and J. Van Leer. 1976. Near bottom velocity and temperature profiles observed by cyclesonde. *Geophysical Research Letters* 3: 633–636.
Nolan, J. P. 2006. Multivariate elliptically contoured stable distributions: Theory and estimation. Preprint revised on 31 October 2006. fs2.american.edu/jpnolan/www/stable/EllipticalStable.pdf.
Okubo, A. 1971. Oceanic diffusion diagrams. *Deep-Sea Research* 18: 789–902.
Perlin, A., J. N. Moum, J. M. Klymak, M. D. Levine, T. Boyd, and P. M. Kosro. 2007. Organization of stratification, turbulence, and veering in bottom Ekman layers. *Journal of Geophysical Research* 112: C05S90. https://doi.org/10.1029/2004JC002641.
Pope, S. B. 2000. *Turbulent Flows*, 807 pp. Cambridge University Press.
Richardson, L.F., and H. Stommel. 1948. A note on eddy diffusion in the sea. *Journal of Meteorology* 5: 238–240.
Roberts, J.W., and D.R. Webster. 2002. Turbulent diffusion. In *Environmental Fluid Mechanics—Theories and Applications*, ed. H.H. Shen, A.H.D. Cheng, K.-H. Wang, M.H. Teng, and C.C.K. Liu, 7–45. Reston, VA: American Social of Civil Engineers.
Schlichting, H. 1933. Laminare Strahlenausbreitung. *ZAMM Journal of Applied Mathematics and Mechanics* 13: 260–263.
Schumer, R., D.A. Benson, M.M. Meerschaert, and S.W. Wheatcraft. 2001. Eulerian derivation of the fractional advection-dispersion equation. *Journal of Contaminant Hydrology* 48: 69–88.
Schumer, R., M.M. Meerschaert, and B. Baeumer. 2009. Fractional advection-dispersion equations for modeling transport at the earth surface. *Journal of Geophysical Research* 114: A07.
Smagorinsky, J. 1963. General circulation experiments with the primitive equations. I. The basic experiment. *Monthly Weather Review* 91: 99–164.
Stacey, M.W., S. Pond, and P.H. LeBlond. 1982. A wind-forced Ekman spiral as a good statistical fit to low-frequency currents in a coastal strait. *Science* 233 (4762): 470–472.
Stommel, H. 1949. Horizontal diffusion due to oceanic turbulence. *Journal of Marine Research* 8: 199–225.
Taylor, G.I. 1921. Diffusion by continuous movements. *Proceedings of the London Mathematical Society* 20: 196–211.
Umlauf, L., and H. Burchard. 2005. Second-order turbulence closure models for geophysical boundary layers. A review of recent work. *Continental Shelf Research* 25: 795–827.
Wygnanski, I., and H. Fiedler. 1969. Some measurements in the self-preserving jet. *Journal of Fluid Mechanics* 38: 577–612.

Yanagi, T., K. Murashita, and H. Higuchi. 1982. Horizontal turbulent diffusivity in the sea. *Deep-Sea Research* 29 (2): 217–226.

Chapter 8
Spreading and Mixing in Near-Field River Plumes

Robert D. Hetland

Abstract Near-field plumes are supercritical, jet-like regions of rapid flow expansion and strong mixing. The characteristics of near-field river plumes are described based on our understanding from numerical ocean models and observations. A simple mathematical model is presented that demonstrates two competing processes within the plume: spreading, which tends to accelerate the flow in the plume, and mixing, which acts to retard the flow. The simple model is used to make statements about the energetics of the flow, and net dilution of water properties flowing through a near-field plume. Shortcomings of the model—including the effects of rotation, and the difficulties in specifying a turbulence closure—are outlined and discussed.

8.1 Introduction

The estuary/river plume system is a mixing region where terrestrial fresh water is transformed into brackish ocean seawater. While in some large systems, this brackish seawater may be observed thousands of kilometers from the source, generally the strongest gradients in salinity, and therefore the areas of most intense mixing, are concentrated either within the estuary or in a near-field river plume.

The near-field plume is associated with energetic flows—Froude numbers above one—and elevated mixing rates. As such, near-field plumes are regions of rapid transition in the character of the estuarine outflow, both in terms of the dilution of fresh water and the structure of the flow. Though both estuaries and near-field plumes can be characterized by large gradients in salinity over an area small compared to the continental shelf, and terrestrial water passing to the ocean must pass through both regions, estuaries and river plumes are often treated separately. One reason may be geographic; estuaries have clear boundaries, distinct ecosystems, and may be next to population centers that care about local water quality. Near-field river plumes on the other hand are ephemeral, generally only occurring during ebb tides, they have no distinct boundaries. Near-field plumes are not associated with any

R. D. Hetland (✉)
Department of Oceanography, Texas A&M University, College Station, College Station, TX, USA
e-mail: hetland@tamu.edu

H. Schuttelaars et al. (eds.), *The Mathematics of Marine Modelling*,
Mathematics of Planet Earth 9, https://doi.org/10.1007/978-3-031-09559-7_8

particular ecosystems as they are transitional, with water parcels traversing the near-field plume quickly—usually a few hours or less. Near-field plumes also have distinct dynamics—supercritical flow detached from the bottom and not constrained laterally by the coastline.

Not every river or estuary entering into the coastal ocean has an associated near-field plume. The mouth of the estuary needs to be narrow enough for hydraulic control to affect the outflow. For wide estuary mouths, rotation will become an important factor in determining the structure of the outflow. If the estuarine flow is given sufficient space, the buoyant estuarine outflow will form a trapped boundary current, hugging the right-hand coast (in the northern hemisphere) as the flow travels seaward. This process breaks the hydraulic control, as the structure of the flow exiting the estuary is determined by rotating dynamics, and not hydraulics. Thus, the first criterion for a near-field plume to exist is that the mouth be narrow compared to the deformation radius, or that the Kelvin number, K, the ratio between the width of the estuary mouth, W and the deformation radius, $R_d = \sqrt{g'H}\, f^{-1}$, be small, so that $K = W R_d^{-1} \ll 1$ is a necessary condition for a near-field plume to form Horner-Devine et al. (2015).

Another condition for the existence of a substantial near-field plume is the presence of relatively quiescent receiving waters. This can be quantified by comparing the potential energy anomaly provided by the buoyant outflow to the dissipative energy associated with winds and tides Pritchard and Huntley (2002); storms and strong tides can mix away a plume before it forms or strongly impact its evolution. In practice, because river discharge varies over many orders of magnitude across different systems and seasons, it is the input of potential energy by the buoyant outflow that is the strongest determining factor in forming a robust plume; large river systems generally have well defined plumes.

The first work on near-field plumes was done in a series of papers by Richard Garvine (notably, Garvine 1982; O'Donnell and Garvine 1983; Garvine 1987). For the cases considered, the estuarine source waters were directed downcoast, so that the plume never separated from downcoast coastline; the focus was on predicting offshore frontal positions. Fronts were treated as shock conditions; the details of the frontal dynamics were explored in an earlier series of papers Garvine (1974); Garvine and Monk (1974). Local entrainment was not considered, so the plume density remained constant.

Building on this work, O'Donnell (1990) created a layer model that included both interior and frontal mixing in a radially spreading plume. The radially expanding plume has similarities to the laboratory experiments performed by Britter and Simpson (1978), who looked at an expanding dense plume flowing from a point source, but O'Donnell's numerical experiments included rotation.

There have been a number of observations of near-field plumes, starting with observations of the outflow of South Pass in the Mississippi Delta Wright and Coleman (1971). Wright and Coleman's observations show how the plume gets denser offshore, and how the jet leans in response to the tide. Luketina and Imberger (1987) discuss observations of a small tidal plume, and identify many key features of near-

field plumes, including the lift-off point, entrainment in the core of the plume, and the expansion of the plume front.

There are many similarities between 'engineering' scale jets and the near-field plume (see Jones et al. 2007). The primary difference between a geophysical scale near-field plume, and for example, a cooling water outflow plume (engineering scale) is the aspect ratio of the plume. Engineering scale jets have an aspect that is $\mathcal{O}(1)$ to $\mathcal{O}(10^{-1})$. Geophysical scale plumes have an aspect closer to $\mathcal{O}(10^{-2})$ or less. Thus for engineering scale plumes, lateral mixing is an important consideration. If eddies caused by shear instabilities scale as a few times the plume depth, it is easy to see how lateral processes can cause significant dilution in a plume that has an aspect of $\mathcal{O}(10^{-1})$ or more. However, with a very small aspect, mixing on the edges will have little influence on the bulk of the plume, so mixing is almost exclusively a vertical process in geophysical scale plumes.

There have been a number of studies that have further investigated the mixing in the near-field plume front (e.g., O'Donnell et al. 1998; Orton and Jay 2005; Kilcher and Nash 2010) and the generation of internal tides by the propagating front Nash and Moum (2005); Stashchuk and Vlasenko (2009). As discussed further below, there is some uncertainty about the relationship between the plume front and trailing core of the near-field plume. As the dynamics of the plume front are distinct from the core of the plume, this manuscript will focus primarily on the plume core.

8.2 Dynamical Regions

The near-field plume is part of a series of regions that process fresh water from rivers by mixing and transporting water through the estuary/river plume system. The near-field plume is an important region because, though small relative to the other regions of the estuary/plume system, mixing can be intense, and a significant fraction of the total mixing that river water experiences through the estuary/plume system can occur in the near-field plume. The near-field plume can thus modify flow in downstream regions, but can also be itself influenced by processes occurring at larger scales. In the next section, the dynamical regions surrounding the near-field river plume are examined in more detail.

Estuarine outflow defines the initial salinity and volume transport of the coastal plume. If the mouth is narrow, a near-field plume will form, and salinity and momentum will be rapidly modified by intense mixing. Otherwise, the estuarine outflow will form a buoyancy driven coastal current where properties will change much more slowly; this type of flow is more a continuation of the flow patterns in the estuary, and is not as dynamically distinct as a near-field plume. A key difference between these two features is that the near-field plume is supercritical, with $Fr = U\sqrt{g'h} > 1$, so that momentum in the near-field plume is strong. The strong momentum in the near-field plume inhibits the immediate formation of a rotating coastal current, and often directs the flow offshore.

As the near-field plume collapses and transitions back to subcritical flow, rotation becomes a dominant factor, and the flow is redirected toward the coast. This creates a recirculating bulge that has been the focus of a number of laboratory Avicola and Huq (2003), Horner-Devine et al. (2006), numerical Fong and Geyer (2002), Isobe (2005), and observational Horner-Devine (2009), Kudela et al. (2010) studies. Connections between the near-field plume and the recirculating bulge are not yet clear, but there are two potential interactions that can influence the near-field plume circulation. First, the transition from (non-rotating) near-field jet to (rotating) bulge region is not abrupt, and rotational effects are important at the end of the near-field region Cole (2014); this may cause a shutdown in near-field plume spreading that then inhibits mixing. The second potential interaction is that the returning, up-coast flow in the recirculating bulge may interact with the near-field plume; the recirculating bulge water may place additional forces on the near-field plume, or modify the water that is entrained.

Downcoast of the bulge region, an along-shore coastal current forms [] that may be affected by tides De Boer et al. (2008), Pritchard and Huntley (2006) or winds (Fong and Geyer 2001; Hetland 2005; Lentz 2004; Jurisa and Chant 2013). Though this region is typically much larger than the near-field plume, the influence of the near-field is important because the estuarine outflow may be significantly modified in the near-field. Many theoretical studies relate the structure of the coastal current flow to properties of the estuarine outflow, but in practice this should be related instead to the water properies leaving the near-field plume.

The initiation of the near-field plume is located at a point of internal hydraulic control. In practice this is usually bottom, topographic control from a tidal bar at the mouth of an estuary, like in the Merrimack MacDonald et al. (2007) or Fraser MacDonald and Geyer (2005) rivers, however there are also cases where the control is created at the end of the jetties, where the channel width goes from finite to infinite, as in the case of some of the Mississippi Delta passes Wright and Coleman (1971). After the hydraulic control point, the seaward flow transitions to supercricital, and this supercritical flow characterizes the near-field plume.

Supercritical flow influences the near-field plume in two ways. First, high Froude numbers imply low bulk Richardson numbers, where $Ri_b = g'hU^{-2} = Fr^{-2}$ which in turn means the flow could be susceptible to internal Kelvin-Helmholtz instabilities. Second, the supercritical flow is often associated with flow separation at the estuary mouth. This can be influenced by the geometry of the estuary mouth; for example, jetties will tend to favor flow separation more than a gradually widening, funnel-shaped estuary mouth.

If a near-field plume separates from the coastline, the plume will be able to freely spread. The spreading rate will be twice the internal gravity wave speed, the edges of the plume will each expand in a direction away from the axis of the plume at a rate defined by the local internal phase speed Hetland and MacDonald (2008). Properties within the core of the plume are fairly constant in the lateral direction, and are primarily a function of the distance from the estuary mouth. As such, the spreading rate is also primarily a function of distance from the mouth, and does not significantly vary laterally across the plume.

Note that if the plume does not separate, the geometry of the estuary and coastline will control the spreading rate instead of internal plume dynamics. In this case, a plume might look more like an expansion within an estuary, where the buoyant water maintains contact with the spreading boundaries (see Geyer et al. 2017); situations like this are also associated with elevated and intense mixing Geyer et al. (2010). Similarly, the numerical simulations by O'Donnell (1990) show solutions for a radial source where the flow does not separate from the coastline; in this case as well, the spreading rate of the plume is specified by geometry, and not a dynamical feature of the plume to be solved for.

Mixing in the near-field plume is driven by shear instabilities that can be quite intense. In both the Merrimack MacDonald et al. (2007) and Columbia plumes Nash et al. (2009), shear squared and stratification frequency squared can both exceed 0.1 s^{-2}, and turbulence dissipation rates well exceeding 10^{-4} $m^{-2}s^{-3}$. A comparison between simulated and observed dissipation rates in the Merrimack river plume MacDonald et al. (2007) showed good agreement in magnitude and spatial distribution, most likely because the turbulence closure schemes work well under the strong signal of intense mixing.

There is a process that may bias estimates of mixing in 0D mixing parameterizations, which includes essentially all modern turbulence closure schemes: there is some evidence that mixing may be enhanced even beyond what is expected from a local Richardson number-based parameterization through stretching and intensification of the vortex tubes. As Kelvin-Helmholtz billows roll up, they are also stretched laterally by the spreading plume. This spreading can further enhance the lateral vorticity associated with the rolling billow, pumping more energy into the turbulent cascade MacDonald and Chen (2012). In practice, this effect may be difficult to separate from variability in mixing within the plume, and a 0D mixing parameterization will reproduce the primary features terms of mixing strength and distribution MacDonald et al. (2007). In other situations, for example when a vortex tube starts as vertical vorticity and is stretched laterally due to baroclinic shear, the intensification in the mixing can be a dominant process (e.g., Farmer et al. 2002).

8.3 A Simple Near-Field Plume Model

Following Hetland (2010), the combined effects of a control point at the estuary mouth (i.e., liftoff), and subsequent plume spreading and mixing can be combined into a simple analytic model of the plume that can be used to approximate plume structure and estimate net mixing through the near-field plume. The key dependant variables are the density anomaly of the plume, $\Delta\rho$, the thickness of the active layer, h, the axial velocity, u, and the plume width, W; see Fig. 8.1.

Consider a rectangular estuary mouth, with width W_0. We will consider the estuarine outflow to be a single active layer over quiescent receiving waters, so we use a reduced gravity model. The outflow velocity is u_0, and the depth of the upper layer is h_0, both subject to the constraint that the flow is exactly critical (i.e., the mouth

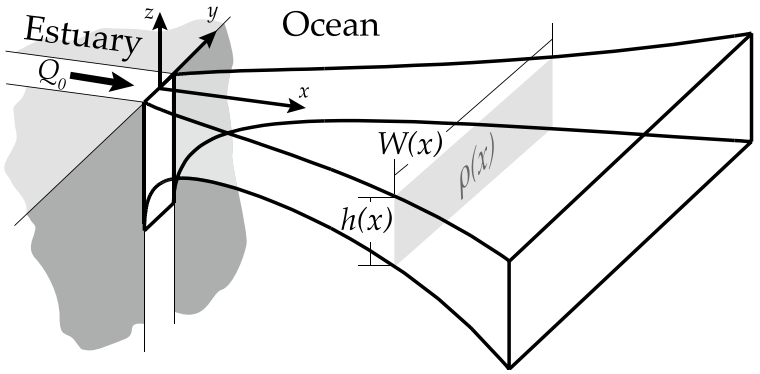

Fig. 8.1 A schematic showing the variables in the simple model of a near-field plume

acts as a constriction, see Armi and Farmer 1986; Farmer and Armi 1986), so that the internal Froude number is one,

$$\mathrm{Fr}\Big|_{x=0} = \frac{u}{\sqrt{g'h}}\Big|_{x=0} = 1, \tag{8.1}$$

where $g' = g\Delta\rho\rho_0^{-1}$ is the reduced gravity, g the gravitational acceleration, $\Delta\rho$ the buoyancy anomaly of the active layer, and ρ_0 the density of the receiving waters.

As the plume evolves, it can entrain receiving waters into the active layer through an entrainment velocity, w_e. The entrainment velocity will be a parameterization of mixing processes, and could therefore be dependent on potential and kinetic energy anomalies in the flow; a more detailed discussion of the parameterization of entrainment follows, but for now it can be treated as an arbitrary function, or to simplify the analysis, constant. Entertainment will affect both momentum and density anomalies in the plume.

Conservation of momentum along the plume axis , x, following a slab of water exiting the estuary mouth, is

$$\frac{Du}{Dt} = -(g'h)_x - \frac{w_e u}{h}, \tag{8.2}$$

where g' must also be considered within the gradient operator as there can be an adverse pressure gradient due to the decreasing density anomaly. Conservation of density can be used to describe the evolution of the density anomaly following the slab of water

$$\frac{D\Delta\rho}{Dt} = -\frac{w_e\Delta\rho}{h}. \tag{8.3}$$

The width of the slab will increase at twice the local gravity wave speed, (see Hetland and MacDonald 2008, as discussed above) requiring

$$\frac{DW}{Dt} = 2\sqrt{g'h} \tag{8.4}$$

Finally, conservation of mass requires

$$\frac{D}{Dt}\left(huW\Delta\rho\right) = 0. \tag{8.5}$$

Assuming that the plume is steady, the total derivative can be converted to an advection term

$$\frac{D}{Dt} = u\frac{\partial}{\partial x}. \tag{8.6}$$

The equations can then be written as a set of ordinary differential equations, in x,

$$\frac{\partial \Delta\rho}{\partial x} = -\Delta\rho\frac{w_e}{u\,h} \tag{8.7}$$

$$\frac{\partial W}{\partial x} = 2Fr^{-1} \tag{8.8}$$

$$\frac{\partial u}{\partial x} = \frac{u}{(1 - Fr^{-2})}\left[\frac{\Delta\rho_x}{\Delta\rho} + Fr^{-2}\frac{W_x}{W}\right] \tag{8.9}$$

$$\frac{\partial h}{\partial x} = -h\left[\frac{\Delta\rho_x}{\Delta\rho} + \frac{W_x}{W} + \frac{u_x}{u}\right] \tag{8.10}$$

where the internal Froude number, $Fr = u(g'h)^{-1/2}$ has been substituted where appropriate. A solution to this set of equations can be found numerically using standard ODE solvers by integrating from the source, $x = 0$, toward the offshore direction. The solution is valid only for the region of the plume that is supercritical, where the wave characteristics are directed only offshore, so the solution ends when Fr returns to one.

An equation for the evolution of the Froude number can be diagnosed from this set of equations,

$$\frac{\partial Fr}{\partial x} = \frac{uh(Fr^2 + 2) - \frac{3}{2}w_e W Fr^3}{Q(Fr^2 - 1)}. \tag{8.11}$$

This equation demonstrates the interplay between mixing an spreading in the plume. In the case with no entrainment, $w_e = 0$, the Froude number always increases, since the near-field plume is defined by the region of supercritical flow, $Fr > 1$. The increasing Froude number is due to the spreading, shoaling, and subsequent acceleration of the plume; the rate of spreading actually decreases as the plume advects offshore as the plume accelerates and the spreading rate decreases due to decreasing plume thickness, resulting in a tulip shaped plume. If mixing is included this term will eventually dominate as the Froude number increases—this is true even if the mixing rate does not depend on the Froude number, but the effect is exacerbated if it

does. When mixing dominates, the Froude number decreases offshore, and the rate of expansion increases resulting in a trumpet shaped plume.

The near-field plume is a supercritical feature, so the Froude number must increase from its initial value of one for the plume to have a region of supercriticality, in other words, $Fr_x|_{x=0}) > 1$. By Eq. 8.11, this requires

$$\frac{weW_0^2}{Q_0} < 2 \tag{8.12}$$

at the estuary mouth, where the subscript 0 indicates values of the width and volume transport at the mouth.

Observations, idealized 3D models, and the simple near-field plume model all suggest that a typical structure is that the Froude number rapidly increases just outside the estuary mouth and quickly reaches a maximum of around 1.5–2. The Froude number then gradually decreases in the bulk of the plume where mixing dominates spreading. This region could be considered similar to an extended hydraulic jump, except for the fact that mixing is slow enough that the plume structure can substantially change over the extent of the mixing region, in particular, the plume can accelerate due to spreading.

The ratio of vertically and horizontally integrated kinetic energy,

$$KE_I = \int_{-\frac{W}{2}}^{\frac{W}{2}} \int_{-h}^{0} \frac{1}{2}\rho_0 u^2 dz\, dx = \frac{1}{2}\rho_0 u^2 hW, \tag{8.13}$$

to vertically and horizontally integrated potential energy,

$$APE_I = \int_{-\frac{W}{2}}^{\frac{W}{2}} \int_{-h}^{0} \frac{1}{2}\rho' g z\, dz\, dx = \frac{1}{2}\rho' g h^2 W, \tag{8.14}$$

is given by Fr^2. The Froude number thus describes the partitioning of integrated energy in the plume, but does not describe the total integraded energy, $KE_I + APE_I$. There are two ways to consider energy in the plume: following a parcel at the surface, and integrating across the entire plume.

The Bernoulli function, derived from conservation of momentum, defines the summed energy of a parcel following the flow at the free surface, given in a steady plume by

$$u\frac{\partial B}{\partial x} = u\frac{\partial}{\partial x}\left(\frac{1}{2}u^2 + g'h\right) = -\frac{w_e u}{h}. \tag{8.15}$$

In the absence of mixing, $w_e = 0$, the total energy of a parcel at the free surface is constant; the total energy of the surface parcel is reduced by entrainment.

The total integrated energy of the plume is more complicated. The change in the total integrated energy may then be calculated as

$$u\frac{\partial}{\partial x}\left(KE_I + APE_I\right) = \sqrt{g'h}\left(\frac{h\sqrt{g'h} - w_e W(Fr^2 - \frac{1}{2})}{Fr(Fr^2 - 1)}\right). \tag{8.16}$$

Similar to the evolution of the Froude number, the total energy in the near-field plume increase away from the estuary mouth in the absence of mixing; entrainment reduces the total energy. The increase in energy can be thought of as caused by pressure forces on the spreading plume. Consider a plume in an expanding channel, such that the expansion is prescribed and not calculated. Pressure forces at the boundaries accelerate the plume, like an inverse form drag. Similar processes are acting here, except it is the receiving waters that are applying pressure to, and thereby accelerating, the plume.

A curious feature of the model is that the net mixing through the near-field plume, as defined by the dilution of the density anomaly at the point where the plume transitions back to subcritical is inversely proportional to the local mixing rate. An example of this is shown in Fig. 8.2, where the final density anomaly of the plume, $\Delta\rho$, normalized by the initial density anomaly $\Delta\rho_0$, is plotted against the normalized entertainment velocity, $w_e W_0^2/Q_0$. The motivation for this choice of normalization is discussed in detail in Hetland (2010), but can be seen as being inspired by the

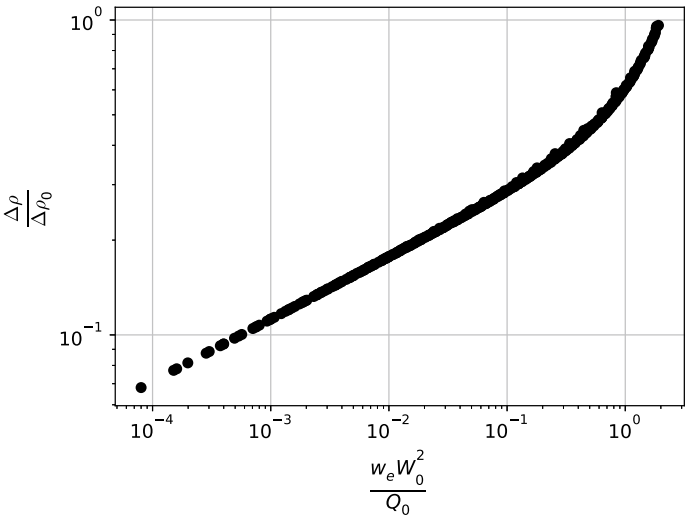

Fig. 8.2 A parameter space of simulations of the simple near-field plume layer model with constant entrainment shows normalized plume dilution, $\Delta\rho\Delta\rho_0^{-1}$, as a function of normalized local entrainment, $w_e W_0^2 Q_0^{-1}$. The near-field plume does not exist, and no dilution occurs for $\Delta\rho\Delta\rho_0^{-1}$ = 1, higher dilution occurs at lower values. Parameters and value ranges include the width of the estuary mouth Wo = 50–3000 m, the fresh water transport Q_f = 10–3000 m^3 s^{-1}, the initial density anomaly $\Delta\rho_0$ = 1–24 kg m^{-3}, and the entrainment velocity w_e = 10^{-4} to 5×10^{-3}. The density difference between the recieving waters and fresh water is constant through the simulations, $\Delta\rho_f$ = 24 kg m^{-3}

criticality condition in Eq. 8.12. For the cases shown, the entrainment velocity is constant for each particular simulation, but varies across the parameter space, along with the initial width, W_0, initial volume flux of the estuarine outflow, Q_0, and initial density anomaly. The result that increased local mixing decreases net plume dilution is robust for different is consistent across different mixing parameterizations, but the functional relationship is shifted, and the collapse is not always as tight.

8.4 Complications to The Simple Plume Model

While the simple model of the near-field plume is a useful conceptual tool that contains many key elements observed in energetic near-field plumes, in particular the interplay between spreading and mixing, there are a number of complications that limit the applicability of this model to predictions of real conditions.

8.4.1 Local Mixing Parameterization

In the absence of mixing, the near-field plume will spread and thin indefinitely, or until some other process arrests the spreading; this can be seen by setting $w_e = 0$ in Eq. 8.11. Using a constant entrainment velocity gives solutions that qualitatively agree with idealized numerical solutions, but the predicted Froude numbers are often too high.

A sensible alternative is to use a mixing parameterization that is dependent on the local Richardson number. However, common closures, such as the classic Ellison and Turner (1959) scheme cease mixing at a critical Richardson number of 0.6, or a Froude number of about 1.12. Without some background or minimum mixing, the plume will never collapse, and after reaching the peak Froude number, the Froude number will decrease, and the Richardson number will correspondingly increase, until it reaches the critical value of 0.8. Then it will remain at this critical value of the Richardson number, as there is a constant acceleration due to spreading that will only be countered when the Froude number is higher than 1.12. Other closure schemes for layer models, such as Christodoulou (1986) and Cenedese and Adduce (2008), allow mixing at Froude numbers as low as 1.0, so these choices are good alternatives that do not rely on an *ad hoc* background mixing rate.

An example of two simulations using the idealized near-field plume model are shown in Fig. 8.3. The horizontal structure of both plumes is similar, with the length and width scales being of similar order, with the plume extending five to six kilometers offshore with a width of eight to twelve kilometers; the plume depth is generally between one to two meters. There are larger differences in the other parameters: there is about 50% more dilution at the end of the near-field in the variable mixing case, and the Froude number is much larger in the constant mixing case. It is not immediately clear which parameterization best matches reality.

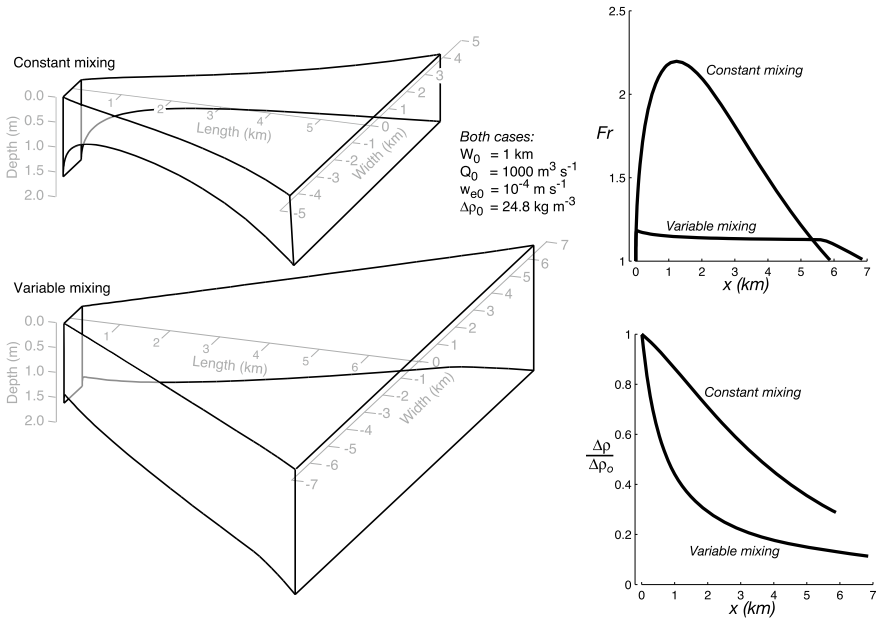

Fig. 8.3 Two idealized near-field plume simulations using constant entrainment, $w_e = w_{e0}$, and the Ellison and Turner (1959) parameterization, with a background (minimum) mixing of w_{e0}. The density anomaly and Froude number along the axis of each plume is shown to the right. The background mixing in the variable mixing case is triggered just before 6 km offshore, and can be seen as a kink in the Froude number profile, and in the layer thickness, but has little effect on the density anomaly

8.4.2 Plume Frontal Mixing

Near-field plume fronts can be regions of intense overturning and mixing. Observations of the Columbia River tidal plume show that fresh water at the plume front can plunge to 30 m below the free surface, about three times the thickness of the plume. Measurements in the Connecticut river plume also show the plume front being about twice that of the plume, though the plume is much thinner at about a meter O'Donnell et al. (1998). While direct measurements of overturning and resultant mixing have so far not been possible due to the rapid translation of the plume front, analogies to gravity current bore heads suggest that mixing is intense.

Despite the fact that mixing at the front is clearly very intense, there is ongoing debate about what percentage of total net mixing within the plume that occurs at the plume front versus the supercritical flow region behind the plume front. Pritchard and Huntley (2006) suggest that essentially all of the near-field plume mixing occurs within the front; Orton and Jay (2005) suggest about 20% of net mixing occurs within the Columbia plume front; Cole (2014) found even less net mixing within the plume front in a series of idealized experiments.

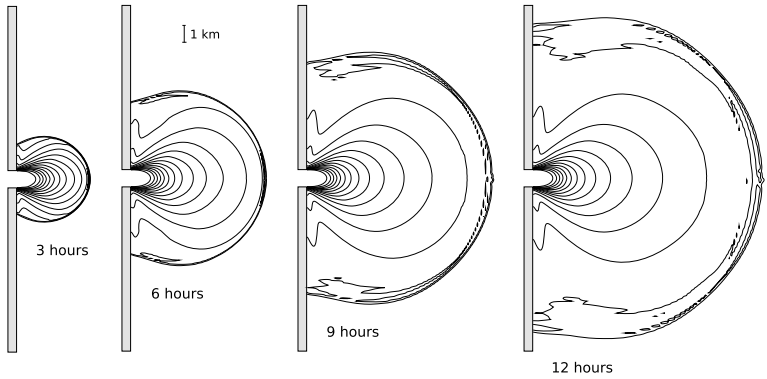

Fig. 8.4 Surface density contours are shown at four stages of plume evolution from a three-dimensional, non-linear hydrodynamic simulation using an idealized configuration

To further emphasize the ambiguity in the interaction between the quasi-steady plume and plume front, idealized experiments using steady fresh water forcing suggest that as the plume front propagates, it exposes a steady near-field plume in its wake (see Fig. 8.4). Thus, studies of mixing within a plume have used both perspectives of flow through a steady plume Hetland (2010), or a Lagrangian perspective following the plume front Jay et al. (2010). Though conceptually distinct, there is considerable overlap in the analytical methods used to solve these two problems.

8.4.3 Rotation and Return to Geostrophy

High Froude numbers within a near-field plume imply strong advection. Thus high Froude numbers are generally associated with high Rossby numbers, $Ro = U(fL)^{-1}$, which in turn implies that rotation may not be a dominant factor in the flow. A key factor is the timescale of flow through the near-field; if this timescale is on the order of, or longer than, the rotational timescale f^{-1}, the flow will likely be influenced by rotation. In practice, the timescales of flow through a near-field plume are rarely greater than an hour, so the impact of rotation is primarily to lean the plume toward the downcoast direction, as defined by the direction of coastal Kelvin wave propagation. But the result of even this minor influence of rotation is that spreading may be suppressed by the turning of the plume so that net plume mixing may be reduced as compared to a non-rotating plume Cole and Hetland (2016).

8.5 Conclusions

The near-field plume, when it exists, is a small region of intense mixing that can strongly alter estuarine outflow before it enters the larger, geostrophic river plume. This manuscript highlighted the importance of two competing dynamical processes that determine the evolution of a near-field plume: mixing and spreading. Unfortunately, the simple analytical description of a near-field plume has a number of problems that prevent it being used for predicting the conditions in realistic plumes, notably the sensitivity to the mixing parameterization and ignoring the effects of other mixing processes, such as winds and tides, and rotation.

The steady plume solution is mathematically similar to models of mixing in a propagating plume front, as the steady plume can be thought of as being exposed in the wake of a propagating plume front. It is not clear which conceptual model is correct, as the relative amounts of mixing in the plume front, and in the steady plume behind the front, are not well established.

Future work in near-field plume dynamics will most likely have to rely heavily on three-dimensional ocean models, as the processes that are unknown are nonlinear, like mixing, or difficult to place into a simple model, like rotation. Simulations in the Merrimack river plume MacDonald et al. (2007); Hetland and MacDonald (2008), or the Columbia river plume MacCready et al. (2009) show that numerical models are capable of reproducing observed features in the near-field, so they may be used as a tool for further investigation and understanding.

References

Armi, L., and D.M. Farmer. 1986. Maximal two-layer exchange through a contraction with barotropic net flow. *Journal of Fluid Mechanics* 164: 27–51.

Avicola, G., and P. Huq. 2003. The characteristics of the recirculating bulge region in coastal buoyant outflows. *Journal of Marine Research* 61 (4): 435–463.

Britter, R.E., and J.E. Simpson. 1978. Experiments on the dynamics of a gravity current head. *Journal of Fluid Mechanics* 88: 223–240.

Cenedese, C., and C. Adduce. 2008. Mixing in a density-driven current flowing down a slope in a rotating fluid. *Journal of Fluid Mechanics* 604: 369–388.

Christodoulou, G.C. 1986. Interfacial mixing in stratified flows. *Journal of Hydraulic Research* 24 (2): 77–92.

Cole, K.L., and R.D. Hetland. 2016. The effects of rotation and river discharge on net mixing in small-mouth kelvin number plumes. *Journal of Physical Oceanography* 46 (5): 1421–1436.

Cole, K.L. 2014. *A numerical study of the mid-field river plume*. Ph.D. thesis.

De Boer, G.J., J.D. Pietrzak, and J.C. Winterwerp. 2008. Using the potential energy anomaly equation to investigate tidal straining and advection of stratification in a region of freshwater influence. *Ocean Modeling* 22: 1–11.

Ellison, T.H., and J.S. Turner. 1959. Turbulent entrainment in stratified flows. *Journal of Fluid Mechanics* 6: 423–448.

Farmer, D., R. Pawlowicz, and R. Jiang. 2002. Tilting separation flows: A mechanism for intense vertical mixing in the coastal ocean. *Dynamics of Atmospheres and Oceans* 36 (1): 43–58.

Farmer, D.M., and L. Armi. 1986. Maximal two-layer exchange over a sill and through the combination of a sill and contraction with barotropic flow. *Journal of Fluid Mechanics* 164: 53–76.
Fong, D.A., and W.R. Geyer. 2001. Response of a river plume during an upwelling favorable wind event. *Journal of Geophysical Research* 106 (C1): 1067–1084.
Fong, D.A., and W.R. Geyer. 2002. The alongshore transport of freshwater in a surface-trapped river plume. *Journal of Physical Oceanography* 32: 957–972.
Garvine, R.W. 1974. Physical features of the Connecticut River outflow during high discharge. *Journal of Geophysical Research* 79: 831–846.
Garvine, R.W. 1982. A steady state model for buoyant surface plume hydrodynamics in coastal waters. *Tellus* 34: 293–306.
Garvine, R.W. 1987. Estuary plumes and fronts in shelf waters: A layer model. *Journal of Physical Oceanography* 17: 1877–1896.
Garvine, R.W., and J.D. Monk. 1974. Frontal structure of a river plume. *Journal of Geophysical Research* 79 (15): 2251–2259.
Geyer, W.R., D.K. Ralston, and R.C. Holleman. 2017. Hydraulics and mixing in a laterally divergent channel of a highly stratified estuary. *Journal of Geophysical Research: Oceans* 122 (6): 4743–4760.
Geyer, W.R., A.C. Lavery, M.E. Scully, and J.H. Trowbridge. 2010. Mixing by shear instability at high Reynolds number. *Geophysical Research Letters* 37: L22607.
Hetland, R.D. 2005. Relating river plume structure to vertical mixing. *Journal of Physical Oceanography* 35 (9): 1667–1688.
Hetland, R.D. 2010. The effects of mixing and spreading on density in near-field river plumes. *Dynamics of Atmospheres and Oceans* 49: 37–53.
Hetland, R.D., and D.G. MacDonald. 2008. Spreading in the near-field Merrimack River plume. *Ocean Modeling* 21: 12–21.
Horner-Devine, A.R. 2009. The bulge circulation in the Columbia River plume. *Continental Shelf Research* 29: 234–251.
Horner-Devine, A.R., D.A. Fong, S.G. Monismith, and T. Maxworthy. 2006. Laboratory experiments simulating a coastal river discharge. *Journal of Fluid Mechanics* 555: 203–232.
Horner-Devine, A.R., R.D. Hetland, and D.G. MacDonald. 2015. Mixing and transport in coastal river plumes. *Annual Review of Fluid Mechanics* 47(1).
Isobe, A. 2006. Ballooning of river-plume bulge and its stabilization by tidal currents. *Journal of Physical Oceanography* 35 (12): 2337–2351.
Jay, D.A., E.D. Zaron, and J. Pan. 2010. Initial expansion of the Columbia River tidal plume: Theory and remote sensing observations. *Journal of Geophysical Research: Oceans* 115: C00B15.
Jones, G.R., J.D. Nash, R.L. Doneker, and G.H. Jirka. 2007. Buoyant surface discharges into water bodies. I: Flow classification and prediction methodology. *Journal of Hydraulic Engineering* 133(9): 1010–1020.
Jurisa, J.T., and R.J. Chant. 2013. Impact of offshore winds on a buoyant river plume system. *Journal of Physical Oceanography* 43 (12): 2571–2587.
Kilcher, L.F., and J.D. Nash. 2010. Structure and dynamics of the Columbia River tidal plume front. *Journal of Geophysical Research*, 115: C05S90.
Kudela, R.M., A.R. Horner-Devine, N.S. Banas, B.M. Hickey, T.D. Peterson, R.M. McCabe, E.J. Lessard, E. Frame, K.W. Bruland, D.A. Jay, J.O. Peterson, W.T. Peterson, P.M. Kosro, S.L. Palacios, M.C. Lohan, and E.P. Dever. 2010. Multiple trophic levels fueled by recirculation in the Columbia River plume. *Geophysical Research Letters* 37 (18): L18607.
Lentz, S. 2004. The response of buoyant coastal plumes to upwelling-favorable winds. *Journal of Physical Oceanography* 34 (11): 2458–2467.
Luketina, D., and J. Imberger. 1987. Characteristics of a surface buoyant jet. *Journal of Geophysical Research* 92 (C5): 5435–5447.
MacCready, P., N.S. Banas, B.M. Hickey, E.P. Dever, and Y. Liu. 2009. A model study of tide- and wind-induced mixing in the Columbia River estuary and plume. *Continental Shelf Research* 29 (1): 278–291.

MacDonald, D.G., and F. Chen. 2012. Enhancement of turbulence through lateral spreading in a stratified-shear flow: Development and assessment of a conceptual model. *Journal of Geophysical Research* 117: C05025.

MacDonald, D.G., and W.R. Geyer. 2005. Hydraulic control of a highly stratified estuarine front. *Journal of Physical Oceanography* 35 (3): 374–387.

MacDonald, D.G., L. Goodman, and R.D. Hetland. 2007. Turbulent dissipation in a near-field river plume: A comparison of control volume and microstructure observations with a numerical model. *Journal of Geophysical Research* 112: C07026.

Nash, J.D., and J.N. Moum. 2005. River plumes as a source of large-amplitude internal waves in the coastal ocean. *Nature* 437: 400–403.

Nash, J.D., L.F. Kilcher, and J.N. Moum. 2009. Structure and composition of a strongly stratified, tidally pulsed river plume. *Journal of Geophysical Research* 114: C00B12.

O'Donnell, J., and R.W. Garvine. 1983. A time dependent, two-layer frontal model of buoyant plume dynamics. *Tellus A: Dynamic Meteorology and Oceanography* 35(1): 73–80.

O'Donnell, J. 1990. The formation and fate of a river plume: A numerical model. *Journal of Physical Oceanography* 20 (4): 551–569.

O'Donnell, J., G.O. Marmorino, and C.L. Trump. 1998. Convergence and downwelling at a river plume front. *Journal of Geophysical Research* 28: 1481–1495.

Orton, P.M., and D.A. Jay. 2005. Observations at the tidal plume front of a high-volume river outflow. *Geophysical Research Letters* 32 (11): 1–4.

Pritchard, M., and D.A. Huntley. 2002. Instability and mixing in a small estuarine plume front. *Estuarine, Coastal and Shelf Science* 55 (2): 275–285.

Pritchard, M., and D.A. Huntley. 2006. A simplified energy and mixing budget for a small river plume discharge. *Journal of Geophysical Research* 111 (3): C03019.

Stashchuk, N., and V. Vlasenko. 2009. Generation of internal waves by a supercritical stratified plume. *Journal of Geophysical Research* 114: C01004.

Wright, L.D., and J.M. Coleman. 1971. Effluent expansion and interfacial mixing in the presence of a Salt Wedge Mississippi River Delta. *Journal of Geophysical Research* 76 (36): 8649–8661.

Chapter 9
Lagrangian Modelling of Transport Phenomena Using Stochastic Differential Equations

Arnold Heemink, Eric Deleersnijder, Syed Hyder Ali Muttaqi Shah, and Ulf Gräwe

Abstract When modelling transport processes in marine waters one might have to solve the advection-diffusion equation or one can simulate the stochastic behaviour of individual particles of the constituent under study. By using the well-established theory of stochastic differential equations (SDEs) it is possible to derive for any advection-diffusion model an underlying SDE governing the behaviour of one particle of the constituent. Using a numerical scheme for approximating this SDE a particle model can then be obtained. In the present Chapter we first briefly describe the results of the theory of SDEs that are relevant for marine transport modelling. Then we derive a number of particle models for solving different types of transport problems and formulate these particle models as SDEs. Finally we discuss the numerical treatment of SDEs and propose a number of numerical schemes for the particle models. The performance of the methods is illustrated by a number of idealized test cases of turbulent dispersion. The test cases considered are inspired by shallow-sea dynamics and large-scale ocean transport processes.

A. Heemink (✉)
Delft University of Technology, Delft, Netherlands
e-mail: a.w.heemink@tudelft.nl

E. Deleersnijder
Université Catholique de Louvain, Ottignies-Louvain-la-Neuve, Belgium
e-mail: eric.deleersnijder@uclouvain.be

S. H. A. M. Shah
Sukkur Institute of Business Administration University, Sukkur, Pakistan
e-mail: syed.hyderali@iba-suk.edu.pk

U. Gräwe
Leibniz Institute for Baltic Sea Research Warnemünde (IOW), Rostock, Germany
e-mail: ulf.graewe@io-warnemuende.de

H. Schuttelaars et al. (eds.), *The Mathematics of Marine Modelling*,
Mathematics of Planet Earth 9, https://doi.org/10.1007/978-3-031-09559-7_9

9.1 Introduction

There are two different approaches to model transport processes in oceanic or coastal waters. One might adopt the Eulerian point of view and, hence, solve numerically the associated advection-diffusion equations. Another option consists in having recourse to Lagrangian models where the behaviour of individual particles of the constituent is considered. By simulating the position of many particles using a random generator the transport processes can be described (Dimou and Adams 1993; Hunter et al. 1993; Visser 1997, 2008).

In most textbooks the relation between the Eulerian and Lagrangian approaches is examined for the very simple case of a diffusion process with constant diffusivity. More general problems are seldom addressed. However, by using the well-established theory of SDEs it is possible to derive for any advection-diffusion model an underlying SDE governing the behaviour of one particle of the constituent. Using a numerical scheme for approximating the solution to this SDE a particle model can then be obtained. The latter is consistent with the advection-diffusion equation under consideration in the following sense: as the number of particles is increased and as the time step is decreased, the results of the particle model converge to the exact solution of the advection-diffusion equation.

The theory of SDEs and the numerical approximation thereof are not straightforward extensions of the deterministic case and, in many respects, seem to be counterintuitive. Most of the mathematical literature on these topics is difficult to comprehend for non-mathematicians. However, we do believe that a sufficient command of SDE theory would be very useful for those dealing with marine transport models. Eulerian and Lagrangian models are respectively based on two different views of the same transport processes. Knowledge on the relation between these two models increases the insight into both types of models and into the question as to which approach is optimal for a given problem. Moreover, if a Lagrangian model is formulated as an SDE then the higher order numerical schemes developed for SDEs can be used to obtain an accurate implementation of the particle model. As was clearly demonstrated by Stijnen et al. (2006), Shah et al. (2011), Shah (2015), Gräwe et al. (2012), just using the very simple Euler scheme is suboptimal in most cases. Therefore in this chapter we would like to bridge the gap between the mathematical theory and applications in oceanography. We do not present any new scientific results, but concentrate our efforts on explaining stochastic calculus and illustrating the theory with practical applications. We do not strive for mathematical rigor or completeness, but focus on the aspects that are relevant for marine transport problems. For a very good introduction on the theory of SDEs the reader is referred to the classical work of Jazwinski (1970) or, the more recent textbook of Oksendal (2003). Regarding the numerical treatment of SDEs, a comprehensive presentation may be found in the excellent book of Kloeden and Platen (1992).

In this chapter we first describe briefly the results of the theory of SDEs that are relevant for ocean transport modelling. We derive a number of particle models for solving different types of transport problems and formulate these particle models as

SDEs. Then we discuss the numerical treatment of SDEs and propose a number of numerical schemes for the particle models. We finally describe a number of relevant transport test cases to illustrate the performance of the Lagrangian approach.

9.2 Stochastic Differential Equations

9.2.1 Introduction

The time varying behaviour of particles moving in a fluid in the absence of diffusive effects can be described by deterministic ordinary differential equations. If we define the state of the physical system as the particle position $\mathbf{x}(t) = (x(t), y(t), z(t))$ we have the following model:

$$\frac{d\mathbf{x}}{dt} = \mathbf{f}(\mathbf{x}, t), \quad \mathbf{x}(t_0) = \mathbf{x}_0. \tag{9.1}$$

In case diffusive effects become important, the particle behaviour can only be described in terms of probability implying that a stochastic component needs to be added. Therefore in this chapter we discuss a SDE as a model for a stochastic process $\mathbf{X}_t$. Here we first consider models of the following type:

$$\frac{d\mathbf{X}_t}{dt} = \mathbf{f}(\mathbf{X}_t, t) + \sigma(\mathbf{X}_t, t)\,\mathbf{N}_t, \quad \mathbf{X}_{t_0} = \mathbf{X}_0, \tag{9.2}$$

where we have introduced a stochastic process $\mathbf{N}_t$ to model uncertainties in the underlying deterministic differential equation. The initial particle position $\mathbf{X}_0$ may also be a random variable. The notations $\mathbf{f}$ and σ refer to deterministic functions while the capital representations $\mathbf{X}_t$ and $\mathbf{N}_t$ are associated with stochastic processes.

Let us first consider the scalar case, X_t, of the stochastic model (9.2):

$$\frac{dX_t}{dt} = f(X_t, t) + \sigma(X_t, t)\,N_t, \quad X_{t_0} = X_0. \tag{9.3}$$

An essential property of this model is that it should be Markovian. This implies that information on the probability density of the state x_t at time t is sufficient for computing the future model state (times $> t$). If the model is not Markovian, then the information on the system state for times $< t$ would also be required. This would make the model very impractical. The SDE (9.3) can be shown to be Markovian if N_t is a continuous Gaussian white noise process with statistics:

$$E\{N_t\} = 0, \quad E\{N_t.N_s\} = \delta(t - s). \tag{9.4}$$

Here $E\{\cdot\}$ represents the expectation operator and $\delta(x)$ is the Dirac function. This is one of the very few processes that guarantee the model (9.3) to be Markovian. The importance of the white noise process lies in the fact that it has a very simple correlation structure. Therefore it is a good candidate for generating another process X_t with a certain probabilistic structure by means of the SDE (9.3). By generating this process X_t using a white noise forcing, the correlation structure of X_t is completely created by the SDE and not partly by the structure of the input N_t. Since we need to be careful when working with delta functions we will rewrite the SDE (9.3) in terms of a Wiener process.

A standard Wiener process $W_t, t \geq 0$ is a process with $W_0 = 0$ and with stationary independent increments such that for any $0 < s < t$ the increment $W_t - W_s$ is a Gaussian random variable with mean zero and variance equal to $t - s$. The formal derivative of the Wiener process can be shown to be the Gaussian continuous white noise process:

$$\frac{dW_t}{dt} = N_t, \tag{9.5}$$

or:

$$dW_t = N_t dt. \tag{9.6}$$

It is now convenient to rewrite the SDE (9.3) in term of the Wiener process:

$$\frac{dX_t}{dt} = f\left(X_t, t\right) + \sigma\left(X_t, t\right) \frac{dW_t}{dt}. \tag{9.7}$$

This equation is usually rewritten as follows:

$$dX_t = f\left(X_t, t\right) dt + \sigma\left(X_t, t\right) dW_t, \tag{9.8}$$

and can also be written as:

$$X_t = X_{t_0} + \int_{t_0}^{t} f\left(X_s, s\right) ds + \int_{t_0}^{t} \sigma\left(X_s, s\right) dW_s. \tag{9.9}$$

The second integral in (9.9) is a stochastic integral and in order to solve (9.9) the stochastic integral needs to be defined precisely. Using the Wiener process as a random driving force introduces some mathematical difficulties in defining and evaluating the stochastic integral in (9.9).

As pointed out above the Wiener process is a very attractive driving noise process in the stochastic model (9.9). There are only a very few alternatives that also guarantee that X_t is Markovian. Among them the Poisson jump process and the Lévy process are the most popular ones (Gardiner 1985). The Wiener process is often used for modelling physical processes, while the other two processes are very popular in finance. More recently the Lévy process (Hanert 2012; Vallaeys et al. 2017) has also been introduced for transport modelling.

9.2.2 Îto Stochastic Integrals

Dealing with stochastic model (9.9) requires the evaluation of a stochastic integral of the following type:

$$\int_{t_0}^{t} \sigma_s dW_s, \tag{9.10}$$

where σ_s is a general stochastic process and W_s is a Wiener process. To illustrate the mathematical difficulties associated with stochastic integrals, let us first consider for example the deterministic integral:

$$\int_{t_0}^{t} s ds. \tag{9.11}$$

The classical Riemann-Stieltjes definition for this integral is:

$$\int_{t_0}^{t} s ds = \lim_{\Delta t \to 0} \sum t_i^* \left(t_{i+1} - t_i\right) = \frac{t^2}{2} - \frac{t_0^2}{2}, \tag{9.12}$$

where the interval $[t_0, t]$ is divided into many small sub intervals $[t_i, t_{i+1}]$ of length Δt and the point t_i^* is chosen somewhere in this interval. Let us now consider the stochastic integral:

$$\int_{t_0}^{t} W_s dW_s, \tag{9.13}$$

where W_s is a Wiener process. Inspired by the deterministic case (9.12) an obvious definition for this stochastic integral would be:

$$\int_{t_0}^{t} W_s dW_s = \text{l. i. m.}_{\Delta t \to 0} \sum W_{t_i^*} \left(W_{t_{i+1}} - W_{t_i}\right), \tag{9.14}$$

where again the interval $[t_0, t]$ is divided into many small sub intervals $[t_i, t_{i+1}]$ of length Δt and choose the point t_i^* somewhere in this interval. The "l.i.m." (limit in mean square sense) refers to a stochastic extension of a limit, i.e. a series of stochastic variables X_n is said to converge in the mean square sense to a limit X if

$$\lim_{n \to \infty} E\left\{(X_n - X)^2\right\} = 0, \tag{9.15}$$

which is denoted by:

$$\text{l. i. m.}_{n\to\infty} X_n = X. \tag{9.16}$$

This definition states that the variance of the stochastic variable defined as the difference between X_n and X will approach zero for large values of n. This implies that the probability that X_n will be significantly different from X will become very small in the limit $n \to \infty$.

Using the definition of the limit in mean square sense and the properties of the Wiener process it is possible to derive (after some clever algebra, Jazwinski (1970)) the stochastic limit of (9.14):

$$\int_{t_0}^{t} W_s dW_s = \frac{W_t^2}{2} - \frac{W_{t_0}^2}{2} - \frac{(t-t_0)}{2} + \sum_i \left(t_i^* - t_i\right). \tag{9.17}$$

From this result we see that unlike in the deterministic case shown in (9.12) this stochastic limit is not uniquely defined. The choice of t_i^* is important for the final result of the integral. Therefore we need another definition for a stochastic integral.

The Japanese mathematician Îto proposed the first and the most well-known definition of a stochastic integral. The Îto integral is defined as:

$$\int_{t_0}^{t} \sigma_s dW_s = \text{l. i. m.}_{\Delta t\to 0} \sum_{\Delta t\to 0} \sigma_{t_i} \left(W_{t_{i+1}} - W_{t_i}\right). \tag{9.18}$$

Using the Îto definition the evaluation point is always chosen at the beginning of the interval. Interpreting the integral (9.17) in Îto sense results in:

$$\int_{t_0}^{t} W_s dW_s = \frac{W_t^2}{2} - \frac{W_{t_0}^2}{2} - \frac{(t-t_0)}{2}. \tag{9.19}$$

This answer is not what we intuitively would expect. Compared to the corresponding deterministic result an additional term $\frac{(t-t_0)}{2}$ is obtained.

9.2.3 *Îto Stochastic Differential Equations*

Having defined the Îto stochastic integral we are now able to define the SDE (9.8)–(9.9) as an Îto SDE:

$$dX_t = f\left(X_t, t\right) dt + \sigma\left(X_t, t\right) dW_t, \tag{9.20}$$

or:

$$X_t = X_{t_0} + \int_{t_0}^{t} f\,(X_s, s)\,ds + \int_{t_0}^{t} \sigma\,(X_s, s)\,dW_s, \tag{9.21}$$

where the stochastic integral has to be interpreted in the Îto sense. Using the definition of the Îto stochastic integral it is possible to derive a simple numerical scheme for solving an Îto SDE (9.20)–(9.21). For a small time step we have:

$$\begin{aligned} X_{t+\Delta t} &= X_t + \int_{t}^{t+\Delta t} f\,(X_s, s)\,ds + \int_{t}^{t+\Delta t} \sigma\,(X_s, s)\,dW_s \\ &\approx X_t + \int_{t}^{t+\Delta t} f\,(X_t, t)\,ds + \int_{t}^{t+\Delta t} \sigma\,(X_t, t)\,dW_s \\ &= X_t + f\,(X_t, t)\,\Delta t + \sigma\,(X_t, t)\,(W_{t+\Delta t} - W_t) \\ &= X_t + f\,(X_t, t)\,\Delta t + \sigma\,(X_t, t)\,\Delta W, \end{aligned} \tag{9.22}$$

where the Wiener increment ΔW is a random variable with mean zero and variance Δt. This approximation is called the Euler-Maruyama scheme. This scheme is consistent with the Îto definition of the stochastic integral and can only be used for an Îto SDE. By using a random number generator realizations of the Wiener increments can easily be obtained.

From the Euler approximation we can also see that X_t is a Markov process. Additional information about X_s for $s < t$ will not help us to obtain more accurate predictions at $t + \Delta t$. The terms in the right hand side of (9.22) are exactly known given the value of X_t. The remaining Wiener increment is independent of previous increments and thus of X_s for all times $s < t$. As a result, information on X_s will not be useful to determine predictions of ΔW. Note that if the Wiener process would not have independent increments the process X_t would not be Markovian.

9.2.4 *Îto's Differentiation Rule*

Having defined the Îto integral we can now discuss Îto's differentiation rule. Consider the process X_t described by the Îto SDE:

$$dX_t = f\,(X_t, t)\,dt + \sigma\,(X_t, t)\,dW_t. \tag{9.23}$$

Let $g(x, t)$ be a sufficiently smooth deterministic function. Then the SDE for g_t is:

$$dg_t = \frac{\partial g}{\partial t}dt + \frac{\partial g}{\partial x}dX_t + \frac{1}{2}\sigma^2\frac{\partial^2 g}{\partial x^2}dt. \tag{9.24}$$

Clearly, from this equation we can see that this result is not what one would expect from classical analysis.

To illustrate the use of Îto's rule let us first consider a deterministic function $g(t) = e^{bt}$, where b is a constant. It is easy to see by differentiation that $g(t)$ is the solution of the deterministic differential equation:

$$\frac{dg}{dt} = bg, \quad g(0) = 1. \tag{9.25}$$

Now suppose we have a Wiener process W_t and let us derive the SDE for the process $g(W_t, t) = e^{bW_t}$. The application of the Îto differential rule for $x = w$, $\sigma = 1$ and for $g(w, t) = e^{bw}$ results in:

$$\frac{\partial g}{\partial t} = 0, \quad \frac{\partial g}{\partial x} = bg, \quad \frac{\partial^2 g}{\partial x^2} = b^2 g. \tag{9.26}$$

Substituting these results in (9.24) provides the SDE for g_t:

$$dg_t = \frac{b^2}{2} g_t dt + b g_t dW_t. \tag{9.27}$$

Note that this Îto SDE for g_t has an extra dt term compared to the deterministic result.

9.2.5 *Stratonovich Stochastic Differential Equations*

The Îto definition is not the only way to define stochastic integral (9.10). Stratonovich has introduced another definition:

$$\int_{t_0}^{t} \sigma_s dW_s = \text{l.i.m}_{\Delta t \to 0} \sum \frac{\sigma_{t_{i+1}+t_i}}{2} \left(W_{t_{i+1}} - W_{t_i} \right). \tag{9.28}$$

In the Stratonovich definition the evaluation point is chosen in the middle of the interval. Interpreting the integral (9.17) in Stratonovich sense results in:

$$\int_{t_0}^{t} W_s dW_s = \frac{W_t^2}{2} - \frac{W_{t_0}^2}{2}. \tag{9.29}$$

This shows that the Stratonovich calculus is in agreement with the corresponding deterministic results. A SDE can also be defined in Stratonovich sense using the Stratonovich integral definition. The relation between the Îto and Stratonovich SDE

is given below without proof. If a physical process X_t can be described by the Îto equation:

$$dX_t = f(X_t, t)\,dt + \sigma(X_t, t)\,dW_t, \tag{9.30}$$

then the same process can also be described by the Stratonovich equation:

$$dX_t = f(X_t, t)\,dt - \frac{1}{2}\sigma(X_t, t)\frac{\partial \sigma}{\partial x}(X_t, t)\,dt + \sigma(X_t, t)\,dW_t. \tag{9.31}$$

On the other hand if a physical process X_t can be described by the Stratonovich equation:

$$dX_t = f(X_t, t)\,dt + \sigma(X_t, t)\,dW_t, \tag{9.32}$$

then the same process can also be described by the Îto SDE:

$$dX_t = f(X_t, t)\,dt + \frac{1}{2}\sigma(X_t, t)\frac{\partial \sigma}{\partial x}(X_t, t)\,dt + \sigma(X_t, t)\,dW_t. \tag{9.33}$$

If σ does not depend on X_t the Îto and Stratonovich interpretations will both produce the same results.

For example, let g_t be again the solution of Îto (9.27):

$$dg_t = \frac{b^2}{2}g_t dt + bg_t dW_t. \tag{9.34}$$

Now from relation (9.31) we can establish that the same process is also the solution of the Stratonovich equation:

$$dg_t = bg_t dW_t. \tag{9.35}$$

From this example we see that the same process can be modelled by an Îto equation or by a Stratonovich equation. The equations are different but their solutions are similar since Îto and Stratonovich equations have to be solved using different rules. Physically, there is no difference between the Îto approach and the Stratonovich one. We can choose the definition we prefer as long as we use the calculation rules that are consistent with this definition. This includes the use of the correct numerical scheme for approximating the SDE.

Both Îto and Stratonovich calculus have their advantages and disadvantages. Îto is more convenient for the analysis of an SDE, while the Stratonovich results are more in agreement with our physical intuition. The Stratonovich SDE is also very important for the development of numerical approximations, since many popular schemes for solving deterministic differential equations can only be used for approximating a Stratonovich SDE.

More recently, another interpretation of the stochastic integral (9.10) called the Îto-backward was introduced:

$$\int_{t_0}^{t} \sigma_s dW_s = \text{l. i. m.}_{\Delta t \to 0} \sum \sigma_{t_{i+1}} \left(W_{t_{i+1}} - W_{t_i} \right). \tag{9.36}$$

Using this definition the evaluation point is chosen at the end of the interval. This stochastic integral is rarely used, but it has been shown by LaBolle et al. (2000) and Spivakovskaya et al. (2007b) that it is attractive for transport problems with diffusivity that strongly varies in space. If a physical process X_t can be described by the Îto SDE (9.30) it is also possible to transform this SDE into an Îto-backward SDE:

$$dX_t = f\left(X_t, t\right) dt - \sigma\left(X_t, t\right) \frac{\partial \sigma}{\partial x}\left(X_t, t\right) dt + \sigma\left(X_t, t\right) dW_t. \tag{9.37}$$

The process X_t can also be described by this backward Îto equation.

9.2.6 Fokker-Planck Equation

Consider now the vector case of the Îto SDE (9.23). To gain insight into the probability density of the particle position X_t which is related to the particle concentration we need to know the probability density function of X_t. Without proof we state that this function can be obtained by solving the Fokker-Planck equation also known as the Kolmogorov forward equation:

$$\frac{\partial p}{\partial t} = -\sum_{i=1}^{d} \frac{\partial \left(f_i p\right)}{\partial x_i} + \sum_{i=1}^{d} \sum_{j=1}^{d} \frac{\partial^2 \left(k_{ij} p\right)}{\partial x_i \partial x_j}. \tag{9.38}$$

The initial condition for (9.38) could be:

$$p(\mathbf{x}, t) = \delta\left(\mathbf{x} - \mathbf{x}_0\right), \tag{9.39}$$

implying that all particles were released at one point. The differential operator in (9.38) consists of the drift vector $\mathbf{f} = f_i$ as well as diffusion term given by a matrix $K = k_{ij}$. This diffusivity matrix K is symmetric and semi-positive definite and is related to the matrix σ in the following way:

$$k_{ij} = \frac{1}{2}\left(\sigma \sigma^{\top}\right)_{ij}. \tag{9.40}$$

Notice that the matrix σ is not uniquely determined by the symmetric matrix $K = k_{ij}$. Two possible choices of σ are the symmetric square root of k_{ij} and the lower triangular matrix given by the Cholesky decomposition of $K = k_{ij}$. All the choices of σ that are consistent with (9.40) give statistically identical diffusion processes.

The probability distribution $p(x,t)$ of the Fokker-Planck equation can be approximated by applying a numerical method to solve deterministic partial differential equation, but on the other hand the distribution $p(x,t)$ can also be approximated by generating the trajectories of the following Îto SDE:

$$d\mathbf{X}_t = f\left(\mathbf{X}_t, t\right) dt + \sigma\left(\mathbf{X}_t, t\right) d\mathbf{W}_t, \quad \mathbf{X}_{t_0} = \mathbf{X}_0. \tag{9.41}$$

The probability distribution of the Îto stochastic process (9.41) will satisfy the Fokker-Planck (9.38).

9.3 Particle Models for Marine Transport Problems

The Fokker-Planck equation describes the evolution in time of the particle concentration for a given SDE. But we can also use the theory the other way round. Although the Fokker-Planck equation models the distribution resulting from advection diffusion processes, it is not exactly equivalent to the classical advection diffusion equation. Therefore it is also possible to start from an advection diffusion equation that is often used for solving transport problems in oceans or coastal waters. By interpreting this transport model as a Fokker-Planck equation it is possible to derive the underlying SDE for the behaviour of the individual particles. In this way the particle model obtained can be considered as a Lagrangian solver for the original transport model.

Let us consider the following 3D advection diffusion equation written:

$$\frac{\partial C}{\partial t} = -\frac{\partial\left(u_i C\right)}{\partial x_i} + \frac{\partial}{\partial x_i}\left(k_{ij}\frac{\partial C}{\partial x_j}\right), \quad t_0 \le t \le T, \tag{9.42}$$

with positive-definite diffusivity tensor K with elements k_{ij} and the velocity field $\mathbf{u} = u_i$. The above equation (9.42) can be rewritten in the form

$$\begin{aligned} \frac{\partial C}{\partial t} &= -\frac{\partial}{\partial x_i}\left(u_i C\right) - \frac{\partial}{\partial x_i}\left(C\frac{\partial k_{ij}}{\partial x_j}\right) + \frac{\partial}{\partial x_i}\left(k_{ij}\frac{\partial C}{\partial x_j} + C\frac{\partial k_{ij}}{\partial x_j}\right) \\ \Rightarrow \frac{\partial C}{\partial t} &= -\frac{\partial}{\partial x_i}\left[\left(u_i + \frac{\partial k_{ij}}{\partial x_j}\right)C\right] + \frac{\partial^2\left(k_{ij}C\right)}{\partial x_i \partial x_j}. \end{aligned}$$

If we set $f_i = u_i + \frac{\partial k_{ij}}{\partial x_j}$ and $C = p$, the above equation will take the form of the Fokker-Planck equation (9.38). Thus the Îto stochastic model corresponding to (9.42) is obtained with this choice of $\mathbf{f}$ and with matrix σ as defined by (9.40) (Spivakovskaya et al. 2007a; Shah et al. 2011):

$$d\mathbf{X}_{\mathrm{t}} = f\left(\mathbf{X}_t, t\right) dt + \sigma\left(\mathbf{X}_t, t\right) d\mathbf{W}_t, \quad \mathbf{X}_{t_0} = \mathbf{X}_0. \tag{9.43}$$

It is also possible to include additional properties of the particle as an additional variable. Consider for example the particle model (9.43) with as additional parameter the age A_t of this particle, i.e. the time elapsed since this particle enters a specified domain:

$$dA_t = dt. \tag{9.44}$$

As long as the particle is in the specified domain A_t increases with time. The corresponding Eulerian model can be derived in this case again from the Fokker-Planck (9.38) for the probability $p(x, y, z, a, t)$to find a particle at location (x, y, z) with age a:

$$\frac{\partial p}{\partial t} = -\frac{\partial p}{\partial a} + \nabla \cdot (K \cdot \nabla p). \tag{9.45}$$

This equation is equivalent to the one derived by Delhez et al. (1999).

9.4 Numerical Approximation of Stochastic Differential Equations

Consider first the scalar deterministic equation:

$$\frac{dx}{dt} = f(x, t), x\,(t_0) = x_0. \tag{9.46}$$

We can approximate this equation numerically with the Euler scheme:

$$x_{n+1} = x_n + f\,(x_n, t_n)\,\Delta t, \tag{9.47}$$

where Δt is the time step. Recall that the order of convergence of a numerical scheme for a deterministic differential equation is defined as follows: The order of convergence is γ if there exists a positive constant c and a timestep Δ such that for fixed $T = N\Delta t$:

$$|x(T) - x_N| \leq c(\Delta t)^{\gamma}, \tag{9.48}$$

for all $0 < \Delta t < \Delta$.

Now consider the Îto SDE:

$$dX_t = f\,(X_t, t)\,dt + \sigma\,(X_t, t)\,dW_t, \tag{9.49}$$

with the Euler scheme introduced in Sect. 9.2.3:

$$x_{t+\Delta t} = x_t + f\,(x_t, t)\,\Delta t + \sigma\,(x_t, t)\,(W_{t+\Delta t} - W_t)\,, \tag{9.50}$$

or with $t_n = n\Delta t$:

$$x_{n+1} = x_n + f\,(x_n, t_n)\,\Delta t + \sigma\,(x_n, t_n)\,\Delta W_n. \tag{9.51}$$

First we have to generalize the definition of the order of convergence to the stochastic case: The strong order of convergence is γ if there exists a positive constant c and a Δ such that for fixed $T = N\Delta t$:

$$E\,\{|X_T - X_N|\} \leq c(\Delta t)^{\gamma}, \tag{9.52}$$

for $0 < \Delta t < \Delta$.

Convergence in the strong sense is a track wise approach. The exact particle track X_t is approximated as accurately as possible by a numerical track X_n. However for many practical particle simulation problems we are not interested in very accurate individual tracks. This is for instance the case if we want to compute the particle concentration or only the position variance of a particle. For these problems we can use a weaker form of convergence: The weak order of convergence is α if there exists a positive constant c and a Δ such that for fixed $T = N\Delta t$:

$$|E\,\{h\,(X_T, T)\} - E\,\{h\,(X_N, N\Delta t)\}| \leq c(\Delta t)^{\alpha}, \tag{9.53}$$

for all $0 < \Delta t < \Delta$ and for all functions $h(x, t)$ with polynomial growth.

If we take $h(x, t) = x$ the definition of weak order convergence reduces to:

$$|E\,\{X_T\} - E\,\{X_N\}| \leq c(\Delta t)^{\alpha}. \tag{9.54}$$

In this case we use the realizations of X_t only to determine the mean at time T, and we evaluate the accuracy of the numerical scheme by computing this quantity. We do not evaluate the accuracy of the underlying tracks. If $h(x, t) = x^2$ we have:

$$\left|E\left\{(X_T)^2\right\} - E\left\{(X_N)^2\right\}\right| \leq c(\Delta t)^{\alpha}, \tag{9.55}$$

and we evaluate the accuracy of the numerical scheme only by computing the second moment.

For deterministic differential equations the Taylor series expansion is an important method to evaluate the order of accuracy, however, for the stochastic case we can use the stochastic version of the Taylor expansion (for more details the reader is referred to Kloeden and Platen (1992)). By analysing the error terms in the stochastic Taylor expansion the strong order of convergence of the Euler scheme can be determined: $\mathcal{O}(\Delta t^{\frac{1}{2}})$. For weak order convergence many realizations are generated and averaged to determine an approximation of the particle concentration. Because of the averaging procedure certain random error terms cancel out and vanish for increasing number of realizations. This results in a weak order of convergence of the Euler scheme of $\mathcal{O}(\Delta t)$. This implies that if we use the Euler scheme and generate many tracks then the individual tracks are only half order accurate (strong convergence) while for example the results on the mean and variance of the tracks are first order accurate

(weak convergence). Certain stochastic errors in the track wise computations cancel out when computing ensemble mean quantities like the mean or variance.

From the stochastic Taylor expansion, more accurate schemes can been obtained, such as the following one:

$$x_{n+1} = x_n + \Delta t f\left(x_n, t_n\right) + \sigma\left(x_n, t_n\right) \Delta W_n + \frac{1}{2}\sigma\left(x_n, t_n\right) \frac{\partial \sigma}{\partial x}\left(x_n, t_n\right) \left(\Delta W_n^2 - \Delta t\right). \tag{9.56}$$

This scheme is called the Milstein scheme and is $\mathcal{O}(\Delta t)$ in the strong sense for scalar equations. For vector systems it is generally of order $\mathcal{O}(\Delta t^{\frac{1}{2}})$ (except for very special differential equations when its accuracy is as in the scalar case). In the weak sense the Milstein scheme has the same order of convergence as the Euler scheme.

By including further terms of the stochastic Taylor expansion, the next higher order scheme is of 1.5 order accuracy in the strong sense and 2.0 order in the weak sense. The 1.5 order strong Taylor scheme is given as:

$$\begin{aligned} x_{n+1} = x_n + \Delta t f \Delta t + \sigma \Delta W_n + \frac{1}{2}\sigma \frac{\partial \sigma}{\partial x}\left(\Delta W_n^2 - \Delta t\right) + \frac{\partial f}{\partial x}\sigma \Delta Z_n + \\ \frac{1}{2}\left(f\frac{\partial f}{\partial x} + \frac{1}{2}\sigma^2\frac{\partial^2 f}{\partial x^2}\right)(\Delta t)^2 + \left(f\frac{\partial \sigma}{\partial x} + \frac{1}{2}\sigma^2\frac{\partial^2 \sigma}{\partial x^2}\right)(\Delta W_n \Delta t + \Delta Z_n) \\ \frac{1}{2}\sigma\left(\sigma\frac{\partial^2 \sigma}{\partial x^2} + \left(\frac{\partial \sigma}{\partial x}\right)^3\right)\left(\frac{1}{3}\Delta W_n^2 - \Delta t\right)\Delta W_n, \end{aligned} \tag{9.57}$$

where all the functions are evaluated at $x = x_n$ and $t = t_n$. In addition to the noise increment ΔW a second random variable ΔZ is needed. ΔZ is also a Gaussian random variable with the following properties: Mean 0, variance $\frac{\Delta t}{3}$ and covariance $E\{\Delta W \Delta Z\} = \frac{\Delta t^2}{2}$.

Weak approximation schemes can be simplified without losing accuracy. Instead of the generation of Gaussian random numbers, numbers can be generated from any probability distribution as long as the mean and variance are the same. The order 2.0 Milstein scheme is a one-step weak simplification of the previous scheme. Because only a weak approximation is needed, some terms of the Taylor 1.5 scheme can be skipped and there is no need for a second random variable. This scheme was proposed by Milstein (1979) and is of 2.0 order accuracy in the weak sense:

$$\begin{aligned} x_{n+1} = x_n + \Delta t f \Delta t + \sigma \Delta W_n + \frac{1}{2}\sigma \frac{\partial \sigma}{\partial x}\left(\Delta W_n^2 - \Delta t\right) + \frac{\partial f}{\partial x}\sigma \Delta Z_n + \\ \frac{1}{2}\left(f\frac{\partial f}{\partial x} + \frac{1}{2}\sigma^2\frac{\partial^2 f}{\partial x^2}\right)(\Delta t)^2 + \frac{1}{2}\left(\frac{\partial f\sigma}{\partial x} + \frac{1}{2}\sigma^2\frac{\partial^2 \sigma}{\partial x^2}\right)\Delta W_n \Delta t. \end{aligned} \tag{9.58}$$

Similar to predictor-corrector schemes for ODEs, there exist equivalent methods for SDEs. This class is often used due to their numerical stability, which they inherit from the implicit counterparts of their corrector scheme. In addition, the difference between the predicted and the corrected values at each time step provides an indication of the

local error. Thus, they can be beneficial in (time) adaptive schemes (Charles et al. 2009).

The lowest order predictor-corrector scheme is as follows:

$$\begin{aligned} x_{n+1}^{p} &= x_n + f\left(x_n, t_n\right) \Delta t + \sigma\left(x_n, t_n\right) \Delta W_n \\ x_{n+1} &= x_n + \frac{1}{2}\left(f\left(x_{n+1}^{p}, t_{n+1}\right) + f\left(x_n, t_n\right)\right) \Delta t + \sigma\left(x_n, t_n\right) \Delta W_n. \end{aligned} \tag{9.59}$$

This is a stochastic version of the trapezoidal method also known as Heun scheme. Note that the predictor step is only applied to the deterministic part, the stochastic part cannot be corrected to keep the numerical approximation consistent with the original Îto SDE (Kloeden and Platen 1992). This Heun scheme is of order $\mathcal{O}(\Delta t)$ in the weak sense and of order $\mathcal{O}(\Delta t^{\frac{1}{2}})$ in the strong sense. At this stage, the question arises as to why another first order scheme is presented. In the limit of vanishing diffusivity, the Euler scheme is equivalent to its deterministic counterpart and is first order accurate. This is not the case for the Heun scheme. Due to the predictor-corrector step, the scheme converges to a second order approximation of the ordinary differential equation.

In case the stochastic term is also evaluated using the prediction step we obtain the Heun scheme that can be used for approximating a Stratonovich SDEs:

$$\begin{aligned} x_{n+1}^{p} =& x_n + f\left(x_n, t_n\right) \Delta t + \sigma\left(x_n, t_n\right) \Delta W_n \\ x_{n+1} =& x_n + \frac{1}{2}\left(f\left(x_{n+1}^{p}, t_{n+1}\right) + f\left(x_n, t_n\right)\right) \Delta t \\ &+ \frac{1}{2}\left(\sigma\left(x_{n+1}^{p}, t_{n+1}\right) + \sigma\left(x_n, t_n\right)\right) \Delta W_n. \end{aligned} \tag{9.60}$$

For approximating a Stratonovich SDE this Heun scheme is first order accurate in the strong sense and also first order accurate in the weak sense.

There are two complications in deriving strong higher order schemes. First the number of error terms grows very rapidly, resulting in rather complicated numerical schemes involving many terms. Secondly, most Wiener integrals appearing in the expansion cannot be solved analytically like in the case of the Milstein scheme. As a result special numerical schemes have to be implemented to approximate these integrals too. For details the reader is referred to Kloeden and Platen (1992).

9.5 Test Cases for Marine Transport Problems

9.5.1 Simple Vertical Diffusion

Firstly, the numerical algorithms are applied to a simple diffusion problem in a domain limited by two boundaries. This can be visualised as a one dimensional water column that is bounded by the sea surface and the pycnocline. The model is

discussed in detail in Deleersnijder et al. (2006) and Spivakovskaya et al. (2007a). The governing partial differential equation for this test case is given by simple diffusion equation:

$$\frac{\partial C}{\partial t} = \frac{\partial}{\partial z}\left(k(z)\frac{\partial C(z,t)}{\partial z}\right), \quad t \geq 0 \text{ and } 0 \leq z \leq H, \tag{9.61}$$

with a "no flux" boundary condition imposed at the boundaries domain and the initial condition is a delta like concentration peak at $z = z_0$:

$$k(z)\frac{\partial C}{\partial z}\bigg|_{z=0,H} = 0, \tag{9.62}$$

$$C(z,0) = \delta\left(z - z_0\right). \tag{9.63}$$

For the sake of generality, the above problem is normalized by introducing the dimensionless variables:

$$t^\star = \frac{t}{H^2/k}, \quad z^\star = \frac{z}{H}, \quad k^\star = \frac{k}{\bar{k}}, \tag{9.64}$$

where $\bar{k}$ denotes the depth averaged diffusivity i.e.

$$\bar{k} = \frac{1}{H}\int_0^H k(z)\mathrm{d}z. \tag{9.65}$$

The parabolic profile is a good approximation of the diffusivity profile in the mixed layer, but it is also a good description for a shallow, well-mixed, coastal region (Burchard et al. 1998; Warner et al. 2005). Moreover, the parabolic profile is until now the only realistic profile, for which analytical solutions exist (beside constant diffusivity). Therefore, the dimensionless diffusivity $k(z) = 6z(1 - z)$ is chosen to be a parabolic function.

The Îto SDE for the particle position Z_t is the 1D version of the case described in Sect. 9.3 and takes the following form:

$$dZ_t = \frac{\partial k}{\partial z}dt + \sqrt{2k(z)}dW_t, \quad Z_{t_0} = Z_0. \tag{9.66}$$

Using this setup, an analytical solution for the dispersion of the initial concentration $C(z,0) = \delta(z - z_0)$ is known (Spivakovskaya et al. 2007a):

$$C(z,t) = 1 + \sum_{n=1}^{\infty}(2n+1)\,P_n(2z-1)\,P_n\left(2z_0-1\right)e^{(-6n(n+1)t)}, \tag{9.67}$$

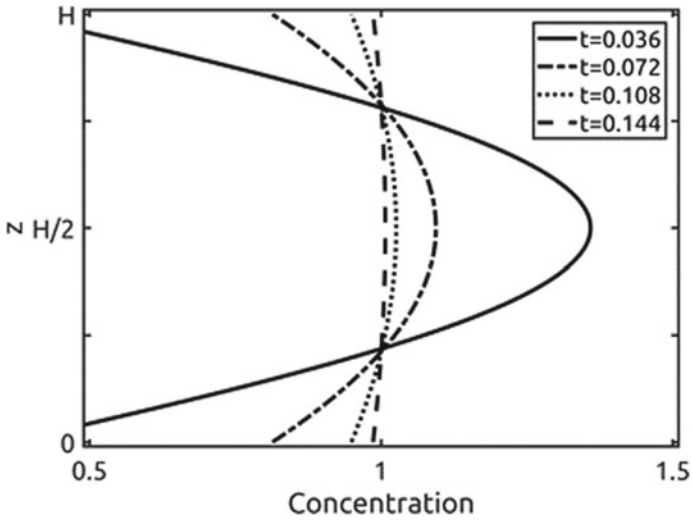

Fig. 9.1 Analytical solution of the 1D diffusion equation at different times

where $P_n(z)$ denotes the nth order Legendre polynomial. Figure 9.1 presents the analytical solution for $z_0 = 0.5$ and for various times t.

We will now use various numerical schemes for the Îto SDEs introduced in Sect. 9.4 to compute the particle concentration and will compare the results with the analytical solution. Table 9.1 summarises the numerical schemes used for this test case.

The results for $z_0 = 0.5$ are shown in Fig. 9.2. The results clearly indicate that all schemes converge to the true solution according to the designed order of accuracy. Hence, by decreasing the time step, all schemes behave as expected and scale according to their designed convergence order.

By increasing the number of particles N, see Fig. 9.2b, the error also becomes smaller. Nevertheless, no differences in the scaling are visible, except from deviations in the offset. This is due to the intrinsic nature of random processes. The results include statistical errors proportional to $N^{\frac{1}{2}}$. Therefore, to increase the accuracy, the "brute-force-method" (using an excessively large number of particles) is an option, but due to the slow convergence, having recourse to a more accurate numerical scheme is much more rewarding. It is important to note that both the chosen numerical schemes and the use of a finite number of particles introduce errors. Preferably both type of errors should be of the same order of magnitude. Therefore, it makes no sense to use the fastest and most simple numerical scheme and a huge amount of particles. But it also makes no sense to use a very accurate scheme and only a limited amount of particles.

Comparing the efficiency, see Fig. 9.2c, it is visible, that the E1 scheme is the fastest, but the M1 and M2 schemes show a better overall scaling. Thus, with moderate time steps, these two schemes provide a higher accuracy at the same runtime.

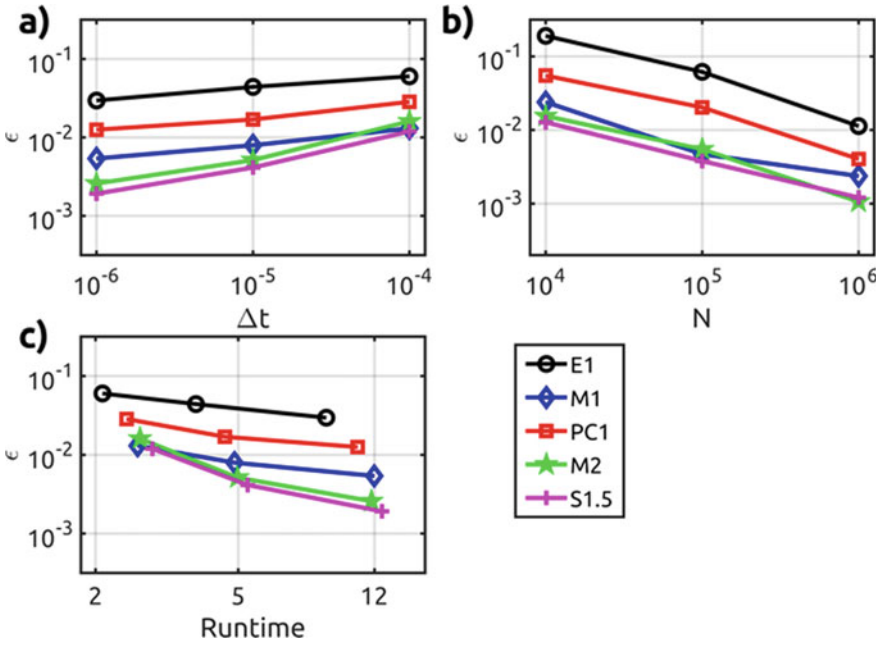

Fig. 9.2 Error of the dispersion test for **a** variation of the time step Δt, **b** variation of the number of particles N, and **c** comparison of the efficiency (accuracy vs. runtime)

Table 9.1 Summary of the numerical schemes used

Scheme	Short name	Strong order	Weak order
Euler	E1	0.5	1
Milstein	M1	1	1
Taylor 1.5	S1.5	1.5	2
Milstein 2.0	M2	1	2
Heun-Îto	PC1	0.5	1

Therefore, these schemes should be preferred. From the efficiency plot, one can also see the additional overhead of the predictor-corrector scheme PC1. Since a predictor steps is needed, the efficiency is clearly lower than for the M1 scheme. Although the S1.5 scheme offers the highest accuracy, it is less efficient due to the high computational demand.

9.5.2 One Dimensional Water Column Including a Pycnocline

The starting point is the test case of Stijnen et al. (2006). The authors performed Lagrangian simulations in the shallow the coastal zone of the Netherlands. They were faced with the challenge of representing inhibition of mixing due to stratification associated with salinity contrasts, caused by river runoff. The stratification, which is associated with a rather thin pycnocline, is a quasi-impermeable barrier to vertical diffusive or turbulent motions. In Stijnen et al. (2006) it is showed that this is easily taken into account by Eulerian models, while obtaining a similar result in Lagrangian simulations is far from trivial. They could show that the pycnocline was no significant barrier to diffusion when the Euler scheme was used. However, when using a higher-order particle tracking scheme, the pycnocline remained almost impermeable to diffusive fluxes—as it is supposed to be.

To construct a possible test case we use the diffusivity profile of Stijnen et al. (2006) as a blueprint. We assume without any loss of generality that the pycnocline is located in the middle of the water column. Accordingly, it is suggested that the idealised vertical eddy diffusivity can be approximated by:

$$\begin{aligned} k(z) =& \frac{2(1+a)(1+2a)}{a^2 H^{1+\frac{1}{a}}} z(H-2z)^{\frac{1}{a}}, \quad 0 \le z \le \frac{H}{2} \\ =& \bar{k} \frac{2(1+a)(1+2a)}{a^2 H^{1+\frac{1}{a}}} (H-z)(2z-1)^{\frac{1}{a}}, \quad \frac{H}{2} \le z \le H, \end{aligned} \tag{9.68}$$

where a is a constant that is larger than or equal to unity, z is the distance to the seabed, which is located at $z = 0$, while the sea surface is at $z = H$. For more details the interested reader is referred to Gräwe (2011).

The important tuning parameter that controls the sharpness of the pycnocline is a. The dependence of the sharpness of the pycnocline on a is shown in Fig. 9.3. The important feature of this analytical eddy diffusivity is that it vanishes at the pycnocline and is small in the vicinity of the latter. The parameter a controls the steepness of the diffusivity profile. The larger the value of a, the larger the vertical diffusivity gradient near the pycnocline. Note, that setting $a = 1$ will produce a double parabolic diffusivity profile.

For this test case, we have considered a pure diffusion problem so the SDE for the particle position Z_t is again described by (9.61). The boundaries are treated again as "no flux" boundaries and the initial release is also in this test case a Dirac function. For an analytical solution of the posed problem in the special case of $a = 1$, the interested reader is referred to Gräwe (2011). The intention of this test case is however not to reproduce the analytical solution. Our aim is to assess the ability of different numerical schemes to treat the pycnocline as the requested impermeable barrier. Thus, if we release particles in the upper half of the water column, a "perfect" scheme is characterised by zero concentration in the lower half of the water column at any instant of time. This is easily done in Eulerian-type numerical model. Lagrangian

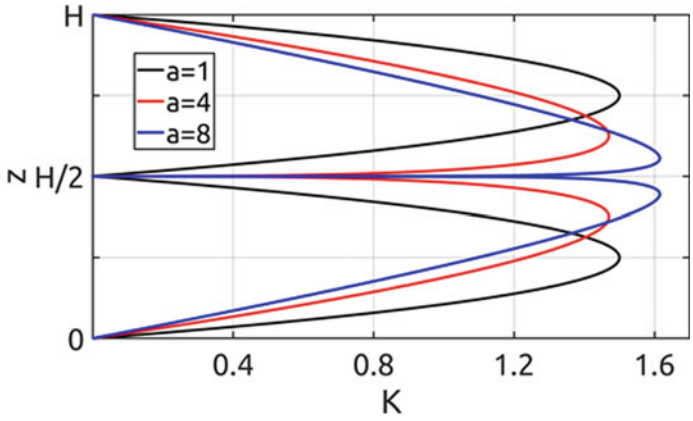

Fig. 9.3 Diffusivity profile $K = \frac{k}{\bar{k}}$ for different values of the parameter a

simulations, however, do show some crossings of the particles through pycnocline, thereby causing simulation errors that have to be assessed. To quantify to what extent the pycnocline is actually a barrier to vertical diffusion, we released N particles in the upper half of the water column. Since the number of particles has to remain constant, we constructed an error measure in such a way that $\epsilon = 0$, if no particles have crossed the pycnocline, and $\epsilon = 1$ if the particles are uniformly distributed in the whole water column. Clearly, the lower ϵ the better the scheme under consideration.

An important point to mention is that although we are looking for the time evolution of a particle distribution and thus weak convergence (9.53), the crossing of the pycnocline tests for strong convergence (9.52). This is related to the fact that the individual particle path in the vicinity of the pycnocline is important and therefore a strong error measure is appropriate.

In Fig. 9.4 we show the time evolution of a point release of particles at $z_0 = 0.75$. We have used again all the schemes presented in Table 9.1. The results clearly indicate that for the E1 scheme the pycnocline is not at all a barrier. This is even true for small values of a. The M2 scheme shows for $a = 1$ no crossing of particles of the pycnocline. For $a = 4$ (Fig. 9.4d) there is a leakage of particles into the lower half of the water column. Hence, by simple visual inspection, it is obvious that the results obtained with the Euler scheme are completely wrong. Furthermore, variations of the time step would not reveal this failure as we are already using a very small time step for this problem (see Visser (1997)).

To visualise the impact for different values of a, we show in Fig. 9.5 the convergence of the error for variations of the pycnocline sharpness. For moderate time steps and small values of a the M1, M2 and S1.5 schemes can treat the pycnocline as a barrier (Fig. 9.5a). However, for values of a larger then 7 all schemes fail this test. Only by decreasing the time step the M1, M2 and S1.5 schemes show a scaling of the error over the whole range of variations of a (Fig. 9.5b). Clearly, the S1.5 scheme

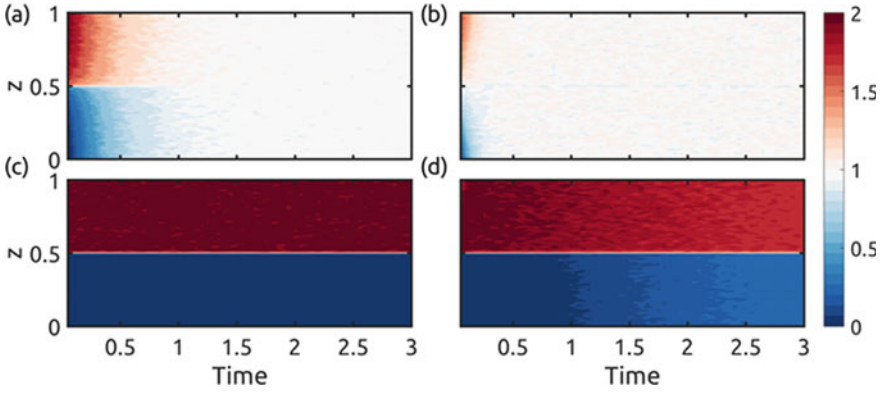

Fig. 9.4 Dispersion of a particle cloud initially located at $z_0 = 0.75$ for two different schemes and for two values of a. Color coded is the particle concentration for **a** E1 scheme with $a = 1$, **b** E1 scheme with $a = 4$, **c** M2 scheme with $a = 1$, **d** M2 scheme with $a = 4$. The time step is 10^{-6}

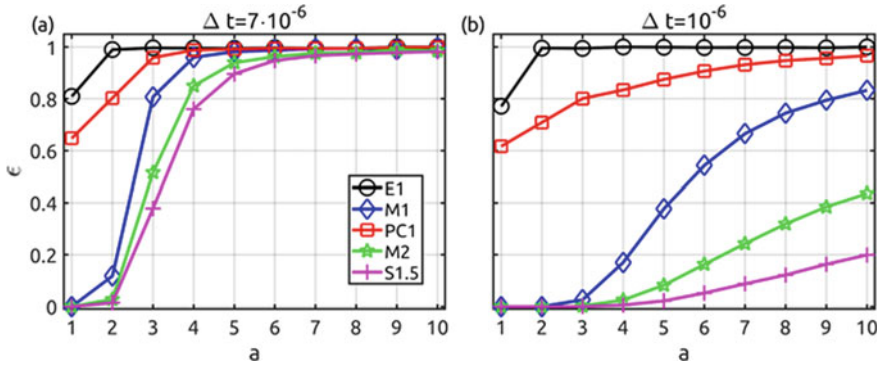

Fig. 9.5 Variation of the error ϵ for the different numerical schemes and **a** a time step of $7 \cdot 10^{-6}$ **b** a time step of 10^{-6}. On the x-axis we show the pycnocline sharpness parameter a and on the y-axis the error ϵ

shows the best performance. Again the E1 scheme and PC1 scheme do not treat the pycnocline correctly for all values of a.

9.5.3 *Multidimensional Diffusion in an Unbounded Domain*

Large-scale diffusion processes in the oceans occur mostly along isopycnal surfaces, i.e. surfaces of equal density. Diapycnal diffusion associated with a diffusion flux orthogonal to isopycnal surfaces is usually very small. The diapycnal and isopycnal diffusion fluxes are commonly parameterised á la Fourier-Fick (Redi 1982).

The natural coordinates for representing diffusive processes in oceans are diapycnal and isopycnal. The slope of the isopycnal surfaces, though generally small, contains significant information about the dynamics of the ocean and its interaction with the atmosphere. Most ocean models do not use iso and diapycnal coordinates. Instead they rely on the horizontal-vertical coordinates, in which the Redi diffusivity tensor is resorted to in order to model diapycnal and isopycnal diffusion. This diffusivity tensor contains off-diagonal terms.

The Eulerian discretisations of isopycnal diffusion terms yield discrete operators that are not monotonic (Beckers et al. 1998, 2000), occasionally producing spurious oscillations and over- or under-shootings in tracer concentration fields, which obviously are unrealistic (Mathieu and Deleersnijder 1998; Mathieu et al. 1999). To overcome these shortcomings Lagrangian numerical schemes can be used. In this Section, idealized test cases are constructed to assess Lagrangian methods for the iso- and diapycnal diffusion problems. For more details see Spivakovskaya et al. (2007a), Shah et al. (2011), Shah (2015).

Iso and Diapycnal Diffusion Along Flat Isopycnal Surfaces

If only large scales of motions are actually resolved, the unresolved motions comprise much more that those giving rise to the molecular diffusion. The unresolved phenomena are usually parameterised as non-isotropic diffusion. Such a formulation resorts to two diffusivity coefficients, K^I and K^d, which are the isopycnal diffusivity and the diapycnal diffusivity, respectively. In the principal axes, the associated diffusivity tensor reads:

$$K = \begin{pmatrix} K^I & 0 & 0 \\ 0 & K^I & 0 \\ 0 & 0 & K^d \end{pmatrix}. \tag{9.69}$$

The z-principal axes is perpendicular to the isopycnal plane. To rotate the coordinate system associated with the isopycnal surface into the geodesic coordinate system we need two angles θ and γ (Redi 1982) and the diffusivity tensor takes the form:

$$K = \begin{pmatrix} K^I \cos^2\theta + \sin^2\theta \left(K^l \sin^2\gamma + K^d \cos^2\gamma\right) & -\cos\gamma \sin\gamma \sin^2\theta \left(K^I - K^d\right) & \cos\gamma \sin\theta \cos\theta \left(K^I - K^d\right) \\ -\cos\gamma \sin\gamma \sin^2\theta \left(K^I - K^d\right) & K^I \cos^2\theta + \sin^2\theta \left(K^l \cos^2\gamma + K^d \sin^2\gamma\right) & \sin\gamma \sin\theta \cos\theta \left(K^I - K^d\right) \\ \cos\gamma \sin\theta \cos\theta \left(K^I - K^d\right) & \sin\gamma \sin\theta \cos\theta \left(K^I - K^d\right) & K^l \sin^2\theta + K^d \cos^2\theta \end{pmatrix}. \tag{9.70}$$

As a test case, it is assumed that the isopycnal surfaces are flat and equally spaced. Furthermore, we assume that the velocity field is zero and that the iso and diapycnal diffusivity are constant. As in Sect. 9.3 we consider the following partial differential problem in an infinite domain:

$$\frac{\partial C}{\partial t} = \nabla \cdot (K \cdot \nabla C), \quad -\infty < x < \infty, \quad C(x, t_0) = \delta(x - 0), \tag{9.71}$$

where δ denotes a Dirac function. The exact solution of problem (9.71) can be shown to be:

$$C(x, t) = \frac{\exp\left(-\frac{x^\top \cdot K^{-1} \cdot x}{4t}\right)}{(4\pi t)^{\frac{n}{2}} \sqrt{\det(K)}}. \tag{9.72}$$

Here $\det(K)$ is the determinant of the constant diffusion matrix K while n is the number of space dimensions considered. Introducing the dimensionless quantities for space and time:

$$t^* = \frac{t}{T}, x^* = \frac{x}{L_h}, y^* = \frac{y}{L_h} \text{ and } z^* = \frac{z}{L_v}, \tag{9.73}$$

where T, L_h and L_v represent the appropriate timescale, horizontal and vertical length scale, respectively. It is also convenient to define:

$$T = \frac{L_h^2}{K^I} = \frac{L_h^2}{K^I}, \quad \alpha = \frac{L_h}{L_v} \text{ and } C^* = \frac{C}{1/L_h^2 L_v}. \tag{9.74}$$

The ratio to the vertical to horizontal length is given by α and the scaled concentration is represented by C^*. Using these quantities (9.73) and (9.74) into (9.70) and dropping the asterisk notation the diffusion tensor takes the following form:

$$K = \begin{pmatrix} \cos^2\theta + \sin^2\theta\left(\sin^2\gamma + \alpha^2\cos^2\gamma\right) & \cos\gamma\sin\gamma\sin^2\theta\left(1-\alpha^2\right) & \cos\gamma\sin\theta\cos\theta\left(\alpha^{-1}-\alpha\right) \\ \cos\gamma\sin\gamma\sin^2\theta\left(1-\alpha^2\right) & \cos^2\theta + \sin^2\theta\left(\cos^2\gamma + \alpha^2\sin^2\gamma\right) & \sin\gamma\sin\theta\cos\theta\left(\alpha^{-1}-\alpha\right) \\ \cos\gamma\sin\theta\cos\theta\left(\alpha^{-1}-\alpha\right) & \sin\gamma\sin\theta\cos\theta\left(\alpha^{-1}-\alpha\right) & \sin^2\theta + \alpha^{-2}\cos^2\theta \end{pmatrix}, \tag{9.75}$$

and the exact solution (9.68) can be rewritten in the form:

$$\begin{aligned} C(x, y, z, t) = {} & \frac{1}{(4\pi t)^{3/2}} \exp\left[-\frac{1}{4t}\left(z\cos\theta - \alpha^{-1}(y\sin\theta\sin\gamma + x\sin\theta\cos\gamma)\right)^2\right] \times \\ & \exp\left[-\frac{1}{4t}(z\alpha\cos\theta + x\cos\alpha\cos\gamma + y\cos\theta\sin\gamma)^2\right] \times \exp\left[-\frac{1}{4t}(x\sin\gamma - y\cos\gamma)^2\right]. \end{aligned} \tag{9.76}$$

The values of the parameters $\theta \approx \alpha \approx 10^{-3}$ are reasonable. The corresponding Îto SDE for the particle position whose probability distribution satisfies the diffusion problem (9.71) reads (see also Sect. 9.3):

$$d\boldsymbol{X}_t = \sigma(\mathbf{X}_t, t)\, d\mathbf{W}(t), \quad \boldsymbol{X}_{t_0} = \boldsymbol{X}_0. \tag{9.77}$$

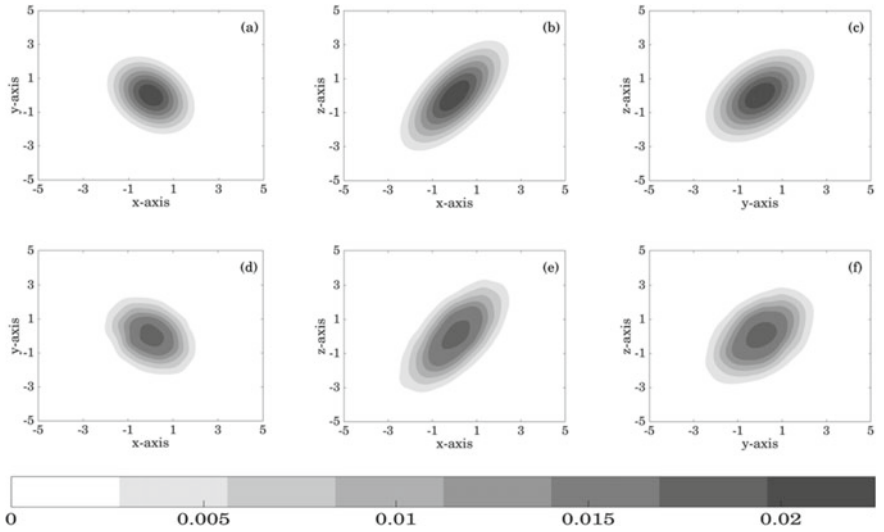

Fig. 9.6 Comparison between the particle model and the exact solution of the diffusion (9.69). This implies the Lagrangian model is indeed consistent with the concentration field of the diffusion equation. **a–c** shows the exact solution along the xy-, xz- and yz- plane and, **d–f** shows the probability distribution of 10^5 Lagrangian particle initially released at origin

Since, the matrix K is symmetric and positive definite it may be decomposed using Cholesky decomposition in following form of σ:

$$\sigma = \begin{pmatrix} \sigma_{xx} & 0 & 0 \\ \sigma_{yx} & \sigma_{yy} & 0 \\ \sigma_{zx} & \sigma_{zy} & \sigma_{zz} \end{pmatrix}, \tag{9.78}$$

with

$$\begin{aligned} &\sigma_{xx} = \sqrt{2k_{xx}}, \sigma_{yx} = \frac{\sqrt{2}k_{yx}}{\sqrt{k_{xx}}}, \sigma_{zx} = \frac{\sqrt{2}k_{zx}}{\sqrt{k_{xx}}}, \sigma_{yy} = \sqrt{\frac{2\left(k_{xx}k_{yy}-k_{xy}^2\right)}{k_{xx}}} \\ &\sigma_{zy} = \frac{\sqrt{2}\left(k_{xx}k_{yz}-k_{xy}k_{zx}\right)}{\sqrt{k_{xx}\left(k_{xx}k_{yy}-k_{xy}^2\right)}}, \sigma_{zz} = \sqrt{\frac{2\left(k_{xx}k_{yy}k_{zz}+2k_{xy}k_{xz}k_{yz}-k_{xz}^2k_{yy}-k_{yz}^2k_{xx}-k_{xy}^2k_{zz}\right)}{k_{xx}k_{yy}-k_{xy}^2}}. \end{aligned} \tag{9.79}$$

The main idea of the Lagrangian model is to simulate the trajectory of many different particles using an appropriate numerical scheme of the SDEs and then construct the probability distribution function which is in this case equal to the particle concentration using non-parametric statistical methods. In our experiment the trajectories of the SDE (9.77) are simulated using the Euler scheme described in Sect. 9.4. In order to obtain the concentration from the particle trajectories a kernel estimator (Silverman 1986; Spivakovskaya et al. 2007a) is used. Here we used the Gaussian kernel and the comparison between the Eulerian and Lagrangian is depicted in Fig. 9.6.

Isopycnal Diffusion Along Non-flat Isopycnal Surfaces

In case the isopycnal surfaces are flat, the Lagrangian simulation reveals that a first order Euler scheme is accurate enough to attain the desired accuracy. If the diapycnal diffusion is zero, the particles should remain on the isopycnal surface they are released on, even if a simple time stepping is used. By contrast, if the isopycnal surfaces are assumed to be not flat, particles tend to leave the isopycnal surface they are released on. In such cases, the first order Lagrangian schemes might fail due to numerical errors and higher order Lagrangian schemes might reduce these errors. This is why assessing different numerical schemes for isopycnal diffusion on a non-flat isopycnal surfaces is important.

The objective here is to simulate diffusion processes along non-flat isopycnal surfaces in the absence of diapycnal diffusion (Shah et al. 2011; Shah 2015; van Sebille et al. 2018). Here, it is more important to accurately reproduce the individual trajectories of the particles rather than the time evolution of a distribution. For approximating particle tracks, higher order strong, in lieu of weak, schemes should be used. A three dimensional idealised test case is constructed for purely isopycnal diffusion along non-flat isopycnal surfaces. Moreover, to validate, numerically, the equivalence between the Îto, Stratonovich and Îto-backward models the Îto, Stratonovich and Îto-backward Lagrangian models for transport along non-flat isopycnal are all considered.

Let x and y denote the horizontal coordinates, while z denotes the vertical coordinate (increasing upward). If ρ is the density, then the isopycnal tensor (Redi 1982) reads:

$$K = \frac{K^I}{\rho_x^2 + \rho_y^2 + \rho_z^2} \begin{pmatrix} \rho_y^2 + \rho_z^2 & -\rho_x\rho_y & -\rho_x\rho_z \\ -\rho_x\rho_y & \rho_x^2 + \rho_z^2 & -\rho_z\rho_y \\ -\rho_x\rho_z & -\rho_z\rho_y & \rho_x^2 + \rho_y^2 \end{pmatrix}. \tag{9.80}$$

Density decreases as z increases, so lighter water lies on the top of heavier water. We consider the following three dimensional density field:

$$\rho(x, y, z) = \rho_0 \left[1 - \frac{N^2 z}{g} + \alpha_x \sin(\kappa_x x) + \alpha_x \sin\left(\kappa_y y\right) \right], \tag{9.81}$$

where $\alpha_x, \alpha_y, \kappa_x$ and κ_y are constants. The following values of these parameters seem to be a reasonable choice:

$$\alpha_\xi = 10^{-3} \text{ and } \kappa_\xi = 10^{-6}, \quad \xi = x, y.$$

Note that the vertical density gradient is assumed to be constant, but the horizontal one is not, so that the isopycnal surfaces are not flat. The horizontal and vertical density gradients are

$$\rho_x = \rho_0 \alpha_x \kappa_x \cos(\kappa_x x), \ \rho_x = \rho_0 \alpha_y \kappa_y \cos\left(\kappa_y y\right) \text{ and } \rho_z = -\frac{\rho_0 N^2}{g}, \tag{9.82}$$

and the corresponding isopycnal surface may be represented as follows:

$$z = \frac{g}{N^2}\left(1 - \frac{\rho^*}{\rho_0}\right) + \frac{g\alpha_x}{N^2}\sin\left(\kappa_x x\right) + \frac{g\alpha_y}{N^2}\sin\left(\kappa_y y\right). \tag{9.83}$$

Substituting the density gradients (9.82) into (9.80) yields the actual expressions of the components of the diffusion tensor and substituting the resulting components (9.78) of σ into (9.43), lead to the following system of Îto SDEs for non-flat isopycnal diffusion:

$$d\mathbf{X}_t = f\left(\mathbf{X}_t, t\right) dt + \sigma\left(\mathbf{X}_t, t\right) d\mathbf{W}_t \quad \mathbf{X}_{t_0} = \mathbf{X}_0. \tag{9.84}$$

Here the components of the drift vector a are given by:

$$f_x = \frac{\partial k_{xx}}{\partial x} + \frac{\partial k_{xy}}{\partial y},\ f_y = \frac{\partial k_{yx}}{\partial x} + \frac{\partial k_{yy}}{\partial y} \text{ and } f_z = \frac{\partial k_{zx}}{\partial x} + \frac{\partial k_{zy}}{\partial y}. \tag{9.85}$$

The components of σ are given in (9.78)-(9.79). This system of SDEs is again consistent with diffusion equation:

$$\frac{\partial C}{\partial t} = \nabla \cdot (K \cdot \nabla C), \quad -\infty < x < \infty, \quad C\left(x, t_0\right) = \delta\left(x - x_0\right). \tag{9.86}$$

For the numerical simulations the particles are all released at the origin $(x, y, z) = (0, 0, 0)$. This point belongs to the isopycnal surface whose equation reads:

$$z = \frac{g\alpha_x}{N^2}\sin\left(\kappa_x x\right) + \frac{g\alpha_y}{N^2}\sin\left(\kappa_y y\right). \tag{9.87}$$

The position $(x_i(t), y_i(t), z_i(t))$, $j = 1, 2, \ldots, J$ of the particles is updated by means of Lagrangian schemes. Since the diapycnal diffusion is zero the particles should not leave the isopycnal surface (9.83), but numerical errors are unavoidable. Their magnitude may be estimated by means of the following error measure:

$$\mu(t) = \sqrt{\frac{1}{J}\sum_{j=1}^{J}\left[z_j(t) - z = \frac{g\alpha_x}{N^2}\sin\left(\kappa_x x_j(t)\right) + \frac{g\alpha_y}{N^2}\sin\left(\kappa_y y_j(t)\right)\right]^2}. \tag{9.88}$$

This expression is approximately equal to the standard deviation of the distance of the particles to the isopycnal surface on which they should remain. Clearly, the better a Lagrangian scheme is, the slower the rate of increase of standard deviation $\mu(t)$ will be.

In order to depict the equivalence between the Îto, Stratonovich and Îto-backward stochastic models. The Îto SDEs (9.80)(80) is transformed into Stratonovich and Îto-backward SDEs. The drift coefficients in (9.80) is modified by using the transformations described in Sect. 9.3. The resulting Stratonovich and Îto-backward SDEs are then used to simulate the trajectories of the particles on the non-flat isopycnal

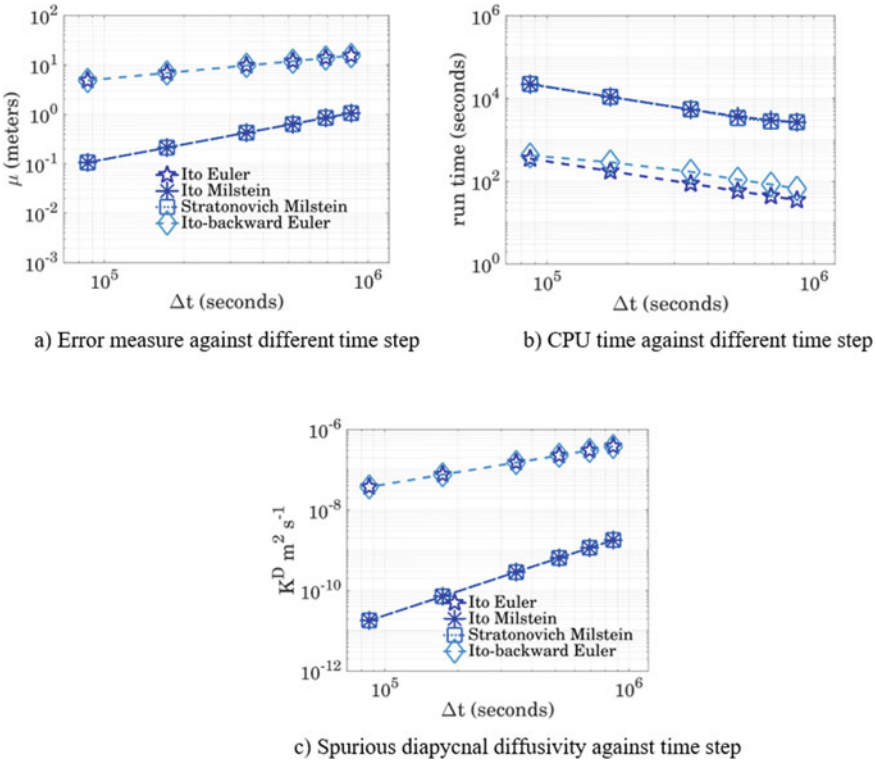

Fig. 9.7 Comparison of the performance of the numerical schemes for different time steps

surface. Note that careful attention is required to implement Lagrangian schemes for Îto, Stratonovich and Îto-backward models (Kloeden and Platen 1992). It is important to recall here that, assessing the pathwise strong approximations for Lagrangian model interpreted in Îto, Stratonovich and Ito-backward sense is a main goal here, that is why attention is not paid to the probability distribution.

The comparison between the accuracy and efficiency of the Lagrangian schemes is shown in Fig. 9.7a, b. The standard deviation μ against the different time steps Δt is shown in Fig. 9.7a, while Fig. 9.7b depicts the CPU time of the Lagrangian schemes. The results reveals that Îto Euler and Îto-backward Euler converges with order 0.5 and Îto and Stratonovich Milstein schemes converges with the order 1.0. It is quite clear from these experiments that the higher order schemes produce better pathwise approximations. Another way of assessing the numerical schemes under consideration consists in estimating the spurious diapycnal diffusion $\left(K^D\right)$ they are associated with. The related spurious diapycnal diffusivity is of the order $\frac{\mu^2(t)}{2t}$. The spurious diapycnal diffusivity of each Lagrangian scheme is determined and the results are displayed in Fig. 9.7c. The spurious diapycnal diffusivity of the Euler and

Milstein schemes differs approximately by a factor of 10^{-4}. This shows the spurious diffusivity in the Milstein scheme is negligible compared with the Euler scheme.

Moreover, it is can also be observed in Fig. 9.7 that the Îto-backward Euler solution converges to the Îto Euler and the Stratonovich Milstein solution converges to the Îto Milstein solution. This implies that if the SDE is interpreted in Îto sense then one can switch to Stratonovich and Îto-backward models by using the transformations described in Sect. 9.3 and one will reach to the same solution. The idealised test case for purely isopycnal diffusion on non-flat isopycnal surfaces was considered to evaluate the performance of the Lagrangian schemes. The idealised test case shows that the Euler approximation is not an appropriate option to simulate the movement of the particle on non-flat isopycnals. The implementation of the Milstein scheme shows that a relatively limited additional computational effort (Fig. 9.7) is required to obtain a good accuracy. The assessment of Lagrangian schemes suggests that one may not obtain satisfactory results with the Euler scheme, while the Milstein scheme is a more accurate and more reliable approximation for simulating the particle paths. Turning to the higher order strong Lagrangian schemes leads to a very significant improvement.

9.6 Conclusion

The Lagrangian random walk model which is dictated by the desired representation of the turbulent diffusion is broadly discussed in this chapter. This chapter provides the foundation to the useful concept to theory of SDEs and it numerical aspects that are used to model diffusive transport processes in marine modelling problems. Implementation of different Lagrangian schemes on various test cases has clearly shown that the order of convergence of the Euler scheme is not sufficient to achieve the desired result. However, the Milstein scheme shows that a relatively limited additional computational effort is required to obtain a good accuracy. The results obtained for the various higher order schemes has shown more accurate results than that of the Milstein scheme. But such schemes are not computationally attractive. Therefore, it is suggested that turning to the higher order strong Lagrangian schemes leads to a very significant improvement.

References

Beckers, J.M., H. Burchard, J.M. Campin, E. Deleersnijder, and P.P. Mathieu. 1998. Another reason why simple discretization of rotated diffusion operators cause problem in ocean models: comment on "iso neutral diffusion in a z-coordinate ocean model. *Journal of Physical Oceanography* 28 (7): 1552–1559.

Beckers, J.M., H. Burchard, E. Deleersnijder, and P.P. Mathieu. 2000. Numerical discretization of rotated diffusion operators in ocean model. *Monthly Weather Review* 128 (8): 2711–2733.

Burchard, H., O. Petersen, and T.P. Rippeth. 1998. Comparing the performance of the k- and the mellor-yamada two-equation turbulence models. *Journal of Geophysical Research: Oceans* 103: 10543–10554.

Campin, J.M., E.J.M. Delhez, A.C. Hirst, and E. Deleersnijder. 1999. Towards a general theory of the age in ocean modelling. *Ocean Modelling* 1: 17–27.

Charles, W.M., E. van den Berg, H.X. Lin, and A.W. Heemink. 2009. Adaptive stochastic numerical scheme in parallel random walk models for transport problems in shallow water. *Mathematical and Computer Modelling* 50 (7–8): 1177–1187.

Deleersnijder, E., J.M. Beckers, and E.J.M. Delhez. 2006. The residence time of settling particles in the surface mixed layer. *Environmental Fluid Mechanics* 6 (1): 25–42.

Dimou, K.D., and E.E. Adams. 1993. A random-walk, particle tracking model for well-mixed estuaries and coastal waters. *Estuarine, Coastal and Shelf Science* 37: 99–110.

Gardiner, C.W. 1985. *Stochastic methods*. New York: Springer.

Gräwe, U. 2011. Implementation of higher-order particle tracking schemes in a water column model. *Ocean Modelling* 36 (1–2): 80–89.

Gräwe, U., E. Deleersnijder, S.H.A.M. Shah, and A.W. Heemink. 2012. Why the euler-scheme in particle-tracking is not enough: The shallow-sea pycnocline test case. *Ocean Dynamics* 62: 501–514.

Hanert, E. 2012. Front dynamics in a two-species competition model driven by Lévy flights. *Journal of Theoretical Biology* 300: 134–142.

Hunter, J.R., P.D. Craig, and H.E. Phillips. 1993. On the use of random walk models with spatially variable diffusivity. *Journal of Computational Physics* 106: 366–376.

Jazwinski, A.H. 1970. *Stochastic processes and filtering theory*. New York: Academic Press.

Kloeden, P., and E. Platen. 1992. *Numerical solution of stochastic differential equations (Stochastic Modelling and Applied Probability)*. Berlin: Springer.

LaBolle, E.M., J. Quastel, G.E. Fogg, and J. Granver. 2000. Diffusion processes in composite porous media and their numerical integration by random walk: Generalised stochastic differential equations with discontinuous coefficients. *Water Resources Research* 36 (3): 651–662.

Mathieu, P.P., and E. Deleersnijder. 1998. What is wrong with isopycnal diffusion in the world ocean models? *Applied Mathematical Modelling* 22 (4–5): 367–378.

Mathieu, P.P., E. Deleersnijder, and J.M. Bechers. 1999. Accuracy and stability of the discretised isopycnal-mixing equation. *Applied Mathematics Letters* 12 (4): 81–88.

Oksendal, B.K. 2003. *Stochastic differential equations: An introduction with applications*. Berlin: Springer.

Redi, M.H. 1982. Oceanic isopycnal mixing by coordinate rotation. *Journal of Physical Oceanography* 12 (10): 1154–1158.

Shah, S.H.A.M. 2015. *Lagrangian modelling of transport processes in the ocean*. PhD thesis, Delft University of Technology.

Shah, S.H.A.M., A.W. Heemink, and E. Deleersnijder. 2011. Assessing Lagrangian schemes for simulating diffusion on non-flat isopycnal surfaces. *Ocean Modelling* 39 (3–4): 351–361.

Silverman, B.W. 1986. *Density estimation for statistics and data analysis*. London: Chapman and Hall.

Spivakovskaya, D., A.W. Heemink, and E. Deleersnijder. 2007. Lagrangian modelling of multi-dimensional advection diffusion with space-varying diffusivities: theory and idealized test cases. *Ocean Dynamics* 57 (3): 189–203.

Spivakovskaya, D., A.W. Heemink, and E. Deleersnijder. 2007. The backward Îto method for the Lagrangian simulation of transport processes with large space variations of the diffusivity. *Ocean Science* 3 (4): 525–535.

Stijnen, J.W., A.W. Heemink, and H.X. Lin. 2006. An efficient 3D particle transport model for use in stratified flow. *International Journal for Numerical Methods in Fluids* 51 (3): 331–350.

Vallaeys, V., R.C. Tyson, W.D. Lane, E. Deleersnijder, and E. Hanert. 2017. A Levy-flight diffusion model to predict transgenic pollen dispersal. *Journal of the Royal Society Interface* 14 (126): 20160889.

Van Sebille, E., S.M. Griffies, R. Abernathey, T.P. Adams, P. Berloff, A. Biastoch, B. Blanke, E.P. Chassignet, Y. Cheng, C.J. Cotter, E. Deleersnijder, K. Döös, H.F. Drake, S. Drijfhout, S.F. Gary, A.W. Heemink, J. Kjellsson, I.M. Koszalka, M. Lange, C. Lique, G.A. MacGilchrist, R. Marsh, C.G. Mayorga Adame, R. McAdam, F. Nencioli, C.B. Paris, M.D. Piggott, J.A. Polton, S. Rühs, S.H.A.M. Shah, M.D. Thomas, J. Wang, P.J. Wolfram, L. Zanna, and J.D. Zika. 2018. Lagrangian ocean analysis: Fundamentals and practices. *Ocean Modelling* 121: 49–75.

Visser, A.W. 1997. Using random walk models to simulate the vertical distribution of particles in a turbulent water column. *Marine Ecology Progress Series* 158: 275–281.

Visser, A.W. 2008. Lagrangian modelling of plankton motion: From deceptively simple random walks to Fokker-Planck and back again. *Journal of Marine Systems* 70: 287–299.

Warner, J.C., C.R. Sherwood, H.G. Arango, and R.P. Signell. 2005. Performance of four turbulence closure models implemented using a generic length scale method. *Ocean Modelling* 8 (1–2): 81–113.

Chapter 10
Morphodynamic Modelling in Marine Environments: Model Formulation and Solution Techniques

H. M. Schuttelaars and T. J. Zitman

Abstract The bathymetry and geometry of coastal seas, barrier coasts and estuaries strongly influence tides and currents, and the associated transport of sediments. In turn, these transports result in a constantly evolving bathymetry and geometry, thus resulting in a feedback loop between bathymetry and geometry, water motion and sediment transport. To capture this evolution, morphodynamic models are employed. In this chapter, first the conservation laws are derived, resulting in a system of strongly coupled partial differential equations that model the morphodynamic evolution. Subsequently, two different solution strategies, indicated as the *initial value* and the *bifurcation* approach, are discussed. In the former approach, the emphasis is on the temporal evolution of bathymetric patterns, whereas the latter approach focuses on the direct identification of asymptotic states of the system under consideration. To exemplify these two approaches, the morphodynamic evolution and asymptotic states of a short, rectangular tidal inlet are considered, showing that these two model approaches result in different and complementary insights.

10.1 Introduction

The geomorphology of coastal seas and estuaries is characterized by complex patterns at vastly different length and time scales. An example of large scale features is given in Fig. 10.1, where the bathymetry is shown of the Dutch and German Wadden Sea and a large part of the southern North Sea. First focussing on the Wadden Sea, many different morphological elements can be identified: on the largest scale of the Wadden Sea itself, a chain of barrier islands is observed. Between the barrier islands tidal inlets are found that connect the back–barrier basins to the North Sea. On the seaward side of these inlets, ebb–tidal deltas are found, whereas complex channel-

H. M. Schuttelaars (✉)
Delft Institute of Applied Mathematics, Delft University of Technology, Delft, The Netherlands
e-mail: h.m.schuttelaars@tudelft.nl

T. J. Zitman
Department of Hydraulic Engineering, Delft University of Technology, Delft, The Netherlands
e-mail: t.j.zitman@tudelft.nl

H. Schuttelaars et al. (eds.), *The Mathematics of Marine Modelling*,
Mathematics of Planet Earth 9, https://doi.org/10.1007/978-3-031-09559-7_10

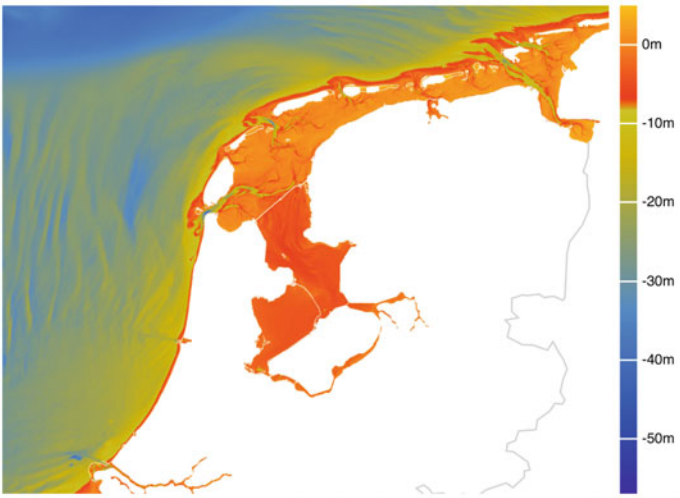

Fig. 10.1 Bed level with respect to mean sea level in the Dutch and German Wadden Sea and a large part of the southern North Sea. Data downloaded from the European Marine Observation and Data Network (EMODnet)

shoal patterns are observed in the back-barrier region. Connected to the seaward side of the most easterly barrier islands and on the closed western coast of the Netherlands, shoreface connected ridges can be seen. In the North Sea itself, large fields of sand banks with wavelengths up to 5 km are visible. Apart from these large scale features, there are extensive fields of sand waves (wavelengths up to 500 m) present in this area as well (Hulscher and Van den Brink 2001).

Furthermore, other smaller–scale morphodynamic features, such as ripples, beach cusps, nearshore bars, are observed in these coastal areas (Dodd et al. 2003).

To understand and predict the origin and evolution of these morphodynamic features, the dynamic interaction among the water motion, sediment movement and the evolution of erodible boundaries (such as the bottom) has to be captured. The water motion is driven by many different forcing agents, such as tides (see Chap. 5), wind stresses exerted at the free water surface (see Chap. 4) and horizontal as well as vertical density gradients (see Chap. 8), resulting in a water motion that varies over a wide range of temporal and spatial scales (from turbulent eddies to large scale sea level changes), that mutually affect each other. The water motion results in the erosion of sediments from the bed, with the erosion flux depending on the velocity and concentration profile close to the bed (mm–cm scale). The sediment is transported close to the bed as bedload transport, or is suspended into the water column where it is transported by advective and diffusive processes. The divergences and convergences of the bedload and suspended load transport result in bathymetric changes, that in turn influence the water motion.

The aim of this chapter is to derive a mathematical model needed to describe this morphodynamic evolution, and to review two different solution strategies, namely the *initial value* approach and the *bifurcation* approach.

Various approaches to model the morphodynamic evolution are discussed in Sect. 10.2. From these approaches, the so–called process–based models are discussed in detail in Sect. 10.3 since these approaches allow for insight in the underlying physical mechanisms. In this section the emphasis is on the derivation of the sediment mass balance, as this equation forms the basis for the study of a wide range of problems in morphodynamics. A derivation of such a mass balance equation for riverine systems was first given by Exner (1920, 1925), hence it is often named the Exner equation. To obtain a balance equation applicable to a wide variety of coastal systems, we follow the generic derivation given by Paola and Voller (2005). Various forms of the morphodynamic equations that are in common use in coastal morphodynamics are presented. In Sect. 10.4 two different solution strategies are highlighted. In the first strategy, the *initial value* approach, the morphodynamic equations are integrated over time, resulting in the morphodynamic evolution of the bathymetry. The *bifurcation* approach focuses on obtaining asymptotic states (such as equilibria) directly, allowing for extensive sensitivity studies. These two approaches are illustrated by considering the morphodynamic evolution of a tidal inlet system (Sect. 10.5), and the pros and cons of both methods are discussed. Finally in Sect. 10.6, conclusions regarding the employability of the two approaches are summarized and major challenges for further advancement are identified.

10.2 Morphodynamic Modelling Approaches

Morphodynamic features in coastal seas result from nonlinear interactions among the water motion, sediment transport and bed evolution, and vary over a large range of length and time scales. The characteristics of these features can either be directly linked to the forcing conditions, or emerge from internal system dynamics (forced and free behaviour, respectively), see De Vriend (2001), Murray (2013). Henceforth, the typical time scale of morphological change for a particular phenomenon is denoted by T_{morph}, and the typical length scale of a morphological element by L_{morph}. Usually, the larger the time scale T_{morph} of some phenomenon, the larger the associated length scale L_{morph} (see Fig. 10.2).

The time scale T_{morph} can be of the same order as the typical forcing time scale T_{forcing} (for example in the swash zone) or much larger than T_{forcing} (for example the evolution of a channel–shoal system in tidal inlet systems)[1] (De Vriend 2001). The phenomena and processes at different length and time scales may interact with each other, with small–scale processes influencing larger scale behaviour and vice–versa (Murray et al. 2014). Apart from this wide range of length and time scales

[1] For later reference, long–term time scales are defined in this chapter as time scales much larger than both the forcing and morphodynamic time scales.

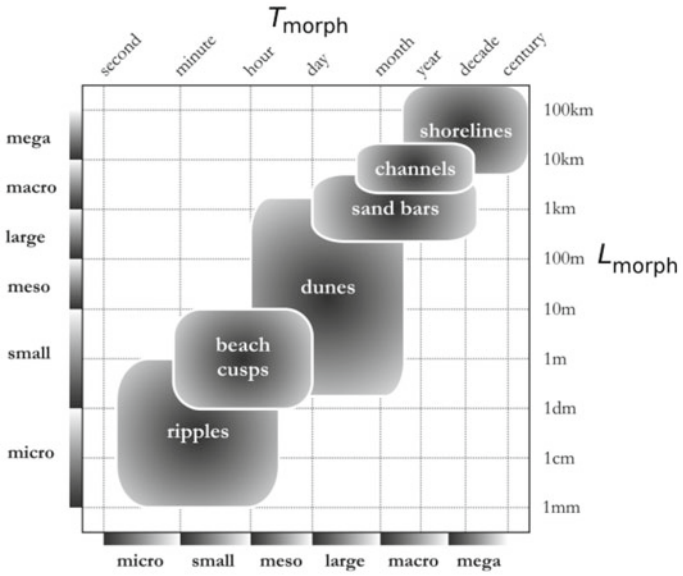

Fig. 10.2 Examples of typical time and length scales of morphological elements in coastal seas

involved, the study of modelling morphodynamic evolution is further complicated by the partial unpredictability of the input signal (waves, storm surges, river discharges).

To deal with these complicating aspects, various modelling strategies have been developed. Following De Vriend (1996), these approaches can be classified as *data–based* models, *empirical relationship* models and *process–based* models (including the semi–empirical long–term and formally integrated long–term models defined in De Vriend (1996)). The first type of models is entirely driven by observations to describe phenomena (e.g. Reeve et al. 2016), for example geostatistical models, models based on the empirical orthogonal function (EOF) analysis (Wijnberg and Terwindt 1995), and neural network models (Pape and Ruessink 2011). Empirical relationship models are derived from a statistical analysis of field data, and establish a relationship between input and output variables. An example of such a relationship is the equilibrium–state relationship given between the cross–sectional area of an inlet and the tidal prism, proposed by O'Brien (1931, 1969). Other examples are the Bruun rule for coastal retreat (Bruun 1962) and the Dean profile for shoreface slopes (Dean 1990). Even though these model types can give valuable information concerning the morphodynamic evolution, the focus in the remainder of this chapter is on process–based models because this type of models allows for generic insight from first principles.

In process–based models, the morphodynamic phenomena are simulated and analysed using a system of coupled (partial) differential equations. Following Murray (2003), these models can be arranged along a continuum with *simulation models* at one end and *exploratory models* at the other. Simulation models are designed

to reproduce as wide a range of morphodynamic features, in as much detail, and with as much quantitative accuracy as can be achieved. To accomplish this goal, a modeller typically strives to include all processes that could significantly affect the quantitative accuracy of the model, in as much detail as is practically feasible. As few processes as possible are parameterised, ideally only those processes on scales smaller than those treated in the model (e.g., parameterisation of turbulence as an effective eddy viscosity and the transport of sediment grains by the bulk behaviour of the sediment/water mixture). In Sect. 10.3.1, the mathematical system of equations, adopting this approach, is derived.

The exploratory models, at the other end of this model spectrum, aim at discovering what processes or interactions produce some poorly understood phenomenon—when searching for the clearest, simplest explanation. In this case, a modeller strives to include only the essential mechanisms, either by systematically simplifying the full system of equations and/or geometry used in the simulation models, or by replacing some (or all) of the balance equations used in the mathematical description for simulation models by empirical relations or rules that are based on physical insight and intuition (Murray 2003, 2007), see Sect. 10.3.2. These empirically–based parameterisations or rules are often employed for accurate modelling of large–scale morphodynamic features, features that are usually difficult to capture by process–based models that resolve much smaller scales (De Vriend 2001; Murray 2007).

10.3 Process–Based Models

The mathematical formulation of the balance laws underlying process–based *simulation* models applied to coastal seas is derived in Sect. 10.3.1. In Sect. 10.3.2 a discussion on the derivation of exploratory models is presented, by either a systematic approach to simplify the laws obtained in Sect. 10.3.1, or by combining or replacing these laws by employing empirically–based parameterisations or rules.

10.3.1 Mathematical Formulation of Simulation Models

Conservation of Sediment

A process–based description of the morphodynamic evolution is derived from conservation of sediment, covering sediment both suspended in the water column and at the bed interface.

In the literature, many different relations for this mass balance can be found, usually based on an adaptation of Exner's original equation (Exner 1920, 1925) to a particular problem. In Paola and Voller (2005), a general expression of the standard Exner equation is derived, including effects of tectonic uplift and subsidence, soil deformation and creep, compaction, as well as chemical precipitation and dissolution.

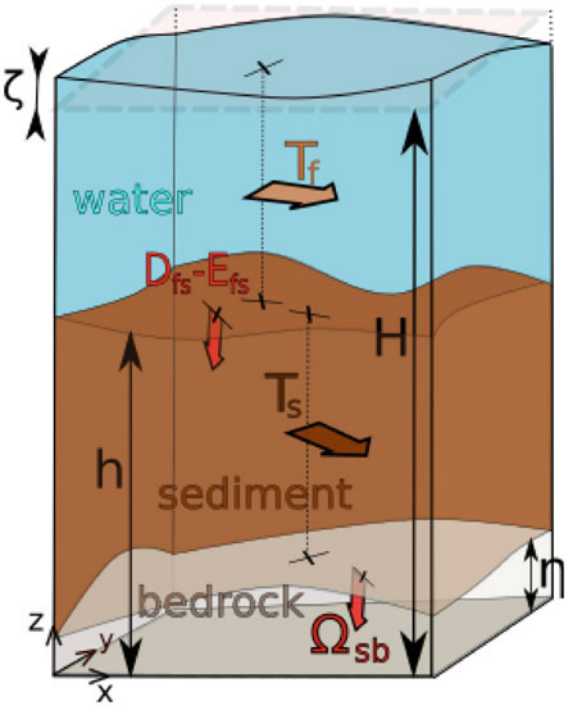

Fig. 10.3 Earth surface, considered as a three layer system, consisting of a water, a sediment and a bedrock layer. For an explanation of the symbols, see text

They apply the continuum approach[2] to a stack of primarily horizontal material layers. For each individual layer, characterised by a typical, distinct density and moving layer interfaces, a sediment mass balance is derived.

Here, this general approach is applied to a system consisting of three distinct layers (see Fig. 10.3), namely a water layer, a bed layer of quasi–static homogeneous particulate matter, and a bedrock layer. Defining an arbitrary reference level $z = 0$, the interface between the bedrock and the sediment is denoted by $z = \eta$, the interface between the sediment and the water by $z = h$ and the free surface is found at $z = H + \zeta$, with $z = H$ the location of the undisturbed water surface. With respect to sediment transport, we discriminate between the water and bed layers, thus ignoring aeolian transport. The transport in the water layer, averaged over its depth, is denoted by $\boldsymbol{T}_{\mathrm{f}}$, with the subscript 'f' referring to fluid. For the bed layer, that is $\boldsymbol{T}_{\mathrm{s}}$ with subscript 's' denoting sediment. The exchange of material between the water layer and the sediment layer is denoted by $D_{\mathrm{fs}} - E_{\mathrm{fs}}$, where the subscript 'fs' denotes that the fluxes are defined at the interface of the water and sediment layer. The deposition of material from the water layer on the bed is denoted by D_{fs}, and E_{fs} denotes the

[2] For a derivation based on spatial averaging of the sub–particle–scale differential equation of solid mass conservation, see Coleman and Nikora (2009).

erosion of the sediment layer[3]. Similarly, a sediment flux, denoted by Ω_{sb} is defined between the sediment layer and the bedrock. This flux is defined positive for a net exchange from the sediment layer to the bedrock layer.

Using this notation, the conservation law for sediment in the flow and sediment layers is derived. First, the sediment balance in the bedrock layer is discussed briefly. Next, in Sect. 10.3.1, the mass balance equations for the three layers are combined with equations that describe the water motion in the water layer, resulting in a system of equations that is typically used to model and simulate morphodynamic phenomena. To make this set of equations suitable for simulating coastal and estuarine morphodynamics, some processes need to be parameterised. This is outlined in subsequent sections.

Concentration Equation and Boundary Conditions

Taking the continuum assumption and considering only one sediment class (see e.g. McAnally and Mehta 2002; Jay et al. 2007 for multiple class models), the sediment balance in the water layer reads (Van Rijn 1993; Ter Brake and Schuttelaars 2010; Burchard et al. 2018):

$$\frac{\partial c}{\partial t} + \nabla \cdot \boldsymbol{u}c - \frac{\partial w_s c}{\partial z} - \nabla_{\mathrm{H}} \cdot (K_h \nabla_{\mathrm{H}} c) - \frac{\partial}{\partial z}\left(K_v \frac{\partial c}{\partial z}\right) = \Gamma_{\mathrm{f}}, \tag{10.1}$$

with $\nabla_{\mathrm{H}} = (\frac{\partial}{\partial x}, \frac{\partial}{\partial y}, 0)^T$, where T is the transpose operator. The sediment mass concentration is denoted by c (units $\mathrm{kg\,m^{-3}}$), w_s is the settling velocity of the sediment particles, and K_h and K_v the horizontal and vertical eddy diffusivities, respectively. The three–dimensional Cartesian velocity vector, denoted by $(u, v, w)^T$, is typically obtained by solving the continuity and Reynolds-Averaged Navier-Stokes equations for shallow waters, using the hydrostatic pressure assumption and Boussinesq approximation (see Chap. 1). For cohesive sediments, the settling velocity may be influenced by hindered settling and flocculation, processes that depend, among others, on suspended sediment concentration, turbulence intensity, and biological factors (Richardson and Zaki 1954; Winterwerp 1998, 2001; Horemans et al. 2020).

The first term on the left–hand side of Eq. (10.1) reflects the temporal changes in the local sediment concentration c, the second term the divergence of the advective sediment flux, the third term the settling of sediments in the water column due to gravitational effects, and the final two terms reflect the horizontal and vertical diffusive fluxes. Sediment sources and sinks in the water column are gathered in the Γ_{f} on the right–hand side of the balance.

[3] The exchange of sediment between the water and/or sediment layer on the one hand and the air on the other hand is not considered here. These fluxes can either be prescribed at the respective interfaces, or may be modeled by introducing a fourth layer that describes the dynamics of sediment in the air (aeolian transport) and the exchange of sediment over the appropriate interfaces.

As boundary condition at the free surface we require that the normal sediment flux vanishes:

$$-w_s c - K_v \frac{\partial c}{\partial z} = 0, \qquad \text{at} \quad z = H + \zeta. \tag{10.2}$$

Furthermore, the sediment flux normal to the bottom has to equal the difference between the erosion flux E_{fs} and deposition flux D_{fs}:

$$-w_s c - K_v \frac{\partial c}{\partial z} = E_{\mathrm{fs}} - D_{\mathrm{fs}}, \qquad \text{at} \quad z = h, \tag{10.3}$$

where the subscript 'fs' henceforth is left out. It is important to note that for these versions of the boundary conditions, surface and bottom slopes are assumed to be small (Kumar et al. 2017).

The horizontal boundary conditions depend on the problem at hand, typical conditions are no–transport boundary conditions at closed walls, prescribed transport conditions at a riverine sides and prescribed concentrations at seaward boundaries.

The deposition flux is defined as $D = w_s c$, with c evaluated at $z = h$, allowing for continuous deposition (Winterwerp and Van Kesteren 2004; Sanford 2008). With this, (10.3) reduces to $-K_v \partial c/\partial z = E$, evaluated at the top of the sediment layer ($z = h$). The erosion flux is usually parameterised to being proportional to a power of the absolute value of the excess bed shear stress $|\boldsymbol{\tau} - \boldsymbol{\tau}_{\mathrm{c}}|$ if this quantity is positive, otherwise it is set to zero. Here $\boldsymbol{\tau}$ is the actual bed shear stress and $\boldsymbol{\tau}_{\mathrm{c}}$ the critical shear stress for erosion (Fredsøe and Deigaard 1992). Specific formulations for sandy beds can be found in Van Rijn (1993), Dyer (1986), while for cohesive material the Ariathurai-Partheniades formulation is typically used (Kandiah 1974; Ariathurai 1974; Winterwerp and Van Kesteren 2004). For high suspended sediment concentrations the proportionality constant in the erosion formulation and both the eddy viscosity and diffusivity become functions of the suspended sediment concentration (Munk and Anderson 1948; Adams and Weatherly 1981; Dijkstra et al. 2019).

Integrating the mass–balance equation (10.1) over depth, using boundary conditions (10.2) and (10.3) (again assuming the horizontal gradients of ζ and h negligible when applying the boundary conditions), results in

$$\frac{\partial}{\partial t} \int_h^{H+\zeta} c \, dz + \nabla_{\mathrm{H}} \cdot \int_h^{H+\zeta} (\boldsymbol{u}_{\mathrm{H}} c - K_h \boldsymbol{\nabla}_{\mathrm{H}} c) \, dz + D - E = 0. \tag{10.4}$$

The second term on the left can be identified as the suspended sediment transport in the water layer $\boldsymbol{T}_{\mathrm{f}}$:

$$\boldsymbol{T}_{\mathrm{f}} = \int_h^{H+\zeta} (\boldsymbol{u}_{\mathrm{H}} c - K_h \boldsymbol{\nabla}_{\mathrm{H}} c) \, dz, \tag{10.5}$$

with $\boldsymbol{u}_{\mathrm{H}} = (u, v, 0)^T$ the horizontal component of the velocity vector. In deriving Eq. (10.4), it has been assumed that there are no source and sink terms in the water column ($\Gamma_{\mathrm{f}} = 0$).

Bed Evolution Equation

Following a similar approach as in the previous section, the depth–integrated mass balance equation for the sediment layer can be derived (see also Paola and Voller (2005)):

$$\int_{\eta}^{h} \frac{\partial \alpha}{\partial t}\, dz + \alpha(h)\frac{\partial h}{\partial t} - \alpha(\eta)\frac{\partial \eta}{\partial t} + \nabla_{\mathrm{H}} \cdot \boldsymbol{T}_{\mathrm{s}} - D + E + \Omega_{\mathrm{sb}} + \int_{\eta}^{h} \Gamma_{\mathrm{s}}\, dz = 0, \tag{10.6}$$

with α the density in the sediment layer and Γ_{s} the volume rate of mass production or destruction, accounting for the production or dissolution of particulate mass within the sediment column. In Eq. (10.6) the first term on the left hand side accounts for changes in the sediment density in the sediment column (e.g., compaction, or inflation of the sediment due to chemical changes). The second and third terms model the rate of movement of the bed surface h and the rate of movement of the bedrock interface η, respectively. The fourth term accounts for the net flow of soil or sediment due to creep in the horizontal plane. The exchange between the water layer and the sediment layer is captured by the deposition and erosion terms ($D - E$). Net sediment outflow across the sediment–bedrock interface is captured by the seventh contribution (Ω_{sb}).

The morphodynamic bed evolution equation, usually deployed for coastal seas, can be obtained from Eq. (10.6) by introducing a number of assumptions. Awareness of these assumptions is crucial to judge whether they are appropriate for the specific problem under consideration. One of these assumptions comprises a fixed interface between the sediment and bedrock layers and zero exchange across it, in which case the third and seventh terms in Eq. (10.6) vanish. This implies that processes such as the lateral flow of bedrock (folding) and tectonic motion are not taken into account (to include these processes, a dynamic equation for the bedrock layer has to be derived, see Paola and Voller (2005) and references therein for appropriate formulations when these terms cannot be ignored). Furthermore, the density α in the sediment layer is assumed to be constant in time, and the net production term Γ_{s} is assumed negligible. If, apart from these assumptions, the sediment layer thickness $h - \eta$ is assumed to be always larger than zero[4] and horizontal transport $\boldsymbol{T}_{\mathrm{s}}$ takes only place in the upper layer (the active layer) as bedload transport[5] $\boldsymbol{q}_{\mathrm{b}}$, Eq. (10.6) reduces to

[4] If only a limited amount of erodible sediment is available, the evolution of a so–called bottom pool, that can be depleted, has to be explicitly taken into account, see Burchard and Baumert (1998), Brouwer et al. (2018), Burchard et al. (2018).

[5] The distinction between bedload and suspended load can be made as follows: the bedload is that part of the load which is travelling in the active layer of the bed, supported by intergranular collisions

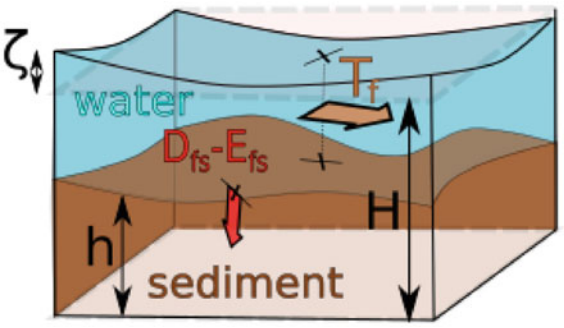

Fig. 10.4 Earth surface, considered as a two layer system. For an explanation of the symbols, see text

$$\alpha \frac{\partial h}{\partial t} + \nabla_{\mathrm{H}} \cdot \boldsymbol{q}_{\mathrm{b}} = D - E, \tag{10.7}$$

i.e., the bed level h only changes due to convergences and divergences of the bedload transport $\boldsymbol{q}_{\mathrm{b}}$ and exchange processes (erosion and deposition) with the water layer. The constant density in the sediment layer can now be related to the density of sediment particles ρ_{s} and the sediment porosity p by $\alpha = (1-p)\rho_{\mathrm{s}}$ (with $\rho_{\mathrm{s}} \sim 2650\,\mathrm{kg\,m^{-3}}$ and $p \sim 0.4$ for sandy material).

Since the bedrock layer is ignored and the sediment layer thickness never vanishes (neither in space nor in time), the three layer system has effectively been reduced to a two layer system: a sediment and water layer, see Fig. 10.4. Combining Eqs. (10.7) and (10.4) results in the bed evolution equation typically used in coastal morphodynamics:

$$(1-p)\rho_{\mathrm{s}} \frac{\partial h}{\partial t} + \nabla_{\mathrm{H}} \cdot \boldsymbol{q}_{\mathrm{b}} + \frac{\partial}{\partial t} \int_{h}^{H+\zeta} c\, dz + \nabla_{\mathrm{H}} \cdot \boldsymbol{T}_{\mathrm{f}} = 0, \tag{10.8}$$

with $\boldsymbol{T}_{\mathrm{f}}$ defined in Eq. (10.5).

Most parameterisations for the mass bedload transport per unit width perpendicular to the transport direction are of the form (Meyer-Peter and Müller 1948; Soulsby 1997)

$$\boldsymbol{q}_{\mathrm{b}} = (1-p)\rho_{\mathrm{s}} \hat{q}_{\mathrm{b}} \sqrt{g' d_{\mathrm{s}}^3}\, (\theta - \theta_{\mathrm{c}})^{b_{\mathrm{bl}}} \left[\frac{\boldsymbol{\tau}}{|\boldsymbol{\tau}|} - \boldsymbol{\lambda} \cdot \nabla_{\mathrm{H}} h \right] H(\theta - \theta_{\mathrm{c}}), \tag{10.9}$$

with $H(\cdot)$ the Heaviside function, $g' = g(\rho_{\mathrm{s}} - \rho)/\rho$ the reduced gravity, g the gravitational acceleration, ρ the water density, d_{s} the typical sediment diameter, and θ the Shields parameter, defined as $\theta = |\boldsymbol{\tau}|/[g d_{\mathrm{s}}(\rho_{\mathrm{sed}} - \rho)]$, expressing the ratio of motion induced forcing and resistance. The critical Shields parameter is denoted by θ_{c}. Furthermore, $\hat{q}_{\mathrm{b}}$, b_{bl} and the elements of the second–rank tensor $\boldsymbol{\lambda}$ are coef-

rather than by fluid turbulence (Wilson 1966). Suspended sediment is that part of the transported particles which mainly is supported by the fluid turbulence.

ficients which depend on the sediment properties and flow conditions (Van Rijn 1993; Soulsby 1997). See also e.g. Soulsby (1997) for other parameterisations of the bedload transport.

Morphodynamic System of Equations

From the above sections, it follows that a *process–based* morphodynamic model for coastal systems consists of equations describing the water motion, the suspended sediment dynamics and the evolution of the bed interface, and the appropriate boundary conditions. The governing equations read:

$$\nabla \cdot \boldsymbol{u} = 0, \tag{10.10}$$

$$\frac{\partial u}{\partial t} + \boldsymbol{u} \cdot \nabla u + fv = -g\frac{\partial \zeta}{\partial x} + \frac{\partial}{\partial x}\int_z^\zeta b\, dz' + \frac{\partial}{\partial z}\left(\nu_t \frac{\partial u}{\partial z}\right), \tag{10.11}$$

$$\frac{\partial v}{\partial t} + \boldsymbol{u} \cdot \nabla v - fu = -g\frac{\partial \zeta}{\partial y} + \frac{\partial}{\partial y}\int_z^\zeta b\, dz' + \frac{\partial}{\partial z}\left(\nu_t \frac{\partial v}{\partial z}\right), \tag{10.12}$$

$$\frac{\partial c}{\partial t} + \nabla \cdot \boldsymbol{u}c - \frac{\partial w_s c}{\partial z} = \nabla_{\mathrm{H}} \cdot (K_h \nabla_{\mathrm{H}} c) + \frac{\partial}{\partial z}\left(K_v \frac{\partial c}{\partial z}\right), \tag{10.13}$$

$$(1-p)\rho_{\mathrm{s}}\frac{\partial h}{\partial t} + \nabla_{\mathrm{H}} \cdot \boldsymbol{q}_{\mathrm{b}} = -\frac{\partial}{\partial t}\int_h^{H+\zeta} c\, dz - \nabla_{\mathrm{H}} \cdot \boldsymbol{T}_{\mathrm{f}}. \tag{10.14}$$

The water motion is described by the incompressible shallow water equations (here with the horizontal eddy viscosity terms neglected), with Eq. (10.10) the continuity equation and Eqs. (10.11) and (10.12) the momentum equations in the x and y direction, respectively. The Coriolis parameter is denoted by f, and ν_t denotes the vertical eddy viscosity. The buoyancy b is defined as $b = -g(\rho - \rho_0)/\rho_0$, with ρ_0 the reference water density. Both at the free surface and the bottom kinematic (i.e., fluid elements cannot escape from these boundaries) and dynamic (continuous tangential (shear) stresses) boundary conditions are applied (see Chap. 1, and references therein). The boundary conditions in the horizontal direction depend on the problem at hand. The suspended sediment dynamics are described by the concentration equation (10.13), together with appropriate boundary conditions, and the bed evolution by Eq. (10.14), with the bedload transport defined in Eq. (10.9) and the depth–integrated suspended sediment transport according to Eq. (10.5).

By adopting the Boussinesq and hydrostatic assumptions, the description of water and sediment dynamics has been focused on comparatively slowly varying conditions. In principle, it is technically feasible to describe conservation of mass and

momentum in a similar fashion for circumstances where also ocean waves play a significant role (which implies the relaxation of the hydrostatic assumption). That, however, is computationally very expensive as it requires a time step that is small compared to the smallest involved wave period. Therefore, the effects of waves (sea and swell) are commonly included in morphodynamic models in a wave–averaged sense. Concerning the water motion, wave–current interaction is usually dealt with by discriminating between effects of waves on currents and effects of currents on waves. This is depicted in Figs. 10.5 and 10.6, showing that waves and currents are computed separately, being that mutual interactions are taken into account, indicated by the *Waves* and *Flow* boxes, respectively. Within the wave computations, the regional wave propagation and generation are usually based on the wave action balance (see for instance Hiswa (Holthuijsen et al. 1989), Swan (Ris et al. 1994; Booij et al. 1999), Wavewatch (Tolman 1991)). Including effects of ambient flow and spatial variations in water depth, obtained from the flow computations, the action balance reads (see e.g. Mei 1983; Komen et al. 1994)

$$\frac{\partial A}{\partial t} + \nabla_{\mathrm{H}} \cdot \left(\left[\mathbf{c}_g + \mathbf{U} \right) A \right] + \frac{\partial (c_\sigma A)}{\partial \sigma} + \frac{\partial (c_\theta A)}{\partial \theta} = \frac{1}{\sigma} S, \tag{10.15}$$

with A the wave action, defined as energy density divided by frequency σ, $\mathbf{c}_g$ is the wave group velocity, θ is the direction of wave propagation and S combines all energy sources and sinks (like wind input, dissipation, non-linear redistribution of wave energy over frequencies). Furthermore, c_σ and c_θ are wave velocities in σ and θ space, respectively (Mei 1983; Dingemans 1997). The ambient flow velocity is denoted by $\mathbf{U}$, and is assumed to be uniform in the vertical direction (SWAN team 2006). It should be stressed that the velocity field, obtained from the flow computations, is a three dimensional flow field. This implies that information from the three–dimensional velocity field has to be reduced to a two–dimensional field, which can be done in various ways. For example, in Moghimi et al. (2013) the surface velocity was used in the two–way coupled experiments.

To include the effects of waves on the flow, two approaches exist in the literature. The first approach incorporates wave effects via a depth–dependent radiation stress formulation (Mellor 2003, 2011, 2015), whereas the second approach uses the vortex force formulation (McWilliams et al. 2004; Uchiyama et al. 2010; Ardhuin et al. 2008; Bennis et al. 2011; Ardhuin et al. 2017). Comparing these two formulations, it was shown that both approaches give similar results, even though some shortcomings were revealed. For a detailed discussion, see Moghimi et al. (2013), Xia et al. (2020). Apart from these conservative wave forces, non–conservative wave forces such as depth–induced breaking, whitecapping induced flow accelerations, and the enhancement of the apparent bed roughness have to be taken into account parametrically (Moghimi et al. 2013; Olabarrieta et al. 2014).

Similar to the hydrodynamic equations, the sediment transport equations and the bed evolution equation are wave–averaged. This implies that the hydrodynamic variables, the suspended sediment concentration and the bed level in Eqs. (10.13) and (10.14) are wave–averaged quantities, including the currents induced by waves (wave boundary layer streaming, breaking–induced currents). Due to wave effects, the sediment diffusivity coefficients in Eq. (10.13) have to be expressed as wave–averaged quantities, which is realised by either employing empirical equations (Van Rijn 2007a, b) or using turbulence closure models. Furthermore, the effect of the waves on the magnitude and direction of the bed shear stress should be taken into account (Zyserman and Fredsøe 1994; Soulsby 1997; Van Rijn 2007a, b).

Waves are also able to generate non–vanishing wave–averaged sediment fluxes, i.e. fluxes related to the correlation between the velocities and sediment concentration that vary on the time–scale of the waves (Green and Coco 2014). In most morphodynamic models, these fluxes, which take place mainly in the wave boundary layer, i.e. the wave–related suspended transport and the bedload transport, are either neglected or included using empirical sediment transport formulae. For a detailed discussion and their importance in the coastal zone, see Van Rijn et al. (2013).

10.3.2 Mathematical Formulation of Exploratory Models

Exploratory models are often derived from the full-blown simulation models by averaging over specific time and length scales, constraining the dynamics and only retaining the processes that are believed essential for explaining some morphodynamic feature. Averaging the equations and reducing the number of processes taken into account are examples of *model reduction*, see Murray (2003) for a discussion.

A model reduction approach, that is often used in morphodynamics, is based on the assumption that resolving the depth–averaged dynamics suffices to capture the essential physical mechanisms. To capture these dynamics, Eqs. (10.10)–(10.13) have to be integrated over the water depth. Employing the vertical boundary conditions and applying Leibniz differentiation rule to interchange derivatives and integrations, and assuming that density gradients and wind stresses are negligible, one obtains the following system of equations (for a detailed derivation of the depth–averaged shallow–water equations and depth–integrated suspended sediment equation, see Nihoul (1975) and Ter Brake and Schuttelaars (2010)):

$$\frac{\partial \zeta}{\partial t} + \nabla \cdot \left[(H - h + \zeta) \hat{\boldsymbol{u}} \right] = 0, \tag{10.16}$$

$$\frac{\partial \hat{u}}{\partial t} + \hat{\boldsymbol{u}} \cdot \nabla \hat{u} + f \hat{v} = -g \frac{\partial \zeta}{\partial x} - \frac{\tau_x}{\rho (H - h + \zeta)}, \tag{10.17}$$

$$\frac{\partial \hat{v}}{\partial t} + \hat{\boldsymbol{u}} \cdot \nabla \hat{v} - f \hat{u} = -g \frac{\partial \zeta}{\partial y} - \frac{\tau_y}{\rho (H - h + \zeta)}, \tag{10.18}$$

$$\frac{\partial C}{\partial t} + \nabla \cdot \hat{\boldsymbol{u}} C - K_h \nabla \cdot \left[\nabla C + \frac{w_s}{K_v} \beta C \nabla h \right] = E - D, \tag{10.19}$$

$$(1 - p) \rho_s \frac{\partial h}{\partial t} + \nabla \cdot \boldsymbol{q}_b = D - E. \tag{10.20}$$

Equation (10.16) is the depth–averaged continuity equation, Eqs. (10.17) and (10.18) are the depth–averaged momentum balance in the x and y direction, respectively. Equation (10.19) is the depth–integrated concentration equation and Eq. (10.20) describes the conservation of sediment mass. In these equations, $\hat{\boldsymbol{u}} = (\hat{u}, \hat{v})^T$ denotes the depth averaged velocity, C the depth–integrated concentration, and β a parameter that depends exponentially on the local water depth (see Ter Brake and Schuttelaars 2010 for an explicit expression). Note that the erosion E, the deposition D, and the bedload transport term $\boldsymbol{q}_b$ still depend on the velocities, shear stresses and concentrations at the bed. However, since the depth–averaged model only results in depth–averaged velocities and depth–integrated concentrations, these contributions have to be parameterised in terms of the depth–averaged quantities (see Sect. 10.5 and Appendix 1 for an example, where the morphodynamic model is applied to a tidal inlet).

The effects of sea and swell can be included as discussed in Sect. 10.3.1, namely by averaging the equations over the time scale associated with waves, resulting in wave– and depth–averaged morphodynamic equations. The generation and propagation of waves again follows from Eq. (10.15), in which the velocity $\mathbf{U}$ is now unambiguous, namely the depth–averaged velocity $\hat{\boldsymbol{u}}$. To include the effects of waves on the flow, the net wave–induced momentum flux is modelled by the divergence of the depth–integrated radiation stress tensor (Longuet-Higgins and Stewart 1964).

Apart from reducing the model equations by formal averaging, empirical submodels can be used in model reduction. In such submodels, complex small–scale processes are lumped together into a simple relationship between larger–scale quantities. In deriving the three–dimensional model equations in (10.10)–(10.14) this approach has been already used, for example in directly relating the bed load transport to the flow parameters. Instead of using such an empirical model only for the bed load transport, the total sediment transport, including both suspended load and bed load transport, may also be given by an empirical formula. This amounts to replacing Eqs. (10.19) and (10.20) in the above model equations by

$$(1-p)\rho_s \frac{\partial h}{\partial t} + \nabla_H \cdot \boldsymbol{q}_t = 0, \tag{10.21}$$

with $\boldsymbol{q}_t$ the *total load* transport, including bed slope effects (Dyer 1986; Soulsby 1997). As shown by Hepkema et al. (2019), it may be important to increase the bed slope coefficient(s) (the elements of the second–rank tensor $\boldsymbol{\lambda}$ in Eq. (10.9)) to include the slope contribution associated with concentration equation (10.19).

When describing large scale phenomena, the morphodynamic evolution is often directly linked to flow velocities. An example is the model reduction developed by Escoffier (1940) to assess the stability and possible closure of a single inlet system by relating the tidal inlet cross–section directly to the cross–sectionally averaged velocity in the tidal inlet. Simplifying the water motion in the backbarrier basin, Van de Kreeke (1990), Van de Kreeke et al. (2008), Brouwer et al. (2012) extended this approach to a double inlet system. Brouwer et al. (2013) extended this analysis by allowing for a dynamic water motion in the backbarrier basin, an approach extended to multiple inlet systems by Roos et al. (2013), Reef et al. (2020).

By only using empirical relations or rules (with rules defined as parameterisations when they are first proposed, to differentiate them from well–accepted parameterisations (Murray 2013), so–called rule–based models can be constructed. Examples of such models can be found in Werner and Fink (1993) for beach cusps, Murray and Paola (1994) for breaded stream models, and Ashton et al. (2001) and Stive et al. (1998) for the formation of large scale coastline features.

10.4 Solution Procedure

Once the morphodynamic process–based model has been formulated (see Sect. 10.3), a solution strategy to solve the resulting mathematical model has to be decided upon. Two different classes of numerical solution strategies can be distinguished, the *initial value* approach and the *bifurcation* approach (Dijkstra et al. 2014). In Sect. 10.4.1 the former approach is discussed in detail, while the bifurcation approach is elaborated upon in Sect. 10.4.2.

10.4.1 Initial Value Approach

In the *initial value* approach, the temporal evolution of the morphology is obtained by integrating the system of mathematical equations forward in time using a so–called morphodynamic loop, see Fig. 10.5. As a first step in the morphodynamic loop, initial conditions for all dependent variables and appropriate boundary conditions have to be prescribed. The boundary conditions usually contain forcing terms that are temporally varying, for example tidal elevations, wave conditions, and concentrations at

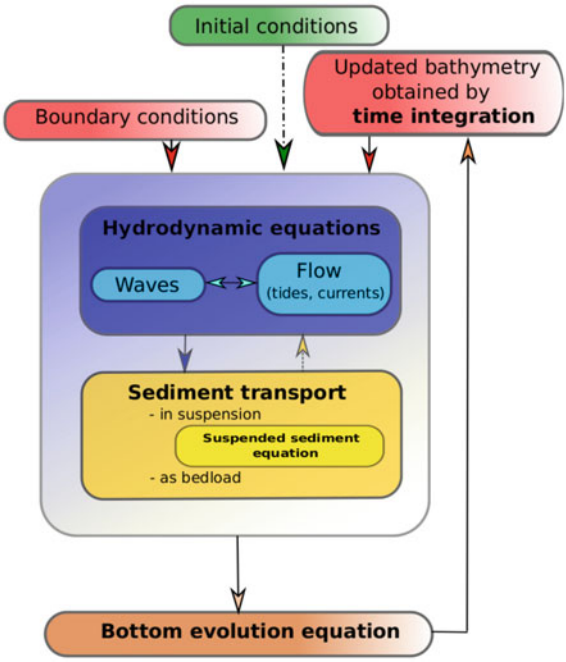

Fig. 10.5 Flow diagram of a morphodynamic model using time–integration. First the initial conditions (green box) and boundary conditions (top red box left) are defined. Next the water motion (blue box) and sediment dynamics, including the sediment transport (yellow box) are calculated. The resulting sediment transport fields are used to update the bed profile (brown box). This updated bed profile is used to close the morphodynamic loop (red box, top right). Often the hydrodynamic variables and the suspended sediment concentration vary on a much shorter time scale than the bed, allowing for various acceleration techniques (see text for a detailed discussion)

open boundaries. Using these initial and boundary conditions, the temporal evolution of the water motion and sediment concentration is calculated by numerically integrating the appropriate equations from an initial point in time $t = t_{\text{ini}}$ to a final time $t = t_{\text{ini}} + T$ with a time step Δt that is small enough to get an accurate solution. If the water motion is not influenced by the suspended sediment concentration, the water motion and suspended sediment concentration can be solved sequentially. However, if the suspended sediment concentrations significantly influence the water motions, the hydrodynamic and suspended sediment equations have to be solved simultaneously. In both approaches, a key assumption is that the bed does not change during the elapsed time T. The water motion and suspended sediment concentrations are used to calculate the cumulative sediment transport over the total elapsed time T. Spatial gradients in the cumulative transport are used to update the bed profile, i.e. the morphological time step is T. The morphodynamic loop is completed by again calculating the hydrodynamic variables and sediment transport, using the updated bed profile, water motion and suspended sediment concentrations at $t = t_{\text{ini}} + T$, and the prescribed boundary conditions.

When updating the bed without making any assumptions concerning time scales, one has to update the bathymetry after each time step Δt, i.e., $T = \Delta t$. Since Δt is typically in the order of seconds to minutes, it is evident that this approach is not feasible for bed changes on the long time scale. By taking advantage of the vast difference between the fast and slow time scales, i.e., employing the observation that the time scales associated with the water motion and transport processes are much smaller than the typical time scales of the significant morphodynamic change, T can usually be chosen much larger than Δt.

Unfortunately, even with this approach, the simulation of the long–term morphodynamic evolution is usually prohibitively time–consuming. To illustrate this, consider a coastal system in which the water motion is mainly forced by tides, for example a tidal inlet (see Sect. 10.5). If the morphodynamic time scale of the phenomenon under study is much larger than the tidal time scale (for example order of years), morphological changes within a single tidal cycle are very small and the bottom can be considered fixed during the computation of hydrodynamics and sediment transport over a tidal cycle (i.e., the morphological time step T defined in the previous paragraph is equal to the tidal period). The bed evolution then follows from the divergence of the *tidally–integrated* sediment transport or the *tidally–averaged* sediment transport multiplied by the tidal period. However, the use of this morphological time step (of approximately 12.5 h) to assess the morphodynamic evolution on the long term (i.e., time scales even larger than the morphodynamic time scale), is still computationally too expensive.

To overcome this problem, various reduction schemes have been developed. Focussing on model reduction (contrasting input reduction techniques, see De Vriend et al. (1993)), these methods can be divided broadly into two groups. The first type of reduction schemes is *intuitive*, as it has not been derived rigorously from the complete mathematical system, while the second *formal* approach is based on rigorous mathematical techniques that exploit the difference between the fast and slow time scales (De Vriend et al. 1993).

In De Vriend et al. (1993), Latteux (1995), Roelvink (2006) an overview of various intuitive reduction schemes is given. Examples are the introduction of an effective morphological time step by multiplying the bed changes after one morphological time step by a prescribed factor (De Vriend et al. 1993), the assumption that the water transport (i.e. the depth integrated velocity) and flow pattern remain constant in time (continuity correction), and the so–named 'online' approach employing a morphological factor (Roelvink 2006). The latter approach is now commonly used in most morphodynamic codes based on the time–integration approach. In this approach, which is similar to the concept of an elongated tide (Latteux 1995), the water motion, sediment transport and bottom are all updated after each time step Δt, associated with the fast time scale. To account for the difference in time scales between the water motion and the morphodynamic evolution, after every time step Δt the bed changes are multiplied by a constant factor N (Lesser et al. 2004; Roelvink 2006). Hence, after a simulation over one tidal cycle, an approximation of the morphologic changes after N tidal cycles has been obtained. At this moment, no robust and objective method to determine the acceleration factor N, resulting in accurate

results when compared to the results obtained without this acceleration factor, has been reported (Ranasinghe et al. 2011). Notwithstanding this problem, the online approach, combined with model input reduction techniques (De Vriend et al. 1993), is now typically used to perform simulations of morphological changes over time periods of years to decades (Luijendijk et al. 2019).

Formal methods exploit the observation that the fast time scale associated with the water motion and sediment transport, is often time periodic, for example in the case of sea waves and tides. One is generally not interested in the details of this short-term motion, but in the residual effects which cause the morphological evolution. Using multiple scale techniques, this residual effect can be obtained by averaging over the short time scale (Sanders and Verhulst 1985), resulting in an asymptotic approximation. Krol (1990) was the first to apply this to a morphological model of a simple tidal basin. He showed that, when the morphodynamic time scale T_{mor} and the tidal time scale T_{tidal} are related as $T_{\text{tidal}} = \delta T_{\text{mor}}$, the approximation $\bar{h}$ of h obtained by averaging the divergence of the sediment transport over the tidal time scale, is an $o(1)$ approximation of the actual bottom topography h, obtained without tidally averaging the divergence of the transport, valid on a $1/\delta$ time scale. In Sect. 10.5 the averaging method will be applied to analyse the morphodynamic evolution of single inlet system.

10.4.2 Bifurcation Approach

In the so–called *bifurcation* approach, the focus is on the computation of the asymptotic states in the morphodynamic models, i.e., the states observed as $t \to \infty$. These asymptotic states can be characterised by their temporal behaviour as steady states, periodic orbits, quasi-periodic orbits or more complicated states, usually referred to as strange attractors of the model (characterised by chaotic, aperiodic behaviour). These asymptotic states, except for the strange attractors, can be obtained systematically and efficiently using the bifurcation approach, resulting in insight in the number of asymptotic states and their stability for a given set of parameter values. Furthermore, the transitions between different states by changes in parameter values, resulting in so–called bifurcations, can be efficiently detected as well. This allows for a detailed framework to understand these transitions.

To find the asymptotic states and identify the transitions, methods of dynamical systems theory are employed. As a first step, the system of morphodynamic equations is discretized, resulting in a (usually large) system of n coupled ordinary differential equations (Dijkstra et al. 2014):

$$\mathcal{M}\frac{d\boldsymbol{u}}{dt} = \Phi(\boldsymbol{u}, \boldsymbol{p}) = \mathcal{L}\boldsymbol{u} + \mathcal{N}(\boldsymbol{u}), \tag{10.22}$$

where $\boldsymbol{u} \in \mathbb{R}^n$ is a discretized solution of the orginal PDEs, and $\boldsymbol{p}$ denotes the vector of prescribed parameters. The matrix $\mathcal{M}$ is called the mass matrix, the discretized

linear operator is denoted by $\mathcal{L}$ and the nonlinear operator by $\mathcal{N}$. In general, these operators will depend on the prescribed parameters $\boldsymbol{p}$.

Given a set of parameters $\boldsymbol{p}$ the aim of the bifurcation approach is to find the possible attractors. The number and type of attractors will typically change when the value of one or more parameters is changed. These transitions occur through bifurcations. The simplest ones, i.e., bifurcations for which the stability of steady states changes by varying only one parameter, are the fold or saddle–node, the transcritical, the pitchfork and the Hopf bifurcation (see Intermezzo for a short discussion on the *supercritical* pitchfork bifurcation). These and other types of bifurcations, as well as the mathematical aspects of dynamical systems, are discussed elaborately in Guckenheimer and Holmes (1983), Kuznetsov (2004), Seydel (2010). Numerical techniques to detect bifurcation points and their type, and continuation methods to follow the attractors are extensively discussed in Keller (1977), Crisfield (1981), Kuznetsov (2004), Seydel (2010).

In Fig. 10.6 the flow diagram associated with the bifurcation approach for *steady states* morphodynamic equilibria is shown. As a first step, a sufficiently accurate ini-

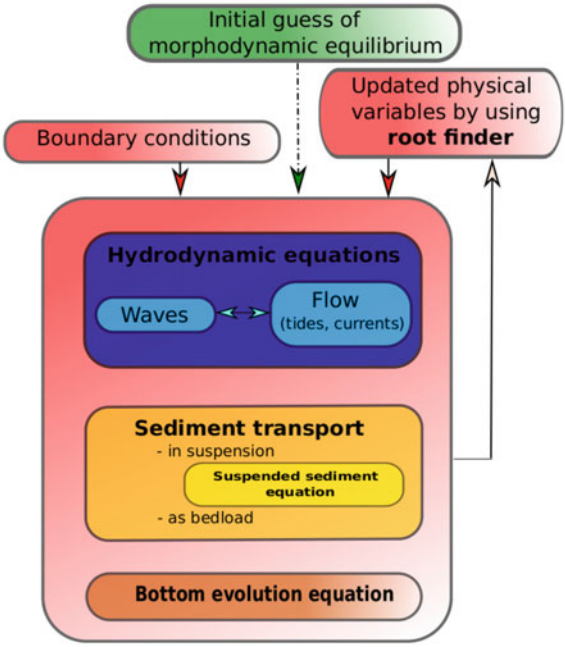

Fig. 10.6 Flow diagram of a general morphodynamic model using a bifurcation approach to obtain steady state morphodynamic equilibria. The initial guess of this morphodynamic equilibrium, consisting of a water motion, sediment concentration and bed in morphodynamic equilibrium close enough to this equilibrium (top green box), together with the prescribed boundary conditions (red box, left), is substituted in the system of equations (large red box, bottom). The resulting deviation from equilibrium is used to update the guess of the morphodynamic equilibrium (red box, top right). This loop is iterated until the updated morphodynamic equilibrium does not change anymore

tial guess of the solution of the morphodynamic problem has to be given. Since this initial guess is usually not a solution of the nonlinear system of equations (10.22), a robust nonlinear solver has to be used to get the associated morphodynamic equilibrium. Usually, the Newton–Raphson method is used, a method that converges quadratically, provided that the initial guess is sufficiently close to the actual equilibrium solution and that the Jacobian is non-singular (Seydel 2010). As soon as a morphodynamic equilibrium is obtained for one set of parameter values $\boldsymbol{p}$, the continuation approach mentioned above can be started. For a discussion on the continuation of periodic and quasi–periodic solutions, we refer to the review of Dijkstra et al. (2014).

Intermezzo

To illustrate the dependency of the number and stability of equilibria on model parameters (here only one parameter is considered, denoted by p), we consider the following equation of an arbitrary quantity $u(t)$:

$$\frac{du}{dt} = u(p - u^2), \tag{10.23}$$

which is the normal form of a (supercritical) pitchfork bifurcation. Concerning steady state solutions, it is found that for $p < 0$ only one (real) solution for u exists, namely $u_{\text{eq}} = 0$. If $p > 0$, apart from the steady state solution $u_{\text{eq}} = 0$, two other stationary equilibrium solutions are found: $u_{\text{eq}} = \pm\sqrt{p}$ (see Fig. 10.7).
To obtain the linear stability of these equilibria, we insert $u = u_{\text{eq}} + u'(t)$ in Eq. (10.23) and linearize the equation w.r.t. the perturbation u', resulting in

$$\frac{du'}{dt} = (p - 3u_{\text{eq}}^2)u'.$$

The linear stability is obtained by solving this eigenvalue problem. This immediately results in the observation that $u_{\text{eq}} = 0$ is stable for $p < 0$, and unstable for $p > 0$. At $p = 0$ the eigenvalue associated with the trivial equilibrium is zero, indicating that a bifurcation occurs: $u_{\text{eq}} = 0$ loses its stability and two new branches of solutions are found for $p > 0$. Both branches are linearly stable.

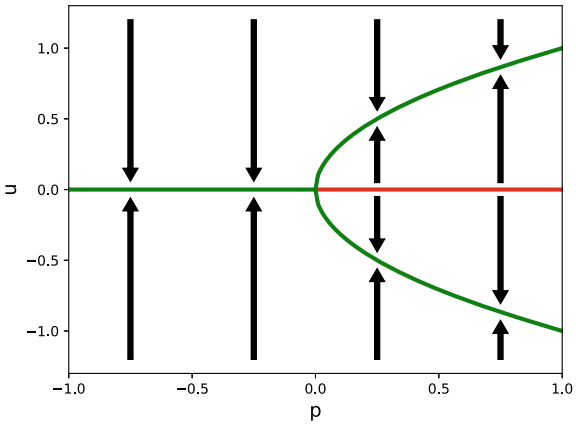

Fig. 10.7 Supercritical pitchfork bifurcation. The green lines indicate the (linearly) stable steady states, the red lines are the unstable solutions. The vertical arrows denote the evolution with respect to time (i.e., going towards the stable solutions). At $p = 0$, a bifurcation occurs: the stability of the trivial solution changes and two new stable solutions come into existence

10.5 Example: Morphodynamics of Tidal Inlet Systems

10.5.1 Introduction

To illustrate the approaches sketched in Sects. 10.4.1 and 10.4.2, the morphodynamic evolution in a short tidal embayment is considered, ignoring the effects of earth rotation ($f = 0$). For both the initial value approach (Sect. 10.5.2) and the bifurcation approach (Sect. 10.5.2), the focus will be on a rectangular embayment of tidally–averaged length L and width B, see Fig. 10.8 for the geometry and Table 10.1 for default parameter values.

The embayment considered can be characterised as *short* because the product of the wavenumber $k = \sqrt{gH}/\sigma$ of the frictionless tidal wave (with g the gravitational constant and σ the dominant tidal frequency, taken in this example as the M_2 tidal

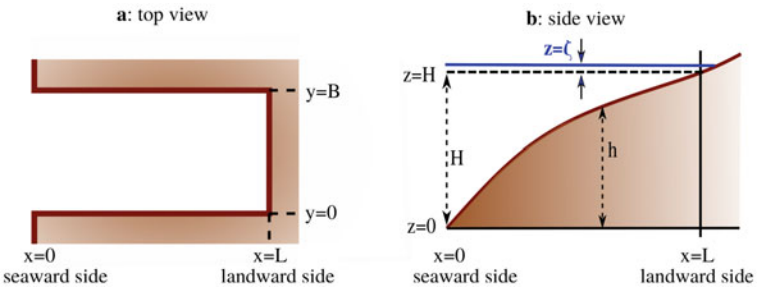

Fig. 10.8 Geometry of a rectangular tidal inlet **a** top view and **b** side view

Table 10.1 Quantities and parameter values for the Frisian inlet system, taken from Ter Brake and Schuttelaars (2010)

Geometry	Tide
$L = 20\,\mathrm{km}$	$A_{M_2} = 0.84\,\mathrm{m}$
$B_0 = 2\,\mathrm{km}$	$\sigma = 1.4 \cdot 10^{-4}\,\mathrm{rad\,s^{-1}}$
$H = 10\,\mathrm{m}$	
Sediment	
$\rho_s = 2650\,\mathrm{kg\,m^{-3}}$	$K_v = 0.1\,\mathrm{m^2\,s^{-1}}$
$d = 130\,\mu\mathrm{m}$	$\alpha = 0.01\,\mathrm{kg\,s\,m^{-4}}$
$w_s = 0.015\,\mathrm{m\,s^{-1}}$	$K_h = 100\,\mathrm{m^2\,s^{-1}}$
$p = 0.4$	$\lambda = 6.8 \cdot 10^{-6}\,\mathrm{m^2\,s^{-1}}$
Non–dimensional parameters	
$\varepsilon \sim 0.15$	$a \sim 0.04$
$\kappa \sim 1 \cdot 10^{-3}$	$b \sim 3$
$\delta_\mathrm{s} \sim 8 \cdot 10^{-4}$	$\delta_\mathrm{b} \sim 5.4 \cdot 10^{-7}$
$\mu \sim 1.8 \cdot 10^{-3}$	$\phi \sim 7^\circ$

frequency), and the tidally–averaged embayment length L is much smaller than one ($kL \ll 1$). The water depth is denoted by $\bar{H} - h + \zeta$, with $\bar{H}$ the width–averaged, undisturbed water depth at the entrance, h the height of the bed (measured with respect to $z = 0$) and ζ is the free surface elevation (measured with respect to the undisturbed water level $z = \bar{H}$).

10.5.2 Cross–Sectionally Averaged Morphodynamic Equilibria

As a first step, the morphodynamic evolution and possible equilibria are studied for a cross–sectionally averaged model. This model is obtained by averaging the system of morphodynamic equations, Eqs. 10.16–10.20, over the width. Using a scale analysis (see Appendix 1 for details), and assuming that the suspended sediment transport is dominated by diffusive processes (neglecting the diffusive transports associated with topographic variations and advective processes), the resulting system of equations reads

$$\frac{\partial \bar{\zeta}}{\partial t} + \frac{\partial}{\partial x}\left[(\bar{H} - \bar{h})\bar{u}\right] = 0, \tag{10.24}$$

$$\frac{\partial \bar{\zeta}}{\partial x} = 0, \tag{10.25}$$

$$\frac{\partial \bar{C}}{\partial t} - K_h \frac{\partial^2 \bar{C}}{\partial x^2} = \alpha \bar{u}^2 - \gamma \bar{C}, \tag{10.26}$$

$$(1-p)\rho_s \frac{\partial \bar{h}}{\partial t} = -\left\langle \frac{\partial}{\partial x}\left(\underbrace{-K_h \frac{\partial \bar{C}}{\partial x}}_{\bar{q}_{x,\mathrm{diff}}} + \underbrace{-\hat{s}\lambda \frac{\partial \bar{h}}{\partial x}}_{\bar{q}_{x,\mathrm{bl}}} \right) \right\rangle, \tag{10.27}$$

with boundary conditions

$$\bar{\zeta} = A_{M_2}\cos(\sigma t), \quad \left\langle \gamma \bar{C} - \alpha \bar{u}^2 \right\rangle = 0, \quad \bar{h} = 0 \qquad \text{at } x = 0, \tag{10.28}$$

$$\frac{\partial \bar{u}}{\partial x} \text{ is finite}, \quad K_h \frac{\partial \bar{C}}{\partial x} + \hat{s}\lambda \frac{\partial \bar{h}}{\partial x} = 0, \quad \bar{h} = \bar{H} \qquad \text{at } x = L, \tag{10.29}$$

where the overbar $\bar{\cdot}$ denotes that the variable is averaged over width and $\langle \cdot \rangle$ denotes that the quantities are averaged over a tidal cycle. The boundary conditions at $x = L$ are obtained by reformulating the boundary conditions at the moving boundary to equivalent conditions at $x = L$, see Ter Brake and Schuttelaars (2010) for details. Note that drying and flooding are not explicitly taken into account. In Eq. (10.27) the first term on the right is minus the divergence of the width–averaged diffusive sediment transport $\bar{q}_{x,\mathrm{diff}}$ and the second term minus the divergence of the width–averaged bedload transport $\bar{q}_{x,\mathrm{bl}}$, where $\hat{s}$ is a coefficient that depends, amongst others, on the velocity and the sediment properties, and λ a bedload coefficient (see the Appendix for a detailed discussion).

Because the bed only evolves on a long morphodynamic time scale, as indicated by the angular brackets in Eq. (10.27), the bed can be considered fixed at the hydrodynamic time scale. This allows for an explicit solution of the comparatively fast varying hydrodynamic quantities, resulting in

$$\bar{\zeta}(x,t) = A_{M_2}\cos(t^*),$$
$$\bar{u}(x,t) = U\frac{x^*-1}{1-\bar{h}^*}\sin(t^*),$$

where the non–dimensional quantities, appearing in these expressions, are defined as $t^* = \sigma t$, $x^* = x/L$, $\bar{h}^* = \bar{h}/\bar{H}$, and $U = \sigma A_{M_2} L/\bar{H}$. Since we are mainly interested in the bed evolution, only the tidally averaged component of the suspended sediment concentration $\bar{C}$, denoted by $\langle \bar{C} \rangle$, has to be calculated. The diffusion term in Eq. (10.26) is much smaller than the erosion and deposition terms, which gives, to a good approximation, that

$$\langle \bar{C} \rangle = \frac{1}{2}\frac{\alpha}{\gamma}U^2\left(\frac{x^*-1}{1-\bar{h}^*}\right)^2.$$

In deriving this expression, corrections of the order $\hat{s}\lambda$ have been neglected. For consistency, these corrections are neglected in the bed evolution equation as well, resulting in

$$\frac{\partial \bar{h}^*}{\partial t^*} = \frac{1}{2}\delta_s^* a^* K_h^* \frac{\partial^2}{\partial x^2}\left(\frac{x^* - 1}{1 - \bar{h}^*}\right)^2, \tag{10.30}$$

with boundary conditions $\bar{h}^* = 0$ at $x^* = 0$ and $\bar{h}^* = 1$ at $x^* = 1$. The non–dimensional parameter $\delta_s^* = \alpha U^2/\rho_s(1-p)\sigma H$ is the ratio of the tidal time scale and the typical time scale T_s at which the bed changes due to suspended sediment transports, $K_h^* = K_h/\sigma L^2$ and $a^* = \sigma/\gamma$ (see Appendix for more details). Since $\delta_s^* a^* K_h^* \ll 1$, the bed indeed evolves at a long time scale, substantiating the assumption that the bed is, to a good approximation, fixed at the short (tidal) time scale.

The resulting bed evolution equation (10.30) can be solved using both approaches discussed in Sect. 10.4. In the next section, the results obtained using the time–integration approach are discussed, followed by a discussion of the bifurcation approach.

Initial Value Approach

The bed evolution equation (10.30) is discretized in time, using the θ–scheme, a generalization of the Crank-Nicolson scheme, with a time step Δt^*. In space the domain is discretized using NX intervals of size Δx^*, and the spatial part of the bed evolution equation is approximated using a central finite difference scheme. The resulting discretized equation reads

$$h_i^{j+1} = h_i^j + \theta \frac{\left(F_{i+1}^{j+1} - 2F_i^{j+1} + F_{i-1}^{j+1}\right)}{\Delta x^{*2}} + (1-\theta)\frac{\left(F_{i+1}^{j} - 2F_i^{j} + F_{i-1}^{j}\right)}{\Delta x^{*2}},$$

with $0 < i < NX - 1$, where i indicates the location $x_i^* = i\Delta x^*$. The superscript j indicates time $t^{*j} = j\Delta t^*$. The function F_i^j reads

$$F_i^j = \frac{1}{2}\delta_s^* a^* K_h^* \left(\frac{x_i^* - 1}{1 - \bar{h}_i^{*j}}\right).$$

As boundary conditions, $\bar{h}_0^{*j} = 0$ and $\bar{h}_{NX}^{*j} = 1$ for all $j \geq 0$. Furthermore, as a closed boundary at $x^* = 1$ is assumed, together with a fixed bed level at that location, the transport at the location $i = NX - 1$ must equal zero. This condition reads

$$\theta \frac{\left(1 - F_{i-1}^{j+1}\right)}{2\Delta x^*} + (1-\theta)\frac{\left(1 - F_{i-1}^{j}\right)}{2\Delta x^*} = 0.$$

In Fig. 10.9a a few snapshots in time of the resulting profile are shown, starting from a bed profile that is ~10 m deep in the largest part of the inlet system (the initial bed

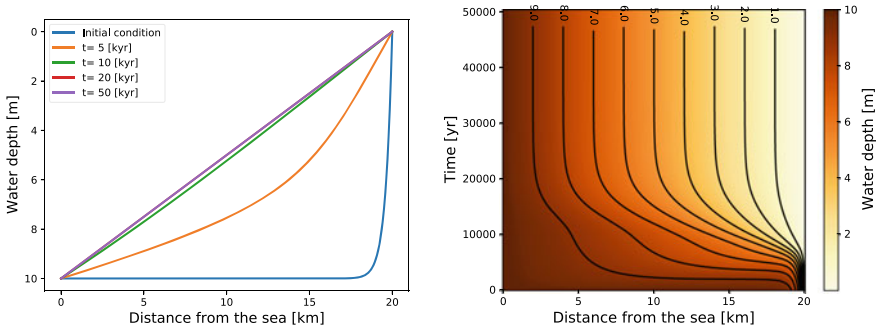

Fig. 10.9 **a** The initial bed profile (blue) as a function of the position in the tidal inlet, and the resulting bed profiles after 5 (orange), 10 (green), 20 (red) and 50 (purple) thousand years. The equilibrium is reached after approx. 20 thousand years, **b** Bed profiles as a function of the location in the tidal inlet system (horizontal axis) and time (vertical axis). Lighter (darker) colors indicate smaller (larger) water depths

profile is prescribed as a power of x^*, $\bar{h} = (x^*)^{50}$, at $t = 0$). Next, the bed evolves on a long time scale towards an equilibrium bed profile, indicated by the purple line (reflecting the bed level reached after 50 thousand years). In Fig. 10.9b, this bed evolution is visualized by a colorplot with on the horizontal axis the location in the tidal inlet system, and the time on the vertical axis. The bed is color coded, with lighter (darker) colors indicating smaller (larger) water depths.

In Fig. 10.10 the tidally averaged import of sediment is shown as a function of time by the red line. This quantity is obtained by calculating the instantaneous sediment transport at the seaward entrance ($x = 0$). This quantity has to be equal to the instantaneous bed change, integrated over the embayment length. These integrated bed changes are shown by the red dots, clearly showing that the numerical scheme used is mass conserving. The blue line indicates the cumulative amount of sediment imported. Since the instantaneous import of suspended sediments goes to zero and the cumulative amount of imported sediments becomes constant, it follows that the system is approaching an equilibrium, that can be characterised as a constantly sloping bed.

In this example, a very simplified morphodynamic model was employed to obtain the cross–sectionally averaged bed profiles through time integration. For results obtained with cross–sectionally averaged models for estuaries of arbitrary length and more general planform geometry, including advective contributions, the reader is referred to Schuttelaars and De Swart (1996), Lanzoni and Seminara (2002), Pritchard et al. (2002), Hibma et al. (2003), Todeschini et al. (2008), Van der Wegen and Roelvink (2008), Bolla Pittaluga et al. (2015), Guo et al. (2016), Xu et al. (2019).

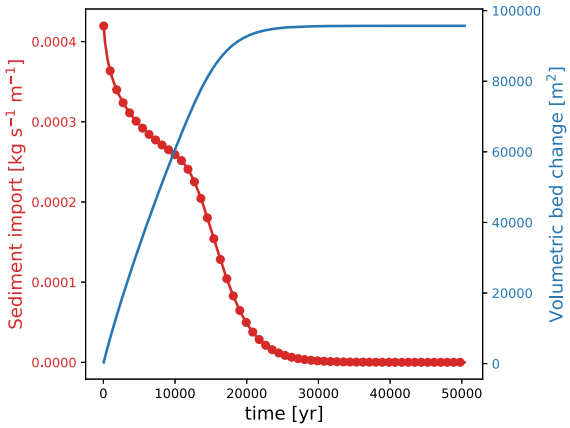

Fig. 10.10 Transport (left axis) and cumulative amount of sediment imported (right axis) as a function of time (horizontal axis). The red line indicated the instantaneous transport of sediment through the open boundary per unit width, whereas the red dots are obtained by integrating the instantaneous bed change over the embayment length at that moment in time. The blue line indicates the total amount of sediment imported per unit width

Bifurcation Approach

When employing the bifurcation approach, the morphodynamic equilibrium is not obtained through time integration. Instead, a combination of $\bar{u}^*$, $\bar{\zeta}^*$, $\bar{C}^*$ and $\bar{h}^*$ is directly searched for, such that the bed $\bar{h}^*$ does not change anymore on the long time scale. In the example considered here, this amounts to finding $\bar{h}^*$, such that

$$\frac{1}{2}\delta_s^* a^* K_h^* \frac{d^2}{dx^2}\left(\frac{x^*-1}{1-\bar{h}^*}\right)^2 = 0,$$

together with the boundary conditions for $\bar{h}^*$, and the requirement that the sediment transport at $x^* = 1$ vanishes. The resulting equilibrium solution is given by $\bar{h}^{*,\mathrm{eq}} = x^*$, i.e., a constantly sloping bed profile. By coincidence, this equilibrium profile also results in a zero tidally averaged transport at $x^* = 1$. If this condition would not be satisfied, the slope contribution of the bedload transport has to be taken into account. Note that this bed profile is also obtained by time integration (see previous section), indicating that this morphodynamic equilibrium is *stable* (see also Schuttelaars and De Swart 1996).

Using this equilibrium, continuation methods can be employed to obtain morphodynamic equilibria for morphodynamic models that are not restricted to short inlet systems or systems that are only forced by an M_2 tidal constituent at the entrance. When allowing for an arbitrary embayment length, the advective contributions in the momentum equation and suspended sediment equation cannot be neglected anymore.

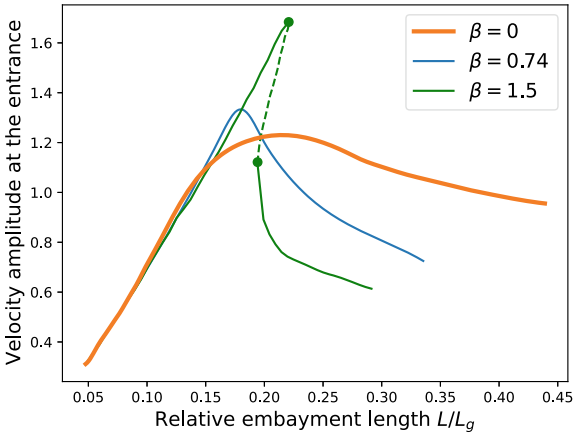

Fig. 10.11 The amplitude of the M_2 horizontal velocity $\bar{u}$ at the entrance of the embayment as a function of the non–dimensional length L/L_g for different values of β, which is the ratio of the M_4 and the M_2 tidal amplitudes of the free surface elevation at the seaward side (with $A_{M_2} = 1.75$ m at the seaward side). The velocity is scaled with $\varepsilon\sqrt{gH}$, with ε the ratio of the M_2 tidal amplitude and the undisturbed water depth at the seaward side. Figure adopted from Schuttelaars and De Swart (2000)

Continuation implies that the embayment length L is gradually increased, starting from the known equilibrium solution for a short basin. This morphodynamic equilibrium is used as the initial guess of the morphodynamic equilibrium for an embayment with a slightly larger length. Imposing that the tidally averaged sediment transport has to be zero everywhere, a root–finding algorithm is employed to iterate to the morphodynamic equilibrium associated with that embayment length.

This process can be continued up to a maximum embayment length $L_{\max}$; for larger embayment lengths no equilibria exist anymore (for a detailed discussion, see Schuttelaars and De Swart 2000). The existence of $L_{\max}$ is illustrated in Fig. 10.11, where the amplitude of the M_2 tidal velocity at the entrance, scaled with $\varepsilon\sqrt{gH}$, is shown as a function of the non–dimensional embayment length L/L_g, with $L_g = 2\pi\sqrt{gH}/\sigma$ the frictionless tidal wavelength. Considering only an M_2 tidal forcing at the entrance, equilibrium tidal velocity amplitudes indicated by the orange line ($\beta = A_{M_4}/A_{M_2} = 0$) are found: for all embayment lengths one unique equilibrium exists, up to a maximum length of $L/L_g \sim 0.44$. Increasing the strength of the overtide to $\beta = 0.15$ results in equilibrium velocity amplitudes indicated by the green line. The morphodynamic equilibria for relatively short embayments are linearly stable (solid lines). By slowly increasing the non–dimensional embayment length to approximately 0.23, a limit point is found: the embayment length has to be reduced to find new morphodynamic equilibria. These equilibria are linearly unstable (dashed lines). For $L/L_g \sim 0.21$ another limit point is encountered, and new morphodynamic equilibria can only be found by increasing the embayment length again. Finally for $L/L_g > 0.3$, no morphodynamic equilibria are found anymore. In this

example, multiple morphodynamic equilibria are found for $0.21 \leq L/L_g \leq 0.23$ and $\beta = 0.15$. These morphodynamic equilibria are associated with different balances between the sediment transport contributions, see Schuttelaars and De Swart (2000) for a discussion.

10.5.3 Depth–Averaged Morphodynamic Equilibria

In Sect. 10.5.2 it was shown that the cross–sectionally averaged bed profile evolves to a morphodynamic equilibrium profile that can be characterised as constantly sloping in the example of a rectangular, short basin with vertical side walls and a steady tidal forcing. Of course, the characteristic channel–shoal patterns, observed in many tidal inlet systems (see Fig. 10.1), cannot be captured in a width–averaged formulation. Therefore the time–integration and bifurcation approach will be discussed below for a short, rectangular inlet system. Again, a depth–averaged formulation is applied and the effects of the Coriolis forcing are neglected.

Time Integration Approach

In Van der Wegen and Roelvink (2008) the morphodynamic evolution in a rectangular tidal inlet was studied using the Delft3D modelling suite (Lesser et al. 2004). The water motion was described using the depth–averaged shallow water equations, neglecting Coriolis effects. The sediment transport was modeled using a total load formula, see Sect. 10.3.2. The parameter used to represent the slope effects was much larger than the typical values used in the literature. This overestimation can be interpreted as including the downslope sediment transport related to the suspended load contribution (Hepkema et al. 2019). The bed evolution followed from the Exner equation, using the online approach, see Sect. 10.4.1, to speed up the morphodynamic calculations. Since Coriolis effects were neglected and the tidal inlet is rectangular, the (quasi–)equilibria obtained from the model run in a width–averaged mode, were also (quasi–)equilibria for the depth–averaged model and hence used as initial conditions to speed up the calculations. This laterally uniform initial condition was randomly disturbed with bed perturbations with amplitudes of maximum 5% of the local water depth. Next, this initially perturbed bed profile was allowed to evolve for 400 years.

In Fig. 10.12 the bed profile after 20 years (left panel) and the resulting bathymetry after 400 years of evolution (right panel) are shown. Initially the major morphodynamic evolution takes place in the relatively shallow part near the head, where relatively small bars are formed. These bed forms resemble the eigenpatterns that are found in linear stability analyses (see the next section, also Schuttelaars and De Swart 1999; Ter Brake and Schuttelaars 2011). After the initial bar formation, channel–shoal patterns develop toward the deeper, more seaward parts of the basin.

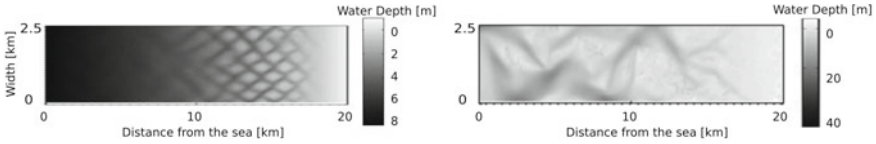

Fig. 10.12 The bed profiles found after 20 years (left panel) and 400 years (right panel), starting from a laterally uniform bed profile. Figure adopted from Van der Wegen and Roelvink (2008)

After approximately 400 years, a meandering channel is found in the seaward side, whereas a branching channel–like structure is found in the shallower region.

Apart from this example, modelling morphodynamic evolution through time integration has been extensively employed to investigate the morphodynamic evolution of tidal inlet systems, e.g. Marciano et al. (2005), Dastgheib et al. (2008), Dissanayake et al. (2009), Van Maanen et al. (2013), Xu et al. (2019) and estuarine systems, see for example Van der Wegen and Roelvink (2008), Ganju et al. (2009), Dam et al. (2016), Nnafie et al. (2018) for more information.

Bifurcation Approach

To obtain depth–averaged morphodynamic equilibria, the following system of equations is used (see Appendix 1 for a derivation):

$$\frac{\partial \zeta}{\partial t} + \nabla \cdot \left[(H-h)\hat{\boldsymbol{u}} \right] = 0, \tag{10.31}$$

$$\frac{\partial \zeta}{\partial x} = 0, \tag{10.32}$$

$$\frac{\partial \zeta}{\partial y} = 0, \tag{10.33}$$

$$\frac{\partial^2 \hat{v}}{\partial x\, \partial t} - \frac{\partial^2 \hat{u}}{\partial y\, \partial t} = -\frac{\partial}{\partial x}\left(\frac{r\hat{v}}{H-h+h_0} \right) + \frac{\partial}{\partial y}\left(\frac{r\hat{u}}{H-h+h_0} \right), \tag{10.34}$$

$$\left\{ \frac{\partial C}{\partial t} - K_h \nabla^2 C \right\} = \alpha \left[(\hat{u})^2 + (\hat{v})^2 \right] - \gamma C, \tag{10.35}$$

$$(1-p)\rho_s \frac{\partial h}{\partial t} = -\nabla \cdot (\underbrace{-K_h \nabla C}_{\boldsymbol{q}_{\text{diff}}} + \underbrace{-\hat{s}\lambda \nabla h}_{\boldsymbol{q}_{\text{bl}}}), \tag{10.36}$$

with boundary conditions

$$\begin{array}{llll} \zeta = A_{M_2}\cos(\sigma t), & \langle \gamma C - \alpha\left[(\hat{u})^2 + (\hat{v})^2\right]\rangle = 0, & \bar{h} = 0 & \text{at } x = 0. \\ (H-h)\hat{u} = 0, & K_h \frac{\partial C}{\partial x} + \hat{s}\lambda \frac{\partial h}{\partial x} = 0, & h = H & \text{at } x = L, \\ (H-h)\hat{v} = 0, & K_h \frac{\partial C}{\partial y} = 0, & \hat{s}\lambda \frac{\partial h}{\partial y} = 0 & \text{at } y = 0,\ y = B. \end{array} \tag{10.37}$$

It can be verified that the one–dimensional solution, obtained in Sect. 10.5.2, is also a solution of this system of equations when the lateral velocity is assumed to be zero. However, this laterally uniform equilibrium bed is not necessarily stable against two–dimensional perturbations. Whether or not the amplitudes of infinitesimally small perturbations will grow or decay follows from a *linear stability analysis* (Dodd et al. 2003). For small friction values, it turns out that all perturbations are damped and hence that the laterally uniform bed is linearly stable. By slowly increasing the friction parameter (continuation), it is found that for a critical value of the friction parameter $r_{\text{cr}}/\sigma H \sim 0.162$ the laterally uniform bed becomes unstable (Ter Brake 2011), and new non–trivial equilibria can be found. To obtain these non–trivial equilibria, the physical variables $\boldsymbol{\Psi} = (u, v, \zeta, C, h)^T$ are written as

$$\boldsymbol{\Psi} = \boldsymbol{\Psi}_{\text{eq}} + \boldsymbol{\Psi}',$$

with $\boldsymbol{\Psi}_{\text{eq}}$ the width–averaged equilibrium solution and $\boldsymbol{\Psi}'$ the deviation from this laterally uniform equilibrium. By substituting this expression in the governing equations, a nonlinear system of equations for $\boldsymbol{\Psi}'$ is obtained. Using the lateral boundary conditions, the lateral structure of the components of $\boldsymbol{\Psi}'$ can be directly identified. Using a Fourier expansion in tidal components for the fast variables $\{u, v, \zeta, C\}$ and an expansion in Chebyshev polynomials $T_i(x)$ for the longitudinal profile of all components of $\boldsymbol{\Psi}'$ the expansions of the physical variables can be made explicit. The expansion for h' reads (for the other components, see Ter Brake (2011)):

$$h'(x, y, \tau) = \sum_{i=0}^{\infty}\sum_{j=0}^{\infty} H_{ij} T_i(x) \cos(\frac{j\pi L}{B} y).$$

Truncating the infinite sums to M Chebychev polynomials in the longitudinal direction ond N lateral modes results in a coupled, nonlinear system of $n = 6NM$ ordinary differential equations (see Eq. (10.22) for a generic notation, where $\mathbf{u}$ in that equation is now replaced by $\boldsymbol{\Psi}'$, and Ter Brake (2011) for explicit expressions).

Given that the laterally uniform equilibrium loses its linear stability at $r = r_{\text{cr}} = 0.162$, the numerical bifurcation approach is employed to find nontrivial solutions associated with this bifurcation point. It turns out that the bifurcation at $r_{\text{cr}} = 0.162$ is a supercritical pitchfork bifurcation, denoted by P1 in the bifurcation diagram in Fig. 10.13. For r slightly larger than $r_{\text{cr}} = 0.162$ three equilibria exist: two stable equilibria and one unstable one. The linear stability of the solutions is indicated by their color: black lines denote stable equilibria, whereas gray lines denote unstable

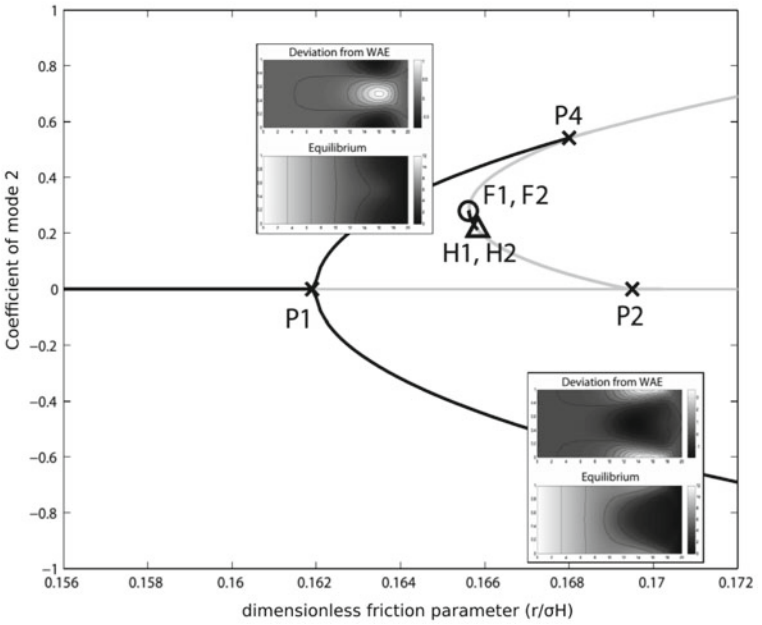

Fig. 10.13 Bifurcation diagram with on the horizontal axis the dimensionless friction parameter and on the vertical axis the coefficient of one of the modes that is used to build up the morphodynamic equilibria. Black solid lines are stable equilibria, whereas gray lines correspond to linearly unstable ones. The bifurcation points are indicated by 'P' for pitchfork bifurcations, 'F' for fold bifurcations (limit points) and 'H' for Hopf bifurcations. Figure adopted from Ter Brake (2011)

ones. The lowest branch of solutions, starting at P1 is stable for all friction parameters shown in Fig. 10.13, whereas the upper branch loses its linear stability through another pitchfork bifurcation around $r \sim 0.169$. This pitchfork bifurcation, denoted by P4, is a subcritical one, resulting in new equilibria for $r < 0.169$. These equilibria undergo a fold bifurction (F1,F2) and a Hopf bifurcation (H1,H2), after which these branches attach to the laterally uniform equilibrium again through a subcritical pitchfork bifurcation P2. In Fig. 10.13, two examples of equilibrium bathymetries (top panels of insets) and their deviation from the underlying laterally uniform equilibria (bottom panels of insets) are shown. The equilibrium bathymetry with the positive value of the coefficient of mode 2 , can be characterised as a two channel system, with a shoal inbetween, whereas the other equilibrium consists of a deep channel, flanked by two shallow regions at either side.

10.6 Summary and Conclusions

To understand and predict the dynamic interaction between the water motion, sediment transport and bed evolution, process–based morphodynamic models are employed. Such a process–based model consists of equations describing the water motion, the suspended sediment dynamics and the evolution of the bed. Focussing on coastal regions, the water motion is typically modeled using the shallow water equations. In this chapter, the equation for the suspended sediment concentration in the water column and the bed evolution equation are derived using conservation of mass in the water and sediment layer, respectively.

This system of equations can be solved by two, complementary, methods: the *time integration* and *bifurcation* approach. In the time integration approach, the emphasis is on the temporal evolution of the bathymetry and planform geometry. With this approach, the impact of human interventions and temporally varying forcings can be studied in detail, especially on the shorter time scale (order of one to two decades). Even though these models can also be employed to obtain approximate long–term results by efficiently taking differences in physical time scales into account in numerical schemes (Roelvink et al. 2016), it is usually not the focus of this modelling approach. Since the morphodynamic evolution depends on the initial bathymetry and geometry, it is difficult to assess the possibile existence of multiple morphodynamic equilibria (i.e., for the same parameter settings and forcing conditions, there can be more than one asymptotic solution, depending on the initial condition); furthermore, unstable equilibria can never be found using the time–integration approach.

The bifurcation approach is specifically geared towards directly finding asymptotic solutions, both the stable and unstable ones, and their sensitivity to parameter variations. This approach allows for a systematic analysis of the number of morphodynamic equilibria that exist for the same forcing conditions (multiple morphodynamic equilibria), and gives direct insight in the physical mechanisms resulting in these equilibria. However, direct assessment of the temporal evolution due to human interventions or changing forcing conditions is not possible.

The above clearly shows that the initial-value and bifurcation approach are complementary, with both approaches giving different, but equally valuable information. This is illustrated by considering the morphodynamic evolution of a short tidal embayment, first in a cross–sectionally averaged sense, followed by model results obtained in a depth–averaged setting. The latter example clearly shows this complementarity: the time–integration approach gives valuable information concerning the evolution towards equilibrium but cannot be directly used to assess the possible existence of multiple morphodynamic equilibria, whereas the bifurcation approach directly identifies these equilibria, their stability and multiplicity, but gives no information concerning the evolution towards these equilibria.

There are many challenges concerning morphodynamic models. At this moment, models using the time–integration approach are much more advanced than models employing the bifurcation approach. To take advantage of the synergistic use of both model types, the bifurcation–type of models have to be extended to include more

advanced processes and allow for more general geometries. Encouraging results concerning these aspects can be found in Boelens et al. (2021), Deng et al. (2021), where a finite element approach is applied that allows for an arbitrary geometry.

Other research challenges that apply to both modelling approaches, remain:

- Are physical processes accurately represented in the morphodynamic models? Examples are the accuracy of the bottom boundary conditions, sediment transport formula's, the interaction of sand and mud mixtures.
- What is the sensitivity and uncertainty in morphodynamic evolution with respect to initial conditions, parameter values and forcing conditions?
- How can extreme events (such as hurricanes and extreme storms) and possible transitions (for example due to climate change) that result in tipping point behaviour, be incorporated in a mathematically correct way and analysed in a systematic manner in morphodynamic models?
- Is there a time horizon for predicting morphodynamic evolution and how does this time horizon depend on the spatial scales under consideration? Additionally, what is the influence of model reduction techniques on this forecasting limit?

Acknowledgements We would like to thank EMODnet Bathymetry Consortium (2018): EMODnet Digital Bathymetry (DTM), http://doi.org/10.12770/18ff0d48-b203-4a65-94a9-5fd8b0ec35f6 for making available the bathymetric data used in Fig. 1.

Appendix

In this appendix, specific parameterisations will be chosen and the depth–averaged morphodynamic system of equations, given in Eqs. (10.16)–(10.20), will be scaled using characteristic dimensions of short tidal inlet systems. Using the non–dimensional equations, an asymptotic expansion of the physical variables is proposed and the leading order system of equations is derived.

As a first step, the bottom shear stresses $(\tau_x, \tau_y)^T$, the erosion function E and the deposition function D have to expressed in terms of relevant physical variables. Concerning the bed shear stresses, observations for turbulent flow conditions and dimension analysis suggest a quadratic dependency on the depth–averaged velocity. However, the gross features of the water motion are well captured by linearizing this quadratic dependency, resulting in a linearized friction law (Lorentz 1922; Zimmerman 1982, 1992), which is the approach taken here:

$$(\tau_x, \tau_y)^T = \rho r_\star \hat{\mathbf{u}}. \tag{10.38}$$

In this expression, $r_\star$ is a friction parameter with units ms^{-1}. The parameter $r_\star$ is chosen such that the net dissipation of energy (averaged over the tidal cycle and embayment) due to the linearized shear stress (10.38) equals that of the bed shear

stress based on the quadratic friction law. This implies that the parameter $r_\star$ is proportional to the tidal current amplitude U and the bottom roughness.

The parameterisation of the friction terms $\hat{\mathbf{F}}^b$ in the depth–averaged momentum Eqs. (10.17) and (10.18), which read

$$\hat{\mathbf{F}}^b = \frac{(\tau_x, \tau_y)^T}{\rho(H - h + \zeta)},$$

becomes unbounded if the water depth tends to zero, as observed near tidal flats. As our model is designed to give only a global description of the tidal flow in an embayment, the friction terms are regularized by increasing the water depth in the denominator of the friction term by a constant h_0 (see Ter Brake and Schuttelaars 2010 for a detailed discussion, and the influence of this parameter on the morphodynamic equilibria).

The erosion function E and deposition function D are due to the pick–up and deposition of the sediment near the bottom. Motivated by field observations (Dyer and Soulsby 1988) and theoretical considerations, the sediment pick–up term E is taken proportional to some power of the absolute value of the difference between the actual bed shear stress and the critical shear stress for erosion. Taking this power to be equal to one (which provides a fair approximation and is computationally beneficial) and assuming the critical shear stress for erosion to be much smaller than the typical bed shear stress in a tidal inlet system, the sediment pick–up term is parameterised as:

$$E = \hat{\alpha}\left(\hat{u}^2 + \hat{v}^2\right),$$

where $\hat{\alpha}$ is a constant which depends on the sediment characteristics. For fine sand (grain size $2 \cdot 10^{-4}$ m) a typical value is $\hat{\alpha} \sim 10^{-2}\mathrm{kg\,m^{-2}\,s^{-1}}$.

The deposition function D is obtained by assuming an approximate balance between settling and vertical diffusion in the three dimensional concentration equation (10.1). Assuming the verical eddy diffusivity to be constant in space and time and that the sediment Peclet number $w_s H/K_v \gg 1$, the resulting bottom concentration can be expressed in terms of the depth–integrated concentration, resulting in $D = \gamma C$, with $\gamma = K_v/w_s^2$.

Using these parameterisations, the morphodynamic system of equations is made non–dimensional by introducing characteristic scales for all physical variables. Focussing on basin–wide phenomena, the tidally averaged basin length L is used as a typical horizontal length scale, and the inverse of the angular frequency σ of the semidiurnal tide as a typical time scale. As a typical water depth the tidally and width-averaged water depth at the open boundary $\overline{H}$ is used, and for the M_2 amplitude of the free surface elevation the width–averaged water level amplitude at the open boundary $\overline{A_{M_2}}$ is employed. The velocity scale follows from the continuity equation (10.16) by requiring a balance between the temporal change in the free surface elevation and the convergence of the water transport, resulting in $U = \sigma\,\overline{A_{M_2}}L/\overline{H}$. The depth-integrated suspended sediment concentration is obtained by assuming an

approximate balance between erosion E and deposition D. Substituting the resulting non–dimensional variables (indicated by an asterisk),

$$(x, y) = L(x^*, y^*); \quad t = \sigma^{-1} t^*; \quad \zeta = \overline{A_{M_2}}\zeta^*; \quad (z, h) = \overline{H}(z^*, h^*);$$
$$(u, v) = U(\hat{u}^*, \hat{v}^*); \quad C = \frac{\hat{\alpha} U^2}{\gamma} C^*, \tag{10.39}$$

into the morphodynamic equations results in the following non–dimensional system of equations:

$$\frac{\partial \zeta^*}{\partial t^*} + \nabla^* \cdot \left[(1 - h^* + \varepsilon\zeta^*)\hat{\boldsymbol{u}}^*\right] = 0, \tag{10.40}$$

$$\frac{\partial \hat{u}^*}{\partial t^*} + \varepsilon \hat{\boldsymbol{u}}^* \cdot \nabla^* \hat{u}^* + f^* \hat{v}^* + \left(\frac{1}{\Lambda^*}\right)^2 \frac{\partial \zeta^*}{\partial x^*} = -\frac{r^* u^*}{(1 - h^* + \varepsilon\zeta^*)}, \tag{10.41}$$

$$\frac{\partial \hat{v}^*}{\partial t^*} + \varepsilon \hat{\boldsymbol{u}}^* \cdot \nabla^* \hat{v} *^- f^* \hat{u}^* + \left(\frac{1}{\Lambda^*}\right)^2 \frac{\partial \zeta^*}{\partial y^*} = -\frac{r^* \hat{v}^*}{(1 - h^* + \varepsilon\zeta^*)}, \tag{10.42}$$

$$a^* \left\{ \frac{\partial C^*}{\partial t^*} + \varepsilon \nabla^* \cdot \left(\hat{\boldsymbol{u}}^* C^*\right) - K_h^* \nabla^{*2} C^* \right\} = \left[\left(\hat{u}^*\right)^2 + \left(\hat{v}^*\right)^2\right] - C^*, \tag{10.43}$$

$$\frac{\partial h^*}{\partial t^*} - \lambda^* \delta_b^* \nabla^{*2} h^* = \delta_s^* \left\{ C^* - \left[\left(\hat{u}^*\right)^2 + \left(\hat{v}^*\right)^2\right] \right\}. \tag{10.44}$$

For simplicity, the diffusive transport resulting from topographic variations is neglected in the concentration equation. Furthermore, the bedload transport has been significantly simplified (compare with Eq. (10.9)): only the contribution related to the topography is retained. Furthermore, this contribution is assumed to be isotropic in space (with the second–rank tensor $\boldsymbol{\lambda}$ reduced to a scalar coefficient λ).

The non–dimensional numbers in Eqs. (10.40)–(10.43) are $\varepsilon = \overline{A_{M_2}}/\overline{H} \equiv U/\sigma L$, which is the ratio of the mean M_2 tidal amplitude at the seaward boundary and the mean water depth at this boundary, $f^* = f/\sigma$ the non–dimensional Coriolis parameter, $1/\Lambda^* = \sigma^2 L^2/gH$ the square of the product of the frictionless tidal wavenumber and the typical lengthscale L, $r^* = r_*/\sigma H$ the non–dimensional friction parameter, $K_h^* = K_h/\sigma L^2$ the non–dimensional horizontal eddy viscosity coefficient, and $a^* = \sigma/\gamma$ the ratio of the deposition time scale and the tidal time scale $1/\sigma$.

In the bed evolution equation (10.44), apart from the non–dimensional parameter $\lambda^* = H\lambda/L$, two other non–dimensional parameters appear. The first one is denoted by $\delta_s^* = \hat{\alpha} U^2/\rho_s(1 - p)\sigma H$ which is the ratio of the tidal time scale and the typical time scale T_s at which the bed changes due to spatial gradients in suspended sediment transport. The second non–dimensional parameter reads $\delta_b^* = \hat{s}/\sigma HL$, with $\hat{s} = (1 - p)\rho_\mathrm{s}\hat{q}_\mathrm{b}\sqrt{g' d_\mathrm{s}^3}(\theta - \theta_c)^{b_\mathrm{bl}}$. This parameter δ_b^* is the ratio of the tidal time scale and the time scale T_b of the bed evolution due to spatial gradients in bedload transport. In the systems under study the time scale T_b is much larger than T_s, hence the bedload transport is much smaller than the suspended load transport. However, bedload effects

cannot be neglected because they are necessary to suppress the growth of small–scale bedforms (Schuttelaars and De Swart 1999; Ter Brake and Schuttelaars 2011).

The fact that both morphodynamic time scales T_s and T_b are much larger than the hydrodynamic time scale σ^{-1} implies that the bed level h can be regarded as slowly varying compared to the other physical variables. Consequently the method of time–averaging can be used: the sediment and the bedrock layer thickness may be considered stationary on the comparatively short tidal time scale and its evolution is only determined by spatial gradients in the sediment transports averaged over a tidal cycle. The mathematical foundations of this approach are discussed in Sanders and Verhulst (1985) and Krol (1991).

This results in the following non–dimensional bottom evolution equation:

$$h^*_{\tau^*} = \left\langle C^* - \left[\left(\hat{u}^*\right)^2 + \left(\hat{v}^*\right)^2 \right] \right\rangle + \lambda^* \langle \nabla^{*2} h^* \rangle, \tag{10.45}$$

with $\langle \cdot \rangle$ denoting averaging over the tidal time scale, $\tau^* = \delta_s^* t^*$ denotes the slow time coordinate, and $\lambda^* = \kappa^* \delta_b / \delta_s$. Using Eq. (10.43), this expression can be rewritten as

$$h^*_{\tau^*} = -\nabla^* \cdot \left(\boldsymbol{q}^*_{\text{diff}} + \boldsymbol{q}^*_{\text{adv}} + \boldsymbol{q}^*_{\text{bl}} \right), \tag{10.46}$$

with the sediment transport contributions defined as

$$\begin{aligned} \boldsymbol{q}^*_{\text{diff}} &= -a^* K^*_h \langle \nabla^* C^* \rangle, \\ \boldsymbol{q}^*_{\text{adv}} &= a^* \varepsilon \langle \hat{\boldsymbol{u}}^* C^* \rangle, \\ \boldsymbol{q}^*_{\text{bed}} &= -\lambda^* \langle \nabla^* h^* \rangle. \end{aligned} \tag{10.47}$$

Considering the rectangular basin geometry, described in Sect. 10.5, the non–dimensional boundary conditions at the sidewalls are given by

$$(1 - h^* + \varepsilon \zeta^*) \hat{v}^* = 0, \qquad K^*_h \frac{\partial C^*}{\partial y^*} = 0, \qquad \lambda^* \frac{\partial h^*}{\partial y^*} = 0 \qquad \text{at } y^* = 0, \, y^* = \frac{B}{L},$$

where the first condition requires the normal transport of water through the wall to vanish, and the second and third conditions require that both the suspended sediment transport and the bedload transport through the sidewalls vanish.

To obtain boundary conditions at the landward boundaries, define the location where the water depth vanishes as $X^*(t)$. At this moving boundary, the velocity is given by $\hat{u}^* = dX^*/dt^*$ and the tidally averaged (diffusive) sediment transport is assumed to vanish. The tidally averaged non–dimensional embayment length is 1, with deviations from this averaged length of $O(\varepsilon)$. Introducing this expansion in the condition of vanishing water depth at $x^* = X^*$, $1 - h(X^*) + \varepsilon \zeta(X^*, t^*) = 1$, using a Taylor expansion, it follows that in leading order $h^* = 1$ at $x^* = 1$. After substitution of this condition in the continuity equation, the boundary condition at the end of the embayment can be reformulated as a boundary condition at $x^* = 1$ and is given by $u^*_{x^*}$ is finite at $x^* = 1$ (Van Leeuwen and De Swart 2001; Ter Brake and Schuttelaars

2011). Apart from this condition, the following boundary conditions are imposed:

$$K_h^* \frac{\partial C^*}{\partial x^*} + \lambda^* \frac{\partial h^*}{\partial x^*} = 0, \qquad h^* = 1 \qquad \text{at } x^* = 1.$$

At the seaward boundary the water motion is forced by a single tidal constituent, the bed level is kept fixed, meaning that erosion is assumed to balance deposition:

$$\zeta^* = \left(A_{M_2}/\overline{A_{M_2}}\right)\cos(t^*), \qquad \left\langle C^* - \left[\left(\hat{u}^*\right)^2 + \left(\hat{v}^*\right)^2\right]\right\rangle = 0, \qquad \bar{h}^* = 0 \qquad \text{at } x^* = 0.$$

The latter expression requires that the bed elevation $\bar{h}^*$, which is h^* averaged over the seaward boundary, is equal to zero. For a more detailed discussion of these boundary conditions, see Schuttelaars and De Swart (1999), Ter Brake and Schuttelaars (2011), Boelens et al. (2021).

Equations (10.40)–(10.43) and (10.46) can be solved using an asymptotic expansion in the small parameter ε, reflecting comparatively small deviations from the $O(1)$ values of primary parameters, see Schuttelaars and De Swart (2000), Ter Brake and Schuttelaars (2011). Assuming that all parameters are $O(1)$, the focus will be on the $O(1)$ equations, neglecting terms of $O(\varepsilon)$ and smaller. Furthermore, for the system under consideration $1/\Lambda^* \gg 1$ which allows for a further simplification of the momentum equations (10.41) and (10.42):

$$\frac{\partial \zeta^*}{\partial x^*} = \frac{\partial \zeta^*}{\partial y^*} = 0,$$

which states that the variations in the free surface elevations are spatially uniform. Information on the zeroth–order velocity field is obtained from the $O((\Lambda^*)^2)$ momentum balance: elimination of the pressure terms results in a vorticity equation, which reads (neglecting earth rotation effects):

$$\frac{\partial^2 \hat{v}^*}{\partial x^* \, \partial t^*} - \frac{\partial^2 \hat{u}^*}{\partial y^* \, \partial t^*} = -\frac{\partial}{\partial x^*}\left(\frac{r^* \hat{v}^*}{1 - h^* + h_0^*}\right) + \frac{\partial}{\partial y^*}\left(\frac{r^* \hat{u}^*}{1 - h^* + h_0^*}\right). \tag{10.48}$$

Converting the system of non–dimensional equations and the associated boundary conditions back to dimensional ones resulting in the equations of Sect. 10.5.3.

References

Adams, C.E., and G.L. Weatherly. 1981. Some effects of suspended sediment stratification on an oceanic bottom boundary layer. *Journal of Geophysical Research* 86 (C5): 4161–4172.

Ardhuin, F., N. Rascle, and K.A. Belibassakis. 2008. Explicit wave-averaged primitive equations using a generalized Lagrangian mean. *Ocean Modelling* 20 (1): 35–60.

Ardhuin, F., N. Rascle, and K.A. Belibassakis. 2017. Erratum: Corrigenda of 'explicit wave-averaged primitive equations using a generalized Lagrangian mean'. *Ocean Modelling* 113: 185–186.

Ariathurai, C.R. 1974. *A finite element model of cohesive sediment transportation*. PhD thesis, Ph. D. Dissertation, University California, Davis, 1974.

Ashton, A., A.B. Murray, and O. Arnault. 2001. Formation of coastline features by large-scale instabilities induced by high-angle waves. *Nature* 414: 296–300.

Bennis, A.-C., F. Ardhuin, and F. Dumas. 2011. On the coupling of wave and three-dimensional circulation models: Choice of theoretical framework, practical implementation and adiabatic tests. *Ocean Modelling* 40 (3–4): 260–272.

Boelens, T., T. Qi, H.M. Schuttelaars and T. De Mulder. 2021. Morphodynamic equilibria in short tidal basins using a 2DH exploratory model. *Journal of Geophysical Research: Earth Surface*, **126** (3).

Bolla Pittaluga, M., N. Tambroni, A. Canestrelli, R. Slingerland, S. Lanzoni, and G. Seminara. 2015. Where river and tide meet: The morphodynamic equilibrium of alluvial estuaries. *Journal of Geophysical Research: Earth Surface* 120 (1): 75–94.

Booij, N., R.C. Ris and L.H. Holthuijsen. 1999. A third-generation wave model for coastal regions 1. Model description and validation. *Journal of Geophysical Research: Oceans*, **104** (C4), 7649–7666.

Brouwer, R.L., G.P. Schramkowski, Y.M. Dijkstra, and H.M. Schuttelaars. 2018. Time evolution of estuarine turbidity maxima in well-mixed, tidally dominated estuaries: The role of availability- and erosion-limited conditions. *Journal of Physical Oceanography* 48: 1629–1650.

Brouwer, R.L., H.M. Schuttelaars, and P.C. Roos. 2013. Modelling the influence of spatially varying hydrodynamics on the cross-sectional stability of double inlet systems. *Ocean Dynamics* 63 (11–12): 1263–1278.

Brouwer, R.L., J. Van de Kreeke, and H.M. Schuttelaars. 2012. Entrance/exit losses and cross-sectional stability of double inlet systems. *Estuarine, Coastal and Shelf Science* 107: 69–80.

Bruun, P. 1962. Sea level rise as a cause of shore erosion. *Journal of the Waterways and Harbors Division* 88: 117–130.

Burchard, H., and H. Baumert. 1998. The formation of estuarine turbidity maxima due to density effects in the salt wedge. A hydrodynamic process study. *Journal of Physical Oceanography* 28: 309–321.

Burchard, H., H.M. Schuttelaars, and D.K. Ralston. 2018. Sediment trapping in estuaries. *Annual Review of Marine Science* 10: 371–395.

Coleman, S.E., and V.I. Nikora. 2009. Exner equation: A continuum approximation of a discrete granular system. *Water Resources Research* 45: W09421.

Crisfield, M.A. 1981. A fast incremental/iterative solution procedure that handles "snap-through". *Computational and Structural* 13 (1–3): 55–62.

Dam, G., M. van der Wegen, R.J. Labeur, and D. Roelvink. 2016. Modeling centuries of estuarine morphodynamics in the Western Scheldt estuary. *Geophysical Research Letters* 43 (8): 3839–3847.

Dastgheib, A., J.A. Roelvink, and Z.B. Wang. 2008. Long-term process - based morphological modelling of the Marsdiep Tidal Basin. *Marine Geology* 256: 90–100.

De Vriend, H.J. 1996. Mathematical modelling of meso–tidal barrier island coasts. Part I: Empirical and semi–emperical models. In *Advances in coastal and ocean engineering*, ed. P.L.-F Liu, 115–149. Singapore: World Scientific.

De Vriend, H.J. 2001. Long-term morphological prediction. In *River, coastal and estuarine morphodynamics*, ed. G. Seminara and P. Blondeaux, 163–190. Berlin: Springer.

De Vriend, H.J., M. Capobianco, T. Chesher, H.E. de Swart, B. Latteux, and M.J.F. Stive. 1993. Approaches to long-term modelling of coastal morphology: A review. *Coastal Engineering* 21: 225–269.

Dean, R.G. 1990. Equilibrium beach profiles: Characteristics and applications. *Journal of Coastal Research* 7: 53–84.

Deng, X., C. Meerman, T. Boelens, T. De Mulder, P. Salles and H.M. Schuttelaars, H.M. 2021. Morphodynamic equilibria in double-inlet systems: Existence and stability. *Journal of Geophysical Research: Earth Surface*, **126** (12).

Dijkstra, H.A., F.W. Wubs, A.K. Cliffe, E. Doedel, I.F. Dragomirescu, B. Eckhardt, A.Y. Gelfgat, A.L. Hazel, V. Lucarini, A.G. Salinger, E.T. Phipps, S.-U. Juan, H. Schuttelaars, L.S. Tuckerman, and U. Thiele. 2014. Numerical bifurcation methods and their application to fluid dynamics: Analysis beyond simulation. *Communications in Computational Physics* 15: 1–45.

Dijkstra, Y.M., H.M. Schuttelaars, G.P. Schramkowski, and R.L. Brouwer. 2019. Modeling the transition to high sediment concentrations as a response to channel deepening in the Ems River Estuary. *Journal of Geophysical Research: Oceans* 124: 1578–1594.

Dingemans, M.W. (1997). *Water wave propagation over uneven bottoms, Vol. 1 and 2*. Advanced Series on Ocean Engineering, Vol. 13. World Scientific.

Dissanayake, D.M.P.K., J.A. Roelvink, and M. van der Wegen. 2009. Modelled channel patterns in a schematized tidal inlet. *Coastal Engineering* 56 (11–12): 1069–1083.

Dodd, N.P., D. Blondeaux, H.E. de Calvete, A. Swart, S.J.M.H. Falqués, and G. Rózy.ński Hulscher, and G. Vittori. 2003. Understanding coastal morphodynamics using stability methods. *Journal of Coastal Research* 19 (4): 849–865.

Dyer, K.R. 1986. *Coastal and estuarine sediment dynamics*. Chichester: Wiley.

Dyer, K.R., and R.L. Soulsby. 1988. Sand transport on the continental shelf. *Annual Review of Fluid Mechanics* 20: 295–324.

Escoffier, F.F. 1940. The stability of tidal inlets. *Shore Beach* 8: 114–115.

Exner, F.M. 1920. *Zur physik der dünen*. Akad. Wiss. Wien Math. Naturwiss. Klasse, **129**

Exner, F.M. 1925. *Über die wechselwirkung zwischen wasser und geschiebe in flüssen*. Akad. Wiss. Wien Math. Naturwiss. Klasse, **134**

Fredsøe, J., and R. Deigaard. 1992. *Mechanics of coastal sediment transport*. Singapore: World Scientific.

Ganju, N.K., D.H. Schoellhamer and B.E. Jaffe. 2009. Hindcasting of decadal-timescale estuarine bathymetric change with a tidal-timescale model. *Journal of Geophysical Research: Earth Surface*, **114** (4).

Green, M.O., and G. Coco. 2014. Review of wave-driven sediment resuspension and transport in estuaries. *Reviews of Geophysics* 52 (1): 77–117.

Guckenheimer, J. and P. Holmes. 1983. *Nonlinear oscillations, dynamical systems, and bifurcations of vector fields*, volume 42 of *Applied mathematical sciences*. New York: Springer-Verlag.

Guo, L., M. van der Wegen, Z.B. Wang, D. Roelvink, and Q. He. 2016. Exploring the impacts of multiple tidal constituents and varying river flow on long-term, large-scale estuarine morphodynamics by means of a 1-d model. *Journal of Geophysical Research: Earth Surface* 121 (5): 1000–1022.

Hepkema, T.M., H.E. De Swart, and H.M. Schuttelaars. 2019. The sensitivity of tidal bar wavelength to channel width. *Journal of Geophysical Research: Earth Surface* 124: 2417–2436.

Hibma, A., H.M. Schuttelaars, and Z.B. Wang. 2003. Comparison of longitudinal equilibrium profiles of estuaries in idealised and process-based models. *Ocean Dynamics* 53: 252–269.

Holthuijsen, L.H., N. Booij, and T.H.C. Herbers. 1989. A prediction model for stationary, short-crested waves in shallow water with ambient currents. *Coastal Engineering* 13 (1): 23–54.

Horemans, D.M.L., Y.M. Dijkstra, H.M. Schuttelaars, P. Meire, and T.J.S. Cox. 2020. Unraveling the essential effects of flocculation on large-scale sediment transport patterns in a tide-dominated estuary. *Journal of Physical Oceanography* 50 (7): 1957–1981.

Hulscher, S.J.M.H., and G.M. van den Brink. 2001. Comparison between predicted and observed sand waves and sand banks in the North sea. *Journal of Geophysical Research: Oceans* 106 (C5): 9327–9338.

Jay, D.A., P.M. Orton, T. Chisholm, D.J. Wilson, and A.M.V. Fain. 2007. Particle trapping in stratified estuaries: Consequences of mass conservation. *Estuaries and Coasts* 30: 1095–1105.

Kandiah, A. 1974. *Fundamental aspects of surface erosion of cohesive soils*. PhD thesis, University of California, Davis.

Keller, H.B. 1977. Numerical solution of bifurcation and nonlinear eigenvalue problems. In *Applications of Bifurcation Theory*, ed. P. Rabinowitz, 359–384. New York: Academix Press.

Komen, G.J., L. Cavaleri, M. Donelan, K. Hasselmann, S. Hasselmann, and P.A.E.M. Janssen. 1994. *Dynamics and modelling of ocean waves*. Cambridge University Press.

Krol, M.S. 1990. *The method of averaging in partial differential equations*. PhD thesis, University of Utrecht, The Netherlands.

Krol, M.S. 1991. On the averaging method in nearly time-periodic advection-diffusion problems. *SIAM Journal on Applied Mathematics* 51 (6): 1622–1637.

Kumar, M., H.M. Schuttelaars, and P.C. Roos. 2017. Three-dimensional semi-idealized model for estuarine turbidity maxima in tidally dominated estuaries. *Ocean Modelling* 113: 1–21.

Kuznetsov, Y.A. 2004. *Elements of applied bifurcation theory*, volume 112 of *Applied Mathematical Sciences*. New York: Springer

Lanzoni, S., and G. Seminara. 2002. Long-term evolution and morphodynamic equilibrium of tidal channels. *Journal of Geophysical Research: Oceans* 107: 1–13.

Latteux, B. 1995. *Techniques for long-term morphological simulation under tidal action* 126: 129–141.

Lesser, G.R., J.A. Roelvink, J.A.T.M. van Kester, and G.S. Stelling. 2004. Development and validation of a three-dimensional morphological model. *Coastal Engineering* 51: 883–915.

Longuet-Higgins, M.S., and R.W. Stewart. 1964. Radiation stresses in water waves; a physical discussion, with applications. *Deep Sea Research and Oceanographic Abstracts* 11 (4): 529–562.

Lorentz, H.A. 1922. Het in rekening brengen van den weerstand bij schommelende vloeistofbewegingen. *De Ingenieur*, 695.

Luijendijk, A.P., M.A. de Schipper and R. Ranasinghe. 2019. Multi-timescale predictions of complex sandy interventions. *Journal of Marine Science and Engineering*, **7** (3).

Marciano, R., Z.B. Wang, A. Hibma, H.J. de Vriend and A. Defina. 2005. Modeling of channel patterns in short tidal basins. *Journal of Geophysical Research: Earth Surface*, **110** (1).

McAnally, W.H., and A.J. Mehta. 2002. Significance of aggregation of fine sediment particles in their deposition. *Estuarine, Coastal and Shelf Science* 54: 643–653.

McWilliams, J.C., J.M. Restrepo, and E.M. Lane. 2004. An asymptotic theory for the interaction of waves and currents in coastal waters. *Journal of Fluid Mechanics* 511: 135–178.

Mei, C.C. 1983. *The applied dynamics of ocean surface waves.* In *Advanced series on ocean engineering*, vol. 1. Singapore: World Scientific Publishing Co. Pvt. Ltd.

Mellor, G. 2003. The three-dimensional current and surface wave equations. *Journal of Physical Oceanography* 33 (9): 1978–1989.

Mellor, G. 2011. Wave radiation stress. *Ocean Dynamics* 61 (5): 563–568.

Mellor, G. 2015. A combined derivation of the integrated and vertically resolved, coupled wave-current equations. *Journal of Physical Oceanography* 45 (6): 1453–1463.

Meyer-Peter, E. and R. Müller. 1948. Formulas for bedload transport. In *World congress of the international association for hydro-environment engineering and research (IAHR)*.

Moghimi, S., K. Klingbeil, U. Gräwe, and H. Burchard. 2013. A direct comparison of a depth-dependent radiation stress formulation and a vortex force formulation within a three-dimensional coastal ocean model. *Ocean Modelling* 70: 132–144.

Munk, W.H., and E.R. Anderson. 1948. Notes on a theory of the thermocline. *Journal of Marine Research* 7: 276–295.

Murray, A.B. 2003. *Contrasting the goals, strategies, and predictions associated with simplified numerical models and detailed simulations.*, vol. 135. Predicition in geomorphologicy. American Geophysical Union, Geophysical Monograph.

Murray, A.B. 2007. Reducing model complexity for explanation and prediction. *Geomorphology* 90: 178–191.

Murray, A.B. 2013. *Treatise on Geomorphology*, volume 2 (Quantitative Modeling of Geomorphology), chapter Which models are good (enough), and when? 50–58. San Diego, CA: Academic Press

Murray, A.B., G. Coco and E.B. Goldstein. 2014. Cause and effect in geomorphic systems: Complex systems perspectives. *Geomorphology* 214: 1–9.

Murray, A.B., and C. Paola. 1994. A cellular model of braided rivers. *Nature* 371: 54–57.

Nihoul, J.C.J. 1975. Hydrodynamic models. In *Modelling of marine systems*, ed. J.C.J. Nihoul, 41–66. Amsterdam: Elsevier Scientific Publishing Company.

Nnafie, A., T. van Oyen, B. De Maerschalck, M. van der Vegt, and M. van der Wegen. 2018. Estuarine channel evolution in response to closure of secondary basins: An observational and morphodynamic modeling study of the western scheldt estuary. *Journal of Geophysical Research: Earth Surface* 123 (1): 167–186.

O'Brien, M.P. 1931. Estuary tidal prism related to entrance areas. *Civil Engineering* 1: 738–739.

O'Brien, M.P. 1969. Equilibrium flow areas of inlets on sandy coasts. *Journal of the Waterways and Harbors Division* 95: 43–52.

Olabarrieta, M., W.R. Geyer, and N. Kumar. 2014. The role of morphology and wave-current interaction at tidal inlets: An idealized modeling analysis. *Journal of Geophysical Research: Oceans* 119 (12): 8818–8837.

Paola, C., and V.R. Voller. 2005. A generalized Exner equation for sediment mass balance. *Journal of Geophysical Research: Earth Surface* 110: F04014.

Pape, L., and B.G. Ruessink. 2011. Neural-network predictability experiments for nearshore sandbar migration. *Continental Shelf Research* 31: 1033–1042.

Pritchard, D., A.J. Hogg, and W. Roberts. 2002. Morphological modelling of intertidal mudflats: The role of cross-shore tidal currents. *Continental Shelf Research* 22 (11–13): 1887–1895.

Ranasinghe, R., C. Swinkels, A. Luijendijk, D. Roelvink, J. Bosboom, M. Stive, and D. Walstra. 2011. Morphodynamic upscaling with the MORFAC approach: Dependencies and sensitivities. *Coastal Engineering* 58: 806–811.

Reef, K.R.G., P.C. Roos, H.M. Schuttelaars, and S.J.M.H. Hulscher. 2020. Influence of back-barrier basin geometry on multiple tidal inlet systems: The roles of resonance and bottom friction. *Journal of Geophysical Research: Earth Surface* 125 (3): 2020.

Reeve, D.E., H. Karunarathna, S. Pan, J.M. Horrillo-Caraballo, G. Różyński, and R. Ranasinghe. 2016. Data-driven and hybrid coastal morphological prediction methods for mesoscale forecasting. *Geomorphology* 256: 49–67.

Richardson, J.F., and W.N. Zaki. 1954. The sedimentation of a suspension of uniform spheres under conditions of viscous flow. *Chemical Engineering Science* 8: 65–78.

Ris, R.C., N. Booij and L.H. Holthuijsen. 1994. Spectral wave model for the coastal zone. In *Proceedings of the 2nd international symposium on ocean wave measurement and analysis, 1993*, 630–641.

Roelvink, J.A. 2006. Coastal morphodynamic evolution techniques. *Coastal Engineering* 53: 277–287.

Roelvink, J.A., D.-J.R. Walstra, M. van der Wegen and R. Ranasinghe. 2016. *Modeling of coastal morphological processes*, 611–634. Cham: Springer International Publishing.

Roos, P.C., H.M. Schuttelaars, and R.L. Brouwer. 2013. Observations of barrier island length explained using an exploratory morphodynamic model. *Geophysical Research Letters* 40: 4338–4343.

Sanders, J.A., and F. Verhulst. 1985. *Averaging methods in nonlinear dynamical systems*. New York: Springer.

Sanford, L.P. 2008. Modeling a dynamically varying mixed sediment bed with erosion, deposition, bioturbation, consolidation, and armoring. *Computers & Geosciences* 34 (10): 1263–1283.

Schuttelaars, H.M., and H.E. de Swart. 1996. An idealized long-term morphodynamic model of a tidal embayment. *European Journal of Mechanics - B/Fluids* 15: 55–80.

Schuttelaars, H.M., and H.E. de Swart. 1999. Initial formation of channels and shoals in a short tidal embayment. *Journal of Fluid Mechanics* 386: 15–42.

Schuttelaars, H.M., and H.E. de Swart. 2000. Multiple morphodynamic equilibria in tidal embayments. *Journal of Geophysical Research* 105: 24105–24118.

Seydel, R. 2010. Practical bifurcation and stability analysis. *Interdisciplinary applied mathematics*, vol. 5. New York: Springer.

Soulsby, R. 1997. *Dynamics of marine sands*. London: Thomas Telfort.

Stive, M.J.F., Z.B. Wang, M. Capobianco, P. Ruol, and M.C. Buijsman. 1998. Morphodynamics of a tidal lagoon and the adjacent coast. In *Physics of estuaries and coastal seas*, 397–407. Rotterdam: Balkema.

SWAN team. 2006. SWAN, technical documentation, http://swanmodel.sourceforge.net/-online_doc-/swantech-/swantech.html. report, Delft University of Technology, Delft, The Netherlands.

Ter Brake, M. 2011. *Tidal embayments: modelling and understanding their morphodynamics*. PhD thesis, Delft University of Technology.

Ter Brake, M.C., and H.M. Schuttelaars. 2010. Modeling equilibrium bed profiles of short tidal. *Ocean Dynamics* 60: 183–204.

Ter Brake, M.C., and H.M. Schuttelaars. 2011. Channel and shoal development in a short tidal embayment; an idealized model study. *Journal of Fluid Mechanics* 677: 503–529.

Todeschini, I., M. Toffolon, and M. Tubino. 2008. Long-term morphological evolution of funnel-shape tide-dominated estuaries. *Journal of Geophysical Research* 113 (5): C05005.

Tolman, H.L. 1991. A third-generation model for wind waves on slowly varying, unsteady, and inhomogeneous depths and currents. *Journal of Physical Oceanography* 21: 782–797.

Uchiyama, Y., J.C. McWilliams, and A.F. Shchepetkin. 2010. Wave-current interaction in an oceanic circulation model with a vortex-force formalism: Application to the surf zone. *Ocean Modelling* 34 (1–2): 16–35.

Van de Kreeke, J. 1990. Can multiple tidal inlets be stable? *Estuarine, Coastal and Shelf Science* 30: 261–273.

Van de Kreeke, J., R.L. Brouwer, T.J. Zitman, and H.M. Schuttelaars. 2008. The effect of a topographic high on the morphodynamical stability of a two inlet bay system. *Coastal Engineering* 55: 319–332.

Van der Wegen, M., and J.A. Roelvink. 2008. Long-term morphodynamic evolution of a tidal embayment using a two-dimensional, process-based model. *Journal of Geophysical Research: Oceans* 113 (3): C03016.

Van Leeuwen, S.M., and H.E. de Swart. 2001. The effect of advective processes on the morphodynamic stability of short tidal embayments. *Physics and Chemistry of the Earth, Part B* 26: 735–740.

Van Maanen, B., G. Coco, and K.R. Bryan. 2013. Modelling the effects of tidal range and initial bathymetry on the morphological evolution of tidal embayments. *Geomorphology* 191: 23–34.

Van Rijn, L.C. 1993. *Principles of sediment transport in rivers, estuaries and coastal seas, 1993*. Amsterdam: Aqua Publ.

Van Rijn, L.C. 2007. Unified view of sediment transport by currents and waves, I: Initiation of motion, bed roughness, and bed-load transport. *Journal of Hydraulic Engineering* 133: 649–667.

Van Rijn, L.C. 2007. Unified view of sediment transport by currents and waves, II: Suspended transport. *Journal of Hydraulic Engineering* 133: 668–689.

Van Rijn, L.C., J.S. Ribberink, and J. van ver Werf and D.J.R. Walstra. 2013. Coastal sediment dynamics: Recent advances and future research needs. *Journal of Hydraulic Research* 51: 475–493.

Werner, B.T., and T.M. Fink. 1993. Beach cusps as self-organized patterns. *Science* 260: 968–971.

Wijnberg, K.M., and J.H.J. Terwindt. 1995. Extracting decadal morphological behaviour from high-resolution, long-term bathymetric surveys along the Holland coast using eigenfunction analysis. *Marine Geology* 126: 301–330.

Wilson, K.C. 1966. Bed-load transport at high shear stress. *Journal of the Hydraulics Division* 92: 49–59.

Winterwerp, J.C. 1998. A simple model for turbulence induced flocculation of cohesive sediment. *Journal of Hydraulic Research* 36: 309–326.

Winterwerp, J.C. 2001. Stratification effects by cohesive and noncohesive sediment. *Journal of Geophysical Research: Oceans* 106 (C10): 22559–22574.

Winterwerp, J.C., and W.G.M. van Kesteren. 2004. *Introduction to the physics of cohesive sediment dynamics in the marine environment,* vol. 56. Elsevier.

Xia, M., M. Mao, and Q. Niu. 2020. Implementation and comparison of the recent three-dimensional radiation stress theory and vortex-force formalism in an unstructured-grid coastal circulation model. *Estuarine, Coastal and Shelf Science* 240: 106771.

Xu, F., G. Coco, J. Tao, Z. Zhou, C. Zhang, S. Lanzoni, and A. D'Alpaos. 2019. On the morphodynamic equilibrium of a short tidal channel. *Journal of Geophysical Research: Earth Surface* 124 (2): 639–665.

Zimmerman, J.T.F. 1982. On the Lorentz linearization of a quadratically damped forced oscillator. *Physics Letters* 89A: 123–124.

Zimmerman, J.T.F. 1992. On the Lorentz linearization of a nonlinearly damped tidal Helmholtz oscillator. *Proceedings of the Koninklijke Nederlandse Akademie van Wetenschappen* 95: 127–145.

Zyserman, J.A., and J. Fredsøe. 1994. Data analysis of bed concentration of suspended sediment. *Journal of Hydraulic Engineering* 120: 1021–1042.

Chapter 11
Wetting and Drying Procedures for Shallow Water Simulations

Sigrun Ortleb, Jonathan Lambrechts, and Tuomas Kärnä

Abstract In the coastal zone, the alternating exposure and submerging of the seabed is an important feature in coastal engineering and marine ecosystems. The wetting and drying of shallow regions challenges the numerical simulation in terms of robustness, efficiency, and the preservation of physical properties. Considering a physically sound representation, desired numerical properties include positivity preservation with respect to the water depth, local and global mass conservation, well-balancedness with respect to lake at rest steady states, and avoidance of artificial pressure gradients. This chapter focuses on recent numerical methods on fixed computational grids based on the depth-averaged shallow water equations where we review and discuss the classes of finite volume methods and discontinuous Galerkin schemes and their respective wetting and drying treatment. In addition, the numerical approaches are classified with respect to either explicit or implicit time integration, and we discuss the advantages and disadvantages accompanying these two alternatives.

11.1 Introduction

The study of ocean dynamics requires the simulation of water flow in diverse regions of varying fluid depth. Part of the considered regions may therefore be subject to alternating wetting and drying processes where the water depth may drastically change. Wetting and drying also occurs on different time scales such as hours in the case of the

S. Ortleb (✉)
Department of Mathematics, University of Kassel, Heinrich-Plett-Str. 40, 34132 Kassel, Germany
e-mail: ortleb@mathematik.uni-kassel.de

J. Lambrechts
Institute of Mechanics, Materials and Civil Engineering, Université catholique de Louvain, Avenue Georges Lemaître 4, 1348 Louvain-la-Neuve, Belgium
e-mail: jonathan.lambrechts@uclouvain.be

T. Kärnä
Finnish Meteorological Institute, PO Box 503, 00101 Helsinki, Finland
e-mail: tuomas.karna@fmi.fi

H. Schuttelaars et al. (eds.), *The Mathematics of Marine Modelling*,
Mathematics of Planet Earth 9, https://doi.org/10.1007/978-3-031-09559-7_11

tides or days in the case of storm surges. The situations relevant to wetting and drying include coastal regions of different characteristics, such as shores, embayments, tidal flats or estuaries. Capturing the fluid dynamics in these areas is significant in order to study and possibly predict the ramifications of singular phenomena such as storm surges or inundations. In addition, repetitive flooding and ebbing is vital to the local ecosystem. Hence, in modelling the occurring biological processes, the time evolution of the flooding and receding water front plays an important role. Furthermore, the periodic occurrence of wetting and drying due to the tides affects sediment transport and the run-up on beaches and dunes and subsequent receding of the water front may cause coastal erosion.

The importance of the alternating wetting and drying water flows in coastal engineering and marine ecosystems is accompanied by challenges with respect to both the development of suitable mathematical models of the occurring processes and the construction of accurate and robust numerical methods.

Considering mathematical models, this chapter focuses on the depth-averaged shallow water equations which are commonly used in coastal areas. These equations are based on the assumption of a small vertical length scale compared to large horizontal ones and a hydrostatic pressure distribution. Near the wet-dry front, however, these assumptions are not fully valid: First, when the fluid depth vanishes, these equations become ill-posed. In addition, if the model includes bottom friction, e.g. in form of a Manning friction term with experimentally determined roughness coefficient, this again involves division by the fluid depth. Second, near the front the horizontal and vertical length scales become comparable. Indeed, the hydrostatic assumption may be violated in certain cases, such as Tsunami modelling which may require the inclusion of non-hydrostatic effects, as discussed in Candy (2017). Nevertheless, on moderate scales as in estuaries or mud flats, the shallow water equations may capture the relevant dynamics quite efficiently and to a sufficient degree of accuracy.

In terms of three-dimensional modeling, most 3D models use a mode-splitting technique in time which means that the free surface dynamics and the internal motion of the fluid are solved separately, possibly using different time step sizes. Some schemes explicitly solve the full 2D shallow water equations, while others introduce a reduced 2D free surface equation where the depth-integrated fluxes are computed from the 3D velocity fields. As such, in most cases, the treatment of wetting and drying essentially reverts to the techniques of the 2D problem.

From the numerical standpoint, several challenges in dealing with wetting and drying in a shallow water model have been stated in the literature. First, the scheme must be positivity preserving, i.e. water depth must remain non-negative in the entire computational domain at all times. As stated above, the governing equations are ill-posed for $H < 0$ and the surface wave celerity $\sqrt{gH}$ is not defined. In addition, the computation of velocity from the discharge $u = (Hu)/H$ becomes ill-posed as H approaches zero.

Second, the model must be locally and globally conservative. The shallow water equations are a system of balance laws which is generally formulated in the conserved quantities of volume and momentum. In addition, in simulations that involve tracers, the wetting and drying treatment should not jeopardize tracer mass conservation. The

tracer advection scheme should also be consistent, i.e. a constant tracer field should remain constant at all times—a property often called local conservation. Arguably the mass and volume conservation properties are essential in most applications, especially in long-term environmental applications where even a small deviation may accumulate over long integration times. Conservation of momentum, on the other hand, is less crucial as the coastal ocean is generally highly dissipative. Nevertheless, a proper resolution of the momentum equation is required for correct representation of the advancing wet-dry front.

Third, the shallow water equations admit certain steady state solutions, most importantly the so-called "lake at rest" steady state consisting of a vanishing velocity vector and a constant sea surface elevation. A numerical scheme which does not discretely preserve this particular steady state is prone to instabilities as it may generate unphysical oscillations due to the improper balance of flux and source terms. In addition, such a scheme will experience difficulties to achieve lake at rest steady state solutions in the long time limit. Therefore, much effort has been taken to construct so-called *well-balanced schemes* preserving the lake at rest steady state in a discrete sense, sometimes by reformulating the shallow water equations in terms of the surface elevation instead of the water height. It should be remarked in this context that it is still not trivial to discretely preserve lake at rest steady states in partially dry cells, e.g. at a shoreline.

A more specific requirement is the non-permeability of dry areas. Coastal domains often feature lakes or ponds that remain wet in the dry stage and become disconnected from larger water bodies. Such emerging dry barriers should remain impermeable, i.e. attain a zero volume flux so that the lakes do not artificially dry out. This condition is often violated by so called porosity schemes that relax the positivity requirement and/or allow water flow beneath the bed.

As water depth reduces, the flow is mostly dominated by the pressure gradient and bottom friction terms. Over a sloping bathymetry the pressure gradient remains non-zero until the water is completely drained, whereas the bottom friction parameterization increases slowing down the flow. The bottom friction term is problematic as it grows without bound as the depth vanishes. The non-zero pressure gradient, on the other hand, becomes an issue in methods that retain a thin water layer over the dry areas: In order to ensure positivity, the *artificial pressure gradient* must be omitted or canceled. In the literature several methods have been developed for achieving this goal, including flux-limiting schemes, direct cancellation of the pressure gradient term, and positivity preserving limiters.

In addition to the properties listed above, an ideal numerical wetting and drying method should also be robust, computationally efficient, and generalizable to unstructured meshes. Robustness implies that the scheme remains stable under rapid flows and highly variable bathymetry. In terms of computational efficiency, many wetting and drying schemes introduce time step limitations which may increase the computational cost significantly and restrict their applicability to realistic problems.

Many techniques to deal with wetting and drying have been suggested and have been classified in at least two classes of methods—*moving mesh methods* and *fixed mesh methods*. With *fixed mesh methods*, the computational grid itself is fixed

throughout the computation of the time-dependent solution. On the other hand, *moving mesh methods*, also referred to as mesh adaption algorithms adapt the boundaries of the computational mesh to precisely match the water front. The general idea is that the moving wet-dry front can be essentially described as a Lagrangian process which bases the moving mesh approach on a sound mathematical formulation. Hence, many difficulties can be circumvented as the equations are always well-defined and there is no artificial pressure gradient. Thus, shorelines can be tracked quite accurately and a non-negative water height is present throughout the computational domain. However, as discussed in Nielsen (2003), Bunya and Kubatko (2009), Lee and Lee (2016), moving mesh methods are computationally more expensive than fixed grid techniques, more difficult to implement especially in case of strongly varying bathymetry and complex boundary shapes. In addition, they can potentially lead to excessively elongated elements along the coastline as stated in Nielsen (2003). In addition, according to Bunya and Kubatko (2009), mesh adaption techniques do not necessarily yield more accurate solutions than fixed grid schemes. Furthermore, front-tracking is difficult to combine with implicit time integration.

For the further discussion of wetting and drying algorithms in this chapter we will concentrate on methods on fixed computational grids. A contemporary review of wetting and drying algorithms for numerical tidal flow models on fixed grids given by Medeiros and Hagen (2013) classifies the wetting and drying fixed mesh methods into four general frameworks: (1) *thin film algorithms*, (2) *element removal methods* that employ checking routines to determine if an element or a node is wet, dry or potentially one of the two, subsequently adding or removing nodes from the computational domain (3) *fluid depth extrapolation* from wet nodes onto dry ones, (4) *negative water depth methods*. As stated in Medeiros and Hagen (2013), the defining feature of *thin film algorithms*, also called *thin layer algorithms*, is the constant presence of a small layer of water within the domain. The algorithm may distinguish between wet and dry cells only by a minimum water height threshold. When the water height drops below the threshold, the velocity of the flow is often set to zero and fluxes between adjacent dry cells are prohibited. Commonly, in finite volume and discontinuous Galerkin schemes, a flux-limiting strategy is employed, where the fluxes are modified, i.e. reduced or cancelled, in the vicinity of dry zones. Recent thin film algorithms have been developed in Ern et al. (2008), Bunya and Kubatko (2009), Gourge et al. (2009), Xing et al. (2010), Xing and Zhang (2013), Warner et al. (2013), Meister and Ortleb (2014), Vater et al. (2015). As discussed in Bunya and Kubatko (2009), since thin film approaches keep a small layer of water in nominally dry regions until these cells become fully wet again, it is difficult to determine an exact shoreline. In addition, an erroneous gradient may be present at the shoreline, possibly generating unphysical flows which are difficult to remove without violating momentum conservation. A recent example of a finite volume implementation of wetting and drying via a thin layer approach is given by Warner et al. (2013). The minimum depth used within their algorithm is a spatially constant user-defined parameter. If the total depth at the cell center is smaller than this thin layer tolerance, the cell is considered dry and no water is permitted to leave the cell, however water is allowed to enter dry cells at any time. Thus, the arrival of incoming

tide is not limited. In addition, the authors state that if the blocking of water relied on the water depth at cell faces, isolated wet patches could be generated for a fluid depth below the tolerance, since the fluid depth at the cell center could in fact be higher.

For *element removal algorithms*, wet elements are included in the computational domain while dry ones are not. At the wetting front, further consideration is needed for the treatment of partially wet cells. For example, this may include distinguishing partially wet cells of dam-break type from those of flooding type as in Bates and Hervouet (1999). The list of element removal algorithms given by Medeiros and Hagen is quite extensive, including the finite element models TELEMAC (Hervouet 2000) and ADCIRC (Luettich 1992), as well as the finite difference models Delft3D-FLOW (Deltares 2009) and MIKE 21 (DHI 2007). As discussed in Bunya and Kubatko (2009), mesh reduction techniques may cause oscillations due to sudden elimination and addition of nodes as well as mass and momentum loss. Considering our list of desirable numerical properties, mass conservation and well-balancedness are hence the most endangered properties when an element removal algorithm is applied.

Most of the above methods rely on detecting the dry elements and applying suitable changes to the numerical procedure. These changes can consist in cancelling fluxes (flux-limiting methods), or omitting pressure gradient terms in partially dry elements. Such "switches" introduce sudden changes in the solver and generally can only be marched in time with explicit schemes. Moreover, they require sufficiently short time steps to prevent oscillations. Due to the discontinuous switches of the method, implicit solvers do not converge because an exact Jacobian is not computable and approximate Jacobians are either discontinuous or highly non-linear.

Depth extrapolation methods focus on the advancing water front from which information is extracted. Mostly, the fluid depth is extrapolated from wet cells onto dry ones, if the algorithm detects an advancement of the front. If new wet cells occur, the corresponding velocities are calculated. In this category, only few approaches are listed by Medeiros and Hagen and it is mentioned that these schemes occasionally lead to artificially wetted elements. In addition, mass conservation has to be dealt with by correction routines.

Negative depth algorithms allow the water surface to drop below the bottom topography, similar to the idea of porosity schemes. While regions with negative depth are considered as dry, fluid flow below the ground is dealt with a porosity approach. The concept of artificial porosity is based on assuming a certain porosity of the sea bed which has to be properly modelled, e.g. by a thin porous layer, and allows for non-zero fluxes in regions formerly considered as dry. The negative depth algorithms are the most recent schemes listed by Medeiros and Hagen and are accredited with a close description of the physical processes involved with the wetting front. The benefit of negative depth methods is that there is no need to detect dry elements or cancel fluxes. In these methods the continuous equations are modified slightly to account for the porosity. As such the artificial pressure gradient issue does not arise, and these schemes are compatible with many discretizations, including implicit time integration schemes. However, negative depth algorithms often break the non-permeability requirement mentioned above. Nielsen (2003) investigated the parameters affect-

ing the performance of the marsh porosity method RMA2. Newer versions of the TELEMAC model include various options of a negative depth approach as well. An alternative approach to negative depth algorithms has been used in Kärnä et al. (2011). Here, the bottom topography is allowed to move in time as the water surface drops.

In the literature, explicit time stepping is implemented in the majority of previous wetting and drying methods. As mentioned above this is required by most flux-limiting and thin layer methods that detect dry elements. However, explicit schemes are subject to time step limitations that may become severe, especially if the mesh is refined in the shallow regions. The choice of explicit or implicit time integration should also be based on the involved time scales of the specific application. In an evaluation of several methods which were developed until 1994 for the simulation of wetting and drying in one space dimension, Balzano (1998) already includes several implicit schemes. In addition, a simple calculation is given regarding the distance which the moving boundary covers within one time step. More precisely, if the speed of the moving boundary is v_b and Δt denotes the time step, we have for this distance

$$v_b \Delta t = \frac{v_b}{\sqrt{gH}} \frac{\Delta t}{\Delta x} \sqrt{gH}\, \Delta x = \mathrm{Fr}\, \mathrm{Cr}\, \Delta x,$$

where Fr and Cr are the Froude number and the Courant number, respectively, Δx is the cell size, H the water height and g is the gravitational constant. Balzano further argues that, in practice, the Courant number is between 0.5 and 1 while the Froude number takes typical values in the interval $[0.01, 0.05]$, hence 20 to 200 time steps would be needed to move the wet-dry boundary over a distance of Δx, i.e. a cell length.

Considering the possibly severe limitation of the allowable time step size, devising implicit time stepping schemes compatible with wetting and drying is generally desirable. A special unconditionally positive implicit time integration scheme is used by Casulli (2009). This approach leads to a mildly nonlinear system to be solved each time step but is mass conserving and guarantees nonnegative water height for any time step size. However, this method is only first order accurate in space and time. In the context of stabilized residual distribution schemes, Ricchiuto and Bollermann (2009) developed a well-balanced and positivity preserving scheme for shallow water flows also considering implicit time integration via the second order trapezoidal rule. In this case, the time step size can be chosen twice as large as for the explicit Euler scheme. Wu (2011) design an implicit finite volume shallow water code on unstructured rectangular meshes based on the backward Euler scheme. Wetting and drying is implemented using the thin layer approach. A different approach is taken by Kärnä et al. (2011). There, the bottom topography is allowed to move in time as water elevation drops, i.e. a user-defined function is introduced which redefines the bottom topography. However, this function has to fulfill certain conditions and hence has to be carefully chosen prior to numerical computation. In Meister and Ortleb (2014), Meister and Ortleb developed an unconditionally positive approach to time integration within a DG scheme in order to obtain non-negative water heights without

time step restriction. This approach was based on a modification of an implicit Runge–Kutta scheme, more precisely the classical third order SDIRK scheme by Cash (1979) via a modified Patankar trick as invented in Burchard et al. (2003). Further recent implicit approaches are given by Marras et al. (2016), combining dynamic viscosity for shock capturing with with a high-order wetting and drying method, a 3D non-hydrostatic implicit model by Candy (2017), and a finite difference implicit 1D code by Kalita (2018).

This chapter is organized as follows. In Sect. 11.2, the most popular variants of the 2D shallow water equations are described. Here, we discuss the different formulations with respect to their impact on well-balancedness. Section 11.3 deals with space discretization where we focus on finite volume methods in Sect. 11.3.1 and discontinuous Galerkin schemes in Sect. 11.3.2. Section 11.4 is dedicated to time discretization where we distinguish wetting and drying treatments with respect to explicit and implicit time integration schemes. Concluding remarks are given in Sect. 11.5.

11.2 Governing Equations

The shallow water equations (SWE) model the flow of water in the case that the horizontal length scale is significantly greater than the vertical one and the vertical velocity is comparatively small with respect to the horizontal velocity. The derivation of the SWE is based on depth-integration of the Navier-Stokes equations which removes the vertical velocity from the set of variables.

In *conservative form*, the SWE in two space dimensions are given by

$$\begin{aligned}
\frac{\partial H}{\partial t} + \frac{\partial Hu}{\partial x} + \frac{\partial Hv}{\partial y} &= 0\,, \\
\frac{\partial Hu}{\partial t} + \frac{\partial (Hu^2 + \frac{g}{2}H^2)}{\partial x} + \frac{\partial Huv}{\partial y} - fHv &= -gH\frac{\partial b}{\partial x} + \frac{\tau_x^s - \tau_x^b}{\rho}\,, \\
\frac{\partial Hv}{\partial t} + \frac{\partial Huv}{\partial x} + \frac{\partial (Hv^2 + \frac{g}{2}H^2)}{\partial y} + fHu &= -gH\frac{\partial b}{\partial y} + \frac{\tau_y^s - \tau_y^b}{\rho}\,,
\end{aligned}$$

where H is the water column height, $(u, v)^T$ is the fluid velocity vector, b is the bottom topography and g denotes the gravitational acceleration. Furthermore, Coriolis forces are included in this formulation, where f denotes the Coriolis parameter depending on the geographic latitude. Forces due to wind stress and bottom friction are contained, denoting the surface stresses by τ_x^s, τ_y^s and bottom stresses by τ_x^b, τ_y^b, while ρ is the density of water. Further influences, such as eddy viscosity, may be included within the momentum equations but have been neglected in the above formulation. The conservative SWE can be written in the more compact form

$$\frac{\partial}{\partial t} U(x, y, t) + \nabla \cdot F(U(x, y, t)) = S(U(x, y, t), x, y), \tag{11.1}$$

where the conservative variables are now collected in $U = (H, Hu, Hv)^T$, while F contains the fluxes and S the sources.

When solving the conservative formulation of the shallow water equations, a central requirement is to satisfy the well-balanced property, i.e. to maintain a lake at rest steady state solution. This precise steady state is given by a constant sea surface elevation $\eta = H + b = const$ and a zero velocity vector, i.e. $u = 0,\ v = 0$. When neglecting wind stresses, these steady states are obviously exact solutions of the analytical equations above, basically due to the fact that the net pressure forces vanish. More precisely, due to the constant sea surface, we have the following balance for the first of the momentum equations

$$\frac{g}{2}\frac{\partial H^2}{\partial x} + gH\frac{\partial}{\partial x}b = gH\frac{\partial}{\partial x}\eta = 0\,,$$

and an analogous one for the second momentum equation. Hence, in the analytical equations the pressure forces are split in two parts which attain non-zero values of opposite signs in case of non-constant bottom topography b and thus cancel each other out. One has to ensure that the numerical scheme satisfies this property as well (within machine-precision). With respect to wetting and drying methods, satisfying both the well-balanced property and non-negativity simultaneously is not trivial, see e.g. Xing et al. (2010). This issue may not arise for slightly modified formulations such as the reformulation

$$\frac{\partial Hu}{\partial t} + \frac{\partial Hu^2}{\partial x} + \frac{\partial Huv}{\partial y} - fHv = -gH\frac{\partial \eta}{\partial x} + \frac{\tau_x^s - \tau_x^b}{\rho}$$

of the first momentum equation, where the pressure gradient term is written directly with respect to the water surface elevation η. This form of the momentum equations is given for example in Balzano's review paper (Balzano 1998).

In the *non-conservative formulation* of the SWE, the pressure gradient term is based on the water surface elevation as well. The first momentum equation is rewritten as

$$\frac{\partial u}{\partial t} + u\frac{\partial u}{\partial x} + v\frac{\partial u}{\partial y} - fv = -g\frac{\partial \eta}{\partial x} + \frac{\tau_x^s - \tau_x^b}{H\rho}$$

and the second momentum equation is rewritten accordingly. Therefore, numerical schemes based on the non-conservative formulation generally behave well for lake at rest steady states. However, in dry areas, the non-conservative form does not admit reasonable values for the velocity since this quantity is in fact not defined in dry areas and artificially setting u and v to zero would lead to a discontinuity at a moving wet-dry front. In addition, the non-conservative form does not hold across shocks or hydraulic jumps.

To alleviate the well-balancedness issue, some methods also use the so called *pre-balanced* shallow water equations. These equations where designed to directly account for the balance of pressure forces acting on a fluid control volume and employ the water surface elevation η as a prognostic variable instead of the water height H. According to Liang and Marche (2009), the main advantage of the pre-balanced formulation is that it maintains the hyperbolicity of the original, conservative formulation and mathematically balances the flux and source terms at the same time. More precisely, the sum of pressure terms $\frac{g}{2}\frac{\partial H^2}{\partial x} + gH\frac{\partial}{\partial x}b$ is rewritten in the variables of surface elevation and bottom topography as

$$\frac{g}{2}\frac{\partial H^2}{\partial x} + gH\frac{\partial}{\partial x}b = \frac{g}{2}\frac{\partial(\eta - b)^2}{\partial x} + g(\eta - b)\frac{\partial}{\partial x}b$$

and algebraically manipulated to obtain the form

$$\frac{g}{2}\frac{\partial(\eta^2 - 2\eta b)}{\partial x} + g\eta\frac{\partial}{\partial x}b\,.$$

If $\eta = const$, both of the above summands have precisely the same form $g\eta\frac{\partial}{\partial x}b$. The pre-balanced form of the SWE is now given by the equations

$$\begin{aligned}
\frac{\partial \eta}{\partial t} + \frac{\partial Hu}{\partial x} + \frac{\partial Hv}{\partial y} &= 0\,,\\
\frac{\partial Hu}{\partial t} + \frac{\partial\left(\frac{(Hu)^2}{\eta - b} + \frac{g}{2}(\eta^2 - 2\eta b)\right)}{\partial x} + \frac{\partial\frac{HuHv}{\eta - b}}{\partial y} - fHv &= -g\eta\frac{\partial b}{\partial x} + \frac{\tau_x^s - \tau_x^b}{\rho}\,,\\
\frac{\partial Hv}{\partial t} + \frac{\partial\frac{HuHv}{\eta - b}}{\partial x} + \frac{\partial(\frac{(Hv)^2}{\eta - b} + \frac{g}{2}(\eta^2 - 2\eta b))}{\partial y} + fHu &= -g\eta\frac{\partial b}{\partial y} + \frac{\tau_y^s - \tau_y^b}{\rho}\,.
\end{aligned}$$

The various numerical methods designed to simulate shallow water flows with wetting and drying are now based on one of the above governing equations. They will be described more cleary in the following Sect. 11.3 dealing with space discretization.

11.3 Space Discretization

In terms of spatial discretization, the first ocean circulation models were based on finite differences (FD). In recent decades, however, the finite volume (FV) formulation has become increasingly popular due to its conservation properties, its suitability for advection dominated problems, and its applicability on quite general grids. Consequently, many recent circulation models use the finite volume formulation, and existing FD models have been reformulated into the FV methodology using conservative numerical fluxes.

In addition, there has been an increasing interest in developing higher-order methods since they require less degrees of freedom to obtain the desired accuracy. Particularly the more modern discontinuous Galerkin (DG) schemes are attractive due to their support of arbitrary meshes, their amenability for hp-refinement and parallel computation, favorable dissipation and dispersion properties, as well as similar local conservation properties as for FV schemes.

In this chapter we therefore focus on the FV method and the DG scheme. The major difference between these approaches consists in the construction of the desired higher order discretizations. While finite volume methods rely on reconstruction of pointwise data using stencils of adjacent cells to achieve higher order in space, for the discontinuous Galerkin approximation, the polynomial degree of the test and basis functions is increased. With respect to the wetting and drying treatment, the approaches used for these classes of schemes differ as well. In the following, we will first review finite volume methods for wetting and drying simulations based on the shallow water equations and then consider the newer class of discontinuous Galerkin schemes.

11.3.1 Finite Volume Methods

Finite volume methods for the shallow water equations commonly start from the conservative formulation based on either the water height and discharge or the surface elevation and discharge. While the numerical representation of the conserved quantities in a finite volume scheme is given by their cell averages, the bottom topography is typically represented either by cell means as in Audusse et al. (2004), Marche et al. (2017), Liang and Marche (2009), Duran et al. (2013), Clain et al. (2016) or by a piecewise linear function which is continuous across cell boundaries as in Kurganov and Petrova (2007), Bryson et al. (2011), Horváth et al. (2015). For the case of one spatial dimension, the basic FV scheme has the form

$$\Delta x_i \frac{d}{dt} U_i(t) + F_{i+1/2} - F_{i-1/2} = S_i, \quad U_i = \begin{pmatrix} H_i \\ H_i v_i \end{pmatrix}, \tag{11.2}$$

where U_i contains the cell means, $F_{i\pm1/2}$ denotes the output of the numerical flux function and S_i is a suitable source term discretization.

As stated in Sect. 11.2, due to the conservative formulation, special consideration has to be taken to ensure the well-balanced property. More precisely, the necessary cancellation of pressure terms $gH\frac{\partial}{\partial x}\eta = \frac{\partial}{\partial x}(\frac{g}{2}H^2) + gH\frac{\partial}{\partial x}b = 0$ for the lake at rest is not fulfilled by the simple source term discretization $-gH\frac{\partial}{\partial x}b \approx -gH_i\frac{b_{i+1}-b_{i-1}}{\Delta x}$ coupled with a classical numerical flux such as the Lax-Friedrichs (LF) flux or the Harten-Lax-van Leer (HLL) flux (Harten et al. 1983). This fact has also been revisited by Clain et al. (2016).

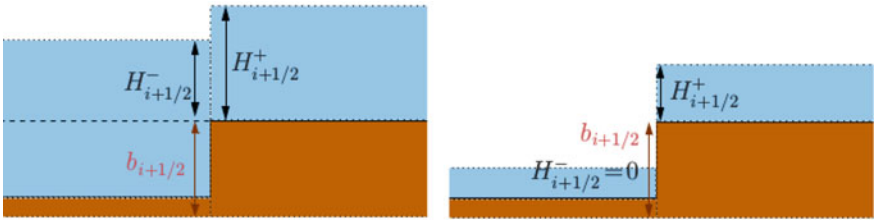

(a) Two adjacent wet cells. (b) Dry cell adjacent to a wet cell.

Fig. 11.1 Illustration of hydrostatic reconstruction approach depicting auxiliary interface bottom topography $b_{i+1/2}$ and reconstructed left and right water heights $H^{\pm}_{i+1/2}$

A very simple and popular technique handling both discontinuous topography and wet-dry interfaces is given by Audusse et al. (2004). Their scheme is designed to achieve the above mentioned well-balanced property, while Clain et al. (2016) demonstrates its viability for Tsunami simulations. Incorporating the hydrostatic reconstruction technique into a finite volume MUSCL scheme, Clain et al. hereby provide numerical results with good agreement both for benchmarks and a realistic historical Tsunami event.

Due to its popularity and simplicity, the hydrostatic reconstruction by Audusse et al. deserves a review in this context. In order to determine the input values for the numerical flux function at a cell interface, the water surface $H + b$ and the bottom topography on the two adjacent cells are taken into account. In a first order scheme, at an interface denoted by $i + 1/2$, the reconstructed left and right water height is given by the non-negative values of

$$\begin{aligned} H^-_{i+1/2} &= \max\{0,\ H_i + b_i - b_{i+1/2}\} \\ H^+_{i+1/2} &= \max\{0,\ H_{i+1} + b_{i+1} - b_{i+1/2}\}, \end{aligned} \tag{11.3}$$

where $b_{i+1/2} = \max\{b_i, b_{i+1}\}$. as illustrated in Fig. 11.1.

The leading order water height values $H^{\pm}_{i+1/2}$ now determine the left and right states of the conserved variables. They are computed as $U^{\pm}_{i+1/2} = \begin{pmatrix} H^{\pm}_{i+1/2} \\ H^{\pm}_{i+1/2} v^{\pm}_{i+1/2} \end{pmatrix}$, where $v^-_{i+1/2} = v_i$ and $v^+_{i+1/2} = v_{i+1}$.

These values are then used as input values for the numerical flux function in (11.2), i.e. $F_{i+1/2} = \mathcal{F}(U^-_{i+1/2}, U^+_{i+1/2})$. In order to achieve well-balancedness, the source term discretization is based on the reconstructed values of water height. If the source term simply contains the pressure forces due to the bottom slope, i.e. the term $-gHb_x$, and all other forces are neglected, its discretization is given by

$$S_i = \frac{g}{2} \begin{pmatrix} 0 \\ (H^-_{i+1/2})^2 - (H^+_{i-1/2})^2 \end{pmatrix}.$$

As mentioned in Audusse et al. (2004), the source term can be redistributed to the cell interfaces. The scheme (11.2) can then be rewritten as

$$\Delta x_i \frac{d}{dt} U_i(t) + \mathcal{F}_l(U_i, U_{i+1}, b_i, b_{i+1}) - \mathcal{F}_r(U_{i-1}, U_i, b_{i-1}, b_i) = 0,$$

where the left and right interface fluxes are given by

$$\begin{aligned} \mathcal{F}_l(U_i, U_{i+1}, b_i, b_{i+1}) &= \mathcal{F}(U^-_{i+1/2}, U^+_{i+1/2}) + \begin{pmatrix} 0 \\ H_i^2 - (H^-_{i+1/2})^2 \end{pmatrix}, \\ \mathcal{F}_r(U_i, U_{i+1}, b_i, b_{i+1}) &= \mathcal{F}(U^-_{i+1/2}, U^+_{i+1/2}) + \begin{pmatrix} 0 \\ H_{i+1}^2 - (H^+_{i+1/2})^2 \end{pmatrix}. \end{aligned} \tag{11.4}$$

In order to achieve a spatial discretization of second order, a piecewise linear representation of the conserved quantities needs to be reconstructed in a way which maintains well-balancedness and non-negativity. Thus, starting with a first order FV scheme, a second order extension may be obtained using reconstructed values at the cell interface. Thereby gradients of the conserved quantities are computed and limited if necessary, in order to avoid overshoots. Based on the situation at an interface between a wet and a dry cell, Audusse et al. argue that of the quantities H, b and $\eta = H + b$, the water height H and water surface η are the variables which should actually be reconstructed while b is to be computed as $b = \eta - H$.

In case of wetting and drying, one of the basic ingredients to ensure non-negativity of water height within a FV discretization is a positivity preserving numerical flux. Used within a FV method and explicit Euler time integration, these numerical flux functions yield non-negative cell means of water height at the next time level under the premise of non-negative cell means at the current time level. Roe-type solvers based on the linearized original equations and the corresponding modified Riemann problems are generally not positivity preserving. Specifically for the SWE, this well-known drawback is discussed in detail in Pelanti et al. (2011) where positivity is guaranteed by a relaxation solver related to Roe's method. Positivity preservation is furthermore given for the local Lax-Friedrichs flux or for the HLL flux mentioned in the beginning of this section. If the well-balanced flux (11.4) designed by Audusse et al. is based on the local Lax-Friedrichs flux for $\mathcal{F}$, positivity in one space dimension can be shown as follows. For the cell averages of water height H_i^n, H_i^{n+1} at two successive time levels t^n, t^{n+1} the first order scheme reads

$$H_i^{n+1} = H_i^n - \frac{\Delta t}{\Delta x_i} \left(\mathcal{F}_1(U^-_{i+1/2}, U^+_{i+1/2}) - \mathcal{F}_1(U^-_{i-1/2}, U^+_{i-1/2}) \right),$$

where $\mathcal{F}_1(U_l, U_r) = \frac{1}{2}((Hv)_l + (Hv)_r - \alpha(H_r - H_l))$ is the first component of the Lax-Friedrichs numerical flux with $\alpha = \max\left\{|v_l| + \sqrt{gH_l}, |v_r| + \sqrt{gH_r}\right\}$. Since $U^-_{i+1/2} = \frac{H^-_{i+1/2}}{H_i}(H_i, (Hv)_i)^T$ and $U^+_{i+1/2} = \frac{H^+_{i+1/2}}{H_{i+1}}(H_{i+1}, (Hv)_{i+1})^T$, we can rewrite the new water height average as the convex combination

$$H_i^{n+1} = \left(1 - \frac{\Delta t}{2\Delta x_i}\frac{H_{i+1/2}^{n,-}}{H_i^n}(v_i^n + \alpha) - \frac{\Delta t}{2\Delta x_i}\frac{H_{i-1/2}^{n,+}}{H_i^n}(\alpha - v_i^n)\right) H_i^n$$
$$+ \frac{\Delta t}{2\Delta x_i}\frac{H_{i-1/2}^{n,-}}{H_{i-1}^n}(\alpha + v_{i-1}^n)\, H_{i-1}^n + \frac{\Delta t}{2\Delta x_i}\frac{H_{i+1/2}^{n,+}}{H_{i+1}^n}(\alpha - v_{i+1}^n)\, H_{i+1}^n\,.$$

Now, since per construction in (11.3) we have $H_{i+1/2}^- \leq H_i$ and $H_{i+1/2}^+ \leq H_{i+1}$, under the CFL condition $\alpha\frac{\Delta_t}{\Delta x_i} \leq 1$, the factors in front of H_i^n, H_{i-1}^n, H_{i+1}^n are all non-negative. This proves non-negativity of the cell average H_i^{n+1}.

The well-balanced and positivity preserving approach by Audusse et al. described above is simple and fulfills the requirements of well-balancedness and non-negativity. It has thus been used as a basic building block in many subsequent FV schemes in one space dimension such as Marche et al. (2017), Liang and Marche (2009) as well as extension to unstructured meshes in Duran et al. (2013) and structured meshes in Clain et al. (2016). It should be remarked that both of the approaches by Liang and Marche (2009) and by Duran et al. (2013) are based on the pre-balanced formulation given in Sect. 11.2.

Furthermore, the possibility to write the scheme in terms of only interface fluxes has lead to its use also as an important ingredient within many of the discontinuous Galerkin schemes to be reviewed in Sect. 11.3.2. In this respect, the approach of hydrostatic reconstruction simply yields a modification of the numerical flux function used within the discontinuous Galerkin scheme in case of a discontinuous representation of the bottom topography.

FV schemes based on a continuous, piecewise linear representation of the bottom topography need slightly different techniques to guarantee well-balancedness and non-negativity at the same time. Approaches of this kind are usually found within the class of central-upwind FV schemes as in Kurganov and Petrova (2007), Bryson et al. (2011), Horváth et al. (2015). The term central-upwind hereby refers to the use of a specific numerical flux function which is a weighted sum of a central and an upwind part with weights determined by the computed characteristic speeds. The central-upwind scheme by Kurganov and Petrova (2007) can essentially be written in the form (11.2) where the conserved variables are now taken as the water surface and the discharge, $U_i = \begin{pmatrix} \eta_i \\ (Hv)_i \end{pmatrix}$ and the source term is computed from the linear bottom topography and the water surface as $S_i = \big(0, -g(\eta_i - b_i)(b_{i+1/2} - b_{i-1/2})\big)^T$. Kurganov and Petrova also explicitly mention the ill-conditioned computation of the velocity by $v = \frac{Hv}{H}$ for very small water height and propose to avoid the division by small numbers via the formula $\frac{\sqrt{2}H(Hv)}{\sqrt{H^4 + \max\{H^4, \varepsilon\}}}$ with the regularization parameter ε chosen grid dependent, i.e. decreasing with decreasing grid size. The algorithm then recomputes the discharge Hv using $(Hv) := H \cdot v$ where it is explicitly mentioned that failing to adjust the discharge may produce negative values of H, in accordance with the proof of non-negativity in Kurganov and Petrova (2007). Furthermore, the

scheme by Kurganov and Petrova has been extended to triangular grids in Bryson et al. (2011).

Horváth et al. (2015) argue that the Courant-Friedrichs-Lewy (CFL) condition for explicit time integration allows for each wave to travel at most one quarter of a grid cell per time step which limits the propagation of information. They extend their central-upwind scheme on structured quadrilateral grids to a method which is well-balancedness also in partially dry cells. Furthermore, they use a draining time step technique similar to Bollermann et al. (2011). The draining time step hereby describes how long it takes for a specific cell to become dry due to outflow fluxes and it is only used at cell interfaces of partially flooded cells. The resulting scheme is reported to allow for larger time steps than the method in Kurganov and Petrova (2007) due to the removal of spurious high velocities at the wet-dry boundaries. The original scheme by Kurganov and Petrova may be classified as a thin-layer method due to the computation of the velocity based on a tolerance ε which may be considered as a "reference" thin layer of water. Comparative numerical experiments in Horváth et al. (2015) also show that for the method (Kurganov and Petrova 2007), a thin layer of water is present once a cell becomes wet which will never dry out. This is different to the result of scheme (Horváth et al. 2015) due to the new reconstruction in partially dry cells and the draining time step technique.

Regarding implicit FV schemes, fewer wetting and drying methods are reported. One of the few algorithms which actually guarantee non-negative water height independent of the time step size, is given by the first order FV method of Casulli (2009). The description in Casulli (2009) contains a mathematically very sound foundation based on the M-matrix property to guarantee positivity. Furthermore, existence and uniqueness of the solution as well as convergence of a Newton-type scheme is derived. The approach by Casulli is based on the non-conservative formulation of the shallow water equations which is discretized in time in a semi-implicit way. The precise formulation is vital to obtain the M-matrix property for the matrices used within the iterations of the Newton-type scheme. More precisely, we will describe this approach for the one-dimensional case and furthermore neglect Coriolis forces and eddy viscosity. Then, the non-conservative momentum equation $H\left(\frac{\partial}{\partial t}v + v\frac{\partial}{\partial x}v\right) = -gH\frac{\partial}{\partial x}\eta - \gamma v$ is discretized. A representative semi-implicit time discretization has the form

$$H_j^n v_j^{n+1} = H_j^n ADV(v^n) - gH_j^n \frac{\Delta t}{\Delta x} D_j \eta^{n+1} - \Delta t \gamma_j v_j^{n+1},$$

where ADV is a space discretization operator of the advective term and D_j is a matrix representing a suitable difference operator applied to the vector of water surface values. Typical of the FV approach, the time evolution of the water volumes $V(\eta_j)$ within the finite volume cells is given by

$$V(\eta_j^{n+1}) = V(\eta_j^n) - \Delta t \left(H_{i+1/2}^n v_{i+1/2}^{n+1} - H_{i-1/2}^n v_{i-1/2}^{n+1}\right).$$

Hereby, the water volumes $V(\eta_j)$ are non-negative by construction as they are defined via integration over the wet part of the cell. Now, the unknown velocity values v_j^{n+1} are formally substituted into this last equation in order to obtain a non-linear equation of the form

$$V(\eta^{n+1}) + T^n \eta^{n+1} = r^n \,.$$

To this last equation, Newton's method is formally applied. Hereby, the Jacobian of $V(\eta^{n+1}) + T^n \eta^{n+1}$ is discontinuous if dry or partially dry cells occur. Moreover, the Jacobian can be proven to possess the M-Matrix property which in particular means that its inverse has only entries ≥ 0. Using the properties of the Jacobian it can furthermore be shown that the Newton iteration generates a converging sequence to the solution of the semi-implicit scheme.

Furthermore, an implicit FV scheme on unstructured quadtree rectangular meshes is constructed by Wu et al. in Wu (2011). Although the focus lies on the quadtree data structure and the coupling of velocity and water level within their algorithm, it is mentioned in a short paragraph on the wetting and drying treatment that the velocity is set to zero at dry nodes and that a wall function approach is used between dry and wet nodes.

11.3.2 Discontinuous Galerkin Schemes

The classical derivation of a DG scheme consists in multiplying the governing equations, e.g. the conservative SWE as in (11.1), by test functions and integrating over the computational domain. In case of unstructured triangular grids, let $\mathcal{T}^h$ be a conforming triangulation consisting of triangular elements K_i of the given computational domain Ω and let $\mathcal{W}^h$ be the piecewise polynomial space defined by

$$\mathcal{W}^h = \{w_h \in L^\infty(\Omega) \mid w_h|_{K_i} \in \mathcal{P}^N(K_i) \quad \forall\, K_i \in \mathcal{T}^h\}\,,$$

where $\mathcal{P}^N(K_i)$ denotes the space of all polynomials on K_i of degree $\leq N$. Now, an approximation $U_h(x, y, t)$ to the exact solution of the conservative SWE is given by a vector of piecewise polynomial functions $U_h(\cdot, \cdot, t) \in (W^h)^3$, which satisfies the semi-discrete equation

$$\frac{d}{dt}\int\limits_{K_i} U_h \cdot W \, dxdy = \int\limits_{K_i} F(U_h) \cdot \nabla W \, dxdy - \int\limits_{\partial K_i} \mathcal{F}(U_i^-, U_i^+, n_i) \cdot W \, d\sigma, \quad (11.5)$$

for any $K_i \in \mathcal{T}^h$, $W \in (W^h)^3$. Hereby, the numerical flux function $\mathcal{F}$ takes into account the outward pointing normal vector n_i of the cell K_i and U_i^-, U_i^+ denote the approximate solution within K_i and an adjacent element, respectively. The DG scheme may generally use any numerical flux function developed within the context of FV schemes. In particular, we note that the approximate DG solution is allowed to be discontinuous across cell interfaces.

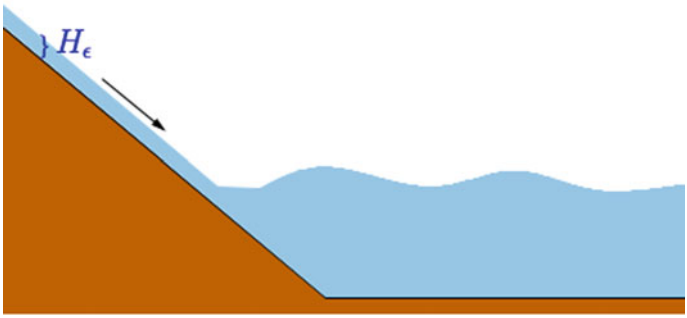

Fig. 11.2 Illustration of the numerical solution of a typical thin layer method. We note that the method conserves a small layer of water of height H_ε in an actually dry region, hence artificial gravity forces are present due to hanging nodes above the water surface

The advancement of wetting and drying approaches for discontinuous Galerkin schemes is more recent. Bokhove (2005) developed a space-time DG scheme which uses mesh adaption to accurately separate wet and dry regions. The thin layer approaches of Ern et al. (2008) and Bunya and Kubatko (2009) generally provide the background for more recent DG approaches. Hereby, Ern et al. design a well-balanced scheme by incorporating the hydrostatic reconstruction numerical flux by Audusse et al. (2004) described in Sect. 11.3.1, i.e. the numerical flux $\mathcal{F}$ in Eq. (11.5) is given by the left and right fluxes in (11.4). For wetting and drying, a slope modification is introduced. Hereby, if the cell average of the water height is negative, the water height in this cell is set to zero. If the cell average of the water height H is non-negative, but the minimum over the integration points is below the drying threshold, a linear representation of H is reconstructed where the slope is modified. In addition the corresponding discharge is set to zero. As long as no negative averages of H occur, mass is preserved by this approach but not momentum. In addition, the method may add mass if non-negativity is violated. In order to rectify the artificial increase of mass, Bunya et al. redistribute the water mass within an element by a modification of the surface elevation to guarantee non-negativity. Additionally, they thereby guarantee local mass conservation. The redistribution process heavily relies on non-negative averages of the water height, so both a sufficient condition on the allowable time step to guarantee non-negativity is derived and a reflection flux is introduced to dispose of the time step restriction. Furthermore, fluxes between dry cells are restricted to prevent unphysical oscillations and to prevent dry cells from loosing their mass.

As stated in Kärnä et al. (2011), the main difficulty in thin layer approaches when used within higher order methods such as DG is treating the wet-dry transition elements. These cells may have "hanging nodes" above the water surface elevation possibly causing an artificial pressure gradient, i.e. gravity forces that drag the water down, as shown in Fig. 11.2. Such a situation may also occur for the lake at rest because, in general, the prolongation of the constant water surface by the dry bottom

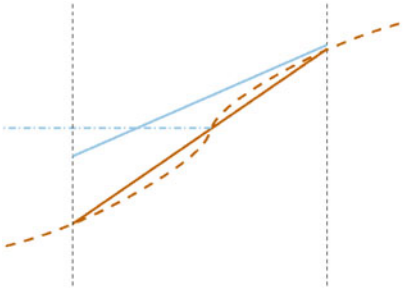

(a) Flooding-type partially dry cell: Lake at rest with artificial surface elevation slope.

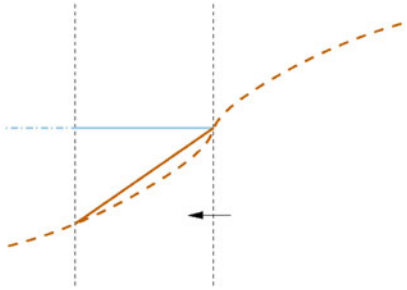

(b) Wet cell: Lake at rest for a moving mesh method.

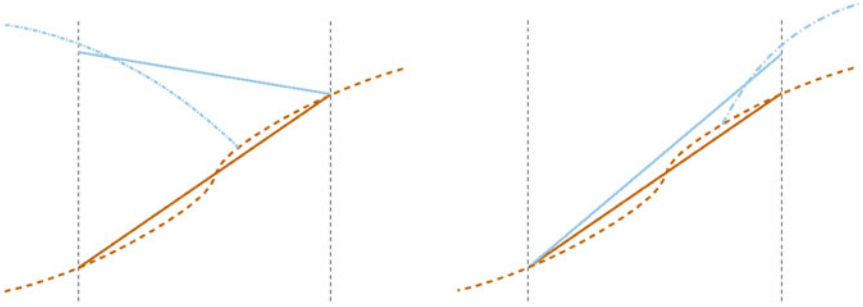

(c) Two different types of dam-break type partially dry cells.

Fig. 11.3 Illustration of surface elevation, bottom topography and shoreline representation in one discretization cell for a second order method in 1D. Black dashed vertical lines: cell boundaries. Blue and brown dashed lines: continuous surface elevation and bottom topography. Solid lines: discrete representation

topography is not a smooth function. In fact, its approximation by a polynomial function then usually yields hanging nodes. This can be seen in Fig. 11.3a where obviously the water surface elevation has an artificial slope creating an artificial pressure gradient. This artifact does not occur for moving mesh methods adapted to the shore line as depicted in Fig. 11.3b and is also prevented in negative depth algorithms. In this context, in order to address this problem in a numerical method, a distinction between dam-break type (Fig. 11.3c) and flooding-type partially dry cells (Fig. 11.3a) has already been proposed by Bates and Hervouet (1999). In case of flooding-type cells which by definition also include lake at rest situations, movement of water in dry cells is only allowed by convective transport. However, for dam-break cells a high water surface level next to the dry cell results in the flow of water due to gravitational forces, which should not be neglected in this case. Flooding-type cells can be identified by considering the representation of water surface and bottom topography within the numerical scheme. Given a cell K_i with water surface elevation $\eta_h(x, y)$ and bottom representation $b_h(x, y)$, then K_i is a flooding-type partially dry cell if we have

$$\max_{(x,y)\in K_i} \eta_h(x,y) - \max_{(x,y)\in K_i} b_h(x,y) < H_\varepsilon \,,$$

where H_ε denotes the drying threshold under which a node is considered dry. This distinction of partially dry cells has also been made by other authors, for example by Bunya and Kubatko (2009), where it is included in the wet-dry status to determine fluxes between dry elements, and by Vater et al. (2015).

Once, partially dry cells are distinguished with respect to their desired behavior, the numerical methods are adjusted. Common to many high order schemes, Bunya et al. use cancellation of gravity to balance the effect of an artificial gradient of the surface elevation in wetting or drying elements. However, their precise choice of the momentum fluxes violates momentum conservation.

In addition, we have to remark that these more or less complicated rules which are applied to partially dry cells in order to remove the artificial pressure forces are difficult to integrate into an implicit time stepping scheme.

Additional difficulties may arise through the combination of wetting and drying techniques with TVB limiters for shock capturing. As reported by Ern et al. (2008) and Bunya and Kubatko (2009), the slope modification of the wet-dry treatment and the TVB slope limiter of the DG scheme may artificially activate each other, possibly leading to instability. Thus, the TVB limiter is commonly only applied to the fully wet region.

In Gourge et al. (2009), a flux limiting wetting and drying DG approach is developed and applied to achieve a realistic simulation of the Scheldt Estuary. The limitation involves computing three intermediate states of the water surface elevation preserving local mass conservation. As in the method of Bunya et al., gravitational forces are neglected within dry elements to allow the water surface to align with the bottom topography. Within a "buffer layer" of very shallow water, bottom stress and eddy viscosity are increased while surface stress is decreased. Due to the many switches in turning the fluxes on or off, the method is discontinuous with respect to the variables. Therefore, Gourge et al. state that implicit time stepping is not directly available for this approach.

The series of works by Xing, Zhang and Shu with the basic ideas given in Xing et al. (2010), Xing and Zhang (2013) deal with the construction of a so-called positivity preserving limiter and the special design of explicit Runge–Kutta time integrators based on convex combinations of explicit Euler steps. Here, the methods are generally in line with the ideas in Ern et al. (2008); Bunya and Kubatko (2009), but a more systematic approach to well-balancedness and positivity preservation is given. Therefore, in principle, the properties of well-balancedness and positivity preservation for the shallow water equations carry over to high order in space and time. One of the basic ingredients of the method by Xing et al. (2010) is a positivity preserving numerical flux function for the shallow water equations as introduced in Sect. 11.3.1. For these flux functions which attain non-negative cell means for explicit Euler time stepping, positivity preservation can be extended to a DG scheme. Hereby, the equations for the water height cell averages are rewritten as convex combinations of finite volume approximations. The occurring factors in this convex combination then

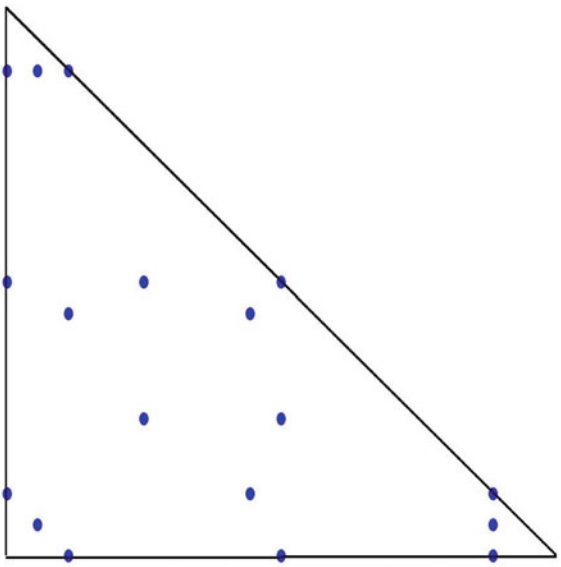

Fig. 11.4 Nodes for positivity enforcement on triangular grids for a polynomial degree of $N = 2$. Figure reproduced with permission from Meister and Ortleb (2014)

determine the CFL condition for positivity preservation, see Xing et al. (2010). More precisely, when writing the DG scheme as a combination of finite volume fluxes, the representation of the scheme is based on values at explicit intermediate nodes within the DG cell. At these nodes, which may be computed a priori, the values of water height are required to be non-negative as well, the mere enforcement of non-negative averages is not sufficient. In order to obtain these non-negative water height values at intermediate nodes, Xing et al. use their so-called positivity preserving limiter which is a simple scaling of the solution around the cell average. This high order positivity preserving limiter is locally mass and momentum conserving and only requires the positivity of water height averages.

In summary, the result by Xing et al. asserts that the new cell averages of water height at time t^{n+1} are non-negative under the premises that a suitable CFL-type time restriction is fulfilled and that the DG representation at time t^n is non-negative at each quadrature point in a set of nodes related to the finite volume representation. As mentioned, this set of nodes can be determined a priori, also for unstructured triangular grids, and depends on the polynomial degree of the DG approximation. To provide an example, for a polynomial degree of $N = 2$, Fig. 11.4 shows the distribution of the set of nodes requiring non-negative water height within a reference triangle. The construction of this nodal set is described by Zhang et al. (2012). In addition, it is possible to extend the approach of Xing et al. to higher order time integration methods which lie within the contents of Sect. 11.4.

In Duran and Marche (2014), Duran and Marche extend a previously constructed FV scheme based on the pre-balanced shallow water equations to a DG discretization. Hereby, the pre-balanced equations reduce the required degree of exactness of the

DG quadrature rule to achieve well-balancedness which is otherwise higher than in the standard approach. Their approach is generally in line with the methods of Xing et al. (2010), Xing and Zhang (2013), as they also use hydrostatic reconstruction as described in Sect. 11.3.1 to determine the input values for the numerical flux, the positivity preserving limiter and strong-stability preserving explicit time integration as described in Sect. 11.4.2. Furthermore, the idea of using the pre-balanced equations has been extended to a DG method which uses finite volume subcells in nearly dry regions by Meister and Ortleb (2016).

The numerically determined velocity in nearly dry regions can be large, especially within a DG scheme which uses a polynomial representation of the conserved variables. In this context, the challenge of computing a stable linear distribution of the velocity within a DG scheme is addressed by Vater et al. (2015) via a velocity-based limiting procedure. Furthermore, favourable properties of monotonicity preserving Bernstein polynomials have been used within a DG model for flooding and drying by Beisiegel and Behrens (2015). In addition, Lee and Lee (2016) extend the approaches in Ern et al. (2008), Bunya and Kubatko (2009) to an implicit treatment of bottom friction terms.

More recently, DG schemes treating wetting and drying for shallow water flow with implicit time integration have been developed.

In Kärnä et al. (2011), Kärnä et al. observe that porosity methods have the advantage of smooth transitions for wetting and drying areas which increases their compatibility with implicit time integration schemes. Their approach to wetting and drying is similar to a negative-depth algorithm but does not need to introduce the concept of porosity since it temporarily moves the bottom topography such that the new surface elevation is always positive. After a DG discretization, the numerical solution is obtained by high order diagonally implicit Runge–Kutta (DIRK) schemes, whereby the nonlinear systems are solved via Newton iteration using a finite-difference approximation to the Jacobian. Due to the removal of switches and discontinuities within the algorithm, the Newton solver is robust and converges rapidly. Difficulties are reported for the third Balzano test case, where the constant presence of the gravitational forces causes the interior pond to dry out. However, this is as a common drawback in porous media methods (Nielsen 2003) and not specific to this scheme. Generally, lakes may be artificially emptied when the water surface is aligned with the non-constant bottom topography, creating an artificial flux at the corresponding cell boundaries which moves water out of the lake.

In Meister and Ortleb (2014), Meister and Ortleb extend the method of Xing et al. to unconditionally positive implicit time integration via the so-called Patankar approach which is also shortly dealt with in Sect. 11.4.2 on implicit time discretization.

In recent work, Marras et al. (2016) incorporate a wetting and drying strategy into a unified continuous/discontinuous Galerkin (CG/DG) scheme with dynamically adaptive viscosity as artificial dissipation used for shock capturing. In their work, they extend the already mentioned strategy by Xing, Zhang and Shu for wetting and drying to their CG/DG method and use a three-stage, second order ESDIRK scheme to advance the numerical solution in time. The scheme belongs to the category of

fixed grid thin-layer methods. As the first stage of the ESDIRK time integration scheme is explicit and equals the last stage of the previous step, effectively only computations of a two-stage scheme are carried out. The non-linear systems are solved by a Jacobian-free Newton-Krylov scheme, where the GMRES method is used to solve the linear system in each Newton step. This basic strategy is similar to the ones used in the works (Kärnä et al. 2011) and (Meister and Ortleb 2014). A closer look at the formulation of the governing equations in Marras et al. (2016) reveals that a very similar form to the pre-balanced shallow water equations is used in this work, the only difference given in the use of H as conserved variable.

11.4 Time Discretization

In the method of lines approach, once a suitable space discretization has been carried out, such as a FV method as in Sect. 11.3.1 or a DG scheme as in Sect. 11.3.2, a system of ordinary differential equations (ODEs) is obtained, as can be seen in Eqs. (11.2) and (11.5). We denote this system of ODEs by $\frac{d}{dt}\mathbf{U} = \mathcal{L}(\mathbf{U}, t)$, where $\mathbf{U}$ now contains all spatial degrees of freedom and $\mathcal{L}$ denotes the operator corresponding to the spatial discretization. The system can be solved by any numerical scheme designed for ordinary differential equations. In the context of the method of lines approach, this process is referred to as time discretization and the chosen numerical scheme is the time integrator. Many of the aforementioned schemes are based on the method of lines, but there are exceptions such as the semi-implicit Casulli scheme described in Sect. 11.3.1, which intertwines space and time discretization as well as other approaches such as space-time methods based on a variational formulation for space and time. Basically, two classes of time integrators can be distinguished: explicit and implicit ones. The various methods discussed in the previous Sect. 11.3 have already been classified with respect to either explicit or implicit time discretization. The current section is dedicated to the specifics of each of these two classes in the context of simulating wetting and drying shallow water flows.

11.4.1 Explicit Time Integration

Many advantages can be listed in favor of explicit time integration schemes. They are easier to implement because they do not require the solution of nonlinear systems, they are usually robust, and provide physically sound results as they can accurately represent the dynamics of the flooding front due to the necessarily small time step sizes.

Explicit time integrators evaluate the right hand side of the ODE given by the spatial operator $\mathcal{L}$ using as input values for $\mathbf{U}$ only already known data, either at the current time level t^n, at computed intermediate stages or at previous time levels. Very popular explicit time integrators are Runge–Kutta (RK) schemes which have

the form

$$\begin{aligned} \mathbf{U}^{(i)} &= \mathbf{U}^n + \Delta t \sum_{j=1}^{i-1} a_{ij}\, \mathcal{L}(\mathbf{U}^{(j)}, t^n + c_j \Delta t), \quad i = 1, \ldots, s, \\ \mathbf{U}^{n+1} &= \mathbf{U}^n + \Delta t \sum_{i=1}^{s} b_i\, \mathcal{L}(\mathbf{U}^{(i)}, t^n + c_i \Delta t)\,, \end{aligned} \tag{11.6}$$

where Δt denotes the time step size, $\mathbf{U}^n$ the approximation to $\mathbf{U}(t)$ at time t^n and $\mathbf{U}^{(i)}$ suitable intermediate stages corresponding to time levels $t^n + c_i \Delta t$. The simplest example is the explicit Euler, or forward Euler method $\mathbf{U}^{n+1} = \mathbf{U}^n + \Delta t\, \mathcal{L}(\mathbf{U}^n, t^n)$.

These explicit schemes are easy to implement, also in parallel hardware environment, need a comparatively small amount of CPU time per time step, and may be constructed to have a high order of accuracy. However, their range of stability is limited. The allowable time step size depends on the characteristic speed and, in case of a global time step size in the computational domain, on the length scale of the smallest cell. Due to this severe time step restriction in case of locally refined grids, explicit time integrators are sometimes used in a multirate fashion, allowing different time step sizes in different parts of the computational domain, see e.g. Seny et al. (2012).

The treatment of wetting and drying, including the maintenance of non-negative water height, hinges on a subclass of RK schemes called strong stability preserving (SSP-RK) methods. As already mentioned in Sect. 11.3.2, in order to achieve non-negativity of the fluid depth, a FV method or DG scheme has to apply a positivity-preserving numerical flux and needs to respect a suitable CFL-type time step restriction for the explicit Euler method. In addition, within the DG scheme, non-negativity of the water height at certain nodes is mandatory, which may be achieved by the positivity preserving limiter by Xing et al. Now, these techniques may be extended to a particular class of Runge–Kutta schemes which may be written as convex combinations of explicit Euler steps. Their precise formulation is

$$\begin{aligned} \mathbf{U}^{(1)} &= \mathbf{U}^n, \\ \mathbf{U}^{(i)} &= \sum_{j=1}^{i-1} \left(\alpha_{ij} \mathbf{U}^{(j)} + \Delta t\, \beta_{ij} \mathcal{L}(\mathbf{U}^{(j)}, t^n + c_j \Delta t) \right), \quad i = 1, \ldots, s, \\ \mathbf{U}^{n+1} &= \mathbf{U}^s\,, \end{aligned}$$

with coefficients $\alpha_{ij}, \beta_{ij} \geq 0$, where a given α_{ij} is zero only if its corresponding β_{ij} is zero. In this respect, positivity preservation with respect to explicit Euler time integration can be extended to higher order in time. More precisely, these SSP-RK schemes have the so-called strong-stability preserving property as they preserve stability properties of the explicit Euler scheme. The respective stability property is defined for a given convex function $\| \cdot \|$ and based on the assumption, that there is a sufficiently small time step $\Delta t_{FE} > 0$ such that the forward Euler scheme satisfies

$$\|\mathbf{U}^n + \Delta t \mathcal{L}(\mathbf{U}^n)\| \leq \|\mathbf{U}^n\|, \quad \forall \Delta t \leq \Delta t_{FE}. \tag{11.7}$$

The above assumption is called *forward Euler (FE) assumption* in this context. Now, a time integration scheme is called SSP method, if there is a constant $c > 0$ such that we have

$$\|\mathbf{U}^{n+1}\| \leq \|\mathbf{U}^n\|, \quad \forall \Delta t \leq c\Delta t_{FE},$$

if the FE assumption (11.7) is fulfilled. Since by $\|\mathbf{U}\| = \max_i\{-U_i\}$ a convex function is given, the positivity requirement $\mathbf{U}^n \geq \mathbf{0} \Rightarrow \mathbf{U}^{n+1} \geq \mathbf{0}$ carries over from the forward Euler method to an SSP scheme, if the time step restriction $\Delta t \leq c\Delta t_{FE}$ is fulfilled. The parameter c is hereby determined by the parameters occurring in the corresponding convex combination of explicit Euler time steps within the SSP scheme as $c = \min_{i,j} \frac{\alpha_{ij}}{\beta_{ij}}$.

This mathematical background on the SSP property is the basis for positivity preservation in higher order time integration schemes, as pioneered by Xing et al. in Xing et al. (2010). Many of the more recent schemes discussed in Sect. 11.3.2 follow this approach when supplementing their respective space discretization by the time stepping routine. In summary, the resulting list of construction principles for methods of this kind consists in: 1. designing a DG scheme for which the FE assumption (11.7) is fulfilled for the above example of a convex function regarding positivity; 2. asserting non-negativity of the cell averages of water height by satisfying the time step constraint of the respective SSP-RK method, given by the parameter c; 3. applying the positivity preserving limiter at each Runge–Kutta stage to obtain non-negative water height at the intermediate nodes, which is relevant to fulfill the first construction principle.

11.4.2 Implicit Time Integration

Implicit time integration methods involve the solution of linear or nonlinear equations to determine the numerical solution in the next time step. Thus, the computational effort per time step is larger than for explicit schemes and parallel computing is more difficult to realize. However, implicit schemes may be preferred over explicit ones if the time step constraints ensuring stability are much more restrictive than those necessary to achieve the desired accuracy of the numerical solution. Then, the implicit scheme can take larger time steps and thus be more efficient. Problems of this kind which are more efficiently solved by an implicit scheme are called stiff. In case of space-discretized partial differential equations such as the SWE, stiffness may be introduced e.g. by the inclusion of bottom friction or by grid-induced stiffness in case of locally refined grids. An

implicit RK scheme is basically of the form (11.6) with stage values now implicitly determined by $\mathbf{U}^{(i)} = \mathbf{U}^n + \Delta t \sum_{j=1}^{s} a_{ij} \mathcal{L}(\mathbf{U}^{(j)}, t^n + c_j \Delta t)$. A very popular subclass of implicit RK schemes are diagonally implicit (DIRK) schemes with $\mathbf{U}^{(i)} = \mathbf{U}^n + \Delta t \sum_{j=1}^{i} a_{ij} \mathcal{L}(\mathbf{U}^{(j)}, t^n + c_j \Delta t)$. For these schemes, the size of the nonlinear systems is reduced since each stage is equivalent, in terms of computational effort, to the implicit Euler scheme $\mathbf{U}^{n+1} = \mathbf{U}^n + \Delta t \mathcal{L}(\mathbf{U}^{n+1}, t^n + \Delta t)$. The resulting nonlinear systems may be linearized by Newton's method leading to a sequence of linear systems to be solved. The solution of these usually large linear systems again involves iterative schemes such as preconditioned Krylov subspace methods.

Although the time step sizes of implicit schemes may by chosen larger for stability reasons, positivity preservation usually still demands a severe time step constraint. In fact, if the order of accuracy of the time integration method exceeds first order, the allowable time step still depends on the finite SSP parameter c. However, the implicit Euler method can be proven unconditionally SSP, i.e. strong-stability preserving for any time step size. Hence, for a first order method, unconditional positivity is possible in principle.

In order to alleviate the time step restriction based on positivity, RK schemes may be modified by the so-called Patankar trick. Hereby, the semi-discrete continuity equation of the FV or DG scheme is written as a production-destruction equation for the cell averages of water height. Production terms are ingoing water fluxes, while outgoing fluxes of water yield destruction terms. Generally, production-destruction equations have the form

$$\frac{dc_i}{dt} = \sum_{j=1}^{I} p_{ij}(\mathbf{c}) - \sum_{j=1}^{I} d_{ij}(\mathbf{c}), \qquad i = 1, \dots, I\,, \tag{11.8}$$

where $\mathbf{c}$ is a vector of positive quantities while $p_{ij} \geq 0$ and $d_{ij} \geq 0$ denote the production and destruction terms, respectively. For fully conservative production-destruction equations, we have $p_{ij} = d_{ji}$ and $p_{ii} = d_{ii} = 0$. While the explicit Euler scheme violates positivity for large enough time steps, it is possible to introduce an implicitly given factor $\frac{c_i^{n+1}}{c_i^n}$ in front of the destruction term in order to reduce outgoing water fluxes. However, this violates conservation. Hence, the modified Patankar scheme developed in Burchard et al. (2003) introduces weighting coefficients for both production and destruction terms.

This Patankar idea has been incorporated into an SDIRK scheme in Meister and Ortleb (2014) to obtain an unconditionally positivity preserving scheme for the SWE. In some cases, difficulties arise with this method in form of a slow convergence of the Newton solver. Basically, the Newton convergence is slowed down by wetting and drying switches. This includes for example the computation of the velocity, which needs a non-zero water height and is unstable for small water height, as well as the Riemann solver, with respect to the computation of the speed of sound and the computation of dissipation parameter α within Lax-Friedrichs flux. The check for neglecting gravitational forces usually is a non-smooth switch as well.

The time step is also restricted by potentially ill-conditioned linear systems as well as the degree of non-linearity of the non-linear system. A large time step can prevent the convergence of the Newton solver or even the convergence of the linear system inside each Newton step. Those restriction are worsened by the presence of wet/dry fronts.

Implicit schemes can yield significant speed-up and permit simulations that would be impossible to carry out with explicit methods. For real applications this substantial increase in efficiency has been documented e.g. in Kärnä et al. (2011). When explicit time step restrictions become far too prohibitive, e.g. due to grid stiffness, implicit time stepping is already a viable alternative. In addition, the interest in the further development of implicit schemes for wetting and drying simulations has increased in recent years and there is still room for improvement.

Many of the switches inherent in wetting and drying techniques may have a negative effect on the convergence rate, as observed in Meister and Ortleb (2014). But not all higher order implicit approaches suffer from difficulties with respect to convergence. One such example is given by the moving topography method in Kärnä et al. (2011) where the realization of a moving bottom topography prevents dry states and the resulting switches. It should also be remarked that Casulli's method (Casulli 2009) is still unique in terms of its mathematical properties, i.e. unconditional positivity preservation and provable convergence of the Newton procedure. The method can be used with unstructured grids, and a similar formulation is used in several circulation models, e.g., ELCIRC, SELFE, and SUNTANS (Fringer et al. 2006). However, this approach is only first order accurate and has not been extended to higher order of accuracy so far.

11.5 Concluding Remarks

This chapter presented a review on numerical methods for wetting and drying shallow water flows on fixed grids in two space dimensions based on finite volume and discontinuous Galerkin space discretization. These restrictions notwithstanding, an overwhelming variety of different wetting and drying treatments is obviously present in current numerical models. Most numerical schemes try to satisfy the key properties mentioned in this review, i.e. positivity preservation, local and global mass conservation, well-balancedness, non-permeability of dry areas, and elimination of artificial pressure gradients. Combining this with the necessity of robustness and efficiency, it is clear that there is not just one road to a satisfactory numerical simulation for all applications of interest which include the influence of a wetting and receding water front.

This review shows that for first order schemes in space and time, wetting and drying is managed more easily because many of the desired properties can already be fulfilled by a suitable choice of the numerical flux function and the source term discretization. Here, we have robust positivity preserving well-balanced schemes equipped with explicit time integration as well as an unconditionally positivity pre-

serving implicit scheme by Casulli with provably convergent Newton iteration. For higher order schemes such as the DG scheme all of these properties require more effort. Positivity preservation, in particular, requires positivity at additional interior nodes, SSP time integration with a specific time step restriction, and the prevention of artificial pressure gradients.

With respect to higher order schemes and suitable time stepping routines, there still is a lot of room for further development. Implicit time stepping may show its full potential once new techniques are found which guarantee positivity preservation, robust computation of velocity from discharge, well-balancedness, and absence of artificial pressure gradients without the additional introduction of discontinuous switches into the method which negatively influence convergence of the subsolvers.

References

Audusse, E., F. Bouchut, M.O. Bristeau, R. Klein, and B. Perthame. 2004. A fast and stable well-balanced scheme with hydrostatic reconstruction for shallow water flows. *SIAM Journal on Scientific Computing* 25: 2050–2065.

Balzano, A. 1998. Evaluation of methods for numerical simulation of wetting and drying in shallow water flow models. *Coastal Engineering* 34: 83–107.

Bates, P.D., and J.M. Hervouet. 1999. A new method for moving-boundary hydrodynamic problems in shallow water. *Proceedings of the Royal Society of London. Series A: Mathematical, Physical and Engineering Sciences* 455: 3107–3128.

Beisiegel, N., and J. Behrens. 2015. Quasi-nodal third-order Bernstein polynomials in a discontinuous Galerkin model for flooding and drying. *Environmental Earth Sciences* 74: 7275–7284.

Bokhove, O. 2005. Flooding and drying in discontinuous Galerkin finite-element discretizations of shallow-water equations. Part 1: one dimension. *Journal of Scientific Computing* 22–23: 47–82.

Bollermann, A., S. Noelle, and M. Lukácová-Medvid'ová. 2011. Finite volume evolution Galerkin methods for the shallow water equations with dry beds. *Communications in Computational Physics* 10: 371–404.

Bryson, S., Y. Epshteyn, A. Kurganov, and G. Petrova. 2011. Central-upwind scheme on triangular grids for the saint-venant system of shallow water equations. *AIP Conference Proceedings* 1389: 686–689.

Bunya, S., E.J. Kubatko, J.J. Westering, and C. Dawson. 2009. A wetting and drying treatment for the Runge-Kutta discontinuous Galerkin solution to the shallow water equations. *Computer Methods in Applied Mechanics and Engineering* 198: 1548–1562.

Burchard, H., E. Deleersnijder, and A. Meister. 2003. A higher-order conservative Patankar-type discretization for stiff systems of production-destruction equations. *Applied Numerical Mathematics* 47: 1–30.

Candy, A.S. 2017. An implicit wetting and drying approach for non-hydrostatic baroclinic flows in high aspect ratio domains. *Advances in Water Resources* 102: 188–205.

Cash, J.R. 1979. Diagonally implicit Runge-Kutta formulae with error estimates. *IMA Journal of Applied Mathematics* 24: 293–301.

Casulli, V. 2009. A high-resolution wetting and drying algorithm for free-surface hydrodynamics. *International Journal for Numerical Methods in Fluids* 60: 391–408.

Clain, S., C. Reis, R. Costa, J. Figueiredo, M.A. Baptista, and J.M. Miranda. 2016. Second-order finite volume with hydrostatic reconstruction for tsunami simulation. *Journal of Advances in Modeling Earth Systems* 8: 1691–1713.

Deltares. 2009. *Delft-3D-FLOW: Simulation of multi-dimensional hydrodynamic flows and transport phenomena, including sediments - User manual*. Delft, The Netherlands: Deltares.

DHI. 2007. *MIKE 21 flow model, hydrodynamic module, user guide*.

Duran, A., and F. Marche. 2014. Recent advances on the discontinuous Galerkin method for shallow water equations with topography source terms. *Computers and Fluids* 101: 88–104.

Duran, A., Q. Liang, and F. Marche. 2013. On the well-balanced numerical discretization of shallow water equations on unstructured meshes. *Journal of Computational Physics* 235: 565–586.

Ern, A., S. Piperno, and K. Djadel. 2008. A well-balanced Runge-Kutta discontinuous Galerkin method for the shallow-water equations with flooding and drying. *International Journal for Numerical Methods in Fluids* 58: 1–25.

Fringer, O., M. Gerritsen, and R.L. Street. 2006. An unstructured-grid, finite-volume, nonhydrostatic, parallel coastal ocean simulator. *Ocean Modelling* 14 (3–4): 139–173.

Gourge, O., R. Comblen, J. Lambrechts, T. Kärnä, V. Legat, and E. Deleersnijder. 2009. A flux-limiting wetting-drying method for finite-element shallow-water models, with application to the Scheldt Estuary. *Advances in Water Resources* 32: 1726–1739.

Harten, A., P.D. Lax, and B. van Leer. 1983. On upstream differencing and Godunov-type schemes for hyperbolic conservation laws. *SIAM Review* 25: 35–61.

Hervouet, J.M. 2000. TELEMAC modelling system: an overview. *Hydrological Processes* 14: 2209–2210.

Horváth, Z., J. Waser, R.A.P. Perdigão, A. Konev, and G. Blöschl. 2015. A two-dimensional numerical scheme of dry/wet fronts for the Saint-Venant system of shallow water equations. *International Journal for Numerical Methods in Fluids* 77 (3): 159–182.

Kalita, H.M., and A.K. Sarma. 2018. An implicit scheme for shallow water flow with wet dry interface. *Water Resources* 45: 61–68.

Kärnä, T., B. de Brye, O. Gourgue, J. Lambrechts, R. Comblen, V. Legat, and E. Deleersnijder. 2011. A fully implicit wetting-drying method for DG-FEM shallow water models, with an application to the Scheldt Estuary. *Computer Methods in Applied Mechanics and Engineering* 200: 509–524.

Kurganov, A., and G. Petrova. 2007. A second-order well-balanced positivity preserving central-upwind scheme for the Saint-Venant system. *Communications in Mathematical Sciences* 5: 133–160.

Lee, H., and N. Lee. 2016. Wet-dry moving boundary treatment for Runge-Kutta discontinuous Galerkin shallow water equation model. *KSCE Journal of Civil Engineering* 20: 978–989.

Liang, Q., and F. Marche. 2009. Numerical resolution of well-balanced shallow water equations with complex source terms. *Advances in Water Resources* 32: 873–884.

Luettich, R.A., J.J. Westerink, and N.W. Scheffner. 1992. *ADCIRC: An advanced three-dimensional circulation model for shelves, coasts and estuaries*. US Army Corps of Engineers, Waterways Experiment Station: Department of the Army.

Marche, F., P. Bonneton, P. Fabrie, and N. Seguin. 2017. Evaluation of well-balanced bore-capturing schemes for 2D wetting and drying processes. *International Journal for Numerical Methods in Fluids* 53: 867–894.

Marras, S., M.A. Kopera, E.M. Constantinescu, J. Suckale, and F.X. Giraldo. 2016. A continuous/discontinuous Galerkin solution of the shallow water equations with dynamic viscosity, high-order wetting and drying, and implicit time integration. https://arxiv.org/abs/1607.04547.

Medeiros, S.C., and S.C. Hagen. 2013. Review of wetting and drying algorithms for numerical tidal flow models. *International Journal for Numerical Methods in Fluids* 71: 473–487.

Meister, A., and S. Ortleb. 2014. On unconditionally positive implicit time integration for the DG scheme applied to shallow water flows. *International Journal for Numerical Methods in Fluids* 76: 69–94.

Meister, A., and S. Ortleb. 2016. A positivity preserving and well-balanced DG scheme using finite volume subcells in almost dry regions. *Applied Mathematics and Computation* 272: 259–273.

Nielsen, C., and C. Apelt. 2003. Parameters affecting the performance of wetting and drying in a two-dimensional finite element long wave hydrodynamic model. *Journal of Hydraulic Engineering* 129: 628–636.

Pelanti, M., F. Bouchut, and A. Mangeney. 2011. A Riemann solver for single-phase and two-phase shallow flow models based on relaxation. Relations with Roe and VFRoe solvers. *Journal of Computational Physics* 230: 515–550.

Ricchiuto, M., and A. Bollermann. 2009. Stabilized residual distribution for shallow water simulations. *Journal of Computational Physics* 228: 1071–1115.

Seny, B., J. Lambrechts, R. Comblen, V. Legat, and J.F. Remacle. 2012. Multirate time stepping for accelerating explicit discontinuous Galerkin computations with application to geophysical flows. *International Journal for Numerical Methods in Fluids* 71: 41–64.

Vater, S., N. Beisiegel, and J. Behrens. 2015. A limiter-based well-balanced discontinuous Galerkin method for shallow-water flows with wetting and drying: one-dimensional case. *Advances in Water Resources* 85: 1–13.

Warner, J.C., Z. Defne, K. Haas, and H.G. Arango. 2013. A wetting and drying scheme for ROMS. *Computers & Geosciences* 58: 54–61.

Wu, W. 2011. An implicit 2-D shallow water flow model on unstructured quadtree rectangular mesh. *Pages 15–26 of:* Sánchez, A., Zhang M. (ed), *Journal of Coastal Research: Special Issue*, **59**.

Xing, Y., and X. Zhang. 2013. Positivity-preserving well-balanced discontinuous Galerkin methods for the shallow water equations on unstructured triangular meshes. *Journal of Scientific Computing* 57: 19–41.

Xing, Y., X. Zhang, and C.W. Shu. 2010. Positivity-preserving high order well-balanced discontinuous Galerkin methods for the shallow water equations. *Advances in Water Resources* 33: 1476–1493.

Zhang, X., Y. Xia, and C.W. Shu. 2012. Maximum-principle-satisfying and positivity-preserving high order discontinuous Galerkin schemes for conservation laws on triangular meshes. *Journal of Scientific Computing* 50: 29–62.

Index

H. Schuttelaars et al. (eds.), *The Mathematics of Marine Modelling*,
Mathematics of Planet Earth 9, https://doi.org/10.1007/978-3-031-09559-7